CONF - 750989
VOLUME I

Distribution category UC-20

PROCEEDINGS OF THE INTERNATIONAL CONFERENCE HELD AT GATLINBURG TENNESSEE, OCTOBER 1-3, 1975

Sponsored By

OAK RIDGE NATIONAL LABORATORY
UNITED STATES ENERGY RESEARCH AND DEVELOPMENT ADMINISTRATION
AMERICAN NUCLEAR SOCIETY
NUCLEAR METALLURGY COMMITTEE OF AIME

RADIATION EFFECTS *and* TRITIUM TECHNOLOGY *for* FUSION REACTORS

Editors

J. S. WATSON
F. W. WIFFEN

Compiling Editors

JULIA L. BISHOP
BRENDA K. BREEDEN
OAK RIDGE NATIONAL LABORATORY

MARCH, 1976

ORGANIZING COMMITTEE

D. Steiner, ORNL, General Chairman
C. J. McHargue, ORNL, Radiation Effects
W. R. Grimes, ORNL, Tritium Technology
J. L. Scott, ORNL, Arrangements

PROGRAM COMMITTEE

Radiation Effects

F. W. Wiffen, ORNL, U.S.A.
J. L. Brimhall, Battelle-Pacific Northwest Laboratory, U.S.A.
B. L. Eyre, AERE-Harwell, U.K.
G. L. Kulcinski, University of Wisconsin, U.S.A.
H. A. Ullmaier, KFA-Jülich, Germany
R. Watanabe, National Research Institute for Metals, Japan
K. M. Zwilsky, Division of Controlled Thermonuclear Research, ERDA, U.S.A.

Tritium Technology

J. S. Watson, ORNL, U.S.A.
F. Coffman, Division of Controlled Thermonuclear Research, ERDA, U.S.A.
E. Hennelly, Savannah River Laboratory, U.S.A.
R. Hickman, Lawrence Livermore Laboratory, U.S.A.
G. McCracken, Culham Laboratory, U.K.
V. Maroni, Argonne National Laboratory, U.S.A..
L. Wittenberg, Mound Laboratory, U.S.A.

An outstanding result during the past few years from both magnetic and inertial confinement experiments was to show the need for larger-scale and more realistic experiments which "burn" deuterium and tritium and produce significant quantities of neutrons and activation products. Some such experiments have been approved and are in advanced stages of design (the Tokamak Fusion Test Reactor, the Joint European Tokamak, and the [illegible]); other more advanced experiments are in early stages of conceptual design (Demo Experimental Power Reactor and Fusion Demonstration Reactor). As fusion research moves into these large, complex experiments, increased attention is required to develop the technology to build and operate the reactor systems. If fusion power becomes a commercial reality and follows patterns set by other advanced technologies (such as nuclear fission), development of the supporting technologies may prove to be more difficult, time-consuming, and expensive than demonstration and evaluation of the fundamental concepts.

A growing interest in fusion technology has been evident in the greater number of national and international meetings to include sessions on fusion technology, the increased attendance at such sessions, and recently the organization of meetings devoted solely to the discussion of technologic[illegible]

As the logical outgrowth of these developments and as a means of fulfilling major current needs of the fusion program, the International Conference on Radiation Effects and Tritium Technology for Fusion Reactors was held in Gatlinburg, Tennessee, on October 1-3, 1975. This conference, which was sponsored by Oak Ridge National Laboratory, the Energy Research and Development Administration, the American Nuclear Society, and the Nuclear Metallurgy Committee of AIME, brought together scientists and engineers to discuss two elements of fusion technology: bulk radiation effects and tritium technology. In many ways, the presentation of papers on the two subjects in parallel sessions gave the effect of two separate conferences; however, several individuals attended sessions on both subjects. The conference was particularly timely because current conceptual design studies of Experimental Power Reactors have shown the immediate need for data on both subjects. In addition, it provided an excellent opportunity for workers from throughout the world to present their most recent results and to share insight into the remaining research needs. Judging from the quality of the papers, the number of attendees, and the interest and enthusiasm generated, the conference was eminently successful. We hope that publication of the proceedings will further enhance the benefits of the conference to all participants and also extend these benefits to others who were not able to attend.

The papers in these proceedings, which were published directly from copy supplied by the authors, are arranged in four volumes. The keynote address, delivered by E. E. Kintner of the Energy Research and Development Administration, is the first paper in Volume I. Papers concerned with radiation effects are included in Volumes I and II, while the tritium technology papers are collected in Volumes III and IV. The arrangement of the papers with regard to subject subdivision and order is the same as that used for presentation at the conference. Each of the four volumes contains a complete table of contents and author index for the entire proceedings.

The editors wish to express their gratitude to everyone who contributed to the success of the conference by assisting in the organization, chairing sessions, presenting papers, or participating in discussions throughout the conference. Special thanks are extended to J. L. Scott for conference arrangements and to D. Steiner, C. J. McHargue, and W. R. Grimes for their assistance with the organization.

J. S. Watson
F. W. Wiffen
Program Chairmen and Editors

CONTENTS

RADIATION EFFECTS

Plenary Session

Swelling and Microstructures (I)

Swelling and Microstructures (II)

Modeling and Damage Analysis

Mechanical Properties of Irradiated Metals

The Effects of Helium in Metals

Stress Effects, Magnets, and Insulators

TRITIUM TECHNOLOGY

Plenary Session

Environmental Considerations

System Design Studies

Experimental Studies, Part I

Experimental Studies, Part II

Special Topics

Permeation

THE EFFECT OF FUSION BURN CYCLE ON FIRST WALL SWELLING

Y. H. Choi
Department of Materials Science and Engineering
and Center for Materials Science and Engineering
Massachusetts Institute of Technology

A. L. Bement
Department of Materials Science and Engineering
and Department of Nuclear Engineering
Massachusetts Institute of Technology

K. C. Russell*
Metallurgy Division, AERE Harwell, Oxfordshire, UK.

ABSTRACT

A mathematical simulation of first wall swelling has been performed for stainless steel under a hypothetical duty cycle of 50 sec burn, 50 sec cool. In most instances steady state nucleation conditions were not established during the burn cycle, thereby necessitating the use of transient nucleation theory. The effects of transmutation helium and of surface active impurities were modelled in an approximate way. Both kinds of impurity were found to give large increases in the void nucleation rate. Suggestions for refining and extending the calculations are also given.

INTRODUCTION

Voids form under irradiation as a result of the preferential agglomeration of vacancies. The process may be aided by the presence of insoluble gases (such as helium) which stabilise the void through internal pressurisation or by surface active impurities (such as oxygen) which reduce the void:matrix surface energy. The gas content (if any) is

*Permanent Address: The Massachusetts Institute of Technology

less than that needed to balance surface energy forces; this distinguishes voids from bubbles.

Voids are typically small (a few hundred $\mathring{A}$ in diameter) but tend to be present in high concentrations ($\sim 10^{15} - 10^{16}/cm^3$) and may give rise to swellings of tens of per cent in fast breeder reactor cladding material[1-4].

The expense and unavailability of in-pile test facilities and the desire for accelerated tests have spurred the development of a number of methods for simulating reactor damage. These include mathematical modelling[5] and irradiation with electrons[6,7], protons[8] and various heavy ions[9-11].

Void swelling is expected also to be a major problem in the first wall of fusion reactors. Atomic displacement rates are comparable to those in the breeder reactor[12] and the high energy neutrons (E ≈ 14 MeV) will produce substantial quantites of transmutation products, in particular helium[12]. The need for simulation procedures in materials testing will be even greater than for the breeder reactor, in that neutron sources of the proper intensity and energy spectrum will not be available for some years, and at least initially will have very small test volumes (probably less than 1 cm^3). Furthermore, the pulsed nature of fusion devices adds a time variable which is missing in the essentially steady-state fission devices, and which will take a great deal of added effort to investigate.

This paper presents a first attempt at mathematical simulation of void nucleation under a hypothetical fusion operating cycle. The time-scale of the cycle necessitates the use of transient void nucleation theory throughout. The effects of insoluble gases and of surface active impurities on the void nucleation rate are modelled in an approximate way.

THEORY

The theory of void nucleation was first developed for the co-precipitation of vacancies and interstitials[13,14]. It was later extended to account for the effects of gaseous[15-18] and non-gaseous[15,16] impurities on the kinetics of void formation.

The Rate Equation

Void nucleation in the absence of impurities is described by the following variables.

$J(n,t)$	flux of n-vacancy to (n+1) -vacancy voids
$\rho(n,t)$	number of n-vacancy voids per unit volume at time t
$\rho^{o}(n)$	equilibrium number density of n-vacancy voids in the absence of interstitials
$\rho'(n)$	number density of voids giving $J(n,t) = 0$ in the presence of interstitials
$\beta_v(n)$	vacancy capture rate of an n-vacancy void
$\beta_i(n)$	interstitial capture rate of an n-vacancy void
$\alpha_v(n)$	vacancy emission rate of an n-vacancy void

Void nucleation is represented by the movement of points along a size axis of n (number of vacancies in the void). Capture of a vacancy moves the point to the right, while the loss of a vacancy or capture of an interstitial moves the point to the left. The flow of voids between size classes n and n+1 is thus given by[13]:

$$J(n,t) = \beta_v(n)\ \rho(n,t) - \left[\beta_i(n+1) + \alpha_v(n+1)\right]\ \rho(n+1,t) \qquad (1)$$

Application of the equation of continuity converts Eq. (1) to a rate equation

$$\begin{aligned}\frac{\partial \rho(n,t)}{\partial t} &= -\left[\beta_v(n) + \beta_i(n) + \alpha_v(n)\right]\ \rho(n,t) \\ &= +\left[\beta_i(n+1) + \alpha_v(n+1)\right]\ \rho(n+1,t) \\ &= +\beta_v(n-1)\ \rho(n-1,t) \qquad (2)\end{aligned}$$

If one makes the physically reasonable assumption that $\alpha_v(n+1)$ is unchanged by the presence of interstitials then

$$\alpha_v(n+1) = \beta_v(n)\ \rho^{o}(n)/\rho^{o}(n+1) \qquad (3)$$

$\alpha_v(n+1)$ may then be calculated from

$$\rho^{o}(n) = N \exp\left(-\Delta G^{o}_{fi}/kT\right) \qquad (4)$$

Eq. (2) may be rearranged in terms of ΔG^{o}_{n}, the free energy of forming the void from the supersaturated vacancies to give:

$$\frac{\partial \rho(n,t)}{\partial t} = \frac{\partial}{\partial n}\left[\beta_v(n)\,\rho'(n,t)\,\frac{\partial \rho(n,t)/\rho'(n,t)}{\partial n}\right] \tag{5}$$

$$\rho' \equiv N\exp(-\Delta G'_n/kT)$$

and $$\Delta G'_n = kT\sum_{j=0}^{n-1}\ln\left[\beta_i/\beta_v + \exp\frac{1}{kT}\left(\Delta G^{o}_{j+1} - \Delta G^{o}_{j}\right)\right]* \tag{6}$$

$\Delta G'_n$ (shown schematically in Fig. (1)) thus plays precisely the same role in void nucleation as the free energy does in conventional nucleation theory. It may be viewed as a kinetically modified free energy.

Eq. (4) may be integrated to give the steady-state production rate of critical sized (n'_k) voids as

$$J_k = Z'\beta_k\, N\exp(-\Delta G'_k/kT) \tag{7}$$

where $1/Z'$ is the width of the activation barrier, kT below the maximum and β_k is the frequency of vacancy capture by the critical nucleus. Z', n_k' and $\Delta G'_k$ are indicated in Fig. (1). Onset of steady-state nucleation conditions will lag the establishment of the point defect supersaturation by a certain characteristic incubation time, τ, which has been calculated as[13]

$$\tau = (2Z'^{2}\beta_k)^{-1} \tag{8}$$

If the supersaturation persists for a time less than τ, or changes appreciably over times the same order, steady state nucleation conditions will not be achieved and Eq. (7) is not applicable. As will be seen presently, proposed fusion burn cycles tend to fall into this category, so in order to simulate void nucleation in the first wall one must return to the original difference equation (Eq. (2)).

---

*β_i/β_v is the ratio of the arrival rates of interstitials and vacancies at a neutral sink. It is equal to D_iC_i/D_vC_v, where the D's and C's refer to diffusivities and concentrations.

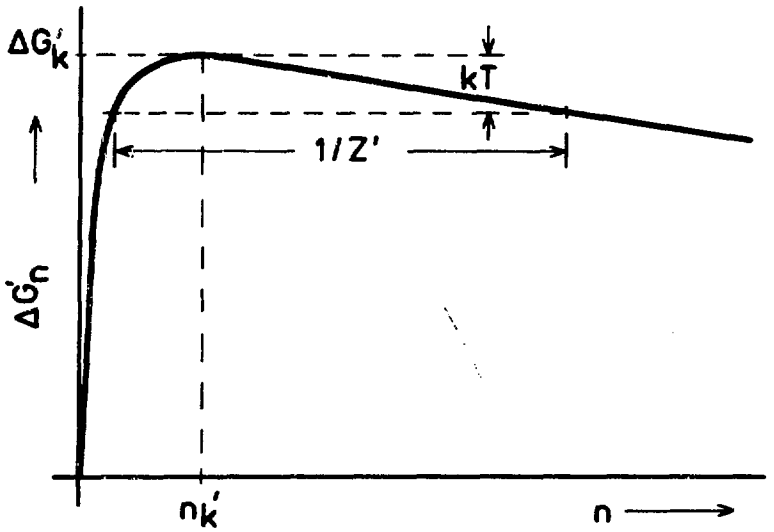

Figure 1 The activation barrier for void nucleation, showing the critical nucleus size (n_k') and the height ($\Delta G_k'$) and width ($1/Z'$) of the barrier. (After Ref. 19).

Evaluation of Equations

Simulation of even the earliest stages of swelling requires consideration of voids of up to several thousand vacancies. Eq. (2) represents a separate difference equation for each size of void and any attempt at direct evaluation results in a prohibitive expenditure of computer time. Any but the simplest representations of the temperature and defect concentrations during the duty cycle was also found to result in consumption of excessive computer time[20].

Consequently, two approximations were made which greatly relieved the computational difficulty, but which did not invalidate the analysis.

1. The duty cycle, temperature and point defect concentrations were taken as step functions of time, as shown in Fig. 2.

2. The void size classes are grouped for evaluation (as shown

in Fig. 3) prior to calculation of the void density.

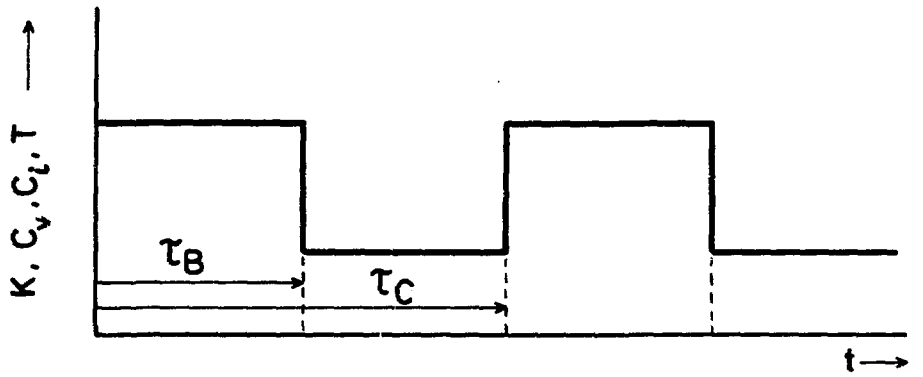

Figure 2 Simplified operating cycle, where τ_B = burn cycle and τ_C = duty cycle

Then $\rho(n,t)$ is the average aged void number density in a group N and the void flux $J(n,t)$ is the summation of the fluxes on the boundary of each group.

The resulting equations are

$$J(n,t) = \left[\beta_v\left(n+\frac{\Delta n}{2}\right)\rho(n,t) - \left[\beta_i\left(n+\frac{\Delta n}{2}\right) + \alpha_v\left(n+\frac{\Delta n}{2}\right)\right]\rho(n+\Delta n,t)\right]/\Delta n \quad (9)$$

and

$$\frac{\partial\rho(n,t)}{\partial t} = \left[-\left[\beta_v\left(n+\frac{\Delta n}{2}\right) + \beta_i\left(n-\frac{\Delta n}{2}\right) + \alpha_v\left(n-\frac{\Delta n}{2}\right)\right]\rho(n,t) + \left[\beta_i\left(n+\frac{\Delta n}{2}\right) + \alpha_v\left(n+\frac{\Delta n}{2}\right)\right]\rho(n+\Delta n,t) + \beta_v\left(n-\frac{\Delta n}{2}\right)\rho(n-\Delta n,t)\right]/\Delta n \quad (10)$$

respectively.

The capture rate of vacancies is the number of vacancies within one jump distance of the void, times the jump frequency toward the void.

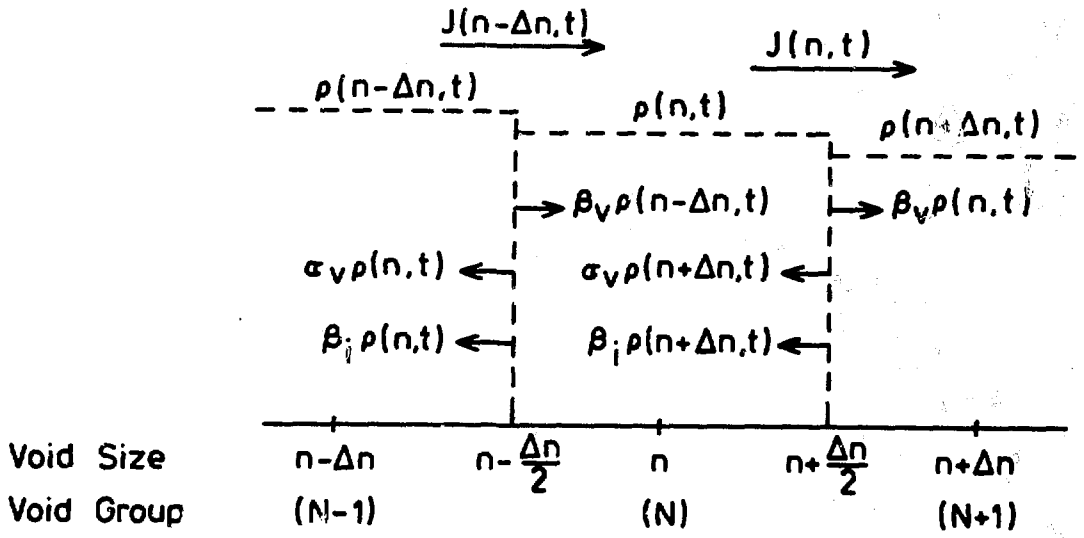

Figure 3 Flux diagram for numerical evaluation of the nucleation equations: n is void size and N is interval number.

The vacancy emission rate is obtained from Eqs. (3,4), where ΔG^{o}_{n} may be calculated from the capillarity model as[13]

$$\Delta G^{o}_{n} = -nkT\ln S + (36\pi V^{2})^{1/3}\gamma n^{2/3} \qquad (11)$$

where S = vacancy supersaturation ratio.

The evaluation procedure was then to

1. Establish the input parameters (Table 1; the materials constants are typical of austenitic stainless steel).
2. Arrange the void size classes into a number of groups consistent with accuracy and computer time required.
3. Evaluate β_v, β_i and α_v at the boundary of each group.
4. Evaluate Equation (10) timewise.
5. Determine the time increment, Δt, as described below
6. Evaluate $\rho(n,t+\Delta t)$.

The void size space was divided into thirty groups to make the average $\Delta n = 100$. Δn was smallest at the smallest void sizes, where $\rho(n,t)$ varies most rapidly.

Table 1 Input Parameters

Symbol	Name	Value
N	Atomic Site density	$8.5 \times 10^{22}/cm^3$
γ	Surface energy (no impurities)	$1000\ erg/cm^2$
γ	Surface energy (with impurities)	$800\ erg/cm^2$
T_B	Temperature during burn cycle	500^oC (21)
T_C	Temperature during cool cycle	300^oC (21)
τ_B	Burn cycle time	50 sec
τ_C	Total cycle time	100 sec
E_v^f	Vacancy formation energy	1.6 eV (17,18)
E_v^m	Vacancy migration energy	1.3 eV (17)
D_v^o	Pre-exponent for vacancy diffusion	$0.6\ cm^2/sec$ (17,18)
P_e	Equilibrium gas pressure	$6 \times 10^9\ dyn/cm^2$
K_i^2	Dislocation sink strength for interstitials	$1.02 \times 10^9/cm^2$
K_v^2	Dislocation sink strength for vacancies	$1.00 \times 10^9/cm^2$
K	Atomic Displacement rates	5.8×10^{-7} dpa/sec
		1.7×10^{-6} dpa/sec
		5.8×10^{-6} dpa/sec
β_i/β_v	Biasing ratio	.98

At each time step Eq. (10) was evaluated for N = 1, 2, 3, ..., 30. The time increment, Δt, was determined by

$$\left.\frac{\partial \rho(n,t)}{\partial t}\right|_{t=t_1} \Delta t_N = \alpha\, \rho(n,t_1) \tag{12}$$

where α is a fixed positive constant. Then

$$\Delta t = \text{minimum of } \Delta t_N \tag{13}$$

Finally, the void number density at time $t_2 = t_1 + \Delta t$ was calculated as

$$\rho(n,t_2) = \rho(n,t_1) + \left.\frac{\partial \rho(n,t)}{\partial t}\right|_{t=t_1} \Delta t \tag{14}$$

The initial condition was $\rho(n,0) = 0$. Starting from this point one could then calculate $\rho(n,t)$ for any n,t of interest. The detailed procedure and a computer program are given elsewhere[20].

Impurity Effects

Highly mobile non-gaseous atoms may be present in the wall material initially or may be formed by transmutation reactions. Elements such as hydrogen and nitrogen are expected to be present in too low concentrations to exert a significant intravoid pressure, but may, however, adsorb at the void:matrix interface, thereby lowering the surface energy and the activation barrier for nucleation[24]. This effect is accounted for by inserting the adsorption-reduced surface energy into the expression for ΔG^{o}_{n} (Eq. 11).

Such inert gaseous impurities as helium reduce the activation barrier by entering the void and exerting a stabilising intravoid pressure[16,18,24]. It is assumed here that the combination of thermal activation and irradiation-induced detrapping provides a high degree of mobility, so that the helium is equilibrated between the void and the lattice. In this case[16]

$$\Delta G^{o}_{n} = -nkT\ln S + (36\pi V^2)^{1/3}\gamma n^{2/3} - nP_e V \qquad (15)$$

where P_e = equilibrium helium pressure and V = atomic volume

During cool-down, however, there is little thermal activation and no detrapping at all, so that the helium content of the voids is expected to remain constant. Then $-nP_eV$ in Eq. (15) is replaced by $-XkT \ln (\frac{eX_e}{X})$ where X_e is the number of helium atoms corresponding to P_e, and X is the number of gas atoms in the void at the end of the burn cycle[16].

It is then a simple matter to substitute the appropriate gas term into the expression for ΔG^{o}_{n} to simulate void nucleation or dissolution.

DISCUSSION

Void swelling was simulated for cases of no impurities and of gaseous and non-gaseous impurities for displacement rates of 5.8×10^{-7}, 1.7×10^{-6} and 5.8×10^{-6} dpa/sec, which are intended to bracket probable first wall conditions. A fusion cycle of 50 sec burn, 50 sec cool was selected on the basis of being physically reasonable and computationally tractable.

Steady-state nucleation rates and incubation times were first calculated (Table 2) for comparison with the results of the transient theory, which are summarised in Table 3.

Table 2 Steady-State Nucleation Parameters

γ (ergs/cm^2)	K (dpa/sec)	S	n_k'	J_k' (voids/cm^3-sec)	$\Delta G_k'$ (eV)	τ (sec)
No Impurities						
1000	5.8×10^{-7}	3429	49	3.2×10^{7}	2.2	543
1000	1.7×10^{-6}	6714	31	1.9×10^{10}	1.8	209
1000	5.8×10^{-6}	13242	21	2.9×10^{12}	1.6	85
Non-Gaseous Impurities						
800	5.8×10^{-7}	3429	25	3.9×10^{14}	1.1	417
800	1.7×10^{-6}	6714	16	1.5×10^{16}	0.93	168
800	5.8×10^{-6}	13242	11	2.7×10^{17}	0.79	73
Gaseous Impurities						
1000	5.8×10^{-7}	3429	31	1.8×10^{10}	1.8	209
1000	1.7×10^{-6}	6714	22	2.7×10^{12}	1.6	85
1000	5.8×10^{-6}	13242	15	1.6×10^{14}	1.3	37

It is seen from Table 2 that (except for one case) the incubation time is larger than the burn time, and is sometimes larger by nearly an order of magnitude. So, as suspected, steady state nucleation theory is inapplicable and the transient treatment employed is needed.

Table 3 Summary of Void Number Density and per cent Swelling after 100 cycles

K (dpa/sec)	Impurities	Void Density[a] (voids/cm^3)	Swelling (%)
5.8×10^{-7}	None	8.9×10^{12}[b]	2.2×10^{-5}
1.7×10^{-6}	None	1.7×10^{14}[c]	1.8×10^{-4}
5.8×10^{-6}	None	2.0×10^{15}	2.0×10^{-3}
5.8×10^{-7}	non-gaseous	6.9×10^{15}	6.7×10^{-3}
1.7×10^{-6}	non-gaseous	5.1×10^{16}	4.8×10^{-2}
5.8×10^{-6}	non-gaseous	2.9×10^{17}	2.7×10^{-1}
5.8×10^{-7}	gaseous	8.0×10^{13}	9.2×10^{-5}
1.7×10^{-6}	gaseous	1.0×10^{15}	9.7×10^{-4}
5.8×10^{-6}	gaseous	9.5×10^{15}	9.0×10^{-3}

[a] Includes only voids larger than the critical nucleus

[b] After 60 cycles

[c] After 68 cycles

Fig. (4) shows typical behaviour of the void number density over a number of duty cycles. In this case (the second line in Tables 2 and 3) the incubation time is 210 sec, and although a few small voids form very quickly, a steady state is not established until the burn time reaches about this value (total time 450 sec). It is important to observe that only the very smallest voids ($n \lesssim 10$) decay during the cool down cycle. For these conditions at least, a 'ratcheting' effect exists with very little void dissolution during the cool cycle.

Figs. (5-7) show the effects of damage rate and of gaseous and non-gaseous impurities on the void number density after 10 burn cycles, which represents approximately steady state conditions.

The effect of gaseous impurities (such as helium) was approximated by assuming an internal pressure of 6×10^9 dyn/cm^2 during the burn cycle, and no gas gain or loss during the cool cycle.

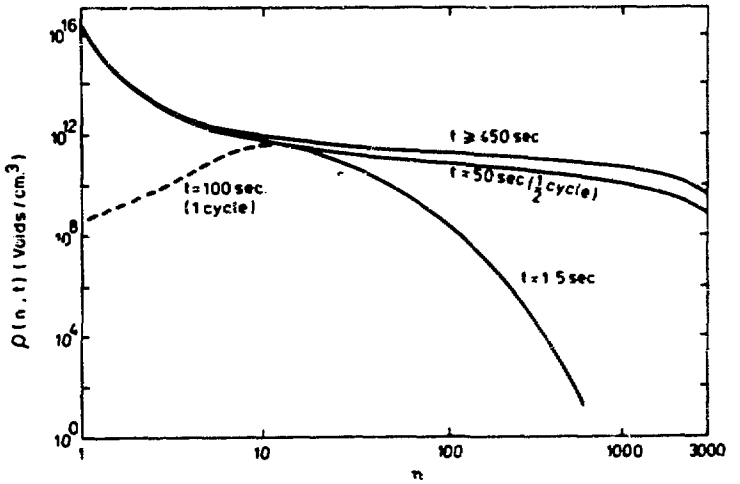

Figure 4 Development of void number density over a number of duty cycles. No impurities, K = 1.7 x 10^{-6} dpa/sec.

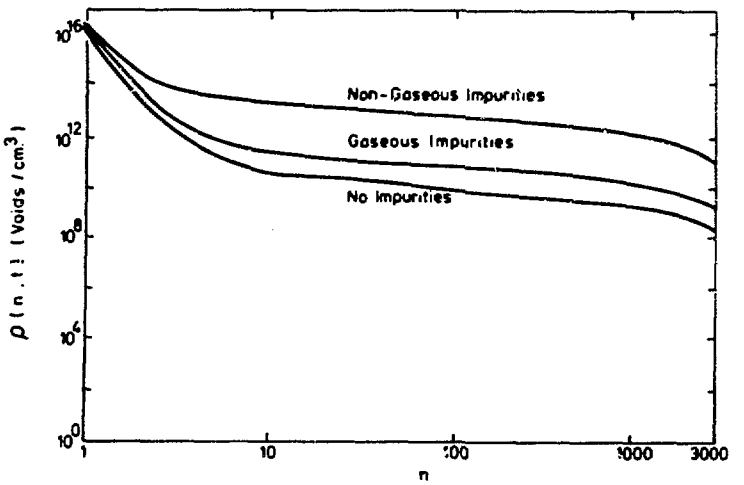

Figure 5 The effect of gaseous and non-gaseous impurities on void number density after five burn cycles (near steady-state) K = 5.8 x 10^{-7} dpa/sec.

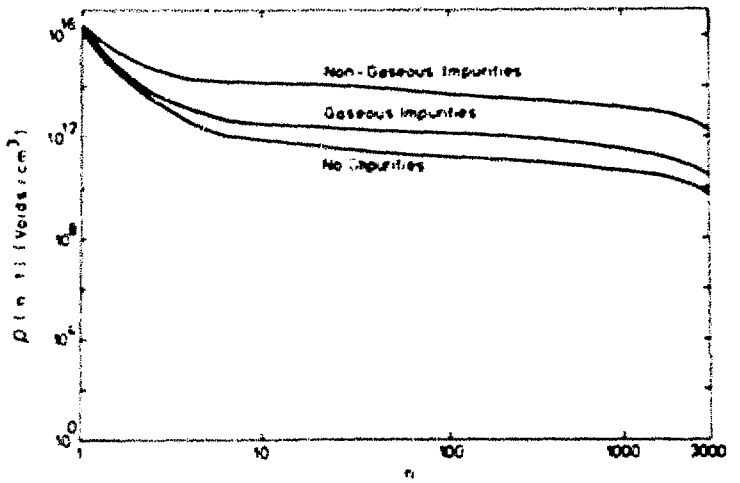

Figure 6 Same as Fig. 5 except K = 1.7 x 10^{-6} dpa/sec. The void number density is somewhat higher than in fig. 5.

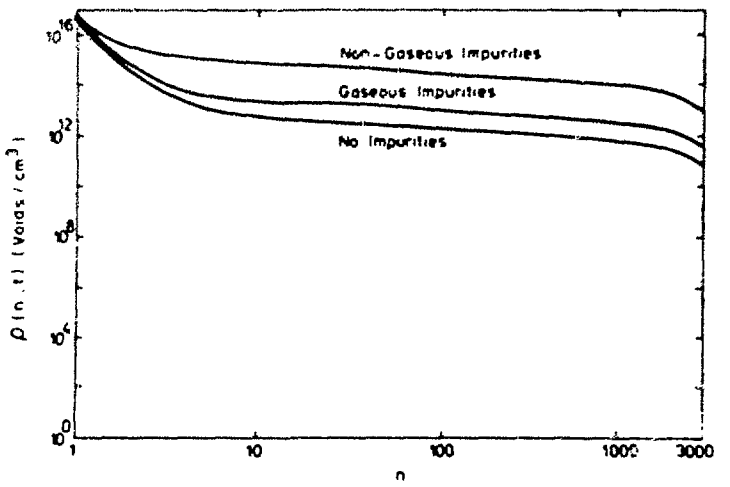

Figure 7 Same as Figs. 5, 6 except K = 5.8 x 10^{-6} dpa/sec. The void number density is higher yet.

The presence of helium is seen to increase the void density by several orders of magnitude, much as happens under steady state conditions. As in the impurity-free case, very little void dissolution occurred during the cool cycle. Under other circumstances, however, helium could have the very important effect of preventing complete dissolution of voids during the cool cycle (which would decay only to bubbles) and would then be prepared to commence growth on the next burn cycle. This could be a very important effect, which would commence only after a number of duty cycles sufficient to produce enough helium to stabilise the voids.

The effect of a mobile, surface active species was approximated by reducing the surface energy to 800 erg/cm^2. This reduction in surface energy is consistent with the effects of adsorption in other systems[25]. The void density is seen to be increased even more by the non-gaseous impurities than by helium, thus illustrating the extreme sensitivity of nucleation rate to changes in surface energy. However, non-gaseous impurities are unlikely to play the same role as helium in preventing total dissolution of voids during the cool cycle. The lowered surface energy will give a slightly lower rate of dissolution, but this is not likely to be of crucial importance.

SUMMARY AND CONCLUSIONS

1. First wall swelling has been simulated by a numerical integration of the equations for void nucleation.
2. Steady-state nucleation conditions were not obtained in most cases, which necessitated the use of the transient formulation of nucleation theory.
3. Very little void dissolution occurred during the cooling cycle.
4. The effect of inert gas or surface-active impurities was to decrease the critical nucleus size and to sharply increase the void nucleation rate.
5. Inert gas may further increase the swelling rate by preventing complete dissolution of voids during the cooling cycle.

FUTURE WORK

It must be emphasised that these calculations represent a first attempt in mathematical simulation of first wall swelling and as such depict a somewhat idealised situation. Certainly more attention should be paid to trends and relative values than to absolute magnitudes.

The applicability and accuracy of the simulation procedure could be improved by:

1. A better representation of the variation of flux, temperature and defect concentrations over the fusion cycle, and calculations based on the various proposed cycles.
2. Extending the upper limit on void size well beyond n = 3000, to perhaps several hundred angstrom diameter voids.
3. Inclusion of the void sink strength in the calculation of defect concentrations, so as to permit a study of swelling saturation.
4. A better model for the concentrations and energetics of the impurities.
5. Nucleation calculations based on only moderately mobile impurities as has been done under fission conditions[25].

ACKNOWLEDGEMENTS

We are indebted to Dr. Farid Abraham and Mr. David Patten for helpful discussions on the numerical calculations.

Financial support by the National Science Foundation, the Energy Research and Development Agency and by an Allegheny Ludlum Fellowship is gratefully acknowledged.

REFERENCES

1. C. Cawthorne and E. J. Fulton, Nature 216, 576, (1967).
2. Voids Formed by Irradiation of Reactor Materials, Proceedings of the British Nuclear Energy Society Conference, AERE Harwell 1971.
3. J. Corbett (ed.) Proceedings of the International Conference on Radiation Induced Voids in Metals, SUNY-Albany, 1972.
4. R. J. Arsenault (ed.) Defects and Defect Clusters in BCC Metals and their Alloys, NBS, Washington 1973.
5. S. D. Harkness and C. Y. Li, in Radiation Damage in Reactor Materials, Vol. II, International Atomic Energy Agency, 1969.
6. M. J. Makin and G. P. Walters, in R. S. Nelson (ed.) The Physics of Irradiation Produced Voids, p299 HMSO, 1975.
7. F. Garner and L. Thomas in Symposium on the Effects of Irradiation on Structural Materials, ASTM 1973.
8. D. W. Keefer, H. H. Neely, J. C. Robinson, A. G. Pard and D. Kramer in Irradiation Effects on Structural Alloys for Nuclear Reactor Applications, ASTM STP 484, p332, ASTM 1970.
9. R. S. Nelson, D. J. Mazey and J. A. Hudson, J. Nuclear Mat. 37, 1, (1970).
10. J. A. Sprague, J. E. Westmoreland, F. A. Smidt, Jr., and P. R. Malmberg, J. Nuclear Mat., 54, 286, (1974).
11. B. A. Loomis, A. Taylor and S. B. Gerber, in Ref. 6, p274.
12. L. C. Ianniello (ed.) Fusion Reactor First Wall Materials, USAEC Washington 1972.
13. K. C. Russell, Acta Met. 19, 753, (1971).
14. J. L. Katz and H. Wiedersich, J. Chem. Phys. 55, 1414, (1971).
15. K. C. Russell, Scripta Met. 6, 209 (1972).
16. K. C. Russell, Scripta Met. 7, 755, (1973).
17. J. Katz and H. Wiedersich, J. Nuclear Mat. 46, 41, (1973).
18. H. Wiedersich, J. J. Burton and J. L. Katz, J. Nuclear Mat., 51, 287, (1974).
19. R. W. Powell and K. C. Russell, Rad. Effects, 12, 127, (1972).
20. Y. H. Choi, Computer Simulation of the Effect of Fusion Burn Cycle on First Wall Swelling, SM Thesis MIT 1975.

21. G. L. Kulcinski, R. G. Brown, R. G. Lott and P. A. Sarger, Nucl. Tech. 22, 20, (1974).
22. A. D. Brailsford and R. Bullough, in Ref. 4, p453.
23. A. D. Brailsford and R. Bullough, J. Nuclear Mat. 44, 121, (1972).
24. K. C. Russell and D. H. Hall, in Ref. 4, p545.
25. R. Mrdjenovich, S. M. Kaufman, T. J. Whalen and C. L. Corey, Met. Trans. 1 2175, (1970).

APPLICATION OF DAMAGE FUNCTIONS TO CTR COMPONENT FLUENCE LIMIT PREDICTIONS

R. L. Simons
D. G. Doran

Hanford Engineering Development Laboratory
Richland, WA 99352

ABSTRACT

Material behavior observed under irradiation conditions in test reactors is not always directly applicable to the design of reactor components such as CTR first wall because of differences in the damage effectiveness of test reactor and service spectra. The interpolation and, under some conditions, extrapolation of material property change data from test conditions to different neutron spectra in service conditions can be accomplished using semi-empirical damage functions. The derivation and application of damage functions to CTR conditions is reviewed. Since limited amounts of data are available for applications to CTR design spectra, considerable attention is placed on the effectiveness of various available and proposed neutron sources in determining a damage function and subsequent fluence limit prediction. Neutron sources included in this study were EBR-II, HIFR, LAMPF (Be and Cu targets), high energy deuterons incident on Be (D-Be), and 14 MeV neutrons (D-T). Several conclusions are drawn from this study: 1) High energy neutron spectra such as from D-Be and D-T reactions are the most effective of those neutron sources studied for reducing uncertainties in the fluence limit prediction for a CTR first wall spectrum. Consequently, material tests should be made in these or similar high energy spectra in order to make useful fluence limit predictions by damage functions. 2) Errors in the damage function and fluence limit prediction are minimized if all available neutron spectra are used. 3) Some neutron sources that are only slightly harder than EBR-II spectra can cause error magnification. 4) If presently available damage functions were applied to CTR spectra (assuming the damage mechanism is the same in the CTR spectra and in the spectra used to derive the damage function) the uncertainty in the fluence limit predictions would be 60% to > 100% at the 95% confidence level.

INTRODUCTION

It is difficult and generally impractical to simulate the exact neutron spectra of a reactor (whether LMFBR or CTR) which is being designed. Consequently, irradiation induced property changes measured in available test reactor spectra must be interpolated or extrapolated to the design spectral conditions. The purpose of the present work is to determine how effective presently available and proposed neutron sources are in determining damage functions for CTR applications. A damage function is, generally speaking, an energy dependent cross section that expresses the neutron energy dependence of an irradiation induced property change. More specifically, the term damage function, or effective damage function (EDF), is used in the present work to refer to a damage cross section that has been adjusted to fit experimental data. Spectral interpolation* with damage functions is, in principle, a relatively simple task. The accuracy of the prediction depends upon the number and variety of different test spectra in which the property change was measured as well as the accuracy of the measurements. Spectral extrapolation involves additional uncertainties as will be apparent in what follows.

A damage function G(E) is derived by an iterative procedure from the set of integral equations

$$M_i = \frac{P}{(\phi t)_i} = \int_0^\infty G(E)\, \phi_i(E) dE, \quad i=1,2,3,\ldots, N \qquad (1)$$

where P is the measured property change due to an irradiation to total fluence $(\phi t)_i$ in the i^{th} neutron test spectrum $\phi_i(E)$ (normalized to unit flux). There is one equation for each test spectrum. The solution begins with an assumed energy dependence $G^\circ(E)$ based on a consideration of damage mechanisms. The result of adjusting $G^\circ(E)$ to give a best fit

---

* Interpolation and extrapolation are not precise terms as used here. They refer to the application of a damage function to a design spectrum that is generally similar to or appreciably dissimilar, respectively, to the test spectra used to derive the damage function.

to the experimental data is a G(E) that applies specifically to the particular property change P. G(E) may be weakly or strongly dependent on G°(E) depending on the extent of the spectral variations of the test data.

The fluence, $(\Phi t)_d$, required to attain the property change P in a calculated design spectrum $\phi_d(E)$ is predicted from the equation

$$(\Phi t)_d = P/\int_0^\infty G(E)\ \phi_d(E)dE. \qquad (2)$$

In the usual application, P is a design-limiting property change and $(\Phi t)_d$ is then the corresponding limiting fluence in the design spectrum.

The principal sources of uncertainty in this method of predicting fluence limits are data errors and the lack of a mathematically unique solution to the set of integral equations. If extrapolation is involved, the question of the existence of a rigorous damage function raises an additional uncertainty. Data errors include those incurred directly in the material property measurement as well as in the irradiation temperature, in the measured fluence, and in the shape of the test spectrum. The uniqueness error arises because, in the absence of assumptions about the form of G(E) and the number and type of test spectra, the set of integral equations does not possess a unique solution. The iterative procedure employed, however, can determine a nearly unique solution in the energy range where appreciable damage is caused by the test spectra if reasonable physical assumptions regarding the form of G(E) are made. Outside of this energy range the iterative procedure can determine an upper bound to the solution; it is important that the initial estimate of G(E) be high enough in this region that one can be reasonably confident that no physically realistic solution exists above the upper bound. This is significant because the upper bound damage function determines the lower bound fluence limit.

Figure 1 shows three steps in the derivation and application of a damage function. In this example, P is 60 ksi yield strength* in

* 60 ksi yield strength was chosen arbitrarily as the reference property level. It is not an established design limiting property level.

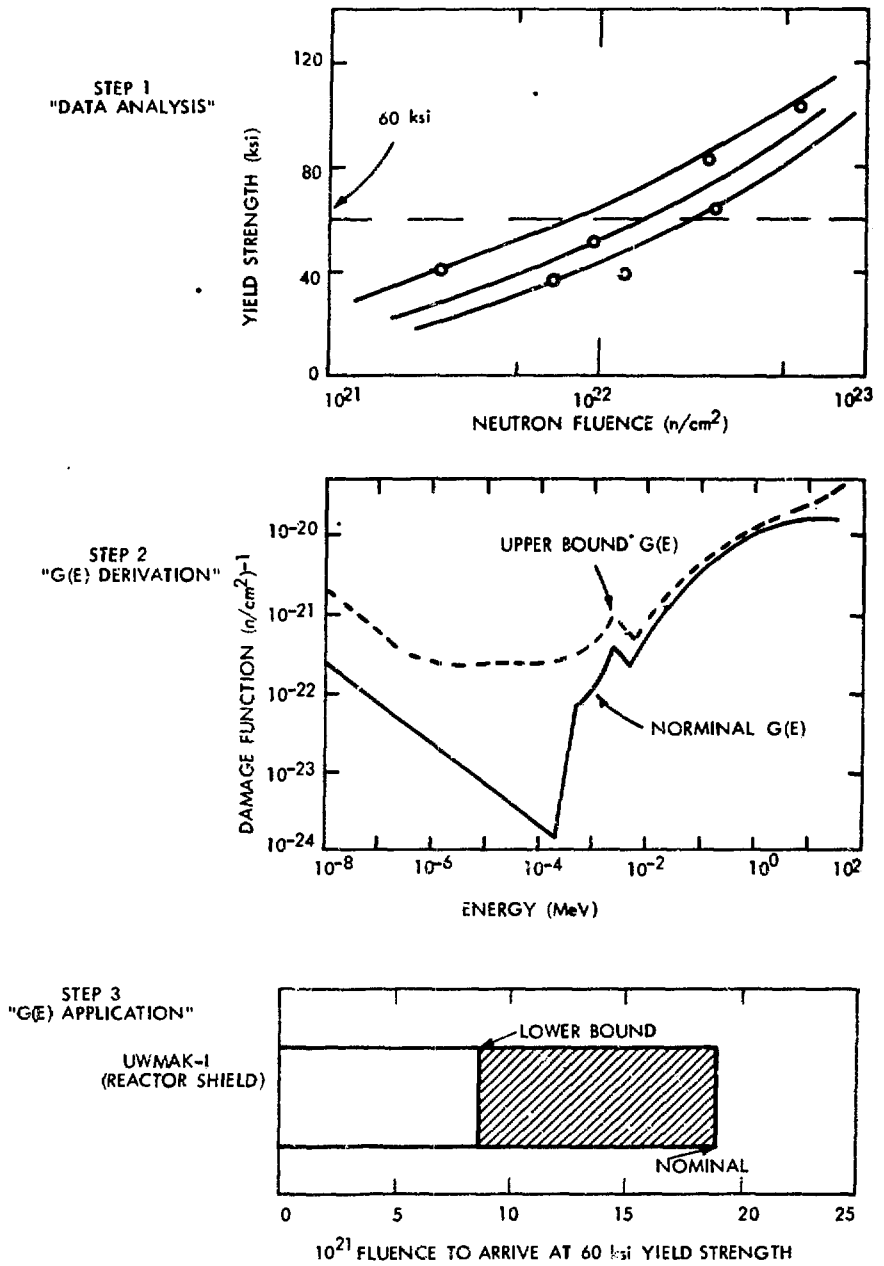

Figure 1. Derivation and Application of Damage Functions.

annealed 304 stainless steel irradiated and tested at 900°F and the design spectrum is for the reactor shield (140 cm from the first wall) of the University of Wisconsin Tokamak I. The first step involved extrapolating or interpolating all available test data from fast and thermal reactors to the reference property level to determine the fluences $(\phi t)_i$. The input data to Eq. (1) are then N values of $M_i = 60/(\phi t)_i$ and a starting function $G°(E)$. In this example, the displacement cross section was used for $G°(E)$. The nominal damage function resulting from the iterative solution to the integral equations is shown in step two. An error analysis of the data and iterative procedure was used to estimate the upper bound solution. Application of the nominal damage function and upper bound damage functions to the step three design spectrum using Eq. (2) gives the nominal and lower bound fluences shown.

A report[1] containing a detailed discussion of the iterative procedure applied to damage function analysis is forthcoming. One objective of that study was to investigate the errors incurred in the extrapolation of data obtained with in-core LMFBR spectra to lower energy, out-of-core spectra. This work is being extended to the problem of interpolating and extrapolating LMFBR and LWR data to the generally higher energies of CTR design spectra. In the present study, the effectiveness of available and proposed neutron sources in determining damage functions for CTR applications was examined by the use of simple damage models to generate data which were, in turn, used to derive damage functions. The effectiveness of various neutron sources in determining a unique damage function and in limiting data error propagation was examined by comparing fluence limits predicted using derived damage functions with those calculated directly from the damage models.

DESIGN AND TEST SPECTRA

The design spectra, all from the University of Wisconsin Tokamak I study,[2] included a first wall spectrum (0.1 cm depth), a lithium blanket spectrum (25 cm from first wall), and a spectrum in the reactor shield (140 cm from first wall). Test spectra typical of the following sources

were included: EBR-II,[3]* HIFR,[4] LAMPF with copper and beryllium beam stops,[5] a linac with 16 and 35 MeV deuterons incident on a beryllium target,[6,7] and a 14 MeV neutron beam (D-t reaction). Several spectra are illustrated in Figure 2.**

DAMAGE MODELS

Three simple damage models were used to generate "data" to determine the effectiveness of the test spectra for damage function analysis. These included a displacement model, a helium model, and an interactive model with vacancies and helium atoms as the defect constituents.

In LMFBRs, atomic displacements appear to be the dominant damage mechanism, as is evident from the relatively good correlation of property change data using displacements per atom (DPA). In the displacement model employed here, the property change, P, is just the total number of DPA, and P was taken to be 1 DPA.

$$P = 1 = \bar{D}_i(\Phi t)_i \qquad (3)$$

where $\bar{D}_i$ is the spectral-averaged displacement cross section D(E) for stainless steel[8] (cm^2) in the i^{th} spectrum and $(\Phi t)_i$ is the total fluence.

* Although the FTR is a potentially valuable facility for CTR irradiation studies, no FTR spectra were included in this analysis because they are effectively covered by the range of EBR-II spectra employed as shown in Table 1.

** The spectra were cut off at 18 MeV, the present upper limit of the group structure in the SAND-II code--only the 35 MeV D-Be spectrum was affected. This truncation has no bearing on the results of this study because 1) it does not exclude any portion of the CTR spectra, and 2) the data generated by the assumed damage models and consequently the unfolded damage functions include the truncation and hence are self-consistent. This study does not address the question of whether the interpretation of radiation effects data obtained in a spectrum having an appreciable component above 18 MeV is complicated by the possibility of different damage mechanisms operating at the higher energies.

Input to Eq. (1) is $M_i = \bar{D}_i$ and the damage function derived from data generated by this model is the displacement cross section.

In CTR design spectra, much more helium is generated than in LMFBR spectra; hence, differences in damage mechanisms can be expected. While displacements could still be the dominate mechanism for some properties such as yield strength, helium production could dominate for properties such as ductility and swelling. Hence, the property for the second damage model is the amount of helium produced (helium atoms per atom or %PA) and P was taken to be 10^{-5} atom fraction.

$$P = 10^{-5} = \bar{H}_i(\phi t)_i \tag{4}$$

where $\bar{H}$ is the spectral-averaged helium cross section, H(E), for iron. In this case, $M_i = \bar{H}_i$ and the derived damage function will be the helium cross section. The iron cross section was used because it has a high energy threshold similar to the helium cross sections of proposed first wall materials such as niobium, molybdenum, etc. This is in contrast to the more complex helium generation process in nickel bearing alloys.

In the third damage model, the property is a defect cluster density calculated from a simple vacancy-helium interaction model. It is shown in Appendix A that this property is proportional to the product of $\bar{H}_i$ and $\bar{D}_i$. Taking the property level arbitrarily to be 10^{16} clusters/cm^3,

$$P = 10^{16} = 2\ K\ \bar{H}_i\ \bar{D}_i(\phi t)_i^2\ , \tag{5}$$

where the proportionality constant K has the value 1×10^{21}. The damage function for this model is

$$G(E,\phi) = K\phi t[\bar{H}D(E) + \bar{D}H(E)]. \tag{6}$$

Note that a true damage function, depending only on E as assumed in Eq. (1), does not exist in this case--$G(E,\phi)$ is spectrum dependent through $\bar{H}$ and $\bar{D}$. The interactive model is clearly a simplified one. However, it enables one to investigate a case in which two damage mechanisms having different energy dependencies interact and consequently violate the assumption of Eq. (1) that a single damage function suffices

for all spectra. Solving Eq. (1) in this case determines an effective damage function (EDF), which is an average of the separate damage functions in their respective energy response ranges. Such an EDF may be suitable for interpolation yet inappropriate for extrapolation.

Figure 3 shows the interactive damage functions for the three UWMAK design spectra used in this study. Note the differences in magnitude for the three spectra and the differences in shape above 1 MeV. These three spectra produce the damage function extremes found with this model. Not all the test spectra exhibit such variations in magnitude. For example, the damage functions for the four EBR-II spectra show much less spectral sensitivity because of smaller variations in helium generation rates.

Table 1 summarizes the input data and characteristics of the test and design spectra. The table shows the spectrum sources or location in the reactor, the mean neutron energies, and the input integral parameters M_i. As indicated above, M_i values for the displacement and helium models are simply spectral-averaged displacement and helium cross sections. Note that the helium cross section is for iron and consequently does not show a high helium production rate in the HIFR spectrum as is expected for nickel-bearing alloys.

DAMAGE FUNCTION DERIVATION STUDIES

Solution Uniqueness

A set of Q "data points" M_i, for a particular set of Q test spectra, was generated with the damage models. The study of the sensitivity of the damage function solution to the input function began by selecting a particular $G^\circ(E)$ containing arbitrary parameters. Ideally, $G^\circ(E)$ represents the best estimate of the energy dependence of the damage mechanisms believed operative. High energy damage due to either displacements or to helium (threshold n,α reactions) should be an increasing function of energy. Therefore, the form chosen for $G^\circ(E)$ was

$$G^\circ(E) = A\,E^b \ .$$

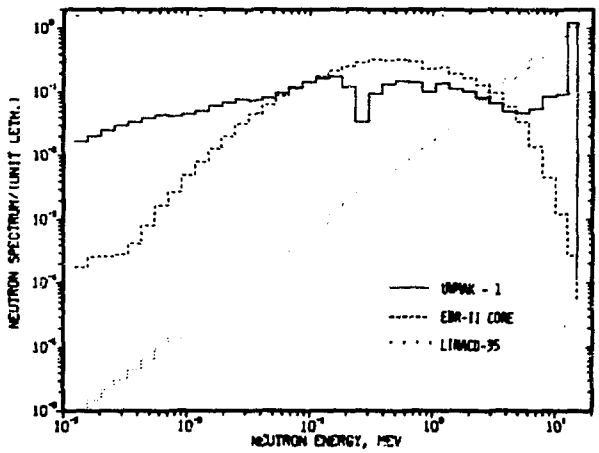

Figure 2. Several of the Test Spectra Used in the Sensitivity Study.

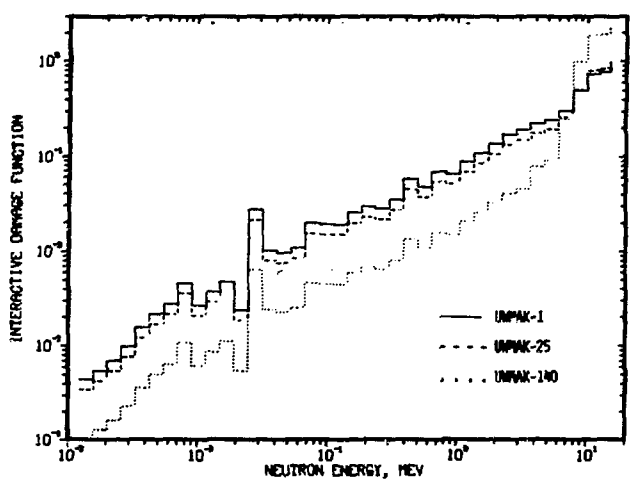

Figure 3. Damage Functions for the Interactive Damage Model for the Three Design Spectra.

Table 1. Characterization of Test Spectra and UWMAK Design Spectra

SPECTRUM	MEAN ENERGY (MeV)	DISPLACEMENT[a] (b)	M_i VALUES FOR THREE MODELS: HELIUM[b] (mb)	INTERACTIVE (10^{-6} Defects/cm^2)/(n/cm^2)
EBR-II, 50 cm above midplane	0.21	167.	0.00328	0.106
EBR-II, 25 cm above midplane	0.48	294.	0.0187	0.335
EBR-II, 18.3 cm above midplane	0.62	359.	0.0325	0.488
EBR-II, 0.0 cm above midplane	0.82	440.	0.0544	0.697
FTR Core Center	0.50	288.	0.0319	0.433
HIFR	0.38	183.	0.0432	0.402
HIFR, Cadmium Shielded	0.72	174.	0.0423	0.387
LAMPF, Cu	0.84	410.	0.416	1.87
LAMPF, Be	1.7	657.	1.08	3.81
LINACD16	6.7	1660.	9.96	18.4
LINACD35[c]	10.8	1943.	22.2	29.7
14 MeV	14.0	2170.	32.8	38.1
UWMAK-1 mm	4.2	855.	8.55	12.2
UWMAK-25 cm	1.7	472.	2.93	5.32
UWMAK-140 cm	0.25	164.	0.0983	0.574

[a] Displacement cross section for stainless steel.

[b] The helium production cross section of iron, rather than that of stainless steel, was used in this study because it displays the (n,α) threshold behavior typical of other proposed CTR materials. The nickel in stainless steel provides a significant source of helium in soft spectra through the two-stage reaction $^{58}Ni(n,\gamma)^{59}Ni(n,\alpha)^{56}Fe$. This source is not applicable to the problem considered here of predicting damage in hard spectra.

[c] Truncated at 18 MeV.

The parameter b in $G^{\circ}(E)$ was systematically varied* about the approximate true energy dependence. Each $G^{\circ}(E)$ and the set of data points were then used in Eq. (1) to derive an adjusted G(E). The process of adjustment, and hence the derived G(E), depends sensitively on the damage responses (i.e., the energy ranges over which significant damage is produced) of the particular set of test spectra. A significant measure of this sensitivity is obtained by using each derived G(E) to predict fluence limits for the design spectra and then comparing these limits with the actual limits corresponding to the assumed damage models. For example, the latter quantity for the displacement model is just 1 DPA $\div \bar{D}_d$ where $\bar{D}_d$ is D(E) averaged over the design spectrum. It should be noted that the errors in the fluence limit predictions obtained in this manner reflect the inability of each set of test spectra to cause adjustment of each $G^{\circ}(E)$ to match the different damage models.

Table 2 shows the mean "uniqueness errors" in the fluence limit predictions obtained for the displacement model, helium model, and interactive model. The number of spectra used is shown at the top and the spectral combination at the bottom of each column. The use of all available spectra generally yields the smallest absolute difference. However, for the first wall spectrum, the two LINAC and the 14 MeV test spectra generally provide the greatest reduction in errors for the displacement model as compared to the other spectra. The LINACD35 spectrum provides slightly better coverage than the 14 MeV spectrum because of the broader energy range of the LINACD35 spectrum. In the lithium blanket spectrum, the LINACD16 appears to give the best overall results and for the structural location, the LAMPF-CU spectrum appears to be best. In all cases, the EBR-II and HIFR spectra were included because these are established neutron sources from which considerable irradiation effects data have and will continue to come.

The helium model shows larger errors than the displacement model

---

* For the displacement and interactive model, b varied from 0 to 1.5, and for the helium model, b varied from 0 to 7. In each case, eight values of b were used.

Table 2. Uniqueness Study--Mean Absolute Difference (%) Between True and Predicted Fluence Limits for Various Sets of Test Spectra

MODEL	DESIGN SPECTRUM	NUMBER OF TEST SPECTRA USED							
		4	5	6	6	6	6	6	11
Displacement	UWMAK-1	40	32	12	25	3.3	1.5	6.2	0.4
	UWMAK-25	30	27	7.6(-)	13	1.3	1.5	10	0.5
	UWMAK-140	3.3(+)	5.3(+)	4.3	6	4.4	4.7	3.7	3.8
Helium	UWMAK-1	57	64	12	19(+)	36(+)	19	7	1(+)
	UWMAK-25	55	61	17	7(+)	26(+)	29	27(-)	4(+)
	UWMAK-140	53	57	21	7.2	20(+)	34(-)	39(-)	5.6(+)
Interactive	UWMAK-1	400(-)	420(-)	67(+)	58(+)	11	13(-)	27(-)	5.2(-)
	UWMAK-25	320(-)	340(-)	53(+)	42(+)	18(-)	31(-)	80(-)	9.6(-)
	UWMAK-140	270(-)	280(-)	29(-)	48(-)	130(-)	150(-)	200(-)	110(-)
Test Spectral Combination									
4 EBR-II		✓	✓	✓	✓	✓	✓	✓	✓
HIFR			✓	✓	✓	✓	✓	✓	✓
LAMPF-Cu				✓					✓
LAMPF-Be					✓				✓
LINACD16						✓			✓
LINACD35							✓		✓
14 MeV								✓	✓

(-) Most predicted fluences were greater than the true value and, hence, nonconservative.

(+) Most predicted fluences were less than the true value and, hence, conservative.

Those values without a sign indicate that the predictions were equally divided between positive and negative.

because of the similarity (and hence redundancy) of the response functions for many of the spectra.

The large errors associated with the interactive model are not surprising when one notes the large variation in magnitude of the individual interactive damage functions in Figure 2. It should also be noted that most all the errors are in the non-conservative direction, i.e., predicted fluence greater than the true fluence. This serves to show that caution should be exercised when dealing with interactive damage mechanisms. It also shows the need to use better damage modeling to identify how interactions take place so that better correlation of irradiation effects data can be obtained.

Solution Errors

In obtaining the fluence limit predictions above, no uncertainties were attributed to the data, M_i, or test spectra, ϕ_i. Major contributions to uncertainty in M_i are errors in the measurement of property change, irradiation temperature, and total fluence. Errors in the fluence and spectral shape can be kept reasonably small by including adequate neutron dosimetry with irradiation effects experiments. For this study the standard deviations assigned to all M_i values were 10% and the standard deviation shape errors assigned to all spectra were 25%. The spectral shape errors are applied to a coarser group structure ($\sim$ 12 groups) than used in the damage function solution (75 groups).

The error analysis (Monte Carlo) procedure is discussed elsewhere in detail[9]. Briefly, it involves determining a large number ($\sim$ 20) of damage function solutions by perturbations of the true set of input data. The perturbations of the data are random and normally distributed with the standard deviations specified above. The error in the fluence limit is the standard deviation of the fluence limits predicted by the large number of solutions.

Data error magnification in the damage function solution is possible in some cases. If the response of a neutron spectrum is small in a particular energy region where no other spectrum responds, then errors in high response energy ranges can be accommodated by disproportionate

changes in the low response energy range. The result is a large error in this energy range. Consequently, a small extension in the response range of a group of spectra can be a disadvantage. The ideal situation is to have at least one dominant spectral response in all energy ranges of interest.

Table 3 shows the standard deviations in the fluence limit predictions for the three UWMAK design spectra obtained using the displacement and helium models and various combinations of test spectra. (Results for the interactive model are not shown because the primary use of that case was to study the adjustment error). The spectral combinations include the four EBR-II and two HIFR spectra in all cases. The second case includes LAMPF-Be; in the third case, LAMPF-Be is replaced by LAMPF-Cu; etc. The last case includes all eleven spectra together. The case with LAMPF-Cu is an example of data error magnification. The LINACD35 and 14 MeV neutron sources are the most effective in reducing the data error magnification for the hard first wall spectrum and are just as effective as the other sources for the softer spectra. Using all available neutron sources generally gives the best overall results.

APPLICATION OF AVAILABLE DAMAGE FUNCTIONS

Damage functions have been determined previously for several properties and irradiation conditions for annealed types 304 and 316 stainless steel.[10] It is instructive to examine the uncertainties incurred in applying several of these damage functions--derived from fission reactor data--to some typical CTR design spectra. Of course, these uncertainties reflect only the errors connected with the derivation of the damage functions. The additional uncertainty as to whether the dominant damage mechanisms in hard CTR spectra are accounted for in the damage functions derived from data taken in softer spectra is under investigation in this and other laboratories. In the present study, this question applies primarily to the first wall spectrum.

Table 4 shows "predicted" fluence limits and percent standard deviations for the three UWMAK design spectra for 60 ksi yield strength,[11] 1% uniform elongation, and 1% swelling[12] in 304 stainless steel. It is

Table 3. Fluence Limit Prediction Uncertainty for UWMAK Spectra by a Monte Carlo Propagation of Data Errors

DAMAGE MODEL	SPECTRAL COMBINATIONS	NEGATIVE 1 STANDARD DEVIATION ERROR (%)[a] FIRST WALL	25 cm	140 cm
DISPL C/S	EBR-II and HIFR	50	37	11
	+ LAMPF-Be	38	25	11
	+ LAMPF-Cu	60	44	10
	+ LINACD16	44	26	12
	+ LINACD35	12	10	10
	+ 14 MeV	13	19	10
	ALL SPECTRA	6.3	5.5	9.1
HELIUM C/S	EBR-II and HIFR	77	73	70
	+ LAMPF-Be	50	38	32
	+ LAMPF-Cu	52	37	34
	+ LINACD16	68	60	55
	+ LINACD35	35	37	40
	+ 14 MeV	9.1	24	30
	ALL SPECTRA	12	17	21

[a] Difference between the nominal fluence limit prediction and the lower bound fluence limit prediction.

Table 4. Fluence Predictions Using Available Damage Functions For Several Property Changes in Annealed Type 304 Stainless Steel

MATERIAL PROPERTY	FLUENCE (10^{22} n/cm^2) ± 1σ[a] FIRST WALL	25 cm	140 cm
60 ksi Yield Strength Irrad. & Test Temp. = 900±100°F	0.62(±70%)	0.92(±53%)	1.9(±39%)
1% Uniform Elong. Irrad. & Test Temp. = 900±100°F	2.2(±40%)	3.8(±38%)	9.8(±36%)
1% Swelling Irrad. Temp. = 840±25°F	1.9(±25%)[b]	3.0(±17%)[b]	6.3(±16%)[b]

[a] The one standard deviation errors were determined by calculating the fluence limit with each recycle damage function resulting from the Monte Carlo error analysis, and then determining the standard deviation of these from the fluence limit predicted by the nominal solution. The uniqueness error was calculated in a similar manner, divided by two since it is arbitrarily defined at the 2σ level, and added to the above.

[b] These % uncertainties do not include a contribution due to nonuniqueness.

important to note that the assigned errors in these cases were smaller than those used in obtaining the values in Table 3. LMFBR applications of G(E) to fluence limit predictions are based upon 95% (2σ) confidence levels. At this level, the uncertainty in most of the predictions in Table 4 is 60% to > 100%.

SUMMARY AND CONCLUSIONS

This study has attempted to supply some quantitative measures of the uncertainty in estimating the damaging effectiveness of neutrons in typical CTR spectra using data from various existing and proposed test spectra. The need for high fluence, high temperature data on mechanical properties of structural materials, obtained in similar spectra, is clear. Because such data will not soon be available, early fluence limit predictions will be based on state-of-the-art knowledge of damage mechanisms.

Several specific conclusions can be drawn from this spectral sensitivity study of damage function analysis as applied to CTR design spectra. It should be kept in mind that they are based on damage models that are oversimplified, particularly as applied to spectra having significant numbers of neutrons above 5 MeV.

1. The 35 MeV D-Be spectrum and a monoenergetic 14 MeV beam are the most effective single neutron sources, of those considered, in reducing errors in predicted fluence limits for a CTR first wall. The former source is superior only in that it provides a broader energy range of neutrons. The 16 MeV D-Be spectrum appears to be too soft for application to a hard first wall spectrum. The tables presented here provide a quantitative measure of the increased accuracy of damage function analysis to be expected by the acquisition of radiation effects data in proposed high energy neutron sources.

2. The best results (i.e., least error) are generally obtained if all available neutron spectra are used in damage function analysis.

3. HIFR provides little, if any, advantage over EBR-II spectra for damage function analysis of iron. A similar conclusion would be expected for most metals. The utility of HFIR for CTR studies is based on the copious helium production in nickel-bearing alloys. This effect,

apparently unique among the structural metals of interest, results from a thermal neutron reaction and therefore is not directly applicable to high energy extrapolations of irradiation effects data. On the other hand HIFR is a valuable source for studying the effects of the large amounts of helium which are anticipated in CTR spectra. Experiments which include varying the thickness of thermal neutron shields could be very effective in this regard.

4. Some neutron sources, such as LAMPF-Cu, if used in damage function analysis without other high energy response spectra, can lead to significant error magnification.

5. If dominant damage mechanisms in LMFBR and particular CTR spectra are the same, the extrapolation of presently available damage functions for 304 SS and 316 SS leads to uncertainties in fluence limit predictions in CTR spectra of 60 to > 100% at the 95% confidence level. Where damage mechanisms are different or interactive mechanisms exist, such predictions are more uncertain. The application of damage function analysis in this situation will be the subject of future studies.

ACKNOWLEDGMENTS

The authors thank T. C. Reuther, K. M. Zwilsky, and C. E. Weber of the United States Energy Research and Development Administration for their interest and continued support of these program efforts. Comments and discussions with W. N. McElroy and G. R. Odette were greatly appreciated.

This work was performed under the auspices of the United States Energy Research and Development Administration.

REFERENCES

1. G. R. Odette, R. L. Simons, and W. N. McElroy, "Reactor Materials Performance Predictions Using Damage Functions: Analysis of Fluence Limit Uncertainties," HEDL-TME 75-43 (May 1975).

2. University of Wisconsin Fusion Feasibility Group, "UWMAK-I A Wisconsin Toroidial Fusion Reactor Design," UWFDM-68 (March 15, 1974).

3. W. N. McElroy, J. L. Jackson, J. A. Ulseth, and R. L. Simons, "EBR-II Dosimetry Test Data Analysis (Reactor Runs 31E and 31F)," BNWL-1402 (June 1970).

4. F. B. K. Kam, and J. H. Swanks, "Neutron Flux Spectrum in the HIFR Target Region," ORNL-TM-3322 (1971).

5. D. J. Dudziak, W. V. Green, T. R. Regenie, and E. G. Zukas, "A Newly Developed Irradiation Facility at LAMPF," Proceedings Amer. Nucl. Society Topical Meeting on Irradiation Experimentation in Fast Reactors, Jackson Lake Lodge, Wyoming (September 10-12, 1973).

6. K. A. Weaver, J. D. Anderson, H. H. Barschall, and J. C. Davis, Nucl. Sci. Eng., 52, p. 35-45 (1973).

7. D. M. Parkin, N. D. Dudey, R. R. Heinrich, and M. J. Fluss, "A Preliminary Neutron Dosimetry Characterization of the Blip Neutron Facility," BNL-50412 (August 1973).

8. D. G. Doran, J. R. Beeler, Jr., N. D. Dudey, and M. J. Fluss, "Report of the Working Group on Displacement Models and Procedures for Damage Calculations," HEDL-TME 73-76 (December 1973).

9. C. A. Oster, W. N. McElroy, J. M. Marr, "A Monte Carlo Program for SAND-II Error Analysis," HEDL-TME 73-20 (February 1973).

10. W. N. McElroy, R. L. Simons, D. G. Doran, and G. R. Odette, "Damage Function Analysis," Journal of Testing and Evaluation, 331, p. 220 (1975).

11. R. L. Simons, W. N. McElroy, L. D. Blackburn, "Damage Function Analysis of Austenitic Steel Neutron Induced Mechanical Property Change Data," Nuclear Technology, 16, p. 14 (October 1972).

12. W. N. McElroy, R. L. Simons, D. G. Doran, and J. L. Straalsund, "Damage Function for Swelling in Type 304 Stainless Steel," Trans. Am. Nucl. Soc., 15, 249 (1972).

APPENDIX I

A Model for Helium-Displacement Interaction*

In order to study the validity of damage function analysis in a situation where a unique damage function does not exist, a simplified model was postulated to describe He - displacement damage interaction. The model is not intended to describe accurately any particular physical phenomena, but it is useful in studying the influence of such interactive effects on the spectral dependence of radiation damage.

The assumptions in the model include:

1. The helium concentration increases linearly with time; the loss of mobile helium to all possible sinks is neglected.

---

* This model was developed by G. R. Odette.

2. Small vacancy clusters of radius R are produced within displacement cascades at a rate of one cluster for every 1000 displaced atoms. These clusters are unstable and will rapidly dissolve at a rate characterized by a time constant τ.

3. If a diffusing helium atom collides with a vacancy cluster, the cluster is stabilized against dissolution.

4. The number density of stabilized clusters is the measure of the amount of radiation damage.

Using these assumptions, an equation for the number density of stabilized clusters as a function of time in various spectral environments can be simply derived. The accumulation of lattice helium is described by

$$\frac{d\ He_i}{dt} = \bar{H}_i N \phi_i \tag{1}$$

or

$$He_i(t) = \bar{H}_i N \phi_i t \tag{2}$$

where He_i is the helium volume density in the i^{th} environment, N the number of atoms/cm^3, ϕ_i the total flux, $\bar{H}_i$ the spectral-averaged helium generation cross section and t the total time. The steady state, unstabilized cluster population V_i^{SS} can be determined from

$$\frac{dV_i^{SS}}{dt} = 0 = \frac{N\bar{D}_i\phi_i}{1000} - \frac{V_i^{SS}}{\tau} \tag{3}$$

or

$$V_i^{SS} = \frac{N\tau\bar{D}_i\phi_i}{1000} = \text{constant} \tag{4}$$

where V_i^{SS} is the vacancy cluster volume density, $\bar{D}_i$ the spectral-averaged displacement cross section, and τ the cluster dissolution time constant.

The reaction rate between helium (diffusion coefficient D) and vacancy clusters to produce the concentration $C_i(t)$ of stabilized clusters of radius R is described by

$$\frac{d\,C_i(t)}{dt} = -\frac{d.He_i}{dt} = K'He_i \qquad (5)$$

where

$$K' \equiv 4\pi RD\,V_i^{SS} \quad .$$

Substituting (2) and (4) into (5) and solving for $C_i(t)$ yields

$$C_i(t) = 2K\,\tilde{H}_i\bar{D}_i\phi_i^2t^2 \qquad (6)$$

where

$$K \equiv \pi RDN^2\tau/1000 \quad .$$

The Influence of First Wall Lifetime on the Cost of Electricity in UWMAK Type Fusion Reactors

by

G. L. Kulcinski[(a)]

J. R. Young[(b)]

ABSTRACT

The effect of first wall lifetime of 0.5 to 8 years on the cost of generating electricity in the UWMAK-I and UWMAK-II reactors is investigated. It was assumed that there was little incentive to develop walls with lifetimes (determined by radiation damage) greater than 10 years because of failures due to conventional mechanisms. Based on this assumption the cost of electricity from these two reactors increased over the 10 year lifetime value by 8 to 10% for a wall life of 4 years, 17 to 28% for 2 years, 35 to 65% for 1 year, and 85 to 150% for 0.5 year lifetimes. It appears that wall lifetimes of <2 years are economically unattractive for these reactors and that there is a great incentive to find materials which will have in-service lifetimes between at least 4 and 10 years.

INTRODUCTION

It has now become quite apparent that the first walls (sometimes referred to as vacuum walls) of fusion power reactors will not last the lifetime of the plant.[1-3] There are many reasons why materials scientists have come to this conclusion, but by far the most prominent one relates to a loss of mechanical integrity under the high stresses and strains associated with typical fusion reactor operations. Void swelling, transmutation effects, neutron and charged particle sputtering would also limit the wall lifetime even if the mechanical property degradation could be eliminated. Current estimates of wall lifetime vary from 2 to 5 years[1-3] under typical 1-5 MW/m^2 neutron wall loadings.

Given the necessity to replace the first walls periodically (and even part of the blanket structure), it is legitimate to ask, "How much does such a replacement effect the cost of generating electricity in a fusion power plant?" It is difficult to give a definite answer to that question at this early stage of reactor design because the absolute cost

(a) University of Wisconsin, Madison, Wisconsin 53706

(b) Battelle Northwest Laboratories, Richland, Washington 99352

of electricity from fusion is not known to probably within a factor of two. Nevertheless, we can gain a qualitative picture of how much of a relative cost penalty is paid by analyzing two rather specific designs in the open literature. We have chosen the UWMAK-I[4] and UWMAK-II[5] reactor designs for this study. It must be noted that the results of this work only apply to these reactors at the 5000 MW_{th} power level and one cannot simply apply these results to other systems at different power levels.

General Effects of Radiation Damage on Fusion Power Economics

The unit cost of electricity from any power source depends on 4 factors;

- Operation and Maintenance Costs
- Fuel Costs
- Return on Capital
- kWh of Energy Generated Per Unit of Time

The necessity to replace the first wall obviously will increase the O & M charges by the cost of replacement material and the labor cost associated with the replacement time. It is fairly easy to calculate the costs associated with the materials but at present one can only make rough estimates of the labor time involved. This latter point is especially true with irradiated components which must be handled remotely. However, we shall see that such costs are not a major factor compared to the material cost.

There is no obvious direct relationship between first wall lifetime and the fuel costs and we shall assume that it is unaffected by radiation damage. There is an indirect relationship in that the need for outage time to replace the walls decreases fuel use. However, the fuel costs for a fusion reactor are so small that the changes will have an insignificant effect in our analysis.

The increase in capital costs of a fusion reactor required by the replacement of the first wall on a regularly scheduled basis is mainly due to:

(A) Inventory costs associated with the spare modules which must be on hand for quick insertion into the reactor.

(B) Larger or more hot cell facilities to handle the repair and/or replacement of the entire reactor component which is removed from the reactor.

(C) Increased long term storage space for the damage components.

Before we address the problem of finite wall lifetime, it is worthwhile to note that fusion reactors will have to be designed for quick and frequent wall repair even if the predicted first wall life is greater than the plant lifetime. This is true because failures will occur which are unrelated to radiation damage. Typical causes might be hot spots, corrosion, inhomogeneties due to fabrication procedures, or abnormal operating conditions. It is reasonable to assume that the entire blanket structure can not function for 30 years at high temperatures and with varying loads without a single failure. Once the concept of replacement is accepted, then all of the procedures, equipment, hot cells, shielding and radioactive component storage areas must be designed, tested and installed. It is also reasonable to assume that at any given time something like 10-15% of the blanket structure may have to be removed per year for external repair or replacement.* This means that the concept of a finite first wall lifetime is only significant if the wall life is less than 10 years or so. We will make estimates for the increased capital costs in UWMAK-I and II based on our knowledge of the system but the reader ought to recognize the qualitative nature of such estimates and not concentrate on the exact numbers.

The last important quantity that is affected by a wall life of $\leq$ 10 years is the time the reactor is unavailable for generation of electricity. This results in lost revenue which can be as high as $700,000 to $800,000 per day. Again, it is certainly recognized that "normal" failures will occur in any power facility and we expect the same will hold true for fusion power plants. In this study, 4 weeks of down time per year is assumed for routine and emergency maintenance unrelated to first wall replacement. Here, we will be concentrating on the additional downtime required for a systematic replacement of the first wall.

---

*A simple pinhole leak could require replacement of a very large component.

Method of Calculation

We will use as a starting point for this study the economic studies published in the UWMAK-I and II reports.[4,5] A summary of the capital and electrical costs for both reactors is shown in Tables 1 and 2. These costs are based on a two year wall life.

Once a decision on the first wall lifetime has been made, the next major task is to determine the optimum time for replacement of the modules. Intuitively, this would appear to be the stated wall life. However, this would require excessively high inventory costs of the blanket modules which must be ready outside the reactor when the shutdown is made. Therefore, one usually tries to remove only a part of the defected parts at a time and replace them with new components. The repair of the damaged components is conducted while the reactor is running. These repaired components then can be reinserted into the reactor at the next outage and the process started all over again. While this means that early in the reactor lifetime some components are changed before their anticipated lifetime, it requires a smaller inventory of components and results in a lower electricity cost.

A simple schematic of how we estimated the major effect of changing the first wall on reactor costs is shown in Figure 1. We first determined the annual outage time as a function of time between replacement. This requires that we know the number of modules replaced per outage. Once this is known, the annual outage time is calculated by

$$\left(\frac{\text{outage days}}{\text{year}}\right) = \left[\left(\frac{\text{X days replacement}}{\text{module}}\right)\left(\frac{\text{No. of modules replaced}}{\text{outage}}\right) + \left(\frac{\text{Y Days Cool Down and Startup}}{\text{outage}}\right)\right] \times \left(\frac{\text{No. of outages}}{\text{year}}\right)$$

One peculiar fact about present reactor designs is that they are usually made up of a finite number of modules which can be conveniently replaced. For example, UWMAK-I had 12 such modules, UWMAK-II had 24, and a more recent design UWMAK-III has 18.[6] Therefore, if one finds that the wall life is 2 years, then he can replace 12 modules every 2 years, or

Table I

UWMAK-I Cost Data

(Prices are 1974 Dollars and Based on a 40 Hour Work Week)

Account Number	Account Title	Total
	DIRECT COSTS:	
Nondepreciating Assets:		
20	Land and Land Rights	$1,200,000
Depreciating Assets:		
	Special Materials	28,290,000
	Physical Plant	
21	Structures and Site Facilities	139,807,000
22	Reactor Plant Equipment	573,636,000
23	Turbine Plant Equipment	170,580,000
24	Electric Plant Equipment	142,859,000
25	Miscellaneous Plant Equipment	9,410,000
	SUB-TOTAL Physical Plant	1,036,292,000
	INDIRECT COSTS (All Depreciating Assets):	
91	Construction Facilities, Equipment	24,300,000
92	Engineering Services	48,500,000
93	Other Costs	76,600,000
94	Interest During Construction	218,618,000
	SUB-TOTAL	367,018,000
	SUB-TOTAL (Total Depreciating Assets)	1,431,600,000
	TOTAL PLANT CAPITAL INVESTMENT:	1,432,800,000
	COST PER KILOWATT GENERATED	$971/kWe

Table 2

UWMAK-1I Cost Data

(Prices are 1974 Dollars and Based on a 40 Hour Work Week)

Account Number	Account Title	Total
	DIRECT COSTS:	
Nondepreciating Assets:		
20	Land and Land Rights	$1,200,000
Depreciating Assets:		
26	Special Materials	5,820,000
	Physical Plant	
21	Structural and Site Facilities	161,590,000
22	Reactor Plant Equipment	775,179,000
23	Turbine Plant Equipment	160,150,000
24	Electric Plant Equipment	84,218,000
25	Miscellaneous Plant Equipment	19,110,000
	SUB-TOTAL Physical Plant	1,200,100,000
	INDIRECT COSTS (All Depreciating Assets):	
91	Construction Facilities, Equipment and Services	24,300,000
92	Engineering Services	48,500,000
93	Other Costs	90,800,000
94	Interest During Construction	250,923,000
	SUB-TOTAL	414,523,000
	Sub Total (Total Depreciating Assets)	1,613,420,000
	TOTAL PLANT CAPITAL INVESTMENT	$1,614,620,000
	COST PER KILOWATT GENERATED	$944/kWe

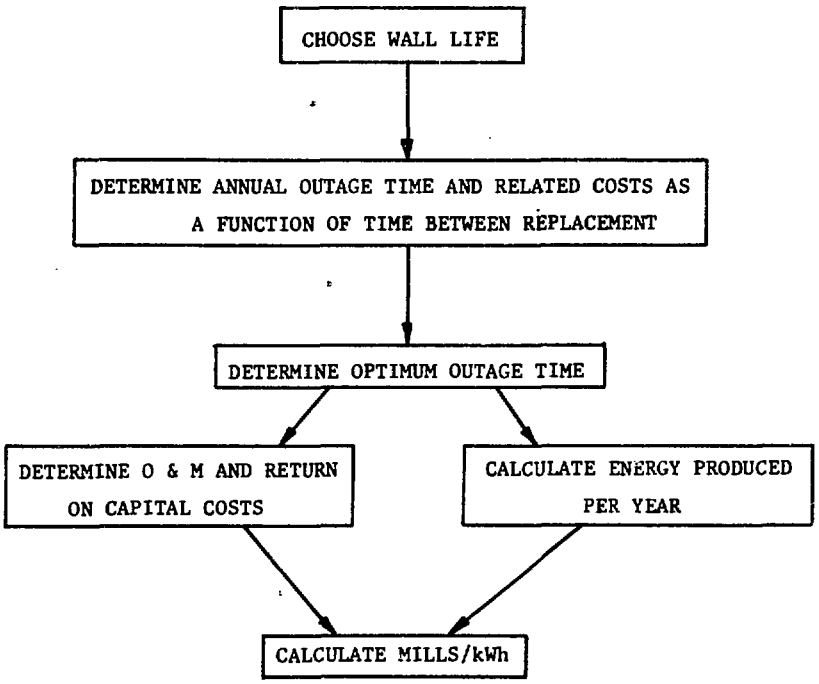

Fig. 1. Method of Calculation of the Effect of First Wall Life on the Cost of Electricity From Fusion Power Plants.

6 modules every year, 3 every 6 months, 2 every 4 months, or 1 every 2 months. The same analyogy can be applied to other systems.

The values of X and Y are somewhat arbitrary at this time because of reactor characteristics but consideration of the mode of construction and afterheat in these reactors led to use of X=3 days for UWMAK-I, X=1.5 days for UWMAK-II, and Y=5 days for both reactors.

We then used this information to calculate the optimum outage time. This depends on three major costs -

(A) Inventory costs for spare modules

$$\left(\frac{\$}{\text{module}}\right) \times \left(\frac{\#\text{ of modules replaced}}{\text{outage}}\right) \times (\text{return on capital})$$

(B) Labor costs to replace modules

$$\left(\frac{\#\text{ of days}}{\text{outage}}\right) \times \left(\frac{\text{Labor costs}}{\text{day}}\right)$$

(C) Revenue lost during time required to change modules

$$\left(\frac{\text{mills}}{\text{kW}_e\text{h}}\right) \times (\text{power level of reactor in kW}_e) \times (\text{annual outage time})$$

Once the optimum outage time is determined, we can calculate increased O & M costs and costs associated with increased capital requirements as well as the reduced kWh generated. This then allows a determination of mills/kWh to be made.

A new wall life is then assumed and the entire process is repeated.

Results for UWMAK-I and UWMAK-II

A comparison of the annual outage time as a function of number of modules replaced per outage and assumed wall life is given in Table 3. There are two points worth noting here, the wall replacement for these two reactors probably will be done on the basis of integral fractions of 12 or 24, and the outage time is the same for I and II except twice as many modules must be changed in II as in I.

The optimum outage time was calculated assuming the following values.[4-5]

Table 3

Annual Outage Time UWMAK-I and II

First Wall Life - Years	Intervals Between Replacement Outages	No. of Modules Replaced per Outage		Annual Outage Time - Days I and II
		I	II	
0.5	6 months	12	24	82
	3 months	6	12	92
	1.5 months	3	6	112
	1 month	2	4	132
	0.5 months	1	2	192
1 year	1 year	12	24	41
	6 months	6	12	46
	3 months	3	6	56
	2 months	2	4	66
	1 month	1	2	96
2 years	2 years	12	24	21
	1 year	6	12	23
	6 months	3	6	28
	4 months	2	4	33
	2 months	1	2	48
4 years	4 years	12	24	10
	2 years	6	12	12
	1 year	3	6	14
	8 months	2	4	17
	4 months	1	2	24
8 years	8 years	12	24	5
	4 years	6	12	6
	2 years	3	6	7
	16 months	2	4	9
	8 months	1	2	12

	UWMAK-I	UWMAK-II
Cost/Module - $	20,300,000	6,250,000
Increased Facility Costs - $ per module	13,000,000[a]	3,300,000[b]
Return on Capital	0.15	0.15
Labor Costs $/Day	28,500	28,500
Loss of Income $/Day (at 20 mills/kWh)	710,000	840,000

(a) for number of modules per outage exceeding 2

(b) for number of modules per outage exceeding 4

The cost per module includes those costs attributable to insurance (~10%) and interest during construction since these modules will probably be long lead time items. The increased facility costs were calculated on the basis of the fraction of the containment facilities attributable to remote handling of components and assuming that the increase in those facilities is 10% per module over the minimum number of modules required for normal outage. For example, we assumed that facilities to handle two damaged modules in UWMAK-I and 4 modules in UWMAK-II would be required regardless of the first wall life. If an extra module had to be changed or held in readiness due to first wall life, then the increased cost is 10% of that required for the basic number in UWMAK-I and 5% for UWMAK-II. These numbers also include the insurance and interest factors.

The cost of labor was calculated on the basis of 96 men working per shift, 3 shifts per day, and these men cost approximately 50% more than the normal maintenance crew (i.e. 20,000 $/man year including fringe benefits).[11] This amounts to labor costs of ~28,500/day of outage.

The loss of revenue has been calculated as if fusion power plants were operating in an economy where electricity is being produced ~20 mills/kWh. Hence, when the plant is shut down it will lose that revenue. For UWMAK-I operating at 1473 MW_e (continuous power) this amounts to ~710,000 $/day. For UWMAK-II at 1716 MW_e, this is 840,000 $/day.

The approximate annual increase in costs due to each of the above items is reported in Table 4 for UWMAK-I and in Table 5 for UWMAK-II. They are also plotted in Figures 2 and 3. The optimum time between outages is

Table 4

Annual Increase in Costs - UWMAK-I as a Function of Wall Life and Time Between Outages

Time Between Outages	Million of Dollars			
	Return on Capital	Labor Costs	Lost Revenue	Total
	0.5 Year Wall Life			
6 months	56.0	2.3	58.2	117
3 months	26.1	2.6	65.3	94
1.5 months	11.1	3.2	79.5	94*
1 month	6.1	3.8	93.7	104
0.5 months	3.1	5.5	136.3	145
	1 Year Wall Life			
1 year	56.0	1.2	29.1	86
6 months	26.1	1.3	33.7	61
3 months	11.1	1.6	39.8	53*
2 months	6.1	1.9	46.9	55
1 month	3.1	2.7	68.2	74.
	2 Year Wall Life			
2 years	56.0	0.6	14.9	72
1 year	26.1	0.7	16.3	43
6 months	11.1	0.8	19.9	32
4 months	6.1	0.9	23.4	30*
2 months	3.1	1.4	34.1	39
	4 Year Wall Life			
4 years	56.0	0.3	7.1	63
2 years	26.1	0.3	8.5	35
1 year	11.1	0.4	9.9	21
8 months	6.1	0.5	12.1	19*
4 months	3.1	0.7	17.0	21
	8 Year Wall Life			
8 years	56.0	0.1	3.6	60
4 years	26.1	0.2	4.3	31
2 years	11.1	0.2	5.0	16
16 months	6.1	0.3	6.4	13
8 months	3.1	0.3	8.5	12*

* Optimum

Table 5

Annual Increase in Costs - UWMAK-II as a Function of Wall Life and Time Between Outages

Time Between Outages	Return on Capital	Million of Dollars Labor Costs	Lost Revenue	Total
	0.5 Year Wall Life			
6 months	32.4	2.3	68.9	104
3 months	15.3	2.6	77.3	95*
1.5 months	6.7	3.2	94.1	104
1 month	3.8	3.8	111	119
0.5 months	1.9	5.5	161	168
	1 Year Wall Life			
1 year	32.4	1.2	34.4	68
6 months	15.3	1.3	37.6	55
3 months	6.7	1.6	47.0	55*
2 months	3.8	1.9	55.4	61
1 month	1.9	2.7	80.6	85
	2 Year Wall Life			
2 years	32.4	0.6	17.6	51
1 year	15.3	0.7	19.3	35
6 months	6.7	0.8	23.5	31*
4 months	3.8	0.9	27.7	32
2 months	1.9	1.4	40.3	44
	4 Year Wall Life			
4 years	32.4	0.3	8.4	41
2 years	15.3	0.3	10.1	26
1 year	6.7	0.4	11.8	19
8 months	3.8	0.5	14.3	19*
4 months	1.9	0.7	20.2	23
	8 Year Wall Life			
8 years	32.4	0.1	4.2	37
4 years	15.3	0.2	5.0	21
2 years	6.7	0.3	5.9	13
16 months	3.8	0.3	7.6	12*
8 months	1.9	0.3	10.1	12

* Optimum

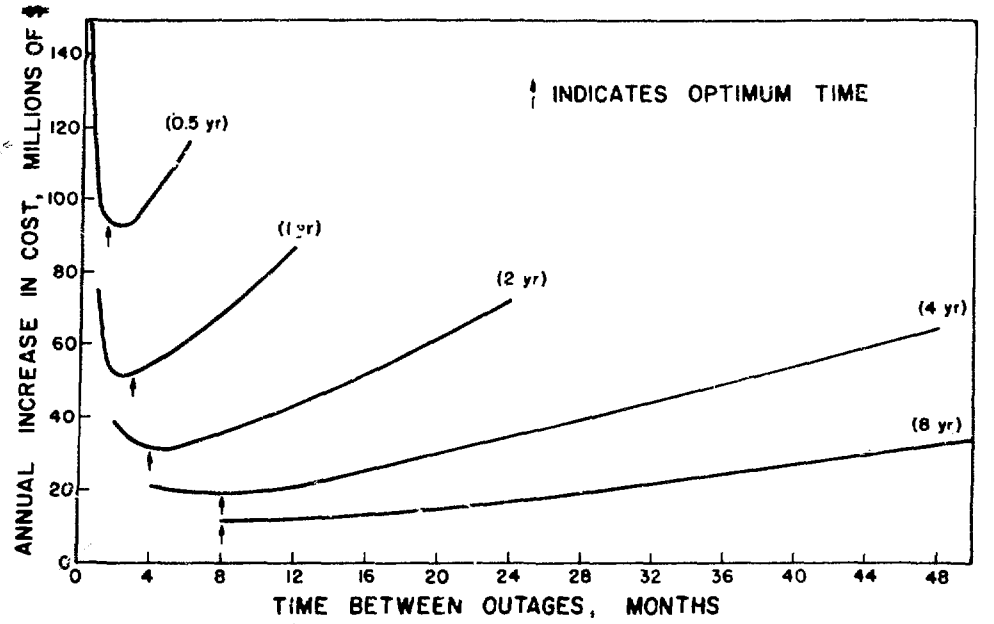

Fig. 2. Determination of Optimum Time Between Outages for UWMAK-I as a Function of First Wall Life.

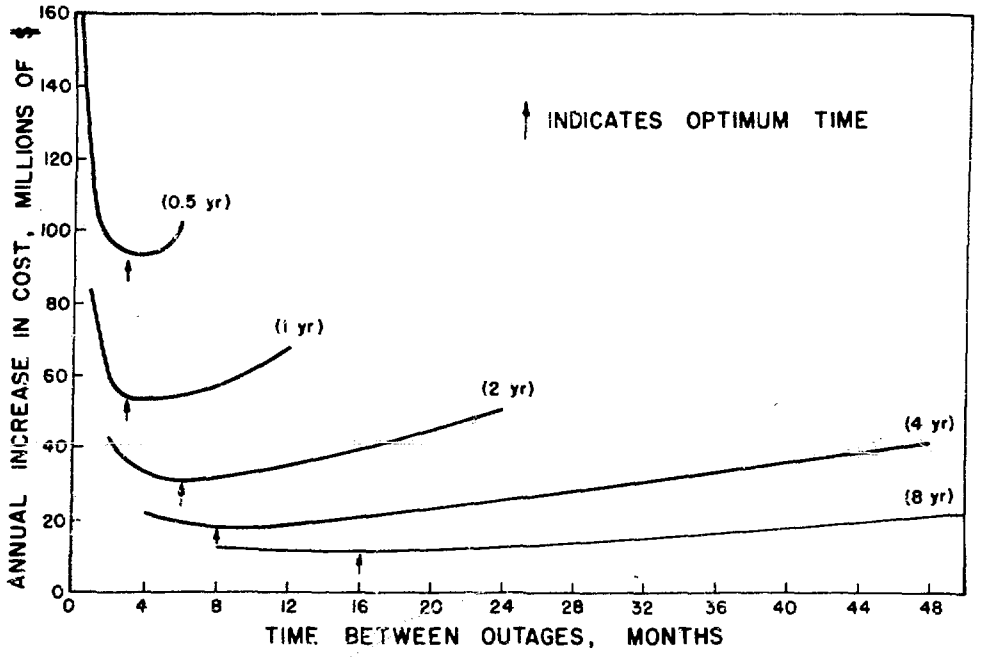

Fig. 3. Determination of Optimum Time Between Outages for UWMAK-II as a Function of First Wall Life.

a balance between the high costs associated with inventory of spare modules (and the increased hot cells to handle them) and the loss of revenue associated with down time.

The optimum time between outages is summarized below from Tables 4 and 5.

Optimum Outage Time - Months

Wall Life - Years	UWMAK-I	UWMAK-II
0.5	1.5	3
1	3	3
2	4	6
4	8	8
8	8	16

It is interesting to note that the optimum outage time does not increase in proportion to the first wall life time, e.g. a factor of 16 increase in wall life only results in less than a factor of 5 increase in the optimum outage time for UWMAK-I and II.

Having determined the optimum outage time, and hence the number of outage days per year due to the first wall replacement (remember that 4 weeks of additional time is set aside for routine maintenance or repairs required by "normal" component failures) we can now estimate the cost of electricity as a function of wall life.

The first area to investigate is that contribution due to O & M costs. The costs are listed for both reactor systems in Table 6 and the explanation for their derivation is given elsewhere.[4] The outside support services are primarily the labor costs determined in Tables 4 and 5. The materials costs of replacing the first wall were determined by using the weights and cost figures from the UWMAK reports.[4-5] For UWMAK-I, this amounts to 17.6 $/kg for the first 20 cm of blanket and 8.8 $/kg for the remainder of the blanket. The stainless steel reflector is assumed to have a lifetime five times that of the first wall due to the neutron attenuation. The total weight of the first 20 cm is 491,000 kg and that of the rest of the blanket is 7,323,000 kg. The amount of 316 SS replaced per year is given in Table 7 as a function of the first wall lifetime.

Table 6

Summary of Operations and Maintenance Costs Associated with UWMAK-I and II

Cost Item	Annual Cost - $ UWMAK-I	UWMAK-II
Salaries (incl. Fringe Benefits)	1,350,000	1,350,000
Misc. Supplies & Equipment	1,000,000	1,000,000
Outside Support Services	350,000+(a)	350,000+(a)
Miscellaneous Costs	200,000	200,000
Subtotal	(b)	(b)
General and Administrative (15% of Subtotal)	(b)	(b)
Replacement of Inner Wall (annual rate)	(a)	(a)
Coolant Make Up	38,000	43,000
Total Annual Cost	(b)	(b)

(a) Depends on Wall Life

(b) To be determined as a function of wall life

Table 7

Cost of Changing First Wall and Associated Blanket Structure
Due to First Wall Lifetimes - UWMAK-I

Wall Life-yr	Wt-First 20 cm MT/yr(a,b)	Wt-Rest of Blanket MT/yr(a,c)	Total MT/yr(a)	Annual Cost-M$
8	61	-	61	1.1
4	123	366	489	5.4
2	246	732	978	10.8
1	491	1465	1956	21.5
0.5	982	2929	3911	43.1

(a) average numbers, MT = metric tonne
(b) 17.60 $/kg
(c) 8.80 $/kg

Table 8

Cost of Materials for First Wall and Blanket Replacement in UWMAK-II

Wall Life-yr	Wt-316 SS First Wall & Tube MT/yr(a)	Wt-316 SS Manifold MT/yr(a)	Wt. of $LiAlO_2$ MT/yr(a)	Wt. of Be MT/yr(a)	Wt. of Graphite MT/yr(a)	Cost $-M/year
8	112		59	54	-	12.4
4	224	170	119	108	65	26.6
2	449	340	238	217	131	53.4
1	897	680	475	433	261	107
0.5	1794	1360	950	866	523	213

(a) average number, MT = metric tonne.

A similar analysis for replacement materials has been conducted for UWMAK-II (Table 8). There is a difference in this reactor because materials other than 316 SS must be replaced due to the high cost of refabricating radioactive material and/or the damage incurred in other materials ($LiAlO_2$, Be or graphite) during their residency in the reactor. Pertinent costs and weights are given below for UWMAK-II.

Component	Metric-Tonnes	Repl. Time (First Wall=1)	$/kg[a]
316 SS-First Wall and Tubes	897	1	17.6
316 - Blanket Manifold	3402	0.2	8.8
$LiAlO_2$[b]	475	1	40
Be[b]	433	1	150[c]
Graphite	1307	0.2	3

(a) fabricated cost
(b) make up neglected
(c) reprocessed Be

There is now enough information to calculate the O & M costs as a function of wall life. The results are given in Table 9 for both UWMAK-I and II. The O & M costs increase dramatically by a factor of 10 to 14 when the wall life decreases from 8 to 0.5 years with the replacement costs of the materials dominating in both of the reactors.

The data for the effect of increased capital costs on the annual costs has already been reported in Tables 4 and 5. In order to get this into a more standard format, we recalculated the total capital costs and the required return on capital. This is shown in Table 10.

The capital costs change less than 5% for a wall life which varies by a factor of 16. This insensitivity is largely due to the fact that we expect the plant will have to be designed for remote changing of first wall components regardless of whether the wall has a lifetime determined by radiation damage.

The last item to be calculated is the number of kWh of energy generated per year of normal operation. The 93.3% duty factor for UWMAK-I and the 94.2% duty factor for UWMAK-II is already taken into account when

Table 9

Calculation of O & M Costs as a Function of Wall Life

Wall Life years	Salaries	Supplies	Fixed O.S. Support	Variable O.S. Support	Misc.	G & A	Material Replacement	Coolant Make Up	Total
				Millions of Dollars					
				UWMAK-I					
8	1.35	1.0	0.35	0.3	0.2	0.48	1.1	0.038	4.8
4				0.5		0.51	5.4		9.4
2				0.9		0.56	10.8		14.9
1				1.6		0.68	21.5		26.7
0.5				3.2		0.84	43.1		49.9
				UWMAK-II					
8	1.35	1.0	0.35	0.3	0.2	0.48	12.4	0.043	16.1
4				0.5		0.50	26.6		30.5
2				0.8		0.56	53.4		57.7
1				1.6		0.63	107		112
0.5				2.6		0.84	213		219

Table 10

Effect of Finite First Wall Life on the Capital Costs of UWMAK Type Reactors

Wall Life Years	No. of Modules Changed per Outage	Capital Costs $ Millions	Return on Capital - $ Millions
	UWMAK-I		
8	1	1379.2	206.9
4	2	1399.5	209.9
2	2	1399.5	209.9
1	3	1432.8	214.9
0.5	3	1432.8	214.9
	UWMAK-II		
8	4	1595.5	239.3
4	4	1595.5	239.3
2	6	1614.6	242.2
1	6	1614.6	242.2
0.5	12	1634.4	245.2

quoting continuous power outputs of 1473 MWe for UWMAK-I and 1716 for UWMAK-II. The calculations also include the four weeks of "normal" downtime in addition to that required to change the first wall. The resulting numbers are summarized in Table 11. The energy produced per year drops from 35 to 45% as the wall life changes from 8 to 0.5 years. We shall see that this has a major effect on the final costs.

The final numbers for the calculation of the cost of electricity are given in Table 12 and plotted in Figure 4.* A few interesting observations can be made about the cost calculations. First of all, the two reactors systems respond remarkably the same considering that they have drastically different designs and coolants. Second, the relative increase in electricity costs (over that for a wall life of >10 years) is low until the wall life drops below approximately two years. The rate of increase in the electricity cost over a projected 10 year life is given below.

% Increase in Electricity Costs Over Those Projected for a 10 Year Life

Wall Life	UWMAK-I	UWMAK-II
10	0	0
8	2	2
4	10	8
2	28	17
1	65	35
0.5	150	85

Thus it can be seen that radiation damage to the first wall can cause an increase of 85 to 150% in the base cost of electricity generated if the wall life is 0.5 years.

The third point to make is that while the relative cost of electricity increases rapidly only below a 2-4 wall life, the absolute costs to the consumer is truly enormous. For example, assuming that fusion is economically competitive in the year 2020 where it may capture some 25 to 33% of the market, we might expect to have some 10^6MWe of installed capacity.[7] If fusion plants were to have an 80% plant factor, then approximately

*These numbers differ slightly from those in Tables 1 & 2[4,5] because we have changed the optimum time between outages in I and because of a slightly different treatment of hot cell costs.

Table 11

Calculation of the Number of kW_eh Generated Per Year as a Function of First Wall Life in UWMAK-I & UWMAK-II

Wall Life Year	Normal Maintenance-hr	First Wall Changes-hr	Production Hours[a]	kW_eh[b]
		UWMAK-I		
8	672	288	7800	1.15×10^{10}
4		408	7680	1.13×10^{10}
2		792	7296	1.07×10^{10}
1		1344	6744	0.993×10^{10}
0.5		2688	5400	0.795×10^{10}
		UWMAK-II		
8	672	216	7872	1.35×10^{10}
4		408	7680	1.32×10^{10}
2		672	7416	1.27×10^{10}
1		1344	6744	1.16×10^{10}
0.5		2208	5880	1.01×10^{10}

(a) basis - 8760 hrs. in a year

(b) Power level averaged over burn - UWMAK-I = 1473 MWe, UWMAK-II = 1716 MWe

Table 12

Effect of First Wall Life on Cost of Electricity in UWMAK-I and II

Wall Life Year	$M			kWh x 10^{10}	Mills/kWh
	O & M	Fuel	Return on Capital		
			UWMAK-I		
8	4.8	0.136	206.9	1.15	18.4
4	9.4	0.134	209.9	1.13	19.4
2	14.9	0.127	209.9	1.07	21.0
1	26.7	0.118	214.9	0.993	24.3
0.5	49.9	0.094	214.9	0.795	33.3
			UWMAK-II		
8	16.1	0.131	239.3	1.35	18.9
4	30.5	0.128	239.3	1.32	20.4
2	57.7	0.123	242.2	1.27	23.6
1	112	0.112	242.2	1.16	30.5
0.5	219	0.098	245.2	1.01	46.0

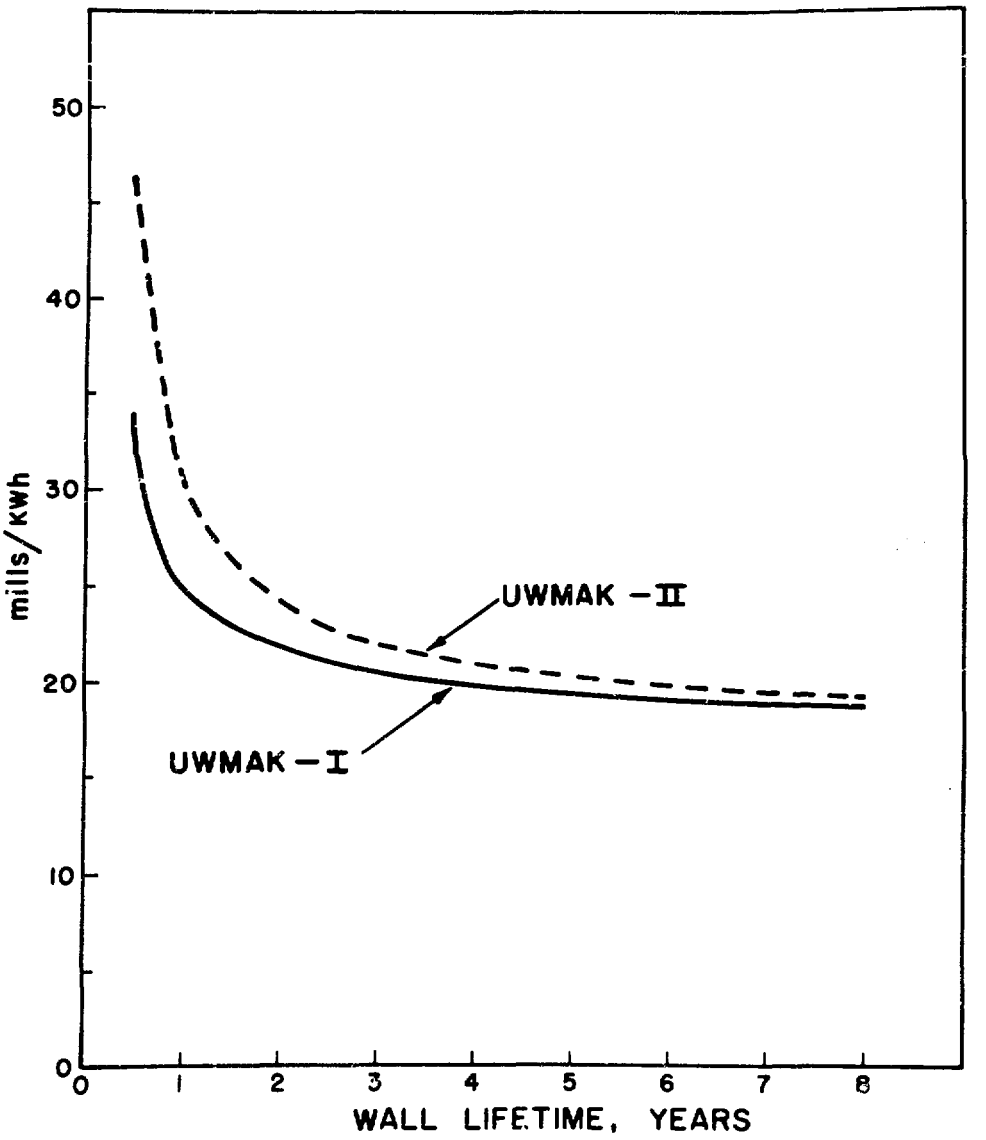

Fig. 4. Effect of Wall Lifetime on Electricity Costs in UWMAK-I.

7×10^{12} kWh would be generated per year by D-T reactions.

Each mill/kWh that fusion is over the competitive price represents some 7 billion dollars. Hence, there is considerable incentive to find first walls which will last at least as long as 2-4 years. It appears, that for the UWMAK reactors, wall lifes of less than 2 years are economically unattractive.

Future studies in this area such as the use of neutron spectral shifters[8-10] may alleviate these problems and can indeed be quite attractive if unprotected walls have lifetimes below 2 years. It is hoped that this admittedly broad brush and somewhat approximate determination of the cost of low first wall life will stimulate designers to alleviate the problem.

Discussion of Results

Periodic replacement of the inner walls of a fusion power reactor can have a significant effect on the unit cost of the electricity production. An average wall lifetime of two years could result in an increase of as much as one-quarter in the unit cost of electricity in comparison to an average wall life of ten years. A wall lifetime of only six months could cause as much as a 150 percent increase in the electricity unit cost.

The actual increase in the electricity cost because of inner wall replacements appears to be dependent primarily on the average wall lifetime, the capital cost of the reactor components kept in inventory to minimize wall replacement outage time, and the average outage time required to replace one wall module. The labor costs for the wall replacement appear to be of much smaller importance.

Study of the three primary determinants of the costs due to replacement of the inner walls reveals several important guidlines for fusion reactor research and design. First, considerable research is justified for determining the characteristics of inner wall materials and methods for increasing the average lifetime. In general, the costs due to replacement are inversely proportional to the average lifetime. A

major effort appears justified for identifying materials which will accumulate radiation damage at a much lower rate and wall designs resulting in less damaging operating conditions.

And, finally, there is a large incentive for developing reactor designs requiring a minimum of outage time for replacing an inner wall segment. The lost revenue while the inner walls are being replaced appears to be over half of the total wall replacement cost for average wall lifetimes of eight years or less. Emphasis should be placed on developing reactor designs which permit rapid removal and replacement of entire reactor segments or inner wall segments. If either reactor or wall segments are replaced, quick disconnect methods are needed for all cooling and instrumentation systems. And, if possible, the connections between reactor segments and foundations or other segments should be simple (or non-existent) requiring no complicated activities such as welding or precision gasketing.

In summary, the costs for fusion reactor inner wall replacement could have a significant effect on the cost of electricity production. Large efforts appear justified for increasing the average wall lifetime, decreasing the inventory costs for spare wall or reactor segments, and reducing the reactor outage time for wall replacement.

REFERENCES

1. G. L. Kulcinski, R. G. Brown, R. G. Lott and P. A. Sanger, Nucl. Tech. 22, 20, 1974.
2. A Fusion Power Plant, R. G. Mills, ed., MATT-1050, April 1974.
3. W. Danner, Max-Planck Institute fur Plasmaphysik Report # IPP 4/130, February 1975.
4. (a) B. Badger, M. A. Abdou, R. W. Boom, R. G. Brown, T. E. Cheng, R. W. Conn, J. M. Donhowe, L. A. El-Guebaly, G. A. Emmert, G. R. Hopkins, W. A. Houlberg, A. B. Johnson, J. H. Kamperschroer, D. Klein, G. L. Kulcinski, R. G. Lott, D. G. McAlees, C. W. Maynard, A. T. Mense, G. R. Neil, E. Norman, P. A. Sanger, W. E. Stewart, T. Sung, I. Sviatoslavsky, D. K. Sze, W. F. Vogelsang, L. J. Wittenberg, T. F. Yang and W. D. Yound, "UWMAK-I, A Wisconsin Toroidal Fusion Reactor Design," Fusion Technology Program, University of Wisconsin, UWFDM-68 - Volume I, March 1974.

   (b) B. Badger, H. Avci, R. W. Boom, E. Cameron, R. W. Conn, D. Graber, A. B. Johnson, G. L. Kulcinski, P. G. Lorenzini, C. W. Maynard, E. Normand, J. W. Lue, H. Pearlman, D. Schluderberg, T. Sung, I. Sviatoslavsky, D. Sze, W. F. Vogelsang, L. J. Wittenberg, T. F. Yang, J. R. Young and W. Young, "UWMAK-I", A Wisconsin Toroidal Fusion Reactor Design," Fusion Technology Program, University of Wisconsin, UWFDM-68-Volume II, May 1975.
5. B. Badger, R. W. Conn, G. L. Kulcinski, M. A. Abdou, R. Aronstein, H. I. Avci, R. W. Boom, T. E. Cheng, J. Davis, J. M. Donhowe, G. A. Emmert, Y. Eyssa, N. M. Ghoniem, S. Ghose, W. Houlberg, J. Kesner, W. Lue, C. W. Maynard, A. Mense, N. Mohan, H. A. Peterson, T. Y. Sung, I. Sviatoslavsky, D. K. Sze, W. F. Vogelsang, R. Westerman, L. J. Wittenberg, T. F. Yang, J. Young, W. D. Young, "UWMAK-II, A conceptual Tokamak Power Reactor Design," Fusion Technology Program, University of Wisconsin, UWFDM-112, October 1975.
6. UWMAK-III, A Toroidal Fusion Reactor, To be published in January 1976.
7. G. L. Kulcinski, Energy Policy, 2, 104, 1974.
8. R. W. Conn, G. L. Kulcinski, H. I. Avci and M. El-Maghrabi, Nuclear Tech., 26, 125, 1975.
9. G. L. Kulcinski, R. W. Conn, H. I. Avci and D. K. Sze, Trans. Am. Nucl. Soc., 21, 50, 1975, see also UWFDM-127, June 1975.
10. H. I. Avci and G. L. Kulcinski, UWFDM-141, October 1975.
11. NUS-531, "Guide for Economic Evaluation of Nuclear Reactor Plant Designs," NUS Corporation, January 1969.

FOIL SPECIMENS FOR THE INVESTIGATION OF MECHANICAL PROPERTIES IN ION SIMULATION EXPERIMENTS

J. Auer and A.A. Sagüés
Institut für Festkörperforschung der Kernforschungsanlage Jülich
D 517 Jülich, Germany

ABSTRACT

In many ion simulation experiments heat dissipation and the moderate range of light ions impose an upper limit for the sample thickness. On the other hand, mechanical property investigations require a certain minimum sample thickness in order to minimize surface and grain size effects. In this work some factors which determine this lower limit are reported for "pure" stainless steel type 316. This material has the same basic composition as AISI 316 but contains only traces of impurities like C, Si, etc. thus eliminating the influence of precipitates by different heat treatments. Cylindrical "bulk" specimens (2 mm diam.) and foil specimens (thickness D between 30 and 100 μm) with grain sizes d between 1 and 45 μm were prepared by a suitable thermomechanical treatment. Tensile tests at room temperature showed that the grain size dependence of the yield stress becomes slightly stronger for small grain sizes, however, the yield stresses are the same for bulk and foil specimens of the same grain size. The uniform elongation ε of the foil specimens (which is here practically equal to the total elongation) is generally only half the uniform elongation of the bulk specimens. For small grain sizes the ultimate tensile strength of foil specimens is only slightly lower than for bulk specimens, however, it drops to very low values if the grain size becomes comparable to the foil thickness (D < 2 - 3d). Creep experiments on similar samples show a substantial decrease in creep rate with decreasing foil thickness probably caused by the increasing influence of surface effects.

INTRODUCTION

High energy ion irradiations are increasingly used for the simulation of neutron damage in reactor materials since they produce high damage levels in relatively short times. One of the main difficulties associated with this technique comes from the restricted penetration range of charged particles. This is especially true if mechanical properties (e.g. in pile creep) are being investigated because of two factors that impose strong limitations upon the choice of specimen shapes:

1. The heating of the sample due to the beam current and the limited range establish an upper limit for the specimen thickness. The thicker the specimen, the more energetic the incident particles must be in order to pass completely through it and thus avoid non-uniform damage rates and alloying effects. This results in inadmissible amounts of heat deposition. Furthermore, the time-advantage of simulation experiments fades away since the damage rate decreases with increasing particle energy.
2. On the other hand, specimens that are too thin bring up effects related with their surface condition and grain structure that are difficult to estimate. This makes extrapolations of mechanical data of irradiated foils to bulk material values questionable.

Several simulation experiments are now in progress at KFA Jülich concerning the tensile and creep behavior of a variety of alloys using foil specimens with thickness between 30 and 100 μ. The following measurements are a preparatory work for these experiments and were intended to establish some of the factors determining the mechanical response of foil specimens and to develop optimal experimental conditions.

EXPERIMENTS AND RESULTS

Specimens

"Pure" 316-stainless steel was chosen as test material for the following reason: This alloy has the same basic components as the commercial AISI 316 material but a much lower impurity content (see Table 1). This prevents the appearance of a variety of precipitates that may make the alloy extremely sensitive to small differences in the thermal treatment of different specimens.

Table 1. 316 "pure" stainless steel-composition[1] (wt.%)

	N	B	S	P	Cl	Mo	Ni	Cr	Fe
....	1.0 ...	<3.3...	0.01...	0	0.01	2.5	14..	17.9	balance

The material received in the shape of polycrystalline rods was axially split, solution treated at 105[0]°C and then cold-rolled down to 1 mm strips. After a second solution anneal, foils were produced by cold rolling down to thicknesses between 5 and 100 μ. Specimens of the shape shown in Fig. 1 were then spark cut from the foils.

The specimens, still cold worked 50 to 97 % were then recrystallized at temperatures from 950 to 1050°C. Some specimens with very small grain size were produced by means of a pulse-annealing technique[2]. This consisted of passing through the sample a current pulse of 60 to 200 msec duration, during which the recrystallization temperature is exceeded (900 - 1200°C). This way grain sizes between 1.3 and 45 μ were obtained.

A number of control "bulk" specimens were produced by turning out of the starting material tensile samples with a gage diameter of 2 mm. This ma-

terial was then recrystallized to several grain sizes.

Tensile Tests

The specimens so produced were pulled to fracture at 20°C and a strain rate of $3 \cdot 10^{-4}$/sec. Fracture occurred always at the point of maximum load. Fig. 2 shows a typical load-elongation curve for a 33 μ foil. The lack of the nonuniform deformation part of the curve is a consequence of the large ratio of gage length to equivalent diameter. In the case of Fig. 2 this ratio is ∿ 200:1, while standard tensile specimens have a ratio close to 5:1.

Fig. 3 shows the yield stress σ_F for foils of different thickness and also for the "bulk" specimens as a function of the grain size d. One can see that the yield stress is independent of the specimen thickness, and that the grain size dependence follows the well known Hall-Petch[3] relationship ($\sigma \sim d^{-1/2}$).

The measurement of grain sizes by optical means (linear intercept method) was difficult for the finer grain material because twins became then almost invisible. Therefore, transmission electron microscopy was used in these cases to determine the average number of twin lines per grain and to provide a correction to the value obtained metallographically.

Fig. 3 also shows that the ultimate tensile stress σ_B is fairly independent of grain size, but that deviations to lower values occur when the ratio of specimen thickness D to grain size d becomes smaller than ≈ 2.5. The lowering of the ultimate stress is coincident with a reduction of the total elongation to fracture, suggesting that those specimens are prone to premature failure. This may be the result of instabilities created by the easy deformation of grains with favorable orientations.

Creep Experiments

Since these investigations are rather time consuming they were limited to material of one grain size (∿ 7.5 μ).

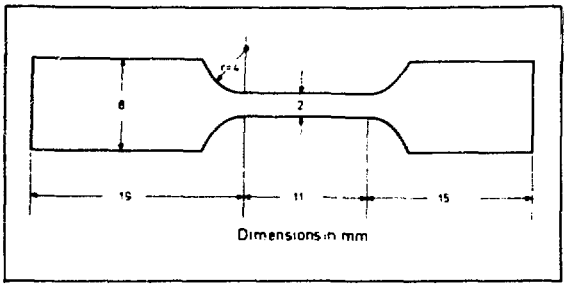

Fig. 1. Shape of Tensile Foil Specimens

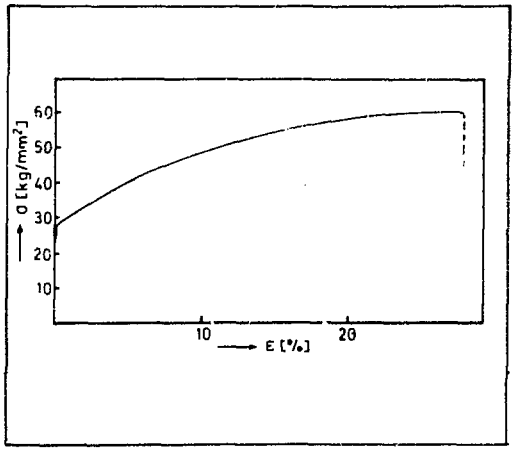

Fig. 2. Stress-strain curve of a "pure" stainless steel 316 foil specimen, thickness D = 33 μ tested at 20°C. Strain rate $\dot{\varepsilon} = 3 \times 10^{-4}$ sec^{-1}

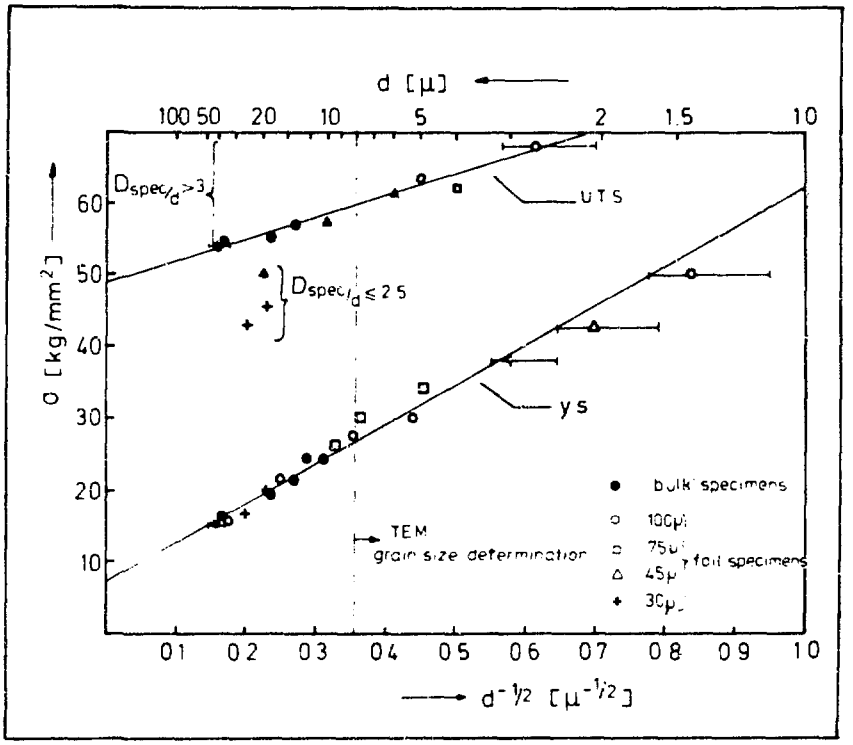

Fig. 3. Grain size dependence of yield strength $\sigma_{y.s.}$ and upper tensile strength σ_{UTS} for "pure" stainless steel type 316 at 20°C

The creep data in Table 2 show a strong dependence of the creep rate on the specimen thickness. The creep rate decreases with decreasing thickness and that is opposite to what would be expected from easier grain boundary sliding conditions. An explanation seems to be possible only by considering surface effects that would naturally become more important for the thinner specimens. This is suggested by electron microscope examinations which showed no significant structure differences between the creep speciment tested.

Table 2. Creep Results ($T = 695^{\circ}C$, $\sigma = 5$ kg/mm^2)

Sample	Annealing temperature	Grain size d(μ)	Thickness D(μ)	steady state Creep Rate (hr^{-1})
1			98	6.83×10^{-4}
2	890°C		98	8.42×10^{-4}
3	1 hour	7.5	74	5.0×10^{-4}
4			31	1.74×10^{-4}
5			31	1.50×10^{-4}

CONCLUSIONS

The flow and ultimate tensile stress of foil specimens are independent of the foil thickness if the latter is larger than 2 - 3 grain diameters. The advantages of thin foil simulation experiments however, must be compromised with the loss of information on the non-uniform part of the load-elongation curve.

The use of "pure" 316 SS foils thinner than 70 - 100 μ for in-pile creep simulation experiments is questionable because uncontrollable surface conditions may be determinant of the creep rate.

ACKNOWLEDGEMENTS

The authors are indebted to Dr. J. Ullmaier for his advice when preparing the paper, and to Dr. E. E. Bloom, ORNL, for supplying the sample material.

REFERENCES

1. J. M. Leitnaker, E. E. Bloom and J. O. Stiegler, ORNL Report TM-4500, p. 2 (1974)

2. see e.g. D. Fahr, ORNL Report TM 3550, p. 110

3. E. O. Hall, Proc. Phys. Soc. London, B64, 747 (1951) and N. J. Petch, J. Iron and Steel Inst., 174, 25 (1953)

IRRADIATION CREEP DURING 4 MEV PROTON IRRADIATION

R.J. McElroy*, J.A. Hudson+ and R.S. Nelson+

+Metallurgy Division, AERE, Harwell, Didcot, Oxford, England.
*Metallurgy Department, University of Oxford, Oxford, England.

ABSTRACT

A technique has been developed for studying irradiation creep during the bombardment of metals by high energy (4 MeV) protons from a Van de Graaff accelerator. The main features of the creep testing and irradiation facility will be described and the important aspects of beam handling and specimen environmental control highlighted. Results have been obtained for thermal and irradiation creep of nickel in the temperature range 400°-600°C. In addition to an irradiation enhancement of creep, a pronounced irradiation hardening was observed. The net effect, therefore resulted from a combination of the two processes and a logarithmic decrease in irradiation creep rate with dose was observed. The irradiation enhanced creep rate after a given time was found to increase linearly with damage rate.

INTRODUCTION

An important requirement of the fusion reactor programme is the study of irradiation effects with 14 MeV neutrons. A fundamental difference compared with the fast fission reactor development programme is the absence of a reactor test facility for many years. Present designs of machines capable of producing 14 MeV neutrons offer fluxes notably less than those anticipated in early reactors or even advanced experiments, so that engineering design will necessarily proceed without fully adequate data. For the immediate future, therefore, it is clear that the use of particle accelerators and fission reactors will form an important part of any materials selection programme.

Based on our experience with fast reactors two important irradiation phenomena will feature signficantly in any fusion reactor programme. These are void swelling and irradiation creep. In the case of void

swelling extensive studies have been carried out in support of the fast reactor programme, using both neutron and charged particle irradiation. In the case of irradiation creep, data are very limited and the physical processes underlying the phenomenon are far from understood. In the present paper we will therefore outline the technique under development at Harwell to simulate neutron induced irradiation creep using proton irradiation. Similar experiments have been set up at Argonne[1] and NRL[2]. The paper will emphasise the roles in which such techniques can be used in the context of the fusion reactor programme, and will present some preliminary data which indicate the usefulness and limitations of the experiments.

In comparison with the simulation of void swelling, a fundamental difficulty is that mechanical tests such as the measurement of strain in a specimen undergoing irradiation creep deformation cannot be performed on the same minute volumes of irradiated material. Thus to attempt a simulation of neutron induced creep, a regime of uniform irradiation damage over large volumes is necessary. This can be realised with lighter particles such as protons, but the increased penetration is achieved at the expense of damage rate. In the present experiments 4 MeV protons from the Harwell Van de Graaff accelerator have been used to bombard thin (25-30 μm) electrically heated specimens held at controlled elevated temperatures under various tensile stresses and the creep strains have been measured. The maximum damage rate achieved with nickel at 500°C is about 10^{-6} displacements per atom per sec (dpa s^{-1}) and a total dose of about 1 dpa can be achieved within a few days.

IRRADIATION REGIME

The range of 4 MeV protons in nickel and stainless steels is about 50 μm, about twice the specimen thickness. In traversing this thickness the protons lose about 1.5 MeV. Most of this energy is lost in inelastic collisions and appears as heat in the specimen whereas a small fraction (~0.02%) is lost in elastic Rutherford-type collisions with nuclei to produce permanently displaced atoms. Details of the displacment cross-section and damage rate calculations are given in standard texts[3]. However, recent refinements to the simple calculations[4] have been applied

by Marwick[5,6] who derived details of the recoil spectra for various regimes of radiation damage used in simulation experiments. Although the mean transferred energy is only a few hundred eV during 4 MeV proton bombardment the form of radiation damage in niobium is not widely different from neutron or heavy ion damage as can be seen from Fig.1, which shows the proportion of displacements produced by recoils of energy less than T as a function of T, the primary knock-on energy, for proton, self ion and C.T.R. neutron bombardment.[7] In the case of a reactor over 90% of the damage is created in niobium by using recoils with energies greater than 1 keV, whereas in the case of 4 MeV protons as much as 60% of the total damage is created by recoils with energies greater than this.

In a typical experiment using a beam density of 10 $\mu A\ cm^{-2}$ the damage rate will be $\sim$1 dpa per 100 hours at 4 MeV. This damage rate is reasonably uniform throughout a 25 μm thick specimen being about 30% higher at the exit surface where the beam energy has fallen by about 1.5 MeV. With the present apparatus it is not possible to bombard the whole specimen uniformly without scanning the proton beam. A beam spot of similar dimensions to the specimen width (4 mm) is scanned over the gauge length (25 mm) at 500 Hz; the instantaneous damage rate can therefore be up to about 5 times the average rate. On the other hand since only $\sim 2 \times 10^{-3}$ s elapses between successive periods of irradiation at any point along the gauge length, negligible enhanced vacancy diffusion ($D' \sim 10^{-15}\ cm^2 s^{-1}$) will occur in these intervals.

An additional feature of the 14 MeV neutron environment to be taken into account in simulation experiments is the inevitable build-up of transmutation products during the irradiation. In particular, helium production from (n,α) reactions is perhaps the most significant, where helium concentrations of up to 1000 ppm can accumulate. As in the case of simulating void swelling, the helium can be pre-injected uniformly throughout the sample prior to the creep tests. It should also be pointed out that the facility can also be used to study irradiation creep in samples previously neutron irradiated to high doses.

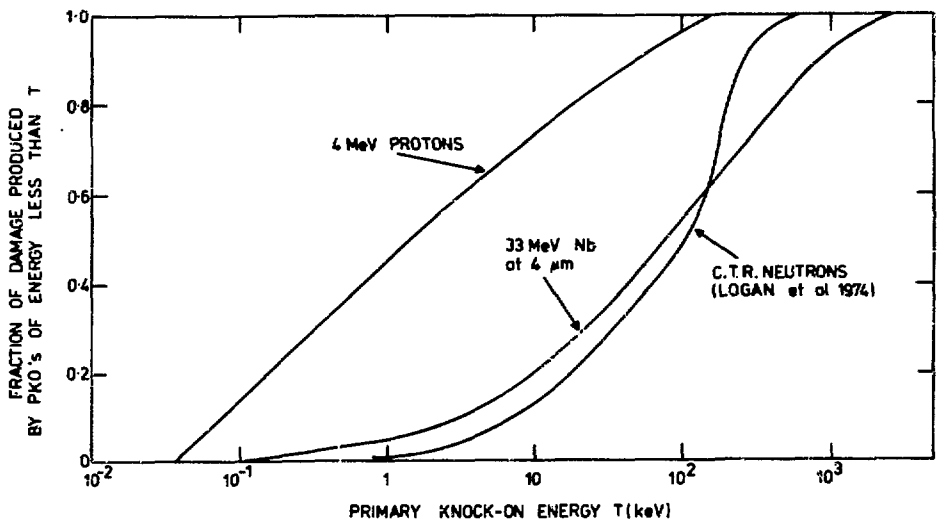

Fig. 1 Proportion of Recoils of Energy less than Primary Knock-On Energy T as a function of T.

EXPERIMENTAL DETAILS

The proton beam is obtained from the Harwell vertical axis Van de Graaf accelerator via a 90° analysing magnet and the beam line optics are arranged so that a focussed spot ~4 mm diameter can be obtained in the plane of the specimen. The specimen is held in a tensile creep apparatus contained in a helium gas enclosure separated from the beam line by a 2.5 μm thick molybdenum window. Variable amplitude horizontal (60 Hz) and vertical (500 Hz) axis electrostatic scanners and beam collimators enable the beam to be profiled to the specimen gauge length (2.5 cm x 0.4 cm). This is particularly important since the temperature profiles arising from beam and DC heating of the specimen gauge length must be accurately matched to avoid steps in strain that would otherwise accompany variations in beam current.

The 25 μm thick creep specimen is held in tension between flat water cooled jaws and the length change continuously monitored by a Linear Variable Differential Transformer (LVDT) having a resolution of 2.5×10^{-6} cm. The strain measuring system is illustrated in Fig.2 and a schematic representation of the beam handling and temperature control systems is given in Fig.3 together with a summary of the various monitoring facilities. Also illustrated in Fig. 3 is a temperature stabilised water circuit which is used to cool the strain measuring system, beam collimators and tantalum beam stop. This is necessary since normal ambient temperature changes and beam heating of the helium environment ultimately limit the strain resolution.

Specimen temperature is sensed by two infra-red pyrometers and the output of one of these, a Barnes RM2A pyrometer with a resolution of better than 0.1°C at 500°C, is used to control temperature during creep via a DC power supply connected across the upper and lower jaws. Position and amplitude fluctuations occur in the proton beam with rise times of 1 to 10 ms and the thermal time constant of a stainless steel specimen at 500°C has been determined as about 300 ms. In order to achieve the optimum temperature control at these response times a three term control system was developed[8] giving control of ± 0.2°C at 500°C at a maximum

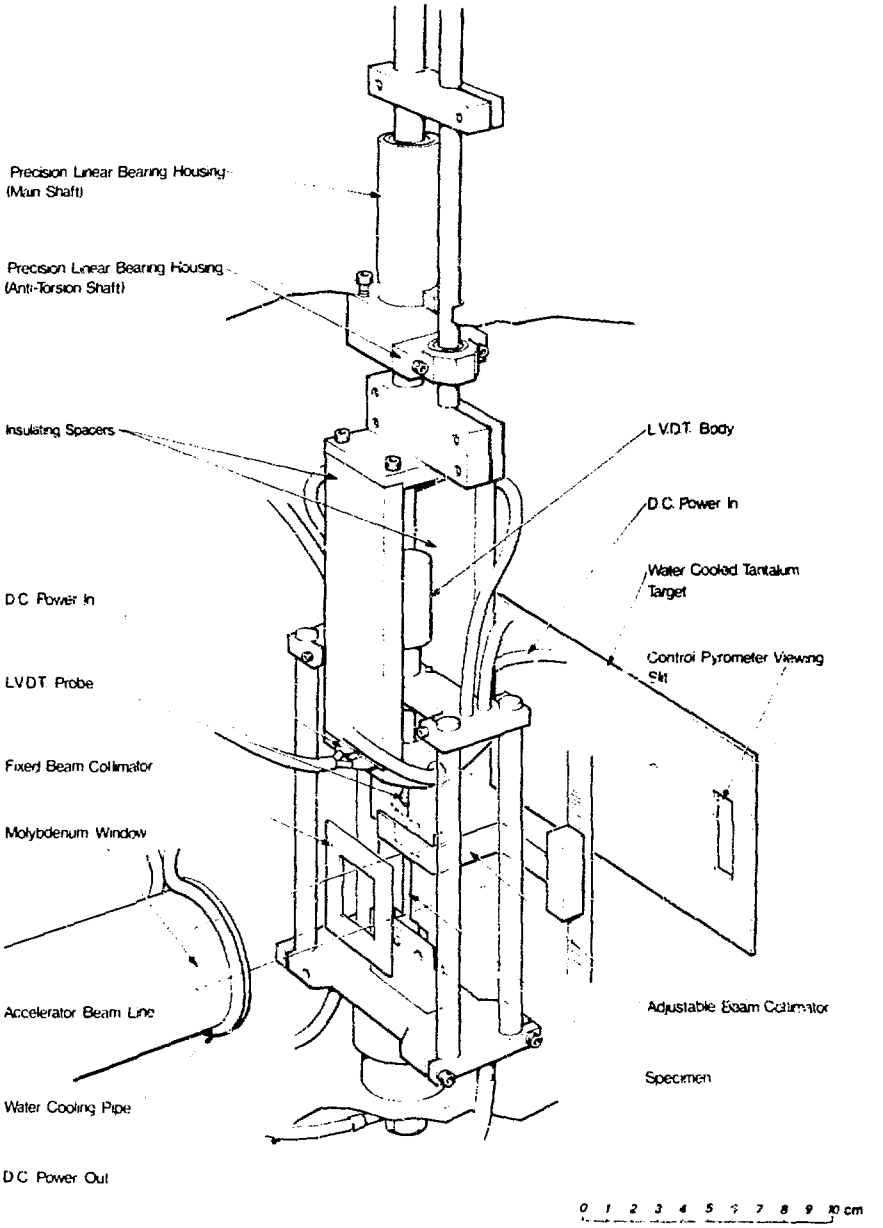

Fig. 2 Strain Measuring System of Irradiation Creep Apparatus.

power dissipation ~11W. In practice the maximum permissible beam current depends on the irradiation temperature required for the experiment. For good temperature control below 550°C the maximum displacement rate obtainable is about 1×10^{-6} dpa s^{-1} (for a displacement energy of 40 eV).

The general characteristics of the irradiation creep apparatus are summarised in the table below.

Table 1. Some Parameters of the Irradiation Creep Apparatus

Irradiation Regime	4 - 5 MeV H^+
Beam Current	0 → 10 μAmp cm^{-2}
Irradiated Area	2.5 cm x 0.4 cm
Specimen Thickness	25 - 30 μm
Damage Rate	0 → 2×10^{-6} dpa per sec
Dose Range	0 → 1 dpa
Temperature Range	300 → 1000°C
Temperature Determination	± 5°C
Temperature Control	± 0.2°C
Strain Sensitivity	5×10^{-6}
Stress Range	0.5 MPa → UTS of Specimen

RESULTS AND DISCUSSION

Early experiments have been carried out to test the apparatus and determine the limits to temperature control and strain measurements. Nickel specimens have been tested over the temperature range 400 - 650°C at stresses of 20 - 200 MPa under thermal and irradiation creep conditions. The relatively high stresses and creep rates ($>10^{-5} h^{-1}$) so far employed, place the experiments in the dislocation creep regime. The thermal creep behaviour of thin specimens was found to be consistent with previous studies in bulk material. For example, the temperature dependence of the secondary creep rate over the range 450 - 650°C gave an activation energy of 2.8 eV in good agreement with values determined from self-diffusion experiments.

In general, two basic phenomena have been identified in the irradiation creep tests; firstly thermal creep is gradually reduced as the damage accumulates, and secondly an irradiation creep well in excess of the thermal component is produced. In the present paper we will limit our discussion to irradiation enhanced creep.

Figure 4 illustrates the general trend which has been observed in all the irradiation experiments with nickel where the irradiation creep rate steadily decreased with increasing dose. In Fig.4 the measured creep strain is plotted against log.(1+ time)for specimens bombarded at 500°C at a damage rate of 7×10^{-7} dpa s^{-1} under tensile stresses of 75, 100 and 125 MPa respectively, and a linear relation is obtained. This behaviour and the relatively large creep rates observed are characteristic of strain developing by dislocation slip. This is in contrast to the mechanisms of assisted climb proposed for irradiation enhanced creep at stresses and temperatures where thermal creep is negligible. In this case a relatively low steady state creep rate, linearly dependent on stress and independent of dislocation density has been predicted[9]. Experiments are now in progress to investigate this regime of irradiation creep with cold-worked stainless steel specimens.

Specimens for transmission electron microscopy have been prepared from several Ni specimens bombarded to 0.2 - 0.4 dpa in the temperature range 450 - 500°C under stresses in the range 40 - 100 MPa. The structures observed in these specimens also suggest dislocation slip as the overiding contribution to the strain. In all cases long dislocation segments intersecting and bowing between a dislocation loop population were observed. Most of the loops were unfaulted and many of the line segments were seen to have originated as large loops when thicker specimens were examined at 1MV in the Harwell High Voltage Electron Microscope. Unstressed specimens bombarded to similar doses at these temperatures do not show such line segments and usually a greater proportion of the small loops are sessile. An example of the structure observed in a stressed specimen is shown in Fig. 5 which is a transmission electron micrograph from a Ni specimen bombarded to 0.3 dpa at 500°C under a tensile stress of 50 MPa. The loops have a mean diameter of 280 Å

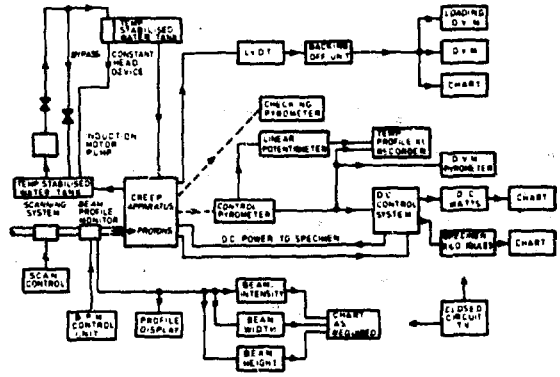

Fig. 3 Schematic Layout of Beam Handling and Temperature Control System.

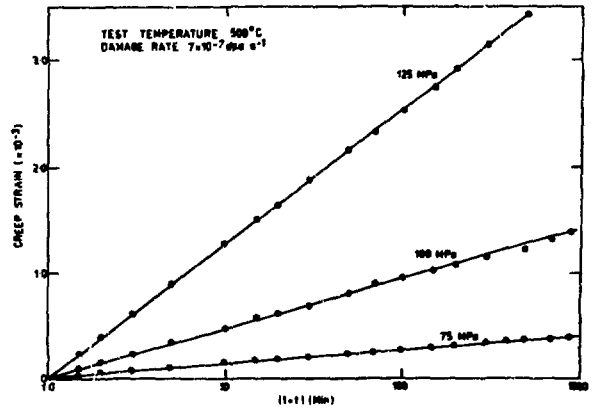

Fig. 4 Irradiation Creep Strain versus log. (1 + time) for Ni specimens bombarded at 500°C under various stresses.

and are present in a concentration of 5×10^{14} cm^{-3}. There was no evidence of significant preferential alignment of loops in any of the specimens investigated.

In Fig. 6 we show the variation of irradiation creep rate (measured after 40 h irradiation) with damage rate, where at 550°C under a stress of 100 MPa a linear dependence in the range $1 - 10 \times 10^{-7}$ dpa s^{-1} was detected.

These preliminary results suggest that the experimental technique has been developed to an extent such that reliable data on the mechanisms of irradiation creep can be usefully studied during 4 MeV proton irradiation. It is too early to make significant deductions at this stage; however some general comments would not be out of place. For instance there is evidence that significant irradiation hardening occurs which steadily reduces both thermal and irradiation creep rates as the irradiation dose builds up. Whether or not a steady state irradiation creep rate will be reached, will depend on the saturation in the dislocation network which forms during irradiation. From our experience in the field of void swelling this occurs around ~10 dpa; however, at this dose void swelling itself may further limit the irradiation creep.

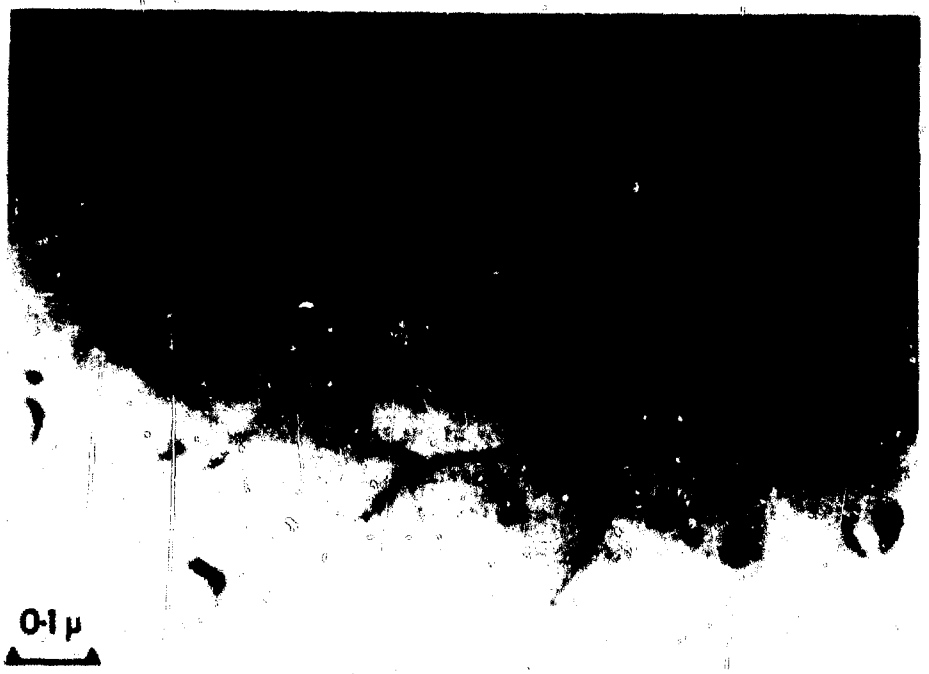

Fig. 5 Transmission electron micrograph for a Ni Specimen bombarded to 0.3dpa at 500°C under a Tensile Stress of 50 MPa

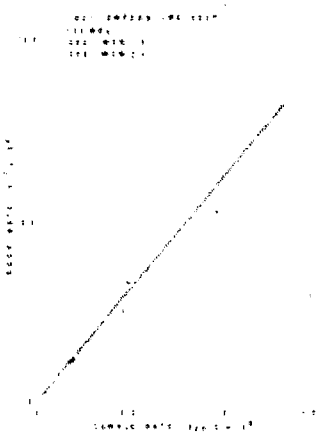

Fig. 6 Irradiation Creep Rate (after 40h) versus Damage Rate for Specimens bombarded at 550°C under a Tensile Stress of 100 MPa.

REFERENCES

1. S.D. Harkness, F.L. Yaggee and F.V. Nolfi in Proceedings of Conf. on "Irradiation Embrittlement and Creep in Fuel Cladding and Core Components" BNES, London 1973, pp259-266

2. P.L. Hendrick, D.L. Michel, A.G. Pieper, R.E. Surratt and A.L. Bement, NRL Memorandum Report 2996, 1975.

3. M.W. Thompson, "Defects and Radiation Damage in Metals", CUP, 1969.

4. M.J. Norgett, M.T. Robinson and I.M. Torrens, AERE Report TP 494,1972.

5. A.D. Marwick, J. Nucl. Mat. 55, 259, 1975

6. A.D. Marwick, J. Nucl. Mat. 56, 355, 1975.

7. C.M. Logan, J.D. Anderson and Z.A. Munir, Nucl. Tech. 22 36, 1974.

8. M.H. Brown, AERE PE MEMO 685, 1975.

9. R. Bullough and M. R. Hayns, AERE Report TP616, 1975.

ION-SIMULATED IRRADIATION-INDUCED CREEP OF NICKEL

P. L. Hendrick D. J. Michel
A. G. Pieper R. E. Surratt
Naval Research Laboratory
and
A. L. Bement, Jr.
Massachusetts Institute of Technology

ABSTRACT

An experimental apparatus has been designed and constructed at the Naval Research Laboratory to measure the ion-simulated irradiation-induced creep of uniaxial tensile specimens bombarded by ions from the NRL Sector-Focusing Cyclotron. High purity nickel tensile specimens were bombarded with 22 MeV deuterons and 70 MeV alpha particles at displacement rates ranging from 13 to 30 x 10^{-3} displacements per atom per second. The experimental technique which was developed during the course of this investigation allowed creep rate to be measured with an on-line computer while temperature, stress, and flux were maintained at the desired level. Irradiations were conducted at 224 C (435 F) and at stresses ranging from 170 to 345 MPa (24,700 to 50,100 psi).

The results obtained demonstrated that charged particle irradiations can successfully be used to simulate irradiation-induced creep in bulk material. Preliminary data is in agreement with a linear flux dependency and suggest a linear to squared dependence on stress over the range investigated. A comparison of deuteron and alpha particle irradiation test results suggests a lower irradiation effect per displaced atom on irradiation-induced creep rate during alpha particle irradiations. A climb-controlled creep model is in agreement with the irradiation-induced creep observed.

INTRODUCTION

An important aspect in the development of advanced breeder and controlled thermonuclear reactors is the prediction of irradiation effects on material properties. Materials will be subjected to unprecedented levels of

radiation damage at elevated temperatures. The dimensional stability of these materials is expected to be limited by the inter-related phenomena of thermal creep, irradiation-induced creep, void swelling, and growth. The accurate assessment of the effect of these phenomena on reactor structural materials over the reactor lifetime is considered essential to reactor designers. Furthermore, the allowance of design margins large enough to incorporate present uncertainties in these effects would place severe economic penalties on reactor performance.

Unfortunately, there exists a lack of irradiation test facilities capable of approximating the environmental conditions of advanced reactor designs. The shortage of test facilities coupled with the long construction lead times, poses a serious dilemma to the successful design of both a fast breeder reactor and, in the longer term, a controlled thermonuclear reactor. However, in the case of the void swelling phenomenon, the charged particle or ion-simulation of neutron irradiation has been used extensively over the past several years in order to develop an understanding of this phenomenon. More recently, it has been demonstrated that charged particle irradiations can be used to simulate irradiation-induced creep under well-controlled conditions[1-4]. Charged particle simulation of irradiation-induced creep offers the potential of fast and efficient irradiation of materials under a variety of controlled conditions in order to gain an understanding of the creep mechanisms involved. Likewise, materials can be efficiently screened as an aid in developing creep-resistant materials.

An experimental apparatus has been constructed at the Naval Research Laboratory, for the purpose of measuring the ion-simulated irradiation-induced creep rate of specimens placed under stress and maintained at constant temperature during charged particle irradiation. Preliminary irradiation

tests validated the technique chosen and provided confidence in the reproducibility of test results[5]. Additional tests are now underway in an effort to characterize the irradiation-induced creep behavior of pure nickel as a function of stress, temperature, and ion flux. Preliminary results of that characterization are presented at this time along with a possible operating creep mechanism.

EXPERIMENTAL TECHNIQUE

General

As reported previously in greater detail[6], an experimental technique has been developed by which the irradiation-induced creep rate of uniaxial tensile specimens, placed under stress and maintained at constant temperature, can be measured during charged particle irradiation.

As illustrated in Fig. 1, the load is applied to the specimen within a vacuum chamber through a lever arm arrangement. A liquid reservoir suspended from the lever arm can be filled or drained to vary the specimen load. The load is monitored remotely by a load cell mounted in the load train below the vacuum chamber. The instantaneous length of the specimen is monitored by three linear variable displacement transformers (LVDTs) which sense pullrod motion external to the vacuum chamber. Two LVDTs are located on opposite sides and at 45 degrees to the plane of the specimen in order to sense any bending moments which may occur in the specimen. The average of the two LVDTs equals the average displacement of the specimen provided extraneous thermal expansions do not occur in the grips, pullrods, or extension rods. The third LVDT senses the average displacement of the specimen directly. This is accomplished by incorporating the magnetic core of the LVDT into the load train below the vacuum chamber.

All functions of the apparatus are remotely controlled and are interfaced with an on-line computer to permit monitoring

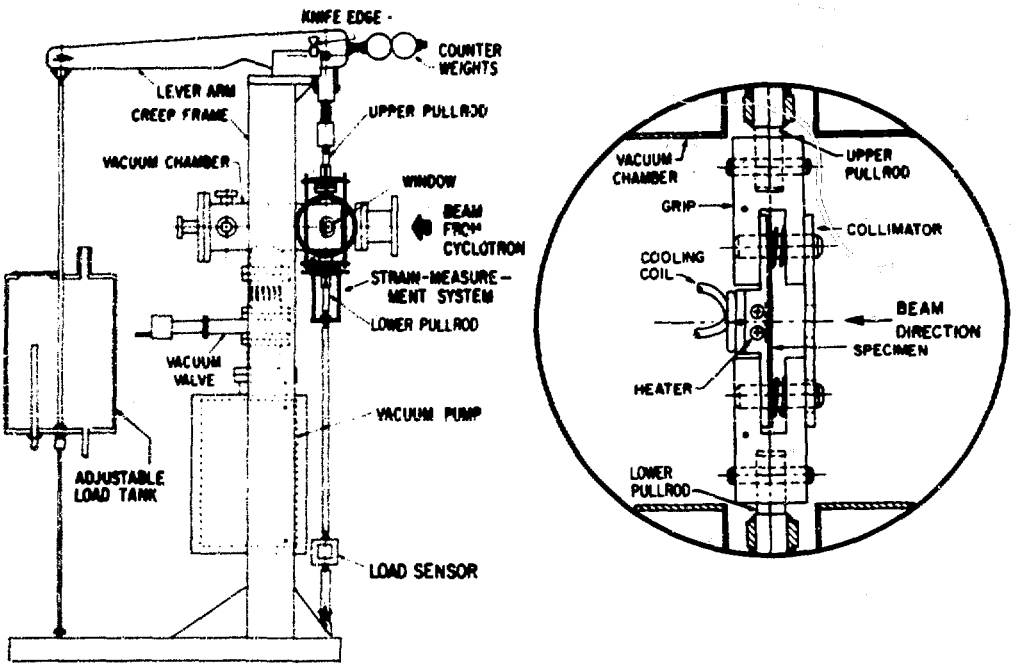

Fig. 1. Ion-Simulated Irradiation-Induced Creep Experimental Apparatus.

and recording of all experimental parameters. These control systems include the specimen temperature control system, the purpose of which is to remove irradiation-induced heat and maintain the specimen temperature at the desired set-point, the pullrod temperature control system, and the environmental temperature control system. The need for care in temperature control is a direct result of the desire to resolve low creep rates during irradiations as short as ten hours. For example, if the average specimen temperature were allowed to vary by as much as one degree centigrade, it would take approximately one hundred hours to resolve a creep rate of 10^{-5} cm/cm/hr to within 10%. This same analogy applies to a greater or lesser degree to each component of the load train and strain measuring system. Therefore, each of these temperature control systems is required in order to achieve less than approximately 2.5×10^{-5} cm (1×10^{-5} in.) long-term displacement resolution.

Specimen Design

Nickel was initially chosen as the specimen material due to the high irradiation-induced creep rate observed by others[2,4,7,8]. The high creep rates would facilitate development of the apparatus and make meaningful results available at the earliest possible date. In addition, results for nickel would be more easily interpretable to permit a more fundamental understanding of the creep mechanisms involved than would a complex alloy such as austenitic stainless steel. Furthermore, nickel is face-centered-cubic (fcc) as is austenitic stainless steel and represents a major constituent of stainless steel. All of these considerations then make nickel an ideal starting point in the investigation of irradiation-induced creep.

In order to determine the stress dependency of irradiation-induced creep rate, it was desired to have a simple and uniform state of stress. For this reason, a uniaxial tensile specimen design was chosen. Following computer calculations of the displacement damage profile of 70 MeV alpha particles on

nickel, using a modified version of the Code E-DEP-1[9], a specimen thickness of 0.38 mm (0.015 inches) was chosen. This decision resulted in a thickness typical of proposed fast breeder reactor cladding and minimized the severity of the displacement damage gradient through the specimen. A preliminary specimen design permitted several irradiation tests to be conducted. During these tests it was found that a beam height of approximately 1.27 cm (0.5 inch) could be readily obtained. Beam profile measurements were made using a modified wire profile scanner developed previously[10]. Therefore, the specimen gauge length was fixed at 1.27 cm (0.50 inches) with a 0.318 cm (0.125 inch) gauge width as shown in Fig. 2. Properties of the nickel specimen material are tabulated in Table 1.

Table 1. Specimen Material Properties

Property	Specimen
Material	nickel
Purity (w/o)	99.995
As-received Dimensions	
Thickness (cm/in.)	0.038/0.015
Width (cm/in.)	2.54/1.00
Length (cm/in.)	61/24
Vendor	Materials Research Corp.
Manufacturer	Materials Research Corp.
Grade	MARZ
Lot Number	28-2236
Metallurgical Condition	95% cold-worked
Grain Size (mm^{-2})	1.3
Yield strength (MPa/ksi) (at 20°C and 0.13 cm/min strain rate)	585/85

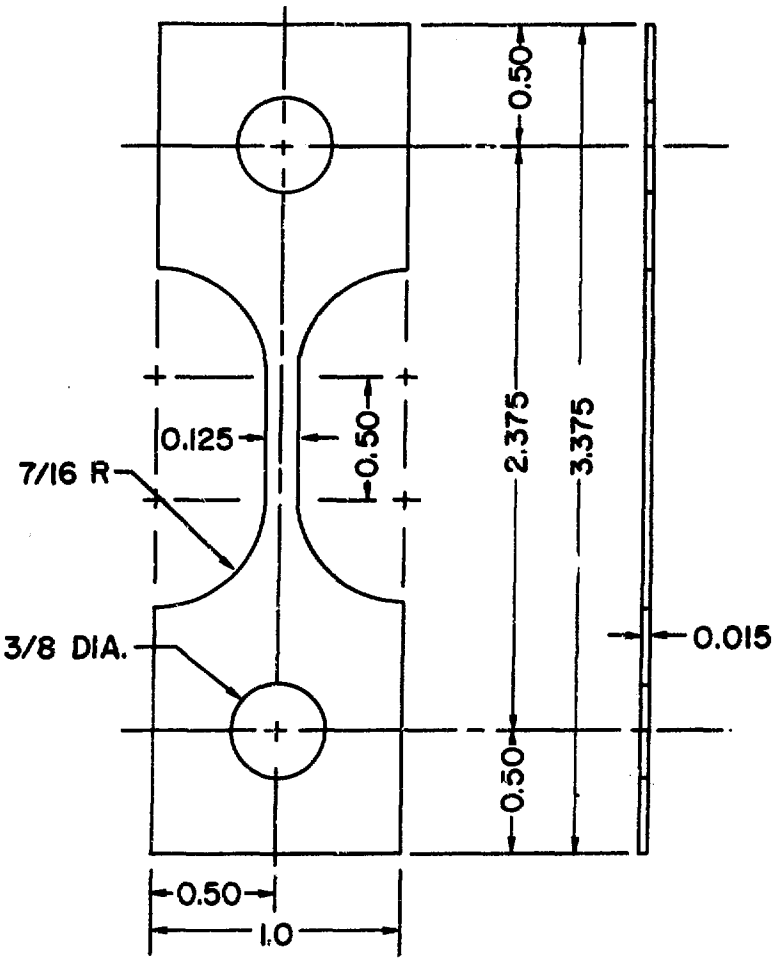

Fig. 2. Irradiation-Induced Creep Tensile Specimen.

RESULTS

Radiation Damage Analysis

As a beam of energetic ions enters the specimen it is considered to lose energy by two separate mechanisms: elastic and inelastic interactions. The inelastic interactions leave the atom on the target in an excited state, but do not result in a movement of the atom from its lattice site. The excitation energy provided is eventually dissipated as heat without creating radiation damage. Elastic collisions, however, can result in the transfer of sufficient momentum from the charged particle to the lattice atom to result in the creation of a primary knock-on atom (PKA) as it is sometimes called. The PKA itself becomes an energetic ion which produces a cascade of displaced atoms often referred to as a displacement spike. It is these displaced atoms which are thought to result in the radiation damage.

A computer program, E-DEP-1, has been developed at the Naval Research Laboratory to calculate the energy loss to displacements for heavy ions[9]. This code has been modified for the creep simulation study to treat the case of light ions ($Z \leq 2$) with energies up to 70 MeV. E-DEP-1 calculates the energy deposited in the creation of displacement damage to the lattice atoms as a function of penetration distance. In order to perform this calculation, the code required both the elastic (nuclear) and inelastic (electronic) stopping power laws. Although the nuclear stopping power is valid for the case of light ions, the electronic stopping power chosen[11]:

$$\left(\frac{dE}{dx}\right)_e = KE^{1/2}, \qquad (1)$$

where

$\left(\frac{dE}{dx}\right)_e$ = electronic stopping power

K = constant

E = energy

is not. In fact, the criterion for validity of this law is that the energy of the ion beam must be less than E_{LIM} given by:

$$E_{LIM} = 0.02481\ A_1 Z_1^{4/3}\ (MeV) \qquad (2)$$

where

A_1 = atomic mass of ion

Z_1 = atomic number of ion.

For the case of deuterons and alpha particles, this results in:

$$E_{LIM\ d^+} = (0.02481)(2)(1) = 0.0496\ MeV$$

$$E_{LIM\ \alpha^{++}} = (0.02481)(4)(2.52) = 0.250\ MeV$$

and, therefore, the electronic stopping power chosen is invalid for the 22 MeV deuterons and 70 MeV alpha particles used in this study over most of their energy range. For this reason, the subroutine, ELCLAW of E-DEP-1 which calculates the electronic stopping power was modified in such a way that for energies less than E_{LIM} the electronic stopping power given by Eq. (1) was utilized. For higher energies the Bethe-Bloch formalism[12] given by:

$$\left(\frac{dE}{dx}\right)_e = \frac{4\pi^4 Z_1^2 Z_2 N}{m_o V^2}\left[\ln\frac{2\,m_o V^2}{I} - \ln(1-\beta^2) - \beta^2\right] \qquad (3)$$

where

e = electronic charge

Z_2 = atomic number of target atom

N = atom density of target

m_o = electron rest mass

V = ion velocity

I = ionization potential

β = ratio of V to speed of light, $\beta = V/c$

was utilized. However, since the lower energy of validity for the stopping power given by Eq. (3) is often above the

upper energy of validity for the stopping power given by Eq. (1), a constant stopping power approximation was used to bridge the gap. The value of the constant was made equal to the value given by the Bethe-Bloch expression at the lowest energy of validity. Thus the code chose the appropriate electronic stopping power for the beam ion energy and calculated the energy deposition profiles accordingly.

In addition to the modification of subroutine ELCLAW, the maximum beam ion energy for which the code will calculate energy deposition curves was increased from 50 to 70 MeV. In order to test the validity of the modifications made, the ranges given by the code were compared with both theoretical and experimental values. This test of validity should be a reasonable one since the ranges are determined to a large degree by the electronic stopping law chosen. Agreement to within the approximations inherent in the code was found[13].

Once the code was run and the curve of energy deposited into the creation of displacements as a function of penetration distance was calculated, use was made of the following expression[14]:

$$\int_o^\infty \rho(x)\ dx = \frac{\eta}{2E_d} \int_o^\infty S_D(x)\ dx \qquad (4)$$

where

$\rho(x)$ = density of displaced atoms at depth, x

η = constant $\simeq 0.8$

E_d = average energy required to create a single displacement $\simeq 40$ eV for nickel

$S_D(x)$ = energy deposition at depth x calculated by modified version of E-DEP-1.

If the assumption is made that the PKA ranges are small compared to the ion range, then Eq. (4) implies:

$$\rho(x) \simeq \frac{\eta S_D(x)}{2E_d} \quad \text{displacements/micron/particle.} \qquad (5)$$

of more interest, however, is the displacement rate per atom (dpa/sec) for a given particle flux. Therefore one must multiply Eq. (5) by the particle flux and divide by the atom density of the target and ion charge to obtain:

$$R_D = 6.24 \times 10^{20} \frac{S_D(x)\varphi}{N Z_1} \qquad (6)$$

where

R_D = displacement rate, dpa/sec
$S_D(x)$ = energy deposition in target, MeV/μ
φ = ion flux, $\mu a/cm^2$
N = atom density of target, atoms/cm^3
Z_1 = electronic charge.

The modified version of E-DEP-1 was run for several cases of interest and the displacement rates were calculated from the energy deposition profiles, $S_D(x)$, using Eq. (6). Figure 3 shows these profiles for several cases of interest. The curves for 3 and 5.25 MeV protons on nickel represent the work of a previous study[4]. The curve for 18 MeV protons on nickel represents an irradiation planned to gain insight into the effect of irradiating particle. The curves for both 22 MeV deuterons and 70 MeV alpha particles represent irradiations performed in this study. In addition, the curve for 22 MeV deuterons is a reasonable approximation to the case of 22 MeV deuterons on stainless steel utilized by Harkness, et al[3]. The displacement damage in stainless steel would be approximately 14% lower than that in nickel. However, the use of a variable energy degrader (gray wedge) by Harkness et al.[3] would have had the effect of raising the curve somewhat. Also indicated in the figure for the case of 70 MeV alpha particles on nickel is the "equivalent" thicknesses of nickel introduced by the aluminum beam window, air gap, and copper beam window of the beam transport system. As shown, the intense damage peak near the end of range occurs in the heat sink transfer film. Displacement rates averaged across

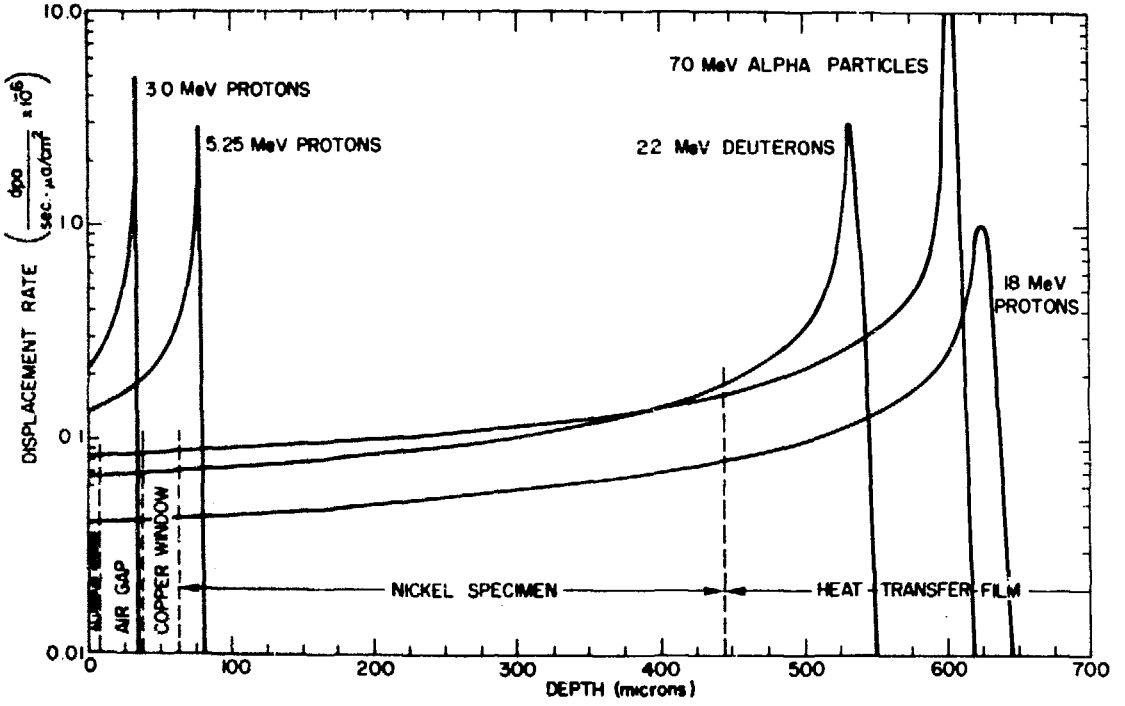

Fig. 3. Displacement Rate Profiles in Nickel for Protons, Deuterons, and Alpha Particles.

the thickness of the specimen were calculated for several cases of interest and are presented in Table 2. For comparison the displacement rate of the Dounreay Fast Reactor is listed[15,16].

Table 2. Average Displacement Rates

Particle	Energy (MeV)	Range (microns)	Material	Specimen Thickness (microns)	Average Displacement Rate (dpa/sec x10^8)
protons	3	32	Ni	25.4	32[b]
	5.25	77	Ni	76.2	25[b]
	18	628	Ni	381	5.7[b]
deuterons	22	536	Ni	381	10.1[b]
alpha particles	70	602	Ni	381	11.3[b]
DFR	0.416[a]		Various	-	63.9[c]

[a] average energy given, where $E = \frac{\int_0^\infty E\varphi(E)\,dE}{\int_0^\infty \varphi(E)\,dE}$.

[b] for ion beam flux of 1 $\mu a/cm^2$.

[c] corresponds to total neutron flux = 1.17×10^{15} neutrons/cm^2 x sec and displacement cross section = 516 barns.

Sources of Error

Any parameter which was found to affect strain and vary enough during a test to have a measurable effect on strain was treated as a critical parameter. An attempt to monitor these critical parameters and correlate them with strain was made. If correlations were difficult or not reproducible, error bars were assigned in order to account for measured variations. If correlations proved successful, corrections were made to the data assuming variations in the critical parameter warranted such correction during a particular test.

The critical parameters, considered elsewhere in detail[6], were load, specimen temperature, grip temperature, pullrod

temperature, and apparatus environmental temperature. Sensitivity coefficients were determined for each of these parameters and then used in conjunction with measured variations in these parameters during a test to calculate errors. It is recognized that other errors not treated explicitly may affect the results. In general, however, these errors are expected to be small compared to those mentioned above. Displacement errors were converted to strain errors by dividing through by the specimen gauge length of 1.27 cm (0.5 in.). In addition, since errors given were total errors, they were divided by two and tabulated as plus or minus. Errors applied to creep rates were divided by the time period over which the rate was derived. For this reason, the errors in steady-state creep rate were typically smaller than those in transient creep rate.

Presentation of Data

Data taken during an irradiation creep test appear similar to that shown in Fig. 4. The tests shown (4D-5-1 and 4D-5-2)* represent an irradiation of nickel with 22 MeV deuterons. The temperature was 224°C (435°F), the stress was 345 MPa (50,120 psi) and the ion flux was 1.34 $\mu a/cm^2$ which was equivalent to a calculated displacement rate of 13.53×10^{-8} dpa/sec. The data shown represents two irradiations conducted at 224°C (435°F) separated by a 40 hour stabilization period due to the unavailability of the cyclotron. As indicated, recovery was not observed under these conditions. The lighter strain trace shown represents the actual strain as measured by the large-bore LVDT while the heavy trace represents a smooth approximation to the data with corrections applied for the systematic error introduced by changes in grip temperature. Also shown for reference is the ion flux and the stress. Although a total of three inadvertent beam-off periods occurred in test 4D-5-1, no

*Test designation: material number-specimen number-test number

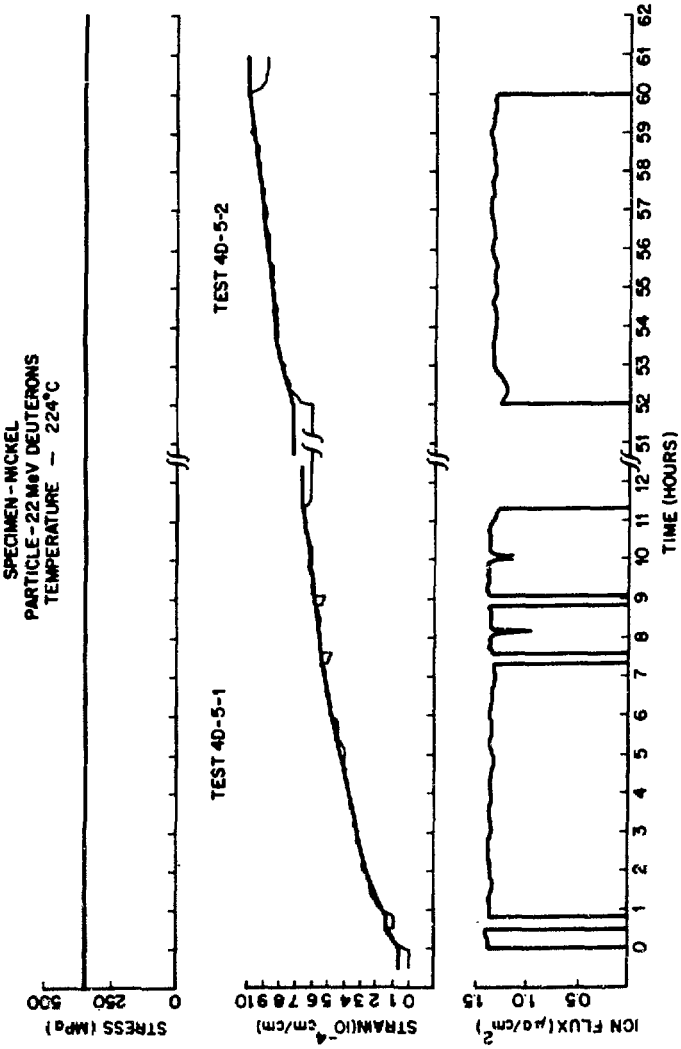

Fig. 4. Irradiation-Induced Creep Tests 4D-5-1 and 4D-5-2.

beam-off periods occurred during test 4D-5-2. As indicated, strain resolution was preserved once the beam was restored on target. Transient creep rate was measured at one hour, for convenience, and was 11.6×10^{-5} cm/cm/hr for test 4D-5-1. Steady-state creep rate* as measured from test 4D-5-2 was 2.7×10^{-5} cm/cm/hr which was only 1.5% lower than the final rate measured for test 4D-5-1. Thus it would appear that transient creep saturated within approximately 12 hours.

The test conditions have been summarized in Table 3. Since two or more irradiation tests were typically conducted on the same specimen under the same conditions in order to achieve steady-state creep and verify reproducibility, several irradiation tests can constitute a single creep test. Irradiation tests have been so grouped in Table 3. Test results and errors are presented in Table 4. All parameters relating to transient creep were derived from the first and/or second irradiation test of a series. Parameters relating to steady-state creep were derived from the last test in a series. Total irradiation time includes all irradiation tests within a given series.

Both primary and steady-state creep rates have been plotted as a function of stress in Fig. 5. The lines drawn through the data correspond to a stress dependency of $n = 1.67$ ($\dot{\epsilon}=\sigma^n$) in the case of the alpha particle irradiations and $n = 2$ in the case of the deuteron irradiations. The primary creep rate observed in test 4D-2-3 is considered low due to the fact that steady-state creep had been achieved in a previous test (4D-2-2) at a lower stress which had the effect of suppressing primary creep somewhat at the higher stress level. Primary and steady-state creep rates have been plotted as a function of ion beam flux in Fig. 6. The line

*The steady-state creep rate, as used in this study, may well be temporal in nature (i.e., specimens irradiated to much greater fluence levels may exhibit lower values of steady-state creep rate due to hardening effects).

Table 3. Summary of Irradiation-Induced Creep Test Conditions

Test[a]	Date	Temperature (°C)	Temperature (°F)	Stress (MPa)	Stress (ksi)	Particle	Energy (MeV)	10N Flux ($\mu a/cm^2$)	Displacement Rate (dpa/sec) x 10^8
4D-2-1	5-30-75	224	435	287	41.72	α^{++}	70	2.69	30.40
4D-2-2	5-31-75	224	435	287	41.72	α^{++}	70	2.69	30.40
4D-2-3	6-4-75	224	435	345	50.12	α^{++}	70	2.69	30.40
4D-2-4	6-6-75	224	435	345	50.12	α^{++}	70	2.69	30.40
4D-2-5	6-7-75	224	435	345	50.12	α^{++}	70	2.69	30.40
4D-3-1	6-13-75	224	435	170	24.70	α^{++}	70	2.69	30.40
4D-3-2	6-14-75	224	435	170	24.70	α^{++}	70	2.69	30.40
4D-4-1	6-20-75	224	435	345	50.12	d^{+}	22	2.69	27.17
4D-4-2	6-21-75	224	435	345	50.12	d^{+}	22	2.69	27.17
4D-5-1	6-25-75	224	435	345	50.12	d^{+}	22	1.34	13.53
4D-5-2	6-27-75	224	435	345	50.12	d^{+}	22	1.34	13.53
4E-1-1	7-1-75	224	435	170	24.70	d^{+}	22	2.69	27.17
4E-1-2	7-2-75	224	435	170	24.70	d^{+}	22	2.69	27.17
4E-2-1	7-8-75	224	435	207	30.00	d^{+}	22	2.69	27.17
4E-2-2	7-9-75	224	435	207	30.00	d^{+}	22	2.69	27.17
4E-4-1	7-15-75	224	435	247	35.95	d^{+}	22	2.69	27.17
4E-4-2	7-17-75	224	435	247	35.95	d^{+}	22	2.69	27.17

[a] Test designation: material number-specimen number-test number

Table 4. Irradiation-Induced Creep Test Results

Test	Total Transient Strain (10^{-5} cm/cm)	Total Transient Time (hours)	Primary Creep Rate[a] (10^{-5} hr^{-1})	Total Strain (10^{-5} cm/cm)	Total Irradiation Time (hours)	Steady-State Creep Rate (10^{-5} hr^{-1})
4D-2-1 4D-2-2	52 ± 1.6	6.5	11.5 ± 1.6	82 ± 3.1	15.8	3.3 ± 0.5
4D-2-3 4D-2-4 4D-2-5	102 ± 2.1	13.3	9.8 ± 2.1	152 ± 2.6	25.0	4.3 ± 0.2
4D-3-1 4D-3-2	22 ± 3.0	5.7	6.4 ± 3.0	36 ± 3.0	17.8	1.2 ± 0.2
4D-4-1 4D-4-2	108 ± 3.2	9.5	18.4 ± 3.2	172 ± 3.2	23.1	4.8 ± 0.2
4D-5-1 4D-5-2	70 ± 2.6	12.7	11.6 ± 2.6	88 ± 2.6	18.7	2.7 ± 0.4
4E-1-1 4E-1-2	50 ± 4.1	10.8	6.4 ± 4.1	76 ± 4.1	19.3	1.8 ± 0.7
4E-2-1 4E-2-2	13 ± 2.1	4.0	4.6 ± 2.1	36 ± 2.1	21.0	1.4 ± 0.2
4E-4-1 4E-4-2	40 ± 2.5	9.0	6.0 ± 2.5	62 ± 2.5	17.0	2.6 ± 0.2

[a]Creep Rate at 1 hour

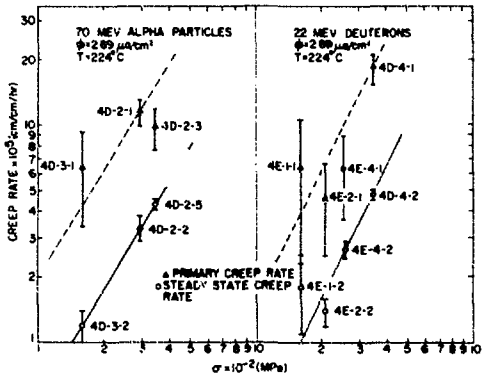

Fig. 5. Stress Dependency of Irradiation-Induced Creep Rate for Alpha Particle and Deuteron Irradiations.

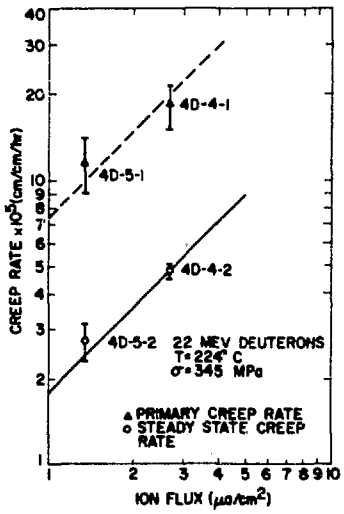

Fig. 6. Ion Flux Dependency of Irradiation-Induced Creep Rate for Deuteron Irradiation.

shown represents a linear fit to the data.

In order to plot alpha particle and deuteron data together as a function of stress, an equation of the form:

$$\dot{\epsilon} = C f_p R_D \sigma^n \qquad (7)$$

where

$\dot{\epsilon}$ = creep rate, primary or steady state
C = material constant
f_p = particle factor
R_D = displacement rate, dpa/sec
σ = stress, MPa
n = stress dependency exponent

was assumed. The particle factor f_p was used to account for differences in irradiating particle. In a physical sense, the particle factor should be proportional to the instantaneous point defect concentration contributing to creep. Since f_p is not known, absolutely, for either deuterons or alpha particles, it was arbitrarily set equal to one for deuterons. The particle factor was then found for alpha particles by equating the value of $\dot{\epsilon}/f_p R_D$ for runs 4D-4-2 and 4D-2-5. These runs were conducted at the same temperature, ion flux, and stress for deuterons and alpha particles, respectively. Therefore, it was reasoned that any differences should be attributed to the nature of the irradiating particle (i.e., displacement spike). The calculation as shown below results in:

$$\left(\frac{\dot{\epsilon}}{f_p R_D}\right)_{\alpha^{++}} = \left(\frac{\dot{\epsilon}}{f_p R_D}\right)_{d^+} \qquad (8)$$

$$(f_p)_{\alpha^{++}} = \frac{(\dot{\epsilon}/R_D)_{\alpha^{++}}}{(\dot{\epsilon}/f_p R_D)_{d^+}} \qquad (9)$$

$$(f_p)_{\alpha^{++}} = \frac{4.3\times10^{-5}/30.40\times10^{-2}}{4.8\times10^{-5}/(1)(27.17\times10^{-2}}\ ,$$

$$(f_p)_{\alpha^{++}} = 0.8\ .$$

Physically, this result would say that 20% fewer point defects at steady-state contributed to creep rate during alpha particle irradiation than during deuteron irradiation. This correlation scheme was then used to plot the data as a function of stress in Fig. 7. For the case of both steady-state and primary creep rate, a slope of n = 2 was indicated. For steady-state creep rate, a slope much less than this value becomes inconsistent with run 4E-2-2 and a slope much greater than this value becomes inconsistent with runs 4E-1-2 and 4D-3-2. For the case of primary creep rate the error bars were such that a lesser slope was inconsistent with 4E-2-1, but a somewhat greater slope (n=2.35) was consistent with the errors indicated. It is of interest to note, as indicated by the dashed line in Fig. 7, that a linear dependency of creep rate on stress in consistent with the data at lower stress (σ <200 MPa). This stress regime, however, must be more fully investigated in order to permit a definitive prediction of stress dependency.

Microscopy Results

Transmission electron microscopy (TEM) was used to investigate the microstructure of the irradiation-induced creep specimens. Examination of the pre-irradiation microstructure of the cold-worked nickel specimens indicated the presence of slip traces, deformation bands, and dislocation cells whose mean diameter was in the range from 0.8 μm to 1.2 μm. The mean dislocation density was estimated to be $>1 \times 10^{11}/cm^2$ with a considerably higher dislocation density in the dislocation cell walls. These values were also typical of unirradiated areas of tested specimens.

TEM examination of the postirradiation microstructure revealed a heterogeneous distribution of defect clusters, small dislocation loops, and random dislocations, and the presence of dislocation cells. An example is shown in Fig. 8 for a specimen irradiated with 70 MeV alpha particles to

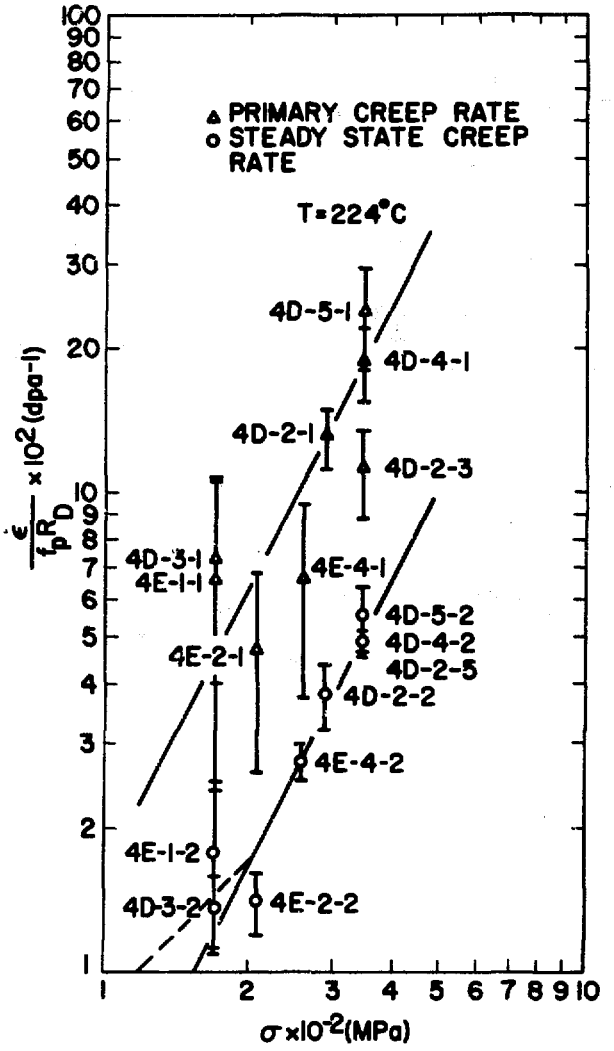

Fig. 7. Stress Dependency of Normalized Irradiation-Induced Creep Rate.

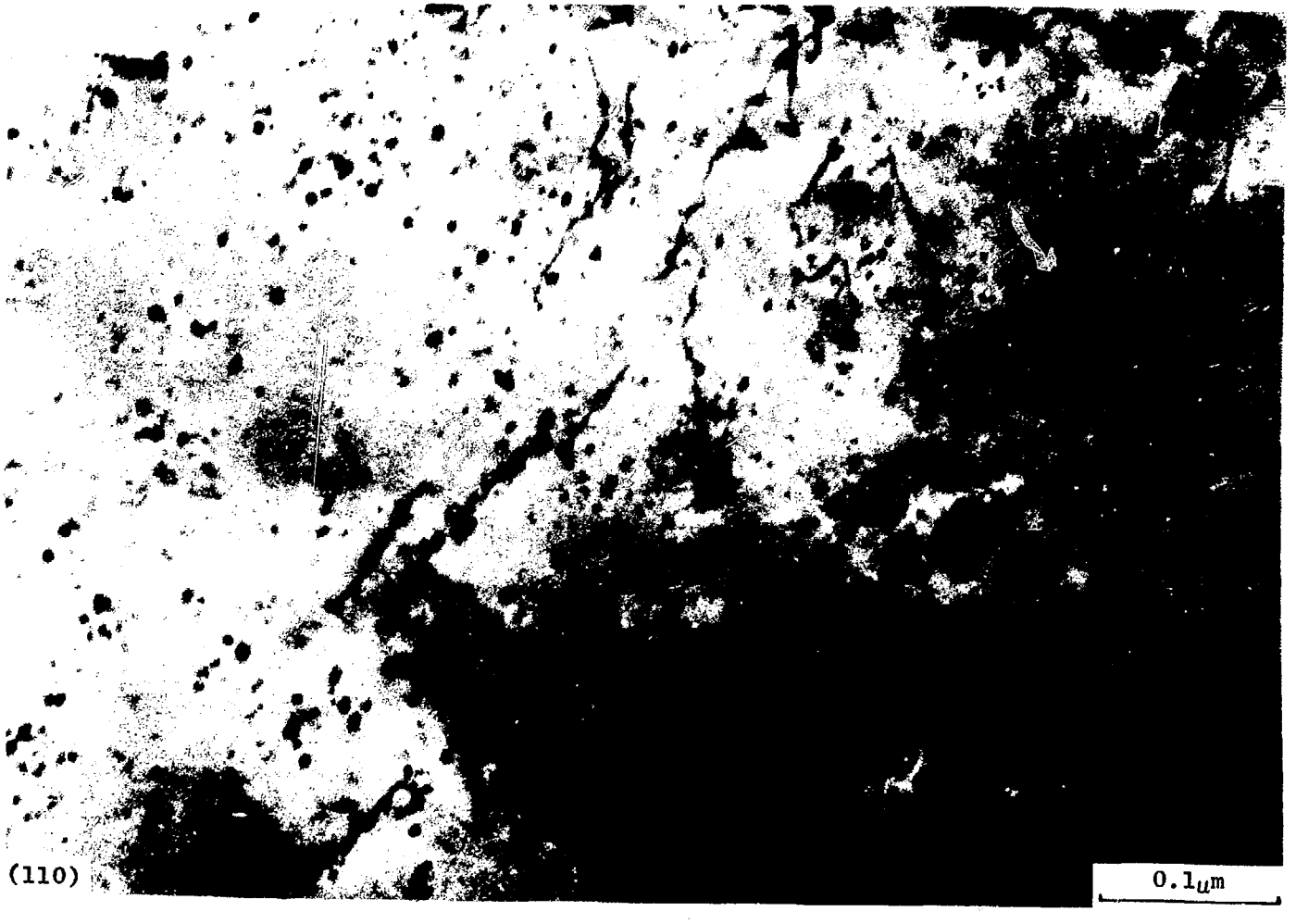

Fig. 8. Nickel, Alpha Particle Irradiated at 224°C to 0.016 dpa at a Stress of 138 MPa.

0.016 dpa at 224°C while uniaxially stressed at 138 MPa parallel to the plane of the paper. Clearly present are small dislocation loops and defect clusters (black spots), also presumed to be loops, which were produced by the alpha particle irradiation. The mean diameter of these loops was determined to be 32 Å with a density of approximately 3×10^{16}/ cm^3. An attempt to determine the nature and extent of any preferential alignment of these loops with respect to the applied stress direction was inconclusive due to their small size. It should be noted, however, that even at this small size, the loops provided effective obstacles to dislocation motion as indicated by the bowing of dislocations between the obstacles observed near the top center of Fig. 8. The observations for this specimen suggest that the microstructure was primarily influenced by the irradiation and not by the stress in view of the decreased dislocation density and relatively unchanged dislocation cell diameter when compared with the pre-irradiation microstructure.

Preliminary examination of specimens irradiated with 22 MeV deuterons has shown a similar microstructure to that in Fig. 8. The results indicate that, for both irradiating particles, an increased loop size is produced by an increased applied stress.

DISCUSSION

Data presented previously was generated in order to demonstrate that the ion-simulation technique chosen could be successfully used to measure irradiation-induced creep in bulk material as a function of those variables considered important. Further testing will be required in order to completely characterize the irradiation-induced creep behavior of nickel as a function of stress, temperature, and flux. In addition, a thorough investigation of both the unirradiated and irradiated microstructure is now being conducted in order

to compliment the irradiation-induced creep data obtained. Also, the correlation of the ion-simulated irradiation-induced creep data with in-reactor data requires additional effort. Displacement rate correlations, such as those described, need to be extended to include the detailed nature of the displacement spike.

The data obtained in this study suggest certain trends and raise several questions. Based upon the data shown in Fig. 6, the value of steady-state creep rate is in agreement with a linear flux dependency. However, the errors are such that the flux dependency could be as low as $\phi^{0.6}$ or as high as $\phi^{1.1}$. Further tests at other flux levels should reduce the uncertainty in flux dependence.

The alpha particle irradiations suggest a stress dependency of $\sigma^{1.67}$ whereas the deuteron data suggest a dependency of σ^2. Since there was no reason to suspect that this dependency should be different, the data were correlated through the use of a modified creep rate, $\dot{\epsilon}/f_p R_D$. The combination of the alpha particle and deuteron data supported the σ^2 stress dependence at stresses between 200 MPa and 350 MPa. At stresses below 200 MPa, the data are in agreement with a linear stress dependence as well. Although the stress dependency was defined to a larger degree than the flux dependency in this study, more tests would be necessary to elucidate detailed variations in stress dependency with stress as different mechanisms may control the creep rate such as has been proposed by Nichols[17,18,19] for zircaloy.

At the 224°C test temperature, no evidence of thermal recovery of the irradiation-induced strain was observed during periods as long as 72 hours. This observation led to the procedure of continuing a creep test during the next scheduled irradiation period. In addition, the value of steady-state creep rate, once established, was reproduced within experimental error during succeeding tests. This fact led to a

degree of confidence in the reproducibility and prediction of the steady-state creep rate.

Although larger error bars were appropriate to the values of primary creep rate, the flux and stress dependency was in overall agreement with that found for steady-state creep rate. Unfortunately, the existing errors in transient strain result in very large errors in the prediction of total transient time. This point was demonstrated by the large variation in total transient time given in Table 4. It should be noted that the flux of tests 4D-5-1 and 4D-5-2 was one-half that of 4D-4-1 and 4D-4-2, but otherwise the test conditions were unchanged. If the saturation of transient creep were fluence dependent, as suggested by Kesketh[20], one would expect the transient period for tests 4D-4-1 and 4D-4-2 to be one-half that of tests 4D-5-1 and 4D-5-2. As indicated, the ratio of these transient periods was only 1.34:1 instead of 2:1. It is expected that a further reduction in errors, accompanied with an increase in strain resolution, will be necessary in order to accurately predict the time for saturation of transient creep rate.

The degree of confidence was greatest in the reported values of steady-state creep rate since time-averaging tends to reduce random errors to a reasonably small fraction of the rate measured. Steady-state creep was observed during a minimum of six hours in test 4D-5-2 (See Fig. 4) and a maximum of 17 hours in test 4E-2-1 and 4E-2-2.

As mentioned previously, the primary creep rate of test 4D-2-3 was presumed low due to a previous irradiation of the same specimen at a lower stress level (i.e., tests 4D-2-1 and 4D-2-2). In order to investigate the hardening law obeyed, a construct of these tests was performed as indicated in Fig. 9. For comparison, test 4D-4-1 and 4D-4-2 were normalized to the conditions of tests 4D-2-3, 4D-2-4, and 4D-2-5 through use of the displacement rate and particle factor.

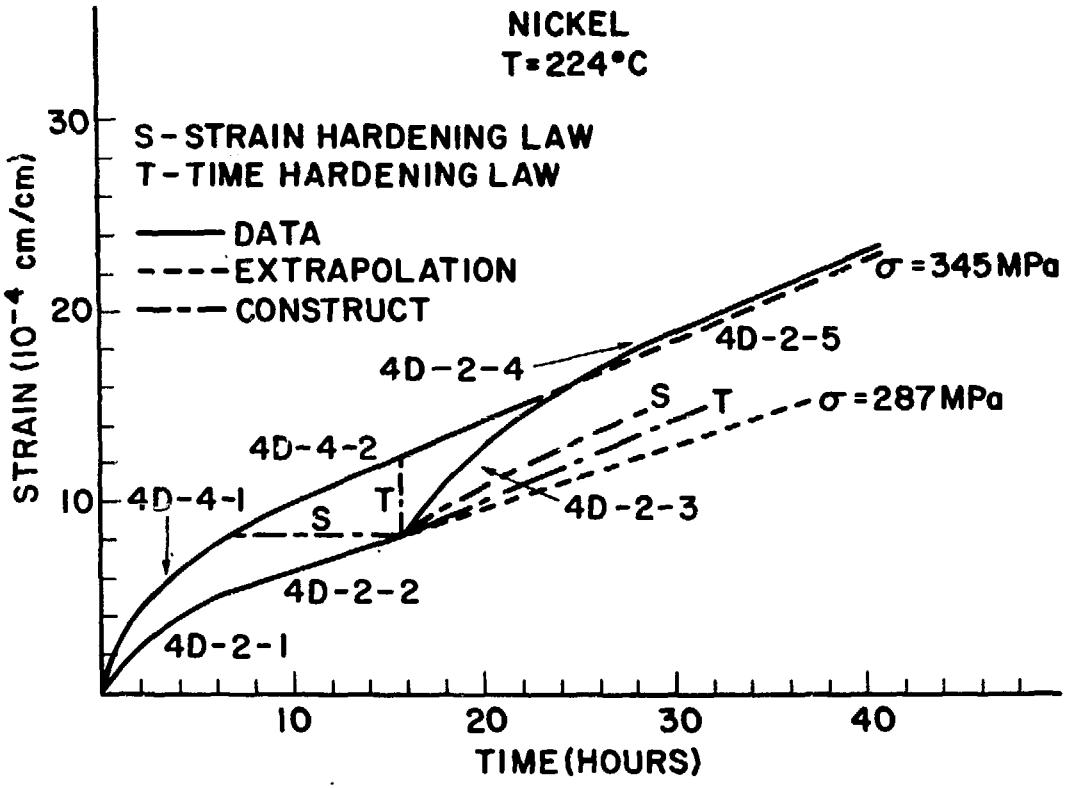

Fig. 9. Irradiation-Induced Creep Behavior Following a Change in Stress at 224°C.

Thus, specimen 4D-4 should, presumably, indicate the behavior of specimen 4D-2 if this specimen had been irradiated from time zero at the stress level of specimen 4D-4 (i.e., 345 MPa). Predictions given by both a strain hardening and time hardening law are given for comparison with the data. As seen, the transient strain amplitude, following an increase in stress, is greater than that predicted by either the time hardening or strain hardening law. In fact, the time hardening law would not have predicted any transient creep strain since the specimen had reached steady-state creep at the time stress was increased. It should be pointed out that an extended beam-off period (100 hours) occurred between the end of test 4D-2-2 and the start of test 4D-2-3. However, creep strain recovery was not observed during this period.

The data obtained in this study were reviewed with respect to possible operating irradiation-induced creep mechanisms in view of the preceeding comments. Based upon an assumed correlation, Eq. (7), which incorporated a linear flux dependency through the term R_D, the data suggest a squared stress dependency above a stress of 200 MPa as illustrated in Fig. 7. The linear flux dependency is in agreement with a previous investigation of nickel[21], but the squared stress dependency represents the upper limit of un-certainty in that investigation. Therefore, the results obtained previously must be considered to be in overall agreement, to within the experimental error, with the present results. Also of interest are the results of Harkness et al.[3] who obtained a stress dependency on solution-annealed Type 304 stainless steel between one and two over a stress range of 130 to 335 MPa (18,930 to 48,745 psi), and at a temperature of 505°C (941°F).

A review of various creep mechanisms by Gilbert[22] reports a number of creep models with a linear stress dependency (n=1) and several with a stress dependence equal to

that of thermal creep ($4 \leq n \leq 7$ for nickel)[23]. Most models predict a linear flux dependency. A mechanism proposed by Harkness et al.[24], however, suggests a squared stress dependency with a flux dependence that is nearly linear. Their creep model was based on a model of climb-controlled glide of dislocations over dispersed obstacles as originally developed by Ansell and Weertman[25]. It was considered by Harkness et al.[24] that the irradiation-induced dislocation loops and voids serve as dispersed obstacles.

A model of this type is consistent with both the creep data and the microstructural observations of the present study since irradiation-induced annihilation of the dislocation structure by both positive and negative dislocation climb will produce a net reduction in dislocation density. Furthermore, the achievement of steady-state creep in these specimens in conjunction with the microstructural observations made in this study suggests that the irradiation-induced defect clusters and small dislocation loops were effective barriers to dislocation motion. The inconclusive results concerning preferential loop alignment in the specimen examined do not permit an assessment of the contribution by a loop alignment mechanism to the observed creep behavior. However, since a linear stress dependence is predicted by loop alignment, this mechanism may contribute to the steady-state creep rate at lower stress levels and/or at higher levels of dpa.

The creep model proposed by Harkness et al.[24] expressed the creep rate as:

$$\dot{\epsilon} = \frac{A\sigma^2 L}{\mu^2 bd} \quad (\nu_{climb}) \tag{10}$$

where

A = constant

σ = applied stress

L = average spacing between obstacles

μ = shear modulus

d = height of the obstacle

b = Burgers vector

v_{climb} = dislocation climb velocity.

At temperatures less than half the melting temperature, the value of the dislocation climb velocity was calculated to be a function of the difference in the fluxes in interstitials and vacancies arriving at a dislocation. The fluxes in turn were a function of the irradiation conditions and microstructure. At temperatures above half the melting temperature, however, the thermally-induced vacancy concentrations were sufficiently large that the in- and out-of-reactor climb rates were nearly identical.

Harkness et al.[24] found, as might be expected, that the defect concentration, and hence the sink annihilation rate to a first approximation, was proportional to flux or the defect generation rate.* Thus, creep rate was approximately linear with flux. Of particular note is the fact that the difference between deuteron and alpha particle irradiations should reflect itself in the value of the recombination rate, and hence on the value of the steady-state defect concentrations. Of additional interest was the fact that a computer solution[24] to the creep rate indicated a weak dependence on temperature and a decrease of creep rate with dose reflecting a fluence hardening effect.

Although Harkness et al.[24] did not distinguish between transient and steady-state irradiation-induced creep, it was assumed that the climb-controlled glide mechanism proposed, accounted for both. This assumption was, therefore, in approximate agreement with the results presented here since

*In a more detailed analysis, account should be taken of the nature of the displacement spike structure and impurity trapping of point defects which are not accounted for in this model.

there was no evidence to suspect that primary creep did not exhibit the same stress and flux dependency as steady-state irradiation-induced creep.

SUMMARY AND CONCLUSIONS

An experimental technique has been developed to simulate the irradiation-induced creep behavior of tensile specimens placed under stress and held at temperature during light ion bombardment. The principal design features were discussed with respect to the maintenance of creep strain resolution on the order of 10^{-5} cm/cm during irradiation testing. Data generated following development was presented along with errors and their sources.

Although the data presented are primarily intended to demonstrate the capability of the technique chosen and, therefore, are preliminary, a number of conclusions can be drawn from this work as follows:

1. Creep rates measured during alpha particle and deuteron bombardment were at least two orders of magnitude greater than those measured in the absence of irradiation at a temperature of 224°C and stresses ranging from 170 to 345 MPa. It was thus demonstrated that deuteron and alpha particle irradiations offer the potential for the direct simulation of irradiation-induced creep in material with a thickness typical of both current and proposed nuclear fuel cladding.

2. Repeated irradiations conducted on separate occasions at the same test conditions yielded identical values of irradiation-induced creep rates to within the experimental error given. This demonstrates that the ion beam profile and current was sufficiently well-characterized so as to permit reproducibility in test results.

3. Intermittent loss of beam did not jeopardize irradiation tests conducted at 224°C. At higher temperatures, however, extensive beam-off periods may permit significant

irradiation-induced creep strain recovery to occur with an effect on test results.

4. The data taken at 224°C were in agreement with a linear flux dependence between 13.53×10^{-8} and 27.17×10^{-8} dpa/sec, but a range of flux exponents from 0.6 to 1.1 cannot be excluded on the basis of data obtained in this study.

5. The data suggest a squared stress dependency between 170 and 345 MPa based upon a linear displacement rate correlation of the deuteron and alpha particle results. However, a multiple stress dependency cannot be ruled out on the basis of data presented for the stress range investigated. A linear stress dependency was shown to be consistent with the data below a stress of approximately 200 MPa.

6. No evidence of recovery of the irradiation-induced creep strain was observed at 224°C. Steady-state creep rates were established within one hour during subsequent irradiations following beam-off periods as long as 72 hours.

7. Based upon a single observation, it appeared that transient creep was reinitiated following an increase in stress level after steady-state creep was achieved at the lower stress level. The transient strain was greater than that predicted by either a time hardening or strain hardening law.

8. Results of both alpha particle and deuteron irradiations correlated well once it was assumed that the damage effectiveness of deuterons for causing irradiation-induced creep was 25% greater than that for alpha particles. This result is qualitatively consistent with the expectation that short-term annealing effects will become more important with displacement spike intensity.

9. An examination of the irradiated microstructure revealed the presence of a heterogeneous distribution of defect clusters, small dislocation loops and random dislocations in

addition to dislocation cells. The relaxation of the pre-irradiated dislocation structure and presence of defect clusters and loops in the irradiated material is consistent with the climb-controlled creep model presented.

10. A climb-controlled creep model proposed by Harkness et al.[24] was in general agreement with both the creep and microscopy data obtained. In this model, irradiation-induced defects serve effectively as dispersed obstacles over which dislocations must climb.

ACKNOWLEDGEMENTS

The authors gratefully acknowledge the assistance provided by Mr. G. E. Miller and the entire NRL Cyclotron staff.

This work was supported by the Office of Naval Research at the Naval Research Laboratory. Support provided to A. L. Bement, Jr., at the Massachusetts Institute of Technology by the Division of Controlled Thermonuclear Research, U. S. Energy Research and Development Administration, is acknowledged.

REFERENCES

1. S. N. Buckley, "Irradiation Growth and Irradiation Enhanced Creep in fcc and bcc Metals," AERE-R-5944, 2, 547 (1968).

2. D. L. Bodde, "Irradiation-Induced Stress Relaxation and Creep in Reactor Materials," S. M. Thesis, Massachusetts Institute of Technology (Feb 1972).

3. S. D. Harkness, F. L. Yagee, and F. V. Nolfi, Jr., "Simulation of In-Reactor Creep of Type 304 Stainless Steel," ANL-7883, Argonne National Laboratory (1972).

4. P. L. Hendrick, A. L. Bement, Jr., and O. K. Harling, Nucl. Instr. and Methods, 124, 389 (1975).

5. P. L. Hendrick, D. J. Michel, A. G. Pieper, R. E. Surratt, and A. L. Bement, Jr., "Simulation of Irradiation-Induced Creep in Nickel," (submitted to J. Nucl. Matl. 1975).

6. P. L. Hendrick, D. J. Michel, A. G. Pieper, R. E. Surratt, A. L. Bement, Jr., "Ion-Simulated Irradiation-Induced Creep," (to be submitted to Nucl. Instr. and Methods 1975).

7. G. Lewthwaite et al, Nature, 216, 473 (1967).

8. D. Mosedale et al, Nature, 224, 1301 (1969).

9. I. Manning and G. P. Mueller, Computer Physics Comm., 7, 85 (1974).

10. C. D. Bond and S. E. Gordon, Nucl. Instr. and Methods, 98, 513, (1972).

11. J. Lindhard, M. Scharff, and H. E. Schiott, Danske Videnskab. Selskab, 33, #14, (1963).

12. R. D. Evans, The Atomic Nucleus, McGraw-Hill NY (1955).

13. P. L. Hendrick, "Ion-Simulated Irradiation-Induced Creep," Ph.D. Thesis, Massachusetts Institute of Technology, (1975).

14. I. M. Torrens and M. T. Robinson, "Computer Simulation of Atomic Displacement Cascades in Metals," USAEC Report CONF-710601, 739 (1972).

15. F. A. Garner, private communications, Hanford Engineering Development Laboratory, Richland, Washington (1975).

16. W. N. McElroy, R. E. Dahl, Jr., and E. R. Gilbert, Nucl. Engr. and Des., 14, 319 (1970).

17. F. A. Nichols, J. Nucl. Matl., 30, 249 (1969).

18. F. A. Nichols, J. Nucl. Matl., 37, 59 (1970).

19. F. A. Nichols, Mater. Sci. Engr., 6, 167 (1970).

20. R. V. Hesketh, Phil. Mag., 8, 1321, (1963).

21. P. L. Hendrick, "Proton Simulated Irradiation-Induced Creep," S. M. Thesis, Massachusetts Institute of Technology, (1974).

22. E. R. Gilbert, Reactor Tech, 14, #3, 258 (1971).

23. E. C. Norman and S. A. Duran, Acta Met., 18, 723 (1970).

24. S. D. Harkness, J. A. Tesk, and Che-Yu Li, Nucl. Appl. and Technol., 9, #24 (1970).

25. G. S. Ansell and J. Weertman, Trans. AIME, 215, 838 (1959).

APPARATUS TO STUDY IRRADIATION-INDUCED CREEP WITH A CYCLOTRON

K. Herschbach and K. Mueller

Kernforschungszentrum Karlsruhe, Institut für Material- und Festkörperforschung, 75 Karlsruhe (Germany)

ABSTRACT

An apparatus is described which allows accurate measurements of length changes of specimens irradiated on a cyclotron while a uniaxial stress is applied. Basic to the design is a "chimney" which establishes a strong convection in the liqu. Na, which serves as a heater bath. Deuterons of high enough energy ($E \geq 50$ MeV) can penetrate into the creep capsule and — with a careful layout of the capsule — irradiation-induced creep can be studied. The precautions necessary to achieve a good resolution are given into some detail.

In the following an apparatus will be described which allows accurate measurements of length changes in specimens irradiated while a uniaxial stress is applied; i.e., irradiation-induced creep. The design outlined below can be used provided that (a) particles of high enough energy are available, f. e. deuterons with an energy of at least 45—50 MeV; (b) the sample material is compatible with liqu. Na.

The basic feature of the creep capsule, shown schematically in Fig. 1, is a chimney which encloses the specimen. A heater below the specimen provides the heat necessary to keep the temperature of the Na-bath. The sodium flows upward due to convection caused by a kind of chimney effect, and leaves the chimney through slots provided above the sample. The specimen temperature can therefore be kept within close limits; both convection as well as conduction can carry away any unwanted heat even when the sample is irradiated with a high-current, high-energy beam. The sodium, unfortunately, has a tendency to form "hot filaments"; this shows as strong, periodic temperature fluctuations which we could measure both at the chimney bottom and top of a fully-instrumented capsule. Nevertheless, the temperature of the sample can be kept within close limits if a very fast temperature

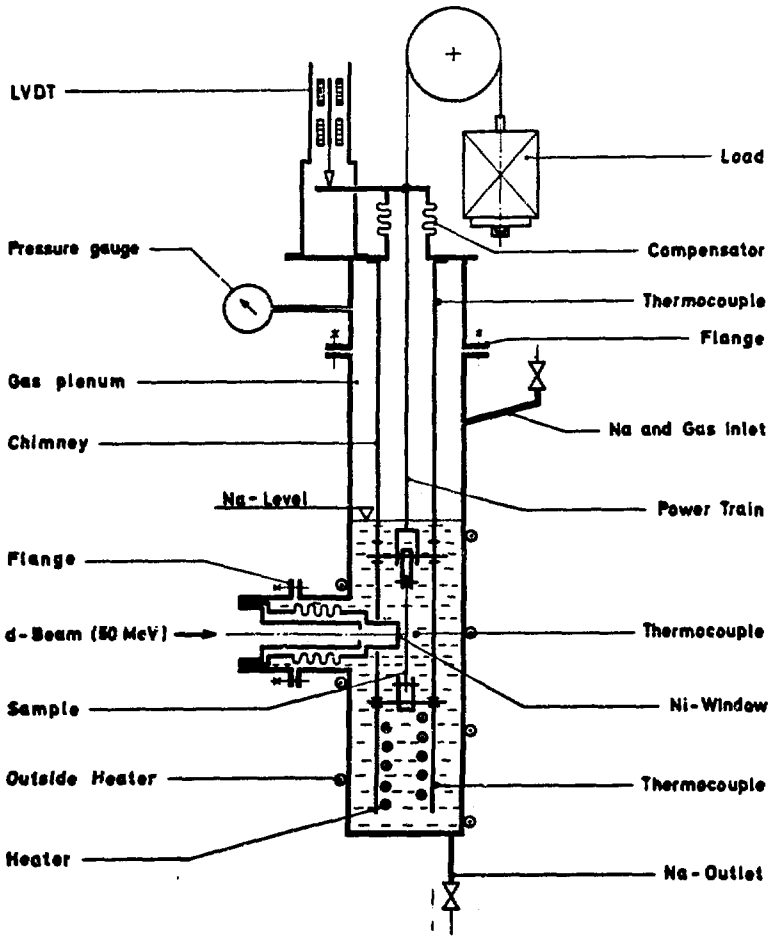

Fig. 1. Schematic Diagram of the Creep Capsule. Not shown are several heaters required to preheat the capsule for filling and draining the Na. The necessary amount of Na is drawn from a small storage vessel so no glove box is required.

controller is employed of the kind which adjusts the power of each half-wave of the ac heater current to the conditions just prevailing. Utilizing the filament effect, we determined the speed of the sodium flow in the chimney to be about 10 cm/sec at 280°C when the capsule outside was cooled with an air blower. The chimney is part of the power train, as can be seen from Fig. 1, which is otherwise quite conventional. The specimen elongation is measured with a Linear Variable Differential Transformer (LVDT).

In order to get a high accuracy of the strain measurements, a number of precautions were found to be necessary:

1. As already discussed, a very fast responding temperature controller was employed to offset the hot filament effect.

2. All parts of the capsule (except the beam window, see below) were fabricated from one kind of steel (German designation 1.4571) and, more important, the power train laid out such that unavoidable temperature fluctuations would affect the up and down part in the same fashion. Therefore, differential expansion was held to a minimum.

3. The LVDT was covered with a small box as indicated in Fig. 1; in addition, the whole upper part of the creep capsule from the Na-level upward was wrapped in heavy layer of stone wool and Al-foil (not shown).

4. The complete creep aparatus was then put into a large metal box to keep the effects of room-temperature changes and drafts to a minimum. The air blower used to cool the lower part of the capsule was also in this box; therefore, even the "cooling air" was conditioned!

Although the capsule was designed for operating temperatures between 200 and 450°C, we have presently employed it mainly at 280°C. The performance parameter at this temperature is: The heater input is approximately 700 watts, depending, of course, on the air blower. The specimen temperature is stable to within ±0.5°C, the specimen elongation to within ±0.5 μ, equaling a strain of $\pm 5 \times 10^{-5}$. The temperature inside the outer box reaches about 80°C and at the LVDT, approximately 100°C, which has to be considered when calibrating the latter.

Because of the larger temperature differences between capsule and ambient, we expect an even better performance at higher temperatures, and actually it is a little worse at 190°C, where we did one irradiation.

To facilitate irradiation, use was made of the fact that 50 MeV deuterons can penetrate quite a bit of material. The beam entrance window is made of Ni, for safety reasons 1 mm thick. The energy loss in this window is 15 MeV (1). The beam is further downgraded in the liqu. Na and hits the sample with an energy of approximately 15 MeV. This energy is a compromise, since on one hand homogenous damage within the specimen (presently Ni foil 0.1 mm thick) is required, which means that the beam has to penetrate the sample; on the other hand, one wants a damage rate as large as possible, which requires low energy. The distance between Ni window and specimen can be adjusted via a kind of micrometer device, the sealing of the capsule being provided by the bellows shown. An exactly-machined distance holder assures that this distance is correct.

Despite the large heat unput within a small volume in front of the specimen (250 watts at a beam current of 5 μamp), no downgrading of the capsule performance was observed during irradiation!

The only drawback we can see in this design is the fact that once irradiation has commenced, the specimen can no longer be exchanged; the irradiation schedule has therefore to be planned carefully.

Needless to say, that because of the large amount of liqu. Na involved (1.5 kg), which will be very radioactive after each irradiation, the utmost care and very stringent inspection requirements have to be employed when the creep capsule is being fabricated.

The authors wish to thank the many members of their institut who helped in various ways to build this apparatus. Special thanks are due to Mr. Chr. Wassilew who took part in designing the first prototype.

REFERENCE

1. C. F. Williamson, J. P. Boujot, and J. Picard, Rapport CEA-R3042.

THE EFFECT OF IRRADIATION TEMPERATURE ON RADIATION-ANNEAL HARDENING IN VANADIUM

K. Shiraishi, K. Fukaya and Y. Katano

Japan Atomic Energy Research Institute
Tokai-mura, Ibaraki-ken, Japan

ABSTRACT

Vanadium samples were irradiated to a fast neutron fluence of 8.0×10^{19} to 1.2×10^{20} n/cm^2 (En≥1 MeV) at temperatures in the range from 70 to 600°C, and the radiation hardening measured at room temperature was investigated in terms of microstructure. The radiation-anneal hardening phenomenon was observed in samples irradiated at 200 and 460°C, whereas the radiation hardening in the sample irradiated at 70°C recovered monotonically with increasing anneal temperature. The density of defect clusters visible in the electron microscope decreased with increase in post-irradiation annealing temperature. The hardening induced by post-irradiation annealing is considered to be due to small interstitial impurity clusters. The sample irradiated at 70°C to a fluence of 1.2×10^{21} n/cm^2 had good ductility on tensile test at temperatures of 450°C and above. The sample irradiated at a temperature of 200°C or below to a fluence beyond 8×10^{19} n/cm^2 exhibited plastic instability or a little work hardening on deformation at room temperature. The irradiation embrittlement was not recovered by post-irradiation annealing at temperatures up to 450°C.

INTRODUCTION

Vanadium has been considered as a candidate material for the first wall in fusion reactors because of its good strength and excellent neutronic characteristics in fusion reactor environment.[1,2] The first wall material is irradiated with high energy neutrons to a high fluence at high temperature. It is required to obtain the data from 14-MeV neutron irradiation and heavy ion irradiation to simulate high fluence neutron irradiation as well as the data

from fission reactor irradiation. In the experiment of 14-MeV neutron and heavy ion irradiations, the damage region of the specimen is limited and the radiation damage could not be evaluated directly by means of mechanical testing. It is necessary to predict the mechanical properties from microstructure of the irradiated specimen.

In previous work the effect of neutron fluence on the radiation and anneal hardening of vanadium irradiated at reactor ambient temperature has been investigated in terms of microstructure.[3] The radiation hardening increased linearly with square root of fast neutron fluence $(\phi t)^{1/2}$ up to a fluence of about 2.5×10^{19} n/cm^2 and appeared to saturate at approximately 25 kg/mm^2; the $(\phi t)^{1/2}$-dependence and saturation effect of the radiation hardening were reported also by Boček et al.[4] The radiation hardening of about 25 kg/mm^2 produced by irradiation to 1.0×10^{20} n/cm^2 can be explained by defect clusters visible in the electron microscope. Upon post-irradiation annealing a substantial increase in yield stress (radiation-anneal hardening) was observed in samples irradiated at low dose (2.0×10^{17} and 1.0×10^{18} n/cm^2), which is closely associated with a change in the density and size distribution of defect clusters. The radiation-anneal hardening has been studied by several investigators[5-13] and considered to be due to the precipitation of interstitial impurities on radiation-produced defect clusters,[6-11] assuming that the clusters' distribution did not change during the annealing treatment. It was reported, for vanadium irradiated to a fluence of 1.6×10^{19} n/cm^2 at 60~80°C, that the magnitude of the radiation-anneal hardening is not dependent on interstitial concentration in the range from 50 to 400 wt ppm;[10] the hardening increases in magnitude with increasing concentration of interstitial impurities beyond the concentration range.[9,10]

In vanadium irradiated to a neutron fluence beyond $1x10^{19}$ n/cm^2, the radiation-anneal hardening has been observed in samples irradiated at temperature above reactor ambient,[9-12] while no radiation-anneal hardening occurs in sample irradiated at reactor ambient temperature;[3] the magnitude of the hardening is very small when the hardening is observed in sample irradiated at 60∿80°C.[10] However, the radiation-anneal hardening has not been understood yet in relation of irradiation temperature and radiation-produced microstructure. The study of the irradiation temperature effects on the radiation-anneal hardening is an initial phase of understanding the radiation hardening or embrittlement of vanadium in terms of microstructure.

This paper describes the radiation-anneal hardening of vanadium irradiated to a fluence of 0.8 to 1.2 $x10^{20}$ n/cm^2 at temperatures up to 600°C in terms of radiation-produced microstructure. The effect of testing temperature on the radiation hardening is also investigated in vanadium irradiated at 70°C to a fluence of $1.2x10^{21}$ n/cm^2.

EXPERIMENTAL PROCEDURE

The vanadium used for this study was prepared from two 55 mm diameter ingots supplied by NGK Insulators, Ltd. The preparation of the specimen was different for each ingot. Specimens, designated material A, were made by hammering and rolling without process annealing. The specimens were finally annealed for 1 h at 950°C in a vacuum better than $2x10^{-7}$ torr and furnace cooled. Specimens of materials B and C were prepared from the other ingot by cold rolling, with process annealing for 1 h at 900°C, in a vacuum of $1x10^{-5}$ torr. Final annealing of the specimen was also carried out for 1 h at 900°C, in a vacuum of $1x10^{-5}$ torr. Prior to the final annealing, tensile specimens having their longitudinal axis parallel to the rolling direction

were machined; 0.3 mm thick specimens with a gage section 5 mm wide and 28 mm long from all the materials, and 1 mm thick specimens of 30 mm in gage length with 4 mm wide from material C. Sheets of 0.2 mm thick were used for the electron microscopy specimens. The grain diameter of the 0.3 mm thick tensile specimens was 38 μm on average, not appreciably different in materials. The 1 mm thick specimen had an average grain diameter of 94 μm. The materials had similar purity of 99.8 wt%, and the impurity content analyzed after final annealing is given in Table 1.

Table 1 Impurity content in 99.8 wt % vanadium

material	concentration (ppm by wt)								
	O	N	C	H	Fe	Ni	Si	Al	Cr
A	190	5	38	15	150	10	52	150	30
B	240	41	32	6	195	130	200	90	120
C	430	3.5	50	21	260	trace	80	120	30

Neutron irradiation of the tensile-test and electron microscopy specimens was performed in an in-core position of either the JRR-2 reactor at Tokai-mura or the JMTR reactor at Oarai. Details of the irradiations are tabulated in Table 2. For irradiations at reactor ambient temperature, samples were contained in a helium-filled aluminum capsule externally cooled with reactor coolant water. Temperatures of the samples were estimated from temperature of the reactor coolant water. For irradiations at temperatures above the reactor ambient, samples were loaded into a helium-filled stainless steel capsule in such a way that all the specimens were in direct thermal contact with the capsule wall. The samples were heated during irradiation by nuclear heating, and temperature control was achieved by an air gap between the stainless

Table 2 Neutron irradiation of vanadium

material	fluence (En≥1MeV) (n/cm^2)	temperature (°C)	reactor
C	1.0×10^{20}	70	JRR-2
B	8.2×10^{19}	200 ∿ 20	JRR-2
A	1.2×10^{20}	460 ∿ 30	JRR-2
A	8.0×10^{19}	600 ∿ 40	JRR-2
C	1.2×10^{21}	70	JMTR

steel capsule and outer aluminum envelope externally contact with reactor coolant water. A contineous record of temperature was made by means of thermocouple located at the center of the stainless steel capsule. Post-irradiation annealing was carried out for 1 h at temperatures up to 750°C in a vacuum better than 2×10^{-7} torr for JRR-2 irradiated specimens; the vacuum was 5×10^{-4} torr for annealing of JMTR irradiated specimens.

Tensile tests were performed with an Instron tensile-testing machine at a strain rate of 2.8×10^{-4} /sec. Specimens were held for 15 min at the test temperature before the start of the test above room temperature. In each of the high temperature tests the temperature was controlled within ±1°C and the vacuum was better than 5×10^{-5} torr. The yield stress was evaluated at the upper yield point or at the maximum stress around yielding determined from the tensile load-elongation curve. When no yield point was apparent, the stress at 0.2% plastic strain was used determining the yield stress.

The microstructure of the irradiated specimen was examined in a JEM-200A electron microscope operating at 200 kV. The damage structure was observed in the foil whose

thickness ranged from 0.15 to 0.3 μm depending on the size and density of the radiation-produced defect clusters. The foil thickness was determined by counting the number of equal-thickness fringes.

EXPERIMENTAL RESULTS

The effect of post-irradiation annealing on the difference in yield stress, $\Delta\sigma_y$ between irradiated and unirradiated samples are shown in Fig. 1; the yield stress in the unirradiated specimens of materials A, B and C were 12.4, 18.6 and 28.1 kg/mm^2, respectively. It is evident from the figure that radiation-anneal hardening occurs in the samples irradiated at temperatures of 200 and 460°C, whereas the radiation hardening of the sample irradiated at 70°C decreases monotonically with increase in the annealing temperature. In the sample irradiated at 600°C, little hardening is observed and the hardening is not much changed by post-irradiation annealing up to 650°C.

Changes in damage structure with post-irradiation annealing for samples irradiated at 70, 200, and 460°C are shown in Figs. 2~4. In the specimen irradiated at 70°C, dislocation lines are observed in addition to fairly large defect clusters of very high density; the image of the clusters overlaps and both the density and size of the clusters could not be estimated precisely. The radiation-produced defect clusters grow to be dislocation loops and develop into dislocation lines with increase in annealing temperature; the density of the loops is about $1x10^{15}$ $/cm^3$ after annealing at 450°C. In the sample irradiated at 200°C, the density of the loops is little changed by post-irradiation annealing at temperatures up to 400°C; it decreases rather rapidly with increase of the annealing temperature above 400°C. It should be noted that the peak of radiation-anneal hardening of the sample appears at around

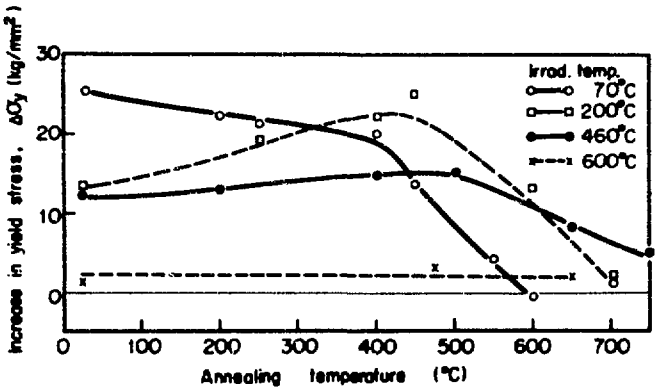

Fig. 1. Change with post-irradiation annealing temperature of the yield stress of vanadium irradiated to (0.8∿1.2)x10 n/cm.

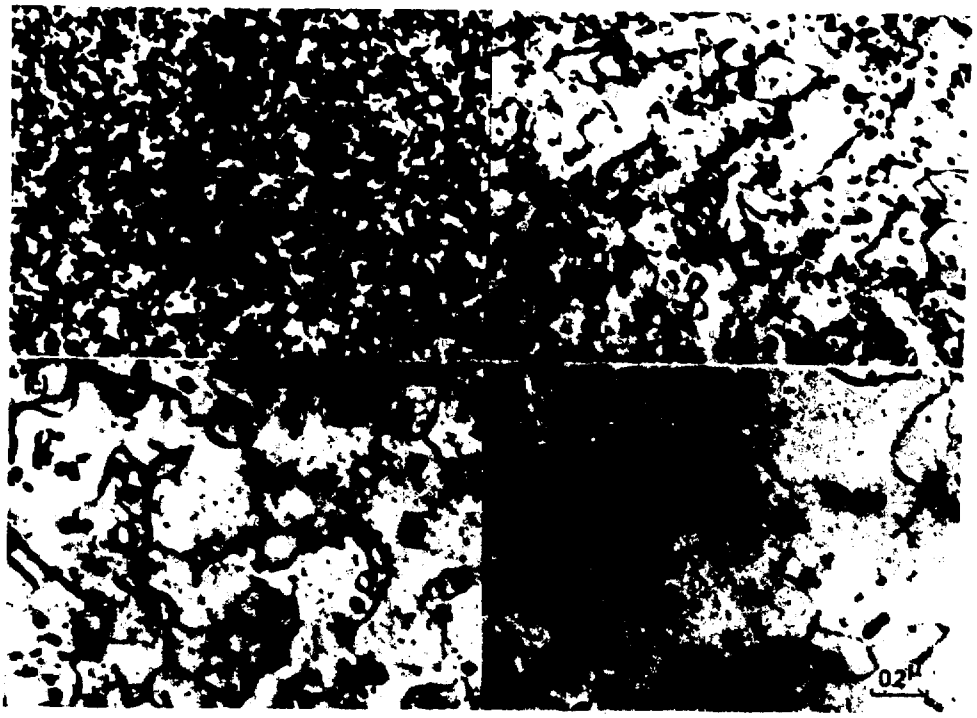

Fig. 2. Damage structure in vanadium irradiated at 70°C to 1.0×10^{20} n/cm (a), and annealed for 1 hr at (b) 450°C; (c) 550°C and (d) 600°C.

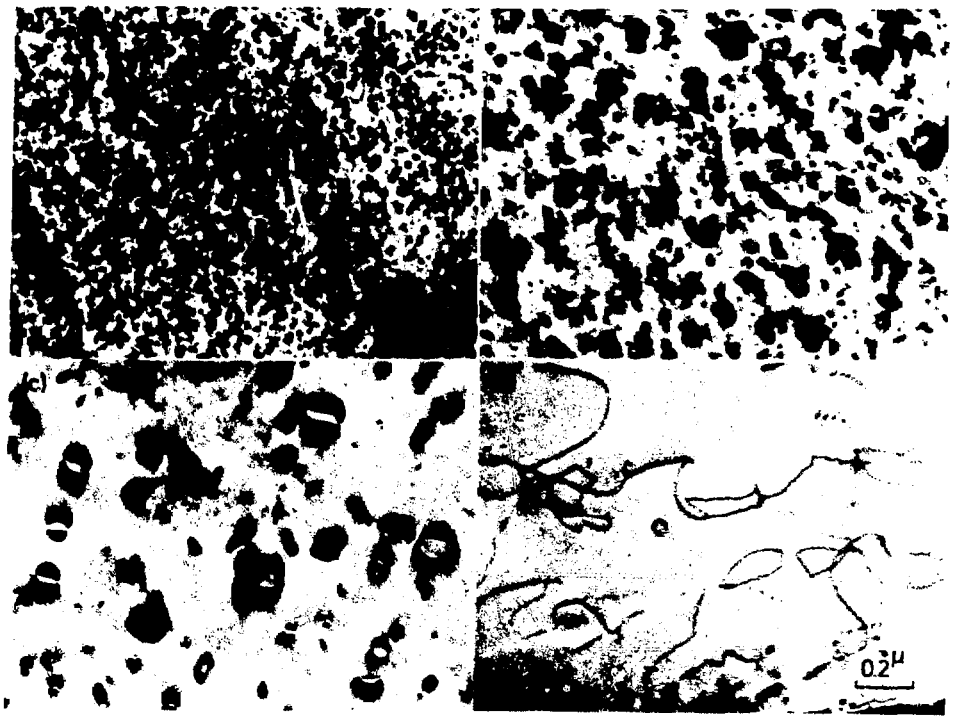

Fig. 3. Damage structure in vanadium irradiated at 200°C to 8.0×10^{19} n/cm (a), and annealed for 1 hr at (b) 400°C; (c) 500°C; and (d) 700°C.

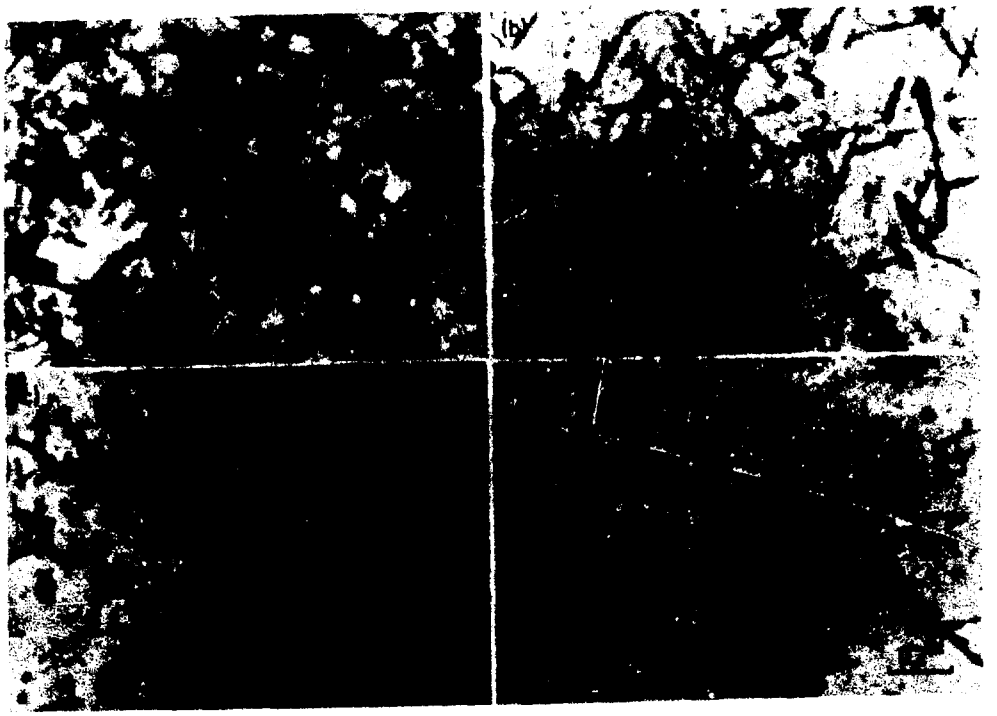

Fig. 4. Dislocation structure in vanadium irradiated at 460°C to 1.2×10^{20} n/cm (a), and annealed for 1 hr at (b) 400°C; (c) 550°C; and (d) 650°C.

450°C (Fig. 1). Dislocation lines are seen in the specimen irradiated at 460°C. Upon post-irradiation annealing, dislocation loops appear with decrease in the density of the dislocation lines. The dislocations seem to be decorated with precipitates, and the density of the dislocation loops is on the order of 10^{13} /cm^3. It should be noted that small voids of 65 Å in average diameter were observed with the density of 2×10^{15} /cm^3 in the as-irradiated specimen, and that the void structure is little changed by annealing at temperatures up to 550°C. The voids decrease in both size and density by annealing at 650°C. Voids of about 550 Å in average diameter and 1×10^{13} /cm^3 in density were formed in the specimen irradiated at 600°C; only a few dislocation segments were seen in the electron microscopy sample.

The yield stress and total elongation at room temperature for the sample irradiated at 70°C to a fluence of 1.2×10^{21} n/cm^2 are plotted in Fig. 5 as a function of annealing temperature. The yield stress and elongation of the irradiated sample is little changed by post-irradiation annealing up to 450°C. On annealing for 1 h at 750°C, the tensile properties almost recover to the unirradiated level. The tensile properties for the irradiated sample are plotted as a function of test temperature in Fig. 6, together with the properties of unirradiated sample. The radiation effect on the tensile properties recovers gradually with increase in the test temperature and no appreciable irradiation effect is seen at 750°C. It can be deduced from Figs.5 and 6 that the radiation hardening measured at room temperature after post-irradiation annealing is not much different from the hardening measured at the temperature equivalent to the annealing temperature if the test and also annealing is made at a temperature above 500°C. The radiation hardening measured at room

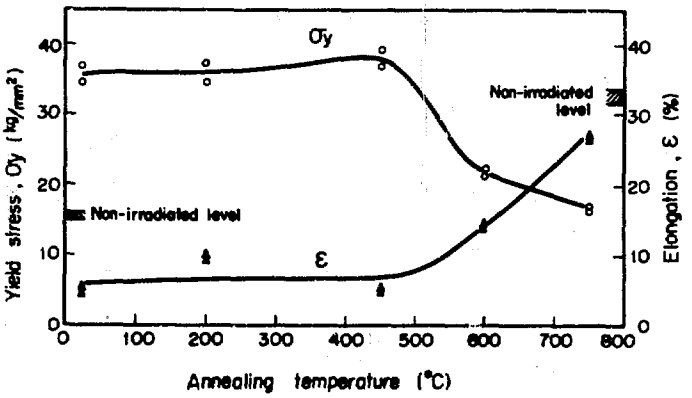

Fig. 5. Change with post-irradiation annealing of the tensile properties at room temperature in vanadium irradiated at 70°C to 1.2×10^{21} n/cm.

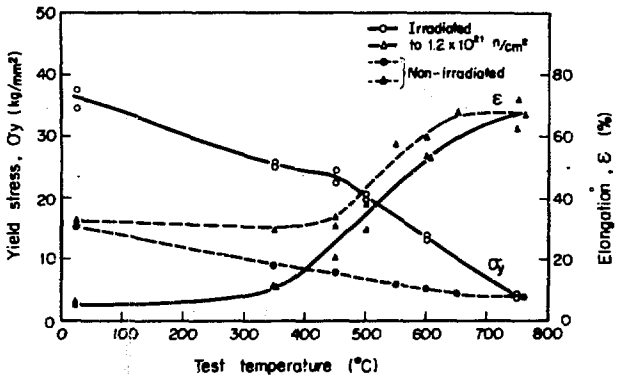

Fig. 6. Change in the tensile properties with test temperature in irradiated (1.2×10^{21} n/cm at 70°C) and unirradiated vanadium.

temperature after annealing at 450°C is considerably greater than that obtained at 450°C tensile-testing.

The sample irradiated at a temperature of 200°C or below to a fluence beyond 8×10^{19} n/cm^2 had only a few percent in total elongation on the tensile test at room temperature. The irradiation embrittlement was not recovered by post-irradiation annealing at temperatures up to 450°C. Most of the tensile specimens from th. sample exhibited a small drop in yield stress followed by plastic instability that led to fracture without uniform longation; some specimens had an ability to work-harden beyond the yield stress. The loss of ductility in the irradiated samples was associated with coarse slip bands at the surface and defect-free channels (dislocation channels) in transmission electron microscope observations of the deformed specimens. The sample irradiated at 70°C to a fluence of 1.2×10^{21} n/cm^2 has good ductility in tensile test at a temperature of 450°C or above.

DISCUSSION

The increase in yield stress caused by dislocation loops,[14] dislocation lines,[15] and voids[16] are, respectively, expressed by the equations,

$$\Delta\sigma_y = \alpha_1 \mu b (\Sigma n_i d_i)^{1/2} \quad (1)$$

$$\Delta\sigma_y = \alpha_2 \mu b \rho^{1/2} \quad (2)$$

and

$$\Delta\sigma_y = \alpha_3 \mu b (ND)^{1/2} \quad (3)$$

where μ is the shear modulus, b is the urgers vector, n_i and d_i are respectively the density and average diameter of loops in a given size interval, ρ is the dislocation line density, N and D are respectively the density and average

diameter of voids, and α_1, α_2 and α_3 are constants.

The size and density of defects clusters observed in the present experiment are tabulated in Table 3 with calculated and experimentally observed $\Delta\sigma_y$; $\Delta\sigma_y$'s were calculated with $\alpha_1=0.5$, $\alpha_2=0.5$, $\alpha_3=1.0$, $\mu=4.76\times10^3$ kg/mm^2, and b=2.63 Å. In the samples irradiated at temperatures of 200°C and 460°C, the peak of the radiation-anneal hardening appears at about 450°C, while the density of radiation-produced defect clusters or dislocation lines in the samples decreases markedly by post-irradiation annealing at 450°C. Moreover, recovery of the radiation hardening in the sample irradiated at 70°C is much less than the extent expected from annealing behavior of defect clusters.

In the sample irradiated at 70°C, radiation-produced defects agglomerate to be visible clusters during irradiation; the radiation hardening is well described by Eq. (1). The defect clusters are considered to be saturated with oxygen and other interstitial impurities in the as-irradiated condition.[3] Then, no further agglomeration of defects nor precipitation of interstitial impurities occurs to increase the yield stress upon post-irradiation annealing, which results in no radiation-anneal hardening to the sample irradiated at 70°C. With a sample containing 250 wt ppm oxygen and 160 wt ppm carbon, Morozumi et al.[11] observed the radiation-anneal hardening after neutron irradiation at 100°C to a fast neutron fluence of 4.7×10^{20} nc/m^2, and reported that the radiation-anneal hardening occurs in two distinct temperature ranges; one of the hardening peaks appears near 200°C and the other peak at about 500°C. The radiation-anneal hardening at around 500°C increases with increase in interstitial carbon content, as in the case of niobium.[17]

The radiation-anneal hardening in the sample irradiated at 200°C and also the hardening of the sample irradiated at 70°C and annealed at about 450°C are considered to be attributable to impurity clusters, possibly to carbon clusters. Oxygen and other interstitial impurities precipitate at radiation-produced defect clusters and strengthen the clusters in the as-irradiated condition. Post-irradiation annealing decreases the density of defect clusters; some of the clusters dissolve into the matrix. The interstitial impurities precipitated on the dissolving defect clusters also resolve into the matrix, which results in recovery of oxygen Snoek damping.[18] During the resolving process interstitial impurities would form the clusters which contribute to the hardening.[12]

According to Morozumi et al.,[11] the solubility of carbon in vanadium is very small and carbides are observed to precipitate in a sample containing 190 wt ppm carbon after annealing at a temperature below 300°C. They also reported, with a sample containing 360 wt ppm carbon, that hardening due to precipitation of fine carbide occurs upon annealing at temperatures up to 400°C, while the carbide resolve into the matrix by annealing at temperatures above 450°C. Although the sample used in the present experiment contains only 30∿50 ppm carbon, the interstitial carbon is localized to precipitate on radiation-produced defect clusters during irradiation. Then, carbon content is considered to be locally high enough for formation of carbon clusters or small carbides around the dissolving defect clusters upon post-irradiation annealing at temperatures up to 450°C; the carbon clusters contribute to the hardening. When the annealing temperature is raised beyond 450°C, interstitial carbon precipitated on the defect clusters resolves into the matrix accompanied by dissolution of the defect cluster. Then the radiation-induced hardening recovers rapidly with

increase in the annealing temperature beyond 450°C.

When the irradiation is performed at reactor ambient temperature, the density of radiation-produced defect clusters is very high, on the order of 10^{17} /cm^3, and the radiation hardening is greater than the hardening resulted from formation of carbon clusters or carbides. Then the radiation-anneal hardening can not be observed in the sample. In the sample neutron irradiated at 200°C, radiation-produced defect clusters are twice as large in average diameter and one-tenth as large in the density as those in the sample irradiated at reactor ambient temperature. Then, carbon content around the dissolving defect clusters during post-irradiation annealing at 450°C is larger in the 200°C irradiated sample than the sample irradiated 70°C. In addition, the radiation hardening produced in 200°C irradiated sample is smaller than that in 70°C irradiated sample. Thus, the radiation-anneal hardening occurs in the sample irradiated at 200°C, even if the phenomenon could not be observed in the 70°C irradiated sample. Moreover, the yield stress after annealing at 450°C in the 200°C irradiated sample can be larger than that in the 70°C irradiated sample.

In the sample irradiated at 460°C, dislocation lines and voids are formed during irradiation. The radiation-anneal hardening of the sample is also attributable to the carbon clusters or carbides formed in place of dislocation lines, as already described; the size and density of voids are little changed by post-irradiation annealing up to 550°C (Table 3). The damage structure of the sample irradiated at 600°C consists of voids and few dislocation lines. The radiation hardening of the sample is attributable to the voids, and the density of voids is not changed by annealing at temperatures up to 650°C, which results in no radiation-anneal hardening. In addition, neutron fluence

Table 3 Density and size of defect clusters and their contribution to the hardening

material	neutron irradiaton		annealing temp. (°C)	loop			$\Delta\sigma_y$ (kg/mm^2)	
	fluence (n/cm^2)	temp. (°C)		density (cm^{-3})	size (Å) average	size (Å) range	calculated	experimental
C	1.0×10^{20}	70	As-irrad.	3×10^{17}	45**		23	25.3
			250	1.8×10^{17}	47	<150	17.8	21.2
			450	1.0×10^{15}	190	<450	2.7	13.8
			550	3.0×10^{14}	450	150<	—	4.4
B	8.2×10^{19}	200	As-irrad.	1.4×10^{16}	70	<120	6.4	13.5
			250	1.1×10^{16}	80	<190	6.5	19.0
			400	1.1×10^{16}	110	<340	7.4	22.0
			450	1.3×10^{15}	160	80∿420	2.9	24.0
			600	2.1×10^{14}	300	110∿730	0.9	13.0
A	1.2×10^{20}	460	As-irrad.	2.2×10^{10}* (1.9×10^{15})	(65)	(30∿80)	9.3 (4.4) 13.7	12.4
			400	6.5×10^{9}* (1.9×10^{15})	(65)	(40∿90)	5.0 (4.4) 9.4	14.8
			500	5.3×10^{9}* (2.0×10^{15})	(65)	(40∿100)	4.6 (4.5) 9.1	15.1
			650	2.3×10^{9}* (4.5×10^{14})	(60)	(30∿100)	3.0 (2.1) 5.1	8.2
A	8.0×10^{19}	600	As-irrad.	(1×10^{13})	(550)	(50∿1600)	(0.9)	1.2

* dislocation line density (cm/cm^3) ** estimated value

The figure in parenthese indicates data for voids.

in the present experiment is not so high that the radiation hardening is very small and no appreciable swelling was observed.

In the sample irradiated to 1.2×10^{21} n/cm^2 at 70°C, the yield stress measured at room temperature is not changed by post-irradiation annealing up to 450°C, whereas the radiation-produced hardening decreases gradually with increase in the test temperature. The fact indicates that the radiation hardening measured at elevated temperature decreases accompanied by annealing of the radiation-produced defect clusters with increase in the test temperature, and also the barrier which causes the radiation-anneal hardening is not effective for dislocation motion at around 450°C.

CONCLUSIONS

(1) The radiation hardening measured at room temperature induced in the sample irradiated at 70°C to 1.0×10^{20} n/cm^2 can be explained by defect clusters visible in the electron microscope.

(2) The radiation-anneal hardening is observed to occur in the sample irradiated at 200 and 460°C to $(0.8 \sim 1.2) \times 10^{20}$ n/cm^2, while the radiation hardening of the sample irradiated at 70°C decreases monotonically with increasing annealing temperature.

(3) The radiation-anneal hardening and the hardening of the sample irradiated at 70°C and annealed at about 450°C are considered to be attributable to interstitial impurity clusters, possibly to carbon clusters.

(4) The hardening in the sample irradiated at 600°C is attributable to radiation-produced voids.

(5) The sample irradiated at 70°C to a fluence of 1.2×10^{21} n/cm^2 has good ductility in tensile-test at temperatures of 450°C and above.

(6) The sample irradiated at a temperature of 200°C or below to a fluence beyond 8×10^{19} n/cm^2 exhibits plastic instability or a little work hardening on deformation at room temperature. The irradiation embrittlement is not recovered by post-irradiation annealing at temperatures up to 450°C.

(7) The embrittlement is associated with coarse slip bands at the surface of the specimen and dislocation channels in transmission electron microscopy.

REFERENCES

1. A.P. Fraas, Nucl. Technol. 22, 10 (1974).
2. D. Steiner, Nucl. Fusion 14, 33 (1974).
3. K. Shiraishi, K. Fukaya and Y. Katano, J. Nucl. Mater. 54, 275 (1974).
4. M. Boček, H. Böhm and W. Scheneider, J. Nucl. Mater. 40, 249 (1971).
5. M. Venetch, A.A. Johnson and K. Mukherjee, J. Nucl. Mater. 34, 343 (1970).
6. G.R. Smolik and C.W. Chen, J. Nucl. Mater. 35, 94 (1970).
7. F.A. Smidt, Jr., Radiat. Eff. 10, 205 (1971).
8. J.F. McIlwain, C.W. Chen, R. Bajaj and M.S. Wechsler, Effects of Radiation on Substructure and Mechanical Properties of Metals and Alloys (ASTM STP 529), p.529, ASTM, Philadelphia, 1973.
9. M.S. Wechsler, D.G. Alexander, R. Bajaj and D.N. Carlson, Defects and Defect Clusters in B.C.C. Metals and their Alloys, p.127, National Bureau of Standards, Gaithersburg, 1973.
10. D.F. Hasson, Defects and Defect Clusters in B.C.C. Metals and their Alloys, p.147, National Bureau of Standards, Gaithersburg, 1973.

11. S. Morozumi, S. Goto and Y. Tsukaue, H. Kayano, J. Jap. Inst. Metals 39, 801 (1975).
12. K. Shiraishi, K. Fukaya and Y. Katano, J. Nucl. Mater. 44, 228 (1972).
13. M. Eto, K. Fukaya and K. Shiraishi, J. Nucl. Mater. 48, 365 (1973).
14. B.A. Loomis and S.B. Gerber, Acta Met. 21, 165 (1973).
15. D.J. Bailey and W.F. Flanagan, Phil. Mag. 15, 43, (1967).
16. P. Coulomb, Acta Met. 7, 556 (1959).
17. S.M. Ohr, R.P. Tucker and M.S. Wechsler, Phys. Status Solidi (a) 2, 559 (1970).
18. M. Eto, Y. Matsuo, S. Ishino and Y. Mishima, J. Nucl. Mater. 52, 309 (1972).

CORRELATION OF THE HOT-HARDNESS WITH THE TENSILE STRENGTH OF NEUTRON IRRADIATED MOLYBDENUM

J. Moteff[1], C. G. Schmidt[1] and F. W. Wiffen[2]

[1]Department of Materials Science
and Metallurgical Engineering
University of Cincinnati
Cincinnati, Ohio 45221

[2]Metals and Ceramics Division
Oak Ridge National Laboratory
Oak Ridge, Tennessee 37830

ABSTRACT

The elevated temperature ultimate tensile strength of recrystallized and of neutron irradiated molybdenum is shown to correlate very well with the corresponding hot-hardness data through the relationship

$$\sigma_u = (H/3)\ (n/0.217)^n$$

where H and n are the hardness values and strain hardening exponent respectively at the given temperatures. It is proposed that the hot-hardness tester be used as a strength microprobe in the preliminary evaluation of the mechanical properties of advanced alloys and of other materials generally available in limited quantities, such as irradiated specimens.

INTRODUCTION

In a recent review paper on the subject of the science of hardness testing and its research applications, Cilman[1] stated that a hardness tester may be considered to be a strength microprobe. Hardness of a material has been identified since classical times with the resistance to non-elastic penetration by a punch, and for a very long while it has also been related to resistance to scratching. These properties have been connected empirically with several other mechanical and physical properties of the material and, within limited ranges of conditions or materials, the relations are sometimes so close that measurement of the other property has been used to determine hardness. This has confused the definition of hardness but it has also added much to the practical value of hardness measurements, for hardness is commonly easier or quicker to determine than is the other property. Hardness measurements at elevated temperatures make the strength microprobe concept even more attractive as a research and development tool. Furthermore, the volume of material required to obtain strength information equivalent to 70 to 100 tensile specimens from only one hot-hardness test specimen is less than 10 percent of that required for one conventional tensile specimen. This circumstance, where less than one tenth of one percent of the volume of material used in a conventional tensile specimen per strength data point is especially an important consideration where (a) small heats of advanced alloys are being evaluated on the basis of strength, (b) irradiation facilities are such that only small quantities of material can be irradiated at a given time and (c) the radioactivity from neutron irradiated specimens requires limited testing in expensive and time consuming hot-cells.

There's no question that a reactor design engineer would prefer to use strenghh data generated from regular

tensile specimens and it is not proposed that the strength microprobe replace the tensile machine in future alloy qualification programs, although the concept has some merits. The engineering use of experimental data generated by the transmission electron microscope, such as the void density and size relationships in the irradiation induced swelling problems and by the scanning electron microscope with an energy dispersive x-ray analysis attachment, such as chemical analysis and second phase particle identifications, are examples of accepted micrometallurgical analytical tools. Preliminary results on the strength microprobe concept are encouraging and clearly suggest that further experimental and especially theoretical investigations of the correlation of hot-hardness to tensile strengths are in order. The purpose of this paper is to show the degree of correlation between the hot-hardness and the tensile properties of neutron irradiated and unirradiated molybdenum.

The general relationship between the hardness (H) and the uniaxial flow stress (σ) of a given material may be given as:

$$H = C\sigma \tag{1}$$

where C is called the constraint factor for the hardness test. As pointed out by Shaw and DeSalvo[2], the presently accepted theory for identation hardness ignores the elastic stress field and considers the material indented to behave in a rigid-plastic manner. Several different analytical solutions of this problem leads to a constraint factor value of C = 2.57. A new approach to plasticity has recently been presented[3] in which the material is assumed to be a plastic-elastic instead of the plastic-rigid model as in all previously existing theories. When an adjustment is made for the elastically loaded area, the constraint factor based on the plastic impression is found[2] to be equal to 3.0, a value of C which is in excellent agreement with the results of many experiments where the

material does not work harden and the indentor is relatively blunt (i.e. Vickers or Knoop).

For the case of room temperature properties Tabor[4] proposed a complex relationship between the ultimate tensile strength (σ) and the hardness (H) in which the strain hardening exponent (n) of the given material is explicitly considered. Following this approach, Cahoon[5] presented a more simplified equation having the form:

$$\sigma = \frac{H}{C}\left(\frac{n}{0.217}\right)^{n} \tag{2}$$

where the C was found by Tabor[4] to be 2.9 for steel and 3.0 for copper and by Cahoon et. al.[6] to have values of 3.0±0.1 for steel and aluminum specimens. Moteff and Sieber[7] used a value of C = 3.1 in the analysis of nine different heats of AISI 304 stainless steel tensile tested at room temperature as well as at 427, 593, and 649°C. In the 304 stainless steel study[7] the average discrepancy between the calculated strength, based on Eq. (2) using C equal to 3.1, and the actual experimental tensile strength level was within about 6 percent. Recently Bhargava and Moteff[8] showed excellent agreement with 304 stainless steel in the temperature range from 22 to 1200°C using a value of C equal to 3.0.

For direct comparison with Eq. (1), the previous equation may be rearranged into the form:

$$H = C'(n)\sigma \tag{3}$$

where the effective constraint factor C'(n) is now a function of the strain hardening exponent and using a value of C = 3.00 is given in the following equation:

$$C'(n) = Cf(n) = 3(n/0.217)^{-n} \tag{4}$$

The strain hardening exponent may be obtained directly through an analysis of the stress-strain diagram of a uniaxial tensile or compression test. The strain hardening ex-

ponent may also be obtained indirectly using several different approaches. One classic method is from a Meyer hardness measurement through the relationship $n = m - 2$, where m is the Meyer hardness coefficient. Another indirect method[9] for the determination of the strain hardening exponent is through the empirical expression:

$$n\lambda = k \qquad (5)$$

shown to agree quite well with direct measurements of n within the limits $0.2 < \lambda < 3.0$ where λ in micron units is the subgrain size of the plastically deformed metal and the constant k is equal to 0.2 microns.

Most of the studies on the correlation of hardness with tensile data are based on the unalloyed fcc metals, the austenitic stainless steels and on some of the ferritic steels with testing performed predominantly at room temperature. Only a few studies have been reported for the case of the higher temperature application refractory metals. Borisenko[10] has examined the connection between the hardness and ultimate tensile strength of tungsten and molybdenum over a wide range of temperatures. Results on the correlation at temperatures up to 1200°C between the hot-hardness and tensile strength of Nb and Nb-1Zr irradiated to a fast neutron fluence of 1×10^{20} n cm^{-2} has been reported by Kamphouse and Moteff[11] and also on molybdenum, tungsten and vanadium by the same authors[12]. Oku and Usui[13] reported their findings on the hot hardness-tensile relationships of tungsten and molybdenum specimens irradiated to 2.7×10^{19} n cm^{-2}. In the Oku and Usui studies the test temperatures ranged from about 150 to 1000°K for tungsten and from about 100 to 600°K for the case of molybdenum.

EXPERIMENTAL PROCEDURES AND RESULTS

A total of 10 tensile tests, conducted at 5 temperatures ranging from RT up to 650°C are compared with 100 separate hardness indentations made at about 16 different temperatures ranging from RT up to 1200°C. About one-half of the experimental data points were obtained from neutron irradiated specimens.

Hot-Hardness

The test specimen, 8 mm x 10 mm by 0.5 mm thick was fabricated from commercial grade arc-cast molybdenum and given a post-fabrication anneal for 1 hour at 1200°C in vacuum. The carbon and oxygen interstitial impurity level is 30 ppm and 25 ppm respectively. Three indents, with hold times of 30 sec and using a 500 gram load, were made at each temperature on the electropolished sample after the specimen soaked at the test temperature for one hour. The furnace atmosphere was high purity argon gas. Details of the hot-hardness test equipment have been presented previously.[14] The hardness measurements were made with a Vickers indentor (sapphire tip) and are reported as diamond pyramid hardness (DPH) units in kg mm^{-2}.

The hardness specimen was irradiated in the Row 2 position of the EBR II facility at a temperature of approximately 425°C and to a fast neutron fluence of about 2.5×10^{22} n cm^{-2}, $E_n > 0.1$ MeV.

Average values of the hardness measurements taken at each temperature for both the unirradiated and the irradiated specimens are plotted in Figure 1. The scatter in the individual hardness values at each temperature was normally small and would fall within the area of the symbol used to designate the data. Exceptions were noted for the case of the irradiated specimen and the scatter is indicated by the length of the bar through the data symbol.

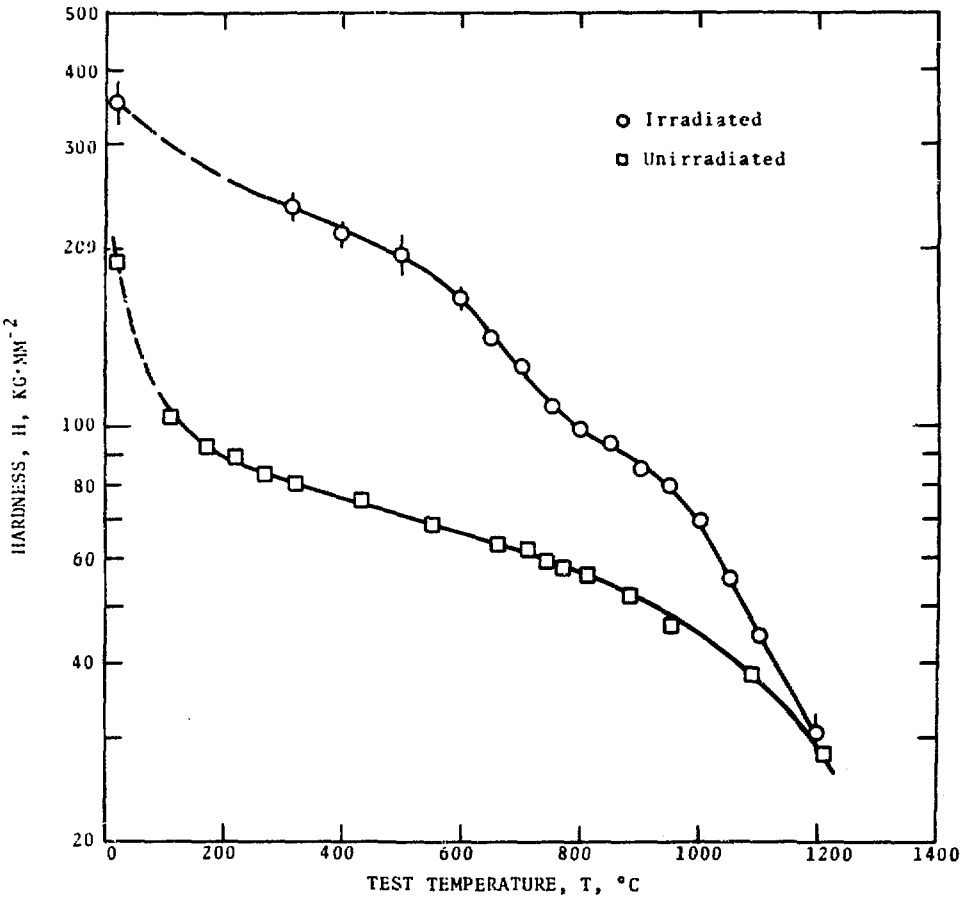

Fig. 1. Hardness of Recrystallized and of Neutron Irradiated Molybdenum as a Function of Temperature. Specimen Irradiated in EBR-II to a Fluence of 2.5×10^{22} n cm^{-2}, $E_n > 0.1$ MeV at 425°C.

At 5 different intervals during the course of the ascending temperature hardness measurements, the furnace temperature would be lowered so that the specimen would be at a constant temperature of about 314°C and a set of indentations would then be made. The purpose of these measurements was to determine the influence of the annealing temperature, and therefore the one variable being the defect state, on the hardness at a given temperature. Normally, when the indentations are made a progressively higher temperatures, both the irradiation induced cluster defect density and size and the dislocation flow and dislocation-defect interaction mechanisms will be variable.

Tensile

The specimens used in this study were made from arc-cast commercial grade molybdenum. The carbon and oxygen interstitial impurity levels are 30 ppm and 7 ppm, respectively.

Tensile tests were conducted on an Instron testing machine in a flowing helium environment. Specimens were held 30 min at temperature before the start of the test. Engineering stresses based on initial specimen dimensions are reported, with the exception of one case, all tests were performed at crosshead speeds of 0.02 in. min^{-1}. As the specimens have an effective gage length of 1.0 inch, nominal strain rates are assumed to be equal to the crosshead speeds.

The specimens were irradiated in Row 7 of the EBR-II facility at a temperature of about 454°C and to a fast neutron fluence of 3.5×10^{22} n cm^{-2}, $E_n > 0.1$ MeV. Details of the irradiation capsule, irradiation conditions and the complete tensile results are reported elsewhere.[15]

Ultimate tensile strengths of the unirradiated and the irradiated specimens used in this study are listed in Table I.

TABLE 1 - TENSILE STRENGTH OF CONTROL AND IRRADIATED MOLYBDENUM

Test Temperature T, °C	Ultimate Tensile Strength[1]				
	Unirradiated		Irradiated		
	σ_u, ksi	σ_u, kg·mm^{-2}	σ_u, ksi (2)	σ_u, kg·mm^{-2} (2)	σ_u, kg·mm^{-2} (3)
22	72.0	50.7	--	--	--
200	51.1	35.9	127[4]	89.3	75.4
400	37.9	26.7	113	79.5	67.2
550	33.5	23.6	101	71.0	60.0
650	32.5	22.9	86.3	60.7	51.3

[1] Tested at a nominal strain rate of 0.02 min^{-1}.

[2] Irradiated in EBR-II to a fast neutron fluence of about 3.5 x 10^{22} n cm^{-2}, E > 0.1 MeV at about 454°C.

[3] Normalized to a fast neutron fluence of 2.5 x 10^{22} n cm^{-2}, E > 0.1 MeV for comparison with the hot-hardness data. Normalization factor $(2.5/3.5)^{1/2}$ equals 0.85.

[4] Tested at a nominal strain rate of 0.0002 min^{-1}.

Since the hot-hardness specimen was irradiated to a fast neutron fluence of 2.5×10^{22} n cm^{-2}, $E_n > 0.1$ MeV, the tensile data was normalized to this fluence so that a direct comparison could be made with the hardness results. It was assumed that the hardening behavior for the elevated temperature irradiations and testing followed a square root fluence dependency and that saturation hardening has not yet been achieved at this relatively low fluence. The normalization factor therefore would be 0.85, i.e. $(2.5/3.5)^{1/2}$ and the normalized ultimate tensile strength values of the irradiated specimens are accordingly listed in the last column of Table I.

DISCUSSION OF DATA

The ultimate tensile strength was calculated by use of Equation 2 and the strain hardening exponents given in Figure 2. It was assumed that the strain hardening behavior of recrystallized molybdenum would not vary significantly and the data published by Bechtold[16] would be representative of the strain hardening characteristics of the present material. The strain hardening behavior of the irradiated molybdenum is estimated based on some unpublished annealing studies.

Figure 3 shows plots (solid lines) of the tensile strength for both the unirradiated and the irradiated molybdenum as calculated from the hot-hardness data. The strain hardening exponent correction parameter $(n/0.217)^n$ was essentially unity for the case of the irradiated specimen and therefore the parameter given by Equation 4 is a constant and equal to 3.0, i.e. $c'(n) = c = 3.0$. The same situation is true for the case of the unirradiated data at temperatures of 650°C and above. The corrections at the lower temperatures are 13, 10, 7 and 4.5 percent for the 200, 300, 400 and 550°C test temperatures, respectively.

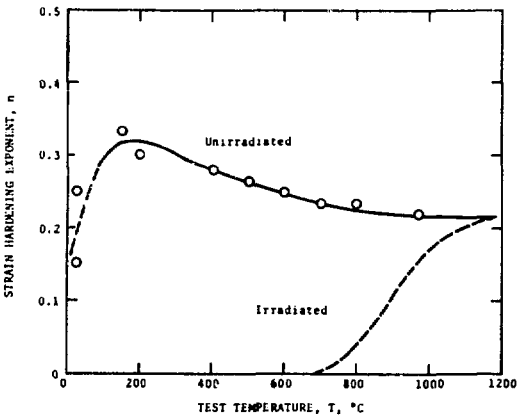

Fig. 2. Strain Hardening Exponent Values of Recrystallized Molybdenum as a Function of Temperature. Dashed Line Represents an Estimate Value for Heavily Irradiated Molybdenum.

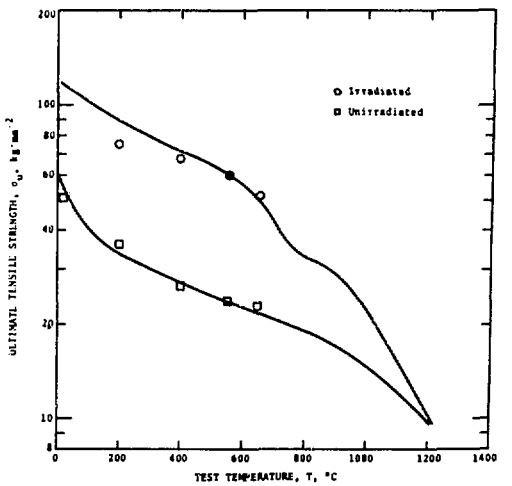

Fig. 3. Calculated (solid lines) and Experimental (data points) Values of the Ultimate Tensile Strength of Recrystallized and of Neutron Irradiated Molybdenum as a Function of Temperature.

The five data points designating the experimental tensile strengths are also plotted in Figure 3. The predicted tensile strengths are within about 7 percent of the experimental values. The comparisons are tabulated in Table II.

With the exception of the 200°C test condition, the predicted tensile strengths fell within 6 percent of the experimental values. The calculated tensile strength for the 200°C test condition was about 15 percent greater than the experimental value. This large discrepancy would be expected since the fracture stress of molybdenum would be in the region of about 70 to 80 kg mm^{-2}. The numbers based on the hardness tests would probably be in much better agreement if the comparisons were made with specimens tested in compression rather than tension.

Although preliminary transmission electron microscopy,[17] performed on molybdenum specimens irradiated under similar conditions to the hardness specimens (2.5×10^{22} n cm^{-2}, $E_n > 0.1$ MeV at 425) did not reveal the presence of voids, it is possible that specimens annealed at temperatures of 200°C and greater may show that small voids are present in the material. This TEM study is now in progress and therefore any detailed quantitative analysis on the exact cause of the irradiation induced hardening will be performed at a later date. Similar TEM studies will also be made on each of the four tensile specimens so that the nature and density of the irradiation induced defects may be established. This important information will also be used to determine a more realistic normalization procedure when comparing samples irradiated under slightly different conditions.

A qualitative evaluation of the expected types and densities of defects which may be present in the specimens when irradiated in the region of 425 to 454°C and followed by anneals to higher temperatures is based on some recent

TABLE 2 - TENSILE STRENGTH DETERMINED FROM HARDNESS MEASUREMENTS

Test Temperature T, °C	Ultimate Tensile Strength			
	Unirradiated		Irradiated	
	σ_u, kg·mm^{-2}	Percent Difference*	σ_u, kg·mm^{-2}	Percent Difference
22	54.0	+6.1	--	--
200	33.5	-7.2	89.0	+15.2
400	27.2	+1.8	71.5	+ 6.0
550	23.6	0	60.0	0
650	21.7	-5.5	49.5	- 3.6

*Using the experimental tensile strengths given in Table I, the percent difference listed in this table is given by

$$\frac{(\sigma_u)_{cal} - (\sigma_u)_{exp}}{(\sigma_u)_{cal}} \times 100.$$

studies by Sikka and Moteff.[18] The normalized void and loop densities are plotted in Figure 4a. It is clear that essentially all the loops are removed by the 800°C anneal conditions and the voids are removed slightly above 1200°C.

Figure 4b shows the normalized irradiation induced hardening at a fixed temperature of 314°C following anneals at higher temperatures. It appears that both loops and voids contribute to the hardening at anneal temperatures below 800°C and that possibly only the voids contribute following anneal temperatures greater than 800°C.

A hardening model of the type

$$\Delta\tau = \alpha \frac{\mu b}{\ell} \tag{6}$$

may be used[19] to describe the irradiation induced hardening, where μb is the product of the shear modulus and the Burger's vector, ℓ is the mean dispersion between the cluster defect barriers and α is a dislocation-defect interaction parameter, assumed to be a constant at a given temperature and for a specified barrier type. The dispersion length may be related to the defect cluster density(N) and size (d) by

$$\ell = (Nd)^{-1/2}. \tag{7}$$

On the other hand, when tests are conducted at progressively higher temperatures, then the values of N and d will change and therefore result in different values for ℓ at each temperature. These changes however would be the same if the tests were conducted at the last anneal temperature or at some lower reference temperature following the high temperature anneal, such as the 314°C used in this study.

Figure 4c clearly shows the influence of test temperature on the values of the parameter α as used in Equation 6. The slight temperature dependence of the shear modulus would not account for the magnitudes of the temperature dependent hardness increments. For instance, at temperatures

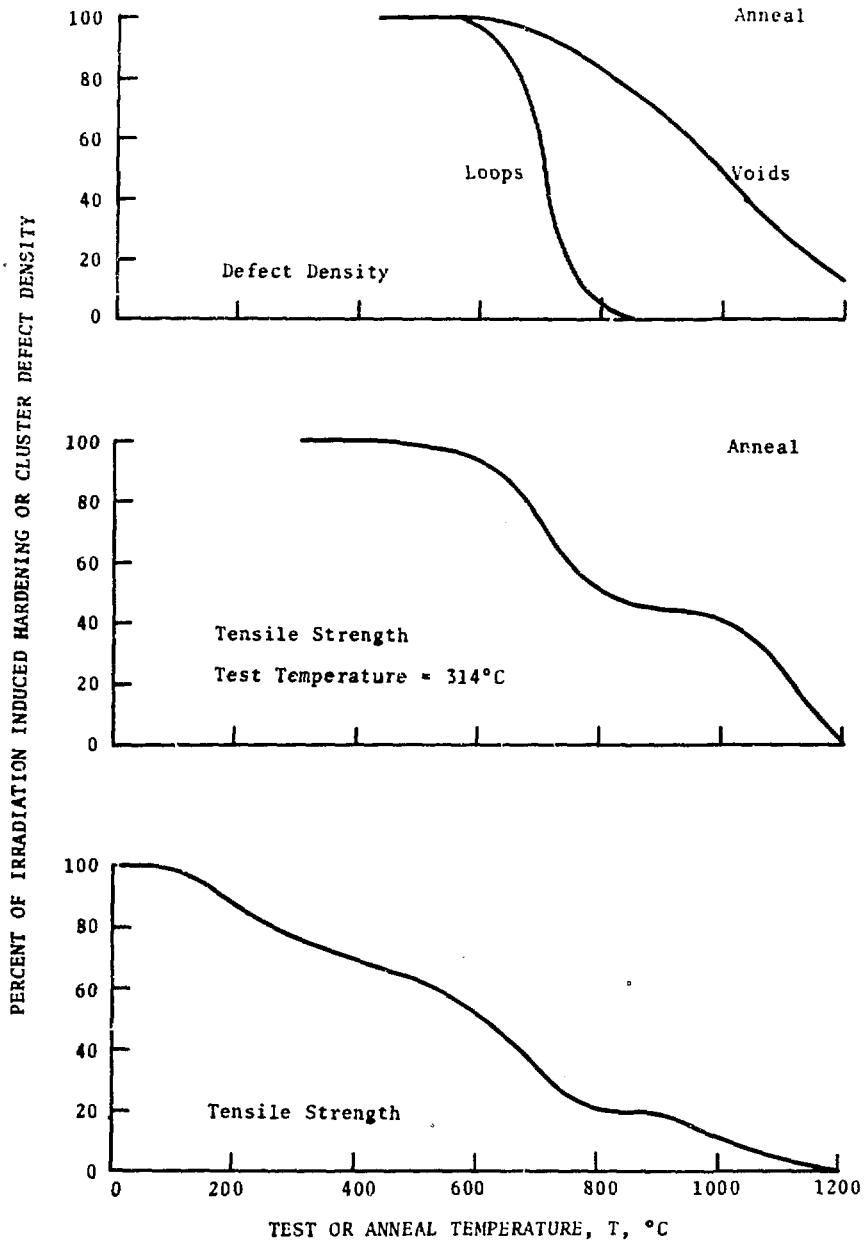

Fig. 4. Variation of the (a) Defect Cluster Density, the (b) 314°C Irradiation Induced Hardness Values as a Function of Anneal Temperature and of the (c) Irradiation Induced Hardness Values as a Function of Test Temperature.

below about 450°C the cluster defect density is constant as well as those defects which would cause changes in the electrical resistivity.[20] Therefore, with the exception of the slight changes in th shear modulus with temperature, the only variable will be the parameter α. The dislocation flow mechanisms are believed to be significantly different above and below a temperature of 0.15 T_m, where T_m is the absolute melting temperature. This may account for the obvious change in hardening behavior above and below a temperature of about 160°C.

SUMMARY

It is concluded that the use of a hot-hardness tester as a strength microprobe is a viable concept in the study of radiation induced hardening. The present studies confirm previous investigations where it has been shown that the hot-hardness data correlates reasonably well with the hot tensile strength of the same material through the relationship

$$\sigma_u = \frac{H}{3} \left(\frac{n}{0.217}\right)^n$$

where H is the hardness, n the strain hardening exponent and σ_u the ultimate tensile strength all at the same temperature.

The degree of agreement between the predicted and the actual stress levels is well within ±7 percent for nine of the ten test conditions evaluated and that the one condition that showed a 15 percent discrepancy can be explained as being due to the fact that the fracture stress was lower than the tensile yield stress of the irradiated material at the 200°C test temperature.

Studies on the detailed microstructure of all the specimens used in this experiment should be performed so that the various hardening models may be evaluated on a

quantitative basis.

Recommendations are made that additional experimental and theoretical studies be performed on the strength microprobe concept and that serious consideration should be given to the application of this tool to the evaluation of the influence of 14 MeV neutrons on the elevated temperature irradiation induced strengthening of metals and alloys.

ACKNOWLEDGMENTS

Research was sponsored by the U.S. Energy Research and Development Administration under contract with Union Carbide Corporation and with the University of Cincinnati. The work at the University of Cincinnati was supported through the Division of Research under Contract AT(11-1)-2093.

REFERENCES

1. J. J. Gilman, The Science of Hardness Testing and Its Research Applications, J. H. Westbrook and H. Conrad, eds., pp. 51-74, American Society for Metals, Metals Park, Ohio, 1973.
2. M. C. Shaw and G. J. DeSalvo, Metals Eng. Quart. 12, 1 (1972).
3. M. C. Shaw and G. J. DeSalvo, Trans. ASME 92, 469 (1970).
4. D. Tabor, J. Inst. Metals 79, 1 (1951).
5. J. R. Cahoon, Met. Trans. 3, 3040 (1972).
6. J. R. Cahoon, W. H. Broughton, and A. R. Kutzak, Met. Trans. 2, 1979 (1971).
7. J. Moteff and P. R. Seiber, Met. Trans. 5, 315 (1974).
8. J. Moteff, R. K. Bhargava and W. L. McCullough, Met. Trans., 6A, 1101 (1975).

9. K. D. Challenger and J. Moteff, Scr. Met. 6, 155 (1972).

10. V. A. Bonisenko, Poroshkovaya Met. Akad. Nauk. Ukr. SSR 2, 57 (1965).

11. J. L. Kamphouse and J. Moteff, ANS Trans. 11, 151 (1968).

12. J. Moteff, unpublished data.

13. T. Oku and T. Usui, J. of Nuc. Matl. 40, 93 (1971).

14. J. L. Kamphouse, J. C. Blake and J. Moteff, Rev. Sci. Instrum. 40, 321 (1969).

15. F. W. Wiffen, Defects and Defect Clusters in BCC Metals and Their Alloys, ed., R. J. Arsenault, 1973, pp. 176-197.

16. J. H. Bechtold, AIME Trans. 5, 1469 (1953).

17. F. W. Wiffen, Radiation-Induced Voids in Metals, ed., J. W. Corbett and L. C. Ianniello, AEC Symp. Ser. 26, CONF-710601, 1972, p. 386.

18. V. K. Sikka and J. Moteff, Nucl Tech. 22, 52 (1974).

19. J. Moteff, D. J. Michel and V. K. Sikka, Defects and Defect Clusters in BCC Metals and Their Alloys, ed., R. J. Arsenault, 1973, pp. 198-215.

20. J. Moteff, Unpublished data.

15 MeV NEUTRON DAMAGE IN Cu AND Nb

J. B. Roberto, J. Narayan, and M. J. Saltmarsh
Oak Ridge National Laboratory
Oak Ridge, Tenn. 37830

ABSTRACT

We have investigated high energy neutron damage in Cu and Nb irradiated with ~15 MeV neutrons at the Oak Ridge Isochronous Cyclotron. The neutrons were generated by bombarding a thick Be target with 40 MeV deuterons resulting in a high energy neutron spectrum broadly peaked at 15 MeV. Single crystals of Cu and Nb were irradiated at room temperature to fluences of ~2 x 10^{17} n/cm^2. The resulting loop-type defect clusters in the crystals were characterized using x-ray diffuse scattering and transmission electron microscopy. The cluster size distributions were found to be generally similar to those characteristic of fission neutron irradiations in these materials and no multiple clusters or sub-clusters were observed. Additional comparisons with fission reactor irradiations in Cu and Nb indicate that the retained displacement damage in these crystals is approximately 3 times greater for the high energy neutrons than for an equivalent fluence of fission neutrons. This result is consistent with detailed damage energy calculations for the Be(d,n) neutron spectrum.

INTRODUCTION

Recent experimental studies[1] and theoretical calculations[2] have suggested that high energy neutrons (E ≈ 15 MeV) are substantially more effective in producing displacement damage than fission neutrons. Such implications are important to the fusion reactor designer who must consider the effects of significant fluences of high energy neutrons on reactor materials. In this work, we have attempted to quantify some of the differences between high energy and fission neutron damage in Cu and Nb and to correlate the experimental results

with theoretical calculations. The experiments have involved irradiations near room temperature followed by characterization of the retained damage in the resulting loop-type defect clusters.

This study is unique in several respects. First, high purity nearly perfect single crystals from the same source material were prepared identically for the high energy and fission neutron irradiations. As a result, spurious effects due to impurities or specimen differences were held to a practical minimum. Secondly, for Cu, both x-ray diffuse scattering and transmission electron microscopy were used to characterize the radiation-induced defects. Finally, the experimental results were compared with very detailed damage energy calculations which explicitly treated the various nuclear reactions which occur in the range of neutron energies present in these experiments.

This work also represents the first utilization of high energy neutrons from the deuteron breakup or "stripping" reaction to perform radiation damage experiments. The deuteron-breakup concept is the subject of considerable interest as a possible mechanism for producing a high-flux large volume source of high energy neutrons for CTR radiation effects research. Several proposals have been made[3,4] and our results provide direct evidence of the usefulness of such a source.

Be(d,n) NEUTRONS

The high energy neutrons were generated at the Oak Ridge Isochronous Cyclotron by stopping a 40 MeV deuteron beam in a thick Be target. The associated deuteron-breakup (d,n) reaction[5] results in a neutron spectrum which is broadly distributed in energy about a maximum at approximately 15 MeV with some neutrons above 30 MeV. The neutrons are strongly forward-peaked and are degraded in both energy and intensity with increasing angle from the deuteron beam axis. The ORIC source[6] produces a maximum flux of $2 \times 10^{12} n/cm^2$-sec

at the specimen chamber with a full-width-half-maximum of approximately 7mm. The results of a recent time-of-flight measurement[4] of the Be(d,n) spectrum are shown in Fig. 1.

The broad energy distribution of the Be(d,n) spectrum presents somewhat of an interpretive problem for radiation damage experiments. In particular, the effects of the high energy tail of the spectrum must be considered. We have approached this problem by computing the displacement damage energy in Cu and Nb as a function of incident neutron energy. The damage energy is that part of the primary recoil energy which is ultimately available for producing atomic displacements. The damage energy concept is therefore useful for comparing displacement damage at various neutron energies. Our calculations are based on the electronic stopping theory of Lindhard[7] and are generally similar to earlier calculations of the energy dependence of neutron damage by Robinson.[2]

For the Be(d,n) spectrum, it is necessary to consider neutron interactions which occur at energies of 30 MeV and higher. Neutron cross-sections are generally unavailable above 15 MeV and we have used theoretical cross-sections[8] based on optical and pre-compound nuclear models for our damage energy calculations. These cross-sections were computed by C.Y.Fu and F.G. Perey of Oak Ridge National Laboratory and include elastic scattering as well as the principle classes of nonelastic interactions. The results of damage energy calculations based on these cross-sections will be published in more detail elsewhere,[9] but we include the damage energy curves for Cu as an example in Fig. 2.

EXPERIMENTAL PROCEDURE

Specimen Preparation

The Cu samples were high purity single crystal platelets approximately 1 x 1 x 0.1 cm which were acid cut from single crystal ingots and lightly polished in 10% H_3PO_4. The Nb crystals were grown from .05 cm thick sheets of zone-refined starting material using the strain-anneal technique. Large single crystal regions up to several

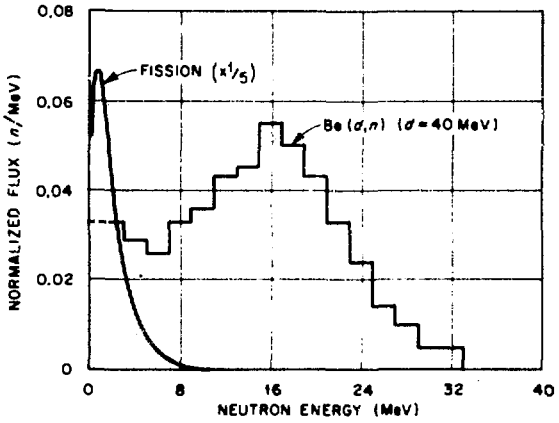

Fig. 1. High Energy Be(d,n) Neutron Spectrum Compared with a Pure Fission Spectrum.

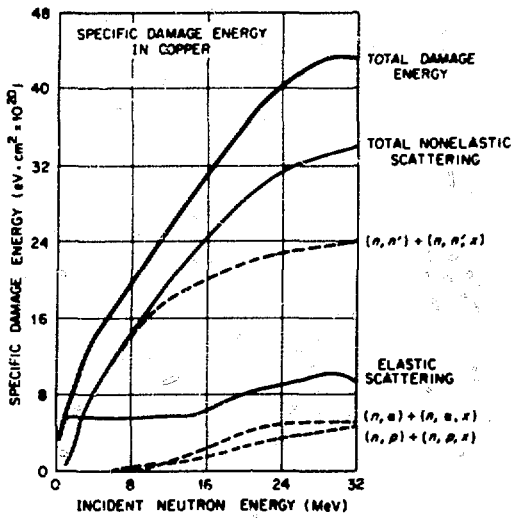

Fig. 2. Specific Damage Energy vs. Neutron Energy in Cu.

square cm in area and with orientations predominately near (110) could be identified in the resulting grain structure. Small platelets 0.5 x 1 x 0.05 cm were spark cut from these single crystal regions and polished using 3:2 HNO_3 and HF.

The resulting Cu and Nb specimens were essentially perfect from the standpoint of Borrmann topography and exhibited near intrinsic Bragg diffraction widths. The Cu starting material was 99.999% pure. The predominate impurities in the Nb starting material were C, O, Ta and W, all at concentrations of 50 wt. ppm or less. The results of residual gas analysis by the vacuum fusion technique for H, N, and O in the Cu and Nb samples after polishing are shown in Table 1. Also shown in Table 1 are the concentrations of C, Ta, and W in the annealed Nb as determined by chemical analysis.

Irradiation Technique

The high energy Be(d,n) neutron irradiations were carried out in an open-ended aluminum capsule with the samples separated by aluminum spacer rings. Two Cu and two Nb specimens were mounted one behind the other along the beam axis. Ni and Co dosimetry foils were placed before and after the sample capsule and the neutron fluence decreased approximately 13% from the first to last sample. The details of the dosimetry have been described elsewhere.[6] The irradiations were carried out at room temperature on a continuous basis over a period of 30 hrs. with a total spectrum dose of $2.0 \times 10^{17} n/cm^2$ at the center of the first sample.

The fission reactor irradiations were preformed at the CP-15 facility of the Solid State Division's bulk shielding reactor. The neutron flux and energy spectrum at the CP-15 position has been carefully measured[10] over the range from 0.6 to 3 MeV and is very similar to a pure fission spectrum. For our fluence and damage energy calculations we have assumed such a neutron distribution. This pure fission neutron spectrum can be compared with the Be(d,n) spectrum in Fig. 1. The fission reactor irradiations were carried out

Table 1. Impurity Analysis of Cu and Nb Samples

(wt. ppm)	H	C	N	O	Ta	W
Cu	30	-	<5	10	-	-
Nb	<5	50	10	50	50	15

at 43°C in a pressurized He-cooled vessel. The total fluences were 1.0×10^{18} and 5.0×10^{17} n/cm^2 ($E > 0.1$ MeV) respectively for the Cu and Nb samples. Following both the high energy and fission neutron irradiations, the samples were allowed to decay for approximately two months and then lightly polished using the techniques described above to remove any surface contamination.

TEM Measurements

Transmission electron microscopy measurements were carried out on both the Nb and Cu crystals using a Hitachi 200 keV electron microscope. The TEM samples were prepared by conventional electropolishing techniques. For the Be(d,n) irradiations, the samples were cut from the high-fluence center region of the crystals. High resolution weak beam (dark field), higher order diffraction (3g), and conventional bright and dark field microscopy were used to determine the size distributions of defect clusters which were present in the form of dislocation loops. Sample thicknesses were determined by stereomicroscopy.

X-ray Measurements

The radiation-induced defects in the Cu crystals were also characterized using x-ray diffuse scattering. These measurements involved collecting the total diffracted intensity into a wide open detector as a function of deviation from the Bragg angle. Care was taken to insure that the measurements corresponded to the high-fluence center region of the Be(d,n) irradiated crystals. Intensity vs. angle

curves about the (111) and (222) reflections were measured both before and after irradiation. The difference in the curves represents the diffuse scattering from the defects themselves and was interpreted using a computed program developed by B. C. Larson.[11] The computer technique uses a least-squares fitting procedure to obtain a size distribution from the scattering data for the loop-type defect clusters. For Cu we have assumed loops on (111) planes with (110) Burgers vectors. Efforts to measure the diffuse scattering from Nb were unsuccessful due to the low retained defect density and high background associated with the Nb samples.

RESULTS AND DISCUSSION

The results of our measurements of the retained defect clusters in Be(d,n) and fission neutron irradiated Cu and Nb are summarized in Figs. 3-6. In Fig. 3, bright field electronmicrographs are shown for ~15 MeV and fission neutron damage in Cu. The micrographs correspond to doses of $2.0 \times 10^{17} n/cm^2$ and $1.0 \times 10^{18} n/cm^2$ ($E > 0.1$ MeV) respectively for the 15 MeV and fission neutron irradiations. Loop size distributions in Cu as determined by TEM and x-ray measurements are compared in Fig. 4. These size distributions represent independent measurements with no adjustable parameters. The absolute agreement within about a factor of two between the TEM and x-ray results is encouraging, but more important is the close agreement on the relative effects of high energy and fission neutron irradiations as determined independently by the two experimental techniques.

Micrographs for the high energy and fission neutron irradiations in Nb are shown in Fig. 5. These micrographs correspond to doses of $1.8 \times 10^{17} n/cm^2$ over the Be(d,n) spectrum and $5.0 \times 10^{17} n/cm^2$ ($E > 0.1$ MeV) for fission neutrons. Loop size distributions from TEM measurements in Nb for both 15 MeV and fission neutron damage are shown in Fig. 6. The average loop size is much smaller for Nb than Cu.

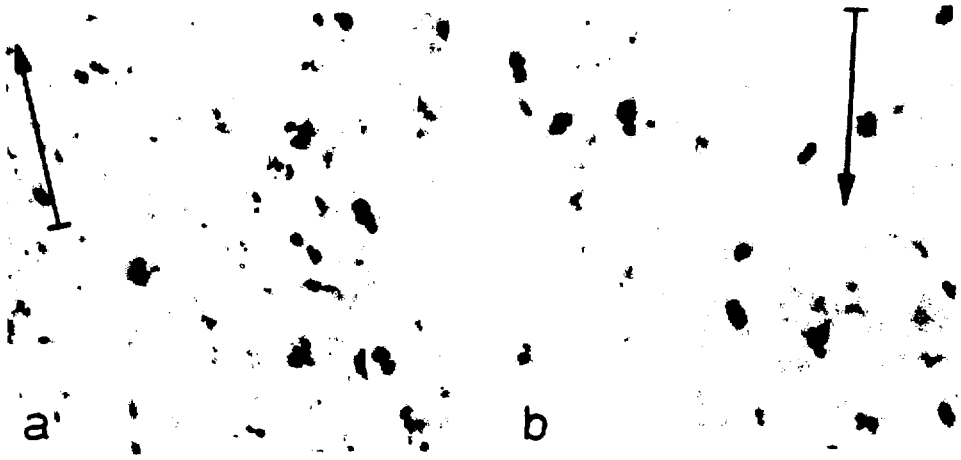

Fig. 3. TEM Micrographs of Cu Irradiated with (a) Fission Neutrons ($1.0 \times 10^{18} n/cm^2$ $E > 0.1$ MeV) and (b) ~15 MeV Neutrons ($2.0 \times 10^{17} n/cm^2$ over the Be(d,n) Spectrum). The arrow indicates the direction of the diffraction vector $[\bar{2}20]$ and corresponds to a length of 0.2 microns.

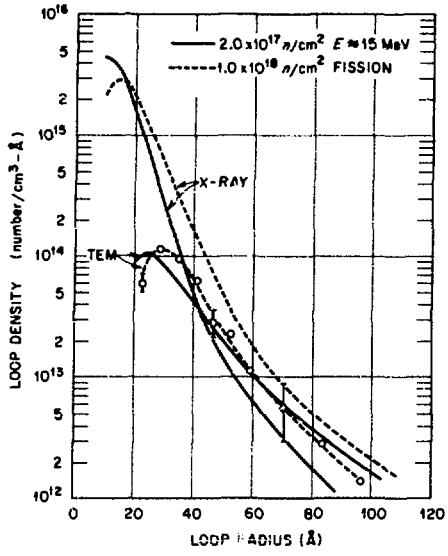

Fig. 4. Loop Size Distributions in Cu for Fission and ~15 MeV Neutron Irradiations as Determined by TEM and X-ray Techniques. The x-ray data for fission neutrons is from ref. 11.

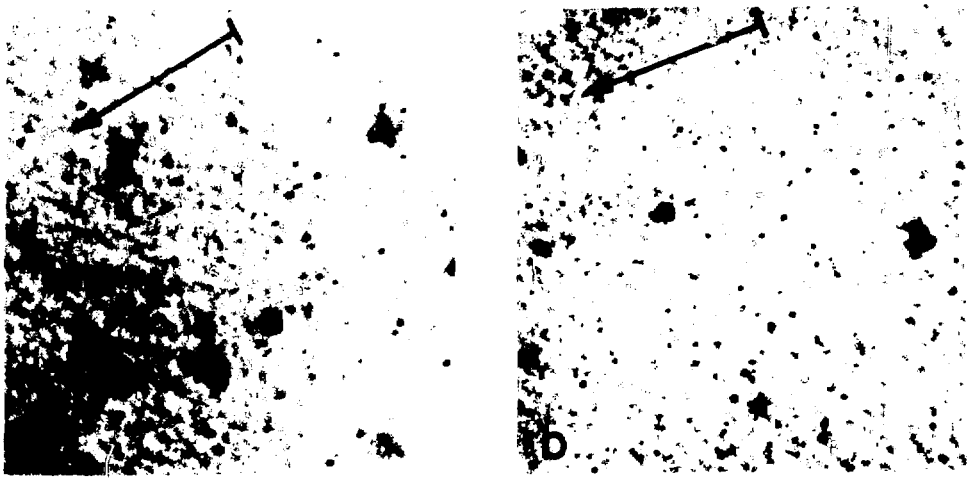

Fig. 5. TEM Micrographs of Nb irradiated with (a) Fission Neutrons (5.0×10^{17}n/cm^2 E > 0.1 MeV) and (b) ~15 MeV Neutrons (1.8×10^{17}n/cm^2 over the Be(d,n) Spectrum). The arrow indicates the diffraction vector [3$\bar{3}$0] and corresponds to a length of 0.2 microns.

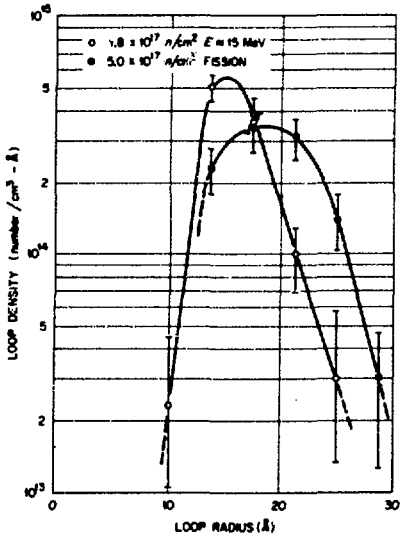

Fig. 6. Loop Size Distributions in Nb for Fission and ~15 MeV Neutron Irradiations as Determined by TEM Measurements.

General similarities between the retained damage from high energy and fission neutron irradiations in both Cu and Nb are apparent in the micrographs and size distributions of Figs. 3-6. Further study will be required to determine whether or not some of the small differences in the observed size distributions for 15 MeV and fission damage are significant. The possible existence of multiple defect clusters associated with the 15 MeV neutron irradiations was also investigated. Careful stereomicroscopy (both weak beam and higher order diffraction techniques) revealed no apparent indications of multiple clusters in either Cu or Nb.

In order to compare the Be(d,n) and fission neutron damage in Nb and Cu on an absolute basis, we have integrated the size distribution curves of Figs. 4 and 6 to determine the retained point defect densities. When adjusted for differences in fluence, these point defect densities give a relative indication of the damage effectiveness of the high energy and fission neutrons. Ratios of the damage effectiveness of Be(d,n) neutrons in terms of fission neutrons as determined from the experimentally observed point defect densities are shown in Table 2. The ratios derived from the TEM and x-ray measurements in Cu are in fairly good agreement and indicate that these independent techniques sample comparable aspects of the damage. Also shown in the table are theoretical ratios based on the damage energy calculations described above.

The agreement between theory and experiment in Table 2 is quite remarkable and indicates that the damage effectiveness of a Be(d,n) neutron with a mean energy of 15 MeV is approximately 3 times greater than a fission neutron in Cu and Nb. Of course, the irradiations were carried out near room temperature where annealing effects are important while the damage energy calculations are appropriate for low temperatures. Nevertheless, the good correlation between theory and experiment for both Cu and Nb suggests that the annealing characteristics of high energy and fission neutron damage are similar and that differences in displacement cascade structure are not striking.

Table 2. Damage Effectiveness of Be(d,n)[a] Neutrons as Compared with Fission Reactor Neutrons

Material	Experiment Retained Damage Be(d,n)/Fission	Theory Damage Energy Be(d,n)/Fission
Cu	3.3 (X-ray) 4.0 (TEM)	3.4
Nb	2.5 (TEM)	2.6

[a]Deuteron energy, 40 MeV.

SUMMARY AND CONCLUSIONS

We have described an experimental investigation of high energy ($E \simeq 15$ MeV) neutron damage in Cu and Nb. Both TEM and x-ray measurements have been used to characterize the surviving loop-type defect clusters in near room temperature irradiations using high energy Be(d,n) neutrons as well as fission neutrons. The resulting cluster size distributions have been compared for high energy and fission neutrons and the defect densities correlated with detailed damage energy calculations. We are led to the following conclusions:

1) The damage effectiveness of a Be(d,n) neutron with a mean energy of 15 MeV is ~3 times that of a fission reactor neutron in Cu and Nb. This result is supported by both experiment and theory.
2) There are general similarities in loop size distributions for the high energy and fission neutron irradiations. Additional studies are required to compare the size distributions in detail.
3) There are no apparent indications for the existence of multiple defect clusters resulting from the high energy neutron irradiations in either Cu or Nb.

4) The deuteron-breakup reaction has proven to be a useful technique for generating high energy neutrons for radiation damage studies. We have shown that we can computationally handle the broad energy spectrum of the neutron source and that the interpretation of the experimental results for Cu and Nb is not particularly complicated by the source spectrum.

The overall results suggest similarities between high energy and fission neutron radiation damage when compared using the damage energy concept. We are currently expanding our experiments and calculations to include Al and Au to represent a broader range in atomic species. Low temperature damage rate measurements are also planned as a complement to our damage effectiveness results. In addition, a detailed analysis of the nature of the defects produced in the high energy and fission neutron irradiations is underway.

ACKNOWLEDGEMENTS

The authors wish to acknowledge many of their ORNL colleagues for their assistance during the course of these experiments. In particular, we wish to thank F. W. Young, Jr. and R. E. Reed for respectively providing the Cu and Nb crystals, C. Y. Fu and F. G. Perey for computing neutron cross-sections and G. J. Smith for performing neutron dosimetry. The authors also acknowledge valuable discussions with M. T. Robinson, B. C. Larson, L. H. Jenkins, and T. S. Noggle as well as the experimental assistance of F. A. Sherrill. This work was supported by the USERDA under contract with Union Carbide Corporation.

REFERENCES

1. J. B. Mitchell, C. M. Logan and C. J. Echer, J. Nucl. Mater. 48, 139 (1973); J. B. Mitchell, R. A. VanKonynenburg, M. W. Guinan and C. J. Echer, Phil. Mag. 31, 919 (1975).

2. M. T. Robinson in Nuclear Fusion Reactors, p. 364, Brit. Nuclear Energy Soc. (1970).

3. A. N. Goland, D. H. Gurinsky, J. Hendrie, J. Kukkonen, T. Sheehan and C. L. Snead, Jr. in Proc. of Int. Conf. on Radiation Test Facilities for CTR Surface and Materials Program, Argonne National Laboratory, July 1975, in press.

4. M. J. Saltmarsh, A. P. Fraas, J. A. Horak and J. A. Martin in ref. 3.

5. R. Serber, Phys. Rev. 72, 1008 (1947).

6. L. H. Jenkins, T. S. Noggle, R. E. Reed, M. J. Saltmarsh and G. J. Smith, Appl. Phys. Lett. 26, 426 (1975).

7. J. Lindhard, V. Nielsen, M. Scharff and P. V. Thomsen, Kgl. Danske Videnskab. Selskab, Mat. - Fys. Medd. 33, No. 10 (1963).

8. C. Y. Fu and F. G. Perey, to be published.

9. J. B. Roberto and M. T. Robinson, to be published.

10. J. M. Williams, private communication.

11. B. C. Larson, J. Appl. Cryst. 8, 150 (1975).

DT FUSION NEUTRON RADIATION STRENGTHENING OF COPPER AND NIOBIUM

J. B. Mitchell* D. M. Parkin+
R. A. Van Konynenburg* C. J. Echer*

*Lawrence Livermore Laboratory, Livermore, CA
+Los Alamos Scientific Laboratory, Los Alamos, NM

ABSTRACT

The initial results of a comparative study of the radiation strengthening and damage structures produced in Cu and Nb by D-T fusion and fission reactor neutrons are described. The radiation strengthening produced by a given fluence of fusion neutrons above about 10^{17} n/cm^2 is equal to that produced by a fluence of fission reactor neutrons (E >0.1 MeV) ten times as great. This difference is about twice as large as would be expected if the strengthening scaled with damage energy or dpa. Initial transmission electron microscopy observations of the damage structures in fusion and fission reactor neutron irradiated copper indicate that the same type of primary structural defects, vacancy and interstitial point defect clusters and small dislocation loops with a/3 ⟨111⟩ and a/2 ⟨110⟩ Burgers vectors, are produced in both cases. The difference in the radiation strengthening produced by fusion and fission reactor neutrons in Cu appears to result from a substantially greater rate of accumulation of damage, in the form of point defect clusters, during irradiation with fusion neutrons than during irradiation with fission reactor neutrons plus a significant difference in the size and spatial distributions of the damage clusters.

INTRODUCTION

The recent growth of interest in controlled thermonuclear reactor (CTR) technology has generated considerable discussion of the effects of 14 MeV D-T fusion neutron radiation damage on candidate structural materials for fusion reactors.

Because experimental facilities that can produce 14 MeV neutron fluxes and fluences comparable to those expected in a fusion reactor do not exist and appear unlikely to be developed in the near future, much of the current effort is being directed toward theoretical predictions and experimental simulations of D-T fusion damage effects.

Theoretical studies have shown that the displacement damage resulting from Frenkel pair generation produced by 14 MeV fusion neutrons in metals such as Cu and Nb should be about 4 to 6 times as great as that produced by the same fluence of fission reactor neutrons. Inspection of (n,α) cross sections for different neutron energies indicates that the rate of internal helium generation could be a hundred to a thousand times as great during fusion neutron irradiation as during irradiation with the same flux of fission neutrons.

Simulation experiments are directed toward producing the same quantities of displacement damage, in terms of damage energy or displacements per atom (dpa), expected from a given fluence of fusion neutrons by irradiation with high-energy ions or fission reactor neutrons. Internal helium quantities comparable to those expected from fusion neutron (n,α) reactions are produced by alpha particle injection, (n,α) reactions in certain materials using high thermal neutron fluxes or by the radioactive decay of dissolved tritium. In most simulations the effects of damage generation rates and possible synergistic effects of damage components are ignored or estimated using classical kinetic and thermodynamic models of damage structure development.

Implicit in these simulation efforts is the assumption that the same processes that determine the nature and distribution of the resultant damage structure and associated physical and mechanical properties under the simulation conditions are also dominant during radiation with fusion neutrons, and that at elevated temperatures and higher damage states they will produce the same effects.

Clearly, one would like to establish confidence in the validity of these simulations by comparing them directly with the effect produced under equivalent conditions by high fluences ($> 10^{20}$ n/cm^2) of fusion

neutrons. However, because of the earlier mentioned limitations on fusion neutron flux and fluence this does not appear to be possible in the foreseeable future.

Some insight into the credibility of some of the aspects of fission reactor neutron simulations of fusion neutron radiation effects can be gained by comparision of the structure and properties produced in a material during irradiation over the fluences within the practical limitation of the Rotating Target Neutron Source (RTNS) at the Lawrence Livermore Laboratory.

Radiation damage experiments on the RTNS can be conducted on small specimens over a wide range of temperatures and environmental conditions in a D-T fusion neutron flux up to approximately 10^{12} n/cm^2-sec and at practical fluence levels up to 10^{18} n/cm^2. These experiments, although not generally useful for yielding engineering design data, can provide a basic understanding of the nature and effects of fusion neutron damage and increased confidence in the predictions and simulations by other sources of radiation damage.

In addition to providing specimens for direct vacuum fusion mass spectroscopy measurements of rates of helium generation in metals and alloys during fusion neutron irradiation, one can also conduct studies to verify the theoretically predicted ratios of displacement damage rates produced by fusion and fission reactor neutrons. Direct comparisons of the resultant physical and mechanical property changes produced during fusion and fission reactor neutron irradiation can be made to determine the validity of the damage energy or dpa criterion for property change simulation.

Finally, an evaluation of the resultant damage structures can be made to assess any differences in the nature, quantities, and distribution of the damage in fusion and fission reactor neutron irradiated materials and to determine if the same or different processes are dominant in determining the resultant structures.

The work described in this paper examines and compares the effect of fusion and fission reactor neutron irradiations on the tensile yield strength and resultant displacement damage structures in copper and niobium.

EXPERIMENTAL PROCEDURE

Sample Preparation

Small tensile samples of Cu and Nb of dimensions shown in Figure 1 were machined from 0.5 mm (0.020-inch) thick cold-rolled sheet stock from LLL stores and from higher purity material purchased from MRC and Cominco†. The chemical analyses of these materials are shown in Table 1.

The Nb tensile samples were annealed for 1 hour at 1200°C in 0.13 μPa ($\approx 10^{-9}$ torr) vacuum and the Cu samples for 1 hour at 600°C in ≈1.3 mPa (10^{-5} torr) vacuum. These times and temperatures were used to obtain grain sizes that would give at least 10 grains over the 0.5 mm (0.020-inch) thickness to insure reproducible polycrystalline tensile behavior. Representative photos of the annealed grain structure are shown in Figures 2 and 3.

The tensile samples were then encapsulated for irradiation in the Rotating Target Neutron Source (RTNS) and the Livermore Pool Type Reactor (LPTR) as described in the next section.

Irradiation Facilities, Neutron Spectra, Dosimetry, Encapsulation, and Temperature Control

A. Rotating Target Neutron Source (RTNS)

The RTNS has been described in detail elsewhere[1-5]. Essentially, it consists of an accelerator which produces a beam of 400 keV deuterons and a tritium-loaded titanium target in which fusion reactions take place and from which neutrons are emitted. The actual neutron-emitting region of the target can be approximated as a disc with a diameter of about one centimeter and negligible thickness. The small size of the tensile samples was dictated in part by the size of this target disc and the fact that the neutrons are emitted nearly isotropically in the

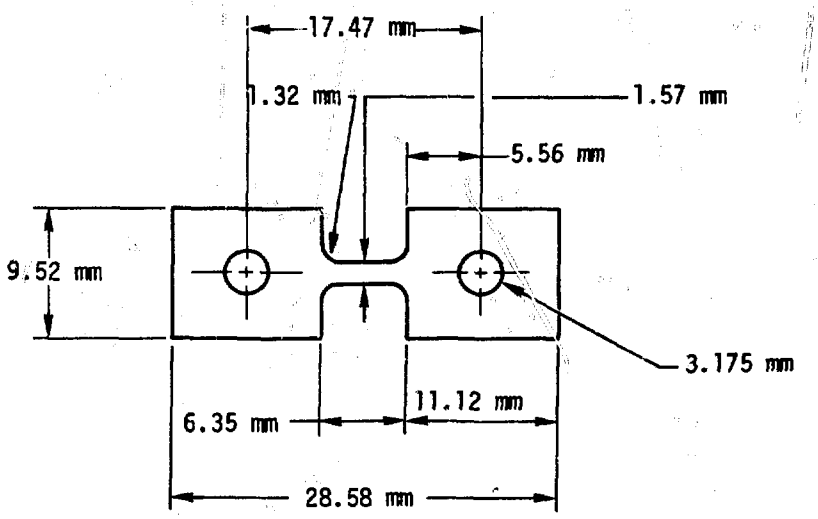

Fig. 1. Tensile Sample Dimensions.

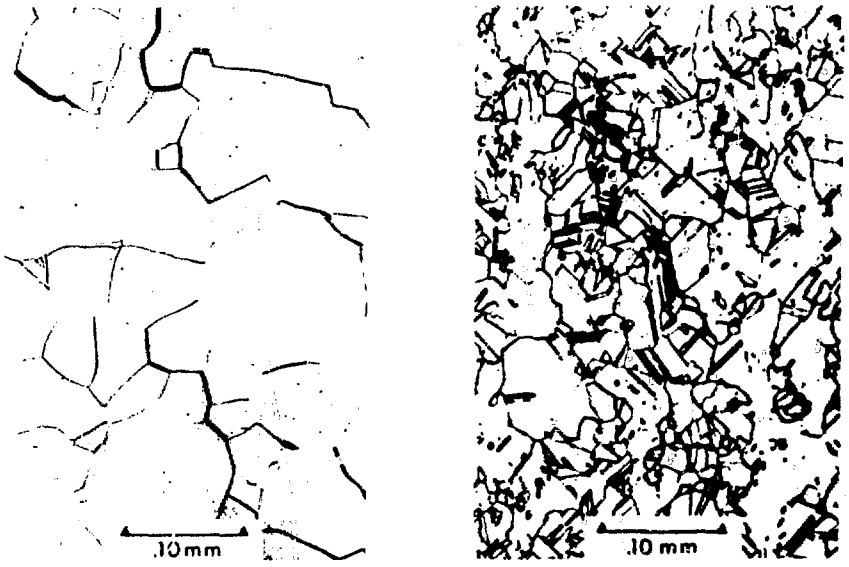

Fig. 2&3. Representative Microstructures of Cu and Nb Tensile Samples.

laboratory coordinate system, which leads to a rapid decrease of the flux with distance away from the source.

The energy of a neutron emitted by a DT fusion accelerator source depends on the energy of the deuteron at the time it enters into the reaction and the angle between the path of the incoming deuteron and the

Table 1. Chemical Analyses of Impurity Elements in Copper and Interatitial Impurities in Niobium

COPPER		
LLL Stores Grade		Cominco
Element:		
Fe	300 ppm	400 ppm
Si	100 ppm	150 ppm
Mg	4 ppm	10 ppm
Ag	50 ppm	2 ppm
Ca	25 ppm	2 ppm
Co	<10 ppm	<10 ppm
Ni	5 ppm	<3 ppm
Al	<3 ppm	<3 ppm
Be	30 ppm	<1 ppm

NIOBIUM		
LLL Stores Grade		Cominco
C	15	15 ppm
O	208	40 ppm
N	70	5 ppm

path of the emitted neutron. In the RTNS, the target is thicker than the deuteron range, so that the deuteron energy at the time of reaction can lie between 400 keV and 15 keV or less. Because of this spread in deuteron energies, the neutrons emitted in the forward direction can have energies between 14.0 and 15.6 MeV, according to calculations involving

conservation of energy and momentum[6]. There is also a range in the angle between the deuteron beam and the paths of neutrons which can strike the sample, because of the finite dimensions of the neutron source and the sample and the small spacing between them. (The spacing was kept small to maximize the flux.) The spread in neutron energy introduced by this effect is less than that arising from the spread in deuteron energy. Account must also be taken of neutron scattering by that portion of the target backing material, cooling water, water spreader, and catch cage which lies between the source and sample. It is estimated that about 5 percent of the neutrons interact with these materials, the majority losing only a small amount of energy. Since several samples were stacked, account must be taken of neutron scattering by the samples located near the sample in question. This is not considered to be a serious problem in the present experiments, however, because the total thickness (13 mm maximum) was less than the mean-free path of the neutrons (40 mm in Cu, 45 mm in Nb). Neutron scattering by materials at larger distances from the target (e.g. water shielding) does not have a significant effect on the fast neutron spectrum at a sample placed close in because of the rapid decrease of the primary flux with distance from the target.

Because of the relatively sharp nature of this neutron spectrum, it has not been possible to characterize its shape by either threshold foil activation or neutron time-of-flight measurements. The most fruitful approach would appear to be a calculation based upon measured cross sections, deuteron energy loss rates, tritium distribution with depth in the target, and the source-sample geometry. This has not been done rigorously for the present experiment, but an indication of the general nature of the shape can be obtained from the calculations of Seagrave[6]. He found that for 400 keV deuterons on a thick tritiated titanium target, the peak in the neutron spectrum in the forward direction (0°) occurs at about 14.8 MeV, and the mean value is about 15.0 MeV. Taking account of the source-sample geometry in these experiments, we estimate that the mean neutron energy on the gauge sections was between 14.8 and 15.0 MeV.

The dosimetry for the RTNS irradiations was accomplished by neutron activation and gamma ray counting of niobium foils. The foils were 0.14-mm thick, cut to the same shape as the tensile specimens, and stacked with them so that each tensile specimen was sandwiched between two dosimetry foils. The dose rate during the irradiations was monitored using proton recoil counters, and these data were used to correct for decay. Only the parts of the foils corresponding to the gauge sections on the specimens were weighed and counted, so that the fluences represent average values over the gauge sections. The reaction used was $^{93}Nb(n, 2n)^{92m}Nb$. This reaction has a threshold at about 9 MeV, and the excitation function is relatively flat in the energy region of interest. The cross section value used was 458 millibarns, based upon the measurements of Nethaway[7]. The dosimetry technique has been described by Van Konynenburg[8].

The fluence values shown are the mean values of the fluences calculated for the dosimetry foils in front and in back of each sample. The absolute accuracy of the mean fluences is ±7.5%. Relative accuracy between any two mean fluences is ±2%. The variation of fluence across the thickness of the samples was ±12% of the mean value in the worst cases. The maximum variation of fluence along the length of the gauge section is estimated to be less than ±12% of the mean value for all specimens.

For the room temperature irradiations, the tensile specimens and dosimetry foils were stacked in small epoxy-fiberglass laminate sample holders, and held in place with thin mylar film at front and back. These irradiations were performed in air at about 25°C. Nuclear heating is not significant with this source because the gamma ray flux is quite small. The neutrons are not very effective in heating, as well as having a relatively low flux themselves. This was verified by irradiating a foil mounted in the same way, with a thermocouple spot-welded to its center. The temperature rose less than 3°C when the accelerator was operated. This may have been due in part to a rise in target cooling water temperature, since the foil was pressed against the back of the water catch cage.

The irradiation at 210°C was accomplished by enclosing the samples and dosimetry foils in a Pt capsule and heating them from behind with a spot heater (Research, Inc.). The Pt capsule was made of 0.75 mm-thick

material, and contained a Pt insert having a slot which conformed to the shape of the specimens. This insert served as a heat sink to insure temperature uniformity, gave protection against deformation of the samples, and reduced dead space inside the capsule. The capsule was evacuated to a pressure of about 13 mPa (10^{-4} torr) and electron beam welded shut. It was cooled by large copper blocks during the welding operation.

Chromel-alumel thermocouples were spot-welded to the capsule at the side and in the center on the front. The capsule was mounted in an insulator made of firebrick and attached to the front of the spot heater. The front of the capsule was insulated with a 1-mm thick layer of Fiberfrax (3M Co.). The spot heater consists essentially of a tungsten quartz iodide light bulb and an ellipsoidal Al reflector. The bulb was placed at one focus and the capsule at the other. Temperature control was accomplished by use of a current-adjusting type controller and a silicon-controlled rectifier power supply which drove the lamp. Temperature was controlled to within ±5°C during the irradiations. The front of the capsule was measured to be at a temperature of 196°C, and the side at 210°C. The capsule was opened by removing the welded bead using a hand shears. Care was taken not to deform the specimens during this operation.

B. Livermore Pool Type Reactor (LPTR)

The LPTR has been described recently[9]. It is a 3 MW heterogeneous tank-type pool research reactor. It is light-water moderated and cooled, beryllium and graphite reflected. It has MTR-type fuel elements, composed of aluminum and enriched uranium. The tensile specimens were irradiated in positions E-1 and E-7 of the reactor core. These positions are located at the northwest and southwest edges of the core, respectively, in the beryllium reflector, adjacent to a large graphite thermal column. Positions E-1 and E-7 have essentially identical environments, from the standpoint of geometry and surrounding materials.

The neutron spectra in these positions have been evaluated by Griffith[10], using multiple foil activation and iterative fitting. The cross sections used in this analysis were taken from McElroy, et al.[11] and from the LLL Evaluated Neutron Data Library. In making the fit, the

lower energy limit was set at 0.025 eV. The main features of these spectra are the fission component above about 10^{-2} MeV and the thermal component below about 1 eV.

In order to minimize thermal neutron activation of the samples, they were surrounded by 0.5-mm thick Cd foil during all LPTR irradiations. It was assumed that the change in the relative shape of the spectrum caused by the Cd can be determined by multiplying the contribution in each energy group by the attenuation averaged over the group as calculated from the Cd cross section. The resulting differential spectra are shown in Figure 4, and the integral spectra in Figure 5. The RTNS spectra are shown for comparison. The LPTR spectra were used to obtain spectrum-averaged cross sections for the reaction $^{54}Fe(n,p)^{54}Mn$, as described by Serpan and Menke[12]. Iron foils were placed next to the tensile samples inside the Cd liner on each run. The absolute fluence values were obtained using the spectrum-averaged cross sections. This procedure accounts for the fact that the Cd lowers the fission rate in the vicinity of the test position relative to the rest of the core. The spectrum-averaged cross sections are shown in Table 2. For comparison, values are shown for position C-53 of the Low Intensity Test Reactor (LITR) (shut down in 1968) and position W-44 of the Brookhaven Graphite Reactor (BGR)(shut down in 1969) from the compilation of Serpan and Menke[12]. The

Table 2.

LOWER ENERGY LIMIT (MeV)	SPECTRUM-AVERAGED CROSS SECTIONS (mb)		
	BGR W-44[12]	LPTR E-1	LITR C-54[12]
>1	69.7	84.8	87.5
>0.1	22.2	28.3	44.6

observation that the present results fall between the others listed is consistent with the fact that the moderation and reflecting material used in the LPTR is a combination of light water and Be as in the LITR, and graphite as in the BGR.

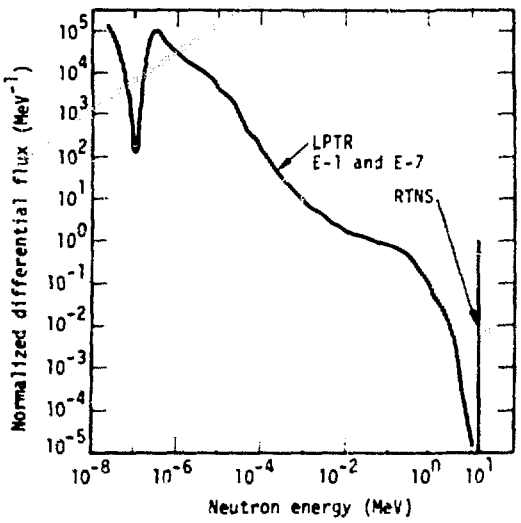

Fig. 4. Differential Neutron Spectra for the E-1 and E-7 Positions of the LPTR Fission Reactor.

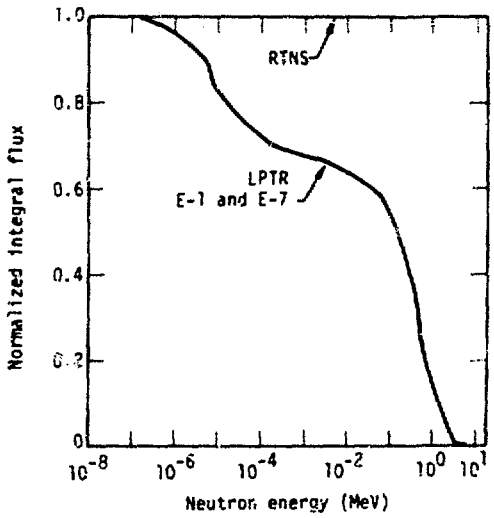

Fig. 5. Integral Neutron Spectra for the E-1 and E-7 Positions of the LPTR Fission Reactor.

The fluence values determined in this way have an estimated overall uncertainty of ±15% for the >1 MeV values and ±30% for the lower threshold values. It is felt that the fluence variation over the gauge sections of the LPTR samples was much less than that over the RTNS samples, because of the volume nature of the neutron source.

As already mentioned, the samples were enclosed in Cd-lined aluminum cans for the irradiation. The cans were cold-welded shut in one atmosphere of air and were vacuum tight. For the 210°C irradiations, the samples were wrapped in Al foil and inserted into the can with little contact with the sides. For the 65°C irradiations, the samples were lightly pressed against a semi-cylinder-shaped Al block, inside the can, using a small spring. The improved thermal contact enabled more efficient heat transfer to the reactor cooling water, which was maintained at 40°C. The temperatures were measured by attaching thermocouples to dummy samples which were irradiated under the same conditions as the actual samples. The temperatures are believed to be accurate to ±10°C. The capsules were opened with a can opener, taking care not to deform the samples.

Tensile Tests

After irradiation and dosimetry measurements were completed the samples were mounted in tensile grips in a specially designed jig to insure against deformation during handling, and tested in an Instron testing machine at about 25°C and a crosshead rate of 0.05 mm/min (0.002 inch/min). Most tests were stopped after about 1 to 2 percent tensile strain so that subsequent TEM observations of the radiation damage structures in the gauge sections would not be obscured by dislocations produced by deformation. The 0.2 percent offset yield stress was determined using the Instron crosshead motion as the sample extension.

TEM STUDIES

Transmission electron microscopy studies of the radiation damage structures in the gauge sections of the tensile samples are being carried out to compare the nature and distribution of the damage as a function of neutron fluence for the fusion and fission reactor neutron irradiations.

Thin foils were prepared by slicing the 0.5 mm (0.020-inch) thick gauge sections into two halves approximately 0.2 mm (0.008-inch) thick with a diamond saw. Circular disks 3 mm in diameter were punched or spark cut from these gauge section strips and jet thinned using a 25% concentrated phosphoric acid, 38% distilled water, and 37% ethyl alcohol electrolyte. Structural examinations were carried out on a JEM 100B microscope.

Analysis of the nature of the primary structural defects, i.e., point defect clusters and small dislocation loops, was performed using a new TEM technique called 2-1/2-D. The description of this technique and its application to studies of point defect clusters is in publication[13] and will be briefly described here.

The 2-1/2-D technique utilizes the shifts in dark-field diffraction contrast images produced by off-optical-axis-diffracted beams, when the objective lens is defocused. As shown in the schematic diagram in Figure 6, when a structural feature in a thin foil is imaged by a diffracted beam that makes an angle α with the optical axis of the microscope, and the objective lens is over-focused by lowering the plane of focus relative to the sample position an over-focus distance ΔD, the image position is shifted parallel to the operating reciprocal lattice vector by an amount

$$y = \Delta D\alpha = \Delta D\lambda g \qquad (1)$$

where λ is the electron wave length, g is the distance in reciprocal space of the diffracted beam from the optical axis, and ΔD is positive for over-focusing and negative for under-focusing.

If two photographs of the dark field image are taken at focus settings differing by ΔD, the shift y of the image between the photographs, produced by the off-axis diffracted beam g, causes an artificial parallax that gives the image a depth position when the photographs are viewed in stereo.

When two structural features F_1 and F_2 are simultaneously imaged under high resolution, dark-field conditions, with diffracted beams g_1 and g_2 which make angles α_1 and α_2 with the optical axis of the

microscope as illustrated in Figure 7, and two photographs are taken at objective lens focus settings differing by ΔD, a relative parallax shift of the images will be produced given by

$$\Delta y = y_1 - y_2 = \Delta D(\alpha_2 - \alpha_1) = \Delta D\lambda(g_2 - g_1) = \Delta D\lambda\Delta g \qquad (2)$$

This relative parallax shift will produce a difference P in depth position of the images of F_1 and F_2 when the photographs are viewed in stereo, given by

$$P = M\Delta y \qquad (3)$$

where M is the overall magnification of the photographs.

The difference in stereo depth of the two images of F_1 and F_2 is determined only by Δg or by the difference in spacing or orientation of the diffracting lattice planes and not by the actual positions of F_1 and F_2 in the foil. Consequently, the stereo view is not a true three-dimensional spatial distribution of the features, but neither is it two-dimensional; hence the term 2-1/2-dimensional.

If the two photographs taken at different focus settings are arranged in a stereo viewer with the photograph that is relatively over-focused on the right and the diffraction pattern is as shown in Figure 8a, the image corresponding to the shorter g vector, in this case g_1, will appear in stereo to be above the image corresponding to the longer vector g_2. In this viewing orientation the parallax is caused only by Δg_s or by differences in the spacing of the diffracting lattice planes of features F_1 and F_2, where in this case F_1 would have a larger lattice spacing than F_2. If the photographs are rotated 90 degrees clockwise as illustrated in Figure 8b, the image of feature F_1 will again appear to be above the image of F_2 in stereo. In this case the parallax is produced only by Δg_r or by the difference in rotational orientation of the diffracting planes of features F_1 and F_2.

Application of the 2-1/2-D technique to analysis of point defect clusters is seen by considering an in-focus high-resolution, dark-field micrograph of vacancy and self-interstitial clusters imaged with the [hkl] matrix g vector. The local elastic strains near point defect

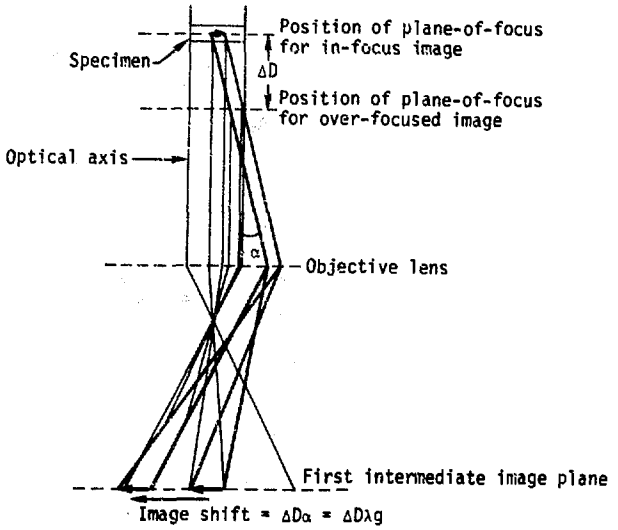

Fig. 6. Schematic Diagram Showing Image Shift Produced by Over-focusing the Objective Lens Under Dark-Field Conditions.

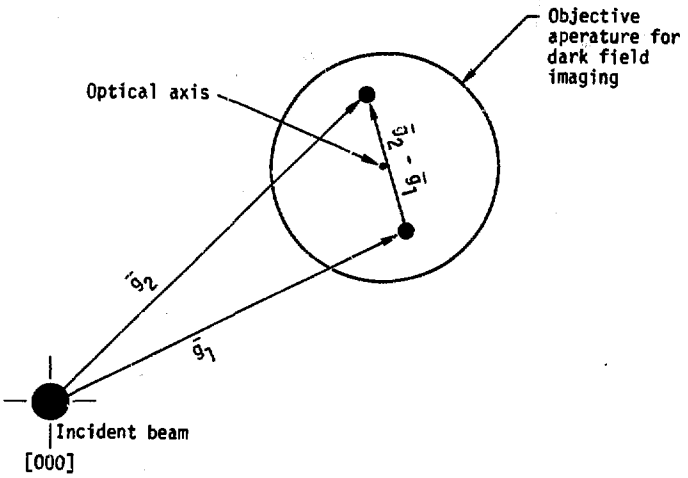

Fig. 7. Diffraction Pattern Arrangement for Taking 2-1/2-D Stereo Pair of Features F_1 and F_2.

clusters produce bending and changes in interplanar spacing of the (hkl) planes as illustrated in Figure 9. Near the interstitial cluster the elastic distortion decreases the (hkl) plane spacing to a value $\overline{d}_{(hkl)i}$ and the vacancy clusters cause a local increase in (hkl) plane spacing to $\overline{d}_{(hkl)v}$. The g vectors corresponding to (hkl) plane diffraction near the vacancy and interstitial clusters $\overline{g}_{(hkl)v}$ and $\overline{g}_{(hkl)i}$ are slightly shorter and longer, respectively, than the $g_{(hkl)}$ vector for the undistorted matrix as shown at the bottom of Figure 9. There is actually a gradient in strain near the clusters and a range of g vectors corresponding to different strains at different points in the matrix. When considering the largest g vector value corresponding to the maximum parallax shift of the defocused dark field image, a large enough volume of material must be involved to diffract enough electrons to produce an observable dark-field image. Figure 10 shows the (220) plane strain gradients at several radii normal to a 4 nm (40 Å) diameter Frank vacancy loop lying on a (110) plane in niobium. These strains were calculated using the isotropic finite elastic displacement field formulations of Kroupa[14] and Ohr[15]. Consider the volumes of material marked A to E in Figure 10. When the image of the Frank loop is defocused, the images of the volumes A to D that are within about 1 nm (10 A) of the loop plane, will shift different amounts proportional to the corresponding strain as illustrated in the figure. These volumes are so small that they alone will not diffract enough electrons to produce observable defocused images. At distances greater than about 1 nm (10 A) from the loop plane, most of the distorted matrix volume marked E in Figure 10, has about the same strain ($\approx$ 4 percent) and will shift the same amount and produce an observable defocused image. Thus, the largest observable image shift for a given lens defocus is expected to correspond to about 4 percent (220) plane strain. This strain has been found to be in good agreement with the values obtained from parallax measurements of 2-1/2-D stereo images of this orientation of Frank loops in niobium[13]. The g vector values corresponding to this maximum parallax shift are designated $\overline{g}_{(hkl)v}$ and $\overline{g}_{(hkl)i}$.

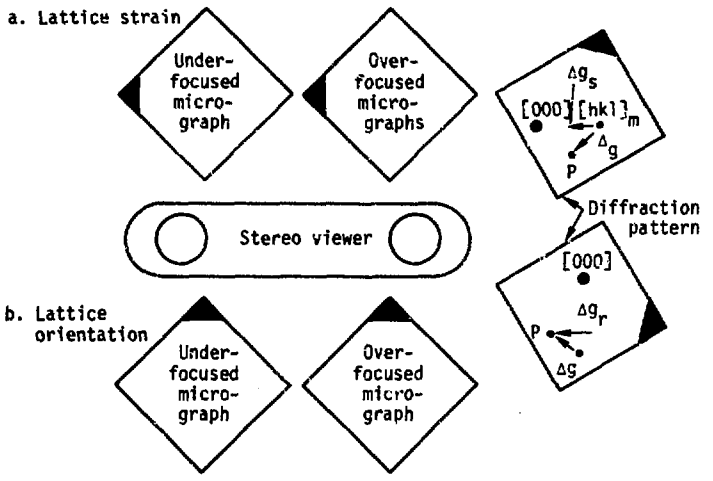

Fig. 8. Stereo Setup for 2-1/2-D Viewing.

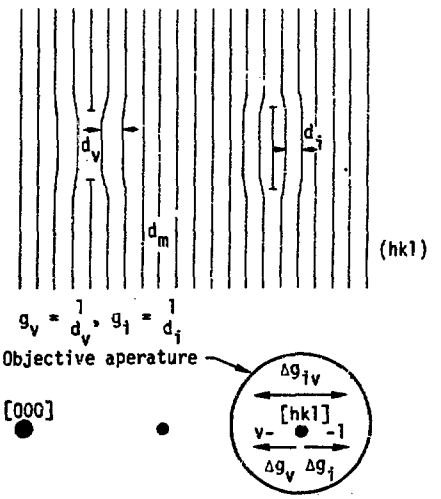

Fig. 9. Illustration of Lattice Strains Produced by Vacancy and Interstitial Point Defect Clusters or Dislocation Loops.

If a second photograph is taken of the point defect clusters under the same diffraction conditions as the in-focus high-resolution dark-field photograph with the objective lens over-focused by ΔD, the images of the vacancy and interstitial clusters will shift parallel to the operating $g_{(hkl)}$ vector in opposite directions relative to their positions in the in-focus photograph by amounts

$$y_i = \Delta D\lambda(\bar{g}_{(hkl)i} - g_{(hkl)}) = \Delta D\lambda\Delta\bar{g}_i \quad (4)$$

$$y_v = \Delta D\lambda(\bar{g}_{(hkl)v} - g_{(hkl)}) = \Delta D\lambda\Delta\bar{g}_v \quad (5)$$

giving a net parallax difference

$$\Delta y_{iv} = y_i - y_v = \Delta D\lambda(\Delta\bar{g}_i - \Delta\bar{g}_v) = \Delta D\lambda\Delta\bar{g}_{iv} \quad (6)$$

and a depth difference in stereo of

$$P_{iv} = M\Delta y_{iv} \quad (7)$$

When the in-focus and over-focused photographs of the point defect clusters are viewed in stereo with the over-focused photograph on the right and the operating matrix $g_{(hkl)}$ vector directed to the right, the vacancy clusters will appear to be in a depth zone which lies above another depth zone containing interstitial clusters as illustrated in Figure 11. When the photographs are reversed or individually rotated 180 degrees, the interstitial clusters will appear to be above the vacancy clusters. If the undistorted matrix is imaged by the (hkl) diffracted beam, it can be used as a reference plane, and the stereo depths of the interstitial and vacancy clusters relative to this plane are given by Equations (4) and (5). The position of a cluster within a depth zone will depend on the orientation and magnitude of its Burgers vector.

The reciprocal lattice point corresponding to the locally distorted (hkl) planes near the point defect clusters is shown schematically in Figure 12 and consists of two cones. Under weak beam conditions where the surface of the Ewald sphere is deviated far from the [hkl] spot, the in-focus images of the clusters will be relatively small and will result from diffraction from the more highly strained and bent (hkl) lattice planes. Under these conditions the out-of-focus images will be quite

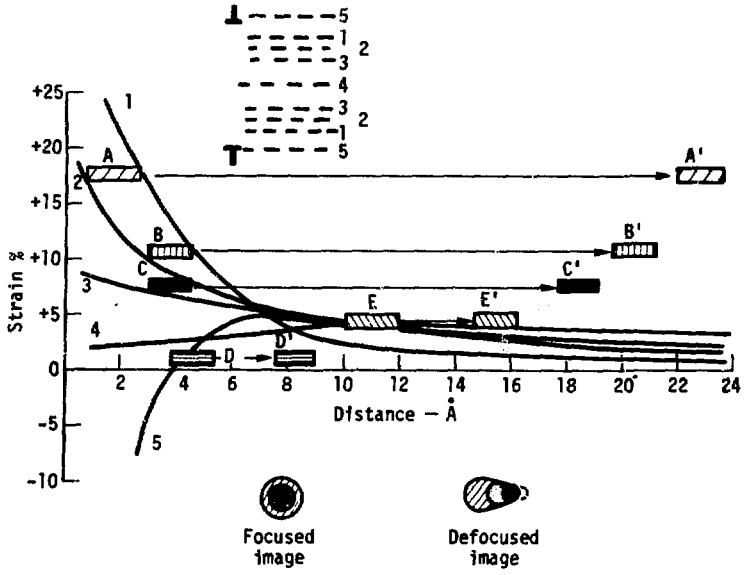

Fig. 10. Illustration of Strain Gradients and Defocusing Image Shifts Near a Frank Vacancy Loop.

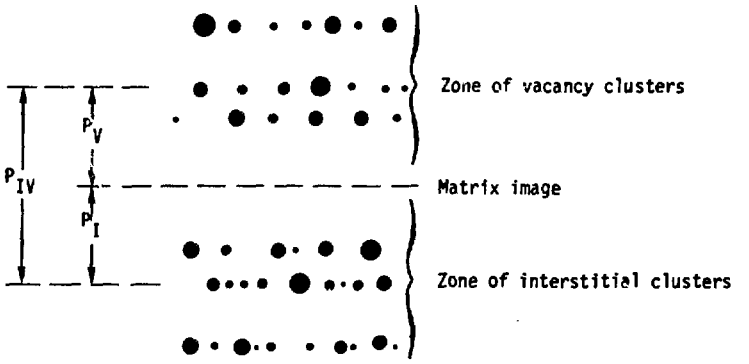

Fig. 11. Schematic Illustration of Vacancy and Interstitial Cluster Distributions in 2-1/2-D Stereo Space.

similar to the in-focus images, except for a little loss of resolution. The stereo images will be small, relatively sharp images that stand above and below the position where the matrix image would be as illustrated in Figure 12. Under stronger diffracted beam conditions, the in-focus images are broader and encompass a larger gradient of strain. The out-of-focus images are elongated in the direction of the $g_{(hkl)}$ vector and the stereo images will appear as tilted plates as shown in Figure 12.

EXPERIMENTAL RESULTS

Radiation Strengthening

The increase in 0.2 percent offset yield stress results are shown vs. neutron fluence in Figures 13 and 14 for Cu and Nb, respectively. Figure 13 shows data for an irradition temperature of 210°C for both neutron spectra and for LPTR irradiations at 65°C and RTNS irradiations at 25°C. Figure 14 shows Nb data for LPTR irradiations at 65°C and RTNS irradiations at 25°C. The increase in yield stress observed for the Cu for a given neutron fluence was independent of the initial material state. In other words, the stores grade Cu had a higher unirradiated yield strength than the Cominco material, but exhibited the same increase in yield stress for a given neutron fluence. The data for the Nb compares fusion neutron irradiated MRC material with fission reactor neutron irradiated LLL stores grade material. LPTR irradiations of the MRC Nb are in progress. The only significant difference between the MRC and LLL stores grade Nb is the higher interstitial content in the latter (see Table 1). Loomis and Gerber[16] have shown that higher concentrations of oxygen impurity significantly increase the radiation strengthening of fission reactor neutron-irradiated Nb. Consequently, the difference in radiation strengthening of the fusion neutron irradiated MRC Nb and the fission reactor neutron-irradiated LLL stores Nb in Figure 14 must be considered less than the difference that would be observed for irradiations of the same material.

It is apparent from these plots that fusion neutrons are considerably more effective than fission reactor neutrons in strengthening both Cu and Nb. If we compare the fusion neutron irradiation of Cu at 25°C

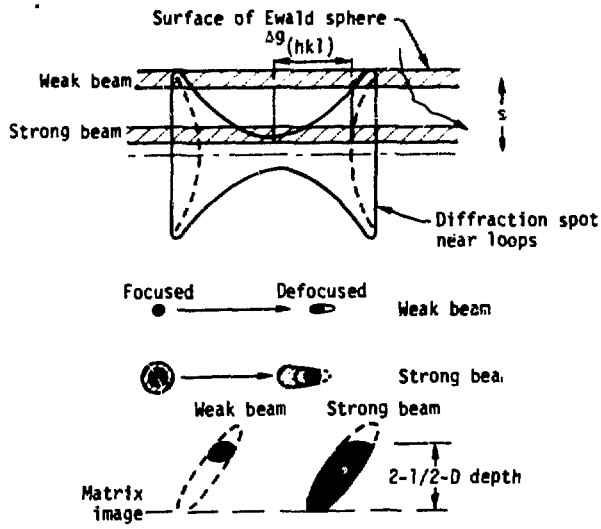

Fig. 12. Illustration of the 2-1/2-D Stereo Images of Clusters for Weak-Beam and Strong-Beam Dark-Field Conditions.

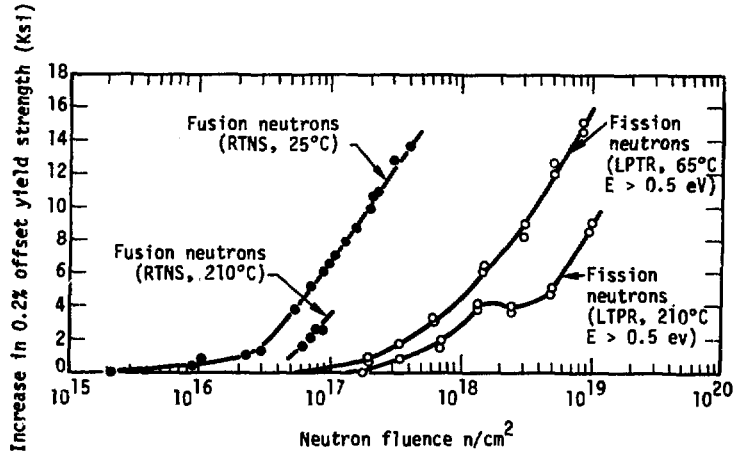

Fig. 13. Increase in Tensile Yield Stress Versus Neutron Fluence in Copper.

with the fission reactor neutron irradiation at 65°C, we find that about 20 times as great a fluence of fission reactor neutrons (E >0.5 eV) is required to produce the same strengthening, for fusion neutron fluences above about 10^{17}n/cm^2. If the fission reactor neutron fluence is expressed in terms of E>0.1 MeV, this ratio reduces to 10. In Nb the fluence ratios are about 17 for E>0.5 eV and 9 for E>0.1 MeV. The radiation strengthening of the Cu samples are slightly greater than that of the Nb for both the fusion neutron irradiations at 25°C and the fission reactor neutron irradiations at 65°C. It should be noted that it is not certain what effect the 40°C difference in RTNS and LPTR irradiation temperatures had on the above results. Experiments are in progress to determine the radiation strengthening at the same temperature of 210 C. This temperature was selected because it is relatively easy to obtain in both neutron sources. Only a limited amount of data are available at the present time on the strengthening of Cu by fusion neutrons at 210°C, and an unequivocal comparison of the fusion and fission reactor neutrons at this temperature cannot be made. The radiation strengthening produced in Cu by fission reactor neutrons at 210°C is significantly less than at 65°C. This decrease is associated with the effect of temperature on the resultant damage structure and will be described later in the section on structure observations.

For Cu at 210°C and the fusion neutron fluences so far attained ($\approx$6 to 9 x 10^{16}n/cm^2), it can be seen that the ratio of fission reactor neutron to fusion neutron fluences required to produce the same strengthening is about the same as for the lower temperatures. This is particularly significant in view of the fact that the 210°C fusion neutron irradiated samples were held at temperature for 80 hours, while the 210°C fission reactor neutron irradiated samples exhibiting the same strengthening were held at temperature only 8 hours. (This resulted from differences in flux between the LPTR and RTNS. Even though the LPTR samples received a greater fluence, the time required for the same strengthening was shorter.) Because of this, more annealing of the damage structure would be expected to have occurred during the fusion neutron irradiation then during the fission reactor neutron irradiation at 210°C. Since the observed ratio was still the same, this suggests that for equal fluxes

at more elevated temperatures, the ratio would be as great or very possibly greater than the ratio observed at the temperatures in Figure 13.

The radiation strengthening results in Figures 13 and 14 are replotted in Figures 15 and 16 versus damage energy. These plots indicate that at the lower damage states, the radiation strengthening produced by fusion and fission reactor neutrons is approximately equal on a damage energy basis. However, at the higher damage states the strengthening for a given amount of displacement damage produced by fusion neutrons at 25°C is greater than the strengthening for the same amount of damage energy for fission reactor neutrons at 65°C. The ratios of damage energy for fission reactor neutrons to that for fusion neutrons for the same increase in yield strength at the higher damage states is about 2.3 for Cu and 1.6 for Nb. Again, the results at the higher damage states are subject to some uncertainty because of the 40°C difference in irradiation temperature.

Damage Structure Observations

A comprehensive transmission electron microscopy study of the damage structures in the tensile samples used to generate the data in Figures 13 and 14 is in progress and will be reported at a later date. Some initial observations were made of the damage structure in Cu samples irradiated with fusion neutrons to a fluence of $1.27 \times 10^{17} n/cm^2$ at 25°C and with fission reactor neutrons to a fluence of approximately $3.0 \times 10^{18} n/cm^2$ (E>0.5 eV) at 65°C and 210 C. As can be seen in Figure 13, the fusion neutron and 65°C fission reactor neutron irradiated samples underwent about the same amount of strengthening while the 210°C fission reactor neutron irradiated sample exhibited significantly less strengthening.

Bright-field electron micrographs of the radiation damage structures, which consist of point defect clusters and small dislocation loops, are shown in Figures 17 through 19. It is apparent from these micrographs that there are significant differences between the spatial distributions of the damage clusters in the fusion neutron and fission reactor neutron irradiated samples.

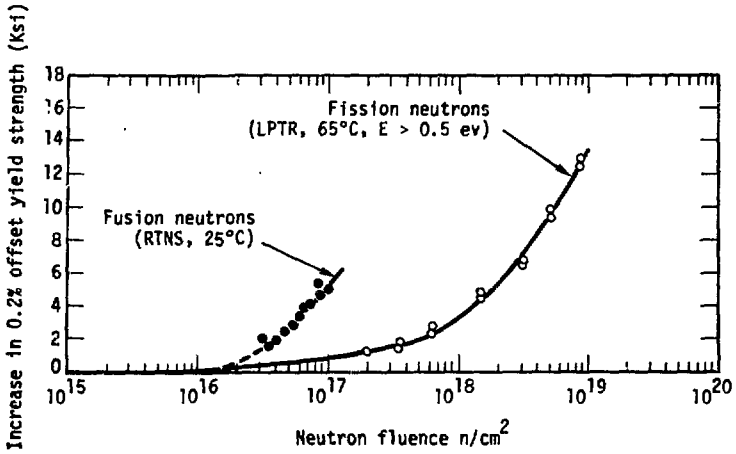

Fig. 14. Increase in Tensile Yield Stress Versus Neutron Fluence in Niobium.

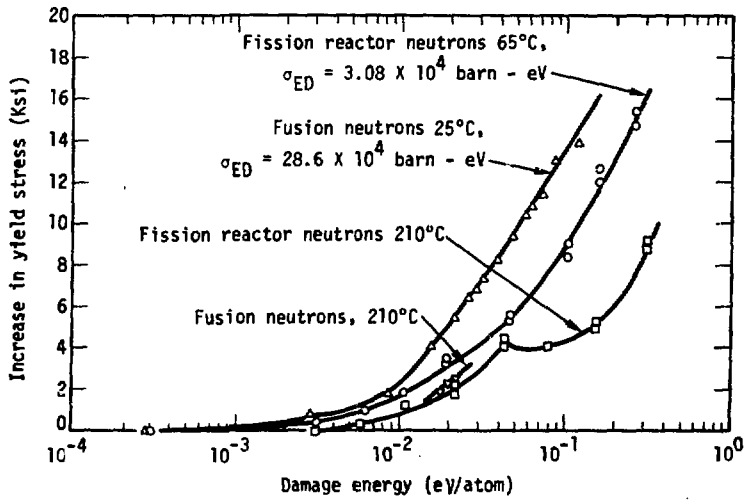

Fig. 15. Increase in Tensile Yield Stress Versus Damage Energy for Neutron Irradiated Copper.

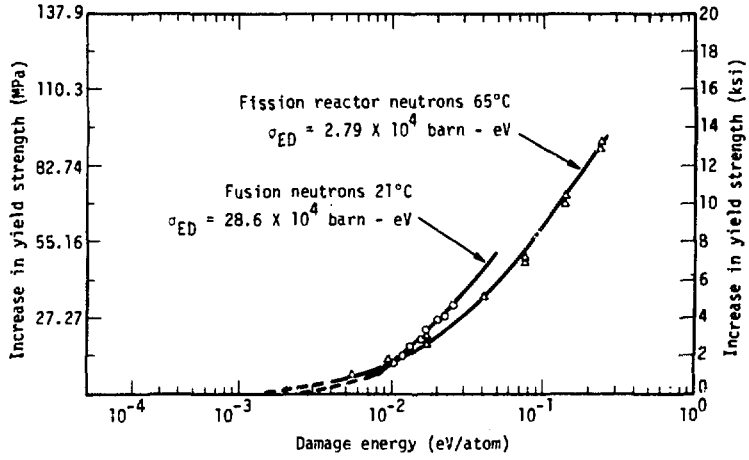

Fig. 16. Increase in Tensile Yield Stress Versus Damage Energy in Neutron Irradiated Niobium.

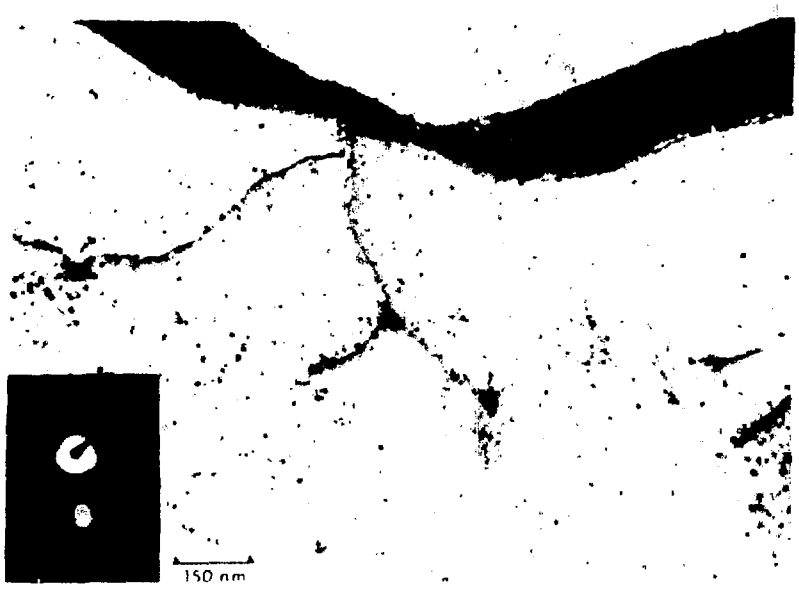

Fig. 17. Bright-Field Transmission Electron Micrograph of Fusion Neutron Radiation Damage in Cu, $\emptyset t = 1.27 \times 10^{7} n/cm^{2}$, 25°C.

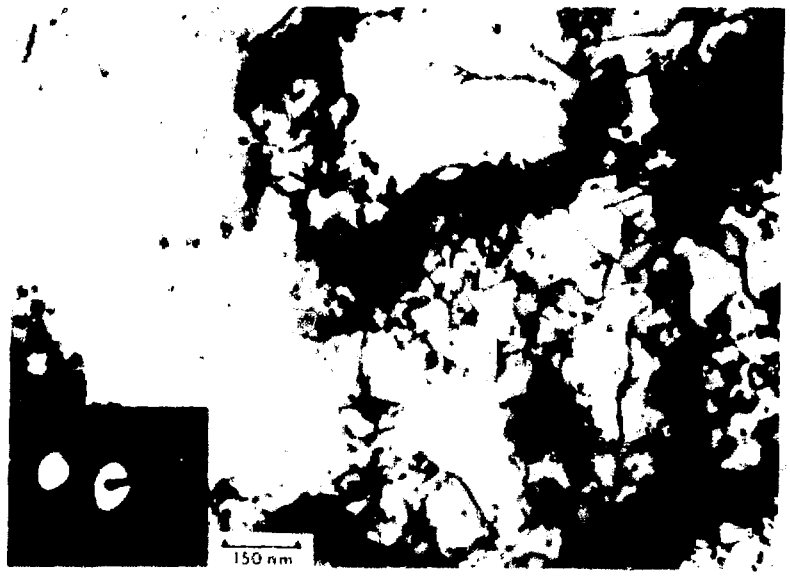

Fig. 18. Bright-Field Transmission Electron Micrograph of Fission Reactor Neutron Damage in Copper $\emptyset t = 3.3 \times 10^{18} n/cm^{2}$, E>0.5 eV, 65°C.

Dark-field 3-D stereo pairs of the fusion neutron and 65°C fission reactor neutron irradiated samples are shown in Figures 20 and 21. The stereo pairs are arranged for viewing with portable or "pocket" stereo viewers. As can be seen in the stereo view of Figure 20, the clusters in the fusion neutron irradiated Cu are uniformly distributed throughout the volume of the foil and range in size from about 1.5 to 10 nm (15 to 100 Å). A number of areas, some of which are shown circled in Figure 20, exhibit close-spaced groups of clusters similar to multiple clusters previously observed in material irradiated with fusion neutrons[17,18,19] and high-energy ions[13,20,21]. The multiple clusters are thought to be produced from multiple cascades created by high-energy primary knock-on events. Although many high-energy primary recoils (>400 keV) do occur in the fusion neutron irradiated Cu, it is not certain whether all of these cluster groups in Figure 20 are multiple clusters. Some of the cluster groups may have resulted from cascade overlap at this fusion neutron fluence. The clusters in the fission reactor neutron-irradiated Cu (Figure 21) have a nonuniform cell-like distribution with cell walls containing a relatively high density of clusters and cell interiors with lower cluster densities. A number of glide dislocations produced during the tensile tests have entangled themselves in the cell wall regions of higher density clusters in the fission reactor neutron irradiated Cu samples.

Estimates of the size-number densities of the clusters in Figures 20 and 21 are shown in Figure 22. The damage in the cell wall regions of the 65°C fission reactor neutron irradiated sample consists of a relatively few large heterogeneously distributed clusters ranging in size from about 7.5 to 20 nm (75 to 200 Å) in diameter and a higher density of smaller clusters about 1.5 to 7.5 nm (15 to 75 Å) in diameter. The interiors of the cells contain a lower density of the smaller clusters. The clusters in the 210°C fission reactor neutron irradiated sample have a distribution similar to that described for the 65°C irradiated sample except that there is an overall reduction in the small cluster density and the larger clusters have grown into resolvable loops 20 to 50 nm (200 to 500 Å) in diameter. The number-density of observed clusters in the fusion neutron irradiated sample is substantially greater

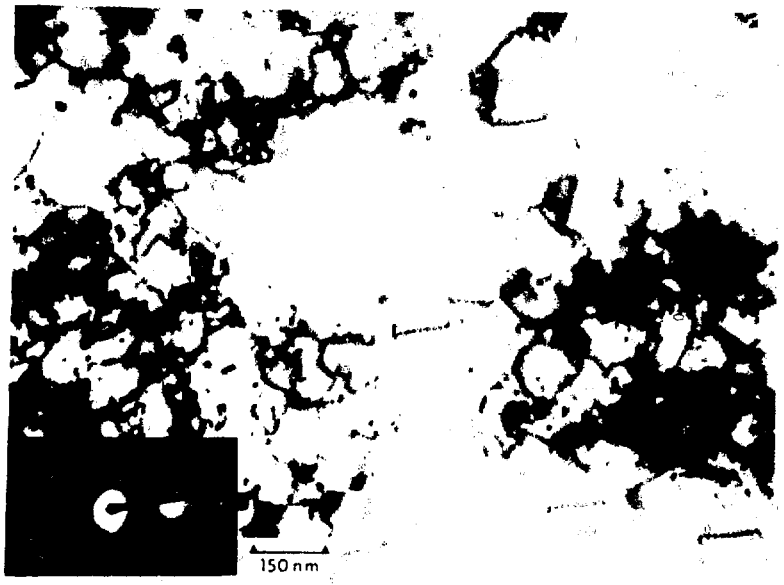

Fig. 19. Bright-Field Transmission Electron Micrograph of Fission Reactor Neutron Radiation Damage in Copper, $\emptyset t = 2.51 \times 10^{18} n/cm^2$, E>0.5 eV, 210°C.

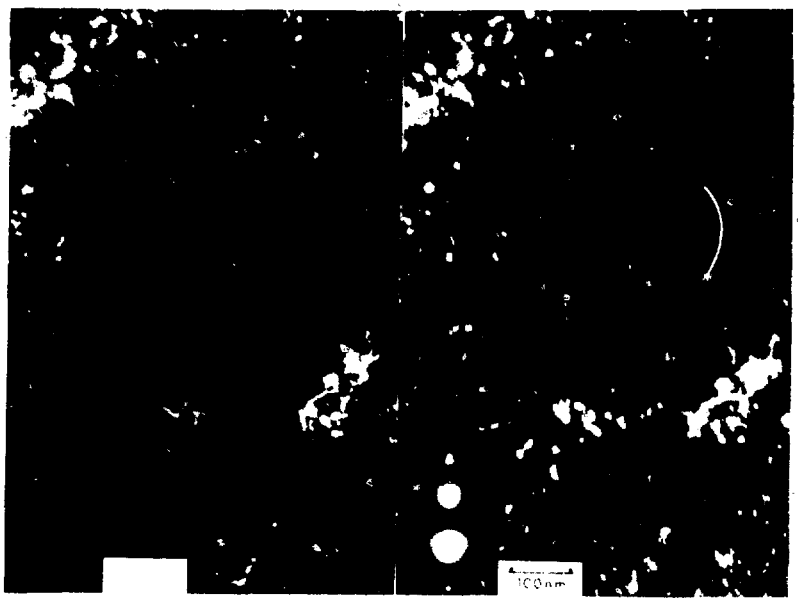

Fig. 20. Dark-Field 3-D Stereo Micrographs of Fusion Neutron Damage in Copper, $\emptyset t = 1.27 \times 10^{17} n/cm^2$, 25°C, z = 001 ,g = [400].

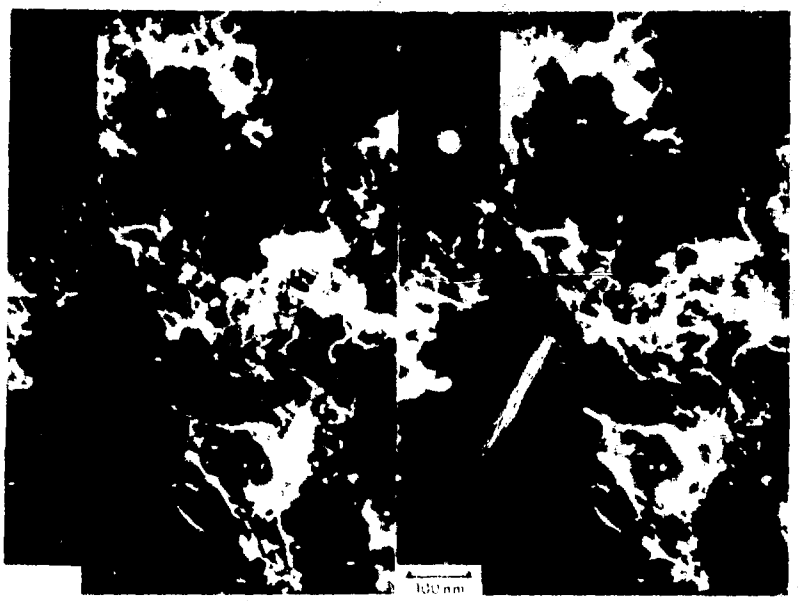

Fig. 21. Dark-Field 3-D Stereo Micrographs of Fission Reactor Neutron Damage in Copper, $\emptyset t = 3.3 \times 10^{18} n/cm^2$, E>0.5 eV, 65°C, $\vec{g} = [001]$, g = [400].

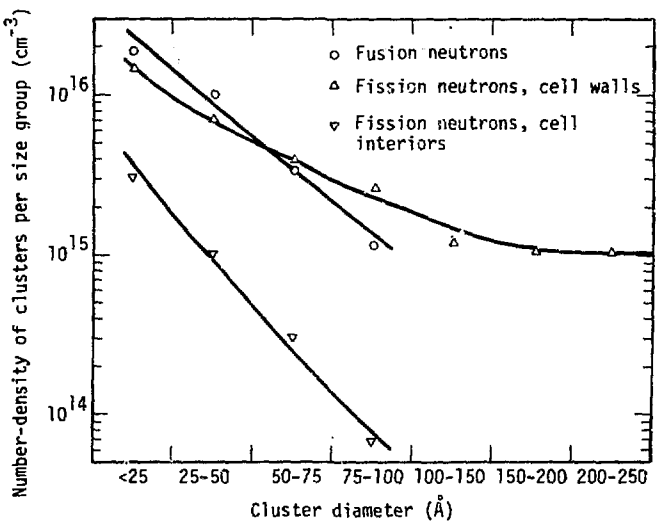

Fig. 22. Size-number Density Distributions of Clusters in Fusion Neutron and 65°C Fission Reactor Neutron Irradiated Copper.

than the cluster density in the cell interiors of the 65°C fission reactor neutron irradiated sample and comparable to the density in the cell walls. Since the fusion neutron fluence was approximately one-tenth as large as the fission reactor neutron fluence (E>0.1 MeV), it appears reasonable to conclude that the rate of accumulation of displacement damage in the form of point defect clusters during irradiation with fusion neutrons is significantly greater than that during irradiation with fission reactor neutrons. This conclusion is in agreement with the results of earlier studies of fusion neutron damage in Cu[17], Nb[18], and Mo[22].

Figures 23 and 24 are 2-1/2-D stereo pairs of the same areas of the fusion and 65°C fission reactor neutron irradiated samples shown in Figures 20 and 21. The micrographs are arranged so that in stereo the vacancy clusters appear above the interstitial clusters. The 2-1/2-D depth distributions of the clusters produced by the fusion and fission reactor neutrons are the same and are shown in Figure 25. The depth positions Va and Ia correspond to vacancy and interstitial clusters with a/3 ⟨111⟩ Burgers vectors and the positions Vb and Ib to clusters with a/2 ⟨110⟩ Burgers vectors. Several clusters in Figures 23 and 24 are so indicated. These Burgers vectors are consistent with those determined from the direction of the axes of the black-white lobes of the dynamical images of the clusters, examples of which are shown in Figures 26 and 27. It can be seen by inspection of the 2-1/2-D stereo view of Figure 24 that the majority of the smaller clusters (<7.5 nm (75 Å) in diameter) in the fission reactor neutron irradiated sample are vacancy-type with predominantly a/3 ⟨111⟩ Burgers vectors while nearly all of the larger clusters (>7.5 nm (75 Å) in diameter) are interstitial-type with many having a/2 ⟨110⟩ Burgers vectors. Inspection of the 2-1/2-D stereo pair of the fusion neutron irradiated specimen (Figure 23) reveals that the interstitial clusters are randomly distributed among the vacancy clusters. The largest clusters observed in this micrograph are interstitial type, but in general the size distribution of the interstitial clusters is similar to that of the vacancy clusters.

The inhomogeneous distribution of the large interstitial clusters in the fission reactor neutron-irradiated samples suggests that they

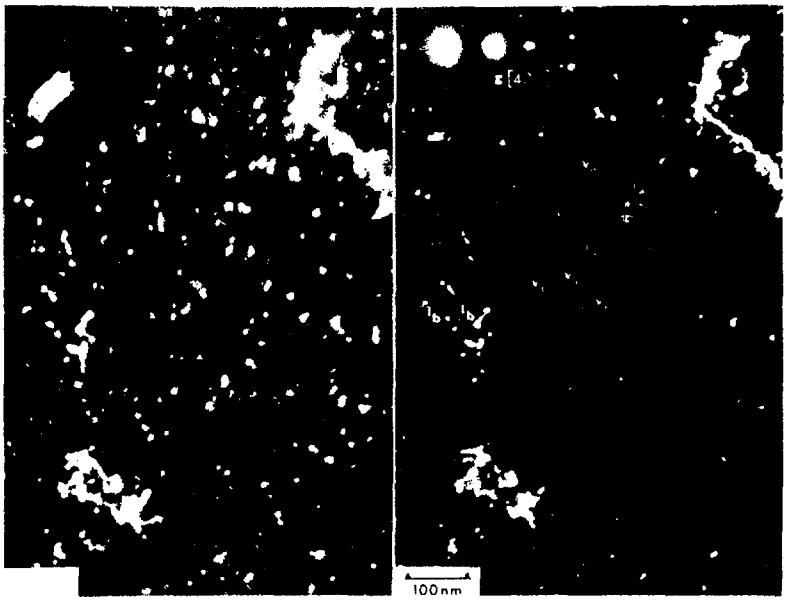

Fig. 23. Dark-Field 2-1/2-D Stereo Micrograph of Fusion Neutron Irradiated Copper of Fig. 20, $\Delta D = 2\mu m$.

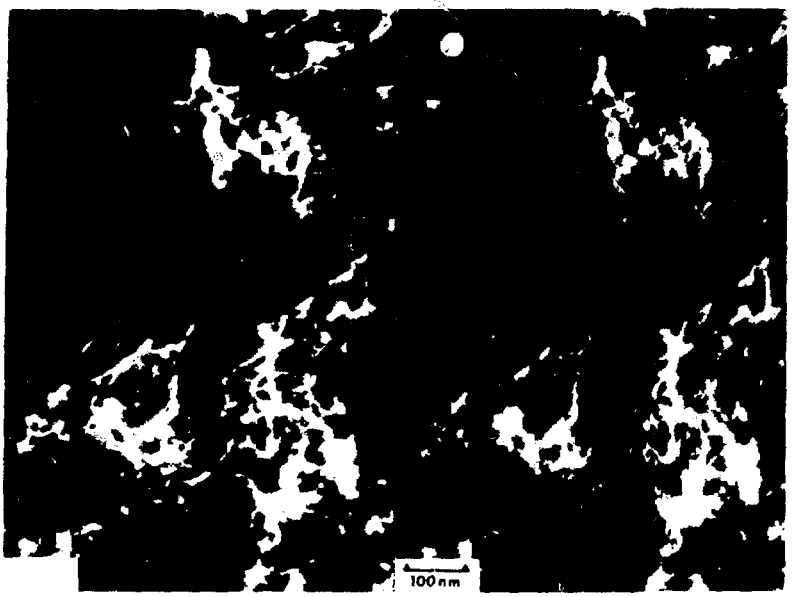

Fig. 24. Dark-Field 2-1/2-D Stereo Micrographs of 65 C Fission Reactor Neutron Irradiated Copper of Fig. 21, $\Delta D = 2\mu m$.

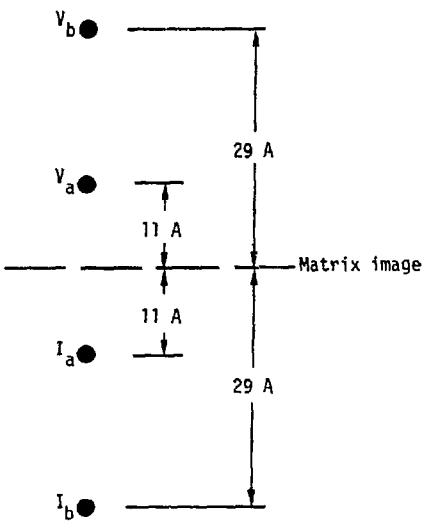

Fig. 25. Stereo 2-1/2-D Depth Distribution of Cluster Images of Fusion and Fission Reactor Neutron Irradiated Copper.

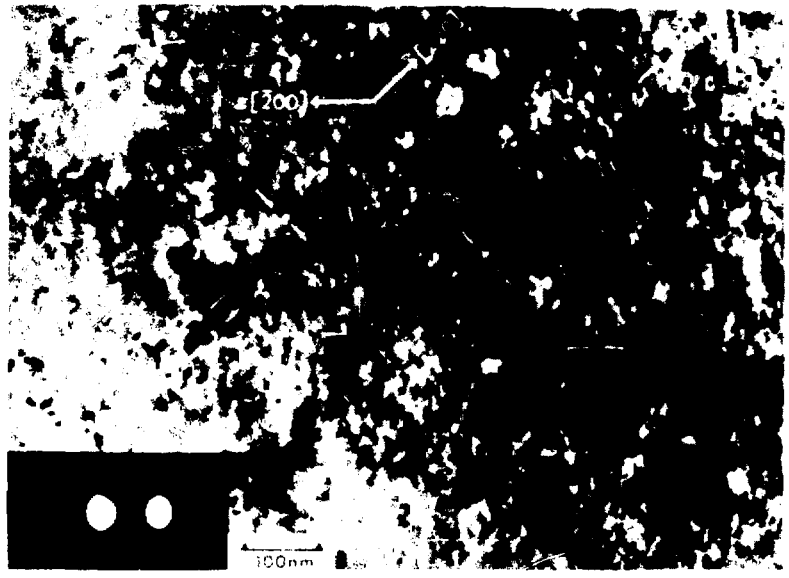

Fig. 26. Dynamical Contrast Micrographs of Clusters in Fusion Neutron Irradiated Copper.

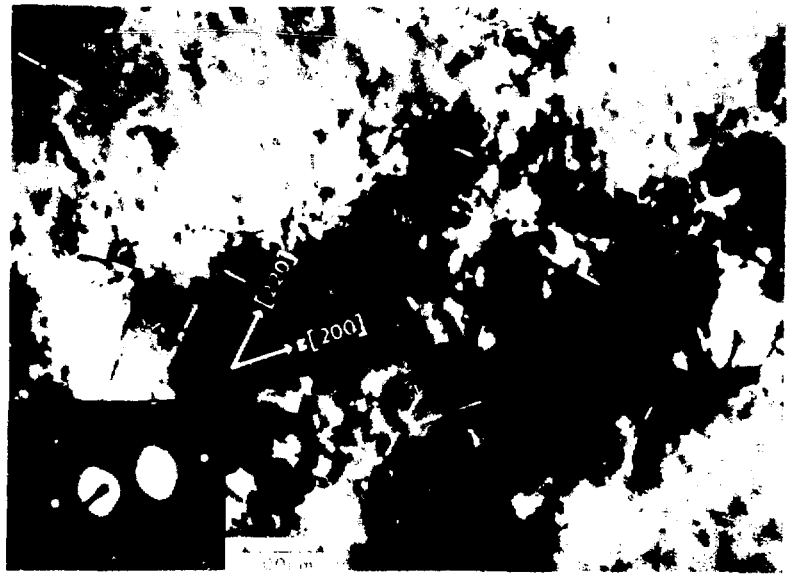

Fig. 27. Dynamical Contrast Micrograph of Clusters in 65°C Fission Reactor Neutron Irradiated Copper.

formed by diffusion and coalescence of self-interstitials at heterogeneous sites in the Cu matrix. These clusters then became preferential sinks for interstitials subsequently produced in their vicinity, leaving a locally higher concentration of vacancies which form the vacancy clusters found at high density in the cell wall region. The lower density of vacancy clusters in the cell interior results from the increased recombination and annihilation of Frenkel pairs in these relatively interstitial-cluster-free regions. The development of the nonuniform structure in the fission reactor neutron irradiated samples evidently results from the long-range diffusion of self-interstitials to interstitial cluster sinks and the shorter range diffusion and coalescence of excess vacancies into vacancy clusters. The more uniform distribution of damage clusters in the fusion neutron irradiated sample indicates either that at the lower irradiation temperature (25°C) the decreased diffusion processes do not influence the structure development in the same way as in the fission reactor neutron irradiated sample (65°C) or that there are some other fundamental differences, such as the spontaneous creation of vacancy clusters from the high-energy displacement cascades that determine the distribution of the clusters..

The results of these initial studies indicate that there are substantial differences in the displacement damage structures and associated tensile properties produced in Cu and Nb by equal fluences of fusion and fission reactor neutrons at temperatures up to about 200°C and fusion neutron fluences up to about 10^{18} n/cm^2. Radiation strengthening differences appear to be about twice as large as those expected from the differences in the amounts of displacement damage produced by the fusion and fission reactor neutrons. TEM observations of the fusion and fission reactor neutron irradiated Cu samples indicate that the damage structures consist of the same kinds of primary structural defects, i.e., vacancy and interstitial point defect clusters and small Frank and prismatic dislocation loops, but that the number-densities, size and spatial distributions of the defects are significantly different. These differences appear to result from differences in the primary recoil spectra as follows: Many high-energy cascades are produced during fusion neutron irradiation, and they spontaneously create stable vacancy clusters and

multiple clusters. The majority of clusters formed during fission reactor neutron irradiation, on the other hand, appear to develop from the diffusion-controlled coalescence of interstitials and excess vacancies. The fraction of the displacement damage retained in the form of point defect clusters appears to be greater during fusion neutron irradiation than during fission reactor neutron irradiation primarily because of the increased recombination of the diffusing vacancies and interstitials during fission reactor neutron irradiation.

ACKNOWLEDGEMENTS

This work was performed under the auspices of the U. S. Energy Research and Development Administration. The samples were prepared by Fay Dishong and Gene Raymond. RTNS irradiation were performed by Donald Rawles, Lewis Mego, Richard Penpraze, and Rex Booth. LPTR irradiations were performed by Wade Richards, Joe Prindle, and Will Burns. Ruth Anderson and Susan MacLean carried out the gamma-ray counting and dosimetry calculations, respectively. Fran Silva encapsulated the higher temperature specimens. Robert Hibbard designed the irradiation furnace. Curtis Rowe gave assistance in setting up and monitoring irradiations. All this help is gratefully appreciated.

REFERENCES

1. R. BOOTH, IEEE Trans. Nucl. Sci. NS14, 943 (1967).
2. R. BOOTH and H. H. BARSCHALL, Nucl. Instrum Methods 99, 1 (1972).
3. R. BOOTH, H. H. BARSCHALL, and E. GOLDBERG, IEEE Trans. Nucl. Sci. NS20, 472 (1973).
4. R. BOOTH, Nucl. Instrum. Methods 120, 353 (1974).
5. R. A. VAN KONYNENBURG, H. H. BARSCHALL, R. BOOTH, and C. WONG, Proc. Int'l Conf. on Radiation Test Facilities for the CTR Surface and Materials Program, Argonne National Laboratory, July 15-18, 1975 (to be published).
6. J. SEAGRAVE, $D(d,n)^3He$ and $T(d,n)^4He$ Neutron Source Handbook, LAMS-2162, Los Alamos Scientific Laboratory (1957).
7. D. NETHAWAY, Nucl. Phys. A190, 635 (1972) and personal communication of later results (Feb. 1975).
8. R. A. VAN KONYNENBURG, Neutron Dosimetry (14 MeV) for Foil Samples Irradiated with the Lawrence Livermore Laboratory Rotating Target Neutron Source, UCRL-51393 Rev. 1, Lawrence Livermore Laboratory (1974).
9. LAWRENCE LIVERMORE LABORATORY, Safety Analysis Report for Livermore Pool Type Reactor, UCRL-51423 (1974).
10. R. V. GRIFFITH, "Activation Foil Neutron Spectra in the Core of the LPTR," in Hazards Control Progress Report No. 49 - July through December 1974, UCRL-50007-74-2, Lawrence Livermore Laboratory (1975).
11. W. N. McELROY and S. BERG, A Computer-Automated Iterative Method for Neutron Flux Spectra Determination by Foil Activation, Kirtland AFB Report AFWL-TR 67-41, 3 (1967).
12. C. Z. SERPAN, JR., and B. H. MENKE, "Nuclear Reactor Neutron Energy Spectra," ASTM Data Series Pub. DS52, Amer. Soc. for Testing and Materials, Philadelphia (1974).
13. J. B. MITCHELL and W. L. BELL, "Characterization of Point Defect Clusters by 2-1/2-D TEM," (to be published in Acta Met. 1975).
14. F. KROUPA, Czech. J. Phys. 10, 384 (1960).
15. S. M. OHR, Phil. Mag. 26, 1307 (1972).
16. B. A. LOOMIS and S. B. GERBER, Acta. Met. 21, 165, (1973).
17. J. B. MITCHELL, D. M. LOGAN, and C. J. ECHER, J. Nucl. Matls. 48, 139, (1973).
18. J. B. MITCHELL, R. A. VAN KONYNENBURG, M. W. GUINAN, and C. J. ECHER, Phil Mag. 31, 919 (1975).
19. K. L. MERKLE, Nucl. Technol. 22, 66 (1973).

20. K. L. MERKLE, Proc. of the Vienna Symposium on Radiation Damage in Radiation Damage in Reactor Materials (Vienna: International Atomic Energy Agency), 59 (1969).

21. F. HAUSSERMANN, Phil. Mag. 25, 537 (1972).

22. J. L. BRIMHALL, L. A. CHARLOT, and H. E. KISSINGER, "14 MeV Neutron Damage in Molybdenum," (to be published in Radiation Effects 1975).

† Reference to company or product name here and elsewhere in this report does not imply approval or recommendation of the product or company by the University of California or the U. S. Energy Research Development Administration to the exclusion of others that may be suitable.

COMBINED EFFECTS OF DISPLACEMENT DAMAGE AND HIGH GAS CONTENT IN ALUMINUM

K. Farrell and J. T. Houston
Oak Ridge National Laboratory
Metals and Ceramics Division
P.O. Box X
Oak Ridge, Tennessee 37830

ABSTRACT

A solid solution alloy of 2300 appm of ^{6}Li isotope in aluminum was neutron irradiated at about 0.36 T_m in high, fast and thermal fluxes producing a damage level of 2 to 3 dpa and simultaneously inducing a gas content of about 2200 appm each of helium and tritium from burnup of ^{6}Li. The gases significantly increased the nucleation of structural defects but did not change the degree of swelling; cavity concentrations were increased ~1000-fold, cavity sizes were decreased ~10-fold and there was ~10-fold increase in the concentrations of dislocations. Also, large cavities were developed on grain boundaries. The cavities were consistent with their being gas-filled bubbles. The refinement of damage structure by the gases caused a considerable increase in radiation hardening. Bend tests at 77 and 296 K revealed severe embrittlement and intergranular fracture. Comparison with data from material irradiated to produce comparable gas levels but relatively little displacement damage indicates that premature intergranular failure is much enhanced by the presence of a defect-hardened matrix. Postirradiation annealing tests showed the cavity and dislocation structures to have high resistance to annealing. Annealing also encouraged the development of a secondary population of large cavities believed to be associated with migration and precipitation of tritium.

---

*Research sponsored by the Energy Research and Development Administration under contract with Union Carbide Corporation.

INTRODUCTION

The question "What will happen to damage structures and to mechanical and physical properties of metals when significant displacement damage and high gas generation rates (and levels) occur simultaneously?" is especially pertinent to the conditions envisaged for the first wall of a controlled thermonuclear reactor (CTR) operating on a D-T reaction. Here the irradiation temperatures will be in the range for void formation, and the generation rates for helium and hydrogen from (n,α) and (n,p) reactions will be much higher than those in existing fission reactors.[1] Moreover, further quantities of these gases will be introduced from the plasma and from the lithium breeder blanket. Concurrently there will be high displacement damage rates. There are no precedents for these conditions and no neutron facilities in which the effects of these conditions can be determined explicitly. We have therefore done a simulation experiment to examine some of the effects of displacement damage and high gas generation rates in a simple material, high purity aluminum.

EXPERIMENTAL CONDITIONS

High purity aluminum is not likely to be used to build a CTR but it does have certain advantages for our simulation experiment. In the first place it readily develops radiation damage structures consisting of the usual loops, dislocations, voids and transmutation products at low and easily attainable neutron fluences.[2-5] Second, it has a very high solid solubility for lithium. We can therefore utilize the large cross-section for the $^{6}Li(n,\alpha)$ reaction with thermal neutrons to produce significant quantities of helium and the hydrogen isotope tritium. And these gases will be created uniformly throughout the test specimens.

Our test material was a dilute alloy of high purity aluminum and 2300 appm (C.052 wt %) of ^{6}Li isotope (added to the melt as a pellet of 98% ^{6}Li + 2% ^{7}Li). The composition of the alloy was analyzed by mass spectroscopy for the ^{6}Li isotope. This alloy, together with unalloyed base aluminum (designated 6-9 Al for six nines purity) was processed to

rods about 50 mm long by 3 mm diam which were annealed for 1 h at 873 K in air then furnace-cooled (FC) or water-quenched (WQ). (Actually we found such big differences in behavior between the 6–9 Al and the Al-Li alloy after irradiation that we did not pursue any effects of prior heat treatment.) The rods were irradiated in the hydraulic facility of the Oak Ridge High Flux Isotope Reactor (HFIR) either in direct contact with the cooling water at about 328 K (0.35 T_m) or packed in aluminum powder in a sealed capsule in which the temperature during irradiation was estimated to be about 348 K (0.37 T_m).

The neutron spectrum in the HFIR has both high thermal and fast components, thus assuring that in the Al-Li alloy displacement damage and high gas generation rates will occur simultaneously. The conventional thermal (2200 m/s or E < 0.0253 eV) flux on the specimens was about 2×10^{19} n/m^2. The fast (E > 0.1 MeV) flux was about 9×10^{18} n/m^2, equivalent to a displacement damage rate for aluminum of 1 to 2×10^{-6} dpa/s. The neutron fluences attained are shown in Table 1, the displacement damage levels being in the range 2 to 3 dpa. The cross-section for the ^{6}Li (n,α) reaction with conventional thermal neutrons is 950×10^{-28} m^2. Consequently, the Al-Li alloy suffered 95–99% burnup of ^{6}Li, resulting in estimated final helium and tritium levels in the region of 2200 appm each. Such gas levels are of the order of those expected to be created in the first wall of a CTR during 10 years of operation. In our experiment they were attained in a period of only about 20 days. The displacement damage rate is of the same order as that expected in a CTR first wall material but the damage level is equivalent to only a few weeks of CTR damage.

OBSERVATIONS

Hardness and Density Measurements

Hardness measurements were made at room temperature on ground and polished specimens cut from the irradiated rods. A Kentron tester was used with a diamond pyramid indentor and a load of 0.5 kg. The average

Table 1. Irradiation Conditions, Hardness, and Swelling Values

	Irradiation Temperature (K)	Neutron Fluence ($\times 10^{25}$ n/m^2)		Hardness (MPa)	Swelling (%)
		E < 0.0253 eV	E > 0.1 MeV		
6-9 Al (FC)		0	0	137	
Al-0.05 Li (FC)		0	0.	137	
Al-0.05 Li (WQ)		0	0	196	
6-9 Al (FC)	~328	5.3	2.2 (3 dpa)	382	
Al-0.05 Li (FC)	~328	5.3	2.2 (3 dpa)	902	
Al-0.05 Li (WQ)	~328	5.3	2.2 (3 dpa)	863	
6-9 Al (FC)	~348	3.3	1.5 (2 dpa)	245	0.64
Al-0.05 Li (FC)	~348	3.4	1.4 (2 dpa)	745	0.56/0.79

hardness values from three indentations for each data point are given in Table 1. The Al-Li alloy displayed considerably greater irradiation hardening than did the 6-9 Al.

Densities (ρ) were measured by Archimedes' displacement on just two of the rods. The degree of swelling, $S = \frac{100(\rho_u - \rho_i)}{\rho_i}$, where the subscripts u and i denote unirradiated and irradiated conditions, is about equal at 0.6% (Table 1) for the pure aluminum and for the Al-Li alloy. The two values of swelling quoted for the Al-Li alloy depend on whether we use the density of Al-Li alloy or of pure aluminum, respectively, for the unirradiated reference material. The use of the density of pure aluminum in this respect allows for the change in composition caused by burnup of ^{6}Li.

Embrittlement

Mechanical testing consisted of bending the rods between two pairs of hand-held pliers in air at room temperature (296 K) and in liquid nitrogen (77 K). At both temperatures the unirradiated materials and the irradiated 6-9 Al could be bent through a full circle without failure. The irradiated Al-Li alloy snapped cleanly with an audible crack and with no measurable bend angle; more force was needed to cause fracture in liquid nitrogen. At both temperatures the fracture path in the irradiated Al-Li alloy was wholly intergranular (Fig. 1a).

Examination of the fracture surfaces of the irradiated Al-Li alloy using scanning electron microscopy and, for better resolution, carbon replicas revealed the boundaries to be riddled with cavities (Fig. 1b,c,d). Fracture occurred by ductile tearing of the grain boundary areas between the cavities. The scale of this ductile tearing was smaller in specimens tested in liquid nitrogen. The shapes and concentrations of cavities varied widely from one grain boundary to another. The photographs in Fig. 1 were selected to show the range of cavitation. Measurements of the cavities indicated that they covered up to 90% of the grain boundary area on some of the fracture facets. On other facets the cavities were relatively small and they covered as little as 10% of the grain boundary area. Typically, the coverage was 50% or more. Frequently the cavities

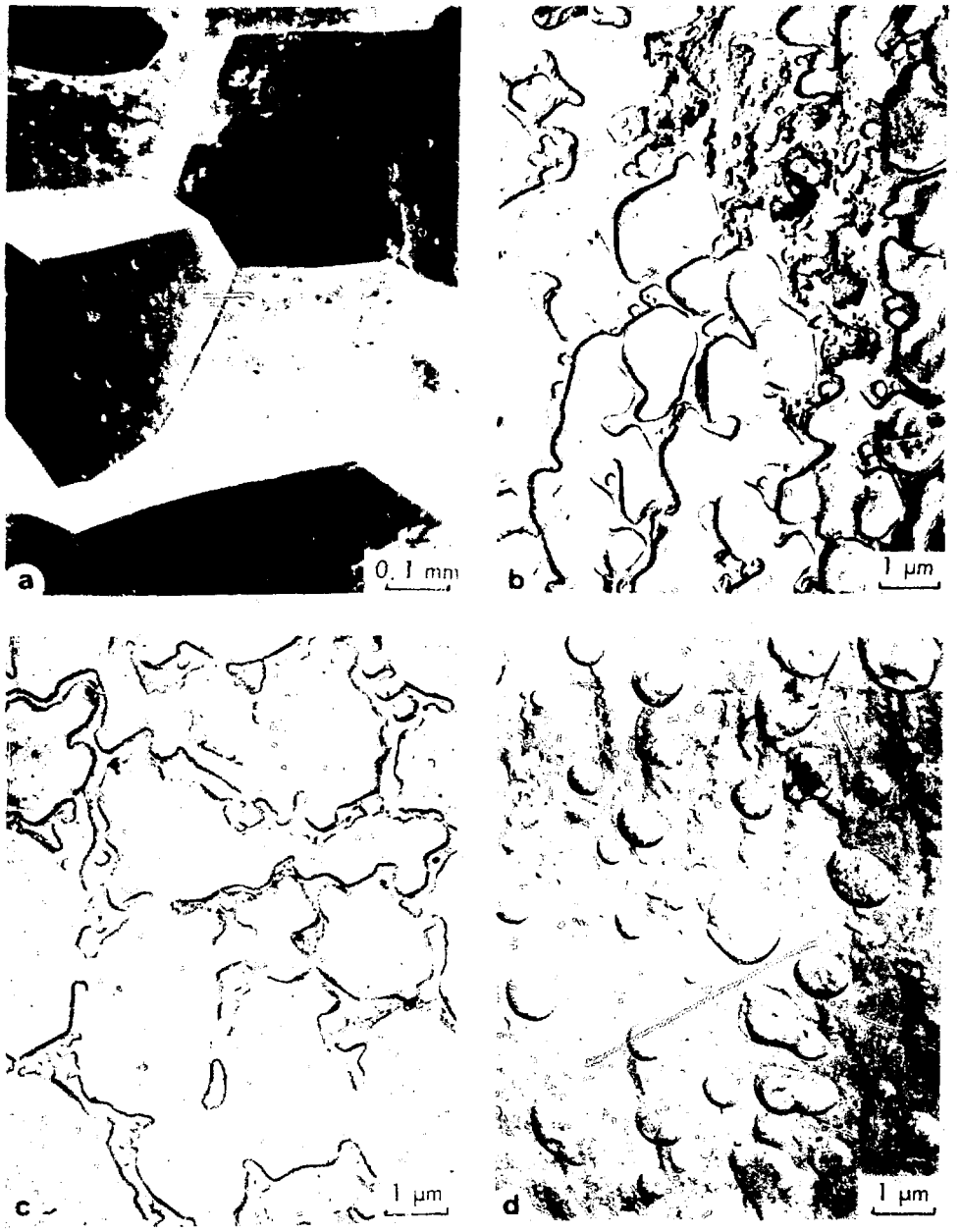

Fig. 1. Intergranular Fracture in Al-Li Alloy Irradiated at 348 K and Bend Tested at 296 K (a,b,c) and 77 K (d).

were interconnected and it was difficult to distinguish individual cavities. Rough measurements indicated that there were at least 10^{12} cavities/m^2 of grain boundary. If these are assumed to be spherical then the size of cavity required to touch one another and give almost complete grain boundary coverage is just 1 μm. This is quite compatible with the observations. These grain boundary cavities did not result from the mechanical testing. They were created during neutron irradiation.

Microstructures

Disks were cut from untested, irradiated rods and were thinned for transmission electron microscopy. The grain size was large, 0.6 mm, and the grain boundaries in the Al-Li alloy tended to be gouged out during electropolishing. The few boundaries that we did manage to retain in thinned areas of the Al-Li alloy are considered to be the better boundaries (i.e., those with the smallest cavities). Two of these are shown in Fig. 2. On such boundaries the cavity sizes ranged from about 15 to 400 nm diam, with concentrations of about $10^{13}/m^2$ of grain boundary area.

There were many tiny cavities within the grains in the Al-Li alloy. These are barely visible in Fig. 2 but can be seen more clearly in Figs. 3b and 4b. Also evident in Fig. 3b is a defect-free zone on each side of the grain boundary. Examination of several grain boundaries indicated that the width of this denuded zone was about equal to the diameter of the largest cavity visible on the boundary.

In the irradiated 6–9 Al there were no cavities on grain boundaries (Fig. 3a) and the denuded regions at the grain boundaries were a factor of 3 or more wider than those in the Al-Li alloy. The cavities within the grains were very much larger and of much lower concentrations than the cavities within the grains of the irradiated Al-Li alloy. Precipitate particles of silicon, a solid transmutation product of aluminum,[6] were present on grain boundaries and on cavities in the 6–9 Al but none was observed in the Al-Li alloy.

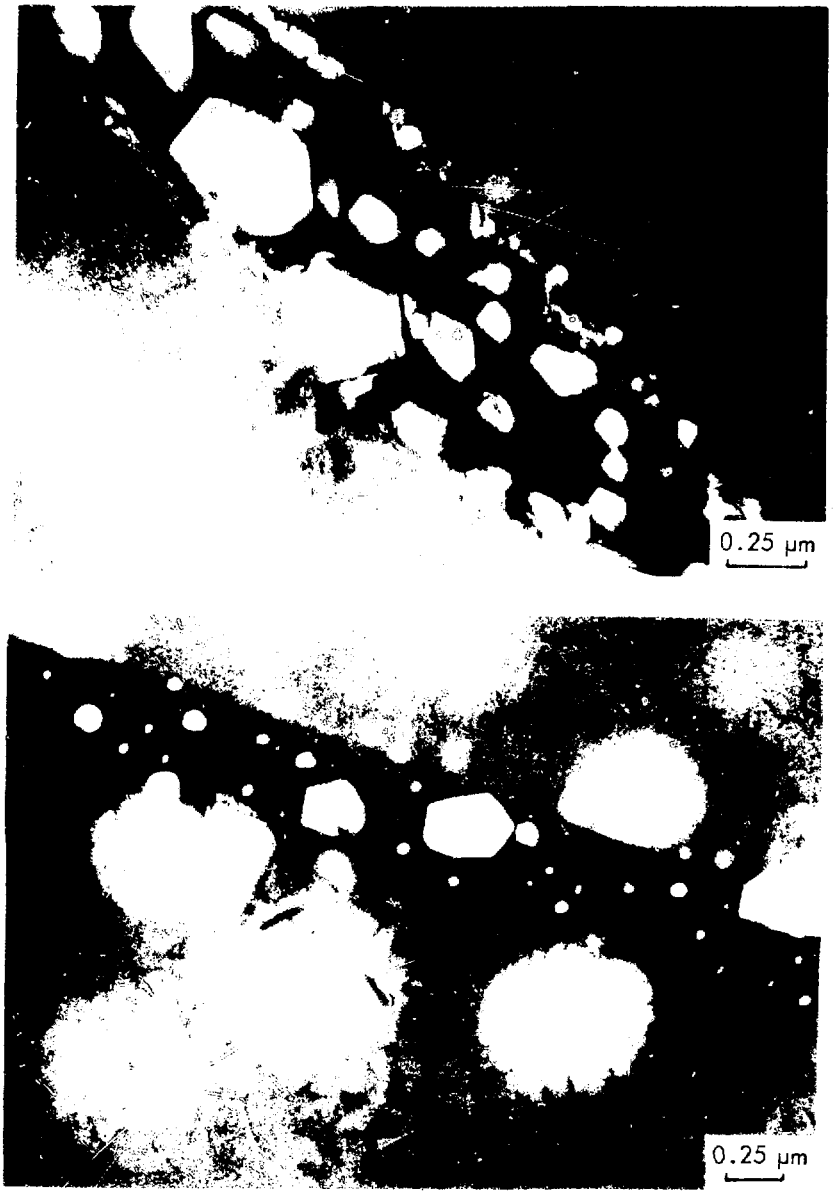

Fig. 2. Large Cavities on Grain Boundaries in Al-Li Alloy Irradiated at 348 K.

Fig. 3. Differences in Grain Boundary Denuded Regions and Matrix Cavities After Irradiation at 348 K. (a) Pure aluminum. (b) Al-Li alloy.

Dislocation concentrations were higher in the Al-Li alloy and were arranged in a uniform configuration as shown in Fig. 4a. There was no discernible association of the dislocations with the numerous, small matrix cavities that can be seen more clearly in Fig. 4b. Quantitative analysis of the microstructures of the irradiated specimens are presented in Table 2. The measured cavity concentrations in the Al-Li alloy are believed to be somewhat low because of significant overlapping of cavity images and because there probably were cavities present whose sizes fell below our resolution limit of about 3 nm.

Annealing Experiments

The microstructures in the irradiated Al-Li alloy were found to have much greater resistance to annealing than those in the irradiated 6-9 Al. Disks about 1 mm thick were cut from each material and were annealed for 1 h in air at temperatures of 573, 673, and 773 K. During 1 h at 573 K all cavities and dislocations completely disappeared in the 6-9 Al and the silicon precipitate coarsened. In the Al-Li alloy the dislocation structure and the small cavities appeared to remain substantially unaffected by the anneal except for a small but obvious growth of some cavities like strings of beads along the dislocations. However, two new features appeared — coarse silicon particles and a uniform distribution of large, secondary cavities within the grains, as shown in Fig. 5 upper (compare with Fig. 4a). These annealing cavities were frequently associated with the coarse silicon particles and they had a wide variety of shapes ranging from rod-like to plate-like, all with crystallographic facets. Their sizes ranged up to 200 nm or so. The formation of these secondary cavities did not involve dissolution of the original, very small cavities in their immediate vicinity (Fig. 5, lower).

At 673 K the dislocation structures and the small matrix cavities were still present in the Al-Li alloy. Growth of cavities on dislocations was no longer obvious but a slight coarsening of the matrix cavities was evident. The large annealing cavities were larger (up to 1 μm) and fewer than those at 573 K, and they were more equiaxed in shape. At 773 K the irradiated Al-Li specimens tended to disintegrate and thinned foils could not be obtained.

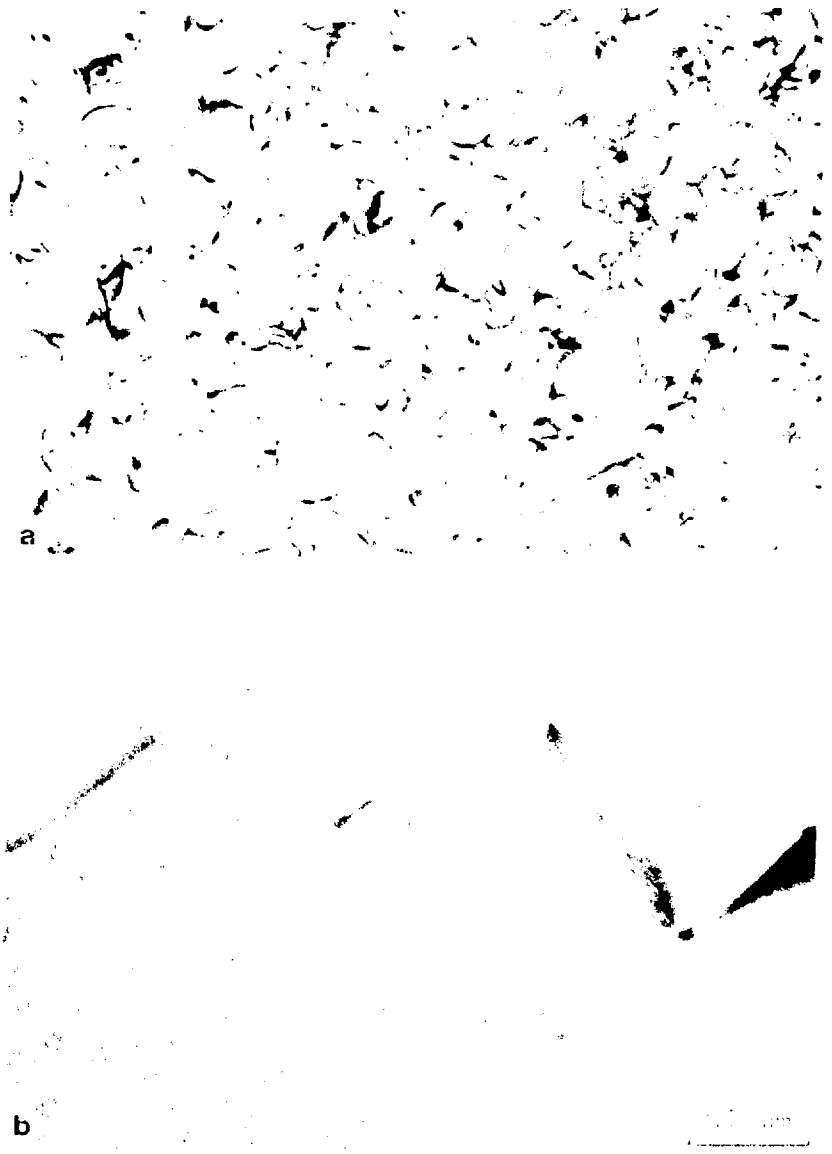

Fig. 4. Dislocations and Small Matrix Cavities in Al-Li Alloy Irradiated at 348 K.

Table 2. Microstructural Data

Material	Irradiation Conditions	Cavities/m^3	Cavity Diameter (nm)	Loops/m^3	Loop Diameter (nm)	Dislocations (m/m^3)
6–9 Al	348 K, 2 dpa	8.7×10^{19}	52	6.7×10^{18}	∿40	1.3×10^{13}
Al–0.05 Li	348 K, 2 dpa	$>7 \times 10^{22}$	∿4	$>8 \times 10^{18}$	∿50	$>6 \times 10^{13}$
Al–0.05 Li	328 K, 3 dpa	2×10^{23}	<4	5×10^{19}	∿20	2×10^{14}

Fig. 5. Large Matrix Cavities Developed in Al-Li Alloy During Postirratiation Annealing for 1 h at 573 K. Black particles are coarsened precipitates of transmutation-produced silicon. Lower photograph shows at high magnification tiny cavities in vicinity of one of the anneal-induced cavities.

DISCUSSION

It is clear that major changes in microstructural defects and in mechanical behavior occur in aluminum when large quantities of tritium and helium are created during displacement damage. These changes are more a matter of difference in the scale or degree of damage than of radical alteration in the nature of the damage. The same neutron-induced structural features (e.g., dislocations, cavities, and precipitates) are involved but there are many more of them when they are created in the presence of the gases. The gases evidently enhance nucleation of the structural defects but do not change their form. The cavities differ in the sense that those in the 6-9 Al are probably empty and can anneal readily whereas those in the Al-Li alloy are undoubtedly gas-filled and are relatively resistant to annealing. The amount of gas required to stabilize the cavities in the 6-9 Al as equilibrium gas bubbles is estimated to be 1.5×10^3 appm (taking a surface energy value of 1.2 J/m^2 for aluminum[7] at 348 K, and using Van der Waals' constant for helium gas[8] of 1.91×10^{-29} m^3/atom and assuming this constant applies to hydrogen, too). The estimated gas levels in the 6-9 Al from Al(n,p) and Al(n,α) reactions are only 4 appm H and 0.7 appm He. In the Al-Li alloy, however, the presence of cavities on the grain boundaries is strong testimony for gas bubbles. Also, the amount of gas present is quite enough to stabilize the cavities; gas levels of 2200 appm each of ^{4}He and ^{3}He can support a population of 4 nm diam bubbles of $1.8 \times 10^{23}/m^3$, which is of the order of the cavity concentrations measured in the Al-Li alloy. These calculations are essentially unaffected by the loss of gas to the large grain boundary bubbles. Even in the extreme case of complete grain boundary coverage with 1 μm bubbles the amount of gas involved at the boundaries is only 30 appm, a negligible quantity with respect to the total gas content.

Despite the large differences in gas content between the 6-9 Al and the Al-Li alloy, and irrespective of whether the cavities are gas-filled or not, both materials swell to the same degree, about 0.6%. The gases greatly increase the concentrations of cavities but do not increase the level of swelling. Presumably at the high cavity concentrations in the

Al-Li alloy the cavities have become the predominant sinks for both vacancies and self-interstitials thus minimizing growth of cavities and controlling the swelling. The distributions of cavities differ in the two materials. There are no grain boundary cavities in the 6-9 Al. Those in the Al-Li alloy are massive compared with the cavities within the grains, but these large cavities do not dominate the swelling. The concentration, N, of large cavities on the grain boundaries in the Al-Li alloy was in the range 10^{12} to $10^{13}/m^2$. The average diameters of such cavities required to completely cover the grain boundaries are the center-to-center bubble spacings on the boundaries (i.e., $N^{-1/2}$ or 10^{-6} to 3.2×10^{-7} m, respectively. Swelling from these cavities is given by $\frac{2N\pi d^3}{6\ell}$ where ℓ is the grain diameter and $\frac{2}{\ell}$ is the grain boundary area per unit volume. In these materials ℓ is 5.8×10^{-4} m, and the maximum swelling from grain boundary bubbles will lie in the range 0.18 to 0.06%. The balance of the measured swelling, 0.5 to 0.6%, must be caused by the small cavities within the grains. The measured concentration of these small cavities is roughly $1 \times 10^{23}/m^3$ and their size is about 4 nm diam (i.e., about 0.33% swelling). This is a reasonably good agreement considering our belief that we have undercounted the small cavities. In fact, as we showed earlier, the concentration of 4 nm diam gas bubbles calculated from the known gas level is $1.8 \times 10^{23}/m^3$, which will give 0.59% swelling.

The tensile strength or flow stress of an irradiated metal containing several species of structural defects is described[9] by an equation of the form

$$\sigma_i = \sigma_u + [(\Delta\sigma_{dis})^2 + (\Delta\sigma_{cav})^2 + (\Delta\sigma_{other})^2 + \ldots]^{1/2} , \qquad (1)$$

where σ_u is the strength of the unirradiated metal, and $\Delta\sigma_{dis}$ is the additional strengthening from a dispersion of radiation-induced dislocations, cavities or other defects that impede dislocation movement. Similarly for hardness,

$$H_i = H_u + [(\Delta H_{dis})^2 + (\Delta H_{cav})^2 + (\Delta H_{other})^2]^{1/2} . \qquad (2)$$

The hardening increment from grown-in dislocation is given by the expression $\Delta H_{dis} = 3\ Gb\ \lambda^{1/2}$, where the factor 3 converts flow stresses to hardness values,[10] G is the shear modulus (2.65×10^4 MPa for Al), b is the Burgers vector (0.286 nm), and λ is the concentration of grown-in dislocations on the slip plane. The contribution from dislocation loops[11] is given by $\Delta H_{\ell} = 6\ Gb\ (Nd)^{1/2}$, where N is the concentration of loops per unit volume of aluminum, and d is their mean diameter; in the present work the hardening component from loops is almost negligible. Cavities make a significant contribution[12] via the equation $\Delta H_{cav} = 6\ Gb\ (Nd)^{1/2}$. Using these equations and the quantitative microstructural data from Table 2 we have calculated the hardness values given in column 5 of Table 3. The calculated values seriously exceed the measured hardnesses at the higher hardness values. This, we believe, is due to the use of the ΔH_{cav} equation which may overestimate ΔH_{cav}. We get a different result if we consider the cavities to act as hard particles opposing dislocation motion, for which we can derive[9] the expression

$$\Delta H_{cav} = \frac{3 \times 1.0^4}{\pi} Gb\ (Nd)^{1/2} \cdot \ell n\ (\frac{d}{4b}) \quad .$$

This reduces the calculated hardness values to those shown in column 6 of Table 3. Note that the two sets of calculated hardnesses now embrace the measured values. Presumably we could play around with hardening equations until we obtained a satisfactory correlation but that is not the primary purpose of this exercise. Rather, we wish to draw attention to the theoretical hardening expressions, all of which indicate that the increase in hardness caused by microstructural defects is an inverse function of the spacing between the defects. Hardness should thus increase with the concentrations of defects which, of course, is qualitatively what we see in our materials. In short, the irradiated Al-Li alloy is much harder than the irradiated pure aluminum because of the finer scale of the damage structure in the Al-Li alloy.

Table 3. Hardness Correlation

Material	Irradiation Temperature (K)	H_u (MPa)	H_i (Meas.) (MPa)	H_i (Calc.) (MPa)	
				Cavities	Hard Particles
6-9 Al	348	137	245	265	235
Al-0.05 Li	348	137	745	912	363
Al-0.05 Li	328	196	863	1520	618

The brittle behavior of the irradiated Al-Li alloy can be related to the irradiation hardening and to the structural modifications induced at grain boundaries. Grain boundaries are distorted lattice regions that are known to be good sources of vacancies and also are sinks for vacancies, self-interstitials and impurities. During irradiation the grain boundaries absorb impurities and irradiation-induced point defects from regions immediately adjacent to, and on each side of, the boundary, leaving clearly visible zones denuded of defects. Such zones are soft compared with the defect-hardened matrix. Gases entering the grain boundaries develop into large bubbles with the aid of readily available vacancies in the boundaries. We have made simple calculations of the amount of gas required to form the observed concentrations and sizes of grain boundary gas bubbles in the irradiated Al-Li alloy and find that adequate quantities of gas can be drawn from the denuded regions alone. These bubbles are built-in holes which can tear open under appropriate shear strains. Shear strains are concentrated at grain boundaries because the boundaries are natural barriers to transmission of slip, and because of the denuded zones at the boundaries. During mechanical testing the hard matrix can support a higher load than the softer denuded zones which must therefore deform prior to the matrix. Plastic strain becomes localized in the grain boundary regions. The grain boundaries, already weakened by the presence of gas bubbles, become overloaded and tear open. The result is highly intense local deformation at grain boundaries with little or no measurable bulk strain, and with intergranular fracture. Similar fracture is avoided in the irradiated 6-9 Al because the matrix is relatively soft, the grain boundary denuded zones are wider, and the grain boundaries are free of irradiation-induced cavities.

The annealing response of the Al-Li alloy deserves comment. The fine matrix cavities were remarkably stable to annealing even despite the strong evidence of vacancy migration. This migration can be seen in the growth of the silicon precipitates and in the development of the secondary population of large cavities during annealing. In previous work on cavity annealing in neutron irradiated aluminum[5,13] of low gas content, as well as as in the present work on 6-9 Al, it was found that growth of silicon precipitates was concomitant with cavity shrinkage or growth, implying a

coupled migration of vacancies and silicon atoms. Also, when large cavities grew, it was always at the expense of their immediate smaller neighbors by a ripening process. This is not so in the Al-Li alloy. Here the small matrix cavities in the vicinity of the anneal-induced large cavities are not dissolved during the anneal. They may shrink a little but they do not disappear. The difference is presumed to be due to the effects of the ^{4}He and ^{3}H. We suspect that in the Al-Li alloy the small cavities retain their inert helium during annealing but release tritium which migrates and precipitates to form the large, annealing cavities. Hydrogen has a very low solubility in aluminum and it readily forms bubbles during proton bombardment;[14] moreover, these hydrogen bubbles coarsen during postbomardment anneals at 573–773 K and eventually disperse, although they may cause extensive grain boundary cracking in the interim. This picture fits nicely with our observations on annealing of the irradiated Al-Li alloy. We certainly had significant tritium migration even at room temperature. Every time we opened our lead storage can to retrieve an irradiated Al-Li specimen we contaminated the walls of our glove box with tritium. Also, when we returned to some thinned electron microscopy foils to reexamine grain boundaries we found that the boundaries had cracked open during storage at room temperature. The most logical explanation of this is that tritium precipitated into the large grain boundary cavities and caused them to burst through the foil surfaces.

These observations and deductions raise the question of the role of tritium in the development of cavities and damage structure. Unfortunately, the irradiated metals contain at least equal quantities of helium and hydrogen (or tritium), and helium is a noted promoter of cavities.[4,15] We cannot readily distinguish a separate role of hydrogen but if hydrogen bubbles can form easily in aluminum during annealing at temperatures above about 370 K we see no reason why they should not develop during irradiation at 328 and 348 K, particularly at grain boundaries. And the grain boundary cavities in the Al-Li alloy are very large. Perhaps they do contain more tritium than helium. The tritium can migrate much more readily than the helium, and its low solubility would force it to precipitate at any free surface. It may also be involved in nucleation of the small matrix

cavities. Evidence in the literature indicates that hydrogen increases the concentration of cavities in neutron irradiated aluminum[4] and in electron-irradiated PE16 alloy,[16] 316 stainless steel[17] and ferritic steels.[18] Until recently hydrogen was not seriously considered an element of radiation damage in most reactor constructional materials, except zirconium, because it was assumed to escape. The writing is now on the wall. In CTR materials the hydrogen generation rates will be many times greater than those of helium, and possible effects of hydrogen should not be overlooked.

It is obvious from this work that when high gas contents and significant neutron displacement damage occur simultaneously in aluminum the resulting effects on damage structures and on mechanical properties are much greater than if the displacement damage occurs alone. It is not clear whether the gas and the displacement damage act synergistically (i.e., whether their combined effects are greater than the sum of their independent effects) since we have not measured the effects of gases alone. Other experimenters[19–22] have studied Al-Li alloys irradiated in predominantly thermal reactors where the neutron spectrum contained relatively minor portions of fast neutrons and hence induced no significant build-up of displacement damage. In these early experiments the major microstructural change was the formation of gas bubbles on grain boundaries and on preexisting dislocations. These bubbles caused some swelling and hardening and loss in ductility but usually considerable ductility was retained and the fracture path remained transgranular except at elevated test temperatures above about 470 K where intergranular fractures occurred and ductility values fell to very low levels at high gas contents. Some of these changes are illustrated by the data in Table 4 for irradiations done at 348 K to give gas levels similar to those in our Al-Li alloy. Note, in Table 4, that with increasing neutron fluence (and gas content) the average size of gas bubbles increases and the average concentration of bubbles decreases markedly. At the gas level of interest to the present work (4480 appm) the concentrations and sizes of bubbles within the grains are quite different from those in our irradiated Al-Li alloy; they are, in fact, almost identical to those of the cavities in the

Table 4. Microstructural Data and Tensile Properties of Al–^{6}Li Alloy (0.3% Li Enriched 96% in ^{6}Li) Irradiated at 348 K in a Predominantly Thermal Reactor (Extracted from References 22a and 22b)

Properties	Thermal Fluence, n/m^2				
	0	6×10^{22}	1.2×10^{23}	1×10^{24}	2×10^{24}
Estimated[a] gas concentration, appm	0	150	280	2350	4480
Size of grain boundary bubbles, nm	0	20+	Occasionally up to 1 μm	20+	250+
Width of grain boundary denuded regions, nm	0	0	0	400	750
Bubble density in matrix, per m^3	0	?	2×10^{22}	1×10^{21}	8×10^{19}
Average diameter of matrix bubbles, nm	0	<2	~5	13	50
Yield stress, MPa					
at 77 K	22	33	45	46	(b)
at 296 K	14	23	33	36	(b)
at 523 K	8	19	21	18	(b)
Ultimate tensile stress, MPa					
at 77 K	124	134	143	128	(b)
at 296 K	68	93	79	69	(b)
at 523 K	17	30	30	22	(b)
Elongation, %					
at 77 K	23	33	26	20	(b)
at 296 K	26	25	13	22	(b)
at 523 K	69	10	8	1	(b)
Matrix Swelling,[c] %	0	?	0.13	0.11	0.52

[a] A gas concentration of 150 appm implies 75 appm ^{3}H and 75 appm ^{4}He.

[b] Specimens contained surface cracks and fissures. Not tensile tested.

[c] Matrix swelling is calculated from the bubble density, N, and average bubble size, d, and is given by $100(V_b/1-V_b)$, where V_b is $N\pi d^3/6$, the volume of bubbles per m^3 of swollen material.

6-9 Al. Consequently, the degree of radiation-induced hardening is expected to be small. Indeed an extrapolation of the ultimate tensile strength from the lower fluence UTS values at room temperature (296 K) indicates no more than about 69 MPa, or a maximum hardness of about 207 MPa which, again, compares more favorably with our irradiated 6-9 Al than with our Al-Li alloy. A similar extrapolation in elongation values would imply retention of significant ductility at 77 and 296 K, again more in keeping with our irradiated pure aluminum than with our irradiated Al-Li alloy. The only points of similarity with our Al-Li alloy observations are the grain boundary bubbles and the degree of swelling.

This comparison strongly suggests a synergistic effect of gases and displacement damage on microstructure and embrittlement. But there is one little flaw in the argument; the data in Table 4 were obtained in a reactor whose thermal neutron flux was undoubtedly much lower (by at least a factor of 10) than that in HFIR. So the data not only represent relative absence of displacement damage but also a lower gas generation rate. We cannot, therefore, conclude that a synergistic effect prevails in our observations. Certainly, however, the combined effects of high gas level and displacement damage are very much greater than the separate effects of displacement damage or high gas level. Another important point illustrated by this comparison is that although gas bubbles on grain boundaries will cause some loss in ductility at low temperatures (Table 4) superimposition of a hardened matrix brings about severe embrittlement (Fig. 1). Indeed, if such hardening, and a weakening of grain boundaries, occurs under CTR conditions then embrittlement and premature fracture, not swelling, is likely to be the Achilles' heel of CTR materials.

CONCLUSIONS

In aluminum neutron irradiated at moderate temperatures ($\sim 0.36\ T_m$) the presence of about 2200 appm each of helium and tritium created concurrently with significant displacement damage causes: (1) No change in overall swelling. (2) Considerable refinement of damage structures without radical change in the type of damage; cavity concentrations are increased 1000-fold, cavity sizes are decreased 10-fold, dislocation concentrations are increased about 10-fold. (3) Development of large cavities on grain boundaries. (4) A narrowing of defect-free regions adjacent to grain boundaries. (5) A large increase in irradiation hardening. (6) Severe embrittlement during mechanical testing associated with intergranular fracture even at very low temperatures.

The combined effects of high gas level and displacement damage are much greater than the effects of displacement damage alone, but it is not clear if there is a synergistic effect. Gases enhance nucleation of defect structures, and at high gas levels the cavities are gas-filled. This refinement of damage structure increases the irradiation-hardening. A combination of a hardened matrix and weakened grain boundary regions leads to severe embrittlement and intergranular fracture. Postirradiation annealing causes the development of a secondary population of large cavities believed to be associated with tritium migration and precipitation. Migration of tritium is evident even at room temperature.

REFERENCES

1. D. Steiner, "The Nuclear Performance of Fission Reactor Blankets," *Nucl. Appl. and Tech.* 9, 83 (1970).

2. J. O. Stiegler, K. Farrell, C.K.H. DuBose, and R. T. King, "High Fluence Neutron Irradiation Damage in Aluminum," pp. 215–232 in *Radiation Damage in Reactor Materials*, Vol. II, Vienna (1969), pub. by International Atomic Energy Agency.

3. N. H. Packan, "Fluence and Flux Dependence of Void Formation in Pure Aluminum," *J. Nucl. Mater.* 40, 1–16 (1971).

4. K. Farrell, A. Wolfenden, and R. T. King, "The Effects of Irradiation Temperature and Preinjected Gases on Voids in Aluminum," *Radiation Effects* 8, 107–114 (1971).

5. K. Farrell and J. T. Houston, "Void Coarsening in High Purity Aluminum During Postirradiation Annealing," *J. Nucl. Mater.* 40, 225–229 (1971)

6. R. E. Gehlbach, J. O. Stiegler, and K. Farrell, "Transmutation-Produced Silicon Precipitates in Irradiated Aluminum," *Metallography* 3, 275–284 (1970).

7. K. H. Westmacott, R. E. Smallman, and P. S. Dobson, "The Annealing of Voids in Quenched Aluminum and a Determination of the Surface Energy," *Metal. Sci., Journ.*, 2, 177–181 (1968).

8. N. V. Tsederborg, V. N. Popov, and N. A. Morozova, "Thermodynamic and Thermophysical Properties of Helium," U.S. Dept. of Commerce Translation TT70-50096 (1971).

9. K. Farrell and R. T. King, "Radiation-Induced Strengthening and Embrittlement in Aluminum," *Met. Trans.* 4, 1223–1231 (1973).

10. D. Tabor, "The Hardness and Strength of Metals," *J. Inst. Metals* 79, 1–18 (1951).

11. A.J.E. Foreman, "Junction Reaction Hardening by Dislocation Loops," *Phil. Mag.* 17, 353–364 (1968).

12. P. Coulomb, "Sur le Blocage des Dislocations par des Cavites ou de Petits Precipites," *Acta Met.* 7, 556–559 (1959).

13. A. Jostsons, E. L. Long, Jr., J. O. Stiegler, K. Farrell, and D. N. Braski, "Annealing of Voids in Aluminum," pp. 363–375 in *Radiation-Induced Voids in Metals*, Proceedings of 1971 International Conference, Albany, New York, pub. AEC Symposium Series 26, USAEC.

14. C. E. Ells and W. Evans, "The Agglomeration of Hydrogen in High Purity Aluminum and Aluminum-Magnesium Alloys, *Trans. AIME* 227, 437 (1963).

15. E. E. Bloom and J. O. Stiegler, "The Effect of Helium on Void Formation in Stainless Steel," *J. Nucl. Mater.* 36, 331–334 (1970).

16. S. B. Fisher, M. J. Makin, and G. P. Walters, "The Diffusion of Hydrogen into PE16 During Electropolishing, and Its Effect on Void Formation During Subsequent HVM Irradiations," Report No. RD/B/N2727, July 1973, Central Electricity Generating Board, Berkeley, England.

17. J. T. Buswell, S. B. Fisher, J. E. Harbottle, and D.I.R. Norris, "High Voltage Electron Microscope Studies of Void Swelling, pp. 170–179 in *Physical Metallurgy of Reactor Fuel Elements*, Proceedings of International Conference at Berkeley Nuclear Laboratories, 2–7 Sept. 1973, published by the Metals Society, London (1975).

18. C. Janssens, L. Stals, J. Van Landuyt, M. Snykers, and W. Vandermeulen, "The Swelling Behavior of Ferritic Steels," in *Properties of Reactor Structural Alloys After Neutron or Particle Irradiation*, Proceedings of Conference held in Gatlinburg, Tenn., June 11–13, 1974, to be published as ASTM STP 570.

19. D. W. Lillie, "Effects of Radiation-Generated Helium and Tritium on the Properties of Al-Li Alloys," *Trans. AIME*, 218, 270 (1960).

20. V. Levy, J. Antolin, J. Espinasse, and Y. Adda, "Contribution a l'Etude de la Precipitation de l'Helium dans un Alliage Aluminum-Lithium," CEA-R2529, Centre de Saclay, France, Juliett, 1964.

21. K. Shiraishi et al., A number of papers on neutron-irradiated Al-Li alloys published in *J. Nucl. Sci. Tech.*, (a) 2 (12), 499 (1965); (b) 3 (11), 466 (1966); (c) 4 (3) 136 (1967); (d) 8 (5) 250 (1971).

22. I. O. Smith and B. Russell, A number of papers on neutron-irradiated Al-Li alloys published in *J. Nucl. Mater.*, (a) 35 137 (1970); (b) 37, 96 (1970); (c) 38 1 (1971).

HELIUM RELEASE FROM TYPE 304 STAINLESS STEEL

J. R. Cost*, R. G. Hickman, J. B. Holt, and R. J. Borg,
Lawrence Livermore Laboratory, Livermore, California 94550

ABSTRACT

Helium in very low concentration (< 1 atomic parts per billion) has been introduced into type 304 stainless steel by radioactive decay of dissolved tritium. The release of this helium during subsequent annealing has then been monitored with a high sensitivity mass spectrometric gas analyzer. With isochronal annealing, helium is released in two temperature ranges, first near 300°C and then between 800°C and the melting point. The latter release is interpreted as being due to helium gas bubbles. The release near 300°C has been studied isothermally between 150°C and 300°C, and has been analyzed in terms of two stages of exponential decay. The fast and slow release stages have relaxation times near 10^2 and 10^3 seconds, respectively and the fast release accounts for roughly 0.85 of the total release at low temperature. From an analysis of the release kinetics, it is concluded that volume diffusion is the controlling mechanism for the outgassing.

INTRODUCTION

Because the presence of even small amounts of helium often results in decreased mechanical properties and premature failure in materials for nuclear power applications, there has recently been a large amount of work devoted to characterizing the behavior of helium in these materials. The problems caused by the presence of helium become particularly important for fusion power reactors in which materials will be exposed to helium ion implantation from the plasma and to helium created by beta decay of tritium, in addition to helium created by (n, α) reactions. In order to deal with materials problems related to the presence of

*On leave of absence from School of Materials Engineering, Purdue University, West Lafayette, Ind. 47907.

helium, it is important to characterize its outgassing behavior, i.e., to determine how such variables as temperature, radiation, material composition, helium concentration, etc., affect the rate at which helium is released. Before such empirical studies are made, it is valuable to study a simple metal-helium system at low helium concentrations and without the complications of radiation damage so that the basic mechanisms by which helium outgassing occurs can be determined. The present study makes use of the radioactive decay of dissolved tritium as a method for introducing controlled low concentrations of helium into type 304 stainless steel. The subsequent degassing behavior of the helium is studied from room temperature to 1300°C.

Use of tritium for the controlled introduction of helium into metals was first described in a review on inert gases in metals by Blackburn.[1] Tritium undergoes spontaneous beta decay with a half-life of 12.3 years, producing ^{3}He as it releases an average energy of 5.7 KeV per event. Its virtues are that it can dissolve in most metals at moderate temperatures and then decay to produce a uniform internal concentration of helium with negligible radiation damage. This is to be contrasted with the implantation of energetic alpha particles which produces non-uniform concentrations and damage in the form of collision cascades. It is noted that the relatively low energy of the tritium decay reaction is below the threshold energy for producing radiation damage in even the lightest metals.[2]

EXPERIMENTAL METHOD

The experimental method has been described previously.[3] After preannealing at 1000°C in ultra high vacuum for an hour, the specimens were exposed to tritium at 300°C and 1.13 atm (114 kPa) for one day. The samples were 0.406 mm thick foils of commercial 304 stainless steel. After the tritium exposure, the greater part of the dissolved tritium was removed by maintaining the specimens at 250°C in a vacuum of 3×10^{-7} Torr ($\sim$ 40 μPa) for one day. After this outgassing treatment, each specimen was analyzed for residual tritium. This was done by snipping a small corner from the foil, slowly dissolving it in aqua regia,

diluting the resulting solution, and measuring the tritium with standard liquid scintillation counting procedures.

The experimental vacuum system used to make the helium release measurements also has been described previously.[3] During a run, helium is collected in the vacuum system for a prescribed time interval while other gases are removed with a titanium sublimation pump. The amount of helium collected in the time interval is then determined mass spectrometrically by sweeping over the m/e = 3 peak, the height of which is proportional to the helium present. Calibration experiments with ^3He gave a calibration factor of 3.19×10^{22} atoms/amp and a minimum detectible amount of helium after subtraction of background of less than 10^{10} atoms.

RESULTS

Helium release was studied for both isochronal and isothermal anneals. The data for the former are shown in Fig. 1 for three different tritiated samples and an untritiated control sample annealed over the temperature range from room temperature to 1300°C. In this figure, the height of the mass spectrometer peak in amps for species with m/e = 3 is plotted versus annealing temperature. This species is exclusively ^3He, the decay product of tritium, since it was determined by experiments on gas mixtures of helium and hydrogen species in controlled concentrations that the hydrogen species were completely removed from the system by the titanium sublimation pump.

It may be observed that releases occur in two widely separated temperature ranges, one a relatively narrow peak near 300°C and the other involving release between 800°C and the melting point. Similar results with a release peak near 300°C and a broad temperature range of release at high temperature have been reported for isochronal annealing of nickel implanted with helium[4] and also for type 316 stainless steel.[3] The helium concentrations released in these two temperature ranges for the three runs shown in Fig. 1 are given in Table 1. Also reported in Table 1 is the concentration of residual tritium measured on a small portion of the sample before the helium analysis. It is noted that the

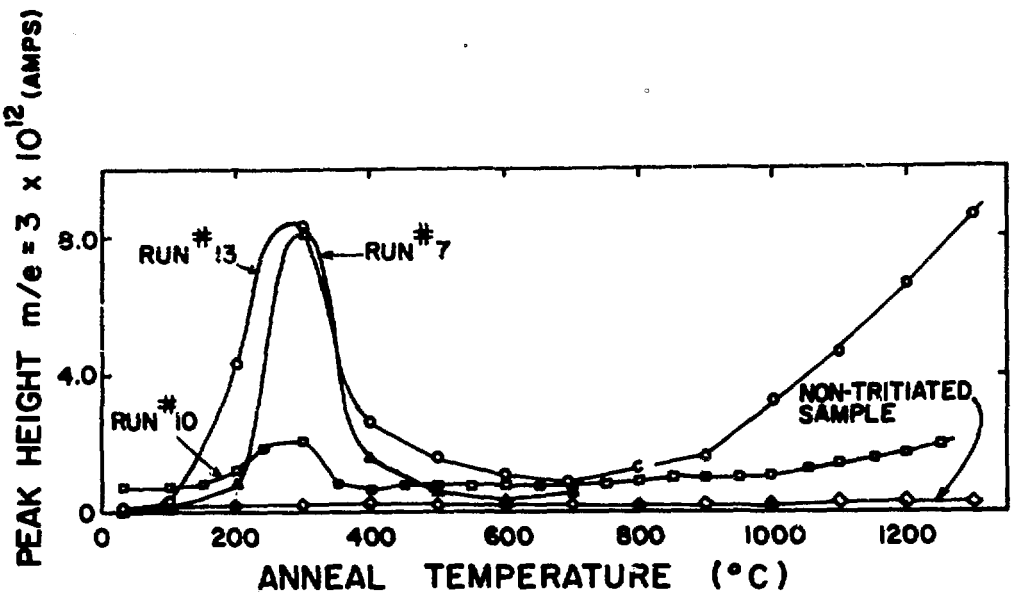

Fig. 1. Isochronal annealing curves for helium release from three different tritiated samples. The time at each temperature was 5 minutes.

Table 1. Summary of Isochronal Annealing Results

Run no.	Sample wt.(g)	Concentration of tritium, c_T (atom fraction)	Concentration of helium released, c (atom fraction)	
			300°C Peak	> 800°C
7	.6691	7.2×10^{-6}	4.7×10^{-11}	not det.
10	.5644	5.3×10^{-6}	1.5×10^{-11}	3.7×10^{-11}
13	.6443	5.4×10^{-6}	7.8×10^{-11}	9.1×10^{-11}

total release above 800°C is somewhat larger than that near 300°C; however, the total helium in the samples could not be determined because the furnace did not reach the melting temperature. One of the goals of this study was to consider the possible mechanisms for these two distinctly different stages of helium release, and in particular the release at low temperature. Thus, the remainder of the experimental results are concerned with the release peak near 300°C.

Fig. 2 shows the release results for four different isothermal annealing temperatures at and below 300°C. These results are plotted semi-logarithmically as the amount still to be released versus annealing time. The solid lines in Fig. 2 are least squares fits of the data at long times (at which the semi-logarithmic plot is linear) to the equation for volume diffusion limited release from a thin slab of thickness h,[5]

$$\bar{c}(t) = c_o \frac{8}{\pi^2} \sum_{x=o}^{\infty} \frac{1}{(2x+1)^2} \exp\left[-(2x+1)^2 t/\tau\right] \qquad (1)$$

where t is time and $\bar{c}$ and c_o are the average instantaneous and original helium concentrations and are proportional to the summed amplitudes of the ^{3}He mass spectrometer peaks remaining to be released with the isothermal anneal. In the above equation, the relaxation time τ is related to the volume diffusivity D by

$$\tau = \frac{h^2}{\pi^2 D} \qquad (2)$$

The least square lines shown in Fig. 2 have a constant slope for times greater than 200 sec corresponding to times at which terms with $x > 0$ are negligible in Eq. 1. It may be observed that the data for each temperature show a good fit to simple exponential decay of the concentration for times greater than 10^3 sec. The slopes of these lines yield values for τ and thus the volume diffusivity. Values for these parameters are reported in Table 2. Because of the uncertainty due to subtraction of the background amplitude for the mass spectrometric measurements, these values are probably no more accurate than 10%. At short times when the terms in the solution to the diffusion equation with $x > 0$ are non-negligible, the least squares fit (solid) lines to Eq. 1

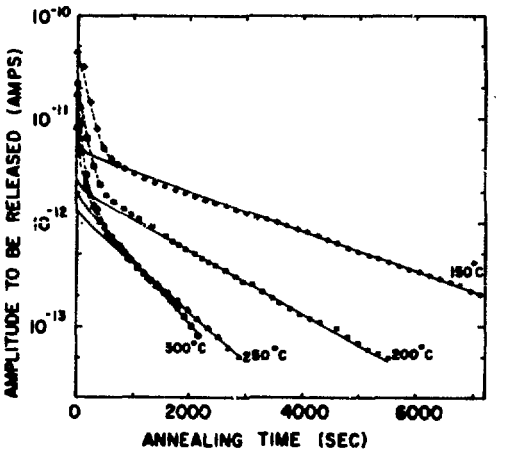

Fig. 2. Semi-logarithmic plot of the data for low temperature isothermal release of helium at four different temperatures. The solid lines which fit the data at long times are least square fits to Eq. 1, the solution to the diffusion equation for volume diffusion controlled degassing of a thin sheet. The lack of a good fit at short times is because the total degassing fits Eq. 1 for a two step process. This figure shows the slow release step and the fast release is shown in Fig. 3.

Table 2. Summary of Isothermal Annealing Results

Temp(°C)	Sample* wt.(g)	Slow release c_s	Slow release τ_s(sec)	Slow release D_s(cm^2/sec)	Fast release c_f	Fast release τ_f(sec)	Fast release D_f(cm^2/sec)	$\frac{c_f}{c_f+c_s}$
150	.6673	2.7×10^{-11}	2.3×10^{3}	8.41×10^{-8}	1.7×10^{-10}	1.3×10^{2}	1.5×10^{-6}	0.86
200	.3411	2.3×10^{-11}	1.5×10^{3}	1.35×10^{-7}	1.67×10^{-10}	1.3×10^{2}	1.5×10^{-6}	0.88
250	.3522	1.3×10^{-11}	9.2×10^{2}	2.12×10^{-7}	5.7×10^{-11}	1.4×10^{2}	1.4×10^{-6}	0.82
300	.6792	9.7×10^{-12}	7.4×10^{2}	2.64×10^{-7}	6.5×10^{-11}	7.7×10^{1}	2.6×10^{-6}	0.83
30 (calculated)	--	--	1.4×10^{4}	1.37×10^{-8}	--	2.5×10^{2}	7.8×10^{-7}	--
		Q_s = 3,800 cal/mole (0.16 eV)			Q_f = 1,200 cal/mole (0.05 eV)			
		τ_{o_s} = 26 sec			τ_{o_f} = 34 sec			
		$D_{o_s} = 7.5\times10^{-6}$ cm^2/sec			$D_{o_f} = 5.8\times10^{-6}$ cm^2/sec			

*All samples were cut from the same tritiated strip for which the concentration of tritium was measured to be 5×10^{-6} atom fraction.

show a small region with increased slope. This region includes about the first 20% of the gas release. It corresponds to the time during which the curved concentration profile for helium is established across the thickness of the sample.

It may be noted that at short times the data do not fit Eq. 1. Instead, an appreciable amount of helium release in excess of that predicted by Eq. 1 is observed. The kinetics of this early or fast release have been analyzed by subtracting away the contribution due to the later or slow release. The gas release after this subtraction is shown in Fig. 3, again as a least square fit to Eq. 1 at each temperature. Because of the short times and thus smaller number of data points for the fast release and the uncertainties involved with subtracting the slow release, the data are not as good as in Fig. 2. However, reasonable fits to exponential decay of the concentration are again obtained. The concentrations, time constants and appropriate diffusivities for the fast release at each temperature are also given in Table 2. One may observe that the fast release accounts for roughly 0.85 of the total helium release at low temperatures. At this point it is to be emphasized that, although it may appear tempting to consider the second and higher number terms in Eq. 1 as an explanation for the results, the magnitudes of these terms are so small that such an explanation is precluded, i.e., the least squares fit lines in Fig. 2 which include these higher number terms definitely do not fit the early release data. It should also be mentioned tnat the isothermal helium release data were found to fit this two stage exponential decay scheme significantly better than other schemes (i.e., mathematical functions) tested, such as kinetics based upon t^n. Although it may be that the data could be fit to other, considerably more complex, multiple-mechanism models, the two-stage volume diffusion-limited model has been chosen because it fits the experimental results and is physically reasonable.

The temperature dependence of the relaxation times from Eq. 1 for both the fast and slow release reactions are shown on the Arrhenius plot of Fig. 4. At each temperature measured, there is roughly a decade difference in the relaxation times for the two releases. There

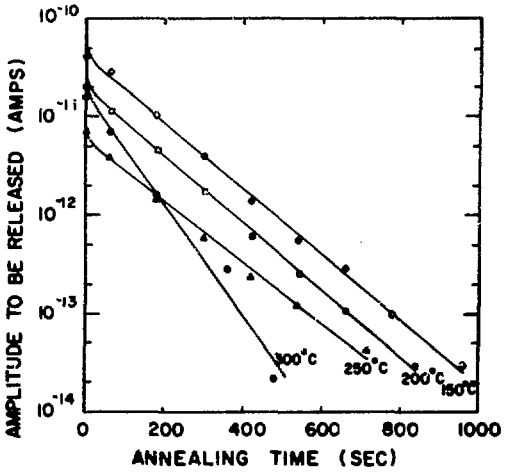

Fig. 3. Semi-logarithmic plot of the low temperature isothermal helium release data after the release shown by the solid line in Fig. 2 has been subtracted. The solid lines are least squares fits to Eq. 1.

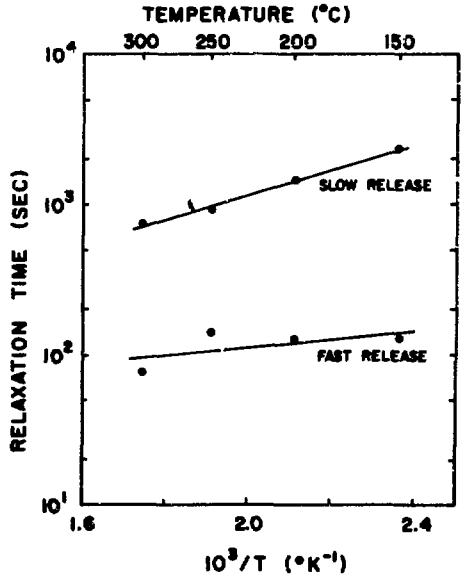

Fig. 4. Arrhenius plot of the relaxation times for both the fast and slow release processes. The parameters obtained from the slopes and intercepts are presented in Table 2.

appears to be less temperature dependence for the faster release, but this probably cannot be stated with certainty because the experimental error is difficult to estimate, especially for the faster release. In Table 2 are reported experimental values of τ_0, D_0, and the apparent activation energies to fit the equation $\tau = \tau_0 \exp(Q/RT)$. In this table the subscripts f and s refer to the fast and the slow release. Also reported are the extrapolated values for the relaxation times at room temperature.

The various annealing treatments were found to cause release of residual tritium from the samples. Since this element is not measured by the mass spectrometer because it is trapped by the titanium sublimation pump, liquid scintillation analyses for tritium were made on various samples before and after annealing. It was found that an isothermal anneal at 300°C for 2000 sec reduced the residual tritium by a factor of six. Also, an isochronal anneal to 1300°C (5 min at 100°C temperature intervals) reduced tritium by a factor of 3.5×10^3. Mass spectrometric analyses for ^{3}He were also made after the above anneals. It was found that the sample which had been given the 300°C anneal (which resulted in helium release) did not show helium release when it was remeasured within an hour after the anneal. This same sample did, however, show a helium release peak, attenuated by roughly a factor of six, after being held several days at room temperature. The sample given the 1300°C anneal, on the other hand, showed no subsequent helium release, corroborating the results of the scintillation counting experiments.

DISCUSSION

Because of the very low or negligible solubility of helium in metals, there is a strong driving force which causes these inert gas atoms which have been introduced to interact with defects which may be present. This interaction may be with point defects, or it may also be a self-interaction in which inert gas atoms aggregate to precipitate and form bubbles. These two kinds of interactions can occur simultaneously and thus be competitive processes. Interestingly, the results of these two processes tend to be quite different. Inert gas atoms

which interact with impurity atoms or point defects can still be mobile and can ultimately outgas by diffusion to free surfaces. On the other hand, the inert gas atoms which form bubbles tend to remain in the metal because, although the small bubbles are mobile and can produce some outgassing, the migrating bubbles tend to coalesce to form larger relatively immobile bubbles. A general pattern for the behavior of helium in various metals has developed from recent studies. At low annealing temperatures, helium atoms interact with point defects to form a complex defect, while at high temperatures they tend to precipitate as bubbles. As previously indicated, these two modes of behavior can both occur at some temperatures. Also, in addition to temperature, the helium concentration can be expected to affect which behavior is dominant. The results of this study will now be discussed in terms of these two kinds of behavior.

High Temperature Release

The release we have found in stainless steel at temperatures above 800°C is believed to be due to bubbles which become mobile in this temperature range. Since bubble mobility decreases with increasing bubble radius, the process of gas release by bubble diffusion to the surface is complicated by the simultaneous process of bubble coalescence in which large relatively immobile bubbles are formed. The kinetics of the combined processes of bubble diffusion to surfaces and coalescence are difficult to analyze quantitatively; however, it is worthwhile to consider the general shape expected for the isochronal annealing curve. The release we observed above 800°C does not appear as a classical release peak, but rather is spread over a wide temperature range up to the melting point. This result is in accord with what one would expect for the bubble migration mechanism of gas release. Because of the large dependence of bubble mobility on the radius and the large width of the distribution of bubble radii,[6] a narrow release peak such as the one at 300°C is not predicted. Instead, the gas release is expected to occur over a wide temperature range up to the melting point where the larger bubbles become mobile. Thus our results are consistent with the

interpretation that diffusion of helium bubbles is the high temperature release mechanism. Also, this interpretation is consistent with results from studies of helium bubble formation in numerous other materials.[7] Obviously this is not an unequivocal interpretation; thus additional studies are suggested to substantiate the mechanism. Unfortunately, although an attempt was made, it was not possible to confirm the presence of bubbles by electron microscopic examination; such a confirmation would be extremely difficult, however, for helium concentrations in the parts per trillion range.

Low Temperature Release

A model for the helium release near 300°C must fit the isothermal annealing results presented in Table 2. In particular, it should be consistent with the result that the release can best be described by the sum of two exponential releases with relaxation times differing by a factor of roughly ten. First, it is useful to consider the kinetics of gas desorption from a surface as an alternative rate-limiting step to that of volume diffusion.

If the helium released is considered to have all originated at the sample surface, it will amount to only about 10^{-4} of a monolayer. Thus, we can consider the possibility that helium originally trapped somehow at a relatively low concentration of surface sites was desorbed during the annealing. It should be mentioned that this is not a likely possibility since there is little reason to believe that chemically inert helium will chemisorb on metal surfaces. The weak Van der Waals bonds would be expected to only produce physical adsorption and then only at pressures well above and temperatures well below those in this experiment.[8] In addition to the above arguments, it can be shown by consideration of the experimental and predicted pre-exponential factors for the time constants that simple surface desorption is not the rate-limiting step for the release. Using the classical model for surface desorption, the rate of release from the surface is $dc/dt = c\,\tau_{surf}^{-1}$ where τ_{surf}^{-1} is the rate constant for the release.[9] Ignoring entropy and geometrical factors which are near unity, this rate constant can be

written as $\tau^{-1}_{surf} = \nu_{surf}(-Q_{surf}/kT)$, where Q_{surf} is the energy of desorption from the surface and ν_{surf}, the vibration rate at the surface, can be estimated to be 10^{12} sec^{-1}. Comparing the desorption energy and pre-exponential factor with the results given in Table 2, we find first that 4,000 cal/mole or less is not an unreasonable value to expect for the desorption energy.[7] Next, comparing the pre-exponential factor for the rate constant, we find a large disagreement, enough to eliminate the surface desorption model. The value $\tau_{0\ surf} = \nu^{-1}_{surf} \cong 10^{-12}$ sec is predicted for surface desorption, while a τ_0 value of roughly 30 sec was determined experimentally. Although we can now reject the simple surface desorption hypothesis for the fast release in the isothermal anneal, the above analysis may not apply to the complex kinetics expected for a two stage process such as we have observed. Thus, it is not ruled out that the surface may have a role in the mechanism for the slow release, although the manner in which a metal surface could trap helium is not known.

The experimental value for τ_0 of roughly 30 sec is large compared to the literature values obtained for volume diffusion of substitutional ($\sim 5 \times 10^{-4}$ sec) and interstitial ($\sim 5 \times 10^{-2}$ sec) solutes.[10] Our data are in better agreement with prior results for interstitial diffusion than for substitutional diffusion. However, the lack of good agreement suggests that either there is not sufficient accuracy in the data for the extrapolation to obtain τ_0 within two orders of magnitude or that the results cannot be interpreted in terms of simple volume diffusion since some other complicating factor such as a trapping effect due to impurities may be present.

Consider now the steady state predicted to exist in samples held at room temperature for long times compared to the relaxation time at this temperature (see Table 2). The rate of production of helium is

$$\frac{dc}{dt} = c_T\lambda \qquad (3)$$

where $\lambda = 1.75 \times 10^{-9}$ sec^{-1} is the radioactive decay constant for tritium, c is the average helium concentration, and c_T is the tritium

concentration. Assuming the surface concentration of helium is zero, the rate of loss of helium by diffusion can be written as

$$\frac{dc}{dt} = - c/\tau \tag{4}$$

Therefore, at steady state we have an average concentration of helium given by

$$c = c_T \lambda \tau. \tag{5}$$

Curves for predicted values of this concentration versus temperature are shown in Fig. 5. They have been calculated using the values from Fig. 4 for the relaxation times for the fast and the slow releases. Also shown in Fig. 5 are the experimental values for the concentration of helium released in the fast and slow stages at each isothermal annealing temperature. Two comparisons between the experimental results and those predicted by Eq. 5 will now be discussed.

First, the gas release predicted for a given temperature should be the difference between the steady state concentration at 30°C and at the appropriate temperature. For the concentrations calculated using the relaxation time for the slow release, the predicted release is nearly independent of temperature for the annealing temperatures investigated; it has a magnitude of 1.0×10^{-10} atom fraction of helium. It may be observed that this value agrees within a factor of two with the release which was observed experimentally at the various temperatures. On the other hand, when the fast release relaxation times are used to calculate the steady state concentration, the predicted release differs by nearly two orders of magnitude from that observed experimentally. From this it appears that the steady state concentration at room temperature is controlled by the slow rather than the fast reaction. It is suggested that a reason for this may be that at room temperature most of the helium does not exist as freely mobile atoms, but instead is trapped, possibly at tritium atoms or as a complex defect with vacant lattice sites.[11,12]

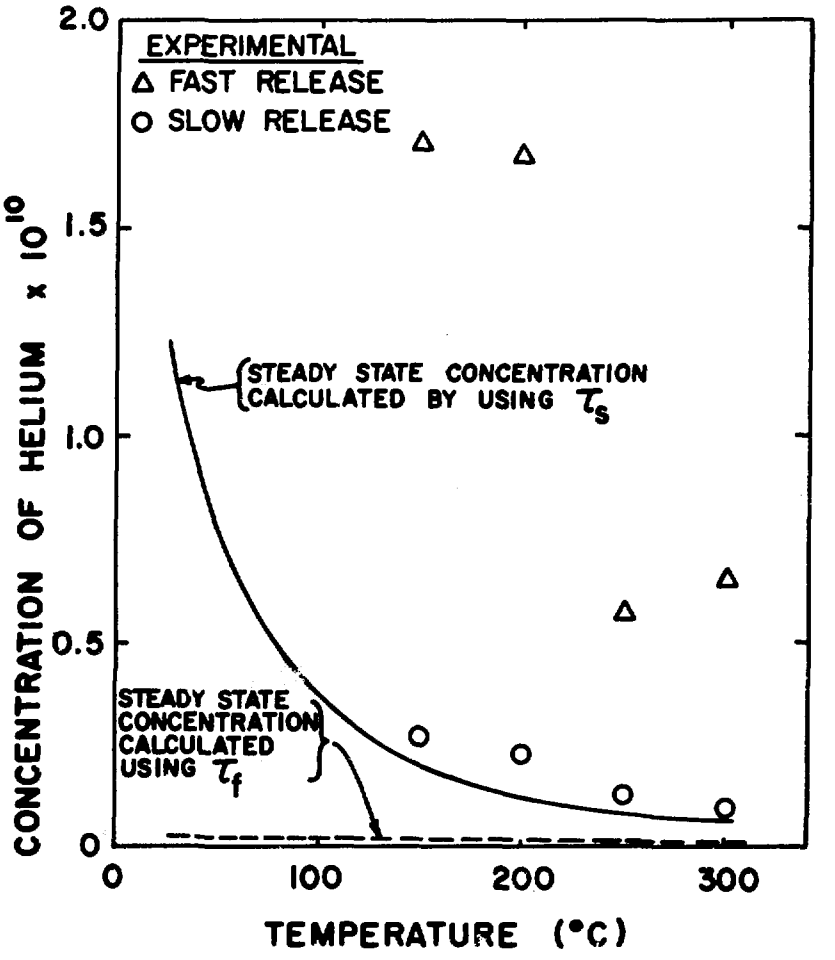

Fig. 5. Concentrations of helium released and calculated to be present at steady state at various temperatures.

Second, it is noted that the amount of helium released at each temperature by the slow reaction (data points with circles in Fig. 5) is the same within experimental error as the steady state concentration calculated using the relaxation time for release by that reaction. This agreement suggests that the slow release reaction actually involves release of the steady state concentration of helium. This would only occur if tritium were also being released. Such a release of tritium is already known to take place since a loss of roughly 0.8 of the tritium was observed for the sample annealed at 300°C. What is interesting in the above discussion is the inference that tritium release is the rate-controlling step for the slow reaction of helium release. This seems to be the most probable, although certainly not the only explanation for the second (slow) stage of helium release. As a part of this explanation there is the requirement that a trapping type of interaction exists between atomic helium and tritium. This does not seem unreasonable. Further studies in which both the tritium and the helium concentrations are monitored will be necessary to properly demonstrate this interaction.

If the slow release stage is governed by diffusion of tritium from the sample, then the fast release stage can be assigned the mechanism of diffusion of atomic helium, or a complex defect involving helium, from the sample. Such an explanation is attractive because of its simplicity, i.e., that roughly 0.85 of the helium will freely diffuse and thus will obey exponential release kinetics and that the remainder is trapped and becomes mobile only when the trapping species can diffuse. From the partitioning of helium indicated above, a binding energy to traps of approximately 11,000 cal/mole (0.48 eV) is calculated at 250°C.

In conclusion we wish to point out that probably the most significant result of this study is the finding that helium degassing occurs by simple exponential decay and thus fits the kinetics predicted for a volume diffusion mechanism. This indicates that the competitive processes of volume diffusion of atomic helium or of a helium complex and of degassing by diffusion of submicroscopic helium bubbles can be studied separately. In our study this has been possible by working at

concentrations low enough so that helium agglomeration and precipitation occurs in a temperature range well above that for volume diffusion. An additional condition which may be important to this experiment and the observation of exponential degassing kinetics is that helium was introduced by a method which is not expected to involve appreciable radiation damage. Future studies with the goal of understanding basic mechanisms for the behavior of helium may for this reason require use of the tritium decay method for the introduction of helium. For such studies, further work will be needed to characterize the interaction between atomic helium and tritium suggested by this investigation.

REFERENCES

1. R. Blackburn, Met. Rev. 11, 163 (1966).
2. M. W. Thompson, Defects and Radiation Damage in Metals, p. 93, Cambridge, London 1969.
3. J. R. Cost and R. G. Hickman, J. Vac. Sci. and Tech. 12 (1975) 516.
4. W. Bauer and W. D. Wilson, Radiation Induced Voids in Metals, p. 230, AEC Symposium Series, vol. 26, edited by J. W. Corbett (U.S.A.E.C. Office of Information Services) 1972.
5. P. G. Shewman, Diffusion in Solids, p. 18, McGraw-Hill, New York, 1963.
6. E. E. Gruber, J. Appl. Phys. 38, 243 (1967).
7. R. Blackburn, Met. Rev. 11, 160 (1966).
8. J. H. de Boer, The Dynamical Character of Adsorption, p. 40, Oxford, London 1968.
9. J. P. Hirth and G. M. Pound, Progress in Materials Science, p. 41, Macmillan, New York, 1963.
10. P. G. Shewman, Diffusion in Solids, p.64 and 111, McGraw-Hill, New York, 1963.
11. C. L. Bisson and W. D. Wilson, Applications of Ion Beams to Metals, p. 423, S. T. Picraux, et al., ed., Plenum Press, New York, 1974.
12. S. T. Picraux and F. L. Vook, Applications of Ion Beams to Metals, p. 407, S. T. Picraux, et al., ed., Plenum Press, New York, 1974.

OBSERVATIONS OF HELIUM BUBBLE FORMATION IN 316 STAINLESS STEEL IMPLANTED BY ALPHA BOMBARDMENT

F. A. Smidt, Jr. A. G. Pieper
Naval Research Laboratory
Washington, D. C.

ABSTRACT

Helium produced by transmutation reactions in the first wall of fusion reactors is expected to affect ductility and swelling. The migration of He during annealing of foil specimens of 316 stainless steel implanted with 20-60 ppm He at <200°C was studied to characterize He behavior under these conditions using transmission electron microscopy to characterize microstructures and the temperature of He bubble formation and bubble migration rates. Bubbles were observed after one-hour anneals at temperatures from 800 to 1100°C (the highest temperature examined) with negligible loss of He from the foils. Strong interactions between He bubbles and dislocations and grain boundaries were apparent. Comparison of the data with published results on neutron data and with theory suggests He migration is accelerated under a radiation flux.

INTRODUCTION

The generation of helium in the first wall of controlled thermonuclear reactors as a result of transmutation reactions arouses concern about its effects on the long-term integrity of the first wall. It has been recognized for some time that the presence of helium degrades the elevated temperature ductility of metals.[1-3] More recently, void formation and swelling of metals have been found to be influenced by the presence of He in metals under conditions where the He pressure would be less than equilibrium.[4] Such problems are of concern in fast reactors where lifetime He concentrations are expected to be of the order of 10 ppm in stainless steel cladding. Generation rates in CTR's are projected to be considerably greater with up to 644 ppm/yr in the Princeton design[5] and 285 ppm in the Wisconsin design[6] so that it is important to understand the effect of He on these phenomena and its behavior in metals.

Knowledge about the diffusion of He in metals is essential to the understanding of both the elevated temperature ductility loss and swelling phenomena during neutron irradiation and in the design of experiments to simulate these effects. At the time these experiments were initiated there were several models for helium mobility described in the literature and it was not apparent which one was applicable to the situation of a metal under irradiation and how to best simulate this situation under accelerated irradiation conditions. Early work on the mobility of helium in metals was associated with studies of fission gas swelling. Transmission electron microscopy (TEM) studies of He in copper[7] showed that bubbles formed at relatively high temperatures and their motion was the dominant process for He transport. A mechanism was proposed in which bubble diffusion took place by a surface diffusion process where metal atoms migrated over the interior surface of the bubble[8] either preferentially in one direction under a driving force or in a random manner in the absence of a temperature or stress gradient. Recent experiments on the behavior of He in copper and gold[9] and aluminum[10] confirmed that He transport by bubble diffusion was occurring. Other recent experiments in which He was injected into specimens by kev energy ion implantation showed re-emission of He at much lower temperatures than those at which bubble formation occurred.[11,12] Migration energies as low as 0.24 ev were deduced from experiments on tungsten suggesting that under some circumstances, He was diffusing by an interstitial mechanism. Other experiments with high He concentrations produced blistering[13] and re-emission of He at rates approaching the incident flux.[14] Thus, a variety of observations related to transport of He in metals had been reported in the literature.

The present experiments were undertaken to determine the behavior of He under conditions where it was implanted

in the interior of the metal at energies up to 70 MeV in a cyclotron at temperatures of less than 200°C and concentrations of 10 to 70 ppm. The samples were then annealed over a range of temperatures in a gradient free furnace, thinned, and examined by TEM to determine the extent of radiation damage and the conditions under which He bubbles form and grow. These experimental conditions are representative of the state of a sample after pre-injection of He in charged particle bombardment experiments to simulate neutron irradiation.

EXPERIMENTAL TECHNIQUES

The present studies of He bubble formation were performed on 316 stainless steel foils rolled to sheet of 62 μm thickness from which 3-mm diameter microscopy specimens were punched. The foils were annealed at 1100°C for one hour in vacuum and cooled rapidly by removing the furnace. Implantation of He was done in the NRL Cyclotron using a 70 MeV alpha particle beam and a beam energy degrader consisting of a series of aluminum foils stacked to various thicknesses and mounted on a remotely positionable water-cooled plate. This variable thickness beam energy degrader controls the depth of a He implant by varying the mean energy of the alpha particles incident on the specimen. Range straggling as a result of this degradation in energy produces a Gaussian shaped depth profile with a full width half maximum of 12 μm in stainless steel. Typical alpha fluxes used during implantation were 4×10^{12} particle/sec/cm^2. A uniform He concentration (±10 percent) was achieved in the center of the specimens by implanting a series of these Gaussian shaped profiles at progressively greater depths as illustrated in Fig. 1. The foil specimens were arranged concentrically around the beam center at a radius of 3.5 mm to specimen center and were bonded to the water-cooled chill block with high conductivity silver paint. This maintained

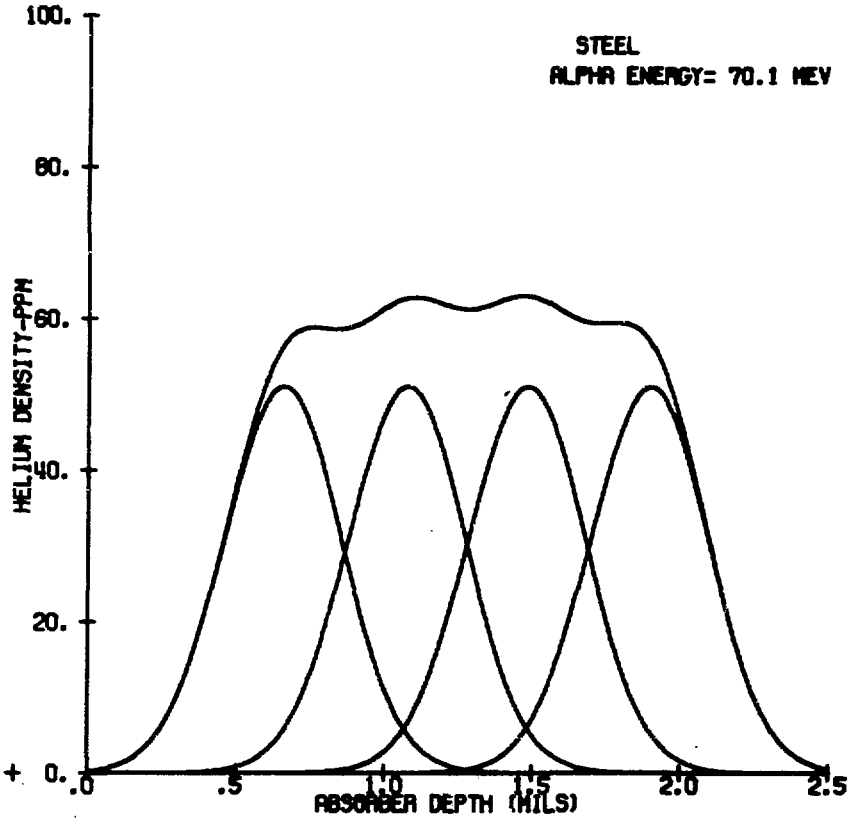

Fig. 1. Helium concentration profile in a .0025-in. foil of 316 stainless steel produced by degrading the energy of a 70 MeV alpha profile beam to sequentially implant four overlapping profiles.

the temperature below 200°C during implantation. He concentrations were calculated from the beam current density and the full width half maximum of the Gaussian depth distribution. Calculated concentrations were verified on selected specimens by a mass spectrometric analysis performed by Atomics International.

Following implantion with He the foils were annealed at the desired temperature in a vacuum furnace having a temperature gradient of less than ±3°C over six inches and with a vacuum of $\leq 10^{-6}$ Torr at temperature. The furnace was arranged so that it could be heated to temperature and then moved into position around the furnace tube to rapidly heat and cool the specimens. Annealing times of one hour at temperature were used in these experiments. The specimens were thinned for TEM using a double jet electropolisher with an electrolyte of 20 ml perchloric acid, 150 ml butyl alcohol, and 250 ml methyl alcohol cooled to -65°C.

TEM examination of the foils was performed with a JEM 200A equipped with a double tilt side entry goniometer stage. All microscopy was performed with the instrument operating at 200 KV. He bubbles were imaged in the weakly diffracting (absorption contrast) condition by the out-of-focus phase contrast technique of Rühle.[15] For overfocus conditions (below the foil), the bubbles appear as a white spot surrounded by a dark ring. Under these imaging conditions the inside of the dark ring should give the true bubble size. Resolution obtainable by this technique has been found to be at least 15Å for He bubbles in a thin section of aluminum, but is probably about 20Å in a thin section of stainless steel. Quantitative measurements of bubble size and size distribution were made with a Zeiss particle size analyzer on positive prints. Foil thickness of the observed areas was determined from stereomeasurements on pairs of photographs taken at tilt angles of 10 to 14 degrees. Accuracy of the thickness

measurements is estimated to be ±20 percent.

EXPERIMENTAL RESULTS

The results obtained from these experiments on He implanted foils include TEM observations of displacement damage and the temperature at which it anneals out, quantitative characterizations of the He bubble populations, observations of the influence of dislocations and grain boundaries on the bubble population and determinations of the He concentration in the foils. The observations will be discussed in the order mentioned above and then the implications of these results will be analyzed in the following section.

Calculations of the displacement damage produced at the end of range by 70 MeV alpha particles in 316 stainless steel have been made from the Mueller-Westmoreland modification of the E-DEP-1 damage code.[16] This code yields a maximum value of the nuclear stopping power, $S_D(x)$, of 9.8×10^{-4} MeV/micron at the peak of the damage-range curve. Displacement damage is then calculated from the formula

$$\text{dpa} = \frac{0.8\ S_D(x)\ \phi t}{2E_d\ N_A} \qquad (1)$$

where

E_d = the displacement energy, 40 ev,

N_A = the atom density,

ϕt = the particle fluence incident on the sample.

The full width half maximum of the $S_D(x)$ curve is 12 microns and drops to values of one-tenth the peak for depths less than the maximum range within the foil. Damage produced in the foil will not be uniform because of the overlapping profiles.but is estimated to be 0.007 dpa at the midplane of the specimen. This is equivalent to a neutron fluence in the high 10^{18} n/cm^2 range.

TEM examination of the as-irradiated specimen showed no visible displacement damage but after a one-hour anneal at 600°C defects showing black-white contrast typical of small dislocation loops were observed as shown in Fig. 2. Another specimen annealed at 700°C for one hour had loops up to 500Å in diameter and is illustrated in Fig. 3. After an 800°C anneal the displacement damage had all annealed out and the first indication of bubbles ~25Å in diameter were found as shown in Fig. 4. These bubbles grew and decreased in density with one-hour anneals at progressively higher temperatures of 900, 1000, and 1100°C, as illustrated in Figs. 5, 6, and 7. A few precipitates began to form at 1100°C. Quantitative microscopy characterizations of the bubble population after various annealing treatments are listed in Table 1. Each set of data represents the average of two or three sets of TEM data weighted by the number of bubbles in the data set.

Table 1. Characterization of Bubble Populations from Quantitative Microscopy

Specimen Number	History	Mean Diameter (Å)	Density (cm^{-3})
SS-4	1 hr - 800°C	~25	$\sim 4.4 \times 10^{14}$
SS-5	1 hr - 900°C	39	1.8×10^{15}
SS-6	1 hr - 900°C	64	2.5×10^{14}
SS-7	1 hr - 1000°C	112	1.1×10^{14}
SS-8	1 hr - 1000°C	86	1.7×10^{14}
SS-9	1 hr - 1100°C	151	5.4×10^{13}

The presence of dislocations in samples can perturb the bubble size distribution and bubble density. This can be noted in Table 1 for samples SS-6 and SS-7 which were inadvertently deformed during removal of the specimens from the chill block following He implantation. Dislocations have many bubbles attached to them and these bubbles tend to be

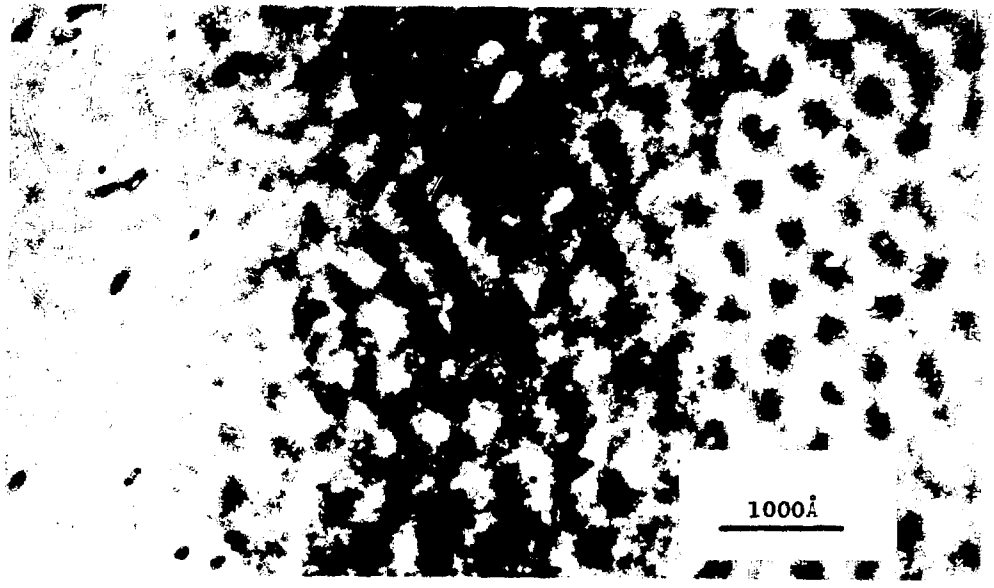

Fig. 2. Transmission electron micrograph of small loops and clusters showing black-white contrast in 316 stainless steel implanted with 40 ppm helium and annealed one hour at 600°C.

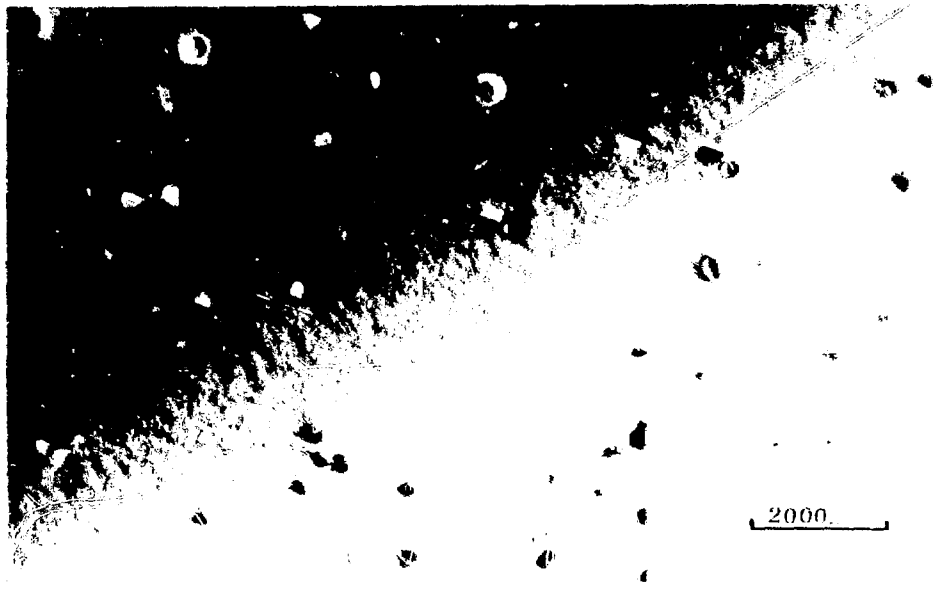

Fig. 3. Transmission electron micrograph of loops in 316 stainless steel implanted with 40 ppm helium and annealed one hour at 700°C.

Fig. 4. Transmission electron micrograph of 316 stainless steel implanted with 40 ppm helium and annealed one hour at 800°C. Note that the loops observed in Fig. 3 have annealed out and numerous small (25Å) bubbles have appeared.

Fig. 5. Transmission electron micrograph of 316 stainless steel implanted with 40 ppm helium after a one-hour anneal at 900°C. Bubbles are clearly visible, are larger than in Fig. 4 and calculations of helium content agree with the concentration implanted.

Fig. 6. Transmission electron micrograph of bubbles in 316 stainless steel implanted with 28 ppm helium and annealed one hour at 1000°C.

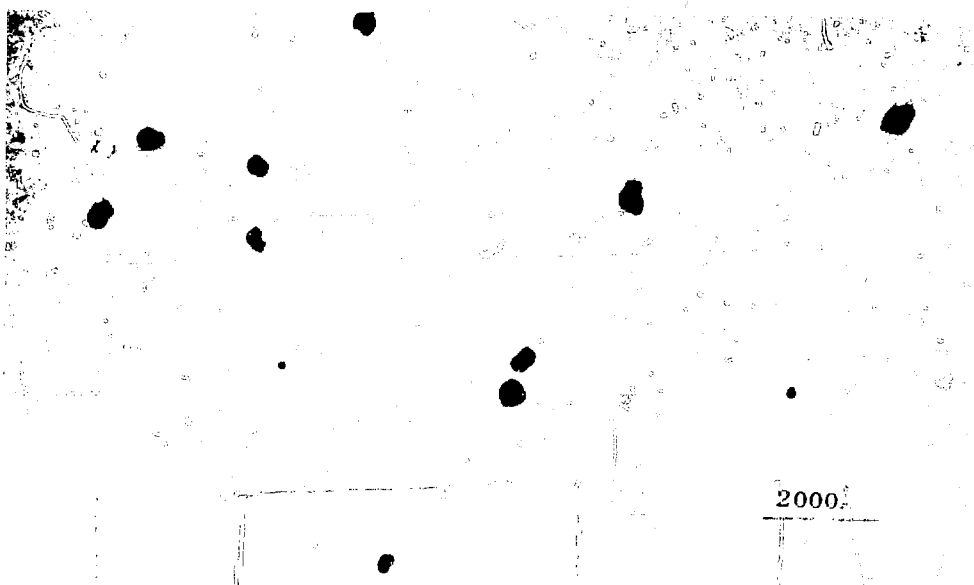

Fig. 7. Transmission electron micrograph of bubbles in 316 stainless steel after one-hour anneal at 1100°C. Note the formation of precipitates under these conditions.

larger than those in the matrix. Nodal points are often the site for He bubbles as in Fig. 8, thus indicating a strong interaction between the dislocations and bubbles. Grain boundaries also have more bubbles than a random section through the matrix. Kramer et al[2] found bubbles in 304 stainless steel implanted with 30 ppm He after a four-hour anneal at 815°C which were 45Å in diameter and bubbles up to 300Å after an eight-hour anneal at 870°C. A recently published study by Mazey and Francis[17] examined the displacement damage produced by 1, 10, 100, and 1000 ppm He implants in 316 stainless steel. Damage was observed after irradiation in the 100 and 1000 ppm specimens and clusters and loops identified as interstitial in character grew on annealing in the 600 to 750°C range. They annealed out above 750°C and bubbles were observed at higher temperatures. Bubble sizes ranged from 45Å at 700°C to 380Å at 1100°F for 100 ppm and 1000 ppm samples. Other observations of bubble formation in stainless steel are qualitatively in agreement with the present results.[18-19]

An independent analysis of the He content of these foils to verify the calculations of implanted He was performed by H. Farrar, IV, using a mass spectrometric technique[20] in which the He^4 content of a small sample is collected by vaporization of the sample and then compared to a known quantity of He^3 injected into the system. Four 3-mm diameter microscopy disks previously implanted with He in overlapping profiles were reduced in thickness by mechanical polishing to remove the surface regions of lower He content and were then cut in half. Samples 1, 2, and 3 were from one implant, while sample 4 was from another run. The results of the analysis are shown in Table 2 and should be compared with the calculated values of implanted He of 61 ±2 ppm, illustrated in Fig. 1.

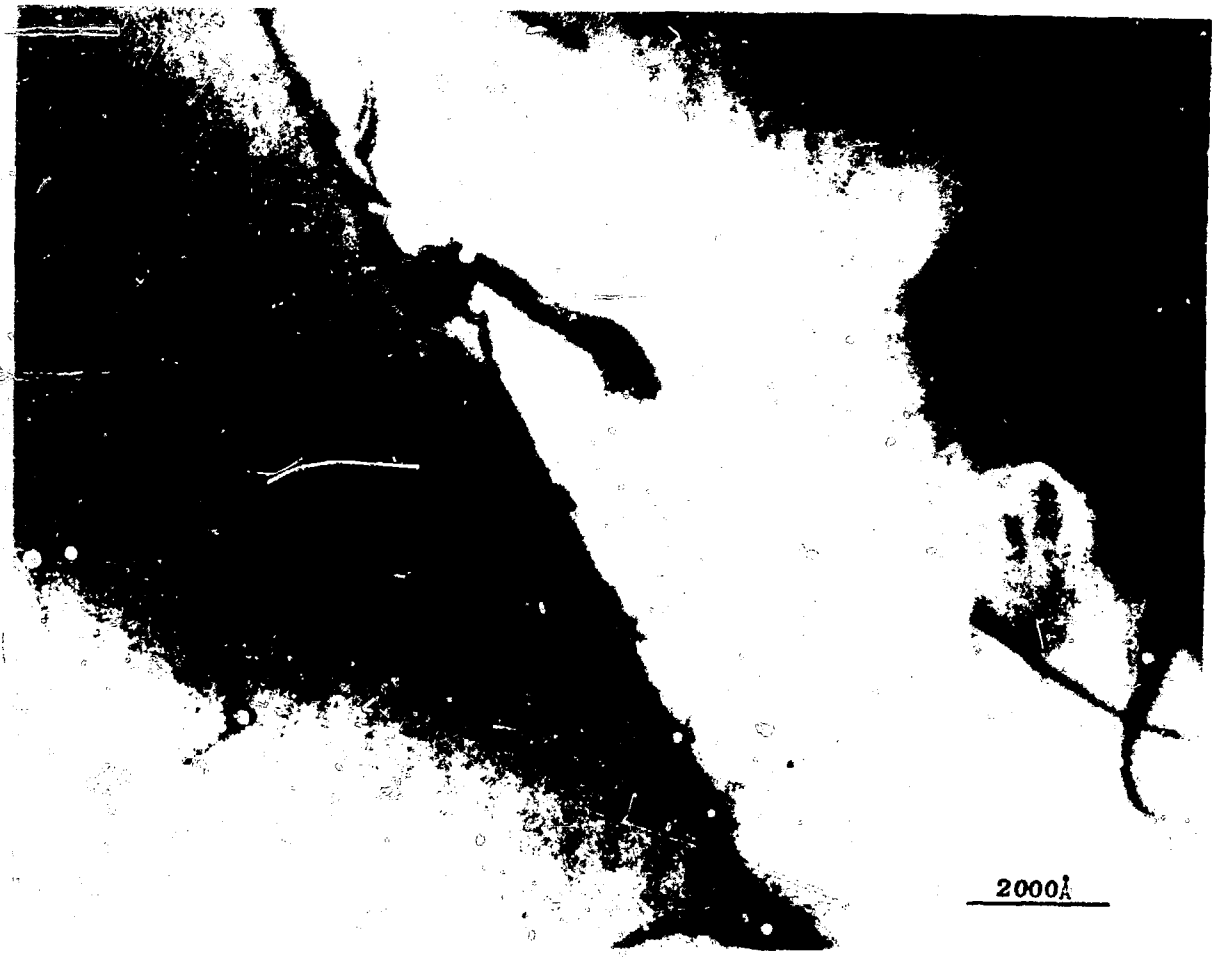

Fig. 8. Transmission electron micrographs of a section of specimen inadvertently deformed and annealed at 900°C for one hour. Note the association of bubbles with dislocations, especially at nodes.

Table 2. Mass Spectrometric Helium Analysis

Sample	Helium Analysis (ppm) ±2.4	Avg.
1A	52.6	61.0
1B	68.4	
2A	68.7	68.9
2B	69.1	
3A	56.6	63.1
3B	71.5	
4A	57.1	57.0
4B	56.9	

Scatter between A and B parts of the samples was traced to a flux gradient across the sample and a slight beam drift off center. Improvement of beam control reduced the scatter to the range shown for sample 4. These analytical results indicate good agreement between calculated implantation concentrations and mass spectrometric analysis when the experimental conditions are carefully controlled during implantation. Analysis of possible variations in implantation conditions during the runs on 316 stainless steel used for microscopy gave outer limits of 20 to 60 ppm with most probable value of 40 ppm for samples SS-4 through 7 and limits of 16 to 40 with most probable value of 28 ppm for samples SS-9 and 9.

ANALYSIS OF EXPERIMENTAL RESULTS

One quantity of considerable interest is the He content of the bubbles. This quantity can be calculated if the internal pressure of He is in equilibrium with the surface tension, $p = \frac{2\gamma}{r}$, and if the surface energy is known. For small bubbles it is also necessary to apply a correction for non-ideal behavior of the gas. The modified Van der Waals

equation of state, P(V-mb) = mkT, is commonly used for this correction, where m is helium concentration, b is the Van der Waals constant, and the other quantities have their usual meaning. Temperature dependent values of b for He with four significant figures are tabulated in reference 21. Surface energies of 1000 ergs/cm^2 are frequently used in void nucleation calculations for stainless steel, but the use of this value leads to calculated He concentrations on the low side. Surface energies measured from creep experiments on 304 stainless steel give surface energies ranging from 2630 ergs/cm^2 at 800°C to 2050 at 1100°C[22] and were used for the calculations in these experiments with good internal consistency between concentration implanted in the foils and calculated values.

The He concentration for each set of micrographs analyzed was calculated from the equation

$$m_i = \frac{2/3\ \pi\ \gamma\ d_i^3}{kT + (4b\ \gamma/d_i)} \qquad (2)$$

for each size class of bubble of diameter, d_i, measured with the particle size analyzer. The total was then summed over all classes. Table 3 gives a comparison between the most probable value implanted and the calculated value from the bubble population.

Table 3. Calculated Helium Concentrations from Transmission Electron Microscopy

Samples	Anneal T (°C)	Implanted Conc. (ppm)	Concentration From Bubbles (ppm)
SS-4	800	40 ±20	2.2
SS-5	900	40 ±20	35
SS-6	900	40 ±20	19
SS-7	1000	40 ±20	28
SS-8	1000	28 ±12	29
SS-9	1100	28 ±12	25

The results calculated from the bubble populations agree reasonably well with the estimates of implanted He except for SS-4 where the bubbles were very small in size and quite obviously all the He had not collected into bubbles in the visible size range. Above 800°C it appears that the amount of He in the bubble population is not changing so that all the He is in visible bubbles after one-hour anneals at 900°C or higher, and it is not lost from the foil at anneals up to 1100°C.

The next question of interest is the process by which the bubbles grow. Effective migration energies for He can be calculated for a simple model which assumes the He in the bubbles comes from a spherical volume of metal uniformly implanted with He. The radius of this volume is then taken as the distance a He atom must move by random walk migration to reach the bubble,

$$\overline{R} = \sqrt{n}\,\alpha = \sqrt{\Gamma t}\,\alpha, \qquad (3)$$

where

n = the number of jumps,

α = the jump distance,

Γ = the jump frequency,

t = the annealing time.

This equation can then be solved for the activation energy, Q, since

$$\Gamma = \frac{\overline{R}^2}{\alpha^2 t} = \nu_D \exp(-Q/kT), \qquad (4)$$

where ν_D is the Debye frequency. The calculation was made for sample SS-5 assuming 35 ppm He concentration and yielded a value of 2.8 ev, for the effective migration energy of a He atom to reach the bubble. This is close to the self-diffusion energy for nickel (2.8 to 2.9 ev) and is therefore consistent with the motion of He as a substitutional atom to form bubbles. It is important to note that if He were moving

as an interstitial atom, a migration energy of about 1.0 ev or less would be expected.

After all the helium implanted in the foils has precipitated out in bubbles, other mechanisms of bubble growth must be considered. The two leading models are growth by collision and coalescence during random walk bubble migration and Ostwald ripening. The random walk migration of bubbles over distance $\bar{R}$ can be described in terms of a bubble diffusion coefficient D_B, $\bar{R}^2 = 6\, D_B t$. Motion of the bubble can be controlled by either vapor transport of material across the bubble, transport by diffusion through the lattice or motion of atoms on the surface of the bubble. Surface diffusivity is generally considered to be the controlling process in the temperature range investigated in these experiments. Gruber[23] has shown the surface diffusivity to be related to the bubble diffusivity by the equation,

$$D_s = \frac{1}{.301}\left(\frac{r}{a_o}\right)^4 D_B. \qquad (5)$$

He has further characterized the bubble size distribution which evolves from collision and coalescence of the bubbles at equilibrium with an internal pressure of an ideal gas. The mean radius of this distribution is related to the surface diffusivity by the equation

$$D_s = \frac{\gamma}{nkT(a_o)^4\, t}\left[\frac{\bar{r}}{1.30}\right]^5, \qquad (6)$$

where

n = the helium content in atoms/cm^3,

a_o = the lattice parameter,

$\bar{r}$ = the mean radius of the bubble population,

and the other parameters have their usual meaning. D_s values for the various bubble populations characterized in these experiments have been calculated and plotted as Arrhenius

equations in Fig. 9 to examine the consistency of the data. The results will be discussed further below.

The other process of bubble growth, Ostwald ripening, is a consequence of the difference in solubility of He in equilibrium with large bubbles and small bubbles so that large bubbles grow at the expense of small ones. The rate controlling process is diffusion of He through the lattice. Markworth[24] has analyzed the evolution of the bubble size distribution for this process and derived equations relating the volume diffusivity to the mean radius of the bubble population,

$$D_v K = \frac{4(\bar{r})^2}{3kT\ t} \ , \qquad (7)$$

where

K = the Sieverts' law coefficient,

$C_r = KP_r$, relating the concentration of gas in equilibrium with a bubble with internal pressure, P, for radius, r.

K was included as part of the argument because it was unknown but as a constant would still permit testing the applicability of the model. Results from these experiments are plotted in Fig. 10.

The 316 stainless steel results show scatter at 900 and 1000°C which is believed to be a consequence of the increased growth rate of bubbles near dislocations. When the high values are discarded for these temperatures, a good fit to a straight line is obtained for the bubble diffusion model with an activation energy of 4.2 ev derived from the slope. The fit of the data to the Ostwald ripening model gave a 1.8 ev activation energy. These results can be compared with a previous analysis of bubble growth in vanadium and aluminum.[25] A rule of thumb for migration energies for surface diffusion above 0.75 T_m is $Q_m = 30\ T_m$ cal/mole,[26] where

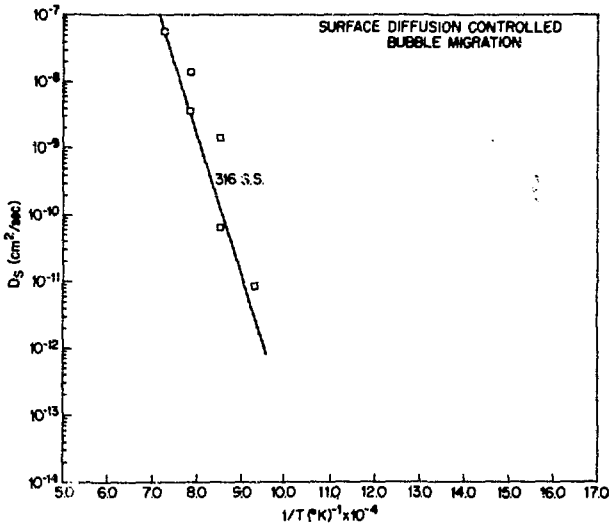

Fig. 9. A plot of surface diffusivity, D_s vs 1/T, D_S values were calculated from Gruber's equation relating bubble size for various annealing times, temperatures, and helium concentrations with surface diffusivity. A linear relationship indicates a fit to the model and the slope yields a value for surface migration energy. The two high points at 900 and 1000°C are attributed to the effect of dislocations. The slope of the line yields a value of 4.2 ev.

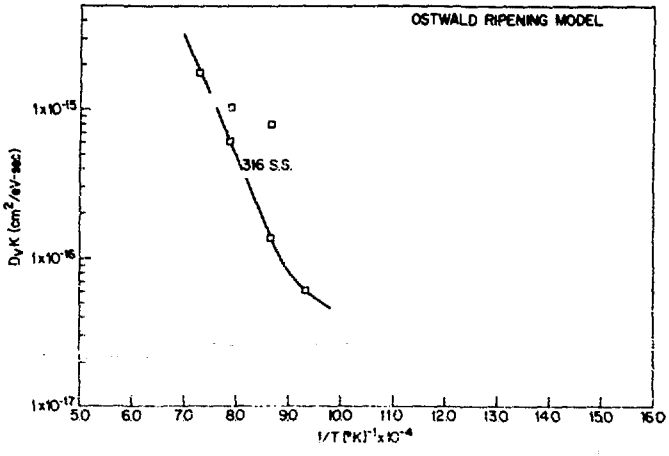

Fig. 10. A plot of D_vK vs 1/T to test the Ostwald ripening model of bubble growth as related to the mean size of the bubble population by Markworth. A linear relation is expected for agreement with this model and the slope of the line gives the activation energy for volume diffusion. The straight line [illegible]

T_m is the absolute melting temperature. A comparison of predicted surface migration energies with values measured from slopes of D_s vs T plots gives 2.8 ev vs 2.4 for vanadium, 1.2 vs 2.1 for aluminum, and 2.2 vs 4.2 for stainless steel. Measurements on gamma iron also gave a value of 2.2 ev.[27] These values are for surface self-diffusion in pure materials and it is possible that impurity effects might modify the results or that a ledge nucleation model might control.[10] The activation energy obtained from the slope of the Ostwald ripening plot for stainless steel yielded a value of 1.8 ev which is less than the self-diffusion energy in nickel (2.9 ev). Another possibility for volume diffusion of He would be as an interstitial for which values ranging from 0.68 ev for nickel to 1.74 ev for palladium have been calculated.[28] If He resides in a substitutional position as a consequence of combining with a vacancy, the rate limiting step for diffusion might be "pop-out" from the substitutional position with activation energies of 3.16 ev in nickel and 1.88 ev in copper.[28] Another mode of diffusion recently suggested on the basis of computer models is a mutual diffusion process in which the He jumps out of a vacancy (substitutional He) into an interstitial position; a lattice atom jumps into the vacant site, and the He jumps back into the new vacancy. The rate limiting step is the first one, where the He jumps into an interstitial position, and for copper has an energy of 2.15 ev.[29] No calculations for this mechanism were found for nickel.

The observations on He bubble formation in the present experiments agree reasonably well with a study of thermal release of He from nickel, 316 stainless steel, and PE-16.[30] Stages attributed to annealing radiation damage, atomic diffusion of He, and bubble migration were observed at 300, 500, and 800°C respectively. In nickel all the He was trapped in bubbles after a 600°C anneal. Only 10% of the He had been released at 800°C in nickel and only 1% in stainless steel was released at 800°C. A migration energy of 2.5 ev was

deduced for migration of He in nickel and a value of 2.3 ev was deduced for stainless steel using a model for trapping during diffusion. Other work on thermal release spectra from low energy alpha implants in 304L stainless steel[31] showed peaks at 411°C and 760°C and activation energies of 1.91 and 2.91 ev were deduced using a different model.

The data available on the behavior of He in stainless steel then can be summarized by saying that during annealing of foils implanted with 0.1 to 100 ppm He, the dominant process is the formation of He bubbles. Although atomic migration of He occurs over distances where the mean free path is less than the separation of bubble nuclei, it is not a long range transport mechanism. Migration energies deduced from thermal release experiments and bubble formation experiments are in the range from 2.0 to 2.8 ev suggesting a substitutional or a mutual diffusion mechanism rather than diffusion as an interstitial He atom. Bubble growth usually results from surface diffusion controlled bubble migration, collision, and coalescence although the current data on 316 stainless steel would require unusually high surface diffusion energies to fit the model possibly due to impurity effects.

DISCUSSION

The experiments described in this paper were intended to investigate the formation of bubbles in He implanted stainless steel to provide base line data about the behavior of He in a specimen implanted at low temperatures and annealed at progressively higher temperatures. We now compare our results to neutron irradiation results and current theories to see if further insight can be gained about the behavior of He under irradiation.

One phenomenon known to be associated with the presence of He is a loss of ductility at elevated temperatures when He collects at grain boundaries and promotes intergranular failure. Kramer et al.[2,32]

ductility above 540°C which became a serious decrease above 650°C in tensile tests of 304 and 316 stainless steels implanted with 30 to 40 ppm He. Bloom and Weir[33] have reviewed data on ductility trends in 304 and 316 stainless steel irradiated to fluences in the low 10^{22} n/cm^2 range and found drastic reductions in tensile ductility at 750°C and above due to He embrittlement with synergistic effects from radiation hardening and He between 450 and 750°C. He transport to grain boundaries to produce He embrittlement requires relatively long range transport such as by sweeping of bubbles. Irradiation does not appear to drastically modify the temperature at which embrittlement occurs so bubble transport by dislocations still appears to be the controlling mechanism.

The other phenomenon for which He transport is important is void nucleation. While the initial experiments with ion damage showed no void nucleation without pre-injection of He^4, subsequent work has shown He is not essential for void nucleation in all cases. If present, He can obviously stabilize a void nucleus because of the internal pressure. Two experiments have been performed in which 304 stainless steel was implanted with He and then neutron irradiated in the void nucleation regime and compared with control samples without He pre-injection. Bloom and Stiegler[34] implanted 20 ppm He in 304 stainless steel and irradiated to a fluence of 7.4×10^{21} n/cm^2 at 390°C. They found the He implanted material had more bubbles of smaller size but less swelling (from visible voids anyway), than control material irradiated under the same conditions. Harkness, Kestel and McDonald[35] performed a similar experiment with 0.1 and 100 ppm He at a fluence of 1×10^{21} n/cm^2 at 450°C. They found heat treatments following implantation that removed the dislocation loops and clusters was more important than He content, at least at this low fluence. Apparently the clusters serve as sinks to delay void nucleation to higher fluences or else many voids below the visible range are nucleated because no

voids formed in specimens not annealed to remove displacement damage prior to neutron irradiation. However, among the samples annealed to remove damage the He implanted samples had greater swelling than the control with no He.

A few simple calculations suggest that irradiation must enhance the diffusivity if a uniform distribution of He is to be redistributed during irradiation into 10^{15} voids at temperatures of 300 to 400°C during a 2000-hr irradiation. Separation between He atoms in a uniform distribution would be 500Å with 0.1 ppm He and 50Å for 100 ppm He. Calculations of the random walk movement of a He atom with 2.5 ev activation energy indicates it would move less than 1Å at 300°C and about 10Å at 400°C. At He concentrations of 0.1 ppm uniformly distributed, 1 He atom would reside in each of 8×10^{15} voids. For 100 ppm, however, 1000 He atoms would reside in each void and the mobilities estimated above are too low to permit this to take place. It seems reasonable then to look for a mechanism by which irradiation can convert He to an interstitial or some other highly mobile configuration. Nelson, Hudson and Mazey[36] report an experiment on 321 stainless steel where the implantation of 100 ppm Ar as well as 10 ppm He prior to ion bombardment suppressed the formation of visible voids. It was postulated that the Ar, which could only move substitutionally, nucleated voids on too fine a scale ($\sim 10^{18}$ cm^{-3}) to be visible in the electron microscope.

Since the time this work on He behavior in metals was initiated, several important theoretical papers have examined the role of He in void nucleation. The two major works by Russell and Hall[37] and by Wiedersich, Burton and Katz[38] have independently solved the problem of nucleation of voids in the presence of He by numerical solution of the kinetic equations of void growth and shrinkage due to vacancy capture and emission, He capture and emission and interstitial capture.

He influences void nucleation by decreasing the rate of vacancy emission and by stabilizing small voids which would otherwise dissolve. Both treatments conclude that He mobility is an important variable and require the arrival rate ratios to be in the range $0.1 < \beta_{He}/\beta_v < 1.0$ to effectively influence nucleation.

We have evaluated this expression for representative substitutional and interstitial migration energies for stainless steel.[39] For substitutional diffusion of He enhanced by radiation induced vacancies, we find,

$$\frac{\beta_{He}}{\beta_v} = \frac{C_{He}\, D_{He}}{C_v\, D_v} = \frac{C_{He}\, C_v\, D_o \exp -\left[(E_m - E_b)/kT\right]}{C_v\, D_o \exp\,(-E_m/kT)} \qquad (8)$$

$$\approx C_{He} \exp\,(E_b/kT),$$

assuming D_o is approximately the same for vacancies and He atoms. Evaluation of this expression for 10 ppm He in the swelling temperature range of 800 to 1100°K for a binding energy of 0.3 ev, gives ratios of the order of 10^{-4} to 10^{-3}. This would indicate that substitutional He would behave essentially the same as immobile He. Diffusion of He by an interstitial mechanism gives,

$$\frac{\beta_{He}}{\beta_v} = \frac{C_{He}\, D_{He}}{C_v\, D_v} = \frac{C_{He}\, D_o \exp\,(-E_m^{He}/kT)}{C_v\, D_o \exp\,(-E_m^{v}/kT)} \qquad (9)$$

The arrival rate ratio would be at least 0.1 for typical conditions of 10 ppm He (all in solution), $C_v = 10^{-6}$, $E_m^v = 1.4$ ev, and 875°K if the migration energy for He were 1.2 ev, or less. It is again concluded that interstitial migration of He is required to enhance nucleation in these theories. The next question then becomes what is the dynamic concentration of He in interstitial positions in equilibrium with the more stable substitutional He.

Wiedersich et al[39] treated this situation for the case

of He trapped at vacancies (substitutional He) and dislocations which were then converted to mobile interstitial He by displacement cascades, thermal detrapping, and interstitial pop-out (the annihilation of the vacancy of a He-v complex).[28] They conclude that for irradiation conditions of interest

$$C_{He}^{free} \approx \frac{C_{He}^{2}}{(D + C_{He})} \qquad (10)$$

where D is the total concentration of trap sites. Their calculations show that under reactor irradiation conditions He can have a major influence on void nucleation rate at concentrations as low as 10^{-10} atom fraction. The influence of He is less potent for simulation experiments performed at higher displacement rates and achieving higher vacancy supersaturations. Similarly, He would be more effective in enhancing nucleation at the high temperature end of the swelling range. As Russell[40] has pointed out, however, sensitivity to as little as 10^{-10} atom fraction of He could apply only at the very earliest times of nucleation since there would be fewer He atoms present than the 10^{15} voids/cm^3 commonly found in neutron irradiated material. Russell suggests a concentration of 10^{-6} is more probable for effective nucleation enhancement. It should also be noted that the Wiedersich et al calculations use a migration energy of 0.08 ev for interstitial He in nickel which was the lowest value obtained for any of the fcc metals (palladium had a value of 1.74 ev)[28] and therefore may overestimate the effectiveness of He for other materials. The conclusion remains, however, that He appears to be more mobile under irradiation than observed in annealing experiments in the absence of radiation.

A final question which should be addressed is the proper way to introduce He in simulation experiments. The easiest method is to do the He implant first at low temperatures and then bombard the specimens at the selected higher

temperature to produce the displacement damage. Simultaneous implantation of He at the same ratio of transmutation rate to displacement rate as produced in reactor has appeal because it duplicates an obvious experimental condition. As noted above, however, this does not guarantee duplication of reactor conditions because the high vacancy supersaturation in simulation may produce homogeneous nucleation rather than He enhanced nucleation. The critical portion of an irradiation as far as He is concerned would be the threshold where the He concentration first influences the nucleation to the point where nucleation is cut off because the voids are acting as sinks to reduce the vacancy supersaturation. In a neutron irradiation, He is produced in stainless steel at the rate of about 0.1 ppm/dpa and nucleation is complete by ~10 dpa (annealed material). In a simulation experiment at 10^{-1} dpa/sec the most critical period would be from 10 to 100 seconds and He concentrations of 0.1 to 1 ppm. During this time period simultaneous bombardment would appear to be advantageous but otherwise would have little advantage. One problem with pre-bombardment implantation that should be avoided is annealing at temperatures and times where He bubbles can form which are larger than the size that can be resolutioned in a displacement cascade. Large bubbles either become the void nuclei or serve as point defect sinks and reduce nucleation. Reference 41 provides an example of the latter.

Experimental results on simultaneous implantation and bombardment have been obtained by Brimhall[42] who compared the void microstructures in molybdenum produced by bombardment with 5 MeV nickel under conditions of: (a) no He implant, (b) implantation of 10 and 150 ppm He prior to bombardment, and (c) simultaneous implantation of He at the rate of 2 ppm He/dpa. A comparison of the microstructure after 6 and 53 dpa showed the no He and simultaneous implant conditions to have essentially identical void size densities

and overall swelling. The samples with pre-injected He had 10 to 30% smaller voids, a higher density, and less swelling than the other conditions. These observations are consistent with the preceding discussion.

CONCLUSIONS

The following conclusions can be drawn from this study of He bubble formation and growth in 316 stainless steel and comparison of the results with published results on neutron irradiated material.

1. Dislocation loops and clustered defects produced by the alpha particle bombardment anneal out below 800°C.

2. He bubbles in dislocation free regions reach visible sizes (25Å) after a one-hour anneal at 800°C for foils containing 40 ppm He.

3. Bubble growth appears to follow a bubble diffusion model with surface diffusion controlled growth although with unusually high surface diffusion energies.

4. He has a very low solubility in the lattice and the "trapping" of He in bubbles keeps long range He transport very low.

5. Comparison of the current results with irradiation results and with theory indicates He must be converted to a more mobile species than observed in the present experiments. Current knowledge suggests He atoms reside in substitutional lattice positions after combining with vacancies. These substitutional He atoms can be converted to more mobile interstitial He by displacement cascades or encounters with self-interstitials produced by the radiation.

6. It is concluded that in simulation experiments the critical period during which the rate of He introduction can influence void nucleation is between a threshold concentration (estimated to be ~0.1 ppm) and the time when

void nucleation ceases. If temperature and dose rate conditions are such that this critical time period is short then pre-bombardment implantation will produce the same results as simultaneous implantation and bombardment.

ACKNOWLEDGMENTS

Financial support for this work was provided by the Office of Naval Research as part of the Cooperative Radiation Effects Simulation (CORES) Program at NRL. The authors wish to thank L. E. Steele and E. A. Wolicki, coordinators of the CORES program, for support and encouragement.

REFERENCES

1. R. S. Barnes, Nature 206, 1307 (1965).

2. D. Kramer, H. R. Brager, C. G. Rhodes, and H. G. Pard, J. Nucl. Matl. 25, 121 (1968).

3. G. H. Broomfield, D. R. Harries, and A. C. Roberts, J. Iron and Steel Inst. 203, 502 (1965).

4. R. S. Nelson and D. J. Mazey, "Void Formation in Stainless Steel During Charged-Particle Irradiation at Elevated Temperatures," in Radiation Damage in Reactor Materials, Vol. II, International Atomic Energy Agency, Vienna, Austria, 157 (1969).

5. R. G. Mills, A Fusion Power Plant, MATT-1050, p. 292 (August 1974).

6. G. L. Kulcinski, R. G. Brown, R. G. Lott, and P. A. Sanger, Nucl. Tech. 22, 20 (1974).

7. R. S. Barnes and D. J. Mazey, Proc. Roy. Soc. (London) 275, 47 (1963).

8. G. W. Greenwood, M. V. Speight, J. Nucl. Matl. 10, 140 (1963).

9. J. E. Willertz and P. G. Shewmon, Met. Trans. 1, 2217 (1970).

10. K. Y. Chen and J. R. Cost, J. Nucl. Matl. 52, 59 (1974).

11. W. Bauer and W. D. Wilson, "Helium Migration in Metals" in Radiation-Induced Voids in Metals (J. W. Corbett and

L. C. Iannniello, Eds.), U.S. Atomic Energy Commission Symposium Series 26, p. 230 (April 1972).

12. E. V. Kornelsen, Radiation Effects 13, 227 (1972).

13. M. Kaminsky and S. K. Das, Appl. Phy. Lett. 21, 443 (1972).

14. W. Bauer and D. Morse, J. Nucl. Matl. 42, 96 (1972).

15. M. R. Rühle, "Transmission Electron Microscopy of Radiation Induced Defects," in Radiation-Induced Voids in Metals (J. W. Corbett and L. C. Iannniello, Eds.,), U. S. Atomic Energy Commission Symposium Series 26, p. 255 (April 1972).

16. G. P. Mueller and J. E. Westmoreland, "Extension of the Energy Deposition Code E-DEP-1 to Higher Energies," NRL Memorandum Report (to be published, 1975), Naval Research Laboratory, Washington, D. C.

17. D. J. Mazey and S. Francis, "Observations of Dislocation Structure and Cavities Formed by Annealing in Type 316 Steel after Ion Irradiation at Ambient Temperature," AERE-R 7934, Consultant Symposium on the Physics of Irradiation Produced Voids (Ed.,R. S. Nelson), p. 257, (1974).

18. G. K. Walker, J. Nucl. Matl. 37, 171 (1970).

19. A. F. Rowcliffe, J. Nucl. Matl. 18, 60 (1966).

20. H. Farrar IV, private communication, 1973.

21. N. V. Tsederberg, V. N. Popov, and N. A. Morozova, Thermodynamics and Thermophysical Properties of Helium, Translation TT 70-50096, NTIS, Springfield, Va., 1971.

22. L. E. Murr, G. I. Wong, and R. J. Horylev, Acta Met. 21, 595 (1973).

23. E. E. Gruber, J. Appl. Phys. 38, 243 (1967).

24. A. J. Markworth, Met. Trans. 4, 2651 (1973).

25. F. A. Smidt, Jr. and A. G. Pieper, "Helium Mobility and Bubble Formation in 316 Stainless Steel, Aluminum and Vanadium," ASTM STP 570, Properties of Reactor Structural Alloys After Neutron or Particle Irradiation (1975), in press.

26. N. A. Gjostein, "Short Circuit Diffusion," in Diffusion, American Society for Metals, Metals Park, Ohio, p. 241 (1973).

27. J. M. Blakely and H. Mykura, Acta Met. 11, 399 (1963).

28. N. D. Wilson and R. A. Johnson, "Rare Gases in Metals" in Interatomic Potentials and Simulation of Lattice Defects (Eds., P. G. Gehlen, J. R. Beeler, and R. I. Jaffee), Plenum Press, New York, p. 375 (1972).

29. N. D. Wilson and C. L. Bisson, Radiation Effects 19, 53 (1973).

30. D. S. Whitmell and R. S. Nelson, Radiation Effects 14, 249 (1972).

31. R. O. Rantanen and E. E. Donaldson, Radiation Effects 23, 37 (1974).

32. D. Kramer, K. R. Garr, C. G. Rhodes, and A. G. Pard, J. Iron and Steel Inst. 27, 1141 (1969).

33. E. E. Bloom and J. R. Weir, Jr., Nuclear Tech. 16, 45 (1972).

34. E. E. Bloom and J. O. Stiegler, J. Nucl. Matl. 36, 331 (1970).

35. S. D. Harkness, B. J. Kestel, and S. G. McDonald, J. Nucl. Matl. 46, 159 (1973).

36. R. S. Nelson, J. A. Hudson and D. J. Mazey, "Some Observations of Void Swelling Produced During 20 MeV C++ and 46.5 MeV Ni^{6+} Ion Irradiation," AERE-R 7934, Consultants Symposium on the Physics of Irradiation Produced Voids (Ed., R. S. Nelson), 119 (1975).

37. K. C. Russell and D. H. Hall, "The Effects of Impurity Atoms on Void Nucleation" in Defects and Defect Clusters in BCC Metals and Their Alloys (Ed., R. J. Arsenault), National Bureau of Standards, Gaithersburg, Md., 545 (1973).

38. H. Wiedersich, J. J. Burton and J. L. Katz, J. Nucl. Matl. 51, 287 (1974).

39. F. A. Smidt, Jr. and A. G. Pieper, Cooperative Radiation Effects Simulation Program, Semiannual Progress Report for the period 1 May 1973-31 October 1973, NRL Memorandum Report 2755, Naval Research Laboratory, Washington, D.C., pp. 57-71 (Feb. 1974).

40. K. C. Russell, "The Effects of Gas on Void Nucleation," AERE-R 7934, Consultants Symposium on the Physics of Irradiation Produced Voids (Ed.. R. S. Nelson), 158 (Jan. 1975).

41. A. T. Santhanam, A. Taylor, and S. D. Harkness, "Charged-Particle Simulation Studies of Vanadium and Vanadium Alloys," in Defects and Defect Clusters in BCC Metals and Their Alloys (Ed., R. J. Arsenault). National Bureau of Standards, Gaithersburg, Md.. 302 (1973).

32. J. L. Brimhall, "Simultaneous Bombardment of Molybdenum with Ni and He Ions," AERE-R 7934, Consultants Symposium on the Physics of Irradiation Produced Voids (Ed.. R. S. Nelson), 197 (Jan. 1975).

HELIUM GENERATION IN COPPER BY 14.8-MeV NEUTRONS*

J. B. Holt
D. W. Hosmer
R. A. Van Konynenburg
University of California, Lawrence Livermore Laboratory
Livermore, California 94550

ABSTRACT

High purity copper foils were irradiated with 14.8-MeV neutrons from the rotating target neutron source facility at LLL. The average energy of the neutrons was 14.75 ± 0.1 MeV, and the average fluence was 7.0×10^{16} n/cm^2. After irradiation each foil was heated to the melting point and the released helium was measured by a mass spectrometer of special design. Isochronal heating was carried out on several samples to establish the type and temperature of maximum release. Calculated cross sections from the literature for the (n,α) and $(n,n'\alpha)$ nuclear reactions were used, and the predicted amount of helium was consistently about 0.5 of that actually measured. Because there is very little data on helium generation in metals irradiated with high energy neutrons, these results are important and will be related to potential CTR materials.

---

*This work was performed under the auspices of the U.S. Energy Research & Development Administration, under contract No. W-7405-Eng-48.

INTRODUCTION

Because helium atoms are not very soluble in metals and alloys, they tend to form bubbles as the temperature increases. These bubbles play an important role in such destructive processes as void-swelling and embrittlement of materials subjected to neutron irradiation. Numerous studies[1] have dealt with the diffusion of helium as a function of temperature. However, the effect of void-swelling, embrittlement, and related phenomena cannot be completely understood until the amount of helium produced for a known neutron fluence can be predicted.

Recent information[2] about helium production at the low neutron energies (1 to 3 MeV) characteristic of fission reactors emphasizes the need for the same data at higher energies. Unfortunately, very little data is available on helium generation in material exposed to 14.8-MeV neutron bombardment. There are indications that helium generation in certain metals during this high energy bombardment can be 1000 times greater than that observed in fission irradiation.

The atomic fraction of helium produced during neutron damage is related to neutron energy through the total cross section of the various nuclear reactions according to the relation

$$^{He}_{(\text{at. fraction})} = \sigma_T \Phi \ ,$$

where Φ is the neutron fluence (n/cm^2) and σ_T is the sum of all cross sections of neutron reactions that generate helium, such as (n,α) and $(n,n'\alpha)$, times their respective isotopic fraction. For a given fluence, the helium content is proportional to the total cross section σ_T. By measuring the helium content and the neutron fluence, the total cross section can be calculated and compared with values measured by activation techniques or computed from theoretical data. In some metals the helium content can be precisely determined by counting those radioactive species produced along with the helium. This method is not applicable when nuclear reactions produce only stable isotopes.

In such cases, direct mass spectrometric measurements of the amount of helium resulting from 14-MeV neutron bombardment would be useful. Copper, because of its well-characterized physical properties, was chosen for this preliminary study in which we developed equipment and procedures. Subsequent to this study, helium generation in refractory metals such as niobium, vanadium and molybdenum are planned.

EXPERIMENTAL METHODS

Disks, 12.7 mm in diameter and 0.05 mm thick, were cut from Marz grade copper foils. These samples were carefully cleaned with methyl alcohol before loading into the target holder of the rotating target neutron source (RTNS) at LLL. The irradiation procedure and beam characteristics are reported elsewhere.[3] After irradiation, the samples were gamma-ray counted to determine the amount of ^{60}Co produced from the ^{63}Cu $(n,\alpha)^{60}Co$ reaction. The amount of helium was measured by heating each disk to the melting point in a specially designed mass spectrometer.[4] This low-resolution, high-sensitivity mass spectrometer can reach pressures lower than 0.13 μPa (10^{-9} Torr) and detect as few as 10^{10} atoms of helium. To maximize the amount of information gained from this study, either an isochronal or an isothermal mode of heating was used prior to the final melting of the sample. The samples were held at the melting point for a period of time (~15 min) sufficient to release all the helium. Several unirradiated disks were run to establish that the background level of helium was negligible.

RESULTS

The amount of helium varied from 1.8×10^{12} to 5.5×10^{12} atoms, more than enough to accurately measure the cross section. Five copper disks were irradiated simultaneously and had an average fluence of 7.0×10^{16} n/cm^2. Another copper sample was irradiated to a fluence of 1.08×10^{17} n/cm^2.

Figures 1 and 2 show typical isochronal and isothermal release of helium from copper. The helium is tenaciously held within the solid until nearly 0.5 of the melting temperature is reached (Fig. 1). The isothermal release is similar to that of other metals. There is an initial accelerated outgassing followed by a rapidly decreasing rate of release. The isothermal curves do not fit those expected from the outgassing of a disk with an initial homogeneous distribution of helium. So, even at these low concentrations (~2 to 3 at. ppb), the release is apparently influenced by the formation of slow moving bubbles.

It would be instructive to know if the helium content is a linear function of fluence. As there are only two data points for fluence, we used the ^{60}Co count from each of the five disks. The ^{60}Co count should be directly proportional to the neutron fluence, and therefore proportional to the amount of helium generated. In Fig. 3, the amount of helium released is plotted vs the ^{60}Co count. In each case, the ^{60}Co was measured with a precision of approximately 0.2%. The absolute accuracy of the measurement is estimated to be ±5%. Even with the scatter in Fig. 3, the linear relation seems valid.

Table 1 shows the helium content of each disk with the calculated total cross section. The five disks have an average cross section of 54 mb. This value is very close to 55 mb for the specimen irradiated to a slightly different fluence. The overall uncertainty of these results is estimated to be ±10%. The important comparison is that of the average experimental value (54 mb) to the value obtained by activation techniques. The main source of helium will be the (n,α) reactions, because the $(n,n'\alpha)$ cross section is too low to be significant. The (n,α) cross sections determined by activation are 34 mb for ^{63}Cu and approximately 21 mb for ^{65}Cu.[5] Taking the isotope fraction into account, the total activation cross section should be about 30 mb. Obviously, the amount of helium experimentally measured is a factor of 1.8 higher than that computed from activation cross sections. We believe the experimentally derived value to be valid because our recent measurements of helium

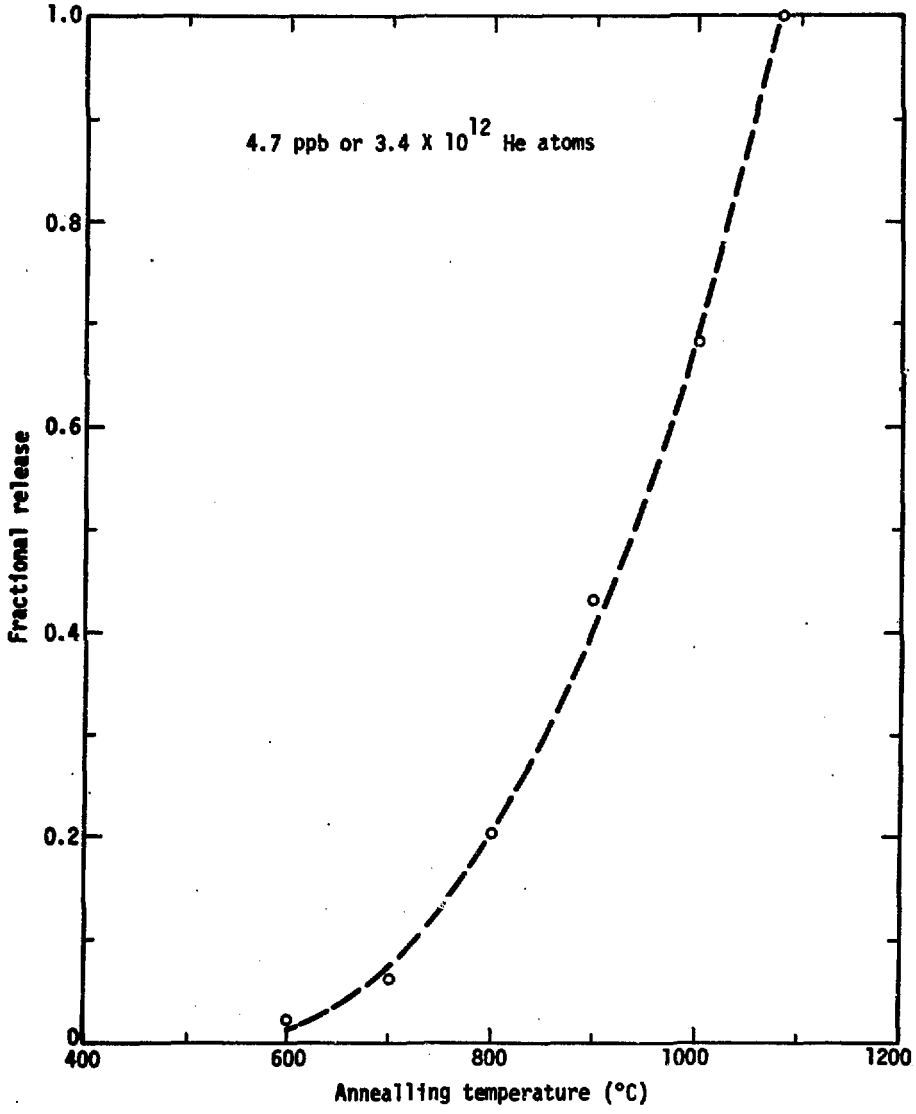

Fig. 1. An isochronal plot of helium release from a copper disk. The time at each temperature was 15 min.

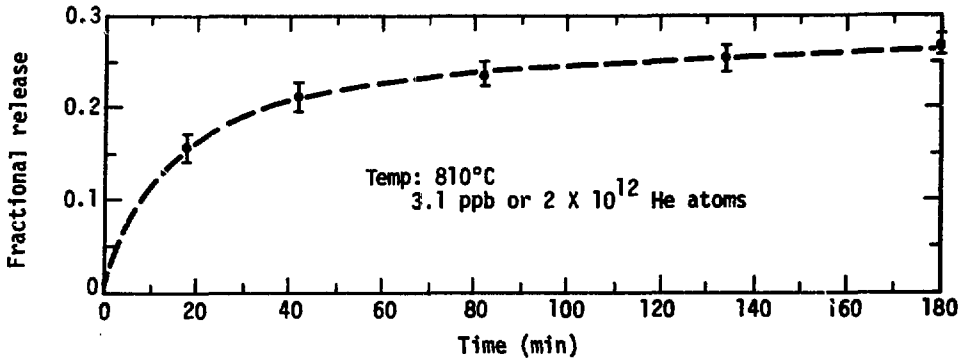

Fig. 2. An isothermal plot of the helium release from a copper disk at 810°C.

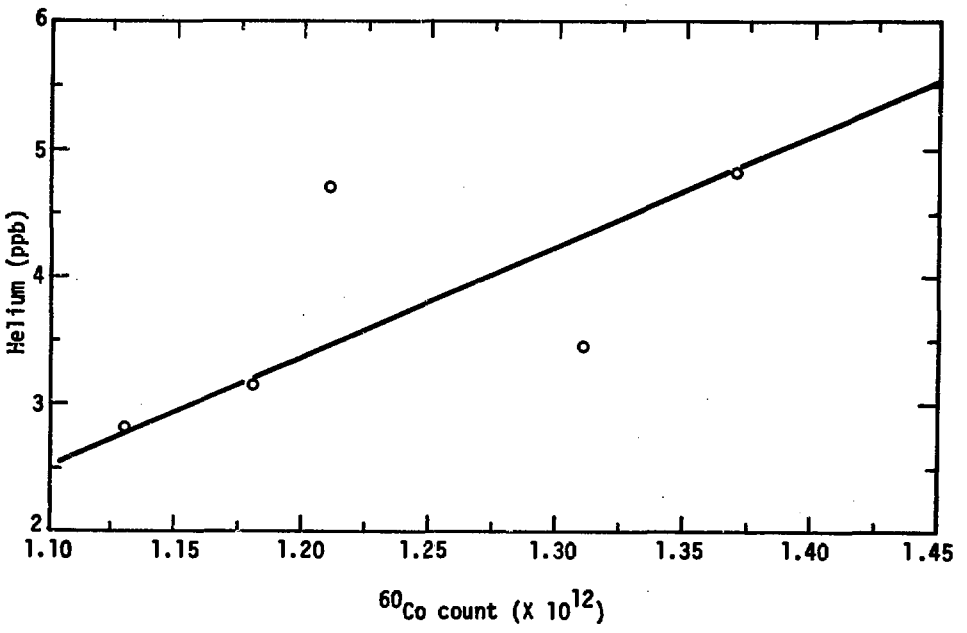

Fig. 3. The measured helium released from each disk is plotted as a function of the ^{60}Co count that is directly proportional to the neutron fluence.

Table 1. Helium content and calculated total cross section of copper disks.

Sample no.	Type of anneal	Amount of helium (ppb)	Fluence	σ_T (mb)
1	isochronal	4.7	7.0×10^{16}	67
2	isochronal	4.8	7.0×10^{16}	68
3	isothermal	3.1	7.0×10^{16}	45
4	isothermal	2.8	7.0×10^{16}	40
5	isothermal	3.4	7.0×10^{16}	49
6	isothermal	5.9	1.08×10^{17}	55
			Average	54
			Uncertainty	±10%

generation in aluminum agree very well with that predicted by the activation cross sections. Aluminum occurs as a single isotope, and its (n,α) cross section is the best known in this energy range.

A possible explanation of the discrepancy in copper might be the presence of impurities within or on the surface of the metal. Most elements in the parts per million range will not increase the helium content significantly. Nevertheless, there are certain elements such as carbon and boron with (n,α) cross sections large enough (~1 b), that when present in parts per million, may make a significant contribution to the inventory of helium. For this reason several copper disks were examined by spectrographic and combustion analysis-mass spectrometry techniques to determine whether boron, carbon or nitrogen might be present in amounts large enough to account for the excess helium.

The analyses are given in Table 2. The carbon contamination might be suspected as a source of helium, because the $^{12}C(n,n')3\alpha$ reaction has

Table 2. The impurity analysis of copper disks (ppm).

Detected	Not detected (limits of detection)
Ag 6	U <1050
Si <6	As, Th <600
Ca 3	Ca, Na <400
Al 1	Ba, Cd, Hg, In, P, Sb, An <100
Mg <1	Bi, Ge, Sb, Sn <40
Be <1	Ga, Co, Cr, Mn, Mo, Nb, V, Sr <15
C 86[a]	B, Ti, Fe <4
	Ni <3

[a]This analysis was by combustion analysis - mass spectrometry.

a cross section of 0.28 b: effectively 0.8 b in terms of helium production. However, the bulk carbon analysis, 86 ppm weight (450 at. ppm), could only contribute 0.025 ppb helium from a fluence of 7.0×10^{16} cm^{-2}, which is a few percent of the amount actually measured. Other low-Z elements have cross sections in the 1-b range, but their concentration also appears to be low. We did not determine if surface contamination is a source of helium. Surface carbon for example, might be a source of helium injected into the metal to a depth of up to 10 μm. To contribute to the helium actually measured however, the carbon layer would have to be over 1 μm thick, much more than expected after our preirradiation clean-up procedure. This seems to negate the probability of impurities contributing to the excess helium generated in the copper.

The discrepancy remains unresolved. The consequence of this preliminary study of helium generation in metals by 14.8-MeV neutron bombardment is to point out the possibility of error in predicting atomic fraction of helium using activation cross sections and to emphasize the importance of high purity, especially low-Z elements, when considering materials in the design of fusion reactors.

ACKNOWLEDGMENT

We appreciate the suggestions and critical review of the manuscript by Ralph H. Condit and Clarence L. Hoenig.

REFERENCES

1 a. L. E. Willertz and P. G. Shewmon, "Diffusion of Helium Gas Bubbles in Gold and Copper Foils," Met. Trans., 1, 2217-2223 (1970).

b. G. Rickers and G. Sorensen, "Diffusion of Inert Gases in Copper," Phys. Status Solidi 32, 597 (1969).

c. A. M. Rodin and V. V. Surenyants, "Coefficient of Diffusion of Helium in Titanium," Fiz. Met. al. Metalloved. 10, 216-222 (1960).

d. J. B. Holt, W. Bauer, and G. 1. Thomas, "Helium Migration in Palladium I Concentration Dependence of Helium Release," Rad. Effects 7, 269-273 (1971).

e. G. J. Thomas, W. Bauer, and J. B. Holt, "Helium Migration in Palladium II Scanning Electron Microscopy Examination of High Concentration Samples," Rad. Effects 8, 27-30 (1971).

f. F. A. Smidt, Jr. and A. G. Pieper, "Studies of the Mobility of Helium in Vanadium," J. Nucl. Met. 51, 361-365 (1974).

g. H. R. Glyde, and K. I. Mayne, "Helium Diffusion in Aluminum," Phil. Mag. 997-1002 (1965).

(These references are a representative cross section and are not a complete bibliography.)

2. N. D. Dudley and S. D. Harkness, "Helium Production in ERR-II Irradiated Stainless Steel," Nucl. Appl. Tech. 9, 700-710 (1970).

3. R. A. Van Konynenburg, H. H. Barschall, R. Booth, and C. Wong, "Characteristics of Rotating Target Neutron Source and its Use in Radiation Effects Studies," Lawrence Livermore Laboratory Rept. UCRL-76857 (1975).

4. R. W. Crawford, J. W. Frazer, and J. B. Holt, "Automatic Apparatus for the Determination of Helium Diffusion in Solids," Rev. Sci. Instrum. 42, 674-677 (1971).

5. M. D. Goldberg et al., "Neutron Cross Sections IIA, Z = 21 to 40," BNL-325, 2nd Ed., Supp. No. 2 (1966).

THE INFLUENCE OF IMPLANTED HELIUM ON SWELLING BEHAVIOR AND MECHANICAL PROPERTIES OF VANADIUM AND V-ALLOYS

K. Ehrlich
D. Kaletta
Kernforschungszentrum Karlsruhe, Germany
Institut für Material- und Festkörperforschung

ABSTRACT

The influence of helium implantation on the swelling behavior and ductility in Vanadium and V-Ti alloys has been investigated by transmission electron microscopy and tensile testing. V and V-20 wt.% Ti has been implanted with He-ions of low energy (240 keV) at irradiation temperatures between 450 and 700° C to fluences ranging from $2.5 \cdot 10^{14}$ to $5 \cdot 10^{17}$ ions/cm^2, which corresponds to peak concentrations of 125 and 250,000 at. ppm He resp. The correlated ion-induced displacement damage is $1.1 \cdot 10^{-2}$ to 22 dpa. For comparison, in the first wall of a CTR about 10,000 ppm He will be generated via (n, α)-reactions in V after a 10 years exposure. In pure V the threshold for bubble formation ($d \geq 40$ Å) is $1 \cdot 10^{17}$ ions/cm^2 at 500° C; it decreases markedly with increasing irradiation temperature ($7 \cdot 10^{14}$ He$^+$/cm^2 at 600° C e. g.). The mean diameters increase hyperlinear with temperature and approximately linear with dose. The strong effect of temperature on the mean diameter can be explained by surface-diffusion controlled coalescence mechanisms. Generally we have observed two different growth processes. The first one can be connected to vacancy trapping and the second one to coalescence. The observed maximum swelling is about 8 % at 625° C. Additions of Ti reduce the concentration of bubbles and their distributions, but have no essential effect on the amount of swelling. Thus in this experiment swelling is mainly due to helium rather than to the displacement damage produced during the implantation. Pure vanadium tensile specimens were homogeneously implanted with 100 MeV He-ions up to 10 ppm helium between 200 and 300° C and tested between 750 and 950° C. No influence upon ductility or yield strength was found in agreement with earlier results on a V-3Ti-1Si alloy.

INTRODUCTION

Vanadium and vanadium base alloys are of interest as potential structural material for the first wall in conceptual designs of fusion reactors. Neutronic analyses of these designs indicated that the neutron-induced activity and associated nuclear afterheat of the vanadium structure were superior to other high-temperature materials such as niobium[1]. Additionally vanadium exhibits an excellent tritium breeding ratio and the compatibility of vanadium-titanium alloys in liquid lithium

up to 700° C is excellent[2].

The generation of helium due to (n, α)-reactions causes one of the most important radiation damages, since helium influences (1) the bulk effects like swelling and high-temperature embrittlement and (2) the surface effects like wall erosion and erosion-induced plasma contamination. The total amount of helium produced in a first wall of vanadium is about 9000 At. ppm within the lifetime of 10 years[3].

In that work the influence of implanted helium of swelling behavior and mechanical properties of vanadium and vanadium base alloys at different temperatures and dose levels is discussed.

EXPERIMENTAL PROCEDURE

The work was carried out with samples of pure vanadium (99,94) and a binary vanadium-titanium alloy of 20 wt.% titanium. The sample size was 10 mm • 0.2 mm. All samples were annealed at 1030° C for 1 hour in an UHV-furnace (10^{-8} Torr) before irradiation. The amount of oxygen and nitrogen was investigated before and after irradiation by chemical and microhardness techniques. To determine the depth within the implanted specimens from which the transmission electron microscopy (TEM) foils were taken, a 3-step procedure was used. In a first step the front surface of the irradiated samples was vibratory polished with an AB Micromet polishing compound, grain size ≤ 0.05 µm, to get a flat, smooth surface. The depth and the parallelity of abraison was controlled by the diameter changes of indents distributed over the sample, a method which is estimated to have an accuracy of ± 0.1 µm. In a second step four discs of 2.3-mm diameter were punched from every polished sample. The discs were thinned electrochemically up to their final depth of 0.6, 0.8, 1.0 and 1.2 µm, respectively, measured from the original surface. This electropolish also eliminated the cold work on the surface introduced by the vibratory polishing. The electrolytes used were 20 % $HClO_4$ + 80 % CH_3COOH for pure vanadium and 20 % H_2SO_4 + 80 % CH_3COOH for V-20 Ti. In the last step the backside of the discs were thinned while the front surfaces were

masked off. Foils were examined with a 100-kV SIEMENS Elmiskop 1A and with a JEOL 200 A electron microscope. The thickness of the foils was determined by stereotechnique. Bubble concentration and the size distribution curves were obtained by counting and classifying the bubbles with a ZEISS particle-size analyser using a standard magnification of 120,000 for the micrographs.

During the implantation the samples were placed in a high vacuum irradiation chamber on a rotable target-holder with twelve target positions. The target-holder was electrically and thermally isolated against the container thus allowing a continuous measurement of the incident beam current. The secondary electron emission was suppressed by a Faraday cup.

The time integration of the flux, i. e. the dose measurement, was accurate within ± 5 %. The dose varied between $2.5 \cdot 10^{14}$ and $5.0 \cdot 10^{17}$ ions/cm^2.

The target holder was held at a constant temperature between 460 and 700° C with a stabilization of ± 0.5° C. Beam induced heat pertubations can be controlled within few seconds due to the low heat capacity of the target holder system and due to the quick response of the temperature stabilizer. The radial and axial temperature gradients are of the order of one degree Celsius per cm. A data acquisition system controlls the irradiation parameter. The beam source was the UNILAC-testinjector at Darmstadt operating with a duoplasmatron ion source. The beam energy was 240 keV. The current density was between 10 and 100 μA/cm^2 corresponding to a particle flux of $6.24 \cdot 10^{14}$ and $6.24 \cdot 10^{15}$ He^+/cm^2s, respectively.

The high energy irradiation with 104-MeV α-particles was carried out at the Karlsruhe cyclotron. The beam current density varied between 2 and 5 μA/cm^2 and the target temperature was about 280° C due to beam heating. Both the current density and temperature were measured at the target holder which was electrically isolated against the container. We used the homogeneous operation mode reducing the ion beam energy of 104-MeV down to zero continuously by a rotating moderator disc. The thickness of the moderator disc varied over twelve segments along the circumference

which have different thicknesses as well as different segment angles due to the nonlinear relationship between range and energy. In this mode we got a uniform helium distribution over the sample thickness which is 500 µm. The gauge length of the tensile specimens was 15 mm and the width 4.2 mm.

We tested only pure vanadium samples from the same batch as the ones used for the low energy implantation. After irradiation all tensile specimens were annealed at specified temperatures and times and thereafter tensile tested under vacuum conditions.

RESULTS AND DISCUSSION FOR THE LOW ENERGY IMPLANTATION

Pure vanadium

Due to stopping and range straggling of the ions implanted the induced damage as well as the ions have no uniform distribution along the penetration depth. In Fig. 1 we show the typical dependence of the bubble concentration and the bubble diameter on the sample thickness measured by TEM technique. The helium ion energy was 240 keV corresponding to a mean penetration depth of 0.8 µm with a small standard deviation of 0.1 µm calculated according to the LSS-formalism and using empirical electronic loss data[4]. The damage peak related to above ion energy is located at 0.7 µm. From Fig. 1 one can see that we also have found bubbles at greater depths than the mean penetration depth. Therefore we can state that at all depths investigated the supply of helium should be sufficient for nucleation or even in oversupply. The quick spread of helium can be explained by the low migration energy for helium in vanadium[5], 0.13 eV, leading to a migration velocity of several µm/s. The dominant trapping mechanism for helium by vacancies can only be effective in the region towards the surface (damage region). For regions towards the bulk the thermal equilibrium concentration of vacancies is not sufficient to effectively trap the high helium flux. The peak broadening of the helium distribution, the reduction of peak height as well as the shift of

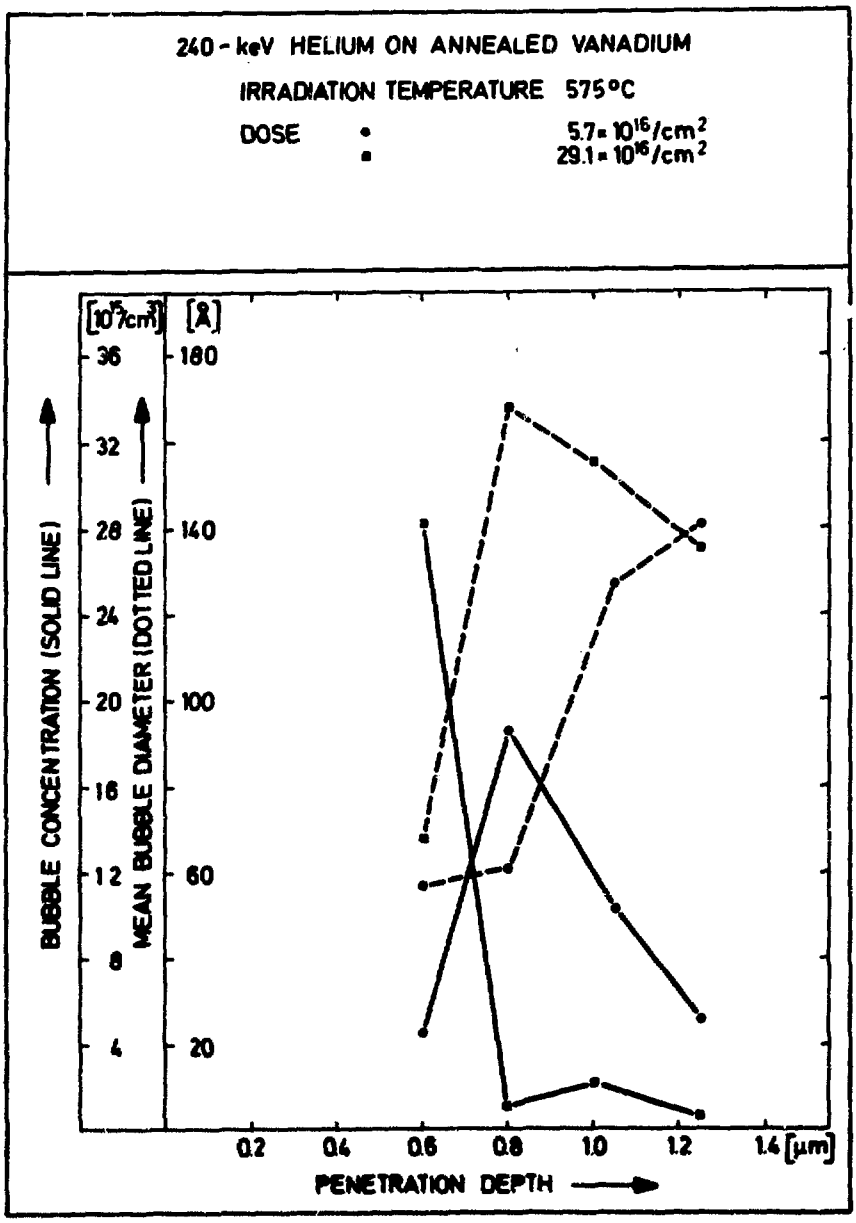

Fig. 1. Bubble concentration and mean bubble diameter in pure vanadium implanted with 240-keV He^+ at two dose levels as a function of penetration depth of helium.

the helium distribution governed by the kinetics of migration are illustrated in Fig. 2. The dotted line indicates the helium build-up during implantation neglecting migration processes. The distribution calculated is assumed to be Gaussian. The solid line represents the helium content calculated from the observed bubble distribution. The bubbles were assumed to be in thermal equilibrium, i. d. the gas pressure (van-de-Waals law) is balanced by the surface pressure using a surface energy of 1000 erg/cm^2. The irradiation conditions are the same ones as used in Fig. 1 for the case of the $5.7 \cdot 10^{16}$ dose level.

From our experiments we can deduce two different growth processes taking place during irradiation at elevated temperatures. The first growth process can be associated with a bubble growth due to vacancy trapping. As seen in Fig. 1 at the depth 0.6 µm the bubble concentration increases with increasing dose accompanied by an increase in bubble diameter. The migration energy of vacancies in vanadium is low enough[6], 0.54 eV, to ensure a quick diffusion through the solid, if no other processes such as recombination lowers the vacancy supply significantly. As confirmed by Evans et al.[7] in 1975 experimentally and as supported by own calculations the dominant traps for vacancies are the helium centers rather than other defect types such as dislocations. The second growth process can be connected to coalescence. The coalescence restricts the increase in bubble concentration due to increasing dose below a threshold and declines the bubble concentration with increasing dose above a threshold. That behavior is demonstrated on Fig. 1 for the peak intervall at 0.8 µm having a width of ± 0.06 µm (the intervall width corresponds to the foil thickness experimentally determined by TEM). For that intervall we calculated the number of Frenkel defects produced by one helium ion to 17 assuming a displacement threshold of 25 eV and a damage efficiency of 0.8. At a dose level of 10^{16} He$^+$/cm^2 there is a helium concentration of 4200 At. ppm and a defect number of 0.071 dpa which are 36 % of the total injected amount of helium, and 16 % of the total induced damage, respectively. The calculations based on a procedure given by Kaletta and Ehrlich[8] in 1974. For that peak intervall one can see that the bubble concentration does decline with increasing dose. The decrease of bubble

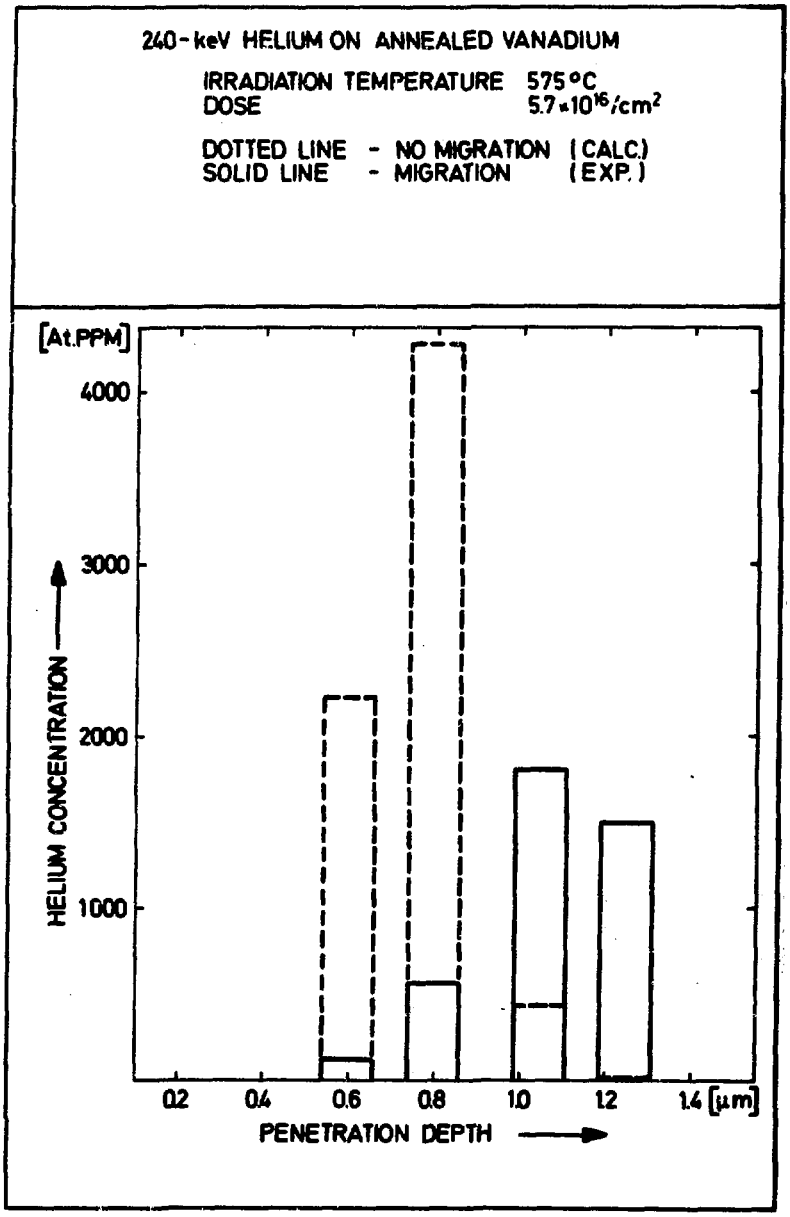

Fig. 2. Helium distributions in pure vanadium after 240-keV He^+ irradiation.

concentration is accompanied by an increase in bubble diameter. The starting point for amalgation depends on the mean separation λ of the bubbles a quantity determined predominantly by the dose $\lambda \sim (\phi t)^{-1/2}$, and by the mobility of the bubbles which in term is determined by the temperature and migration mechanism. The correlation between the mean free path and the diffusion path indicates that the migration mechanism of bubbles should be a surface diffusion mechanism.

It is believed that the peak in the bubble concentration vs. dose curve is governed by the vacancy supply and demand. Up to a critical bubble concentration there are continuous nucleation and growth processes with dose. At the concentration maximum the vacancy demand by bubbles is balanced by the vacancy supply; there is no further increase in concentration but only in diameter. Simple estimates confirm that the damage induced vacancy supply at high bubble concentration levels can only support a growth process because the vacancy demand by bubbles for growing is of one order of magnitude lower than the vacancy demand for building up a new bubble of some diameter before growing. For the case that bubble growth above a critical bubble concentration is due to vacancy trapping one gets a saturation effect in the bubble concentration vs. dose curve, and for the case that bubble growth above a threshold is due to coalescence one gets a peaked curve

At elevated temperatures we observe that the vacancy supply is still sufficient to enable a bubble growth under thermal equilibrium conditions. As seen in Fig. 3 the cubic morphology of bubbles even at high depths is unchanged and there are no stress fields around the bubbles indicating thermal equilibrium.

In Fig. 4 we show the temperature dependence of the two growth processes as observed at the peak-intervall of 0.8 µm. At a given dose there is initially a build-up of the bubble concentration up to a critical temperature and thereafter a decrease with temperature. That behavior can be explained in terms of current theories based on temperature dependence of the vacancy supersaturation. With increasing dose at a given flux, however, we observe the decrease in bubble concentration discussed above and a temperature shift of the bubble peak concentration to lower

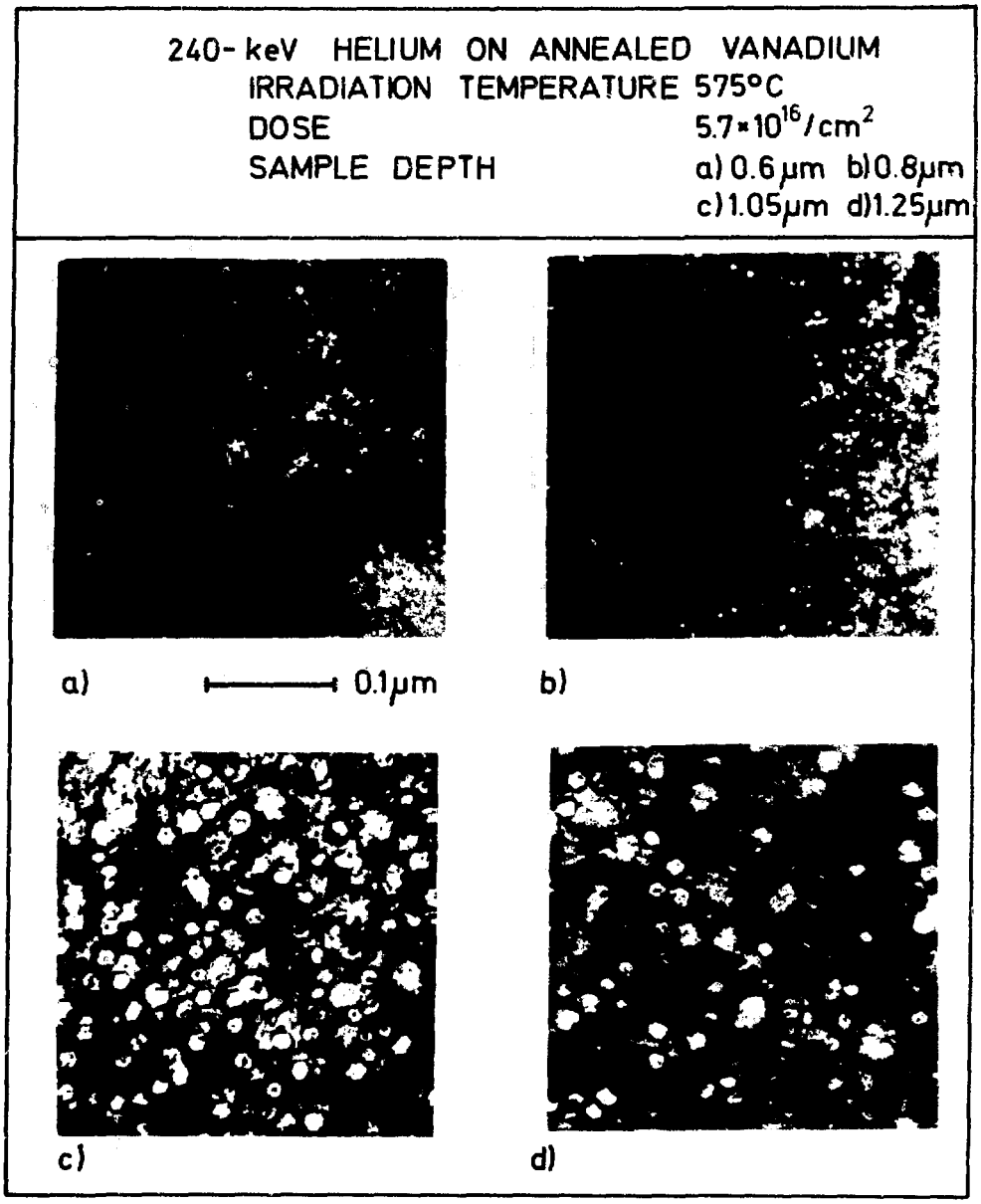

Fig. 3. TEM micrographs: bubble concentration and mean bubble diameter in pure vanadium implanted with 240-keV He^+ as a function of penetration depth of helium (Fig. 3 is related to Fig. 1).

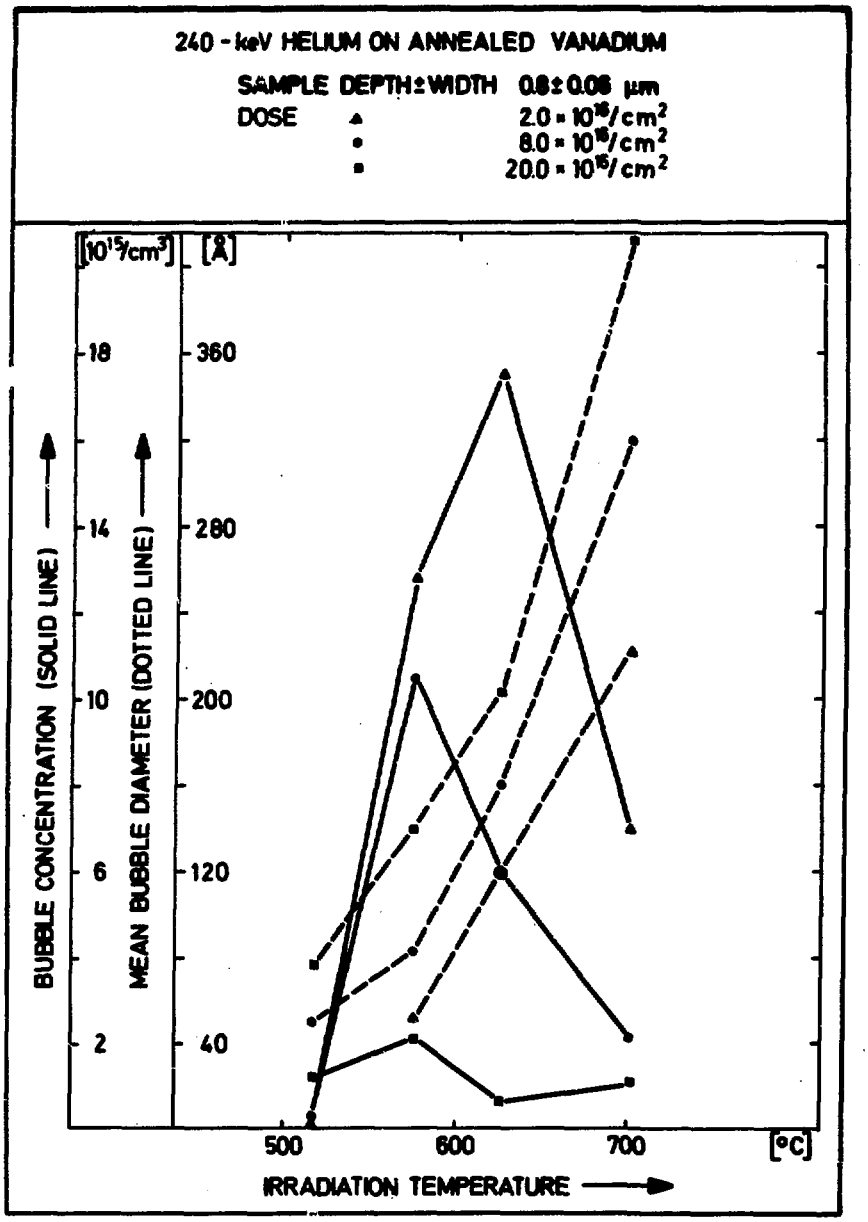

Fig. 4. Bubble concentration and mean bubble diameter in pure vanadium implanted with 240-keV He^+ at three dose levels as a function of irradiation temperature. The sample depth is 0.8 µm.

temperature with increasing dose. The sign of that temperature shift is opposite to the sign resulting from variations of the defect production rate. That behavior can be ascribed to coalescence: The higher the dose is the shorter the bubble distance is and the bubbles need a lower mobility or temperature to grow by coalescence.

From our dose vs. temperature data for bubble diameters we can extrapolate a threshold dose for bubble occurence. In Fig. 5 we show the strong influence of irradiation temperature on the threshold dose for observing bubbles with 40-Å diameter. This diameter has been chosen as a lower limit for bubble observation. The extrapolation procedure which extrapolates from large bubble diameter data to low bubble diameter ones, should be handled carefully because the diameter data involve two different growth processes. We believe, however, that within a factor of 2 the threshold values should be correct.

In Fig. 6 we show the dependence of the swelling volume $\Delta V/V$ of the samples due to bubbles upon dose and temperature. We have found that the magnitude of swelling is an increasing function with dose showing a maximum of 8 % at T = 625° C.

Vanadium-20 wt.% titanium

In the case of the V-Ti alloys we found a nearly unaltered swelling volume compared to the case of pure V under the same irradiation conditions which is in contrast to the swelling behavior due to voids[9]. The microstructure of the V-Ti alloy samples exhibit large precipitates (TiO_2) corresponding to the high oxygen content of these samples. In accordance with the altered microstructure we found an altered bubble structure which differs in three points from the bubble structure of pure V. At first the bubble morphology was changed in V-20 Ti; the bubbles grow in a direction exhibiting an elongated and plate-like form instead of cubic shape as seen in Fig. 7. Secondly the mean bubble diameter is mostly more than twice greater than for bubbles in pure V and the bubble diameter distribution curve is broadened. That means that the σ/μ ratio increases (σ is the standard deviation of the average μ). The increase in diameter was accompanied by a decrease in bubble concentration. And thirdly the bubbles grow along grain boundaries and precipitates prefe-

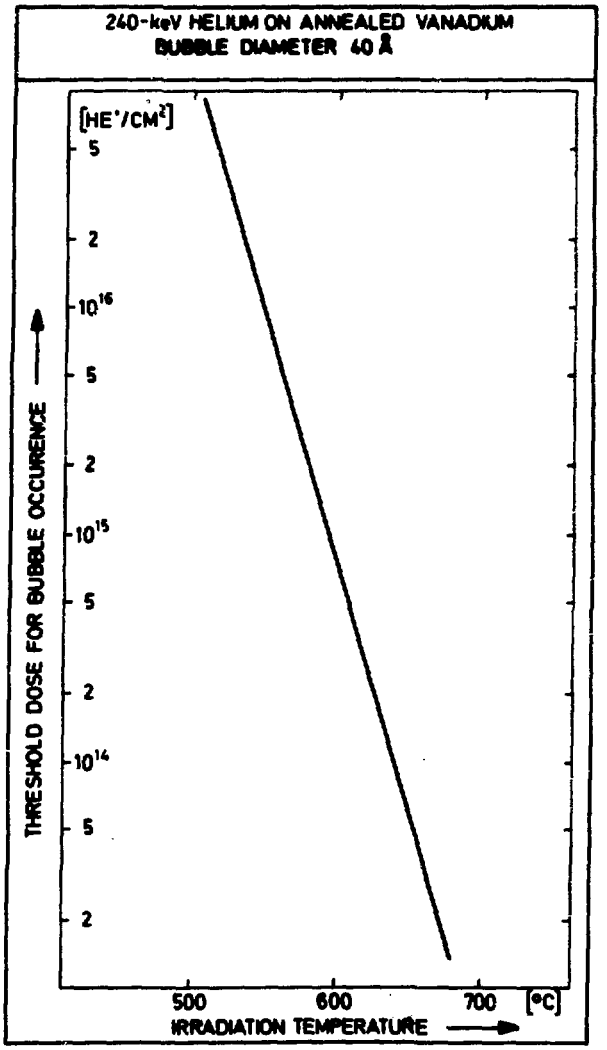

Fig. 5. The threshold dose for bubble occurence as a function of irradiation temperature. The bubble diameter chosen is 40 Å.

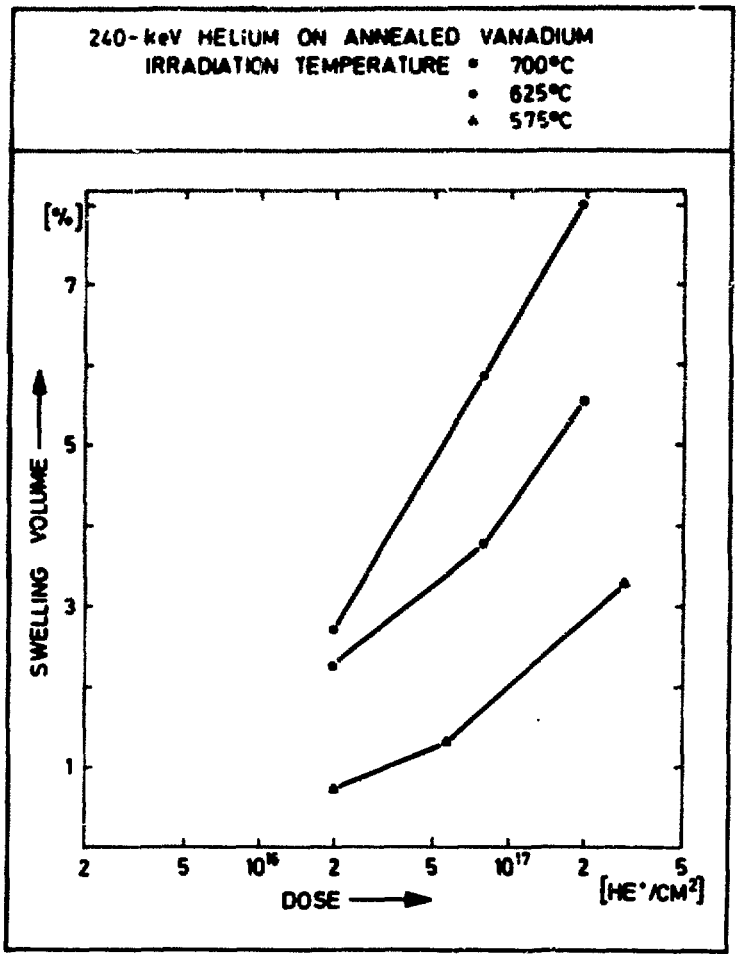

Fig. 6. The swelling volume of pure vanadium implanted with 240-keV He^+ at three temperatures as a function of dose.

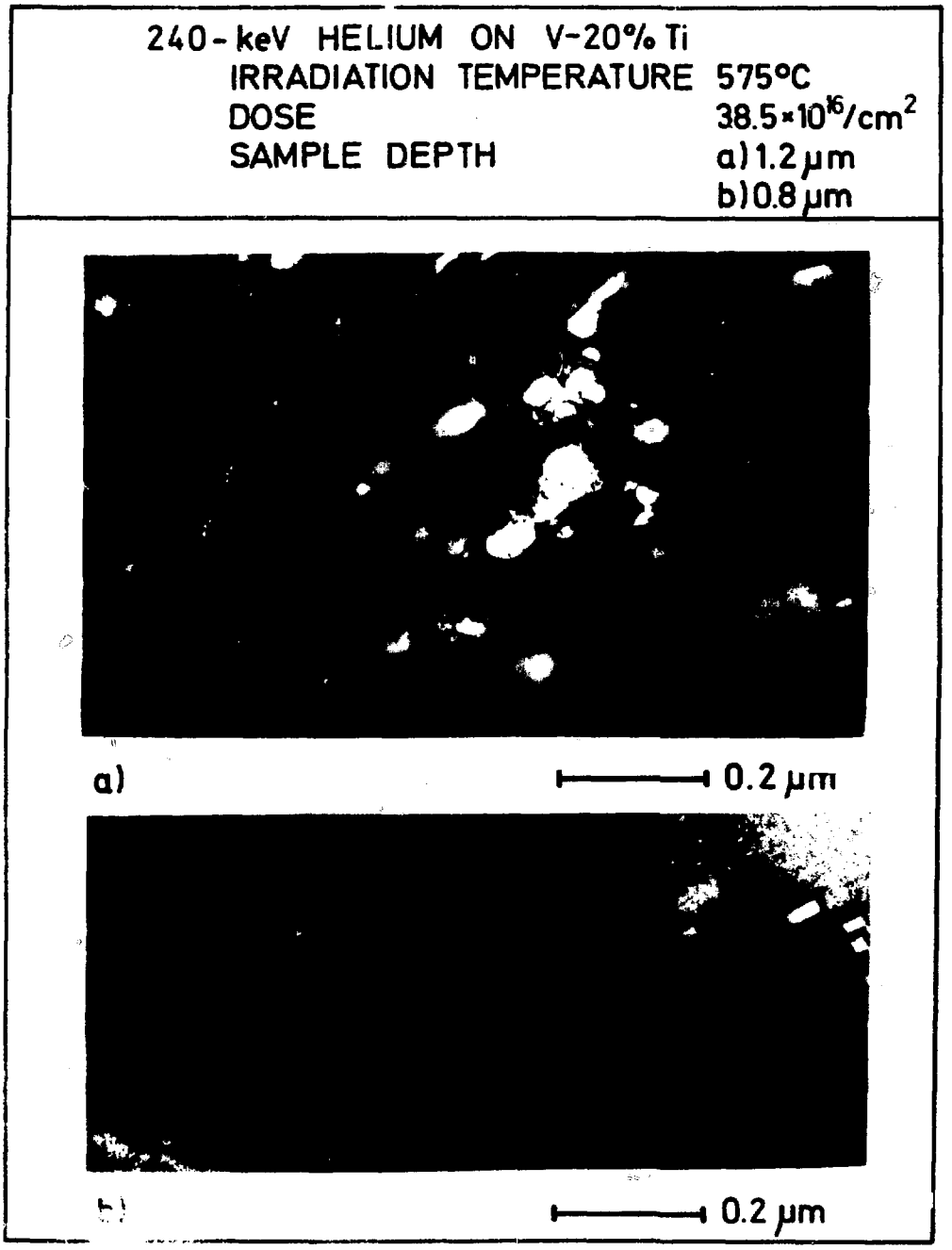

Fig. 7. TEM micrographs: bubble morphology in V-20 wt.% Ti implanted with 240-keV He.

rentially (Fig. 7); there is no uniform distribution within the grains as for the case of pure V.

The preferred bubble growth along grain-boundaries does not only affect bulk-phenomena, but does affect related surface phenomena, too. Using REM techniques we could clearly observe that the vanadium alloys exhibit an intergranular structural fracture with pronounced brittle fracture behavior.

THE EFFECT OF HELIUM ON THE TENSILE PROPERTIES OF VANADIUM

In former experiments[10] it was shown that some investigated vanadium alloys of high tensile and creep strength were sensitive to a preimplantation of helium at test temperatures of about 0.5 T_M and higher. The observed embrittlement could however not be correlated to the appearance of helium bubbles at grain boundaries which in the case of nickel alloys and austenitic stainless steels is being claimed to be the important mechanism for high temperature embrittlement[11]. Similar results had been found by Santhanam et al.[12] on a vanadium-15 % Cr-5 % Ti alloy. They could establish that the embrittlement was associated to an increasing tendency to intergranular fracture - which is supposed to be the general characteristic for helium embrittlement. But again the formation of bubbles along grain boundaries was observed only in exceptional cases.

The results of our investigations on pure vanadium where helium was homogeneously implanted at about 280° C parallel our findings on a V-3Ti-1Si alloy. In both cases (Fig. 8) nearly no influence of preimplanted helium on the ductility is observed even at the highest test temperatures (900 - 950° C). Preannealing of samples at 850 resp. 950° C for 16 hours followed by tensile testing at the same temperatures had no influence on yield stress and elongation. Electronmicroscopic investigations of the samples showed no helium bubbles along grain boundaries.

The reason for the different behavior of several vanadium alloys after preimplantation with helium when tensile testing at temperatures of 850° C and higher is not known. Maybe the very high yield strength of V-Nb-Ti-alloys promotes a preferred intergranular cracking in these

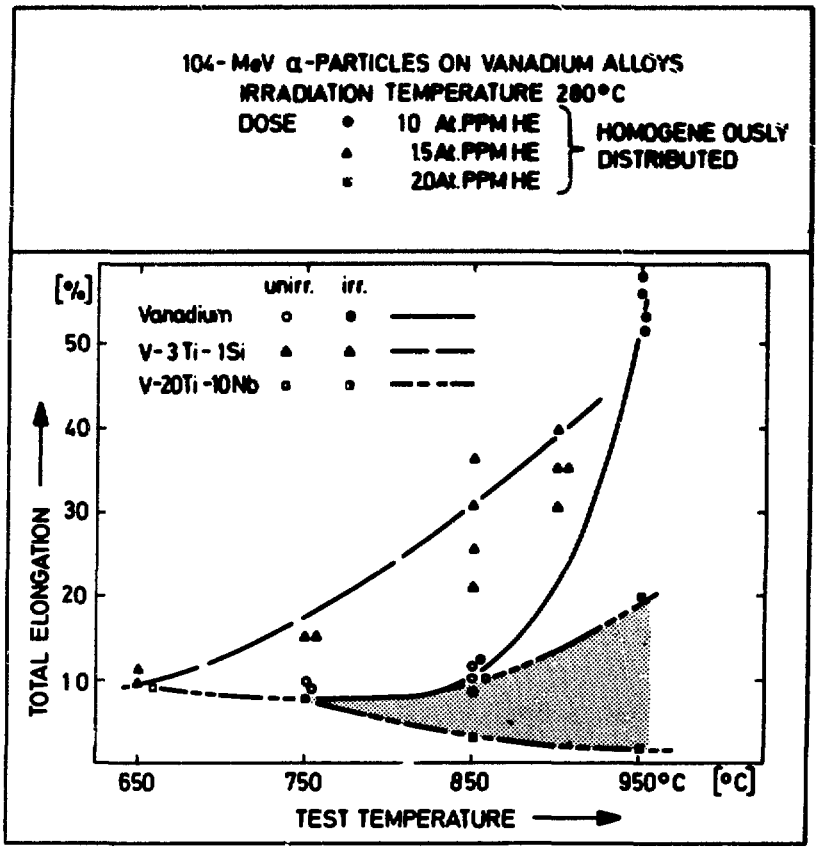

Fig. 8. Total elongation of vanadium and two ternary alloys implanted with 104-MeV α-particles as a function of test temperature.

materials. Also the recovery behavior of both groups of materials is very different. Finally the recent results on Vanadium and V-3Ti-Si show a very steep increase of total elongation at temperatures of 900° C and higher indicating some sort of superplastic deformation at this temperature region. Further experiments are necessary to clearify the reasons for this very different behavior.

SUMMARY

From our experiments we can conclude:

(1) At an initial stage of irradiation helium is enabled to diffuse through the solid quickly. There are no dominant traps for helium trapping thus helium can be act as a nucleation center far behind the mean penetration depth of helium injected.

(2) The bubble nucleation and growth due to vacancy trapping increase with dose up to a critical bubble concentration. Above the threshold the bubble growth is governed by coalescence and the bubble concentration declines.

(3) With higher temperature the threshold dose for 40-Å bubble occurence is lowered drastically.

(4) The addition of Ti to V alters the bubble morphology, concentration and diameter as well as their distributions but has no influence on the swelling volume when compared to pure vanadium.

(5) The injection of helium in the ppm-range at low temperatures has no significant effect on tensile properties at elevated test temperatures, when the yield strengths of the alloys are comparable to that of pure vanadium.

ACKNOWLEDGEMENTS

The authors are indebted to GESELLSCHAFT FUER SCHWERIONENFORSCHUNG, DARMSTADT, for utilizing; the accelerator-system; especially they wish to thank Drs. N. Angert and H. Krupp. The authors are grateful to G. Przykutta and Mrs. B. Zeckai for providing technical assistance.

REFERENCES

1. D. Steiner, Nucl. performance of vanadium as a structural material in fusion reactor blankets, ORNL-TM-4353 (1973).

2. Memorandum über die technolog. Probleme des Fusionsreaktors, ed. by Forschungszentren Deutschland, Sept. 1973.

3. H. U. Borgstedt, J. Nucl. Mat. 51, 226 (1974).

4. C. F. Williamson, J. P. Boujot and J. Picard, Tables of range and stopping power of chemical elements for charged particles of energy 0.5 to 500 MeV, CEA-R 3042 (1966).

5. W. D. Wilson and R. A. Johnson, Rare Gases in metals, p. 375, in: Interatomic potentials and simulation of lattice defects, ed. by P. C. Gehlen, J. R. Beeler, Jr. and R. J. Jaffee, New York - London, 1972.

6. R. A. Johnson and W. D. Wilson, Defect calculations for fcc and bcc metals, p. 301, in: ibid.

7. J. H. Evans, J. Mazey, D. L. Eyre, S. K. Erents and G. McCracken, A TEM study of gas bubbles and surface blisters in Mo bombarded with helium ions in the energy range 25 - 60 keV, on: Internat. Conf. on "Application of ion beams to materials", Warwick, U. K., Sept. 8 - 12, 1975.

8. D. Kaletta and K. Ehrlich, J. Nucl. Mat. 51, 227 (1974)

9. H. Böhm, The effect of neutron irradiation on the high-temperature mechanical properties of vanadium-titanium alloys, p. 163, Nucl. Metallurgy vol. 18 (Aug. 1973).

10. K. Ehrlich and H. Böhm, Irradiation effects in vanadium-base alloys, p. 349, in: Proc. IAEA-Conf. on "Radiation damage in reactor materials", Vol. II, Vienna 1969.

11. D. R. Harries; J. Brit. Nucl. En. Soc., p. 74 (1966).

12. A. T. Scanthanam, A. Taylor and S. D. Harkness, Charged-particle simulation studies of vanadium and vanadium alloys, in: Nucl. Metallurgy 18, 302 (1973).

EFFECTS OF HELIUM IMPLANTED BY TRITIUM DECAY ON THE HIGH TEMPERATURE MECHANICAL PROPERTIES OF NIOBIUM

D.G. Atteridge A.B. Johnson, Jr.
L.A. Charlot J.F. Remark
R.E. Westerman
Battelle-Pacific Northwest Laboratories
Richland, Washington

ABSTRACT

Helium-induced mechanical property degradation is one of the major material problems which must be assessed in predicting the lifetime of CTR first-wall structures. The effects of helium on the high-temperature short-time tensile properties of commercial purity niobium are being determined as a first step towards attaining a better understanding of inert gas/metal matrix interactions on mechanical properties. Helium concentrations from 30 to 500 appm were implanted in the niobium matrix by tritium decay. The tritium was introduced into the matrix by a gas-charging technique and then removed after a sufficient decay time at room temperature for the helium concentrations to build up to the desired values. Subsequent tensile tests at 1020°C, utilizing buttonhead specimens of 0.41 cm gage diameter, revealed a decrease in uniform and total elongation with increasing helium content, accompanied by a helium-induced grain-boundary-decohesion failure mechanism. Microstructures and fracture surfaces are being investigated optically and by SEM and TEM; results of these studies are presented.

INTRODUCTION

Helium-induced mechanical property degradation is a major material problem which must be assessed in predicting the lifetime of CTR first-wall structures. The ability to resist the embrittling effects of helium formed within the material by (n, α) reactions between neutrons and metal atoms is one of the most significant factors affecting the lifetime of the internal walls of these vessels. The helium born in the metal lattice is in a thermodynamically unstable state, as helium is essentially insoluble in metals under normal conditions. This unstable

helium removes itself from the metal lattice by combining with structural defects in the metal such as dislocations, voids, incoherent interfaces, and grain boundaries. Helium-induced mechanical property degradation results from these interactions.

This paper describes the effects of internal helium on the high-temperature short-time tensile properties of commercial purity niobium. The helium implantation technique used in this study is based on the so-called "tritium trick" in which tritium decays to helium.[1] This helium charging technique consists of diffusing tritium into the niobium, allowing sufficient decay time to reach the required helium concentration and then outgassing the remaining tritium. The specimens are tensile tested following tritium removal.

The tensile test results represent the first substantial test program using the tritium-decay, helium-charging method for studying helium-induced mechanical property changes in refractory metals. These results also represent the initial segment in a PNL study directed toward attaining a better understanding of inert gas/metal matrix interactions and their effects on mechanical properties.

SPECIMEN PREPARATION AND TEST PROCEDURE

The material used in this study is annealed commercial purity niobium purchased from Teledyne Wah Chang; the composition is shown in Table 1. The niobium was obtained as 0.96 cm diameter rod and was subsequently machined into buttonhead tensile specimens 7.6 cm long with a gage section diameter of 0.4 cm and a gage length of 3.2 cm (Figure 1).

Table 1. Composition of Commercial Purity Niobium

Element	ppm	Element	ppm	Element	ppm	Element	ppm
Al	< 20	Cu	< 40	Mo	< 20	Sn	< 10
B	< 1	Fe	< 50	N	< 20	Ta	377
C	< 30	H	< 5	Ni	< 20	Ti	< 40
Cd	< 5	Hf	< 50	O	< 70	V	< 20
Co	< 10	Mg	< 20	Pb	< 20	W	52
Cr	< 20	Mn	< 20	Si	< 20	Zr	1000

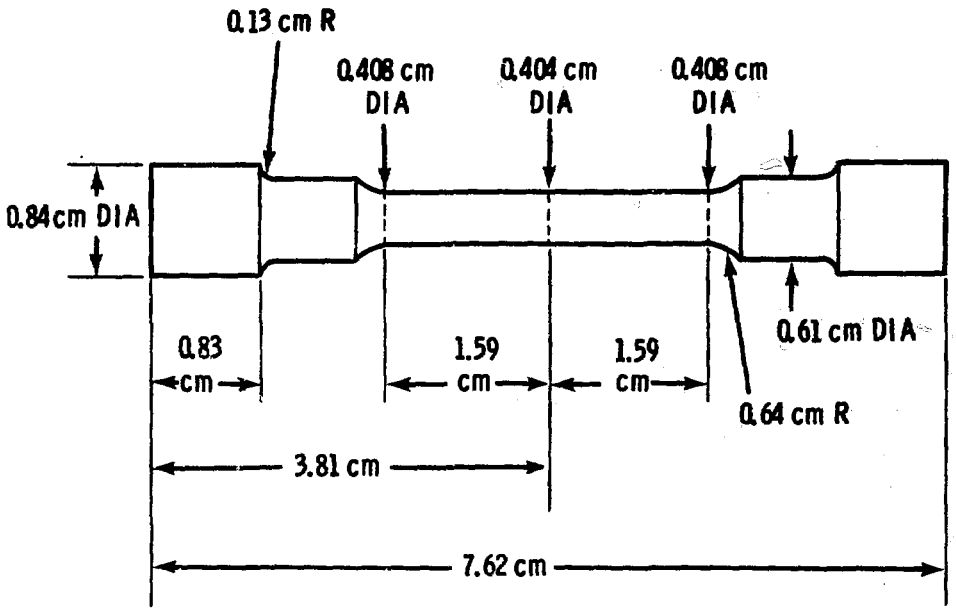

Fig. 1. High-Temperature Tensile Specimen Configuration.

The specimens were charged with helium by the tritium-decay, helium-charging technique. The basic steps are:

- Introduction of tritium into the metal lattice by intermediate temperature (500°C) gas-phase tritium charging.
- Generation of helium in the metal matrix by allowing sufficient decay time at room temperature to accumulate a predetermined concentration of helium through tritium transmutation.
- Removal of the remaining tritium by hot vacuum extraction at ∿ 900°C. The helium is left behind in the metal lattice.

A detailed discussion of this helium charging method is presented elsewhere.[2]

Niobium specimens containing from 30 to 520 appm helium have been prepared and tested. Helium is accumulated at ∿ 75 appm per month, based on a typical beginning tritium content of 15,000 appm (the room temperature terminal solubility of hydrogen in Nb is 30,000 appm)[3] and the tritium half-life of 12.26 years. This specimen charging rate compares to a predicted helium accumulation rate of 25 appm per year for niobium in a fusion reactor first-wall application exposed to a 14 MeV neutron current of 4.4×10^{13} n/cm^2 sec.[4]

The helium concentrations reported in this paper are from theoretical calculations based on initial tritium concentrations in the specimens and the known tritium half-life. The calculated concentrations were found to agree within $\pm$ 10 percent with subsequent helium spectroscopic analysis.[2]

High temperature tensile tests at ∿ 0.48 T_m (1020°C) were carried out on annealed niobium from zero to 520 appm helium; the test temperature corresponds to the maximum predicted CTR use temperature for niobium alloys. The tensile specimens were heated in a radiant heated quartz tube vacuum apparatus and tested in a 5 kgm Instron tensile machine. They were given a 30-minute pretest soak at test temperature and were tested at a pressure of $< 10^{-5}$ torr and a strain rate of 0.02 min^{-1}.

RESULTS

The 1020°C tensile test results are presented in Figure 2. Several major mechanical property trends are apparent:

- The uniform and the total percent elongation decreases with increasing helium content.
- The yield and ultimate strengths increase with increasing helium content.
- The amount of strain hardening decreases with increasing helium content, i.e., the difference between yield and ultimate strengths decreases with increasing helium content.

The total elongation decreases from 50 percent for as-received niobium to 15 percent for the 520 appm helium specimen resulting in a $\sim$ 7 percent drop in elongation per 100 appm helium. There is, however, the possibility of a threshold helium concentration of less than 100 appm below which helium does not affect elongation. The uniform elongation remains relatively unaffected by increasing helium content until a concentration greater than 250 appm helium is reached (it decreased at a rate of $\sim$ 1 percent per 100 appm helium up to 250 appm helium). At 350 appm helium the uniform elongation drops to less than 2 percent and remains at this value for 520 appm helium also.

The yield and ultimate strengths increase rapidly with low-level helium additions and then remain relatively constant at concentrations above 100 appm helium. The yield strength approaches the ultimate strength at high helium concentrations, with a resultant decrease in the amount of matrix strain hardening.

The stress-strain curves for specimens of selected helium contents are given in Figure 3. Two general types of curves are present. Type I behavior is found in specimens with concentrations $\leq$ 250 appm helium. This type of curve exhibits a substantial strain hardening region between yield and ultimate, a second substantial strain region of slowly decreasing load bearing capability, and finally a relatively abrupt load drop region terminating in specimen fracture. These characteristics result in the high uniform and total elongation values mentioned above for specimens with $\leq$ 250 appm helium. Type II behavior is found in

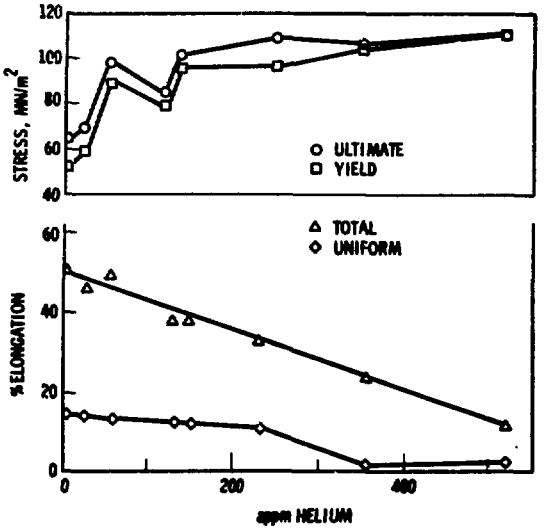

Fig. 2. Short-Time Tensile Properties for Annealed Niobium Tested at 1020°C.

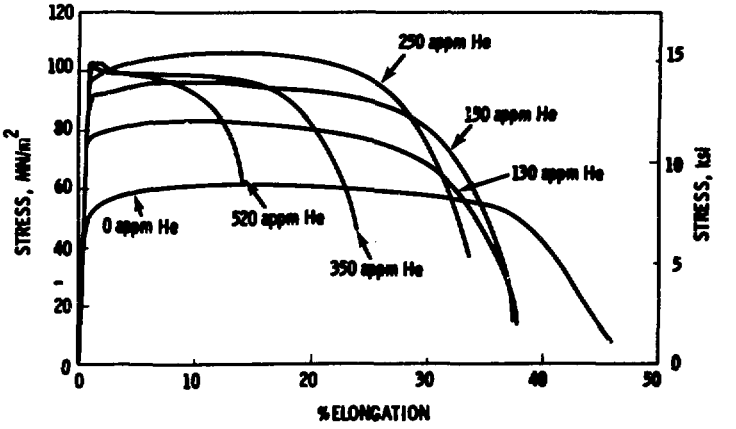

Fig. 3. Effect of Helium on Tensile Characteristics of Annealed Niobium Tested at 1020°C.

specimens with greater than 250 appm helium. These curves exhibit a small strain hardening region after the proportional limit is reached, a region of relatively constant load bearing capacity, and then an abrupt load drop followed by a sustantial strain region of decreasing load carrying capacity terminating in a specimen failure region similar to Type I curves. The abrupt change from the strain hardening region to the constant load region at low strain results in the low uniform elongation values in Figure 2, as the values are based on elongation at ultimate strength.

The physical appearance of selected fractured specimens is illustrated in Figure 4. The fracture tip appearance changes gradually from a chisel-point to a pseudo cup-cone fracture with increasing helium content. No abrupt change in fracture appearance is evident between the 250 and 350 appm helium specimens, the compositions where the stress-strain curves change from Type I to Type II. Magnified views of the fractured end of the zero and 520 appm helium specimens are shown in Figures 5 and 6; their as-tested microstructures are seen in Figures 5 through 8.

The as-received niobium (Figures 5 and 7) exhibited the following high-temperature deformation characteristics:

- Extended uniform plastic elongation.
- Extended necked region, terminating in a chisel-point fracture.
- Highly deformed and elongated grains.

The high-helium niobium (Figures 6 and 8) exhibited the following high-temperature deformation characteristics:

- Reduced uniform plastic elongation.
- Limited necking deformation, terminating in a pseudo cup-cone fracture.
- Lack of highly deformed grains in the necked region.
- Significant amounts of grain boundary decohesion in high deformation regions.

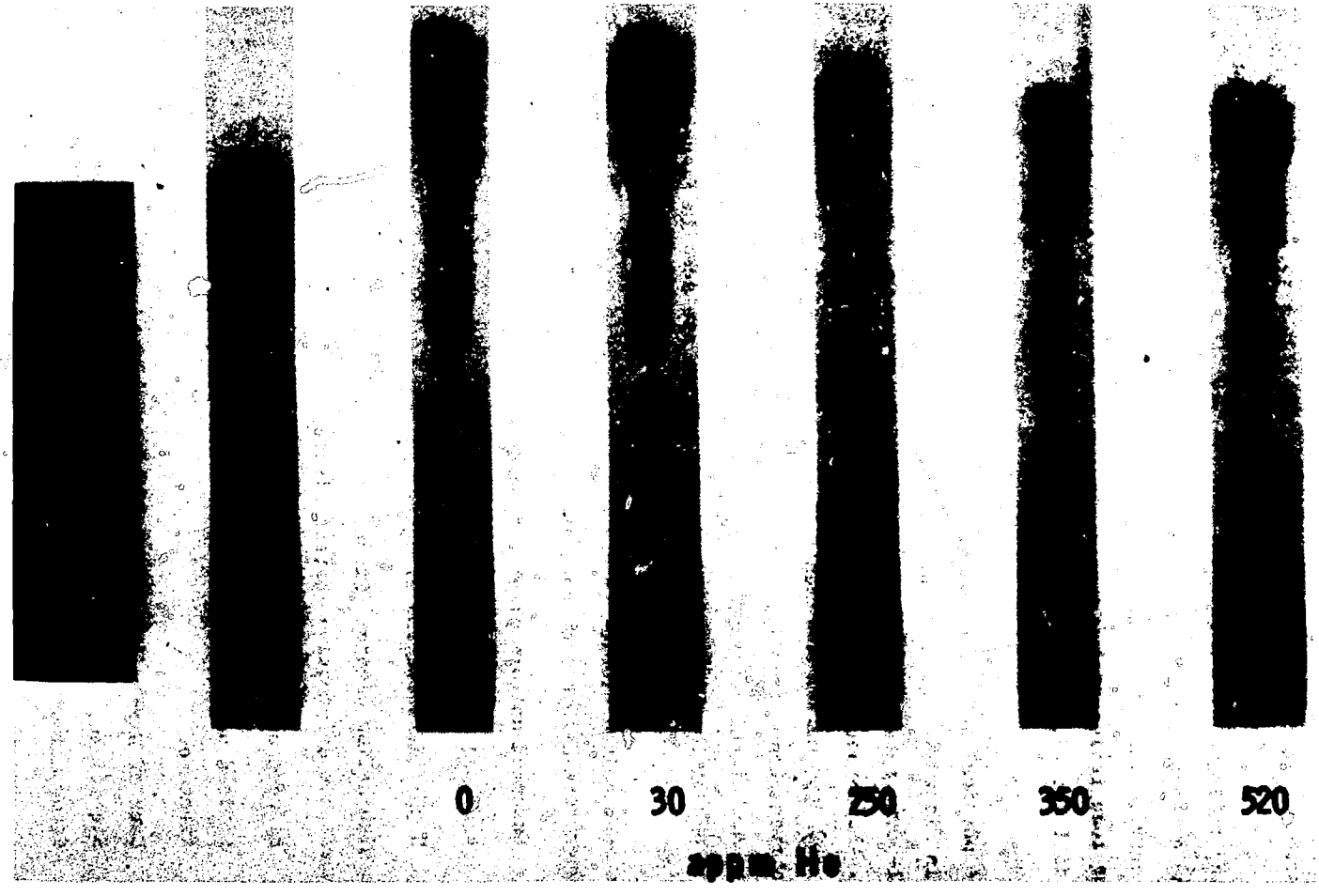

Fig. 4. Annealed Niobium Tensile Specimens Tested at 1020°C.

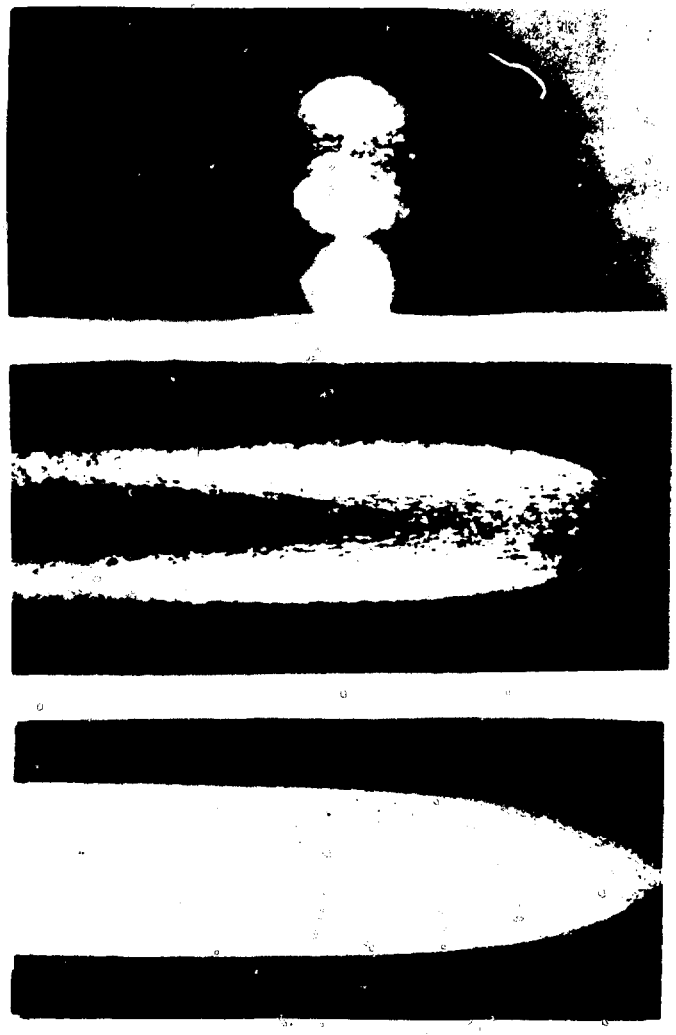

Fig. 5. Fracture Morphology and Microstructure for Zero-Helium Niobium Tested at 1020°C. 8×.

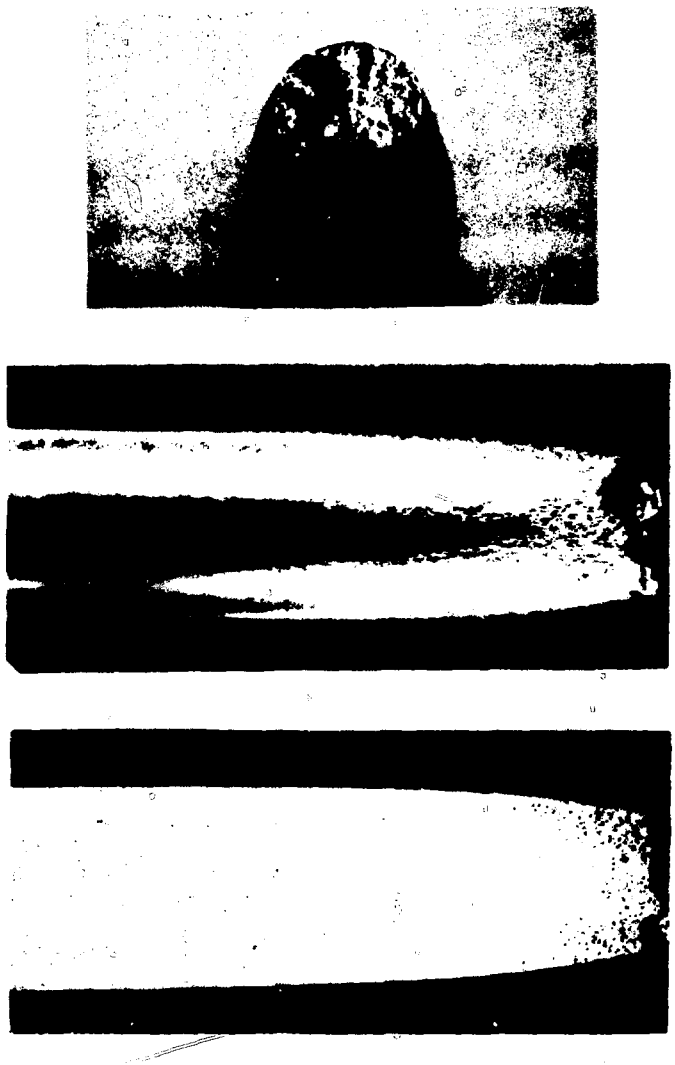

Fig. 6. Fracture Morphology and Microstructure for 520 appm Helium Niobium Tested at 1020°C. 8×.

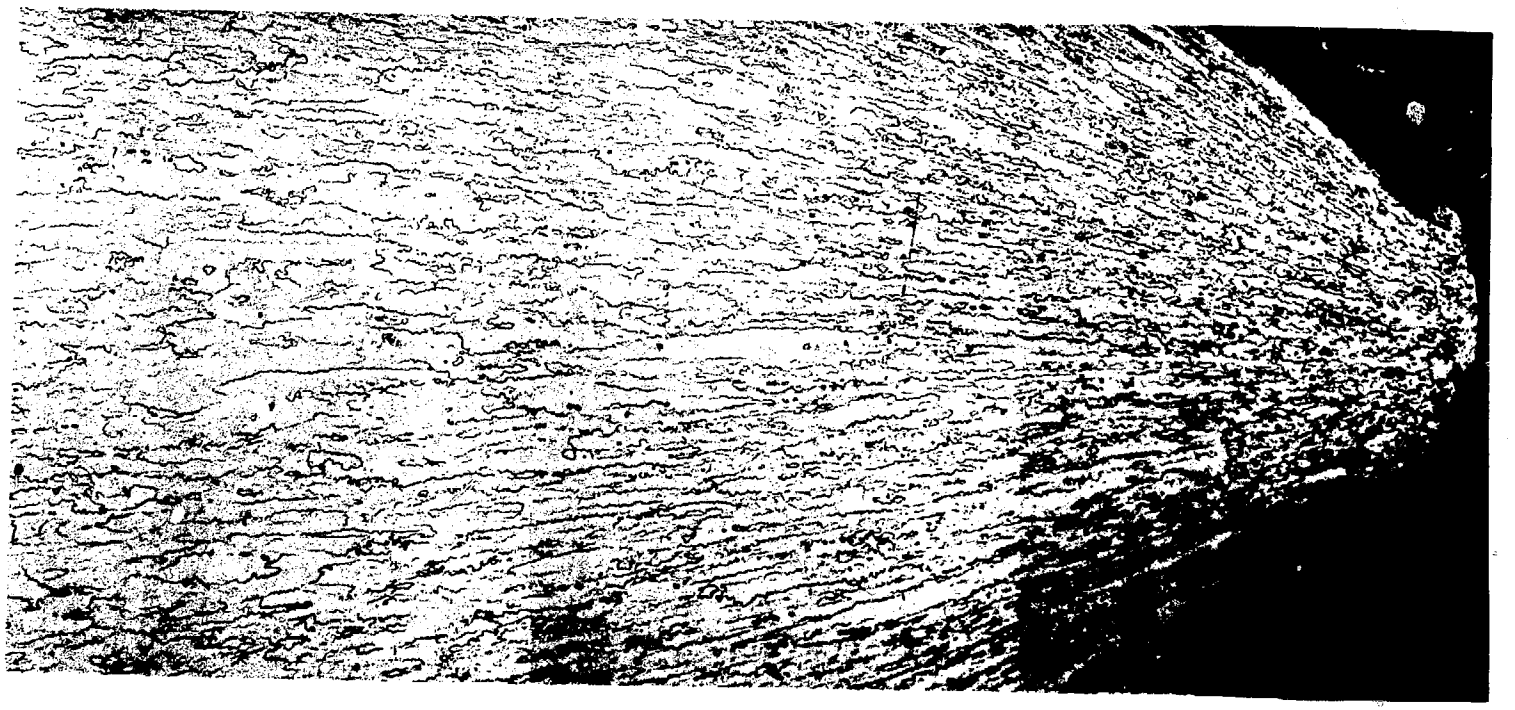

Fig. 7. Microstructure of the Fractured Region of Zero-Helium Niobium Tested at 1020°C. 100×.

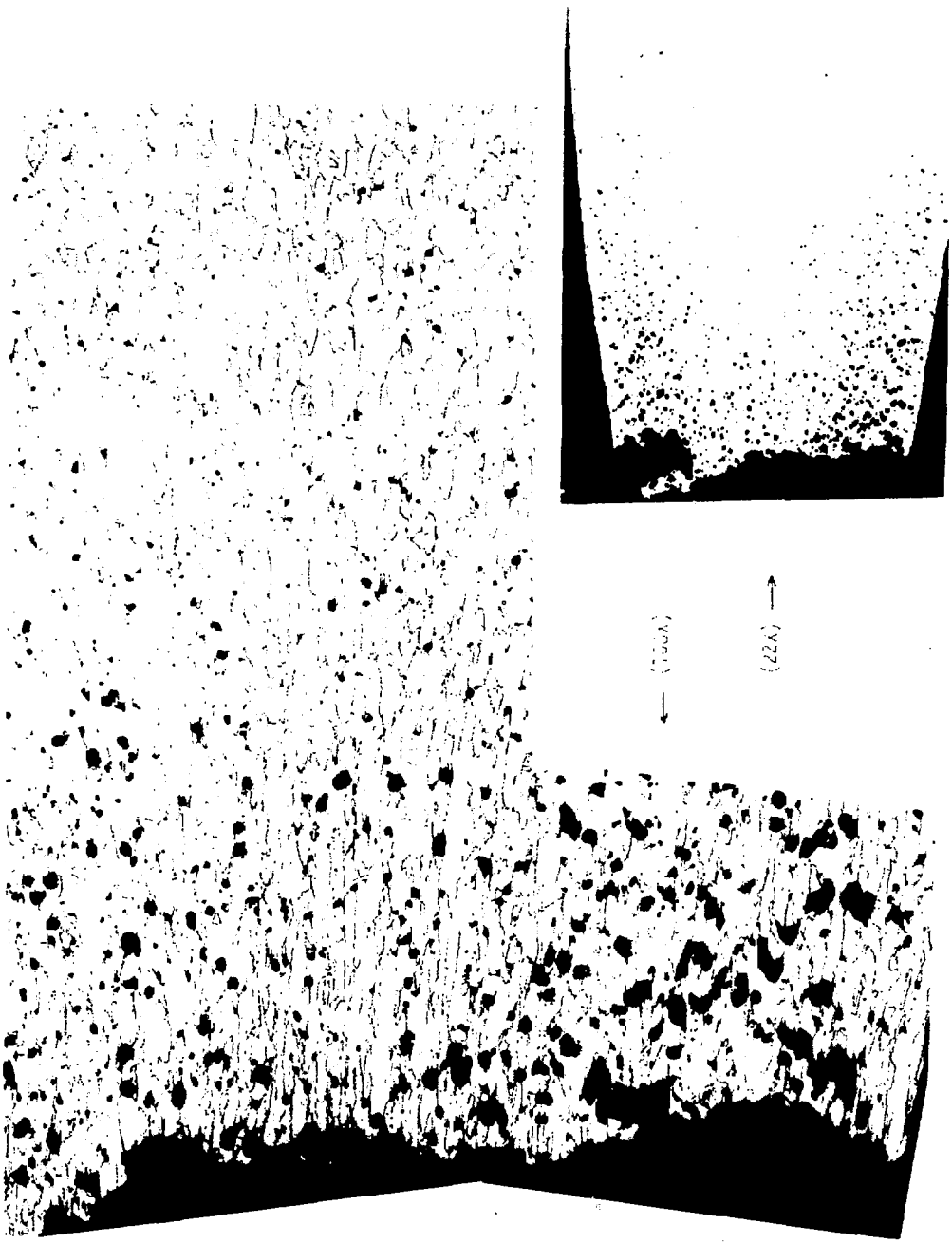

Fig. 8. Microstructure of the Fractured Region of 520 appm Helium Niobium Tested at 1020°C.

The 520 appm helium specimen microstructure shown in Figure 8 and again in the Scanning Electron Microscope photomicrographs in Figure 9 demonstrates that grain boundary decohesion is a major deformation mechanism at high plastic strains in high-helium content specimens.

The grain boundary separation in the high-helium niobium initiated preferentially at triple points and on boundary surfaces approximately perpendicular to the tensile axis. The series of photomicrographs in Figure 9 show that the grain boundary void size decreases with distance from the fracture surface. The void density was observed to decrease with increasing distance from the fracture surface; the last voids detectable by SEM approximately coincide with the beginning of the necked region. Figures 6 and 7 indicate that grain boundary separation after void nucleation continued by a grain boundary slip mechanism and resulted in a grain pull-out failure mechanism. The high-helium niobium fracture surface morphology presented in Figures 10 and 11 also indicate that the failure mechanism is grain boundary pull-out. Individual grains can be identified in Figure 10; however, no intergranular or transgranular cleavage is present. The lack of cleavage, along with the large amounts of localized plastic flow exhibited in the matrix near the grain boundaries in Figure 11, indicates a lack of helium-induced matrix embrittlement at the 1020°C test temperature.

A post-test Transmission Electron Microscopy (TEM) study revealed that no resolvable helium bubbles were present in the specimens with 30 or 60 appm helium. Very small isolated matrix and grain boundary helium bubbles were detected in the 130 appm helium specimen. Substantial numbers of helium bubbles were found in the specimens containing $\geq$ 250 appm helium. Figure 12 illustrates the typical size and distribution of helium bubbles found in the high-helium niobium. Both preferential grain boundary bubble nucleation and dislocation decoration are present.

DISCUSSION

This paper presents mechanical property degradation results for annealed commercial purity niobium helium charged by tritium decay. This helium charging method was chosen for two major reasons: the technique provides relatively fast charging rates, (up to three years

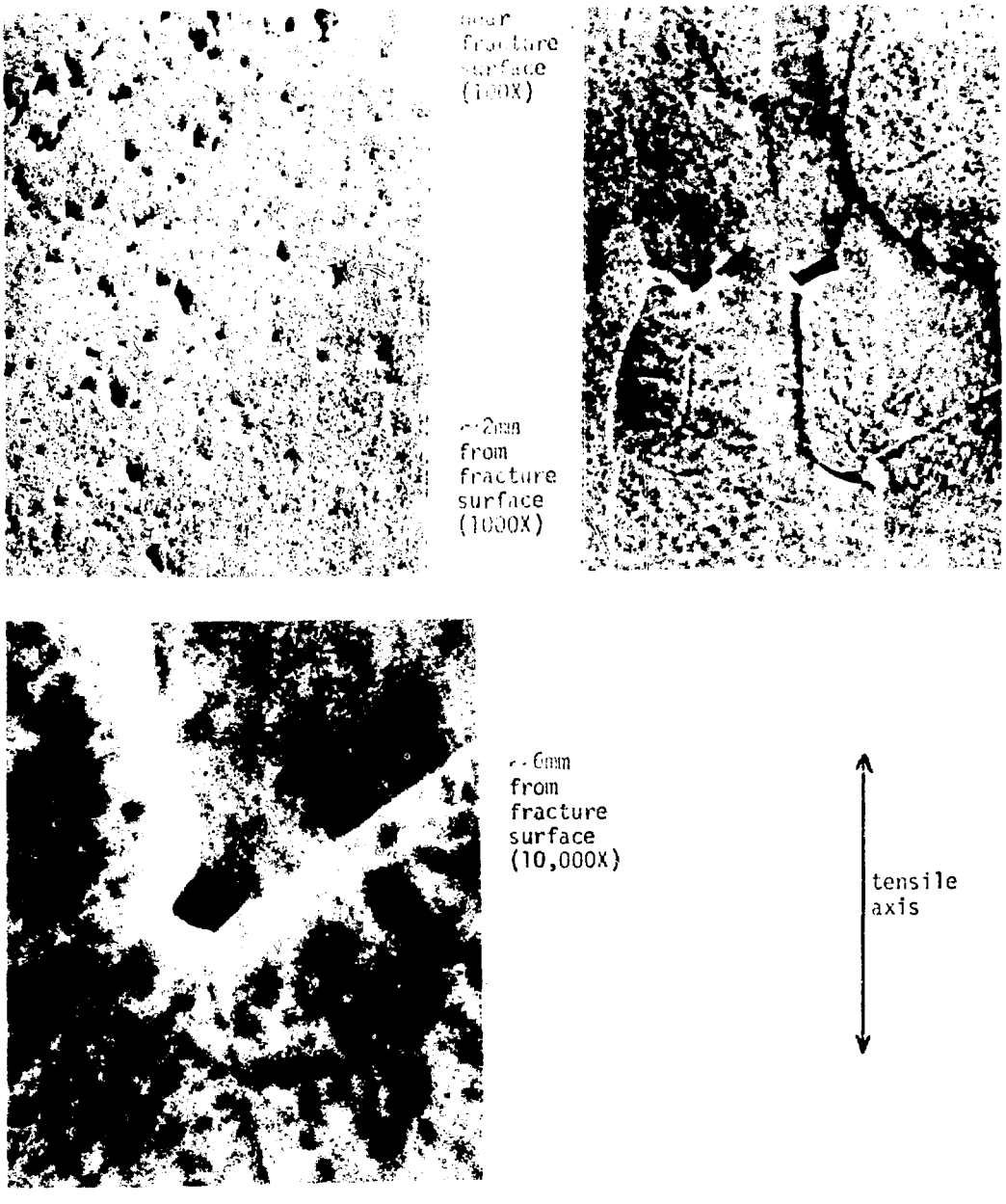

Fig. 9. Metallographic Evidence of Grain Boundary Decohesion in 520 appm Helium Niobium Tested at 1020°C.

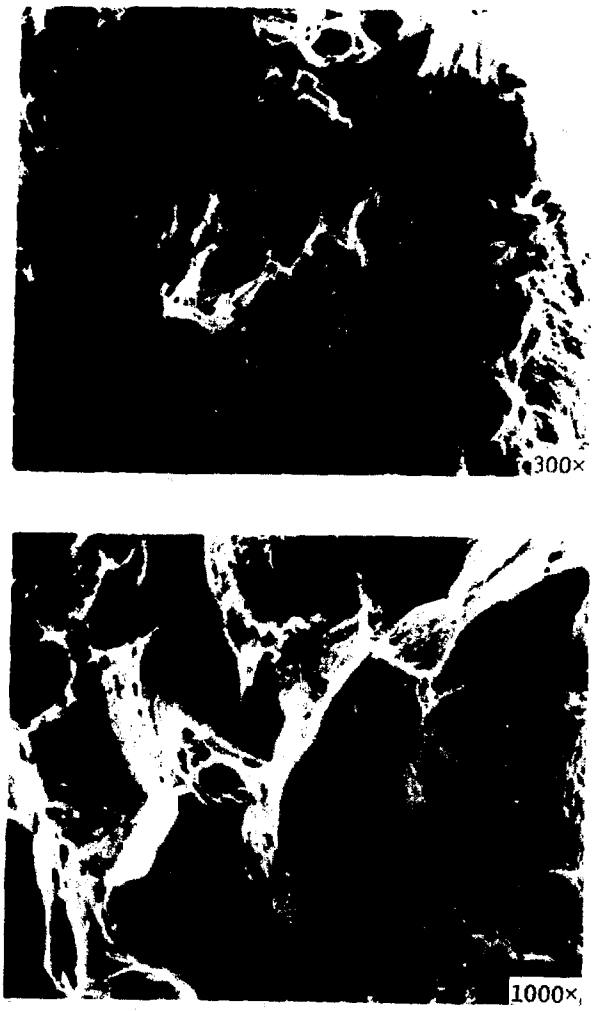

Fig. 10. Fractography of the Edge Region of the Fracture Surface of the 520 appm Helium Niobium Tested at 1020°C.

Fig. 11. Fractography of the Central Region of the Fracture Surface of the 520 appm Helium Niobium Tested at 1020°C.

Fig. 12. Typical Helium Bubble Distribution for 250 appm Helium Niobium Tested at 1020°C.

simulated helium accumulation per month of charging time were achieved in this study), and there is essentially no specimen thickness restriction, as this technique depends solely on tritium diffusing into the metal matrix. Helium analyses performed after the high temperature tensile tests indicate that uniform helium distributions were achieved in these specimens and that the predicted helium concentrations were attained with $\pm$ 10 percent.[2]

Experimental evidence indicates that helium produced by tritium decay is mobile at the 1020°C test temperature used in this study, as substantial amounts of both matrix and grain boundary bubbles are present in high-helium niobium (Figure 12). Bubbles were detectable in specimens containing $\geq$ 130 appm helium. The helium bubble distributions appear to be manifestations of a preferential bubble nucleation at grain boundaries; they thus duplicate the defect structures found in both neutron radiation induced helium damage and alpha bombardment specimens.[5,6]

The high temperature tensile test data (Figure 2) show definite helium-induced mechanical property changes. The most pronounced change is the decrease in both uniform and total elongation with increasing helium content. In general, the total elongation continuously decreases with increasing helium concentration, while the uniform elongation exhibits an abrupt drop around 300 appm helium.

The short-time high-temperature test cycle used in this study corresponds to that used by Santhanam[7] in the testing of thin foils of an alpha-bombarded high-strength vanadium alloy, V-15 wt% Cr - 5 wt% Ti. Testing of this alloy was conducted at elevated temperatures comparable on an absolute melting scale to the test temperature used in this study of niobium.[8] Helium contents of 25 appm drastically reduced the elongation of the vanadium alloy at elevated temperatures $\geq$ 750°C (0.47 T_m), as compared to the greater than 250 appm helium contents required to reduce the uniform elongation of annealed niobium at 1020°C (0.48 T_m). A joint PNL-ANL study is currently underway to determine if alloy effects, specimen thickness or helium charging technique is responsible for this large embrittlement discrepancy.

The abrupt drop in "uniform" elongation seen in Figure 2 coincides with a distinct change in stress-strain behavior of the niobium, i.e., there is a substantial strain hardening region after yield for specimens containing < 300 appm helium while there is essentially no strain hardening region for specimens containing > 300 appm helium (Figure 3). This abrupt change in stress-strain behavior, coupled with the other post-test specimen analysis results presented above, suggests that two competing deformation mechanisms are active under the high temperature tensile test conditions. The deformation mechanisms responsible for the observed stress-strain behavior are plastic deformation within the niobium grains and grain boundary sliding (GBS) and/or grain boundary decohesion.

Plastic deformation within the grain is to be expected at these test temperatures and appears to be the dominant mode of deformation at concentrations below 300 appm helium. It is postulated that GBS is responsible for the abrupt elimination of strain hardening shortly after the proportional limit is reached in specimens containing > 300 appm helium (Figure 3). The initiation of gross grain boundary separation (as seen in Figure 9) may be responsible for the abrupt load drop following the short "no-strain-hardening" region of these high helium specimens.

Grain boundary sliding is known to become a significant deformation mechanism at test temperatures near one-half the absolute melting temperature of a given metal. This deformation mechanism is, however, usually associated with creep tests rather than the relatively high strain-rate tensile test. Nevertheless, GBS can be induced during high strain-rate tests by a change in the strength properties of the matrix and/or the grain boundary, as the site of deformation is determined by the relative strength of the grain boundary compared to that of the matrix. The onset of significant GBS or grain boundary decohesion is controlled by the loss of the ability of the grain boundary to sustain the stress needed to actuate slip in adjacent grains in order to retain intimate contact between these grains.

Grain boundary sliding or decohesion takes place in order to accommodate external shape changes when the stress needed to actuate slip in adjacent grains is greater than the strength of the grain boundary.

Increasing the matrix strength and simultaneously decreasing the grain boundary load carrying area through the addition of helium and the formation of helium bubbles results in the critical stress for GBS being reached under the high-helium specimen test conditions used in this study.

A substantial concentration of helium bubbles on the grain boundaries of low strength niobium is required, however, before GBS becomes the dominant deformation mechanism. This is illustrated by the 250 appm helium specimen, for although there is a substantial helium bubble concentration on the grain boundaries in the 250 appm helium specimen, (Figure 12), its deformation characteristics are still controlled by plastic deformation within the matrix grains.

The stress-strain behavior of the high-helium specimens ($\geq$ 350 appm) can be rationalized when broken down into a multi-step process. The initial small strain-hardening region can be explained if a finite amount of strain (or strain hardening) is required to reach the stress needed to start GBS. After this critical stress is reached, GBS predominates during the "no-strain-hardening" stress-strain region. Gross grain boundary separation is initiated at the high-stress grain boundary triple points in this stress-strain region, thus reducing still further the load carrying area of the grain boundary. After sufficient grain boundary separation has taken place to initiate localized necking grain boundary separation becomes the predominant deformation mechanism, resulting in a substantial decrease in load carrying area with increasing strain; this results in an abrupt load drop until all, or nearly all, boundaries in the necked region perpendicular to the tensile direction are separated. A combination GBS and grain boundary decohesion then takes place, resulting in localized grain pull-out and specimen fracture. Evidence of grain boundary pull-out can be seen in the fracture surface morphology and fractured specimen cross-section photomicrographs in Figures 8 through 11.

The observation that detectable grain boundary separation is first seen in or near the beginning of the necked region suggests that necking in the high-helium specimens is instigated by grain boundary separation.

Theoretical modeling of GBS and grain boundary decohesion[9] indicates that a finite amount of GBS is required before the initiation of grain boundary separation, although helium bubbles may reduce or eliminate this nucleation strain. In the high-helium specimens, the presence of a stress strain region controlled by GBS is supported by the substantial amount of total elongation that cannot be accounted for by a combination of strain hardening and necking strain.

Two helium-induced phenomena observed in these niobium specimens are felt to enhance GBS. The first is the preferential nucleation of helium bubbles on the grain boundaries, as seen in Figure 12. Grain boundary bubble formation decreases the boundary's load carrying area, thus decreasing the grain boundary's shear strength relative to that of the matrix. The second effect is the matrix strengthening seen in the increase in yield strength with increasing helium content. This also increases the matrix strength relative to that of the grain boundary. Thus, both helium bubble formation and matrix strengthening enhance the probability of GBS.

The matrix strengthening with increasing helium content observed in these specimens as well as in other refractory metals and alloys[7,8,11] may come from helium atoms pinning dislocations, helium bubble formation, and/or interstitial and substitutional strengthening. Interstitial helium is expected to be present in niobium containing helium implanted by tritium decay as the parent tritium atom occupies an interstitial site. It is expected that this interstitial ^{3}He will tend to drop into substitutional lattice sites, as this has been reported as the ^{4}He diffusion site.[10] It is probable that interstitial helium is also present in neutron irradiated niobium. It has been proposed that helium implanted with concurrent radiation damage may end up in interstitial as well as substitutional sites and will be capable of interstitial diffusion until it drops into substitutional lattice sites or removes itself from the matrix by interaction with structural defects. Thus neither interstitial nor substitutional helium effects in CTR materials can be ruled out a priori. Lattice parameter studies are being conducted concurrently with density measurements and strengthening model calculations in the hopes of determining the various helium-matrix interactions responsible for the observed matrix strengthening.

The maximum helium concentration contained in the specimens prepared for this study correlates with ∿ 21 years predicted helium accumulation for a niobium CTR first-wall. However, the helium distributions present in these specimens are not expected to be directly comparable to those found in CTR-exposed niboium as the first-wall will see a neutron lattice damage component and a long-time high-temperature exposure not seen by the specimens in this study. Helium-induced defects are predicted to be the controlling mechanical property degradation mechanism at these high temperatures. It is expected that exposure to neutron-induced damage and the corresponding long times at elevated temperature will mainly accelerate diffusion processes and not substantially change the observed deformation mechanism sequence.

The increased helium diffusion (and possibly bubble nucleation kinetics) under fusion reactor conditions is expected to reduce the amount of helium needed to initiate GBS from that found in this study, due to an expected increase in the concentration of helium bubbles on grain boundaries. The helium-induced strengthening effect would be expected to decrease due to a depletion of helium in the matrix with increasing bubble formation if dislocation decoration or solid solution hardening is the strengthening mechanism; this would decrease the probability of GBS. The strengthening effect would increase if helium bubble formation in the matrix is the strengthening mechanism; this would increase the probability of GBS.

It is predicted, however, that the matrix strengthening effect on GBS initiation will be less important than the increased helium bubble formation, resulting in GBS at a lower helium concentration than required in the present tests. A high temperature anneal study is currently proposed in hopes of achieving a closer simulation of the actual material condition to be expected after CTR exposure in order to experimentally determine the interaction of the various deformation mechanisms and their effects on mechanical properties.

CONCLUSIONS

The experimental results illustrate the potential of the tritium-decay helium-charging technique for studying the effects of internal helium on materials with high tritium solubilities, such as the refractory metals. The on-going research effort at PNL using this helium implantation method is directed toward developing an understanding of helium phenomena in metals which will serve as a basis for determination of alloy design parameters capable of predicting material requirements needed for maximum resistance to helium-induced degradation.

The helium-induced mechanical and microstructural property changes noted for the annealed commercial purity niobium tested at 1020°C are listed below:

- Elongation decreases with increasing helium content. Total elongation decreased continuously at a rate of $\sim$ 7 percent per 100 appm helium; uniform elongation decreases continuously until 350 appm helium is reached and then abruptly drops to less than 2 percent elongation.
- Yield and ultimate strengths increase with increasing helium content.
- Helium bubbles were detected in niobium at helium concentration $\geq$ 130 appm; preferential bubble formation on grain boundaries and dislocations was observed.
- Grain boundary decohesion was present in the necked region of the 500 appm helium experiment.

ACKNOWLEDGMENTS

This work was performed under ERDA contract No. AT(45-1)-1830.

REFERENCES

1. W.V. Green, "Tritium Effects and Some Possible Fatigue Effects in Pulsed Reactors," WASH-1206, 57 (April 1972)

2. J.F. Remark, A.B. Johnson, Jr., H. Farrar IV, and D.G. Atteridge, Helium Charging of Metals by Tritium Decay, to be presented at the San Francisco ANS Meeting (November 1975)

3. W.M. Mueller, J.P. Blackledge, G.W. Lidowitz, Metal Hydrides p. 597, Academic Press, New York, 1968

4. G.L. Kulcinski, O.G. Doran and M.A. Abdou, Comparison of Displacement and Gas Production Rates in Current Fission and Future Fusion Reactors, UWFDM-15 (April 1974)

5. E.E. Bloom and F.W. Wiffen, The Effects of Large Concentrations of Helium on the Mechanical Properties of Neutron-Irradiated Stainless Steel, ORNL-TM-4861 (May 1975)

6. F.A. Smidt, Jr. and A.G. Pieper, Studies of the Mobility of Helium in Vanadium J. Nucl. Mater., 51, 361 (1974)

7. A.T. Santhanam, Effects of Helium on High Temperature Tensile Properties and Swelling of Vanadium and Vanadium Alloys, IEEE-73-CH0843-3-NPS (November 1973)

8. J. Moteff, Irradiation Effects on the Mechanical Properties of BCC Metals, WASH-1206 (April 1972)

9. F.W. Grossman and M.F. Ashby, Acta Met., 23, 425 (April 1975)

10. D.C. Johnson and J.R. Cost, Nuc. Metallurgy, 18, 279 (1973)

11. D. Kramer, K.R. Gan, A.G. Pard and C.G. Rodes, A Survey of Helium Embrittlement of Various Alloy Types, in Irradiation Embrittlement and Creep in Fuel Cladding and Core Components, p. 109, British Nuclear Society, London (1973)

MECHANICAL BEHAVIOR OF Nb-1%Zr IMPLANTED WITH He AT VARIOUS TEMPERATURES

A.A. Sagüés and J. Auer
Institut für Festkörperforschung der Kernforschungsanlage Jülich
D 517 Jülich, Germany

ABSTRACT

Nb-1%Zr polycrystalline foils of commercial purity were He-implanted at 50°C and 600°C by a cyclotron α-particle beam of variable energy to homogeneous concentrations in the 10^{-6} to 10^{-4} at. range. Tensile tests were made after implantation at a 10^{-4} sec^{-1} strain rate and temperatures from 20°C to 800°C. The material implanted at 50°C exhibited radiation damage effects that annealed out when tested at the higher temperatures. In the whole temperature range the mode of foil fracture is transgranular and its characteristics appear unaffected by He concentrations of up to 80 at. ppm even when the foils are annealed under stress at temperatures between 650°C and 1000°C prior to the tensile test. The material implanted at 600°C presents some reduction in ductility but still shows transgranular fracture. T.E.M. samples were prepared from the tensile specimens and from implanted material subjected to anneal under stress at up to 1300°C, and preliminary examinations reveal no features that can be identified with He segregation. Helium release measurements are discussed together with the T.E.M. results in terms of He distribution during implantation and post-treatment.

INTRODUCTION

Nb-Zr alloys are an important candidate for the first wall material of fusion reactors. Present designs[1] foresee total neutron fluences between 10^{22} and 10^{23} n/cm^2/year resulting in the production of He through (n, α) reactions at rates varying from 10 at. ppm/yr to 200 at. ppm/yr. Since such concentration levels are known to strongly reduce the ductility of other reactor alloys operating at high equivalent temperatures, is necessary to determine the extent and nature of the effects of

comes more pronounced because most of the He embrittlement data available now concerns austenitic steels while few body centered cubic alloys have been studied in this direction.

As a result, a commercial purity Nb-1Zr alloy was chosen to characterize its behavior in the temperature and He concentration range expected in a fusion reactor application.

TECHNIQUE AND RESULTS

He concentrations of the magnitude earlier mentioned cannot yet be produced in a reasonable time by means of (n, α) reactions, and some type of simulation technique had to be used. The choice was made of He implantation by means of a variable energy cyclotron beam because of its simplicity and because the high-damage environment of the just implanted atom is presumed to resemble actual conditions better than what is expected in other techniques (for example, tritium decay[2]).

The alloy was supplied by Hereaus, W. Germany, in the form of sheets 50 μ thick. The sheets were spark cut to the standard tensile specimen shape shown in Fig. 1. The interstitial impurity content of the as-received material is indicated in Table 1. The specimens were then degreased and annealed for 1 hr. at 1500°C in a vacuum of $5 \cdot 10^{-10}$ torr. This results in a structure that remained stable during the subsequent tests. The annealing temperature is a compromise between tolerable contamination and convenient grain size. The latter is $\sim$ 20 μ, or 2 to 3 grains per specimen thickness.

Table 1. Nominal interstitial impurity content of the as-received Nb-1% Zr alloy

	C	H	N	O
at. ppm	1000	1000	700	2500

Fig. 2 shows the experimental arrangement used for the cyclotron implantation. A defocused α-particle beam was swept along the specimens while its energy was varied by continuously moving the interposed aluminum wedge. The excursion of the wedge was adjusted so as to obtain penetration ranges varying from zero to just above the thickness of the overimposed specimens that made the target. Uniform He deposition through and along the specimens was thus achieved. Plate A serves the purposes of final energy degrader, of holding the specimens in place and, together with plate B stabilizes the temperature of the specimens. Temperature fluctuations due to beam current and energy variations were compensated by the regulated oven block. The pressure in the irradiation chamber was of $1 \cdot 10^{-5}$ torr. Irradiation times and currents were adjusted to obtain He concentrations between 8 and 100 at. ppm.

Tensile tests were performed at a strain rate of 10^{-4}/sec in a He atmosphere with an estimated Oxygen partial pressure of $2 \cdot 10^{-7}$ torr, and in the temperature range from 20 to 800°C. Oxygen pick up as determined from resistivity ratio measurements on control Nb strips was not enough to alter significantly the mechanical response of the commercial alloy. However, as it will be considered later, contamination effects become important in the high temperature implantations done in the 10^{-5} torr atmosphere of the cyclotron chamber. Typical stress-strain curves for the sheet specimens at low and high temperatures are shown in Fig. 3. The specimen geometry and loading conditions reduce strongly the non uniform deformation of the curve. At room temperature the yield stress is well defined and the curve is rather smooth. At or above 650°C the yield stress is less defined and serrated flow is observed in all apecimens.

Fig. 4 summarizes the ultimate and yield stress data for He implanted as well as uninplanted control specimens. The yield stress of implanted specimens tends to be higher at low temperatures than that of the controls. This effect, is probably due to irradiation damage produced during implantation and anneals out at the higher temperatures. The ultimate tensile stress results are practically the same for implanted or unimplanted specimens.

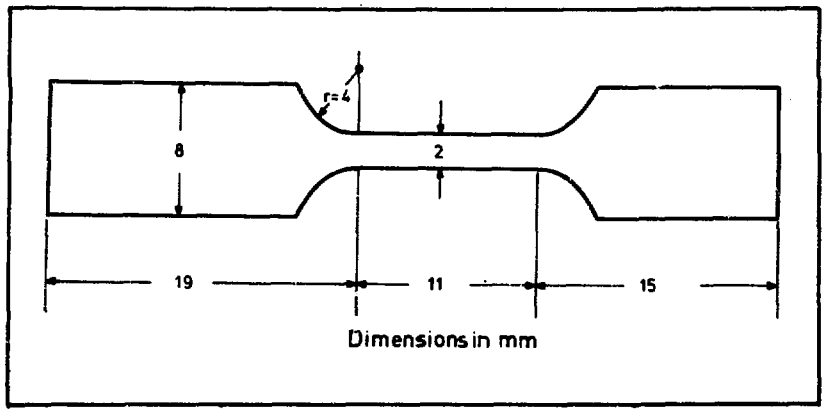

Fig. 1. Shape of Tensile Foil Specimens

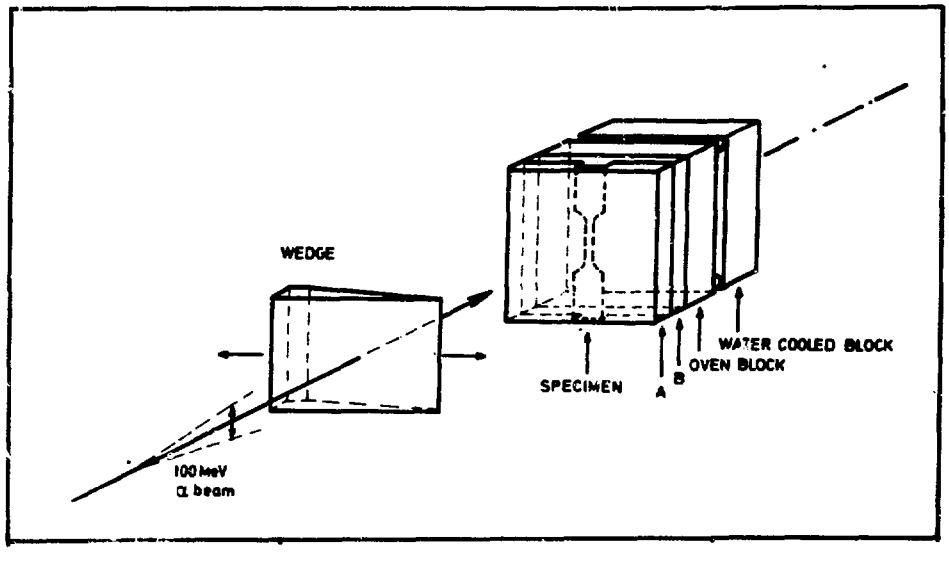

Fig. 2. Helium Implantation Arrangement

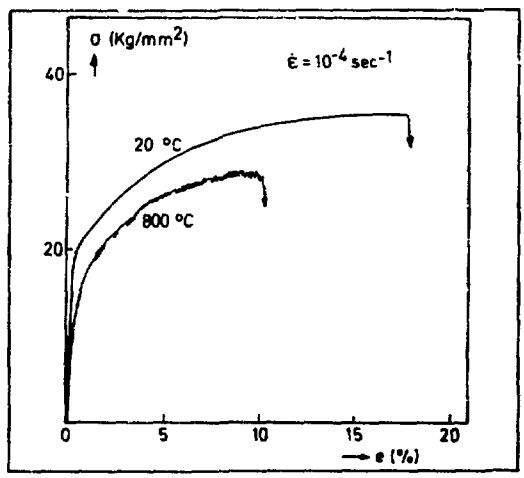

Fig. 3. Load Elongation Curves of Control Specimens

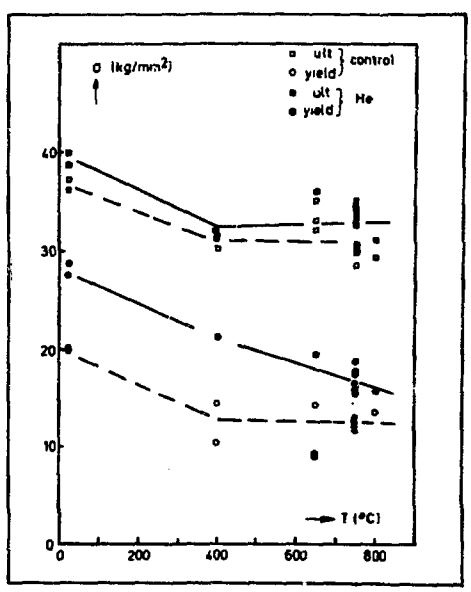

Fig. 4. Ultimate and Yield Stress Data

The implanted specimens had He concentrations varying from 8 to 80 at. ppm, but their yield and ultimate stress values show no trend with changing concentrations. The shape of the stress-strain curves was not affected by He at the high temperatures. Fig. 5 shows the values of total elongation to fracture (which in our case is the same as uniform elongation). This parameter is again unaffected by He concentrations implanted at 50°C between 8 and 80 at. ppm. Some of the specimens (□) were held near the yield stress at the test temperature for 60 minutes before continuing the test. This procedure did not affect the total elongation. Specimens marked (▽) were annealed on a vacuum of $1 \cdot 10^{-9}$ torr for 300 minutes at 1000°C while being spring-stressed at 10 kg/mm^2. The subsequent tensile test again showed no difference between implanted and control specimens.

Some preliminary experiments with thicker (100 μ) foils agree with the results of the 50 μ material.

The material irradiated at 600°C (x) shows some decrease in total elongation but this material presented also a visible surface contamination layer after being implanted.

Scanning electron micrographs of the fracture surfaces revealed ductile, transgranular fractures in all cases (Fig. 6). No instances of intercrystalline fractures were observed.

Transmission electron microscope examination of the tensile tested specimens showed no hints of bubbles or other He segregation feature either at the grain boundaries or inside the grains. The minimum detectable bubble size was set at ∿ 50 Å after taking into consideration the presence of a high density of dislocations.

A group of 50°C implanted specimens containing from 8 to 100 at. ppm He was annealed for periods of 300 minutes at temperatures ranging from 1000°C to 1300°C, while being spring-stressed at 10 kg/mm^2. As before this treatment was done in a $1.0 \cdot 10^{-9}$ torr vacuum. Transmission electron microscopy failed again to reveal He segregation. Bubbles were also absent in samples loaded with 30 at. ppm He and annealed unstressed at 2200°C for 15 minutes in the same ultra high vacuum conditions. However,

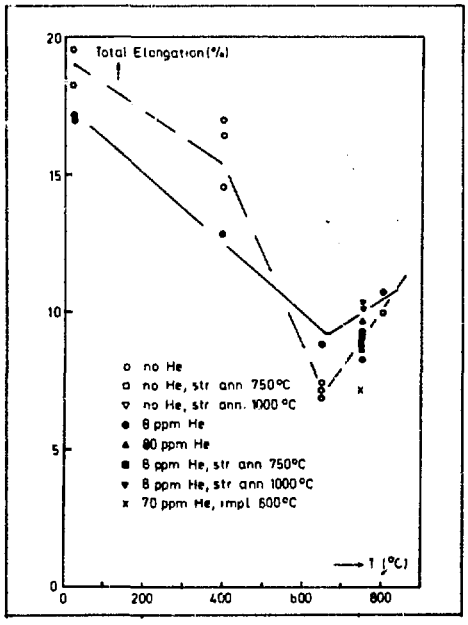

Fig. 5. Total Elongation to Fracture

Fig. 6. Fracture Surface of a Specimen containing 70 at. ppm He and tested at 750°C (X 1250)

it must be noted that in this case the large grain size resulting from the high temperature anneal made impractical the examination of the grain boundaries with the electron microscope.

Some preliminary experiments measured the release of He out of a specimen loaded with 8 at. ppm when its temperature was being increased at a constant rate of 1.7°C/sec. Fig. 7 shows the rate of emission and the integrated emission as a function of temperature. The total amount emitted is, within the present accuracy of our measurements in agreement with the amount of He calculated from the cyclotron implantation parameters. (This specimen was implanted at 50°C.)

In order to emphasize the insensitivity of the alloy to the introduction of He a comparison is made with the results of experiments being now conducted in a parallel study of He embrittlement of austenitic steels, using the same implantation and mechanical test equipment. Fig. 8 shows some of the TEM evidence of He bubble formation in commercial 316 stainless steel and DIN 1.4970 stainless steel after He implantation and subsequent anneal. Table 2 exemplifies loss of ductility. These results will be fully presented elsewhere.

Table 2. Total elongations to fracture (%) for commercial 316 stainless steel at 700°C

	$\dot{\varepsilon}(sec^{-1})$		Creep Test
	$3 \cdot 10^{-4}$	$7 \cdot 10^{-5}$	700°C
Control	17.7	17.4	32.6
8 ppmHe	13.4	13.4	14.5

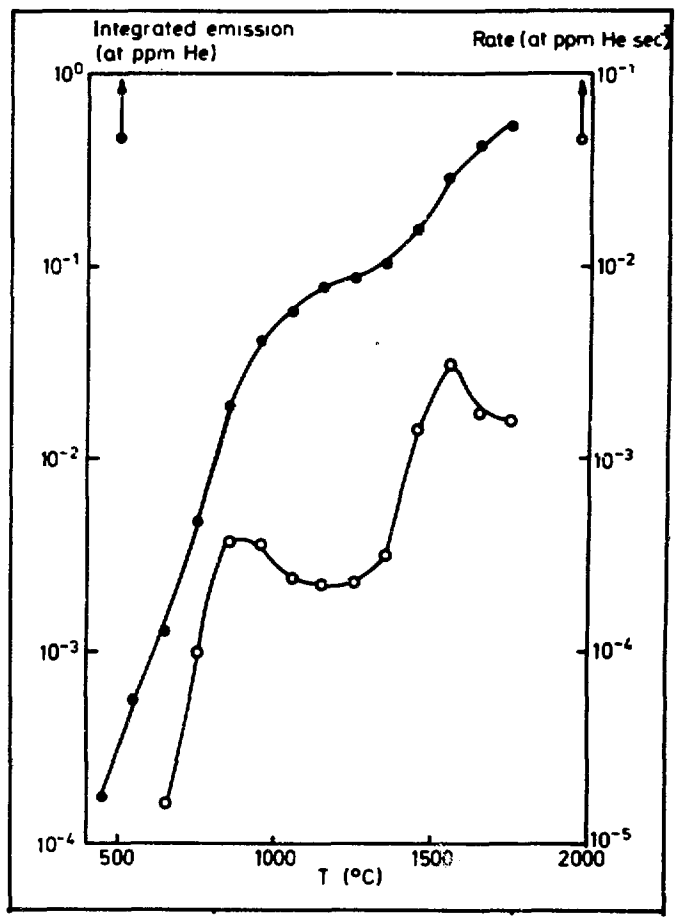

Fig. 7. He release from a Nb-1%Zr specimen loaded with 8 at. ppm He. $T = 1.7^{\circ}C\ sec^{-1}$

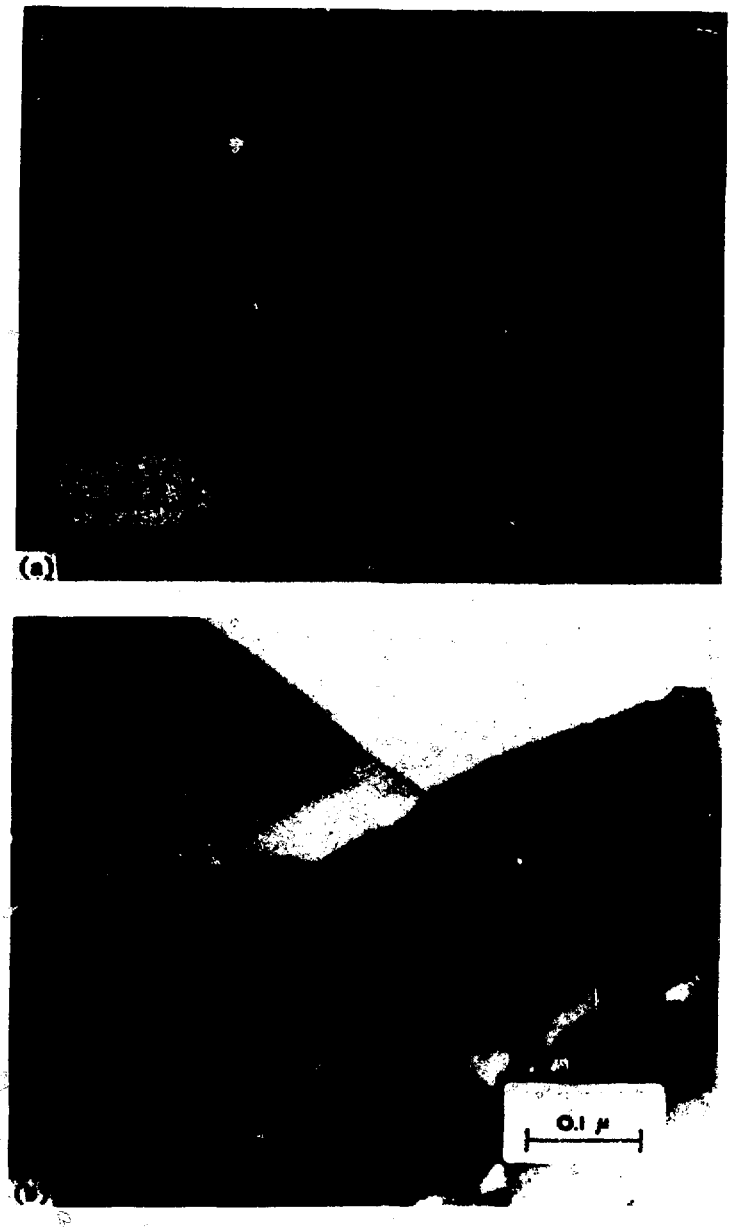

Fig. 8a. He bubbles on a AISI 316 stainless steel loaded with 8 at. ppm He and annealed for 1 hr at 1000°C

Fig. 8b. He bubbles on a DIN 1.4970 stainless steel loaded with 100 at. ppm He and annealed for 1 hr at 900°C

DISCUSSION

It seems clear that at the strain rate, temperatures and concentration range on which the tensile experiments were performed no embrittlement effect due to the presence of He is observed. The small loss of ductility at the lower temperatures is satisfactoryly explained by the radiation damage expected from the implantation procedure (about 10^{-2} dpa typical), and its annealing out at the higher temperatures is in agreement with previous observations[3]. The small effect observed for the material implanted at 600°C is not accompanied by changes in the appearance of the fracture surface. The poor vacuum conditions existing in the cyclotron chamber, coupled with surface decoloration observed after implantation suggest that interstitial impurity absorption resulted in a small reduction of ductility[4].

The present tensile experiments were conducted at relatively high strain rates. The extension of these results to the expected first wall conditions may require some creep measurements, which are in the case of thin Nb-base foils seriously limited by gas contamination even on UHV conditions. On the other hand most alloys that present He embrittlement on creep tests do have residual effects at strain rates similar to the one used here. The absence of such effect would indicate that its magnitude in the most favorable conditions is not very large. This impression is further substantiated by the insensitivity of the fracture parameters to the anneals in situ near the yield stress. These were intended to provide enough time and elastic energy to initiate an embrittlement mechanism that would involve helium segregation; for example, stress induced bubble growth at the grain boundaries, resulting in bubble coalescence and intergranular fracture[5,6]. The same applies to the specimens annealed at up to 1300°C under stress before being tensile tested.

The absence of He bubbles at or away from the grain boundaries in all the specimens favors the interpretation of the mechanical experiments given above. Previous publications[7] report the presence of He bubbles in Nb loaded with ∿ 150 at. ppm He after annealing above 1000°C. This observation does not conflict with our conclusions since the size of

those bubbles was at or below our detection limit. Moreover, their size and density was not seen to change when the annealing temperature was increased, an indication that growth or coalescence was being hindered. Should the application of tensile stress result in appreciable bubble growth, bubbles would have become observable in our stress annealed specimens, which was not the case.

The He release results are in general agreement with previous investigations in pure Nb[7], suggesting that the presence of substitutional Zr has little effect on the internal distribution and mobility of He. Some experiments are now in progress concerning He emission at various temperature rates and electron microscopy of polycrystalline samples with much higher, localized concentrations of implanted He.

The results of mechanical tests with foil specimens can be extrapolated to the bulk material with certain restrictions, as discussed elsewhere in this meeting[9].

The absence of He bubbles at the grain boundaries of the material examined should be fairly unrelated to specimen thickness in our experiments. This is supported by the observation of He intergranular bubbles in the stainless steel foils, which have a similar grain size to thickness ratio.

CONCLUSIONS

In the temperature range 20 to 800°C the ductility of Nb-1 Zr is not significantly affected by the presence of up to 80 at. ppm of implanted He.

The above result is valid for foil specimens tested at strain rates of 10^{-4}/sec, and there is evidence that it could be extended to the bulk material.

ACKNOWLEDGEMENTS

The authors are indebted to Dr. P. Jung for the He release experiments.

REFERENCES

1. W. F. Wiffen, Private Communication

2. R. G. Hickman, Proc. of the First Topical Meeting on the Technology of Controlled Nuclear Fusion, Vol. II, p. 535, J. R. Hopkins, Editor, San Diego, Calif. 1974

3. M. J. Makin and F. J. Minter, Acta Met. 7, 361 (1959)

4. C. R. Tottle, J. Inst. Metals 85, 375 (1957)

5. R. S. Barnes, Nature 206, 1307 (1965)

6. E. E. Bloom, Irradiation Embrittlement and Creep in Fuel Cladding and Core Components, p. 93, The British Nuclear Energy Society, London 1973

7. D. L. Johnson and J. R. Cost, Defects and Defect Clusters in B.C.C. Metals and Their Alloys, p. 279, R. J. Arsenault, Editor, Maryland 1973

8. J. Auer and A. A. Sagüés, this Conference

CREEP AND TENSILE PROPERTIES OF HELIUM INJECTED Nb–1% Zr

F. W. Wiffen

Metals and Ceramics Division
Oak Ridge National Laboratory
Oak Ridge, Tennessee 37830

ABSTRACT

Specimens of commercial purity Nb–1% Zr were helium doped by cyclotron α-bombardment near room temperature to gas contents near 2 and 20 appm He, corresponding to helium production in a CTR first wall during approximately one month and one year of operation at 1 MW/m^2 neutronic wall loading. These specimens were tensile and creep tested to evaluate the effect of helium, in the absence of other components of CTR radiation effects, on the mechanical properties. Tensile tests at 1000 and 1200°C show no significant effect of either helium level on the strength or elongation values. Creep-rupture tests at the same temperatures on Nb–1% Zr showed rupture elongations somewhat reduced in the helium injected samples but the dependence on helium content and on test temperature does not fit the usual effect of helium on elevated temperature ductility. We thus conclude that in the absence of displacement damage this alloy is resistant to elevated-temperature embrittlement for helium contents up to 20 appm. The resistance to embrittlement results from the precipitation of helium on a submicroscopic level and from the alloy's inherent resistance to grain boundary separation.

INTRODUCTION

A distinct difference in the radiation response for a structural material in a CTR and in a fission reactor lies in the much higher rate of helium production in the fusion reactor. The helium is the product of transmutation reaction; including (n,α) and more complex reactions. The general conclusion of radiation effects experience is that the amount of helium generated will affect the changes produced in

*Research sponsored by Union Carbide Corporation under contract with the Energy Research and Development Administration.

engineering properties during neutron irradiation. In particular, it has been found that helium can affect the swelling, through both its influence on the cavity nucleation process and through control of the cavity growth rate.[1] Helium also has a very important influence on the mechanical properties through its influence on the fracture mode at elevated temperatures. The influence of helium has been documented in a number of cases to result in severely reduced elongation by promotion of high-temperature intergranular fracture.[2] Although the details of the machanism remain in doubt, it has been well documented that in many systems the insoluble helium is collected preferentially at the grain boundaries, forming bubbles visible by electron microscopy techniques. Under the influence of stress, these grain boundary cavities expand along the boundary, in many cases linking up, and lead to failure by separation of the boundary. This process results in a loss of elongation (compared to a helium-free test) with little or no effect on the strength properties.

Among the many candidate alloys proposed by conceptual design studies for use as the CTR first-wall material is Nb—1% Zr. Attractive features of this alloy include strength and compatibility with liquid metals, making it suitable for use at temperatures higher than possible with stainless steel or nickel-base alloys, and formability, weldability, and low-temperature ductility superior to many of the other refractory alloys. Another point in favor of the use of Nb—1% Zr is its status as a developed, available commercial alloy. In this regard it is superior to possible vanadium-base alloys, where alloy optimization has not yet been accomplished. On balance, there are also unattractive features associated with the possible use of Nb—1% Zr. Major difficulties with the use of this alloy would include the long-term induced radioactivity and the problems associated with the alloy's affinity for oxygen and other interstitial contaminants.

Niobium in service in a CTR at a first-wall neutronic wall loading of 1 MW/m^2 (typical of current conceptual designs) will transmute to produce helium at a rate of 24 appm per year of operation.[3] The main solid product of the transmutation reactions will be Zr, produced at

about 0.12% per MW-year/m^2 of reactor operation,[4] and this will have only a modest effect[5] on the properties of interest of Nb–1% Zr. In contrast to this, irradiation of the same alloy in the currently available high-flux fission reactors will produce much lower helium concentration, ≈1 appm per year in EBR-II or ≈2 appm per year in HFIR. Displacement damage will be produced at high rates in any of these systems, 7.2 dpa per year for a CTR, 23 for EBR-II, and 20 for HFIR. Thus, while adequate simulation of the displacement rates for CTRs can be achieved in current fission reactors, the right combination of dpa and helium content cannot be achieved for Nb–1% Zr. A necessary first step to the prediction of CTR radiation effects in Nb–1% Zr is the separate examination of helium effects in the absence of displacement damage.

An attempt can be made to predict the effect of helium on the elevated-temperature mechanical properties of Nb–1% Zr by application of available information on helium effects in other alloy systems. In alloys based on aluminum, iron, and nickel, helium has been found to reduce tensile ductility in tests at temperatures of half the melting point (0.5 T_m) or higher.[2,6] Although there is little experimental data on the bcc refractory metals, one experiment on a complex niobium alloy[2] and a series of experiments on vanadium alloys[7,8] show that the helium embrittlement process is not restricted to fcc alloys, but also occurs at about the same homologous temperatures in at least some bcc metals. In the vanadium alloys, embrittlement was found for tensile test temperatures of 750°C or greater (~0.5 T_m). As with the fcc alloys, the embrittlement of vanadium alloys was accompanied by intergranular fractures. A promising phase of the vanadium alloy work, however, was the demonstration that some of the alloys tested were resistant to the embrittlement.[7] On the basis of this evidence, it can be hoped that other promising alloys can be identified that possess unusual resistance to the helium embrittlement.

The experiment reported here was designed to investigate the effects of helium, in the absence of high levels of displacement damage, on the ductility of Nb–1% Zr. The temperature range of interest was

800 to 1400°C (0.4 to 0.6 T_m) and both tensile and creep tests were used to determine failure elongations. Post-test examination of the fractures and near-fracture material include optical metallography, transmission electron microscopy, and scanning electron microscopy.

EXPERIMENTAL DETAILS

The material used in this study was commercial grade Nb—1% Zr, obtained from the Wah Chang Corporation, with partial chemistry given in Table I. Metallic impurities included 610 ppm Ta, <300 ppm W and lower levels of other elements. The material was received from the vendor as 0.060-in. sheet, containing at least 40% cold work. The sheet was further cold-rolled (without intermediate heat treatment) to a final thickness of 0.0105 ± 0.0005 in. Tensile specimens with a length of 2.75 in. and a reduced gage length section 0.25 in. wide by 0.75 in. long were machined from the sheet. The cleaned specimens were annealed in a vacuum at pressures $\leq 1 \times 10^{-6}$ torr for 1 hr at 1200°C.

Table I. Chemical Analysis of Nb—1% Zr

Element	Content, wt %	
	Vendor[a]	ORNL
Zr	0.95	0.91
O	0.0205	0.0160
N	0.0090	0.0085
H	0.0002	
C	0.0065	0.0045
Si	<0.010	

[a]Wah Chang Corporation, Heat No. 1012-946.

Helium was injected into the flat sheet specimens by degrading a ~50-MeV α-beam from the Oak Ridge Isochronous Cyclotron with a rotating energy degrader of continually variable thickness. Target specimen racks

scanned in two dimensions through the beam produced a nearly uniform helium concentration throughout the test portion of the sample. Specimens were mounted on a water-cooled rack and were further cooled by a refrigerated jet of air directed at the target position. The temperature of the specimens spiked to somewhat less than 200°C each time the specimens passed through the beam, but the exact temperature on each pass is not known. The specimen temperature dropped rapidly to ~20°C as it moved out of the beam on each pass. The helium injection technique has been described in detail by King.[6]

Helium contents of 1.7 and 18 appm were achieved in the injection runs, with helium contents determined by H. Farrar IV of Atomics International by a technique using sample vacuum fusion and mass spectrometer analysis of the released gases. Absolute uncertainty in gas contents determined by this method is estimated to be less than 2%.

Mechanical property tests were performed in cold-wall, resistance-heated vacuum chambers which were pumped with liquid-nitrogen cold-trapped oil diffusion pumps. The vacuum during tensile tests was typically $<1 \times 10^{-6}$ torr and $\leq 2 \times 10^{-7}$ torr during creep tests. Tensile tests were conducted on an Instron testing machine and creep tests were in ORNL-developed test stands. The creep load was transmitted via a dead-weight load and direct-ratio pulley system to a pull-rod that passes through the vacuum chamber in a conventional U-cup vacuum seal. Strain measurements were taken from cross-head travel in tensile tests and from pull-rod motion in creep tests.

RESULTS

The tensile properties of samples tested at 1000 and 1200°C are given in Table II. The data on strength and elongation properties scatter within the normal scatter range expected for tensile tests, with no indication of either strengthening or ductility reduction that could be attributed to the presence of the injected helium. Reduction in area was effectively 100% in all tests, with fracture occurring only after necking to form a chisel point.

Table II. Tensile Properties of Nb–1% Zr Alloy Containing Helium[a]

Test Temperature (°C)	Helium Content (appm)	Stress, psi		Elongation, %	
		Yield	Ultimate	Uniform	Total
1000	0	14,040	22,390	15.7	30.5
1000	1.7	11,430	21,430	19.7	28.2
1000	18	12,540	22,890	14.6	26.9
1200	0	9,160	12,050	9.2	77.1
1200	18	9,060	11,740	9.3	80.3

[a]Strain rate 0.027 per min.

Results of creep-rupture tests are given in Table III and Figs. 1 and 2. These results indicated slightly higher strength and lower ductility than for the same heat of material tested under comparable conditions, but with a greater cross-section thickness, 0.060 in. thick as compared to 0.010 in. in the present experiments.[9]

The data at 1000°C show only a modest dependence of ductility of the control tests on stress, with the ductility in a 1-hr test three-quarters that in 30- and 800-hr tests. Samples containing 1.7 and 18 ppm helium tested at 1000°C and 14,000 psi had rupture lives approximately twice that of the control tests, reduced minimum creep rates and rupture elongations approximately one-half that of the control values. However, there is no dependence of rupture elongation on the helium content for the two helium levels tested. The creep curves for the three tests at 1000°C and a stress of 14,000 psi are shown in Fig. 1. All three tests show the three-stage creep behavior. The lower ductility in the helium-doped samples is reflected in a reduced third-stage creep.

Creep tests at 1200°C showed a generally greater ductility than tests at 1000°C, with fracture elongations approximately twice those at the lower temperatures. At this temperature, the lowest elongation was recorded in the lowest stress-longest time test (36% elongation in a 456-hr test), while other tests lasting from 3 to 250 hr at various stresses had elongations of 64 ± 4%. In tests at 1200°C and 6000 psi,

Table III. Creep-Rupture Properties of Helium Containing Nb–1% Zr

Test Temperature (°C)	Helium Content (appm)	Stress (psi)	Minimum Creep Rate (%/hr)	Rupture Life (hr)	Elongation (%)
1000	0	10,000	0.0192	781	33.8
1000	0	14,000	0.199	32.9	33.9
1000	1.7	14,000	0.0506	61.5	14.9
1000	18	14,000	0.0558	61.3	16.9
1000	0	21,000	11.9	1.0	26.5
1200	0	4,000	0.0313	456	35.7
1200	0	5,000	0.122	242	62.6
1200	0	6,000	0.328	77.0	62.2
1200	1.7	6,000	0.378	53.2	46.5
1200	18	6,000	0.518	65.3	46.2
1200	0	7,000	0.675	37.6	67.0
1200	0	8,000	3.376	7.3	66.0
1200	0	9,000	10.05	2.9	60.0
1200	18	9,000	3.2	3.1	51.5
1400	0	5,000	a	580[a]	85.6
1400	18	5,000	a	297[a]	97.1

[a]Creep tests at 1400°C were interrupted several times by binding of stress transfer system. Rupture lives are therefore not characteristic of the temperature and stress condition, but elongation values are.

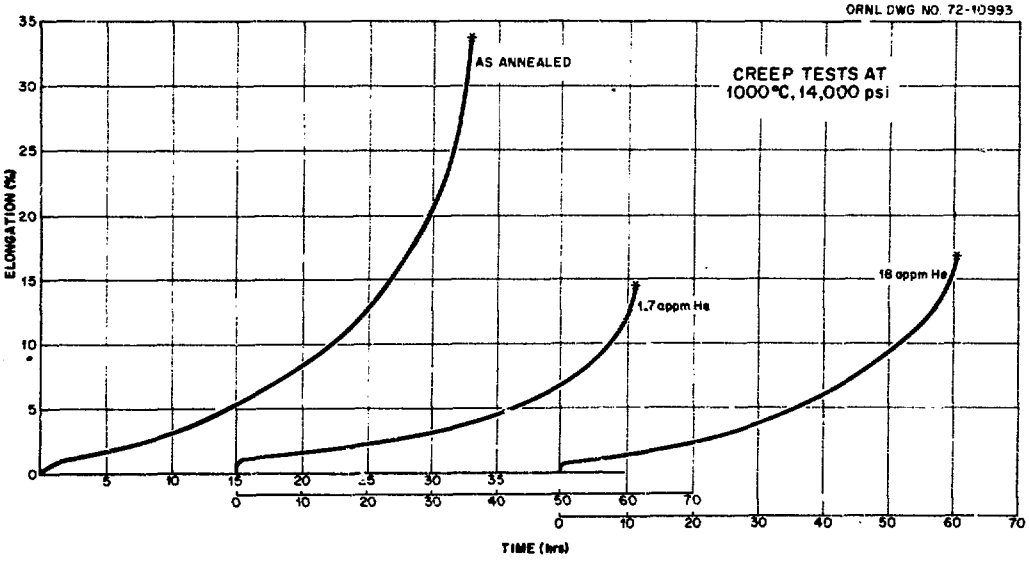

Fig. 1. Elongation vs Time Curves for Creep Tests of Nb–1% Zr at 1000°C at a Stress of 14,000 psi. Curves are shown for a control sample and samples with 1.7 and 18 ppm He. Note different scales on abscissa.

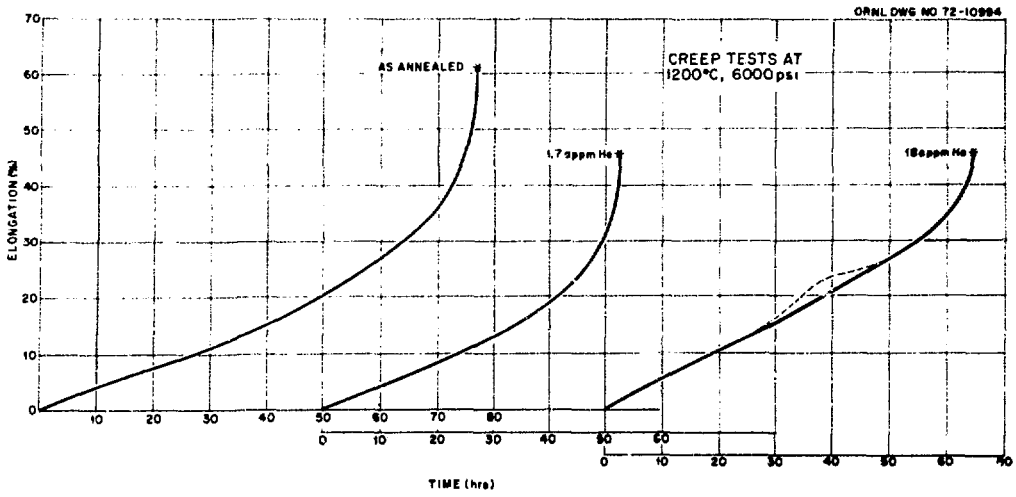

Fig. 2. Elongation vs Time Curves for Creep Tests of Nb–1% Zr at 1200°C at a Stress of 6000 psi and Helium Contents Shown. The dotted line shows recorded data, believed to be due to a slight temperature excursion.

helium-injected samples had slightly shorter rupture lives and approximately three-quarters of the rupture elongation of the control sample. Creep curves of a control sample and samples with the two helium levels are shown in Fig. 2. (The broken curve for the 18-ppm helium sample shows the recorded data. It is believed that this irregularity was due to a slight temperature excursion during the test.) In these curves, too, the general form of the curves is the same for both control and helium-doped samples. The reduced ductility in the helium-doped samples has resulted from the reduced amount of third-stage creep. Again, as at 1000°C, there is no dependence on the amount of helium in the two samples containing gas. Tests at a higher stress, and thus shorter creep-rupture time, showed less effect of the 18 ppm helium than found at longer rupture times. In these tests at 1200°C and 9000 psi, the creep-rupture times were comparable for control and helium-containing samples, with the helium-injected sample having 85% of the rupture elongation of the control sample.

Tests conducted at 1400°C at a stress of 5000 psi showed 13% more elongation to rupture in the 18-ppm helium-doped specimen than in the control. Equipment failure during the 1400°C tests limit the amount of data obtained. Only the elongation values in these tests are reliable. Creep rates and rupture lives were lost due to binding of components in the load train.

In all creep tests, as in the tensile tests, chisel-edge fractures formed with ~100% reduction in area. Figure 3 shows a macroscopic view of the samples tensile tested at 1000°C. Fractures of all samples across the specimen width were at an angle of 70 to 80° to the stress axis.

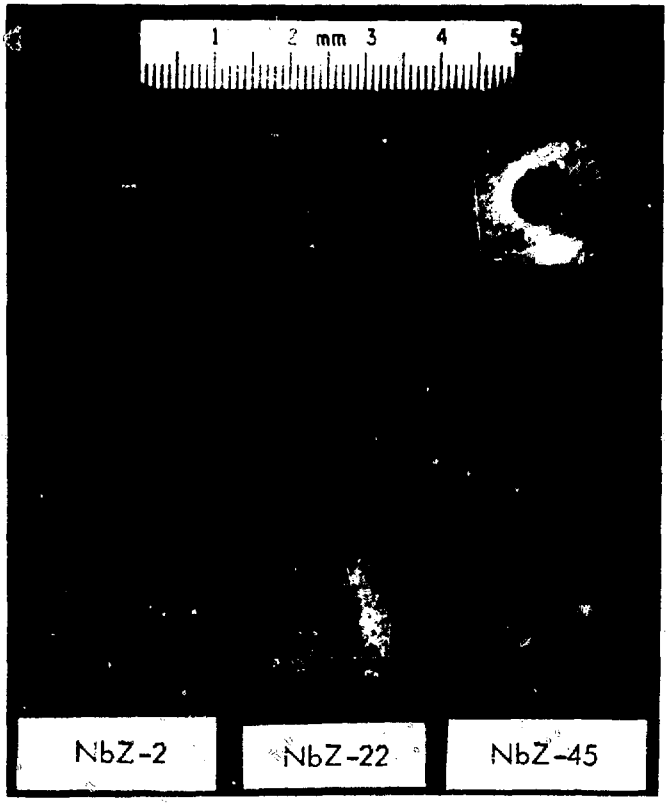

Fig. 3. Nb–1% Zr Samples Tested at 1000°C and a Tensile Strain Rate of 0.027 per min. Helium contents are NbZ–2, 18 appm; NbZ–22, 1.7 appm; and NbZ–45, no helium. All necking occurred in the thickness direction and cannot be seen in this view of the specimens.

The fracture angle on the thickness direction was not determined. Scanning electron micrographs of the fracture surfaces of specimens creep tested at 1000°C are shown in Fig. 4. This shows clearly the chisel-edge nature of the fractures formed in these tests. Fractures from creep tests at 1200°C and tensile tests at both 1000 and 1200°C looked identical to those shown in Fig. 4. The sharp edge in all fractures was interrupted occasionally by the small cavity-like pockets that are believed to be the dimples characteristic of ductile-mode fractures. There was no evidence of grain boundary separation, the characteristic fracture mode that accompanies helium embrittlement.

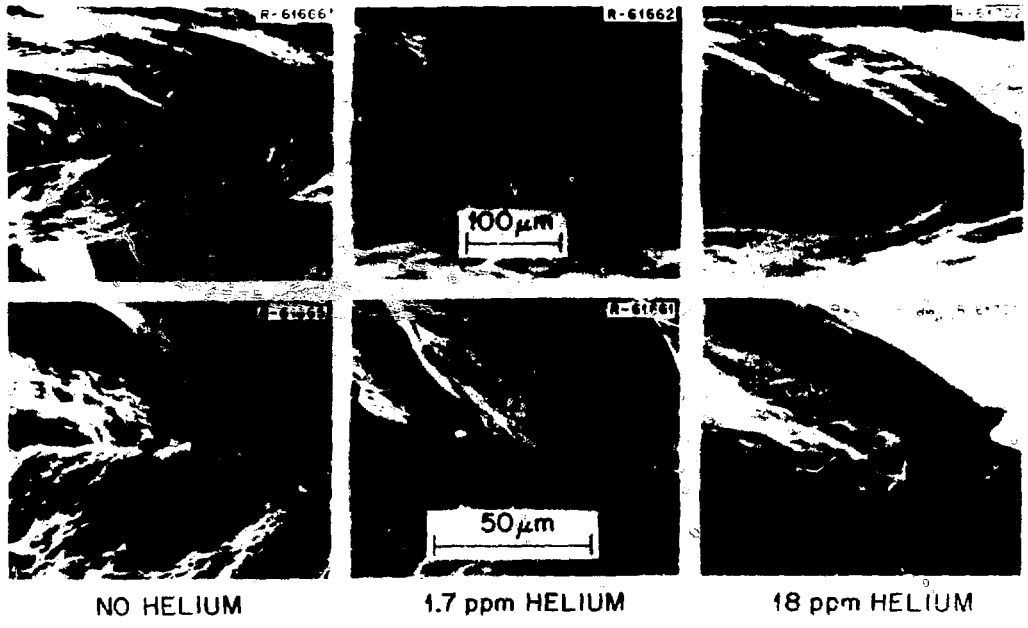

Fig. 4. Scanning Electron Micrographs of Chisel-Point Fractures in Helium-Doped Nb–1% Zr Creep Tested at 1000°C and 14,000 psi. Helium contents as shown.

Cross sections through the fractures were examined metallographically for representative tests. Figure 5 shows metallographic sections on specimens tensile tested at 1200°C, and Fig. 6 shows specimens creep tested at the same temperature. In both figures the structures of helium-free and 18 appm helium samples are compared. At this magnification, the deformation is uniform throughout the zone examined, with elongated grains reflecting the large amount of deformation that has occurred. The optical metallography showed more precipiate phase in the helium-injected samples than in the control samples, and in both 0 and 18 appm helium samples the grain boundaries are serrated and irregular. This suggests a fine-scale grain boundary pinning, which appears qualitatively to be more complete in the doped samples. The most important feature of the metallography is the lack of difference in the fracture produced by helium. It is also important to note that there is no observed grain

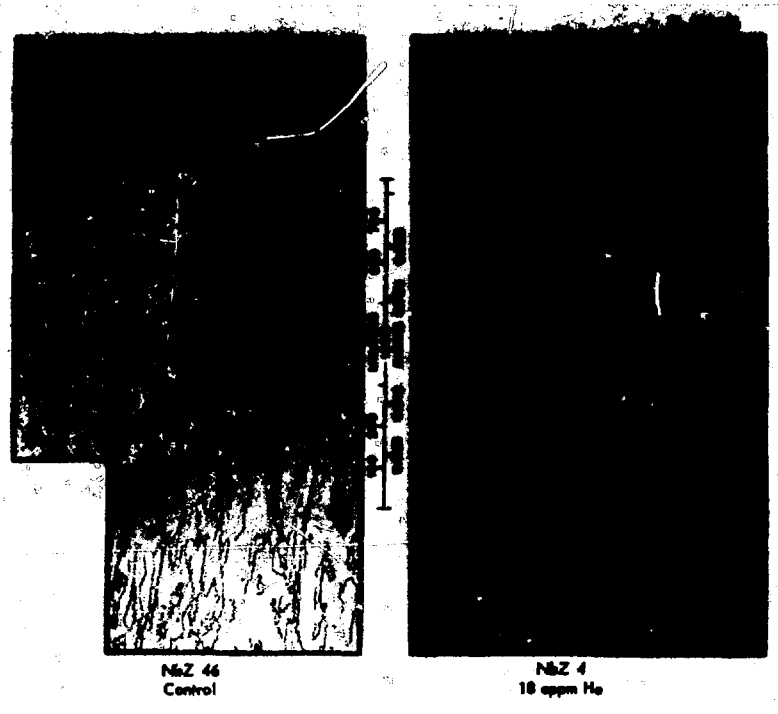

Fig. 5. Metallographic Section Through Fracture of Nb–1% Zr Specimens Tensile Tested at 1200°C. Tensile axis vertical.

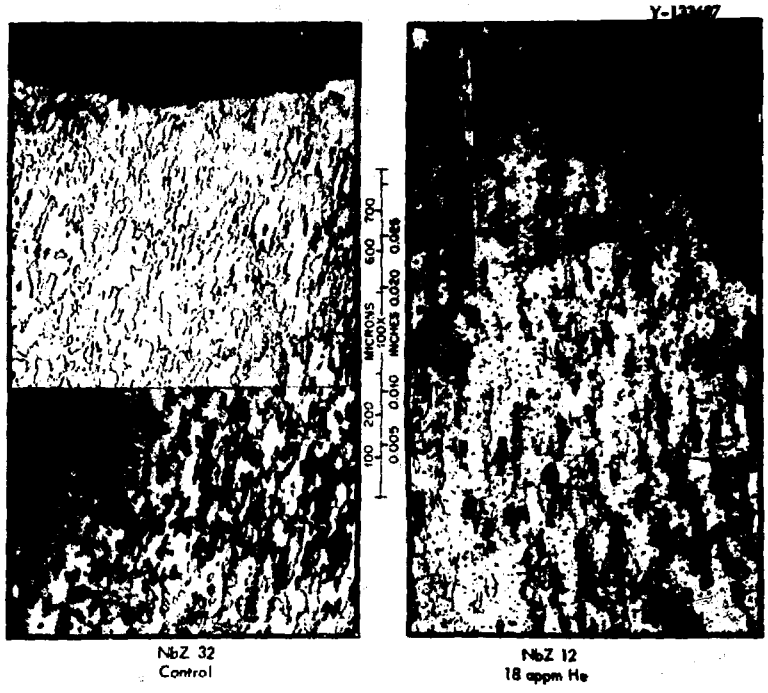

Fig. 6. Metallographic Section Through Fracture of Nb–1% Zr Specimens Creep Tested to Failure at 1200°C and 6000 psi.

boundary separation in either the control or gas-doped sample. In all specimens examined, only one or two isolated cracks were found and these could not positively be identified as grain boundary separations.

Sections from the stressed gage portion of tested specimens were electrochemically thinned and examined by transmission electron microscopy. No effect of helium could be detected in the microstructure of these samples. In general, the grain boundaries in all samples examined were precipitate free, but some grain boundaries were pinned on precipitates. The matrix of all samples contained a low concentration of relatively large precipitates, and most samples also contained a population of smaller precipitates with linear dimensions of the order 200 to 2000 Å. The highest concentration of the small precipitates was found for specimens creep tested at 1200°C, and examples of micrographs are shown in Fig. 7. It must be noted immediately that the white features in this figure are believed to be mainly pits left when the precipitates

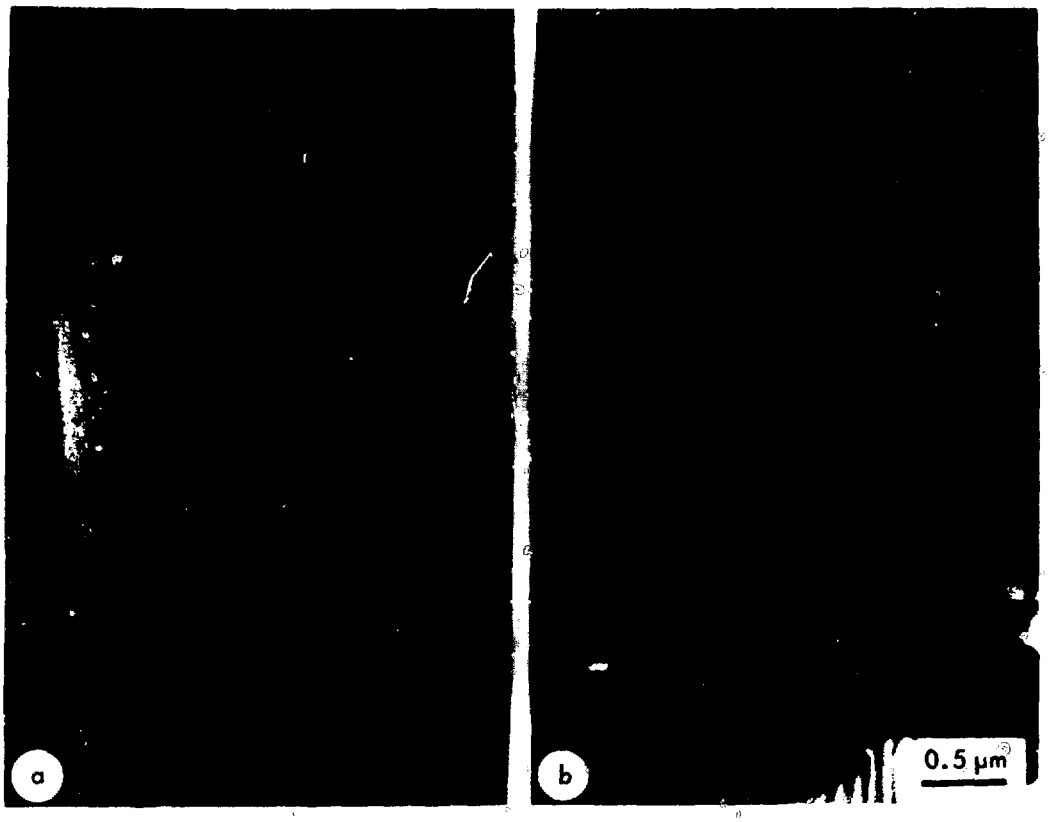

Fig. 7. Microstructure in Nb–1% Zr Sample Creep Tested to Rupture at 1200°C and 6000 psi. (a) Helium-free control. (b) 18 appm cyclotron-injected helium.

were preferentially attacked by the polishing solution. Stereo microscopy confirmed that the great majority of these pits intersected one of the surfaces. There were, however, a few white features that appeared to be contained in the foil and these could be gas bubbles. The ratio of these pits to the precipitates was about the same in helium-free as in helium-doped samples. Lower precipitate concentrations were found for samples tensile tested at 1200°C and still lower concentrations for samples creep or tensile tested at 1000°C. This could indicate more impurity pickup during the longer times at the higher temperatures, an effect of the precipitation kinetics of impurity-containing phases, or a combination of both. The highest dislocation densities were found

for tensile tests at 1000°C, with densities decreasing for longer test times (creep) or for tests at the higher temperatures. Most samples contained segments of dislocation networks, as seen in Fig. 7, with some pinning of the network on the precipitate particles. Subgrain boundaries were also commonly observed, and the tensile samples creep tested at 1000°C also contained some finer scale dislocation arrays. The undoped and helium-injected samples creep tested at 1400°C showed similar microstructures. The grain boundaries were clean in these samples. The matrix contained a low concentration of large, random precipitates but were free of the fine-scale precipitate seen for the two lower test temperatures. Only isolated dislocation segments were contained in these samples, with most segments pinned on the precipitates or arranged in low-angle boundaries.

DISCUSSION

The experimental evidence indicates that helium contents up to at least 18 appm do not reduce the ductility of Nb–1% Zr for test temperatures in the range 1000 to 1400°C. Tensile tests showed only differences that are expected from normal data scatter. Creep-rupture ductility values at first seemed to indicate helium embrittlement. However, lack of dependence on the helium contnet, an apparently smaller effect at 1200°C than at 1000°C, and absence of the classical features of helium embrittlement in fractography, metallography, and microscopy examination all suggest that the creep ductility reduction is not due to helium. The observed precipitate phase suggests that the embrittlement in creep tests is probably due to interstitial impurity pickup in the Nb–1% Zr during the helium injection. Precipitation of this impurity, possibly as ZrO_2, occurred during elevated-temperature testing and was especially effective in reducing creep-rupture ductility.

The source of the precipitating impurity phase has not been definitely established. While some of the impurity was present in the starting material, the thin samples required for helium injection make the samples more susceptible to contamination. The precipitate observed in helium-free samples thus suggests possible impurity pickup during annealing or

during elevated-temperature testing. The observation of more precipitate phase in the helium-injected samples than in the control samples shows that some contamination must have occurred during the α-bombardments conducted in air. The only significant differences found in these experiments could be attributed to impurity pickup. Since testing conditions were identical, the injection technique is suspect.

The effects of intentionally added oxygen on the creep properties of niobium[10,11] and Nb–0.6% Zr[12] have been determined. Oxygen was reported to reduce creep rates of niobium for temperatures less than 1050°C, but have little effect on creep strength at higher temperatures.[10] This is in agreement with the effects observed here, of reduced creep rate and longer rupture lives for bombarded samples (assumed to have higher impurity content) in tests at 1000°C, but little effect at 1200°C. The result may be due to an overaging of precipitate, perhaps ZrO_2, at the higher temperatures, rendering the precipitate distribution less effective in strengthening the alloy. The study of the effect of oxygen on slow-bend creep of Nb–0.6% Zr was restricted to tests at 1000°C. Oxygen introduced before creep testing reduced the creep rate while oxygen introduced during testing had more complex effects.[12] Although the data scatter considerably, Stoop and Shahinian's[11] work also indicates that increased oxygen content may reduce creep-rupture elongation. (It must be noted that Stoop and Shahinian chose to describe their data as showing "no deleterious effect on ductility".)

The observed resistance of Nb–1% Zr to helium embrittlement is encouraging. The resistance to degradation is promising and is one more plus in evaluating the possible use of this alloy in CTR application. Explaining the resistance, however, is beyond the present understanding of helium effects in metals. The lack of embrittlement is, of course, a result of the lack of effect on the fracture mode. The key to understanding may be in the resistance of Nb–1% Zr to grain-boundary cracking under the test conditions examined. In none of the tested specimens examined, either control or helium-doped samples, were grain-boundary cracks observed. In many alloys where helium embrittlement has been observed at comparable homologous temperatures, occasional grain-boundary

cracks are seen in helium-free samples. (An example for a vanadium alloy is seen in the metallography in Ref. 8.) In a study of a series of ferritic steels, Böhm and Hauck[13] showed that a tendency toward intergranular fracture in helium-free steels greatly enhanced the embrittlement produced by helium doping when compared with steels more resistant to grain-boundary separation. Whether or not the inherent resistance to grain boundary cracking of Nb–1% Zr is associated with the very irregular, serrated grain boundary morphology cannot be established without further work.

The absence of large gas bubbles on grain boundaries that have been stressed at elevated temperatures during testing was also unexpected. However, a similar result was found by Johnson and Cost[14] in niobium containing helium. Based on Johnson's observations, and the apparent lack of helium bubbles in samples examined here, it appears that the helium is precipitating into very small bubbles, too small to be observed by routine TEM examination, and that it remains stable in this size distribution during testing.

The possiblity that helium is lost through migration and release at the free surfaces cannot be totally dismissed. However, Bauer and Thomas[15] and Johnson and Cost[14] found incomplete helium release from niobium under similar conditions in thinner specimens. An unrelated experiment at ORNL showed that annealing Nb–1% Zr for 1 hr at 1650°C did not release a significant fraction of the contained helium. We thus conclude that although some helium may have been lost during elevated-temperature testing, it is unlikely that this influences the results.

CONCLUSIONS

Helium contents up to at least 18 appm do not degrade the properties of Nb–1% Zr in the absence of irradiation-induced displacement damage. This observation makes the material attractive for possible CTR application and justifies the investigation of the synergistic effects of both helium and displacement damage. The resistance to embrittlement may be associated with the inherent resistance of Nb–1% Zr to grain-boundary separation

during tests at 1000 and 1200°C and to the inferred tendency of helium to precipitate on a fine scale under these conditions, resulting in the absence of microscopically visible gas bubbles on the grain boundaries.

ACKNOWLEDGMENTS

The author is grateful for the help on this project provided by a number of people at ORNL. B. L. Cox, L. K. Egner, and E. Bolling helped with various phases of the experimental work. R. T. King kindly provided his helium-injection equipment, as well as invaluable assistance on the α-bombardment operation. R. S. Crouse and T. J. Henson performed the scanning electron microscopy and W. H. Farmer the optical metallography. Thanks, also, to J. O. Stiegler for discussion of the work and to E. A. Kenik and R. W. Carpenter for manuscript review. The assistance of Jo Anne Zody and Julia Bishop in preparing the manuscript is greatly appreciated.

REFERENCES

1. P. J. Maziasz, F. W. Wiffen, and E. E. Bloom, "Swelling and Microstructural Changes in Type 316 Stainless Steel Irradiated Under Simulated CTR Conditions," this conference proceedings.

2. D. Kramer, K. R. Garr, A. G. Pard, and C. G. Rhodes, "A Survey of Helium Embrittlement of Various Alloy Types," p. 109 in *Irradiation Embrittlement and Creep in Fuel Cladding and Core Components*, British Nuclear Energy Society, London (1973).

3. G. L. Kulcinski, D. G. Doran, and M. A. Abdou, "Comparison of Displacement and Gas Production Rates in Current Fission and Future Fission Reactors," to be published by ASTM in Proceedings of June 1974 Radiation Effects Symposium, Gatlinburg, Tennessee, ASTM-STP 570.

4. D. Steiner, "The Nuclear Performance of Vanadium as a Structural Material in Fusion Reactor Blankets," *Nuclear Fusion* 14, 33 (1974).

5. M. J. Klein and A. G. Metcalfe, "Effect of Solutes in Binary Columbium (Nb) Alloys on Creep Strength," *Met. Trans.* 4, 2441 (1973)

6. R. T. King, "Cyclotron Simulation of Neutron-Transmutation Produced Gases in Reactor Cladding and Structural Material," p. 492, *The Uses of Cyclotrons in Chemistry, Metallurgy, and Biology*, Butterworths, London (1969).

7. K. Ehrlich and H. Böhm, "Irradiation Effects in Vanadium-Base Alloys," pp. 349–55, *Radiation Damage in Reactor Materials*, Vol. II, IAEA, Vienna (1969).

8. A. T. Santhanam, A. Taylor, and S. D. Harkness, "Charged-Particle Simulation Studies of Vanadium and Vanadium Alloys," p. 302 in *Defects and Defect Clusters in BCC Metals and Their Alloys*, ed. R. J. Arsenault, Nuclear Metallurgy, Vol. 18.

9. H. E. McCoy, "Creep Properties of the Nb–1% Zr Alloy," *J. Less-Common Metals* 8, 20 (1965).

10. J.D.W. Rawson and B. B. Argent, "The Effect of Oxygen and Carbon on the Creep Strength of Niobium," *J. Inst. Metals* 95, 212 (1967).

11. J. Stoop and P. Shahinian, "Effect of Oxygen on Creep-Rupture of Niobium," NRL Report 6095 (July 10, 1964).

12. T. K. Roche, *Effect of Degree of Vacuum on the Slow-Bend Creep Behavior of Columbium–0.6% Zirconium at 1000°C*, ORNL-3569 (June 1964).

13. H. Böhm and H. Hauck, "Investigation of Radiation Induced High-Temperature Embrittlement of Ferritic Steels in the Temperature Range of the α-γ-Transformation," *J. Nucl. Mater.* 29, 184 (1969).

14. D. L. Johnson and J. R. Cost, "Characterization and Behavior of Atomic Helium in Niobium," p. 279 in *Defects and Defect Clusters in BCC Metals and Their Alloys*, ed. R. J. Arsenault, Nuclear Metallurgy, Vol. 18.

15. W. Bauer and G. J. Thomas, "Helium Re-emission and Surface Deformation in Niobium, Vanadium, and Molybdenum," p. 235 in *Defects and Defect Clusters in BCC Metals and Their Alloys*, ed. R. J. Arsenault, Nuclear Metallurgy, Vol. 18.

STUDY OF HE DISTRIBUTIONS IN NIOBIUM BY MEANS OF (n,p) REACTIONS

J.P. Biersack D.Fink

Hahn-Meitner-Institut für Kernforschung, Berlin DE

ABSTRACT

Helium will be introduced into fusion reactor first wall materials as low energy ions from the plasma, as neutron knock-ons from the coolant, and also from (n,α) reactions in the bulk. Direct observation of He which is distributed inside a metal is extremely difficult, and few attempts of detecting He profiles have been successful so far [Blewer using RBS in thin metal foils; Picraux et al, and Behrisch et al using the $^{3}He(d,p)\,^{4}He$ reaction]. In short, detailed studies of He in metals are still lacking, despite of considerable practical and theoretical interest.

The present investigation utilizes the thermal neutron induced reaction $^{3}He\,(n,p)T$ of cross section 5000 barn which can be applied for detecting He profiles as well as He lattice locations. An advantage over other methods is seen in the facts that thermal neutrons cause practically no displacements of He or lattice atoms prior to detection, and that there is less background and higher sensitivity than in RBS or (d,p) detection.

The method is applied for measuring depth profiles of He in Nb after implantation and after subsequent thermal anneals. A comparison with theoretical predictions yields the following results: (i) Mean ranges of 70 to 300 keV He^{+} in Nb agree with theory after increasing the k value of Lindhard and Scharff. (ii) The width of the range distributions is slightly higher, the skewness is much lower than predicted. (iii) Upon anneal, implanted He does not diffuse, but is detrapped with an activation energy of 1.4 eV which does not correspond to He atoms bound to single vacancies.

INTRODUCTION

Mainly two aspects are studied in the present work: The range distributions of implanted He in niobium, and the thermal detrapping and release of implanted He.

The observation of He depth distributions in metals is difficult, and few methods of detecting He profiles are known so far. Blewer [1] has successfully applied the method of proton Rutherford back scattering (RBS) from He-4 which was implanted in thin copper foils. Picraux et al [2] introduced the ^{3}He(d,p) reaction as a means of detecting He profiles in tungsten. For the present studies of He in niobium a different detection method is proposed and tested: The thermal neutron induced reaction ^{3}He (n,p) T of cross section 5000 barn. The advantage of using this reaction is seen not only in the high sensitivity, but also in the fact that thermal neutrons cause no displacements of He or lattice atoms, except through the detecting (n,p) reaction itself. Since practically no radiation damage develops, even extended channelling/blocking measurements seem feasable for lattice location studies of He in metals.

For investigations on the thermal release (detrapping probability) of implanted He, the change of concentration profiles is observed in connection with the amount of released gas through many successive steps of thermal anneal. Helium is expected to be trapped or precipitated in defects or defect structures which result from the He implantation itself. However, no experimental evidence has been achieved so far about the nature of such He traps, and in particular about the binding energy. Extensive theoretical studies, however, on the binding energy of He atoms to single metal vacancies have been published by Bisson and Wilson[3].

HELIUM RANGE DISTRIBUTIONS

Experimental. -- Cold rolled foils and polished single crystals of niobium (supplied by MRC) are implanted at room temperature with 70 ... 300 keV $^3He^+$ to helium concentrations of 1 ... 7 % atomic fraction. This is about one order of magnitude below the dose of blistering. Single crystals are tilted about 7° from the <111> direction in order to avoid channeling effects.

The resulting He depth profiles are measured by the $^3He(n,p)$ reaction in a thermal neutron beam which is extracted from a nuclear reactor. High energy radiation background from the reactor is eliminated by using either a slightly curved neutron guide tube (FMRB, 1 MW reactor facility of the PTB Braunschweig), or by using Bi filters in a linear collimator assembly (BER, 5MW reactor at HMI Berlin).

The $^3He(n,p)$ reaction has a cross section of about 5000 barns for neutrons of thermal energies (0.025 eV), and even higher cross sections (by a factor up to 3) for the "cold" neutrons of the curved beam guide according to the $E^{-1/2}$ absorption law.

The emitted protons of initially 580 keV which leave the sample surface near normal direction, are detected by a surface barrier detector in connection with a multi channel analyser. The resulting proton energy loss spectra are converted into depth profiles using the stopping power of 120 keV/μm. This stopping power value has been chosen on the basis of theoretical estimates (Northcliffe, Schilling [4], Northcliffe [5], Biersack [6]), but has not yet been experimentally checked. The position of the surface in the multichannel spectrum is determined quite precisely for each depth profile by means of a calibration sample which has been implanted with He-3 of only 100 eV.

Results and Discussion. -- The resulting He range distributions in Nb are depicted in Fig. 1, and compared to theoretical predictions in Fig. 2. The mean projected ranges denoted as r in Fig. 2a, agree well with theory [7] after increasing Lindhard's k value by a factor 1.2. This is a rather common correction for Nb, similar to the correction obtained for Li range and damage distributions in Nb [8]. A particularly high electronic stopping power for He^+ in niobium has also been theoretically anticipated by Rousseau et al [9], and experimentally verified for the energy range 0.3 ... 2 MeV by Lin et al [10].

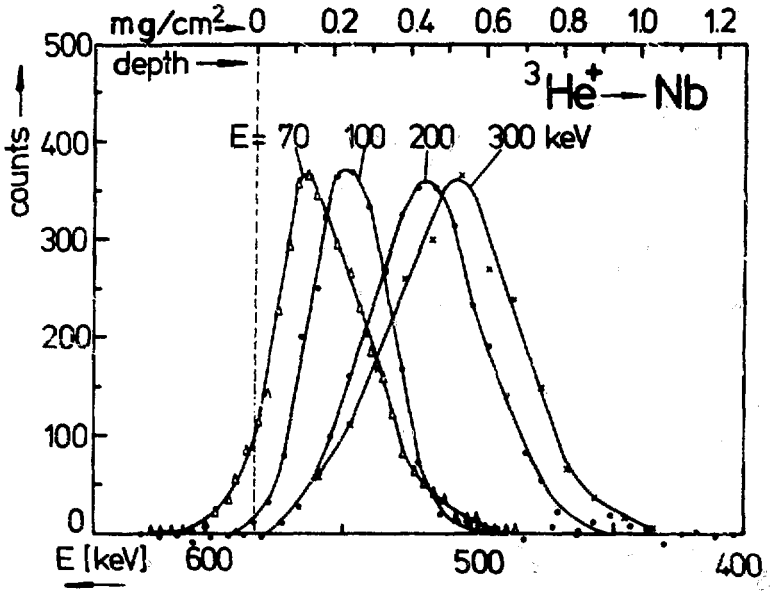

Fig. 1. Depth profiles of helium implanted in niobium. The 100 keV profile is obtained with single crystalline Nb implanted at random direction, the other profiles correspond to polycrystalline materials.

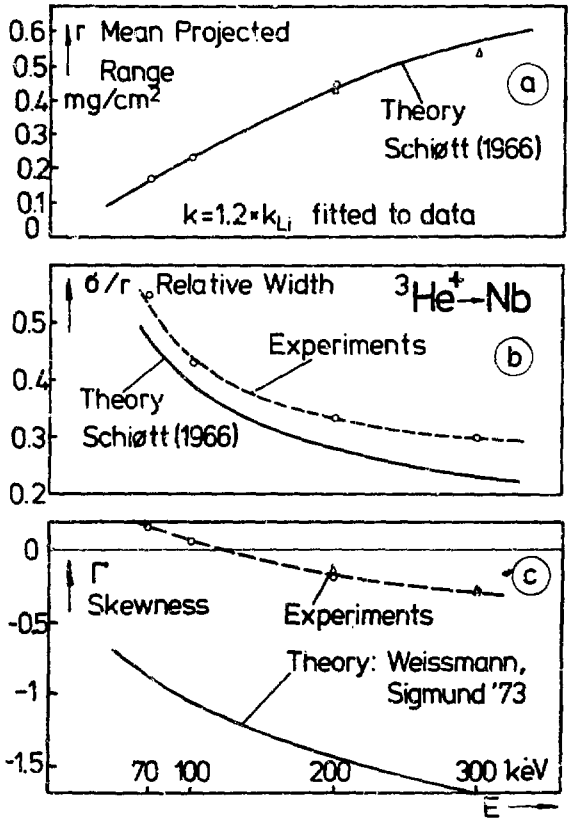

Fig. 2. Comparison of the experimental results with the analytical theory of Schiøtt [7], and Weissmann and Sigmund [11].

The relative width of the profiles, σ/r in Fig. 2b, follows the theoretically expected trend, but is in general slightly higher. The difference can not be accounted for by the detector resolution.

Agreement with theory [11] is rather poor in the case of the skewness $\Gamma = \langle \Delta x^3 \rangle / \sigma^3$, as depicted in Fig. 2c. This may be due to the approximations used in theory, including the neglection of the surface. Particularly at lower energies, particles are removed from the left side of the distribution when slowing down near the surface. This particle loss tends to shift Γ towards positive values, whereas the theoretical model [7,11] accounts for too many particles at the left of the peak, including those which are "stopped" in the fictitious negative half space.

HE RELEASE BETWEEN 500° AND 1600°C

At high implantation doses, as encountered in the present experiments as well as in future thermonuclear fusion reactors, a strong interaction of He with radiation induced damage is anticipated. In particular, a strong binding of He atoms to vacancies is expected [3].

For the present measurement of He detrapping and release, a single crystalline Nb disk is implanted at a random direction with 200 keV ^{3}He to a maximum concentration of 7 %, as depicted in Fig. 3, upper curve. The thermal annealing experiments are carried out in an ultra high vacuum chamber ($p < 10^{-9}$ Torr) by mounting the Nb crystal between resistively heated Nb foils. Temperatures up to 1600° C are achieved, and controlled by thermo couples and pyrometer. The amount of He-3 gas released is measured by the Ultek partial pressure analyser (magnetic mass spectrometer) in two different ways: Either following the partial pressure increase with pumps turned off, or observing the equilibrium pressure (obtained within seconds) with pumps on, after having calibrated the pumping speed.

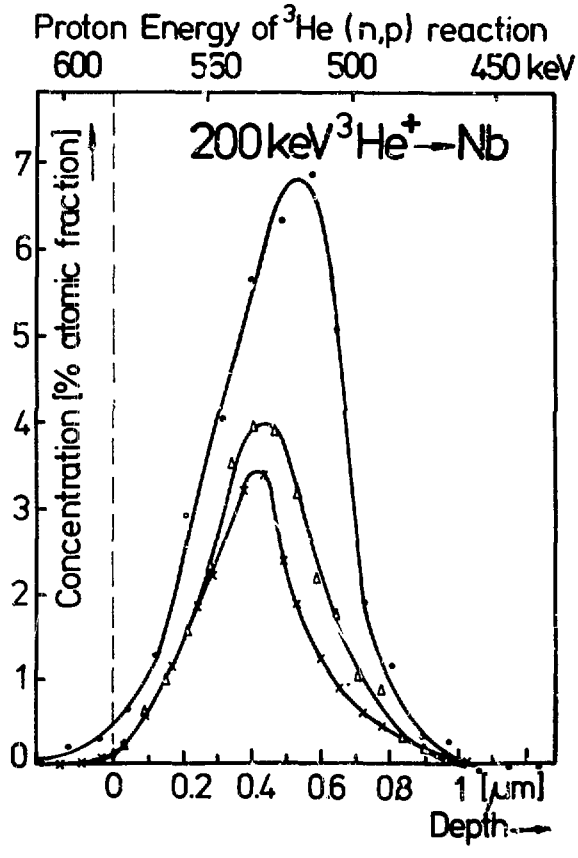

Fig. 3. Depth profiles of He in Nb after successive anneals, indicating that detrapping but not diffusion occurs.

An initial burst of He is observed below 700°C. Thereafter, the largest fraction of He is released with release rates following closely the Arrhenius diagram shown in Fig. 4, which indicates a binding energy of 1.43 eV to the traps. That indeed detrapping is observed and not diffusion (of either He atoms or agglomerations) becomes evident from the depth profiles which are measured after several steps of anneal, see the lower curves in Fig. 3. There occurs no diffusional broadening. The half width is even reduced after anneal which may be attributed to He precipitations near the center of the distribution, or - more precisely - in the region of highest damage (slightly left of the initial He peak).

As a result, the Arrhenius plot, Fig. 4 , can be interpreted as a detrapping probability of 0.016 exp (- 1.43 eV/kT) per He atom per second which applies for the larger fraction of helium. The nature of the traps, however, remains a puzzle: For He atoms trapped at single vacancies, one would expect a higher binding energy [3], and a fore factor of the order of $10^{13}\,sec^{-1}$. The energy of 1.4 eV also seems too low for returning a helium atom from a bubble into the Nb lattice.

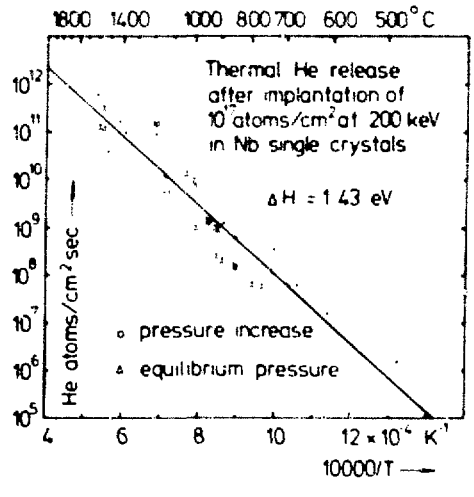

Fig. 4. Release rates of He at various annealing temperatures.

RESUME

(i) Mean ranges of 70 ... 300 keV He^+ in niobium agree with theoretical predictions after increasing the k value of the Lindhard-Scharff electronic stopping power by about 20 %.

(ii) The range distributions are slightly broader, but less skew than predicted.

(iii) He implanted at 200 keV to a maximum concentration of 7 %, does not diffuse at thermal anneals up to 1600°C, but is detrapped with an activation energy of 1.4 eV.

ACKNOWLEDGEMENT

We are indebted to the Physikalisch-Technische Bundesanstalt (PTB), Braunschweig, in particular to Prof.Dr.W.Heintz for the permission to use the FMRB reactor facility and his neutron guide tube. Mr. E. Santner kindly helped in implanting the samples.

REFERENCES

1. R.S.Blewer, p. 557 in "Applications of Ion Beams to Metals", ed.Picraux, EerNisse, Vook; Plenum, New York, 1974.

2. S.T. Picraux, and F.L. Vook, p. 407 in "Applications of Ion Beams to Metals", ed. Picraux, EerNisse, Vook; Plenum, New York, 1974 .

3. C.L.Bisson, and W.D. Wilson, in "Applications of Ion Beams to Metals", ed. Picraux, EerNisse, Vook; Plenum, New York, 1974 .

4. L.C.Northcliffe, and R.F. Schilling, Nuclear Data Tables, A 7, 233 (1970).

5. L.C.Northcliffe, Annual Rev. Nucl.Sci.13, 67 (1963).

6. J.P.Biersack, and D. Fink, p. 737 in "Atomic Collisions in Solids", Vol. 2, Plenum, New York (1974).

7. H.E. Schiøtt, Mat.Fys.Medd.Dan.Vid.Selsk. 35, No. 9 (1966).

8. J.P.Biersack, and D. Fink, J.Nucl.Mat. 53, 328 (1974), and p. 211 in "Ion Implantation in Semiconductors and Other Materials", edit. S. Namba, Plenum, New York (1974).

9. C.C. Rousseau, W.K.Chu, and D. Powers, Phys.Rev.A4 , 1066 (1971).

10. W.K. Lin, H.G. Olson, and D. Powers, Phys.Rev. B8 ,1881 (1973).

11. R.Weissmann, and P. Sigmund, Rad.Effects 19, 7 (1973).

HELIUM EMBRITTLEMENT OF CTR MATERIALS SIMULATED BY ION IMPLANTATION AND HOT ISOSTATIC PRESSING OF METAL POWDERS

L. R. Fleischer
J. A. Spitznagel
W. J. Choyke
Westinghouse Research Laboratories
Pittsburgh, Pennsylvania 15235

ABSTRACT

Helium embrittlement is currently considered a limitation on the lifetimes of CTR structures exposed to high energy neutrons. The phenomenon has been observed in fast fission reactor irradiated materials and has been studied in helium ion bombarded foil samples. In this study, helium ions were implanted in stainless steel and refractory metal alloy powder particles. The 150 keV ion energies used require particle size distributions with mean particle diameters of about 3 μm to get a suitably homogeneous initial distribution of helium atoms. The helium implanted powders were consolidated by hot isostatic pressing; the helium remained in solid solution. Subsequent thermomechanical processing permitted the preparation of tensile specimens with controlled helium bubble distributions. In general, grain boundary migration concentrated helium bubbles on the boundaries, while conditions favoring stationary boundaries allowed intragranular bubble nucleation on dislocations. It remains to be seen whether the distributions available through these processes are representative of those that will be generated *in situ* by (n,α) reactions in CTR neutron spectra. Specimens for bulk properties measurements prepared in this way are most suitable for study of helium embrittlement as an isolated effect. Many of the constraints encountered in other sample preparation methods are mitigated.

INTRODUCTION

Helium embrittlement may be the limiting factor in fusion reactor containment design.[1] Loss of high temperature ductility was first observed in fission reactor irradiated metals.[2,3] The effect is attributed to the stress-induced growth of intergranular bubbles of transmutation product gases.[3,4] Studies of the embrittlement mechanism

and of the susceptibilities of various alloys have been carried out, in general, by two sample preparation methods: fission reactor neutron irradiation[5] and high energy helium ion bombardment of thin strip specimens.[6]

Both techniques, however, have inherent limitations. Access to the machines producing the radiation is necessary -- usually a fission reactor or a high energy cyclotron (or other accelerator). Reactor irradiated sample materials must contain or be doped with an isotope which has a substantial (n,α) cross-section in the neutron spectrum available. Even then, in most cases, acceleration of the time scale is unlikely; accumulation of the desired amount of transmutation helium will take as long or longer in a fission reactor than in the projected fusion reactor. Fission reactor irradiation is a good geometric simulation of fusion reactor irradiation, but it is not possible to unambiguously separate helium embrittlement effects from some other forms of radiation damage.

Helium implantation by ion bombardment is limited by the ion energy available. In most applications of this technique,[6,7] ions accelerated to more than 40 MeV were used. Even with energies of this magnitude, sample thicknesses were limited to the order of 0.025 cm (10 mils) by the penetrating power of the ions.

This paper describes a method for preparing helium doped samples which eliminates most of these limitations. Geometries suitable for a variety of mechanical strength and fracture toughness specimens can be prepared. A variety of microstructures and gas bubble arrangements can be achieved. By implanting the helium in powder particles, restrictions to high energy accelerators are eased since ion ranges on the order of micrometers rather than millimeters are involved.

EXPERIMENTAL

Overview

The powder method for preparing helium embrittlement samples falls conceptually into three steps:

- Ion implantation
- Consolidation
- Thermomechanical processing.

In the first step, helium is implanted in the individual particles of metal powder by ion bombardment. The second step involves fabricating a bulk solid from the He-containing powder. The third step is intended principally to control the microstructure of the product and the distribution of helium bubbles within it. Each of these steps, with its attendant technical problems, is discussed below along with descriptions of the experimental work we have done.

Ion Implantation

The Powder

The most difficult aspect of this method is obtaining suitable powders. Ideally, the powder particles should have diameters two to three times the available range of the helium ions. With ion energies of 150 keV, particles on the order of one to three micrometers diameter were required. 316 stainless steel powder with particle sizes in the micrometer range could not be procured from commercial sources except by separating fines estimated to be about 4% by weight from a nominal -325 mesh powder. Molybdenum powder, with commercial applications in flame spraying and wire drawing, is available with particle size distributions in the micrometer range.

Fine particle size powders are characterized by high chemical activity and tend to absorb relatively large amounts of oxygen when exposed to air. Even the -325 mesh stainless steel powder contained on the order of 6000 appm oxygen which showed up as an oxide grain boundary phase when the powder was hot isostatically pressed (HIP).

The fine molybdenum powder used in this study contained on the order of 16,000 appm oxygen. Treatment to reduce the oxygen content will be described below.

The accelerator used produced helium ions with an energy of 150 keV; this energy corresponds to a range of approximately 0.5 μm in molybdenum, as calculated according to the LSS[8] theory. A commercial molybdenum powder with small particle sizes was treated to obtain a very fine distribution by dispersing the powder in benzene, allowing time for sedimentation, and displacing the upper portion of the settling medium by pumping in fresh liquid. The measured particle size distributions of the as-received and extracted powders are given in Fig. 1. The particle size distributions were determined by x-ray sedimentation analysis* using a dilute water suspension of the powders. The suspensions were ultrasonically dispersed for 30 minutes prior to analysis. These data represent mass distributions as a function of particle size. Also plotted in Fig. 1 is a curve showing the number distribution of particle sizes in the extracted powder. This curve was calculated from the mass distribution assuming spherical particles of theoretical density. The calculated curve suggests that the mean particle diameter was just greater than twice the ion range, and that 90% of the particles had diameters less than four times the ion range. Thus, a reasonably uniform distribution of implanted helium atoms could be achieved since most of the volume of a spherical particle lies close to its surface.

The extracted powder was heat-treated for eight hours at approximately 700°C under slowly flowing dry hydrogen (dew point −60°C). The effluent gas was monitored for moisture content; at the end of the treatment the moisture level in the effluent gas had dropped to the initial moisture level in the source gas. The treatment was effective in reducing the oxygen content of the powder. The measured oxygen level in the helium implanted powder was 8750 appm (down from

*A Micromeritics Particle Size Analyzer, Model 5000, was used.

~16,000 appm). This must be taken as an upper limit since some oxygen contamination during transfer of the samples to the vacuum fusion analyzer is likely. After the hydrogen treatment, care was taken not to expose the powder to air. After sieving to break up agglomerates, the powder was loaded in the accelerator target chamber.

Ion Bombardment

Helium ions were accelerated to 150 keV with a linear accelerator with magnetic mass analysis. The 150 keV ion beam passed through a 3 cm^2 aperture and was then bent 45° into a rotating sample cup. The rotating sample cup and associated equipment is illustrated schematically in Fig. 2. Ion beam currents of 75 to 100 microamperes were used.

The powder, lying in the corner of the inclined cup, tumbled and mixed as the cup rotated. Thus, all powder particles were randomly exposed to the ion beam. Scattered ions and ions passing through the outer layers of particles provided lower energy helium to distribute throughout the powder particle volume. Tumbling and mixing of the powder was enhanced by including several 1.6 mm (1/16 inch) long slugs cut from 0.3175 cm (1/8 inch) molybdenum rod in the cup.

After helium implantation the powder was sieved (down to -400 mesh) to break up aggregates. Samples were taken for gas analysis, crimped in platinum envelopes, and sealed in glass vials. The bulk of the powder was loaded in 0.089 cm (0.035 inch) wall 304 stainless steel tubes with one end welded closed.

Analysis for residual and added gases was done by vacuum fusion extraction of the gases and mass spectrographic analysis. The duplicate powder samples were wrapped in platinum (which acts as a fluxing agent) and heated by induction in graphite crucibles. Blanks were run to account for the outgassing of the graphite, platinum, and apparatus.

Consolidation

The powder filled stainless steel tubes were connected to a vacuum system. The valves attached to each tube were "cracked" to evacuate

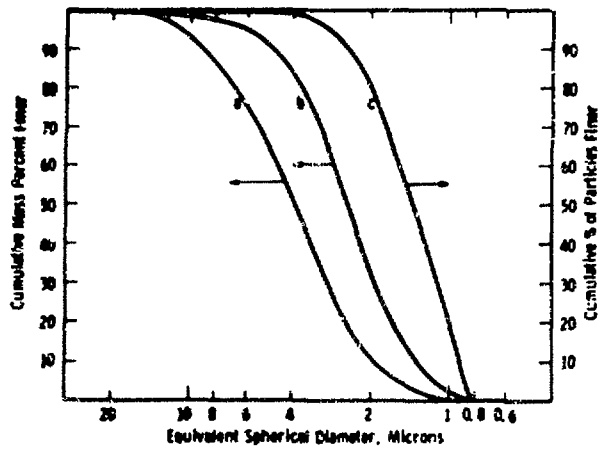

Fig. 1. Particle size distribution curves for molybdenum powders. (a) as-received powder, mass basis; (b) extracted powder, mass basis; (c) extracted powder, number basis.

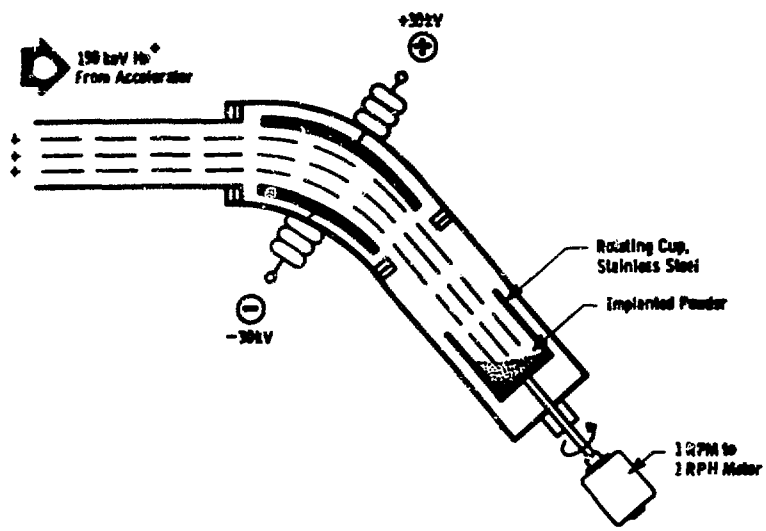

Fig. 2. Schematic illustration of ion implantation apparatus.

the tubes slowly, avoiding bubbles which might carry powder up the tubes. When the pressure fell to about one torr, the valves were opened wide and high frequency vibrations applied to the tubes. Several hours of pumping to about 10^{-4} torr removed all accessible adsorbed or trapped gases. Then the tubes were sealed at the top of the powder bed.

The sealed tubes were loaded in the hot isostatic press (HIP). The machine was first pressurized to 6.9 to 7.6 MPa (1000 to 1100 psi), then heated to about 500°C. Both pressure and temperature were gradually increased to the desired hold points with the control routine set to reach final pressure before final temperature. These conditions were held for two hours followed by cool down (initially rapid) and depressurization.

In preliminary tests it was found that the consolidation of active molybdenum powder was more dependent on pressure than temperature. Pressing temperatures below 0.5 T_m were preferred to avoid premature precipitation of helium bubbles. Therefore, the terminal pressing conditions selected were 138 MPa (20,000 psi) and 1120°C (0.48 T_m). The resulting compacts contained less than 1% porosity. It can be seen in Fig. 3 that the pores present are very fine, with average diameter less than 1 μm.

Thermomechanical Treatments

The compacted powder in rod form was rolled to prepare microstructures for controlled precipitation of helium bubbles. The thermomechanical treatments were intended to: (a) produce a reasonably homogeneous helium bubble distribution; (b) produce dislocation networks to act as nucleation sites for gas precipitation; and (c) recrystallize the molybdenum to concentrate helium bubbles on the grain boundaries.

Prior to rolling, however, an interdiffusion zone, Fig. 3, at the surface of the as-pressed molybdenum compact had to be removed. It was feared that if the interdiffusion zone was a brittle intermetallic phase, cracks formed in the surface layer during rolling could propagate into the sample. Therefore, the original can and the

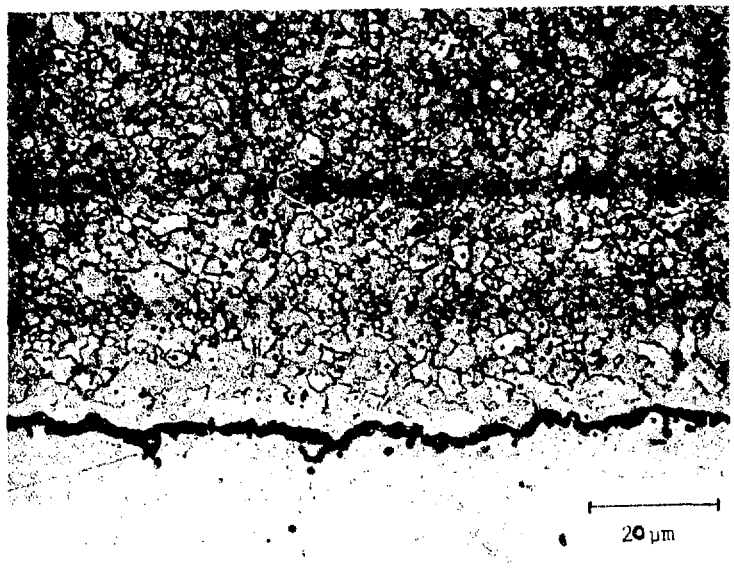

Fig. 3. Photomicrograph of as-hot isostatically pressed, helium implanted molybdenum powder at compact/can interface (1000X) (etched in Murakami's solution).

surface zone were removed. The stainless steel cans were dissolved in hot HCl. The interdiffusion zone was apparently not affected by this treatment, but dissolved in a solution of HCl and HNO_3 (about 50-50).

With the interdiffusion zone removed, the compacts were reclad. Tantalum tubes were collapsed onto the molybdenum rods and the ends welded closed. The tantalum provided a ductile, compatible barrier to further surface reactions. The tantalum clad rods were inserted in holes bored in stainless steel rectangular blocks. Steel plugs were located above and below the rods. The holes were evacuated before the blocks were sealed. The rectangular blocks were used to transfer the rolling load as uniformly as possible to the cylindrical compacts

and to give a reasonable measure of reduction in area achieved. The blocks were heated to 760°C before rolling and reheated between passes. The reduction in area was approximately 80%.

After removal of the outer steel casing, the rolled molybdenum was sectioned and annealed at several temperatures to find the best conditions for the desired recovery and recrystallization processes. The effectiveness of the heat treatments were determined by hardness measurements. The anneals for recovery or recrystallization were followed by heat treatment at 1600°C to precipitate helium bubbles.

Following heat treatment, samples were cooled to liquid nitrogen temperature and broken. The fracture surfaces were then examined by scanning electron microscopy (SEM) to determine the fracture mode and to look for evidence of helium bubbles on the fracture surfaces. Companion samples were examined by transmission electron microscopy (TEM). Three millimeter diameter discs were electro-discharge machined (EDM) from slices of the samples. The discs were ground to thicknesses of 125 to 200 μm, then electrochemically thinned to perforation.

RESULTS AND DISCUSSION

The results of the vacuum fusion analyses for the residual gas content of the as-received and implanted molybdenum powders are given in Table 1.

Table 1. Residual Gas Analysis of Molybdenum Powders (appm)

	H	He	O	N	Ar
As-Received	1617	0	15,560	1114	0
After Implantation	1575	686	8750	409	4

The powder was composed of a fine fraction extracted from the as-received powder and was hydrogen annealed to reduce the oxygen content before helium ion implantation. The oxygen and hydrogen concentrations in the processed powder following implantation were approximately 50 and 15 times higher than the respective solubilities at the pressing temperature.[9,10] The microstructure of the helium implanted and consolidated molybdenum powder, Fig. 3, was characterized by low porosity (<1%) and the absence of solid state inclusions. There were few indications of second phase particles at the powder particle boundaries in thin foils observed by transmission electron microscopy. Apparently, the relatively large concentrations of oxygen and hydrogen exerted little influence on the consolidation of the powder and on the resultant microstructure. The influence of these impurities on bubble formation is unknown. Previous runs with higher concentrations of oxygen and hydrogen but lower helium levels had resulted in fewer and smaller bubbles for the same powder processing conditions.

The powder was tumbled during ion implantation to minimize local beam heating and particle sintering. However, occasional fusing of particles did occur. In some regions of the as-consolidated sample helium bubbles were visible and were observed to be reasonably homogeneously distributed, Fig. 4. Very few bubbles were visible in thin foils made from other sections of the as-consolidated sample, however, or samples annealed at temperatures up to 1200°C after rolling. These observations suggest that implanting the helium at elevated temperatures can result in reasonably homogeneous bubble formation without the necessity for a subsequent high temperature anneal to precipitate the helium. Similar observations have been made on helium bombarded niobium strip by Bauer and Thomas.[11]

Selection of a 760°C rolling temperature and 80% reduction in area represented an attempt to introduce the maximum amount of "cold work" without cracking the samples. This was moderately successful. Some cracking was observed in sections of the as-rolled strip. The rolling deformation resulted in grain size aspect ratios of up to 8:1 with the

Fig. 4. Helium bubbles in as-implanted and consolidated molybdenum powder compact (TEM).

initially equiaxed grains (originally powder particles) elongated in the rolling direction. No significant increase in dislocation density or extensive network formation occurred as a result of the plastic deformation of these ultra-fine grained samples.

The range of annealing temperatures listed in Table 2 was selected to establish conditions for stress-relief annealing, recrystallization and grain growth.

Optical metallography and transmission electron microscopy showed that no significant changes in microstructure occurred for annealing temperatures up to 1200°C. Similarly, the hardness decreased rapidly above 1200°C, Table 2. The very rapid softening from 1400°C to 1600°C was accompanied by selective grain growth and increasing porosity. Scanning electron micrographs of the surfaces of samples broken in liquid nitrogen after annealing at 1400-1600°C showed intergranular

Table 2. Annealing Conditions and Resulting Hardnesses for Molybdenum Compacts

Annealing Conditions	3 kg Vickers Hardness
as-rolled	370 ± 5
870°C, 2-1/2 hr	391 ± 1
980°C, 2 hr	375 ± 0
1093°C, 2-1/4 hr	340 ± 2
1200°C, 1 hr	304 ± 16
1400°C, 1 hr	173 ± 4
1600°C, 1 hr	102 ± 4

fractures. Cavities were clearly visible at facets and grain boundaries, Fig. 5a. Transmission electron microscopy of thin foils of these samples from regions where appreciable grain growth had not occurred showed accelerated growth of grain boundary pores as well as extensive helium bubble formation within the grains, Fig. 5b.

Table 3 summarizes the effects of the thermomechanical processing on the resultant helium distributions in molybdenum. In every case, some partitioning of helium between competing nucleation sites occurred. For example, thermomechanical processing to produce a homogeneous bubble distribution also resulted in accelerated growth of bubbles at the grain boundaries and precipitation on existing dislocations. Table 3 merely indicates that it was possible to establish a dominant "sink" for the helium. Additional work will be required to: optimize the control of the helium distribution; evaluate the correlation between mechanical properties and distribution of helium; and compare the mechanical property response to that of samples with conventional cast and wrought microstructures.

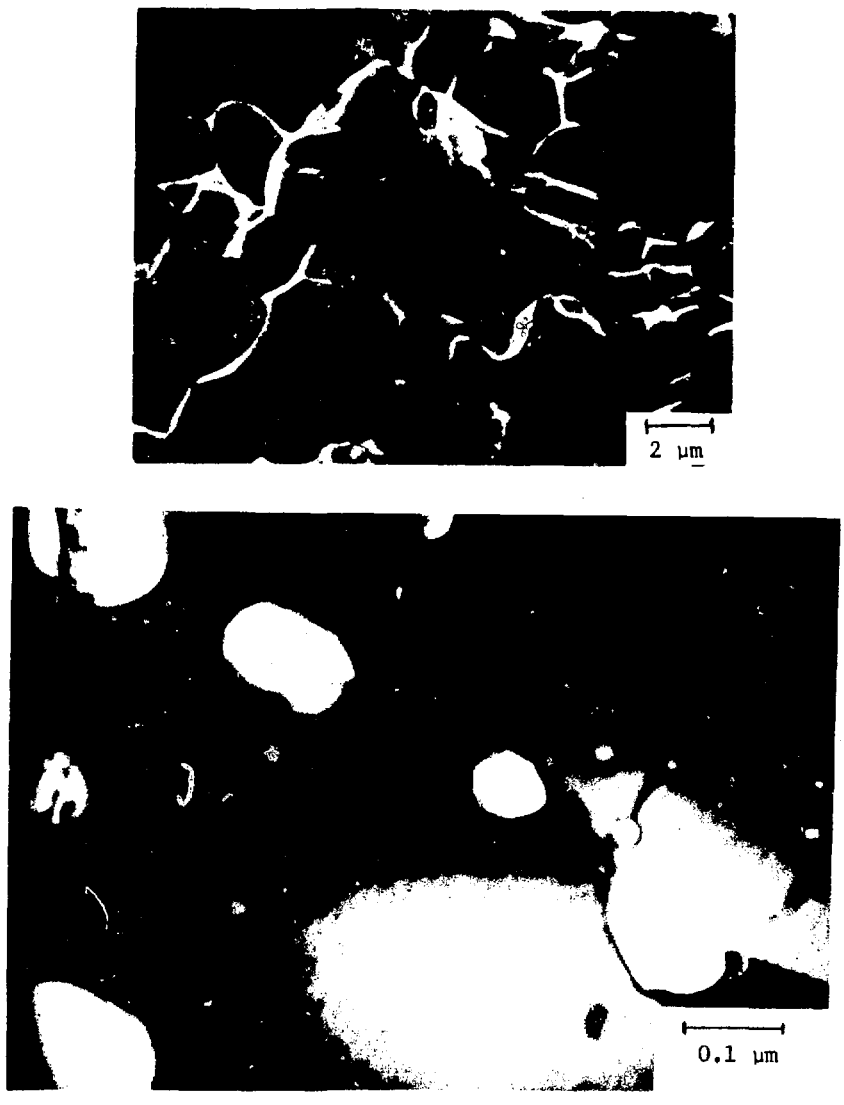

Fig. 5. Electron micrographs of helium implanted, consolidated, and precipitation annealed (1 hr at 1600°C) molybdenum powder compact. (a) Fracture surface SEM. (b) Bubbles at grain boundary intersection TEM.

Table 3. Effects of Thermomechanical Processing on Helium Bubble Distribution in Molybdenum

Post Consolidation Thermomechanical Treatment (TMT)	Bubble Distribution, (Dominant Locations)
Precipitation anneal (0.65 T_m)	Homogeneous
(Implantation at high temperature, no TMT	Homogeneous)
Warm rolled (760°C) to 80% RA, Stress relief anneal (0.40 to 0.47 T_m) Precipitation anneal (0.65 T_m)	Heterogeneous, on dislocations and some grain boundaries
Warm rolled (760°C) to 80% RA, Grain growth anneal (0.51 to 0.65 T_m)	Heterogeneous, primarily on grain boundaries

CONCLUSIONS

It has been shown that helium implanted molybdenum powder can be successfully consolidated to form specimens for studying the effects of helium on properties despite supersaturation levels of other gas contaminants. The microstructures produced were clean and free of oxides and other heterogeneous phases. Clear-cut placement of helium bubbles on a single type of nucleating site was not achieved. However, homogeneous precipitation, bubble formation predominantly on dislocations, and collection of bubbles mainly on grain boundaries -- each with a minor component of the other modes -- was accomplished by variation of heat treatment and mechanical working conditions. It seems clear that more careful powder preparation and handling techniques are needed to minimize contamination. But with these improvements this method may provide a means for studying helium effects on mechanical and physical properties independently of synergistic atom displacement phenomena.

ACKNOWLEDGMENTS

Helpful discussions and technical assistance were provided by R. W. Buckman and R. E. Gold. The assistance of N. J. Doyle in implanting the molybdenum powder is gratefully acknowledged.

REFERENCES

1. G. L. Kulcinski and R. W. Conn in Proc. of the First Topical Meeting on the Technology of Controlled Nuclear Fusion, Vol. 1, G. R. Hopkins, ed., NTIS, Springfield, Va., CONF-740402-P1 (1974), p. 38.

2. P. C. L. Pfeil and D. R. Harries, ASTM STP No. 380, 202 (1965).

3. A. F. Rowcliffe, J. Nucl. Mater. 18, 60 (1966).

4. G. J. C. Carpenter and R. B. Nicholson in Radiation Damage in Reactor Materials, Vol. II, IAEA, Vienna (1969). IAEA-SM-120/G-6, p. 383.

5. E. E. Bloom and F. W. Wiffen, "The Effects of Large Concentrations of Helium on the Mechanical Properties of Neutron Irradiated Stainless Steel," ORNL-TM-4861 (May 1975).

6. A. T. Santhanam, A. Taylor, and S. D. Harkness, in Defects and Defect Clusters in B.C.C. Metals and Their Alloys," R. J. Arsenault, ed., NBS, Gaithersburg, MD. (1973), p. 302.

7. D. Kramer, H. R. Brager, C. G. Rhodes, and A. G. Pard, J. Nucl. Mater. 25, 121 (1968).

8. J. Lindhard, M. Scharff, and H. E. Schiott, Kgl Danske Videnskab Selshab. Mat. Fys. Medd. 33 (1963).

9. R. P. Elliott, Constitution of Binary Alloys, First Supplement, p. 500, McGraw-Hill, New York, 1965.

10. F. A. Shunk, Constitution of Binary Alloys, Second Supplement, p. 517, McGraw-Hill, New York, 1969.

11. W. Bauer and G. J. Thomas in Defects and Defect Clusters in B.C.C. Metals and Their Alloys, R. J. Arsenault, ed., NBS, Gaithersburg, Md. (1973), p. 255.

RADIATION DAMAGE BY ^{252}Cf FISSION FRAGMENTS AND ALPHA PARTICLES*

T. H. Gould, Jr.
W. R. McDonell

Savannah River Laboratory
E. I. du Pont de Nemours & Co.
Aiken, S. C. 29801

ABSTRACT

Rates of atom displacement and helium injection in materials exposed to ^{252}Cf fission fragments and alpha particles were calculated to establish the potential for use of ^{252}Cf sources for radiation damage studies. Maximum displacement rates of about 10^{-6} dpa/sec at the surface of typical targets exposed to a ^{252}Cf fission fragment source were comparable to those experienced by materials in a fast breeder reactor or in a controlled thermonuclear reactor (CTR) first wall, though much lower than the displacement rates achieved using particle accelerators. Helium was concurrently accumulated at a rate of 3×10^{-4} atom ppm/sec at the target surface, yielding a He/displacement ratio 10^3 times that produced in the fast breeder reactor materials, but only about 20 times that produced in the CTR materials. These comparisons suggest that ^{252}Cf fission fragment sources may find useful applications in studies of effects of high-He content on radiation damage in CTR materials.

INTRODUCTION

Accelerator-generated charged-particle irradiations have proved effective for simulating fast-neutron damage in materials for fast breeder or controlled thermonuclear reactors (CTR).[1] The intense beams of high-energy particles that can be generated by the accelerators produce in a few hours effects that are equivalent to several years of reactor service. Intensities of charged particles such as alpha particles

*The information contained in this article was developed during the course of work under Contract No. AT(07-2)-1 with the U. S. Energy Research and Development Administration.

from radionuclides are generally too low for practical use in such damage-simulation studies, although fission fragments produced during neutron irradiation of fissionable ^{235}U have been employed in some studies.[2]

During studies of effects of ^{252}Cf radiations on neutron-source capsule materials, it became apparent that ^{252}Cf fission fragments could cause significant atom-displacement damage to adjacent materials. The displacement damage produced by the fission fragments would be accompanied by injection of high concentrations of helium resulting from ^{252}Cf alpha decay, indicating that the ^{252}Cf sources might prove useful in simulating radiation damage in high-helium generating environments, such as the CTR.

RESULTS

Californium-252 decays with a half-life of 2.65 years by competitive alpha emission (97%) and spontaneous fission (3%).[3,4] Of the 1.28×10^{12} fission fragments produced per gram per second, half (light group) are emitted with average kinetic energy of 104.1 MeV, average atomic number of 42, and average mass of 106.4. The heavy group of fission fragments are emitted with average energy 79.25 MeV, atomic number 55, and mass 141.7. Like other heavy particles, the ^{252}Cf fission fragments displace atoms in materials in which they are absorbed, forming vacancies and interstitials which agglomerate at appropriate temperatures into microscopically observable voids and dislocations.[5] Alpha particles also produce lattice damage and leave implanted helium atoms that promote formation of voids at intermediate temperatures and form gas bubbles at high temperatures. The ultimate consequences of these effects are a potentially deleterious swelling of the exposed material and changes in other properties such as mechanical strength. Quantitative assessments of the damage produced by the ^{252}Cf fission fragments and alpha particles are made in the following sections.

Displacements Produced by Fission Fragments

The rate of target-atom displacement produced by ^{252}Cf-source fission fragments was calculated using a modification of the method of Kulcinski, et al.[6,7] to predict displacement rates produced by accelerator-generated heavy ions. The model, as described in the Appendix, employs the Lindhard, Scharff, and Schiott (LSS) theory[8] to determine the energy lost by fission fragments in primary nuclear collisions, and the Kinchin and Pease approximation[9] to determine the rate of displacement of atoms in a target lattice. The fraction of energy given up by the fission fragments in primary collisions which subsequently goes into the production of higher order displacements is determined by the method of Doran and Kulcinski.[7]

In contrast to the accelerator-generated ions, which are emitted as a monoenergetic, unidirectional beam, fission fragments from a ^{252}Cf source are generated within a discrete source volume and are emitted with variable energy and direction. This characteristic of the fission fragments requires that the displacement rate at a given point in a target be determined by integration of effects of fragments originating at different points in the californium source. If the simplifying assumption that the range of the fission fragments in the source material is equal to their range in the target material is made, and a Gaussian distribution about the mean particle range is used for the spatial dependence of the rate of nuclear energy transfer in the source and target, the rate of atom displacement at a given penetration distance in a target material exposed to a ^{252}Cf source is approximated by Eq. (1), as derived in the Appendix:

$$D(x) \simeq \frac{N_f E_T}{4E_d N}\left(1 - \frac{x}{R}\right) \text{ for } x \leq R\text{-}2\alpha \qquad (1)$$

where

$D(x)$ = rate of atom displacement at x, dpa*/sec,

x = penetration distance into target, μm,

N_f = number of fission fragments generated in source/cm^{3}sec,

E_T = energy transferred to lattice atoms in nuclear collisions, eV,

N = number of target atoms/cm^3,

* Displacements per atom (dpa) represents the fraction of total atoms displaced during irradiation.

E_d = displacement energy, eV,

R = mean range of fission fragments in source and target materials, μm,

α = effective range-straggling parameter, μm.

Values for E_T, R, and E_d that were used to calculate the displacement rate for aluminum and iron targets exposed to ^{252}Cf fission fragments are listed in Table 1. Since α is about 1/10 the range R, Eq. (1) applies over about 80% of the total penetration distance of the particles.

For a source with a density of 10 g/cm^3 containing 20% $^{252}Cf_2O_3$ (remainder impurities), the number of fission fragments (N_f) in each of the mean light (MLF) and mean heavy (MHF) groups is 1.2 x 10^{12}/cm^3 sec. Exposure of a 0.3-cm^2 target area to a source containing 6 mg ^{252}Cf* would displace atoms at a maximum rate of about 9 x 10^{-7} dpa/sec in aluminum and about 1 x 10^{-6} dpa/sec in iron. The atom-displacement rates for the MLF and MHF groups are shown as a function of penetration distance into the aluminum targets in Fig. 1. Damage decreases approximately linearly from a maximum at the target surface to about 50% at a penetration distance of 7 μm (40% of the particle range).

The maximum displacement rates produced by ^{252}Cf fission fragments at the target surface are comparable to those expected for materials in EBR-II and a CTR first wall,[10,11,12] as shown in Fig. 2, and are at least an order of magnitude higher than the displacement rates obtained in a thermal reactor. They are, however, several orders of magnitude lower than those typically produced with charged-particle accelerators. Irradiation of a highly enriched ^{235}U source in a thermal reactor would be required to achieve the displacement rates obtained with a particle accelerator.

Helium Atom Concentrations

Concurrent with fission fragment emission, ^{252}Cf emits alpha particles with average kinetic energy of 6.1 MeV at the rate of 1.92 x 10^{13} alphas/g sec, resulting in the deposition of helium atoms in an adjacent target. If, as in Eq. (1), equal range for the alpha particles in

* The 6-mg ^{252}Cf source, equal in thickness to that required for maximum He concentration in an adjacent target, is about twice the thickness required to produce the maximum displacement rate.

Table 1. Parameters used to Calculate Displaced-Atom Densities in Aluminum and Iron

Parameter	Aluminum		Iron	
	MLF	MHF	MLF	MHF
Energy Transfer, E_T(MeV)	2.0	3.0	2.6	3.8
Range,[a] R (μm)	16	13	8.0	6.3
Displacement Energy, E_d (eV)	30	30	25	25
Range-Straggling Parameter Ratio, α/R	0.08	0.11	0.08	0.11

a. Calculated from LSS theory.[8]

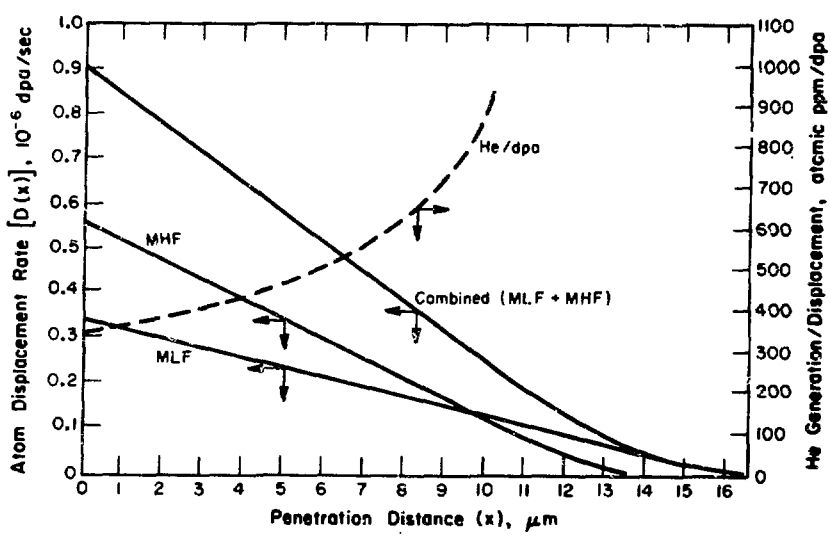

Fig. 1. Atom Displacement Rate and He Generation-to-Displacement Ratio Produced in Aluminum by ^{252}Cf Radiations.

source and target material is assumed, and the unidirectional deposition of alpha particles is approximated by a Gaussian distribution about the particle range, the rate of deposition of helium atoms as a function of penetration distance in the target is of similar form to Eq. (1):

$$N(x) \simeq \frac{S_V}{2}\left(1 - \frac{x}{R}\right) \text{ for } x \leq R - 2\alpha \qquad (2)$$

where

$N(x)$ = rate of He deposition at x, particles/cm^3 sec,

x = penetration distance into target, μm,

S_V = rate of generation of alpha particles, particles/cm^3 sec,

R = mean range of alpha particles in source and target materials, μm,

α = effective range-straggling parameter, μm.

Eq. (2) applies over about 98% of the alpha-particle range, since the range-straggling parameter α is about 0.01 R.[13] The range in aluminum of the 6.1-MeV ^{252}Cf alpha particle, as calculated from range data for protons,[13,14] is about 30 μm, or twice that of the ^{252}Cf fission fragments. An aluminum target exposed over a 0.3 cm^2-area to a 6 mg-^{252}Cf source emitting 3.5 x 10^{13} alpha particles/cm^3 sec would be injected with He atoms at a maximum rate of 3 x 10^{-4} atomic ppm/sec at the target surface, decreasing approximately linearly to zero at the 30 μm particle range. The maximum concentrations of helium produced, compared in Fig. 2, are a factor of 30 times that expected in the CTR first wall materials,[10,11,12] and 1000 times that in EBR-II.[12,15] The ratio of He atoms to displaced atoms at the specimen surface is about 350 atomic ppm/dpa, increasing with increasing penetration due to the greater range of the alpha particle, as shown in Fig. 1. In iron, the relative concentration of He atoms to displaced atoms at the surface is about 225 atomic ppm/dpa. Californium-252 sources having thicknesses between the ranges of the fission fragments and the alpha particles would have lower He-to-displaced-atom ratios.

The displacement damage induced in the metal target by 6.1 MeV-^{252}Cf alpha particles was estimated using the model derived by Kinchen and Pease for Rutherford collisions.[9] In aluminum about 300 displacements per alpha particle occur. If a damage distribution similar to

that defined by Eq. (2) is assumed, the alpha-induced displacement rate at the target surface will be about 9×10^{-8} dpa/sec or 10% of the number of displacements produced by the fission fragments.

Radiation Damage Effects

The radiation damage produced by ^{252}Cf fission fragments and alpha particles would be manifested in several ways, depending on target material. Displaced-atom densities of 10 dpa can be realized in target materials exposed to a 6-mg $^{252}Cf_2O_3$ source for 120 days. At intermediate temperatures (0.3-0.6 absolute melting point), microscopically observed voids and interstitial dislocation loops are formed in pure metals after 0.1 dpa and produce volume changes exceeding a few tenths of a percent after 1 dpa.[5,16] Equivalent effects are produced in more swelling-resistant alloys, such as stainless steel, at 10 times these exposures or higher. In the low-melting materials, such as aluminum, such damage is produced at just above room temperature, but in higher-melting materials, such as stainless steel, damage is observed at temperatures of 500°C or more.

The high He-to-displacement ratio provided by ^{252}Cf sources, compared to the ratio for other radiation sources in Table 2, should produce effects that are of special interest in CTR materials studies. Helium generated during HFIR irradiations of Type 316 stainless steel by the successive slow neutron capture reactions $^{58}Ni(n,\gamma)^{59}Ni(n,\alpha)^{56}Fe$ concurrent with displacement damage by fast neutrons produces swelling at intermediate temperatures that is considerably greater than that expected from void formation in the absence of helium.[12] The swelling, moreover, persists to high temperatures because of gas-bubble formation. Concentrations of cavities generated in the high-helium environment are an order of magnitude greater than those expected for void concentrations in the absence of helium, and the cavities, like gas bubbles, form preferentially at grain boundaries and precipitate-matrix interfaces. Similar or more-pronounced effects of high-helium content should be produced by ^{252}Cf fission fragment sources in a variety of target materials.

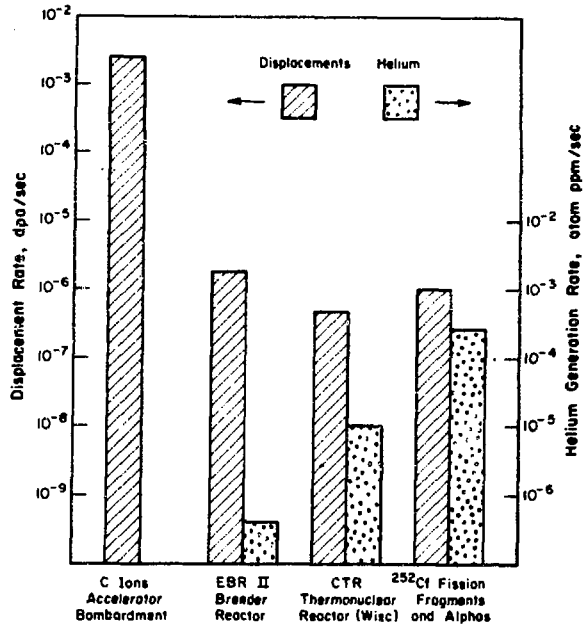

Fig. 2. Rates of Displaced Atom and Helium Generation Produced by Several Radiation Sources.

Table 2. Rates of Displaced Atom and Helium Generation

Source	Generation Rates (per year)		
	dpa	He(ppm)	He(ppm)/dpa
EBR-II[a]	60	12	0.2
^{235}U fiss. frag. (0.03 a/o bu)[b]	60	90(Xe + Kr)	1.5
CTR (Wisc)[a,c]	18	285	16
HFIR[a]	60	1,900	32
^{252}Cf fiss. frag. + alpha (6 MeV)	28	8,300	300

a. Ref. 12

b. Assuming 200,000 displacements per fission (Ref. 20).

c. Ref. 10 and 11.

d. Assuming exposure over 0.3 cm^2 area to 20% pure Cf_2O_3 source containing 6 mg ^{252}Cf.

Atom displacements caused by fission fragments in non-cubic metals such as orthorhombic uranium produce anisotropic growth effects as well as swelling. Such effects, due to preferred orientations of the defect agglomerates produced by vacancies and interstitials, are well known in uranium fuel elements.[17,18,19] Typical consequences include external changes in shape and surface roughening indicative of severe internal grain distortions at low temperatures and large irregular cavities due to related intergranular stresses at intermediate temperatures. Such effects are pronounced in uranium after burnups that produce about 3×10^{19} fission fragments/cm^3, which is approximately equivalent to 1-1/2 years' exposure to a ^{252}Cf source. A ^{252}Cf source could thus be employed to characterize the anisotropic growth effects expected during reactor exposure of nonfissionable hexagonal metals such as magnesium, zirconium, and titanium. Effects of high-He content on the damage sustained by these metals are also of interest. The gas-to-displacement ratio produced by ^{235}U fission fragments is included in Table 2 for comparison with the ratio provided by a ^{252}Cf source.

LIMITATIONS ON USE OF ^{252}Cf SOURCES

Limitations on the use of ^{252}Cf fission fragment sources in radiation damage studies do not appear to present insurmountable difficulties. The ^{252}Cf must be employed in relatively large quantities (3-6 mg) for maximum effect. However, inventories of the nuclide that would accommodate use of these quantities are available. The ^{252}Cf must be handled behind relatively thick neutron shielding, typical of that employed during source preparation.[3]

Since the ranges of the fission fragments and alpha particles are limited, only thin sections of target materials exposed to ^{252}Cf radiation would suffer damage. Thin foils would be best suited as target specimens. Special fission fragment source designs that would allow close proximity of source and target would be required, and provision for removal of heat generated in the target would be necessary. Microscopic examinations and volume measurements of target foils could be performed by using techniques that were developed for specimens irradiated with accelerator-generated charged particles.

Sources of radioactivity in the exposed target include ^{252}Cf contamination, neutron-induced activities, and residual fission products. Contamination could be eliminated by appropriate cleaning. The neutron-induced activity levels would depend on cross sections of the target material and its impurities. Calculations of activity from residual fission products indicate that dose rates of less than 10 mr/hr at 1 meter would be encountered from the targets after 120-day exposures.

APPENDIX

Displacement Rate Calculations

To reduce the complexity of calculating the atoms displaced by fission fragments emitted from a source of finite volume, the following two assumptions were made:

1. The ranges and rates of energy loss of the fission fragments are equal in source and target materials.
2. The nuclear energy transfer function, $S_n(r)$, calculated by the method of Ref. 6 can be replaced by a Gaussian distribution about the mean range R of the fission fragment group (see Fig. A.1).

The first approximation (equal fission fragment ranges in source and target) slightly overestimates the damage rate in aluminum, since the calculated ranges of the MHF and MLF fragments in californium oxide (taken as Cf_2O_3) are about 20% less than those in aluminum. For an iron target, the damage rates calculated by this model are slightly underestimated.

The second approximation greatly simplifies the spatial integration over the product of flux and energy transfer function $S_n(r)$. The energy transferred in primary collisions can be expressed as

$$S_n(r) = \frac{E}{\alpha \sqrt{\pi}} \exp\left[- \left(\frac{r-R}{\alpha} \right)^2 \right] \qquad \text{(A1)}$$

where

$S_n(r)$ = nuclear energy transfer function, eV/μm,

r = distance along particle track in source or target material, μm,

E = total energy transferred in primary collisions, eV (integral of $S_n(x)$, Fig. A.1),

α = effective range-straggling parameter, μm,

R = mean range of fission fragments in source and target materials.

The effective range-straggling parameter α was estimated from $\alpha^2 = \alpha_L^2 + \alpha_E^2$ where α_L represents range straggling from LSS theory,[8] and α_E, the range dispersion associated with the group's energy distribution. The range-dispersion parameter α_E, which is the dominant term of this equation, was determined from the experimental energy distribution of ^{252}Cf fission fragments measured by Schmitt and Pleasonton.[21] Conversion from energy dispersion to range dispersion was made with the aid of energy-range relationships derived from LSS theory. Values of effective relative straggling for the MLF and MHF fragments are given in Table 1.

The source geometry considered by this model is shown in Fig. A.2. The fission fragment flux at a distance r from a small volume element dV in the source is $N_f \cdot dV/4\pi r^2$, where N_f is the source density (fission fragments/cm^3). The displacement rate D(r) (in dpa/sec) at r due to fission fragments emitted from dV can be approximated by

$$D(r)dV = \frac{N_f dV}{4\pi r^2} \bullet \frac{wS_n(r)}{2E_d N} \text{ for } dV = 2\pi r^2 \sin\Theta \, dr d\Theta \qquad (A2)$$

where w is a correction factor to account for energy lost to electrons by primary and secondary knockons, E_d is the displacement energy, (in eV), N is the number of target atoms/cm^3, and Θ is the angle of fission fragment track in target (Fig. A.2). Integrating over the effective source volume gives

$$D(x) = \frac{-wE}{2E_d N} 2\pi \int_{x/R_m}^{1} \int_{x/\mu}^{R_m} r^2 dr \, \frac{N_f}{4\pi r^2} \bullet \frac{1}{\alpha\sqrt{\pi}} \exp\left(-\frac{r-R}{\alpha}\right)^2 \qquad (A3)$$

where

D(x) = rate of atom displacement at x, dpa/sec,

x = penetration distance into target, μm,

μ = cos Θ (Fig. A.2),

R_m = maximum projected range of fission fragment, μm.

The upper limit on the second integral can be extended to infinity without changing the value of the integral. Carrying out the integrations in Eq. (A3) as far as possible in closed form gives

$$D(x) = \frac{E_T}{8E_dN}\left[(1-x/R) + \alpha x \int_{\frac{R-R_m}{\alpha}}^{\frac{R-x}{\alpha}} \frac{\mathrm{erf}(\nu)d\nu}{(R-\alpha\nu)^2}\right] \qquad \text{(A4)}$$

where $\nu = \frac{1}{\alpha}(R-x/\mu)$ and $E_T = wE$. For practical purposes, the maximum range can be set equal to the mean projected range plus twice the straggling parameter, that is $R_m = R + 2\alpha$. If this substitution is made for R_m, Eq. (A4) can be approximated by

$$D(x) \simeq \frac{N_f E_T}{4E_dN}\left[1-x\left(\frac{R}{R^2-4\alpha^2}\right)\right] \quad \text{for } x<R-2\alpha$$

or

$$D(x) \simeq \frac{N_f E_T}{4E_dN}\left(1-\frac{x}{R}\right) \qquad \text{(A5)}$$

for α of the order of 0.1R or less. Thus, the atom displacement rate is expected to decrease almost linearly with the depth of penetration of the fission fragments.

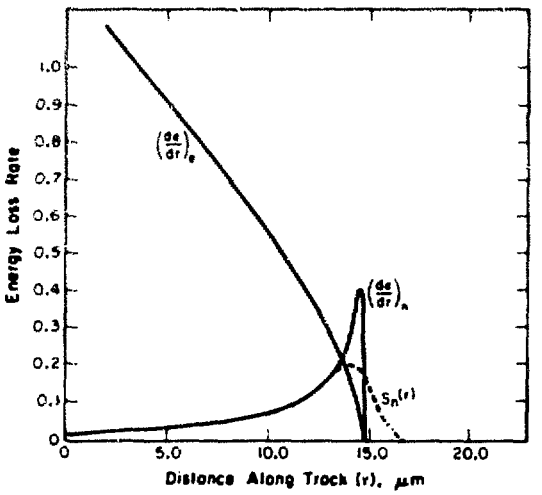

Fig. A.1. Energy Loss Rates for the Mean Heavy Fission Fragment in Aluminum.

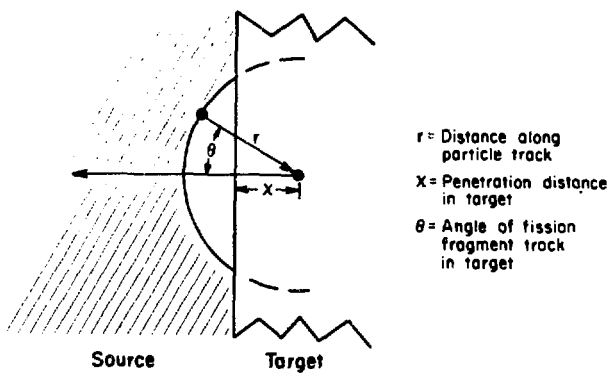

Fig. A.2. Source-Target Geometry.

REFERENCES

1. G. L. Kulcinski, J. L. Brimhall, and H. E. Kissinger, "Production of Voids in Pure Metals by High Energy-Heavy Ion Bombardment," p 449 in Radiation-Induced Voids in Metals — Proceedings 1971 International Conference, Albany, N.Y., June 1971, J. W. Corbett and L. C. Ianniello, Eds. (CONF-710601) U. S. Atomic Energy Commission, 1971.

2. J. Leteurtre, J. L. Pouchou, J. Soullard and L. Zuppinoli, J. Nucl. Mater. 54, 254 (1974).

3. Californium-252 Guide for Fabricating and Handling ^{252}Cf Sources, U. S. Atomic Energy Commission Report SRO-153 (January 1971).

4. D. H. Stoddard, Radiation Properties of Californium-252. DP-986, (June 1965).

5. D. I. R. Norris, Radiat. Eff. 14, 1 and 15, 1 (1972).

6. G. L. Kulcinski, J. J. Laidler, and D. G. Doran, Radiat. Eff. 7, 195 (1971).

7. D. G. Doran and G. L. Kulcinski, Radiat. Eff. 9, 283 (1971).

8. J. Lindhard, M. Scharff, and H. E. Schiott, Mat. Fys. Medd., Kgl. Dan. Vid. Selsk. 33, No. 14 (1963).

9. G. H. Kinchin and R. S. Pease, Rep. Progr. Phys. 18, 1 (1955).

10. G. L. Kulcinski, R. G. Brown, R. G. Lott, and P. A. Sanger, Nucl. Technol. 22, (1974).

11. G. L. Kulcinski and G. A. Emmert, J. Nucl. Mater. 53, 31 (1974).

12. F. W. Wiffen and E. E. Bloom, Nucl. Technol. 25, 113 (1975).

13. S. V. Starodubtsev and A. M. Romanov, The Passage of Charged Particles Through Matter, AEC-tr-6468, Chapt. 1 (1965).

14. J. F. Janni, Calculations of Energy Loss, Range, Path Length, Straggling, Multiple Scattering, and Probability of Inelastic Nuclear Collisions for 0.1 to 1000 MeV Protons, AFWL-tr-150 (1966).

15. W. N. McElroy and H. Farrar, "Helium Production in Stainless Steel and Its Constituents as Related to LMFBR Development Programs," p 187 in Radiation-Induced Voids in Metals — Proceedings 1971 International Conference, Albany, N.Y., June 1971 (CONF-710601) U. S. Atomic Energy Commission, 1971.

16. J. O. Steigler, "Void Formation in Neutron-Irradiated Metals," Radiation-Induced Voids in Metals (Proceedings 1971 International Conference, Albany, N.Y., June 1971) (CONF-710601), p 292. U. S. Atomic Energy Commission, 1971.

17. W. R. McDonell, ANS Trans. 15, 185 (1972).

18. W. R. McDonell, "Void Model for Cavitational Swelling of Uranium." Int. Conf. on Phys. Metallurgy of Reactor Fuel Elements, Berkeley, England, Sept. 1973 (to be published).

19. R. D. Leggett, T. K. Bierlein, B. Mastel and H. A. Taylor, "Basic Swelling Studies," p 303 in Radiation Effects (AIME Symposium, Asheville, N. C., Sept. 1965), W. F. Sheely (ed), Gordon & Breach, N. Y., 1967.

20. J. Leteurtre and Y. Quéré, p 21 in Irradiation Effects in Fissile Materials, American Elsevier Publ. Co., N. Y., 1972.

21. H. W. Schmitt and F. Pleasonton, Nucl. Instrum. Methods 40, 204 (1966).

[illegible]
[illegible] für Kernverfahrenstechnik
[illegible], [illegible], Germany

The aim of this review is a discussion of data (already existing or to be required) which should allow prediction of the behavior of large superconducting coils in the radiation field of a future fusion reactor. The electrical and mechanical stability of such magnets is determined by the irradiation induced deterioration of the magnet components, i.e. by changes in critical current, field and temperature of the superconductor (NbTi, A-15 phases), by resistivity increase in the stabilizer (Cu, Al), and by changes in mechanical and dielectric properties of insulators and spacers. Recent low temperature simulation experiments with fission neutrons and heavy ions show that the superconductor will not be the critical component of a fusion magnet - at least as far as radiation damage is concerned. Much more severe is the loss of stability due to the resistivity increase of the stabilizing material. It seems, however, that the magnitude of this effect can be predicted rather reliably and therefore taken into account in the coil design. Almost no data exist about the low temperature behavior of insulator and spacer materials in a radiation field. Furthermore, very little is known about the nature of the radiation damage in non-metals, which makes extrapolations of the few existing data to other materials or to other doses highly speculative. Only future experiments can decide if the insulators will be the limiting component of a CTR magnet or not.

EXPECTED ENVIRONMENTAL DATA FOR CTR MAGNETS

Already in the first conceptual designs, power balance estimates very clearly showed that superconducting coils must be used in fusion reactors. This requirement adds another problem to the abundance of new technologies which are involved in CTR technology. Although reliable small and medium size superconducting coils are now available, magnets with dimensions and fields needed for large fusion devices have not yet

been built and grievous experiences in the past have shown that scaling laws should be used with caution when the performance of small superconducting coils is extrapolated to larger systems. But apart from problems connected with their large size and stored energy, CTR magnets are exposed to a considerable flux of fast neutrons, i.e. they will operate in an environment which is not very hospitable for superconducting components.

As far as we know at present, the neutron irradiation will have two detrimental effects on superconducting magnets. First, energy in the form of heat is deposited in the coil volume. This causes (a) temperature gradients from the bulk of a coil section to the coolant channels and (b) increased power and refrigerator costs. Second, radiation damage usually deteriorates the properties of superconducting magnet components. In order to keep both effects sufficiently small a fusion reactor must have a shield between the blanket and the magnet windings. Several designs of such shields which usually consist of a mixture of iron, borated water and lead have been proposed[1] and an excellent review on this subject together with a critical analysis of the two design criteria (thermal and radiation damage) has been published by McCracken and Blow[2] in 1972. Nevertheless, it appears to be appropriate to review the problem of radiation damage again at this point of time since most of the irradiation experiments on superconductors which are meaningful for CTR magnets have been carried out in the last two or three years[3-11].

Before discussing radiation damage effects in the different magnet components, it is necessary to arrive at some numbers about typical neutron fluences and spectra in the magnet region. These data can be obtained in the following way: Using the thermal criterion that the maximum power allowed for refrigeration is e.g. 1 % of the thermal reactor output (corresponding to an energy attenuation of 10^{-5}) McCracken and Blow[2] showed that the neutron flux through the first wall must be attenuated by a factor of about 1.6×10^{-6} when reaching the magnet region. In the model of Fig. 1 this is achieved by a blanket and shield thickness of 1 and 0.55 m, respectively. For a total first wall loading of 10 MWm^{-2} ($\simeq 3 \times 10^{14}$ of 14 MeV $ncm^{-2}sec^{-1}$) this would correspond to a neutron

flux of around 4×10^{9} $nem^{-2}sec^{-1}$ through the innermost windings of the magnet (see Fig. 1).

However, both the 1 J thermal criterion and the wall loading of 10 MWm^{-2} are extremely high values (e.g. for UWMAK II, the energy attenuation to the magnets is 4×10^{-5} and the neutron wall loading is only 1.16 MWm^{-2}). Therefore, one is certainly still on the safe side if a maximum neutron flux of $\phi = 1 \times 10^{9}$ $nem^{-2}sec^{-1}$ through the magnet components is assumed. This corresponds to a fluence of $\phi t = 3 \times 10^{17}$ nem^{-2} in 10 years of continous reactor operation.

The neutron energy spectrum in the coil region has also been calculated by McCracken and Blow[2] and is shown in Fig. 2 where it is compared with a first wall spectrum and a typical fission research reactor spectrum. Since the spectrum in the magnet region is rather similiar to the fission spectrum, research reactors are ideally suited for irradiation experiments on CTR magnet components if they are equipped with low temperature facilities like in ANL or Garching. The last requirement is essential since all CTR magnet components operate at low temperatures (4.2 K) where irradiation effects are usually quite different from those observed at room temperature or above. Although this entails considerable experimental handicaps, there is also a positive consequence: since all irradiation produced defects are immobile at such low temperatures, no defect reactions and thus no dose rate effects will occur. This is rather important because the simulation experiments on CTR magnet components in fission reactors[3-10,12,13] are performed at much higher dose rates than will actually occur in CTR magnets.

In the following I will try to review measurements of property changes in magnet materials which were subject to irradiation conditions similiar to the ones stated above. We shall discuss each group of materials separately, going from the least critical component (structure) to the most uncertain one (insulators).

RADIATION DAMAGE DATA OF COMPONENTS IN SUPERCONDUCTING MAGNETS

Structural Materials

It is expected that the limiting factor in the performance of large coils will be the strength of the conductor and the structural material (steel) which have to withstand extremely large forces[14,15]. However, yield and tensile stress of steels and other metals are generally increased by neutron irradiation at low temperatures[16]. Another effect, namely irradiation induced ("in pile") creep, requires mobile interstitials which are not present at 4 K in most metals. We therefore expect no adverse effects on the mechanical stability of a coil system as far as radiation damage in structural materials is concerned.

Superconductors

The applicability of irreversible type II or "hard" superconductors which are used as magnet conductors is essentially characterized by the three parameters T_c (transition temperature), B_{c2} (upper critical field) and $j_c(B)$ (critical current density as a function of the magnetic field B). T_c is mainly determined by the electronic properties of the material and is only slightly influenced by the defect structure whereas B_{c2} and particularly j_c strongly depend on the concentration and kind of defects present in the material. Since fast particle irradiation of metals produces cascades of vacancies and interstitials (Frenkel pairs), we expect B_{c2} and j_c to vary with irradiation dose and large changes of these parameters have indeed been observed in pure superconductors with an initially low defect density[17].

However, technologically useful materials contain structural imperfections (dislocations, precipitates, grain boundaries) already in the unirradiated state (otherwise they would not be "good" superconductors). The density and effectiveness of these defects is much higher than that of irradiation induced defects which makes hard superconductors rather insensitive to radiation damage. Nevertheless, small effects can be observed and will be discussed in the following.

NbTi-Alloys

Extensive irradiations of commerical NbTi single and multifilament conductors at ∿ 5 K were carried out by Soell and his coworkers[3-5] in the low temperature irradiation facility in Garching near Munich. The neutron energy spectrum of this reactor is comparable to the expected spectrum in the CTR magnet region (Fig. 2). Typical results of the field and dose dependence of the critical current density j_c are shown in Fig. 3 (the initial critical current density j_{co} of this material was 1×10^5 Acm^{-2} at 5 T). At constant dose one finds a relative reduction of j_c which is almost independent of the magnetic field. Annealing at different temperatures causes a recovery of the critical current density which is almost completed at room temperature. The dependence of j_c on the neutron dose $\phi \cdot t$ has the linear form

$$j_c = j_{co}(1 - k\,\phi\,t) \qquad (1)$$

and can be qualitatively understood by a simple pinning model[17]. Comprehensive simulation experiments with protons[18] confirm the neutron results and show that the transition temperature T_c and the upper critical field B_{c2} of alloy superconductors are also little affected by irradiation.

For a material with a relatively high initial current density j_{co}, the relative change of j_c/j_{co} is around 0.98 at our assumed maximum fluence of 3×10^{17} ncm^{-2} (Fig. 3). Since k decreases with decreasing j_{co} (see hatched area in Fig. 7) and even changes sign for very low j_{co} materials[5], we can assume that the maximum critical current degradation in a NbTi CTR magnet caused by the superconductor itself will never be more than 2 %. As will be shown later, this is much less than the degradation caused by the stabilizer. This shows that the NbTi superconductor will not be a critical component of a fusion magnet as far as radiation damage is concerned.

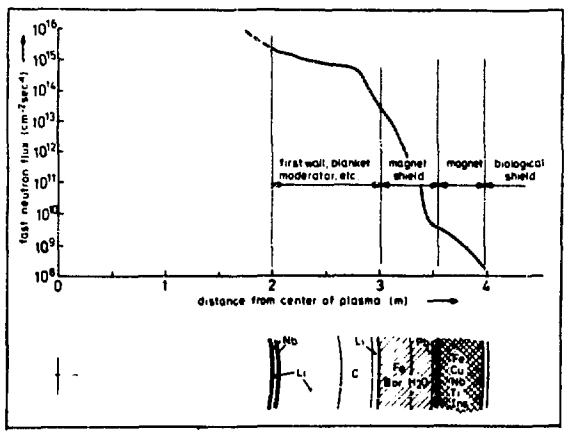

Fig. 1. Neutron flux in the different regions of a typical conceptual fusion reactor with total wall loading of 10 MWm^{-2} (after McCracken and Blow[2]).

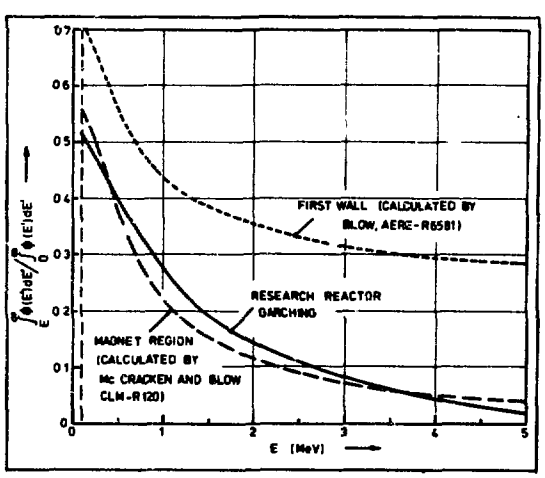

Fig. 2. Comparison of neutron spectra in the energy range 0.1 MeV < E < 5 MeV.

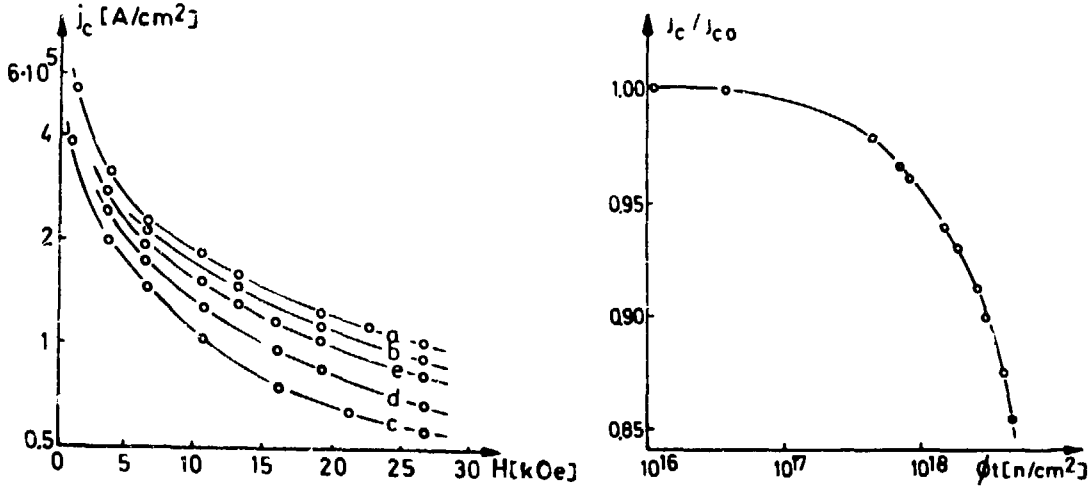

Fig. 3. (a) Critical current density j_c versus applied transverse magnetic field H for Nb-50 wt % Ti at 5.3 K. Curve a unirradiated, b irradiated with 3.2 x 10^{18} ncm^{-2} (E > 0.1 MeV), c irradiated with 7.5 x 10^{18} ncm^{-2}, d annealed at 100 K, e annealed at 270 K.

(b) Relative change of j_c at zero field as a function of neutron dose $\phi \cdot t$. j_{co} is the current density before the irradiation (after Soell[4]).

A-15 Compounds

Although A-15 materials (Nb_3Sn, V_3Ga etc.) have excellent superconducting properties (high T_c, H_{c2} and j_c), they were not very popular among reactor design teams up to now, mainly because of their brittleness and limited available conductor dimensions. Recently, however, flexible multifilament conductors of various cross sections and sizes which are intrinsically stable have been developed[19,20] and are now commercially available. This recommends A-15 compounds for certain high field coils in CTR reactors and raises the question of their radiation resistance.

Whereas in alloy superconductors irradiation produced defects essentially change only the pinning structure[21] we may expect a second effect to occur in highly ordered compounds. During fast particle irradiation, vacancies and interstitials are created by replacement collisions which lead to an interchange of atoms between sites and therefore to a disorder of the compound. Such disorder effects have indeed been observed in recent experiments[6,7,9-11]. Because of the highly nonlinear dose dependence of this effect[22], they are substantial only at doses which are much larger than those expected in CTR magnets (Fig. 4). It is interesting to mention that in these special investigations room temperature and low temperature irradiations are equivalent since only the (temperature independent) number of replacement collisions is important.

At fluences below 3×10^{17} ncm^{-2} the detrimental disorder effects are almost completely masked by an increase of the critical current density[8,9] which is caused by the irradiation produced defect cascades acting as pinning centers (Fig. 5). The relative j_c enhancement increases with increasing magnetic field which might lead to stability problems. An extension of the measurements to higher fields is therefore desirable. However, the magnitude of all radiation induced changes of j_c and T_c is again small and the conclusions for NbTi are expected to hold also for Nb_3Sn superconductors.

No low temperature irradiations have been reported for V_3Ga.

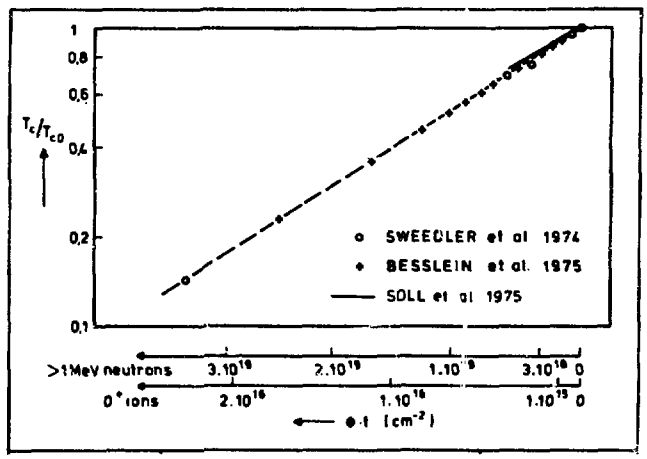

Fig. 4. Change of transition temperature T_c in Nb_3Sn as a function of irradiation dose $\phi \cdot t$.

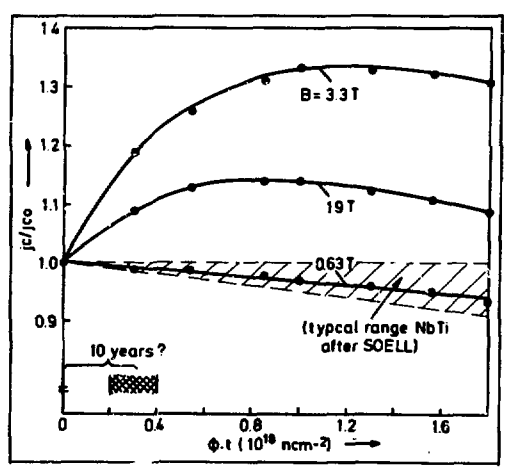

Fig. 5. Relative change of critical current in neutron-irradiated Nb_3Sn diffusion layers (after Brown, Blewitt, Wozniak and Suenaga[8]).

Stabilizer Materials

Because of safety reasons, the design of CTR magnets is generally based on the socalled cryogenic stabilization principle[23]: If a thermomagnetic instability drives a section of the superconductor into the normal state, an alternative path for the current is provided by a highly conducting normal metal (Cu, Al) which is in close contact with the superconductor ("stabilizer"). If, with the whole current flowing in the stabilizer, the heat flux does not exceed a critical value Q_c, the current will commutate back into the superconductor as soon as the instability has disappeared. Q_c is given by the condition that during this event the temperature of the conductor can be kept below the transition temperature. This can only be achieved if the heat transfer to the coolant (liquid He) is accomplished by the nucleate boiling mechanism. The maximum stable current I_{St} of a compound conduction (superconductor + stabilizer) is therefore given by

$$\frac{I_{St}^2 \rho}{A} \leq Q_c \cdot p \qquad (2)$$

where Q_c = heat flux below which film boiling cannot be sustained
ρ = stabilizer resistivity
A = stabilizer cross-sectional area
p = cooled conductor circumference

Eq. (2) shows that neutron irradiation will have an adverse effect on the stability of a CTR magnet since radiation induced Frenkel pairs cause an increase in the resistivity ρ of the stabilization material which is given by

$$\rho = \rho_o + \rho(B) + \rho(\phi \cdot t) \qquad (3)$$

where ρ_o residual resistivity
$\rho(B)$ magnetoresistance
$\rho(\phi t)$ resistivity from radiation induced Frenkel pairs

A fourth term which is due to radiation induced transmutation products can be neglected in this context[2]. Reliable data for $\rho(B)$ and $\rho(\phi t)$ exist for both stabilizer materials:

Copper

Using magnetoresistance data by Hsu and Kunzler[24] and radiation damage data by Burger et al.[12], the total resistivity ρ at 4.2 K and 8 T is plotted in Fig. 6 for Cu with two different initial residual resistivity ratios RRR = ρ at 273 K/ρ_o. For a fluence of 3×10^{17} ncm^{-2} the resistivity is increased by about 60 % for RRR = 170 and by 30 % for RRR = 35. This corresponds to a decrease in maximum stable current by 30 % or 15 %, respectively, which is much more than the degradation caused by the superconductor (see Fig. 7). Such losses in stability have indeed been observed experimentally by Soell[4] and Brown et al.[8] who irradiated NbTi/Cu and Nb_3Sn/Cu compound conductors. A typical voltage-current characteristic is shown in Fig. 8.

The decrease of the maximum stable current of the conductor with increasing fluence must be compensated by an oversized stabilizer volume; but an increase of 30 % with all its consequences on superconductor inventory, increased coil volume etc. would certainly be unacceptable on the grounds of the extra capital cost involved. Fortunately, radiation damage in metals recovers at relatively low annealing temperatures (in Cu, about 80 % of the radiation induced resistivity anneals out at room temperature). Therefore, by allowing say 5 annealing cycles in a 10 year period, the current degradation would be around 12 % for the RRR = 170 material which might already be tolerable.[+)]

Aluminium

Although having lower mechanical strength, aluminium is gaining increasing importance as a stabilizing material because of its low magnetoresistance and low residual resistivity in commercial material. In CTR-magnets, these advantages disappear at first sight because $\rho(\phi t)$ rises more than three times faster[13] than in Cu, i.e. at 3×10^{17} ncm^{-2} the total resistivity ρ of Al is already above the value for Cu with RRR = 170 (see Fig. 6). However, considering again an annealing period each two years ($\phi t = 6 \times 10^{16}$ ncm^{-2}) the resistivity would still be only half of the value for Cu (in Al, $\rho(\phi t)$ is completely recovered at room temperature).

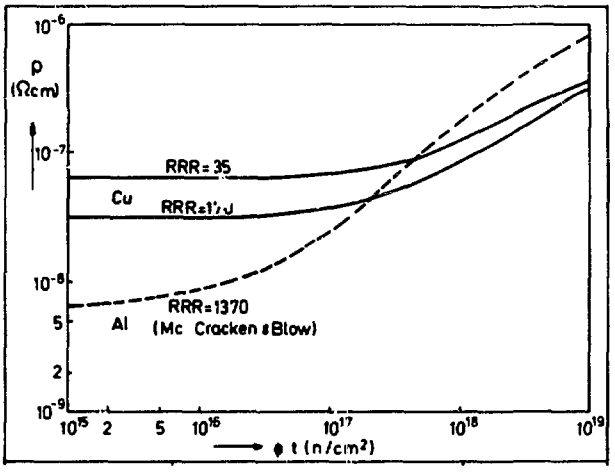

Fig. 6. Resistivity ρ of Cu and Al at 4.2 K and 8 T as a function of neutron flux $\phi \cdot t$.

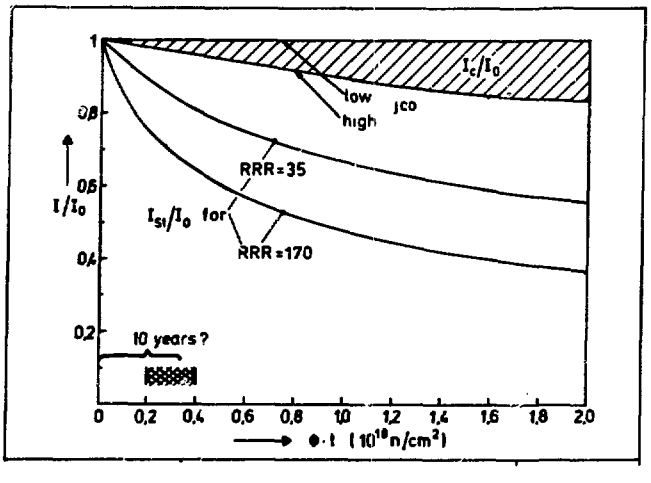

Fig. 7. Typical fluence $\phi \cdot t$ dependence of stable current I_{st} and critical current I_c for NbTi/Cu composite wires.

Insulators

Refractory Insulators

Since radiation damage effects in these materials which will be used for the electrical insulation of coil terminals will be covered by four following papers in this section, they will not be discussed here.

Polymers

The insulators used in present superconducting magnets are (a) thin layers of polyester (Mylar), PTFE (Teflon) or similiar material for the insulation of the conductors and (b) reinforced epoxy resins for potting of coils. Whereas the mechanical and thermal properties of these materials at cryogenic temperatures are rather well known[25], very little information is available about low temperature irradiation effects. From the few existing data which have been reviewed by Brechna[26], it is difficult to predict general tendencies - even for such fundamental properties like tensile strength, etc. This is illustrated by Figs. 9 and 10 which show the tensile strength σ_B of PTFE[27] and polyester films[28], respectively, under different irradiation conditions: in PTFE σ_B decreases slightly with dose whereas Mylar shows an increase of about 25 %. But in most cases these changes are rather small compared to the temperature effect on σ_B (see Figs. 9 and 10). Much more pronounced is the reduction in ultimate elongation which was observed in most irradiation experiments[29] (see e.g. Fig. 11). It seems, however, that most insulators can meet the mechanical strength requirements even when exposed to a γ-dose of several 10^8 rad (corresponding to a neutron fluence of 3×10^{17} ncm^{-2}).

It would be premature to express a similiar optimistic view for the dielectric strength of insulators under irradiation because, as far as I know, not a single measurement in this field has been reported up to now. Although under normal conditions the electric fields in a magnet are extremely small, high voltages between layers are induced when the coil goes normal. In order to complete our knowledge on radiation damage in CTR magnet components, data on dielectric properties of insulators under low temperature γ and neutron irradiation are therefore

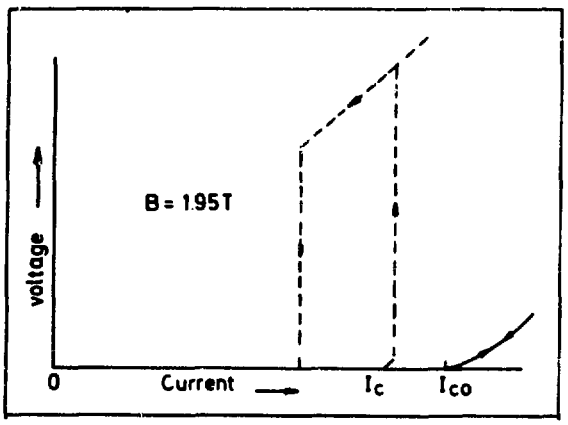

Fig. 8. Typical voltage-current curves of a 46 strands NbTi multifilament wire before (solid line) and after (dotted line) low temperature irradiation with 4.7×10^{18} ncm^{-2}. The copper to superconductor ratio was 3 : 1 and the initial resistivity of the copper was 5×10^{-8} Ωcm (after Soell[4]).

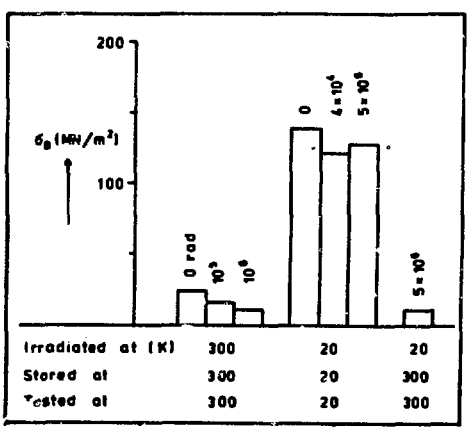

Fig. 9. Tensile strength of irradiated PTFE (Teflon) (after Van de Vorde[27]).

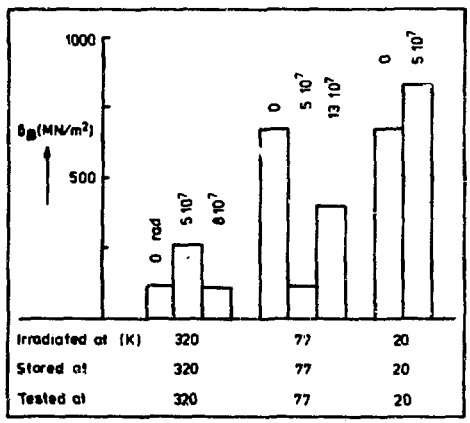

Fig. 10. Breaking strength of irradiated polyester film (Mylar) (after McKannan and Gause[28]).

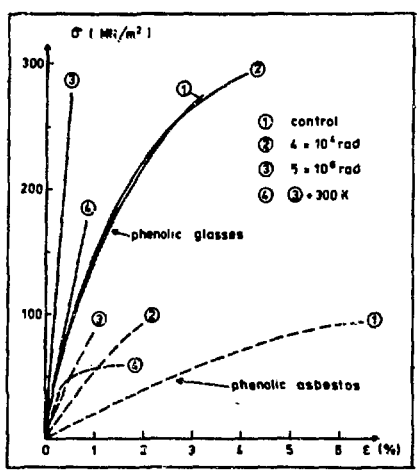

Fig. 11. Stress-strain curves at 20 K for irradiated phenolic materials (after Weleff[29]).

urgently needed.

EFFECT OF LOW TEMPERATURE NEUTRON IRRADIATION ON COIL PERFORMANCE

The above review shows that today most of the radiation induced property changes of CTR magnet components can be predicted rather accurately. However, investigating each component more or less isolated does not a priori guarantee that the behavior of the entire magnet can be predicted with the same reliability because changes caused or enhanced by a combination of effects can easily be overlooked (e.g. is there an influence of large stresses on the radiation damage in insulators?) In order to avoid costly experiences, an extension of low temperature irradiations to entire coils would be desirable. Actually, a first experiment of this kind has already been performed in 1967 by Benaroya et al.[30] who irradiated a very small coil (0.75" O.D., 0.9" length) consisting of 1200 turns of unstabilized NbZr wire in the ANL CP-5 reactor to a fluence of 7×10^{17} ncm^{-2}. No significant changes in the coil behavior could be defected. However, results for magnets of this size and field strength have hardly any relevance for CTR magnets and tests on larger coils are required. Unfortunately, this is more easily said than done because the present facilities allow only small volumes to be irradiated at low temperatures. Irradiation of successively larger coils may become possible when some of the intense neutron sources under construction are available and will be equipped with powerful refrigeration facilities. An alternative way would be to bypass this generation of experiments and wait until results for full size CTR-magnets in engineering test reactors like TETR[31] become available. A decision in favor of one of the two directions of research requires a detailed analysis which is far beyond the scope of this short review.

I am grateful to Dr. B.S. Brown, Prof. G. Ischenko, Prof. T. Okada and Dr. M. Söll for informing me about some of their results prior to publication.

REFERENCES

1. See e.g. W. G. Homeyer, Thermal and chemical aspects of the thermonuclear blanket problem. MIT Technical Report 435, 1965;
A. Fraas, Cryogenic system for the superconducting magnets of a full scale thermonuclear power plant. ORNL-TM-3097, 1970;
D. Steiner, priv. comm., 1972;
R.W. Conn, G. L. Kulcinski, et al., Proc. of the Fifth IAEA Conference on Plasma Physics and Controlled Nuclear Fusion Research, Tokyo, Japan, Nov. 11-15, 1974

2. G. M. McCracken and S. Blow, The shielding of superconducting magnets in a fusion reactor, Culham Report CLM-R 120, 1972

3. M. Soell, S. Wipf and G. Vogl, Proc. Appl. Supercon. Conf., Annapolis, 1972

4. M. Soell, Thesis TU München, Sept. 1974

5. M. Soell, C. A. M. van der Klein, H. Bauer, and G. Vogl, IEEE Trans. Magnetics, MAG-11, 178 (1975)

6. A. R. Sweedler, D. G. Schweitzer, and G. W. Webb, Phys. Rev. Letters 33, 168 (1974)

7. A. R. Sweedler and D. E. Cox, Phys. Rev. B12, 147 (1975)

8. B. S. Brown, T. H. Blewitt, D. G. Wozniak, and M. Suenaga, Bull. Am. Phys. Soc. 20, 296 (1975) and to be published

9. M. Soell, H. Bauer, K. Boening and R. Bett, Phys. Lett. 51A, 83 (1975)

10. M. Soell, K. Boening and H. Bauer, to be published

11. B. Besslein, G. Ischenko, S. Klaumünzer, P. Müller, H. Neumüller, K. Schnelz and H. Adrian, Phys. Lett. 53A, 49 (1975) and G. Ischenko, priv. comm.

12. G. Burger, H. Meissner and W. Schilling, phys. stat. sol. 4, 281 (1964)

13. K. Böning, H. J. Fenzl, E. Olympios, J. M. Welter and H. Wenzl, phys. stat. sol. 34, 395 (1969)

14. D. W. DeMichele and J. B. Darby, Jr., Proc. 1st Topical Meeting on the Technology of Controlled Nuclear Fusion, San Diego, 1974, Vol. I., p. 462

15. W. F. Westendorp and R. W. Kilb, Stresses in Magnetic Field Coils, 2nd Intern. Conf. on Magnet Technology, Oxford (1967)

16. See e.g. J. Diehl in Vacancies and Interstitials in Metals (Proc. Int. Conf. KFA, Jülich 1968), North Holland Publ. Co., Amsterdam 1969, or Aerospace Structural Metals Handbook, Vol. 1, Belfour Stulen, Inc., 1975

17. For a review of these effects see e.g. H. Ullmaier in: Defects and Defect Clusters in BCC Metals and their Alloys (ed. R. J. Arsenault) Gaithersburg 1973, p. 363

18. K. Wohlleben, J. Low Temp. Phys. 13, 269 (1973)

19. K. Tachikawa and Y. Iwasa, Appl. Phys. Letters 16, 230 (1970) and M. Suenaga and W. B. Sampson, Appl. Phys. Letters 18, 584 (1971)

20. M. Suenaga, T. S. Luhman and W. B. Sampson, J. Appl. Phys. 45, 4049 (1974); W. A. Fietz and C. H. Rosner, IEEE Transact. on Magnetics 10, No. 2 and R. M. Scanlan, priv. comm. (1974)

21. For a review of the interaction between structural defects and flux lines in hard superconductors see: A. M. Campbell and J. E. Evetts, Adv. Phys. 21, 199 (1972) or H. Ullmaier, Irreversible properties of type II superconductors, Springer Tracts of Mod. Phys., Vol. 76 Springer Verlag, Berlin, 1975

22. R. E. Somekh, J. Phys. F: Metal Phys. 5, 713 (1975) and J. Appel, to be published

23. C. Laverick, Proc. Intern. Symp. Magnet Techn. UC-28, Stanford Univ. (1965), p. 560, A. R. Kantrowitz and Z. J. J. Stekly, Appl. Phys. Letters 9, 306 (1965) or B. J. Maddock and G. B. James, Proc. I.E.E. 115, 543 (1968)

24. F. S. L. Hsu and J. E. Kunzler, Rev. Sci. Instr. 34, 297 (1963)

25. For a recent extensive review see M. B. Kasen, Cryogenics 15, 327 (1975)

26. H. Brechna, Proc. of the 1968 Summer Study on Superconducting Devices and Accelerators, Brookhaven Nat. Lab. Report BNL 50155, Part III, p. 1023

27. M. Van de Voorde, IEEE Trans. Nucl. Sci, NS-20, 693 (1973)

28. E. C. McKannan and R. L. Cause, J. Spacecraft 2, 558 (1965)

29. W. Weleff, Adv. in Cryogen. Eng. (Ed. K. D. Timmerhaus), Plenum Press, New York 1966, Vol. 11, p. 486

30. R. Benaroya, T. H. Blewitt, J. M. Brooks and C. Laverick, IEEE Trans. Nucl. Sci, NS-14, 383 (1967)

31. R. W. Conn and D. L. Jassby, University of Wisconsin Report UWFDM-119, March 1975

+) An optimazation of the Cu/supercond. ratio in connection with radiation effect problems is presented by T. Okada in one of the following papers of this session (T. Okada, H. Tsubakihara, S. Katoh, T. Horiuchi, Y. Monjhu, and S. Tsurutani, this conference)

HIGH-ENERGY NEUTRON IRRADIATION OF SUPERCONDUCTING COMPOUNDS*

A. R. Sweedler and C. L. Snead
Brookhaven National Laboratory
Upton, New York 11973

L. Newkirk, F. Valencia, and D. M. Parkin
Los Alamos Scientific Laboratory
Los Alamos, New Mexico 87544

T. H. Geballe and R. H. Schwall
Stanford University
Stanford, California 94305

R. T. Matthias and E. Corenswit
Bell Laboratories
Murray Hill, New Jersey 07974

ABSTRACT

The effect of high-energy neutron irradiation (E>1 MeV) at ambient reactor temperatures on the superconducting properties of a variety of superconducting compounds is reported. The materials studied include the A-15 compounds Nb_3Sn, Nb_3Al, Nb_3Ga, Nb_3Ge and V_3Si, the C-15 Laves phase HfV_2, the ternary molybdenum sulfide $Mo_3Pb_{0.5}S_4$ and the layered dichalcogenide $NbSe_2$. The superconducting transition temperature has been measured for all of the above materials for neutron fluences up to 5×10^{19} n/cm^2. The critical current for multifilamentary Nb_3Sn has also been determined for fields up to 16 T and fluences between 3×10^{17} n/cm^2 and 1.1×10^{19} n/cm^2.

INTRODUCTION

In most present designs for fusion reactors superconducting magnets will be utilized to provide plasma confinement. In such an application the superconductor will be subjected to neutron irradiation, the exact level depending on the particular design and length of exposure.[1] It

*This work was performed under the auspices of ERDA.

is therefore necessary to have information concerning the effect of such radiation on the superconducting properties of potential magnet material, particularly the effect on the superconducting transition temperature T_c and the critical current density J_c.

In this work we report the effect of high-energy neutron (E>1 MeV) irradiation at ambient reactor temperatures on the superconducting properties of a variety of intermetallic compounds that have potential use for high-field magnets. Although the neutrons produced in a fusion vessel will have energies of ~14 MeV, by the time they reach the region where the magnets will be located, their energy is expected to be ~1 MeV with a spectrum similar to that of a fission reactor.[2] It is therefore possible to gain meaningful information concerning the behavior of superconducting materials to be used in fusion reactors by irradiation with neutrons from a fission reactor.

The materials studied here include the A-15 compounds Nb_3Sn, Nb_3Ga, Nb_3Ge, Nb_3Al and V_3Si. Nb_3Sn has been developed into multifilamentary conductors for magnet use[3] and besides the effect of neutron irradiation on T_c, extensive J_c data, up to fields of 16 T and fluences of $\sim 10^{19}$ n/cm^2, are reported. Nb_3Ga has also been developed into usable form for magnet construction[4] and the effect on T_c up to fluences of 5.0×10^{19} n/cm^2 is also reported. Nb_3Ge, currently possessing the highest T_c, ~23 K,[5] of any known superconductor is investigated up to fluences of 5.0×10^{19} n/cm^2 and annealing experiments to 900°C are described.

Other compounds studied include the ternary molybdenum sulfide $Mo_3Pb_{0.5}S_4$,[6] which has the highest reported upper critical field

of any bulk material, ~50 T[7] making it extremely desirable for magnet use if it could be prepared so as to carry reasonable currents, a prospect not yet realized.[8] The C-15 Laves phase HfV_2, and pseudobinary compounds with Zr having this structure, also are potential magnet conductors as J_c's as high as 10^5 A/cm^2 at 13 T at 4.2 have been obtained[9] despite its relatively low T_c of 10 K. These materials are also less brittle than the A-15's, making wire and tape fabrication somewhat easier. Finally we mention the layered dichalcogenide $NbSe_2$ even though it is not a good candidate for magnet material to show how neutron-induced disorder can be correlated with disorder brought about by deintercalation.

EXPERIMENTAL

The characteristics of the samples before irradiation along with the preparative techniques are listed in Table 1. The irradiations were carried out in the Brookhaven High Flux Beam Reactor (HFBR), the fluence being obtained by multiplying the time of irradiation by the fast flux (E>1 MeV) which is known to be $(1.0\pm0.5)\times10^{14}$ n/cm^2 sec. The measured temperature of the samples during irradiation was 140°C. T_c was measured inductively in a manner previously[15] described and J_c determined by noting the current at which a 3-μV signal appeared across the superconductor.[16]

RESULTS AND DISCUSSION

Transition Temperatures

Figure 1 shows the effect of high-energy neutron irradiation on the T_c's of the various materials used in this work. T_c is the value after irradiation and T_{co} is the value before irradiation listed

in Table 1. The data are presented on a normalized plot to indicate the relative change in T_c as a function of fluence.

The materials most extensively studied are those having the A-15 (β-W) structure Nb_3Ge, Nb_3Al, Nb_3Sn, Nb_3Ga and V_3Si. When plotted on a normalized plot we see that the depressions in T_c due to the neutron irradiation are very similar for the Nb-base A-15 compounds. Up to $\sim 10^{18}$ n/cm^2 there is very little change in T_c ~4-6% relative to the unirradiated value. Above this fluence, T_c begins to be rapidly depressed. For fluences $\sim 5 \times 10^{18}$ n/cm^2 T_c has been decreased by ~20%, for $\sim 10^{19}$ n/cm^2 ~40% and above 10^{19} n/cm^2 reductions greater than 90% in T_c are observed. In the case of Nb_3Al no superconductivity was observed for fluences $>1 \times 10^{19}$ n/cm^2 to a temperature of 1.2 K and recent data indicate that at 5×10^{19} n/cm^2 Nb_3Ge also shows no superconductivity to 1.2 K.[17] V_3Si lies somewhat below the curve for the Nb-based A-15 compounds at fluences below 10^{19} n/cm^2 indicating that the relative depression of T_c for this material is somewhat greater than for the Nb A-15 compounds.

The large depressions in T_c shown in Fig. 1 for the A-15 materials are due to replacement collisions brought about by the fast-particle irradiation resulting in a decrease in the degree of long-range order.[18] This has been confirmed directly in the case of Nb_3Al where measurements of the degree of long-range order before and after irradiation showed the order to decrease with increasing neutron dose.[12] We also note that with respect to T_c both low-temperature irradiations (30 K)[19] and ambient-temperature irradiations (140°C) give similar depressions in T_c for Nb_3Sn. In both cases the results are well described by a site-

Table 1. Sample Characteristics Before Irradiation

Sample	Transition Temp. T_{co}(K)	Lattice Parameter a_0(Å)	Method of Preparation	Comments
Nb_3Ge	20.6	5.142	Ref. 10	Chemically vapor deposited. ~70% A-15 + Nb_5Ge_3 phase
Nb_3Ga	20.3	5.165	Ref. 11	A-15 + ~50% Nb_5Ga_3 phase
Nb_3Al	18.7	5.183	Ref. 12	>98% single phase
Nb_3Sn	18.1	5.290	Ref. 13	Used for T_c measurements - single phase
Nb_3Sn	15.0		Ref. 3	19 core multifilamentary conductor J_c=1.0x10^6 A/cm^2 at 4 T
V_3Si	17.1			Single phase - arc cast
$Mo_3Pb_{0.5}S_4$	13.0		Ref. 6	Sintered powder compacts
HfV_2	9.4		Arc cast	
$NbSe_2$	7.1	a=3.45 c=12.56	Ref. 14	Double layer hexagonal type

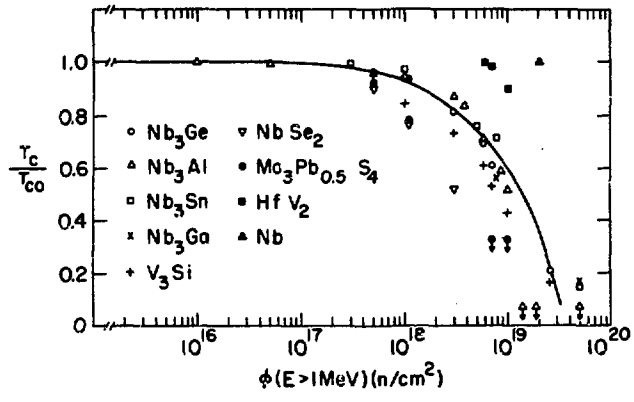

Fig. 1. Reduced transition temperature T_c/T_{co} as a function of high energy neutron (E>1 MeV) fluence for different superconducting compounds. T_c is the transition temperature after irradiation and T_{co} is the value before irradiation. Values of T_{co} are found in Table 1. Curve is drawn as a visual aide. Arrows indicate no superconductivity observed to the indicated temperature.

exchange-disorder model yielding depression rates of 2-3 K per percent of B atom on the Nb chains in the A-15 structure.

The ternary molybdenum sulfides have recently been prepared with T_c's in the range 10-13 K[6] and upper critical fields of the order 50 T[7] have been reported. The extremely high critical fields and reasonably high T_c's make these materials attractive as potential magnet materials. However, recent attempts to fabricate the sulfides into usable conductors have resulted in rather low current densities, $\sim 10^3$ A/cm^2 at 4 T.[8] Whether these low J_c values are inherent to the material or are the result of the preparative techniques employed to prepare the material in conductor form is not known.

Figure 1 shows the effect of neutron irradiation on the T_c of $Mo_3Pb_{0.5}S_4$. We see immediately that T_c is extremely sensitive to neutron bombardment at all fluences studied. Even at the relatively low fluence of 5×10^{17}, T_c is depressed by 8% relative to its unirradiated value. At 10^{18} n/cm^2 T_c is down by 22% compared to the A-15 compounds whose T_c has decreased by only about 6%. At levels close to 10^{19} n/cm^2 no superconductivity was detected to 4.2 K, indicating a depression in T_c of >65%. We thus see that the T_c of $Mo_3Pb_{0.5}S_4$ is quite sensitive to neutron irradiation. Although we have not made any crystallographic measurements to determine the changes taking place in the structure during irradiation, as with the A-15's, the superconducting properties of the ternary molybdenum sulfides are known to be extremely sensitive to pressure and strain and thus it is not surprising that T_c would be sensitive to heavy-particle irradiation.

$NbSe_2$, although of not much promise as a magnet material, is

interesting from the point of view of superconductivity in layered compounds.[14] These layered compounds consist of two close-packed planes of metalloid, Se in this case, with Nb atoms in between in trigonal prismatic space lattices. The bonding between the Nb and Se atoms within the layers are of the strong covalent type while the bonding between layers are of the weak Van der Waals type. The effect of neutron irradiation on 2H-$NbSe_2$ is shown in Fig. 1 where it is seen that this material is also extremely sensitive to heavy-particle irradiation. For fluences of $3x10^{18}$ n/cm^2 a reduction in T_c of almost 50% is observed, which may be compared to the A-15's where T_c at the same fluence is decreased only 20%.

The rapid decrease in T_c for 2H-$NbSe_2$ upon irradiation with high-energy neutrons may be understood by noting the sensitivity of T_c to the occupation by Nb atoms of the Nb sub-lattice as shown by Antonova et al.[20] Antonova et al. prepared 2H-$NbSe_2$ with different stoichiometries and T_c was determined as a function of changes in the occupation of the Nb and Se sub-lattice sites as the concentration was varied. A correlation between T_c and the degree of ordering of the Nb sub-lattice was observed suggesting that occupation of the Nb sub-lattice by Nb is important in determining the superconducting properties. The depressions in T_c observed by Antonova et al., from ~6 K to 2 K, are similar to what we observe for the neutron-irradiated samples and most likely arise from the same cause, disruption of the Nb sub-lattice. In the case of the experiments of Antonova et al. disorder in the Nb sub-lattice is produced by a change in composition whereas in the present study disorder is brought about by displacement collisions resulting

from the high-energy irradiation without compositional changes.

The effect of irradiation on HfV_2, which crystallizes in a cubic C-15 Laves phase ($MgCu_2$-type), is also indicated in Fig. 1. Of all the materials studied to date this is the only one that is relatively radiation resistant. At fluences where the T_c of the A-15's have been depressed about 30%, the T_c of HfV_2 is decreased only 1%. For high fluences, $\sim 10^{19}$ n/cm^2, where the T_c of A-15 superconductors are down by approximately 40%, the T_c of HfV_2 is depressed only 10%. A maximum T_c of 10.1 K and H_{c2} of 23 T have been reported in pseudobinary alloys based on HfV_2 and Tachikawa[9] and co-workers have prepared tapes carrying currents as high as 10^5 A/cm^2 at 13 T making the Laves phase interesting materials for magnet conductors. Their resistance to radiation degradation in the high 10^{18} n/cm^2 range make these materials potentially useful as magnet conductors where such high radiation levels might be expected. Although their T_c's at 10^{19} n/cm^2 would be in the range of 9 K as compared to Nb_3Sn of ~11 K at that fluence, the critical currents and fields of the Laves phases would be much higher than those of Nb_3Sn.

For the A-15 compounds recovery of T_c to close to its unirradiated value is possible by annealing at moderate temperatures, ~700-900°C for various periods of time ranging from 20 minutes to 20 hours depending on the compound. This reversibility of T_c has been observed in Nb_3Sn, Nb_3Al, Nb_3Ga and Nb_3Ge.[15,17,18]

Critical Currents (I_c)

Figure 2 shows the effect of neutron irradiation on the I_c of multifilamentary (19-core) Nb_3Sn wires for fluences from 3×10^{17} to

1.8×10^{19} n/cm^2 (E>1.0 MeV) at transverse magnetic fields up to 16 T. All measurements were made at 4.2 K. For doses below 10^{18} n/cm^2 I_c is enhanced over the unirradiated value, the degree of enhancement being greater at higher field values. This behavior is consistent with an interpretation in which the upper critical field $H_{c2}(4.2)$, increases with increasing dose because of the increase in the normal-state resistivity of the Nb_3Sn caused by defects and increasing disorder. The T_c does not change over this range (see Fig. 1) so changes in I_c are not due to changes in T_c for doses up to $\sim 10^{18}$ n/cm^2. Above 10^{18} n/cm^2, however, the continuing decrease in the order begins to produce substantial reductions in T_c, which effect outweighs that of the increasing normal-state resistivity. Thus, decreases in I_c are produced as T_c is depressed for doses above 10^{18} n/cm^2. H_{c2} also decreases causing the large depressions in I_c observed in this fluence range.

The change in the reduced critical current I_c/I_{co} as a function of fluence for different fields is shown in Fig. 3. One expects the enhancement to increase in such a plot as the applied field approaches the upper critical field of the unirradiated Nb_3Sn which by extrapolation would lie at ~17 T, and indeed this is what is observed. The peak in the enhancement occurs at a dose of 5×10^{17} n/cm^2 with H_{c2} and I_c decreasing from that dose on. One speculates, then, that at this dose of 5×10^{17} n/cm^2 the tendency to increase H_{c2} caused by the increasing normal-state resistivity is balanced by the tendency to decrease H_{c2} owing to a decreasing T_c. Above 5×10^{17} n/cm^2 the rapidly decreasing T_c thus dominates, causing I_c to rapidly degrade.

These data are interesting to compare to low-temperature

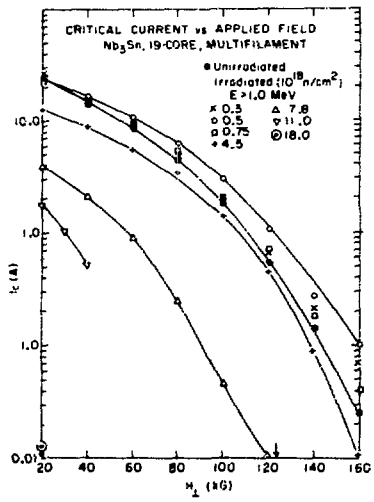

Fig. 2. Critical current I_c vs applied transverse magnetic field H for 19 core multifilamentary Nb_3Sn wire for different fluences. Unirradiated value of $J_c=10^6$ A/cm^2 at 4 T. To convert I_c to current density divide by 1.5×10^{-5} cm^2.

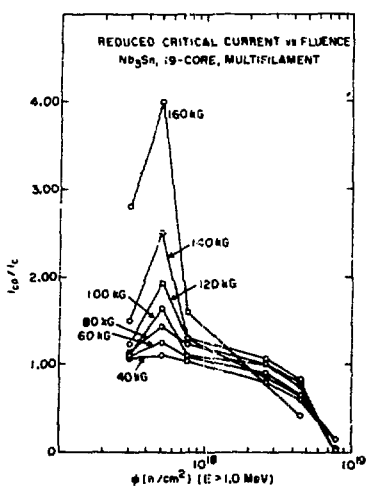

Fig. 3. Reduced critical current I_c/I_{co} as a function of fluence at different fields for 19 core multifilamentary Nb_3Sn wire.

irradiations on similar material. Brown et al.[21] irradiated identical multifilamentary Nb_3Sn to fluences of 1.8×10^{18} n/cm^2 at 6 K (to compare fluences from the Argonne reactor with the Brookhaven reactor divide the Argonne fluences by ~3). They found increases in J_c of ~32% relative to the unirradiated value at a field of 3.32 T for an equivalent fluence of 3×10^{17} n/cm^2. The fluence range where the maximum increases are found are close to our ambient temperature results and the magnitude of the increase is of the same order of magnitude.

It should be noted that the Nb_3Sn multifilament wire used in this work was fabricated so as to maximize the critical current density and thus I_c. Many experiments have shown that for Nb_3Sn that is not so optimized, increases in I_c with irradiation are produced, the size of the increases increasing with the lowering of the initial J_c. Our initial value of H_{c2}, ~17 T, is not of the best that can be obtained for Nb_3Sn, ~20 T. It would be instructive to repeat these kinds of measurements with higher initial values of H_{c2} to determine if further enhancement of H_{c2} could be achieved. The ramifications for I_c in this case would also be of interest. The interactions between these critical properties may be an important factor in tailoring metallurgically the best possible A-15 superconductor to use in a fusion reactor where levels to 10^{18} n/cm^2 over a 10-year lifetime might be expected.

CONCLUSIONS

The effect of the radiation field on the superconductor in a magnet used in a CTR device will not present a serious problem with respect to deterioration of the superconducting properties provided the fluence is below ~10^{18} n/cm^2 (E>1 MeV). Below this fluence no significant

deterioration in T_c is observed for the A-15 compounds and for Nb_3Sn increases in J_c have been observed. Above this fluence as far as the A-15 compounds are concerned severe degradation takes place both in T_c and J_c making these materials unsuitable for magnet conductors in such high radiation fields. It is possible to restore the superconducting properties by annealing in the 700°C range, but this may not be practical in a working reactor. If such high fluences are to be expected, the Laves phases $(Hf,Zr)V_2$ may be an appropriate material to consider as an alternative to the A-15 compounds. A more serious problem than the superconductor appears to be the normal metal used for stabilization, as discussed in the previous paper.[1]

It is also interesting to compare results of ambient-temperature irradiations (70-150°C) with low-temperature irradiations (6-30 K). With respect to T_c there is very little difference in the depression of T_c for Nb_3Sn whether irradiated at low temperatures or at ambient temperatures.[1,19] The critical-current increases observed for Nb_3Sn when irradiated at low temperatures and low fluence have now also been seen in the ambient temperature irradiations (Fig. 3). Where comparable data exist the effect on I_c for low-temperature and ambient-temperature irradiation are similar.

In order to obtain an understanding of the performance for the complete magnet (superconductor, stabilizer, insulator) low temperature irradiations of the component assembly will be necessary. However, as far as the superconductor is concerned the effects of low-temperature and ambient-temperature irradiations are similar. This means that with respect to the behavior of the superconductor, one can gain

meaningful results by irradiation at ambient temperatures.

ACKNOWLEDGMENTS

We would like to thank M. Suenaga for preparing the multifilamentary Nb_3Sn. The expert technical support of R. H. Jones is also greatly appreciated.

REFERENCES

1. H. Ullmaier, this journal (previous article).

2. G. M. McCracken and S. Blow, Culham Report CLM-120 (1972).

3. M. Suenaga and W. B. Sampson, Appl. Phys. Letters 18, 584 (1971).

4. S. Foner, E. J. McNiff, Jr., L. J. Vieland, A. Wicklund, R. E. Miller and G. Webb, Appl. Superconductivity Conf. 404 (1972).

5. J. R. Gavaler, Appl. Phys. Letts. 23, 480 (1973); L. R. Testardi, J. H. Wernick and W. A. Royer, Solid State Comm. 15, 1 (1974).

6. B. T. Matthias, M. Marezio, E. Corenswit, A. S. Cooper and H. E. Barz, Science 175, 1465 (1972).

7. S. Foner, E. J. McNiff and E. J. Alexander, Phys. Letts. 49A, 269 (1974).

8. T. S. Luhman, O. Horigami and D. Dew-Hughes, Bullet. of the APS 20, 343 (1975). T. S. Luhman (private communication).

9. K. Inoue and K. Tachikawa, Appl. Phys. Letts. 25, 94 (1974).

10. L. R. Newkirk, F. A. Valencia, A. L. Giorgi, E. G. Sklarz and T. C. Wallace, IEEE Trans. on Magnetics, Mag 11, 221 (1975).

11. G. W. Webb, L. J. Vieland, R. E. Miller and A. Wicklund, Solid State Comm. 9, 1769 (1971).

12. A. R. Sweedler and D. E. Cox, Phys. Rev. B12, 147 (1975).

13. J. J. Hanak, K. Strater and G. W. Cullen, RCA Rev. 25, 342 (1964).

14. R. E. Schwall, Ph.D. Thesis, Stanford Univ. (1973).

15. A. R. Sweedler, D. Cox, D. G. Schweitzer and G. W. Webb, IEEE Trans. on Magnetics, Mag 11, 163 (1975).

16. D. M. Parkin and D. G. Schweitzer, Nucl. Tech. 22, 108 (1974).

17. A. R. Sweedler, D. E. Cox and L. R. Newkirk (to be published).

18. A. R. Sweedler, D. G. Schweitzer and G. W. Webb, Phys. Rev. Letts. 33, 168 (1974).

19. B. Besslein, G. Ischenko, S. Klaumunzer, P. Muller, H. Neumuller, K. Schnelz and H. Adrian, Phys. Lett. 53A, 49 (1975).

20. Ye. A. Antonova, K. V. Kiseleva and S. A. Medvedev, Fiz Mettallov Metallovedenie 27, 441 (1969).

21. B. S. Brown, T. H. Blewitt, D. G. Wozniak and M. Suenaga, J. of Appl. Phys. (to be published).

NEUTRON IRRADIATION EFFECTS ON SUPERCONDUCTING[+] Nb-Ti ALLOYS IN THE MAGNETS FOR FUSION REACTORS

T. Okada, H. Tsubakihara, S. Katoh
Department of Nuclear Engineering,
Osaka University
Yamadakami, Suita, Osaka

T. Horiuchi, Y. Monjhu, and S. Tsurutani
Asada Fundamental Research Laboratory,
Kobe Steel, Ltd.
Aza-Maruyama, Gomo, Nada-ku, Kobe

ABSTRACT

A study was made on the reactor irradiated single core copper-clad Nb-Ti wire, of which T_c and J_c were followed. A systematic preparation of the samples before irradiation involves followings;(i) composition, (ii) degree of cold work, and (iii) ageing time.

Our new findings in the present study are that the neutron irradiation depressed J_c(at 5.0 T & 4.2 K) as much as 15% at certain condition and that T_c decreased by $\sim$6% due to the same irradiation. The conditions that brought above results are as follows; the sample: Nb-59.8 at %Ti, cold work: 99.87%, heat treatment: 5×10^3min at 380°C, irradiation: 1.3×10^{18}n/cm^2 ($E_n \geq$ 0.1MeV). Specific feature of this sample is that α -phase of Ti precipitates are dispersed in the β = matrix. It is stressed that superconducting Nb-Ti wire with J_c enhanced by precipitates does not appear very resistant to neutron irradiation.

Based upon above results and taking irradiation effects on stabilizing normal conductor into consideration we have evaluated the over all effect to transport current density J_T, which is presently believed to be one of the most convenient parameters for the evaluation of superconducting coil performance in the light of application to large scale magnets. In connection with CTR technology we have successfully obtained normal/super ratio and further the performance of the coil (J_T^m) as a function of neutron fluence.

[+] A part of this work was done in the Research Reactor Institute, Kyoto University.

INTRODUCTION

It has been generally agreed that fusion power technology will need superconducting magnets for the economical production of power[1-3]. In the view of radiation damage it is significant to reveal important parameters which seriously affect the overall performance of the superconducting coil when it is used for the D-T plasma fonfinement in full scale fusion reactors. In that case 14MeV neutrons unavoidably arrive at magnet region even with considerable thickness of shielding. For example, according to Hancox model[4] the fast neutron flux amounts to 10^9-10^{10}n/cm^2/sec, the maximum fluence in the magnet used in a 5,000MW(t) fusion reactor has been estimated to amount up to approximately 10^{18}n/cm^{2}assuming reactor life of 20 years and no intermission of operation. The neutron flux is of course sensitive to radiation shield as well as the first wall loading. The data for radiation sensitivity of magnet materials, therefore, are strongly coupled with power density, shielding design and so on.

In the present paper we shall firstly make a brief survey on the available data of actual conditions(we may call it "CTR condition") on the superconducting coil which will be used in the eventual full scale fusion reactors. Secondly, irradiation effects on typical superconducting properties such as J_c and T_c are reported on copper stabilized Nb-Ti wires which are carefully prepared so that they have systematical change in the internal metallurgical structure. Finally, making use of these results combined with radiation effects on stabilizing normal conductors we shall attempt to obtain some indication on the choice and combination of superconducting and/or stabilizing materials in view of magnet design taking radiation effects into consideration.

ANTICIPATED CTR CONDITIONS IN TERMS OF RADIATION DAMAGE

Practical use of superconducting magnets for the full scale fusion reactor with plasma confinement requires various knowledge on irradiation effects to component materials as well as to the overall performance of

magnets. Specific features of irradiation condition for superconducting magnet materials are as follows:

(I) Working temperature: near liquid helium temperature
(II) Stress : large electromagnetic force
(III) Radiation : intensity and spectrum
1. Neutrons
2. Gamma photons

Although these factors. of course, depend on the design detail, it will be of value to review recently published conceptual design of CTR from the view point of radiation effects. Typical figures are listed on Table 1 which somewhat emphasizes the details in magnet region.[5]

From this table it is immediately seen that the detail of radiation in magnet region is not so clearly specified in most of present conceptual CTR design. It is not certain whether this is due to the lack of material data on superconductor or due to the idea that the damage on the superconductor itself is not so significant compared with other materials such as stabilizing normal conductor and/or insulating materials. Even accepting that the degreeof severeness of radiation damage to the component material of superconducting magnet is in the order of (i) insulator (ii) stabilizer (iii) superconductor, there are avariety of problems to be solved on the overall radiation effects to the performance of the superconducting magnet. This in turn influences shielding and eventually magnet and reactor cost. The importance of these studies, therefore, has been stressed.

IRRADIATION EFFECT DATA ON COIL MATERIALS

We have listed up previously reported examples of radiation effects on alloy superconductors in Table 2[6]. These data seem to show that their hebavior is so much varieted that any definite prediction cannot be derived a priori. They also suggest radiation effects greatly depend upon initial condition of the sample. In order to predict the radiation effect on superconductor, it is, therefore, emphasized to use the sample whose initial metallurgical structure is known as clear as

Table 1. Typical CTR Conditions

	ANL-TEPR	UWMAK-I	UWMAK-II	PRINCETON	JAERI	ITALY	ORNL	CULHAM
Power								
Thermal, P_T(MWt)	129	5000	5000	5305	2000	170	1000	——
Electrical, P_E(MWe)	25	1500	1700	2030	800	——	518	2500
Dimensions								
Major radius(m)	6.25	13	13	10.5	10	11.25	21	——
Minor radius(m)	2.1	5	5	3.2	2	2.25	5.6	——
Core plasma								
Average plasma temp.(Kev)	9.6	11.1	15.2	30	15	23	20	——
Average plasma density($X10^{14}cm^{-3}$)	0.56	0.8	0.646	0.5	1.0	0.19	0.2	——
Toroidal magnetic field(T)	3.4	3.82	3.57	6	6	4.5	2.47	——
Plasma current I_p(MA)	4.8	20.7	14.9	14.6	8	5	——	——
Operation mode								
Current rise phase(sec)	1	0	10	10		——		——
Beam heating phase(sec)	3	11	20	20		——		——
Burn phase (sec)	20—50	5300	5400	5400	6000 (total)	——	120 (total)	——
Shut down phase (sec)	5	100	100	180		——		——
Exhaust & replenishment phase(sec)	15	100	100			——		——
Neutronics								
Total 1st wall neutron flux($n/cm^2/sec$)	$7.2x10^{16}$	——	——	$3x10^{14}$ (E_n 1Mev)	$3.3x10^{14}$	——	$2.4x10^{14}$	10^{15}
Neutron wall load, $P_W(MW\cdot m^{-2})$	0.16	1.25	1.16		1.4	0.095	0.69	4.6
Toroidal field coil								
Superconductor/stabilizer/support	NbTi/Cu /SS	NbTi/Cu /SS	NbTi/Cu /SS	Nb_3Sn	Nb_3Sn-NbTi hybr.	NbTi/Cu /SS	NbTi/Cu	
Number of coils	16	12	24	48	24	36	148	——
Shape	D	D	D	D	D	D	——	——
Major bore(vertical)(m)	11.9		28	19	14	13.2	——	——
Minor bore(horizontal)(m)	7.7		19	12	12.3	9.4	——	——
Peak field, B_{max}(T)	7.5	8.66	8.13	16	11.5	8.0	5.3	14
Current density(KA/cm^2) Coil (Average)	2.38	2.55	2.105	2.17	10		4.85	
Bobin (Gross)	1.28	1.32	1.5	1.6	1.25	1.2		
Operating temp.(K)	4.2	4.2	4.2	4.2	4.2	4.2	4.2	
Stored energy(GJ)	15.6		223	250	160	86		
Magnetomotive force(MAT)	$1.05x10^8$				300			
Ampare-turns(per Coil)	$6.54x10^6$						$2.78x10^6$	
(total)	$104.6x10^6$							
Design strain in conductor(%)		0.2		0.3				
Design strain in stabilizer(%)		0.02	0.2	0.3	0.2			
Maximum hoop stress in the support(psi)	24,000	60,000	60,000					
Maximum field ripple(%)	2				0.5			
Radiation in magnet region								
Neutron flux($n/cm^2/sec$)	$3.0x10^8$							
Gamma flux(photons/sec)								
Heat input($watt/cm^3$)	$5x10^{-6}$		$6x10^{-8}$*					
Reference	a	b	c	d	e	f	g	h

* Energy attenuation

Table 2. Radiation Effects on Superconducting Alloys

Materials	Neutron Fluence (n/cm^2)	Irrad. Temp.	J_c	T_c	H_{c2}	Ref.
Nb-50wt%Ti	7.5×10^{18} $E_n>0.1$MeV	5 K	↘			(i)
Nb-50%Ti	3.5×10^{18} $E_n>0.1$MeV	R.T.	↗	↘		(j)
Nb-25%Zr	3.5×10^{18} $E_n>0.1$MeV	R.T.	↘			(j)
Nb-25%Zr	2×10^{18} f.n.	50°C	→			(k)
Nb-Ti-V	3.7×10^{19} f.n.	lower than 70°C	↘	↘	↘	(l)
Nb-30%Ta	5×10^{16} f.n.	R.T.	→			(m)
Nb-47.6at%Ti	1.3×10^{18} $E_n>0.1$MeV	lower than 70°C	↗	→		(n)
Nb-59.8at%Ti aged at 380°C up to 100 min	1.3×10^{18} $E_n>0.1$MeV	lower than 70°C	↗	→		(n)
Nb-59.8at%Ti aged at 380°C longer than 100 min	1.3×10^{18} $E_n>0.1$MeV	lower than 70°C	↘	↘		(n)
Nb-Ti	9.0×10^{18} f.n.	77 K	↘			(p)

R.T.; room or reactor temperature

f.n.; fast neutron

possible. Our first efforts are concentrated on this point.

In actual CTR conditions superconductors are of course to be irradiated at low temperature near 4K. However, we consider that the present results on radiation effects on superconductors obtained at fission reactor temperature give the first order approximation of the effect within the limit that it is rather insensitive to irradiation temperatures. Until the neutron energy spectrum in actual CTR magnets become clear, we shall assume that it is not so different from that in Kyoto University Research Reactor[7] (see Fig.1)in which samples used in the present study were irradiated.

Radiation Effects on Nb-Ti Wire

Sample Preparation--We have made a systematical study by taking two kinds of Nb-Ti composition and changing the length of ageing time of the sample to give different metallurgical structures which in turn give corresponding superconducting properties. These samples were prepared as follows. Sample A(Nb-47.6 at.%Ti):The 50mm rod was cold worked to 2.5mm, clad with OFC and drawn to 0.25mm core. The reduction ratio is 99.99%: Sample B(Nb-59.8 at.%Ti): The 7mm bar was cold worked to 2.5mm in diameter clad with OFC and drawn to.25mm in core: The reduction ratio is 99.87%. Both samples were aged at $380^{\circ}C$ for 0 - 10^{4} min. in a vacuum of $\sim 10^{-6}$torr.

Neutron Irradiation--Samples encased in silica tube in Al capsule were irradiated in the Kyoto University Research Reactor. The fast neutron flux up to $3.9 \times 10^{13} n/cm^2/sec$ (En>0.1MeV). Irradiation temperature is believed less than $70^{\circ}C$.

Critical Current--The standard four terminal method was used. The critical current Ic was determined with the awake of 5μV across the potential terminals.

Critical Temperature--The critical temperature was determined by standard dc method with accuracy of ±0.005K using the calibrated Ge sensor(Cryocal Inc. CR-500).

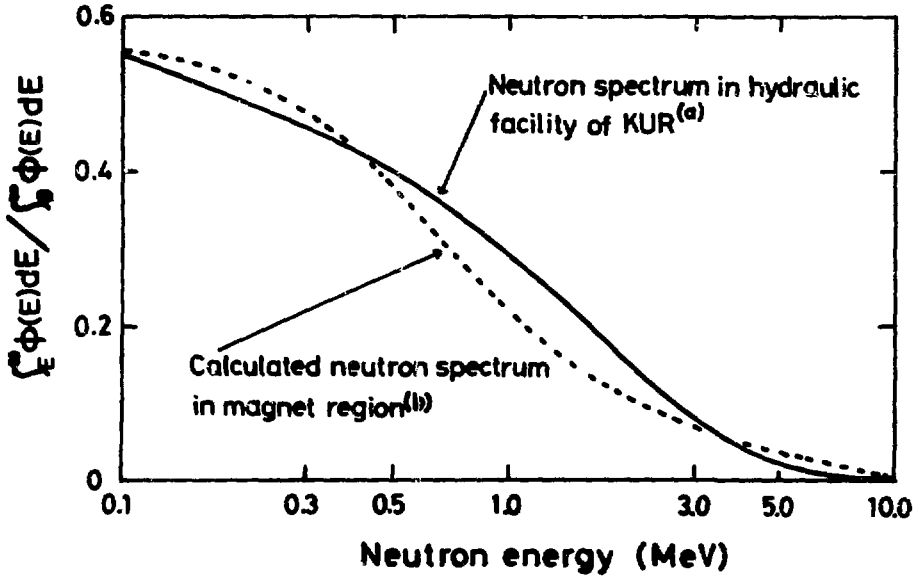

Fig. 1. Comparison of neutron energy spectrum in hydraulic irradiation facility of Kyoto University Research Reactor [(a):Ref.7] with calculated spectrum in magnet region of CTR [(b):Ref.9].

Results--The figures 2(a) and (b) show the irradiation effects on critical current density J_c of samples A and B, respectively, at the external transverse magnetic field of 3.1 T. Very little effects are seen in sample A. Figs. 3(a) and (b) and Figs. 4 (a) and (b) show the behaviors in the samples A and B where the J_c's were measured at 5.0 and 8.0 T, respectively. The general tendency of these results is that the radiation effects are larger in sample B than that in A. The maximum decrease in J_c measured at 5.0 T amounts up to 15% in sample B which was aged for 5×10^3min.. Considerable effect of J_c in sample B has been attributed to the neutron irradiation induced destruction of α-Ti precipitates which play an important role as flux line pinner. The detail will be published elsewhere. The effect to critical temperature shown in Figs. 5 (a) and (b) are to reflect above change in internal structure: i.e., only sample B showing drastic change after irradiation.

Effects on Copper and Aluminum

Usually copper or aluminum has been adopted as a stabilizer because of their low electrical resistivity. Blewitt et al[8] have shown that induced resistivity increase ($\Delta\rho$) of Cu due to neutron irradiation at 14.5K takes independent value of 1.2×10^{-26}ohm.cm/n/cm^2 to residual resistivity. McCracken and Blow[9] have also reported that the values of $\Delta\rho$ for Cu and Al at 4.2K irradiation are 6.2×10^{-26} and 2.1×10^{-25} ohm•cm/n/cm^2, respectively.

OPTIMIZATION IN COMPOSITE CONDUCTORS

In the following we shall attempt to obtain maximum transport current density (J_T^m) of a composite conductor under the boundary conditions: (1) The critical current density $J_c(T,B)$ of the superconductor is influenced by the irradiation. (The data for this were described in the previous section.) (2) The resistivity of the normal conductor(Cu or Al) increases after the irradiation which then degrades the stability of the conductor. (The data for this were taken from McCracken's review article[9]). (3) Magneto-resistance is assumed independent of initial resistivity.

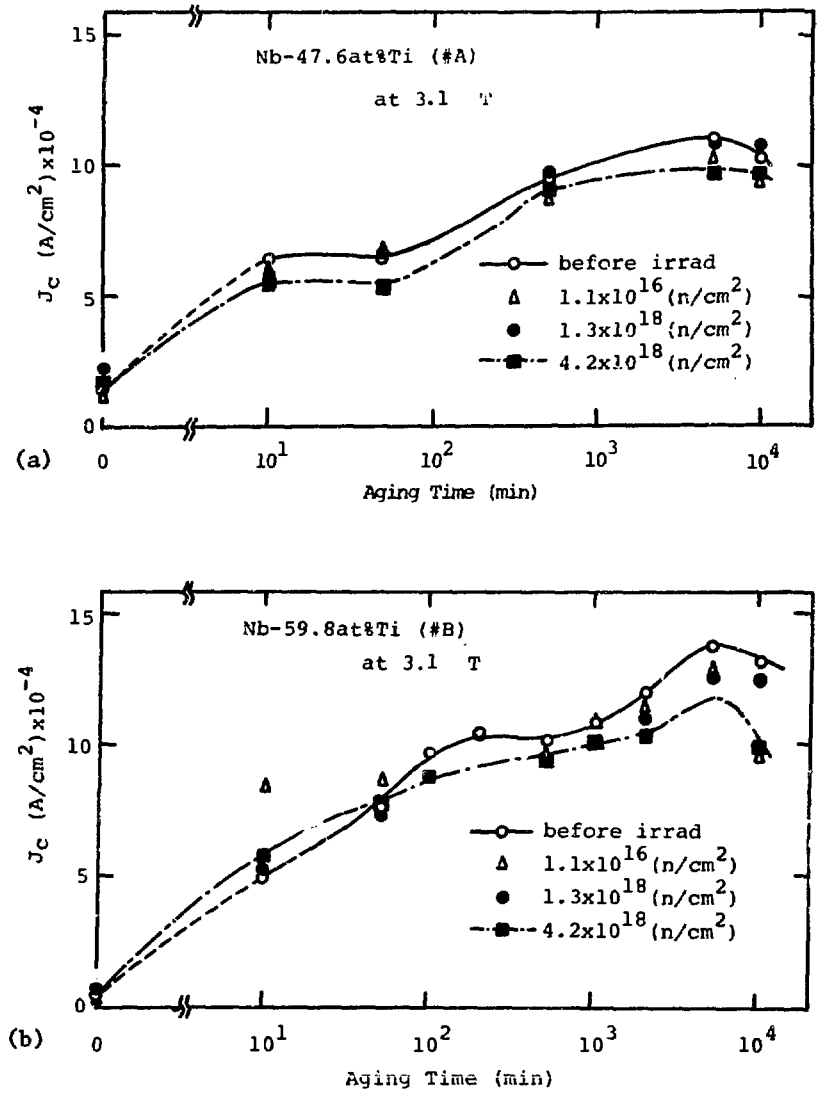

Fig. 2 Dependence of neutron irradiation effects on J_c vs aging time; a) sample A, b) sample B, measured at 3.1 T.

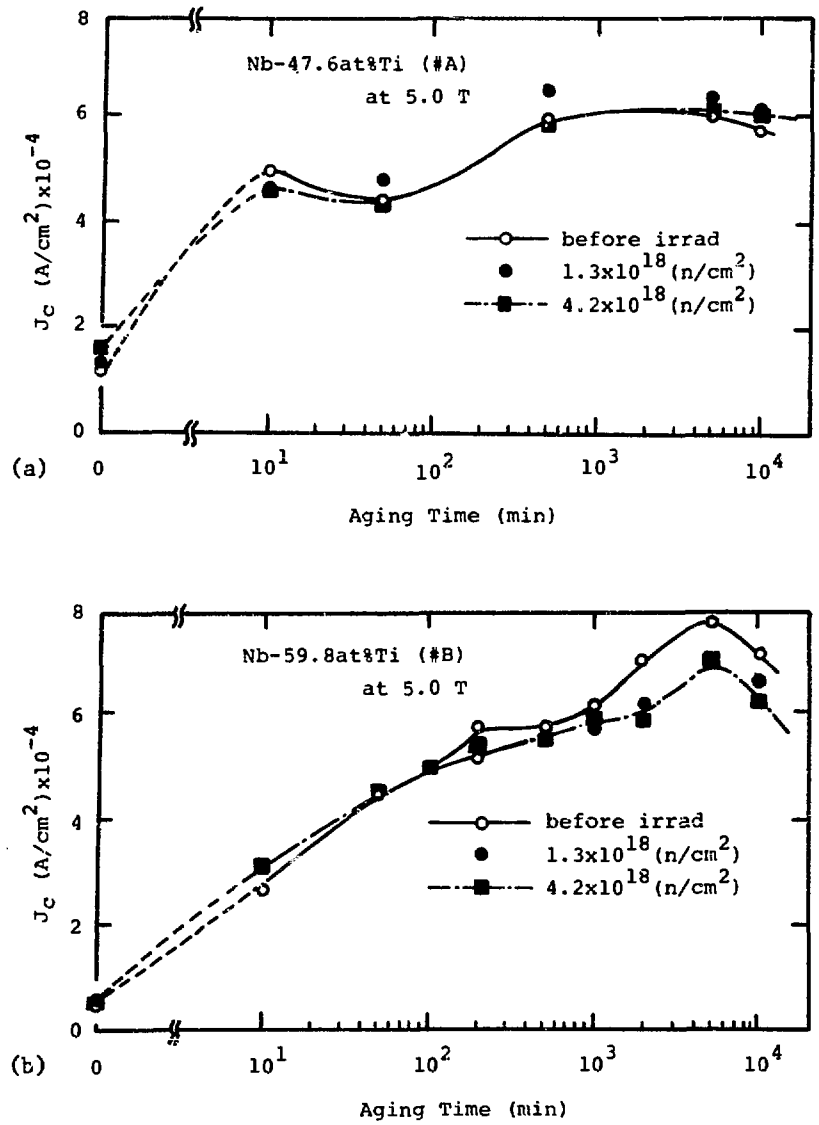

Fig. 3. Dependence of neutron irradiation effects on J_c vs aging time; a) sample A, b) sample B, measured at 5.0 T.

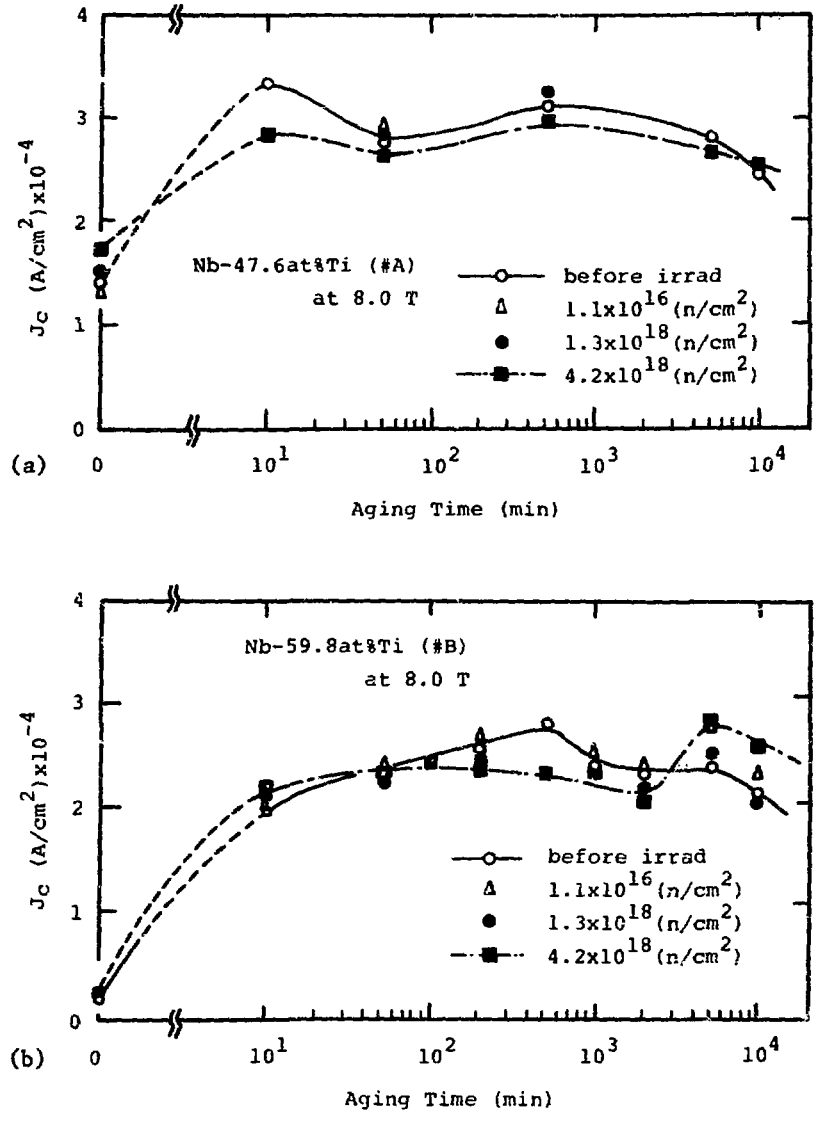

Fig. 4. Dependence of neutron irradiation effects on J_c vs aging time; a) sample A, b) sample B, measured at 8.0 T.

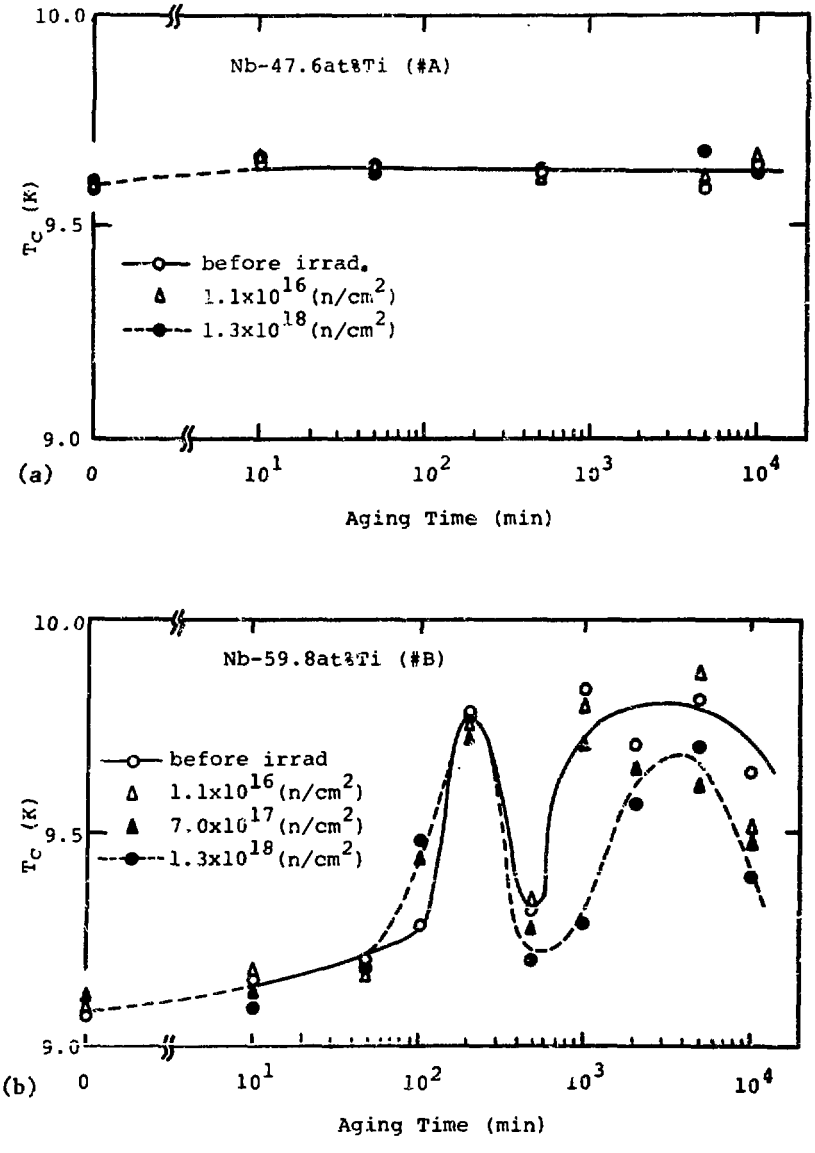

Fig. 5 Dependence of neutron irradiation effects on T_c vs aging time; a) sample A, b) sample B.

The values (ρ_H) used in the following analyses are 3×10^{-9}ohm.cm/T and 5×10^{-9}ohm.cm/T for Cu and Al, respectively.

Geometrical Specification of Composite Conductors

A rectangular composite multifine superconductor was assumed as shown in the inset of Fig.6(a) for the purpose of analysing the effect of radiation on the cryostatic stabilization. The cross section is given by nd^2 ($n \geq 1$). Wider faces are assumed to be cooled. The combination of superconductor of Nb-Ti and stabilizer of Cu or Al is assumed. Notations are given below.

J_c	:	critical current density of superconductor	(A/cm^2)
T_b	:	temperature of the coolant	(K)
T_c	:	critical temperature of superconductor	(K)
A_S	:	cross section of superconductor	(cm^2)
A_N	:	cross section of stabilizer	(cm^2)
A	:	total cross section of composite conductor ($A = A_N + A_S = nd^2$)	(cm^2)
ρ	:	electirical resistivity of stabilizer	(ohm.cm)
P	:	perimeter (=2nd)	
R_{NS}	:	normal super ratio, N/S ratio ($=A_N/A_S$)	
h	:	heat transfer coefficient	($watt/cm^2/K$)

Optimized Normal to Super Ratio and Maximum Allowable Transport Current Density

The maximum allowable transport current (I_T) of a composite superconductor is requested to be less than not only critical current of superconductor but also stabilized current. Stabilized current involves (i) fully stabilized current, (ii) recovery current, and (iii) minimum propagation current, in the order of the severeness of the conditions. For the sake of simplicity we shall examine recovery current hereafter.

The recovery current can be given in the following way. Suppose that the transport current I(amp) is flowing in the composite conductor and that total current happens to flow in stabilizer caused by destruction

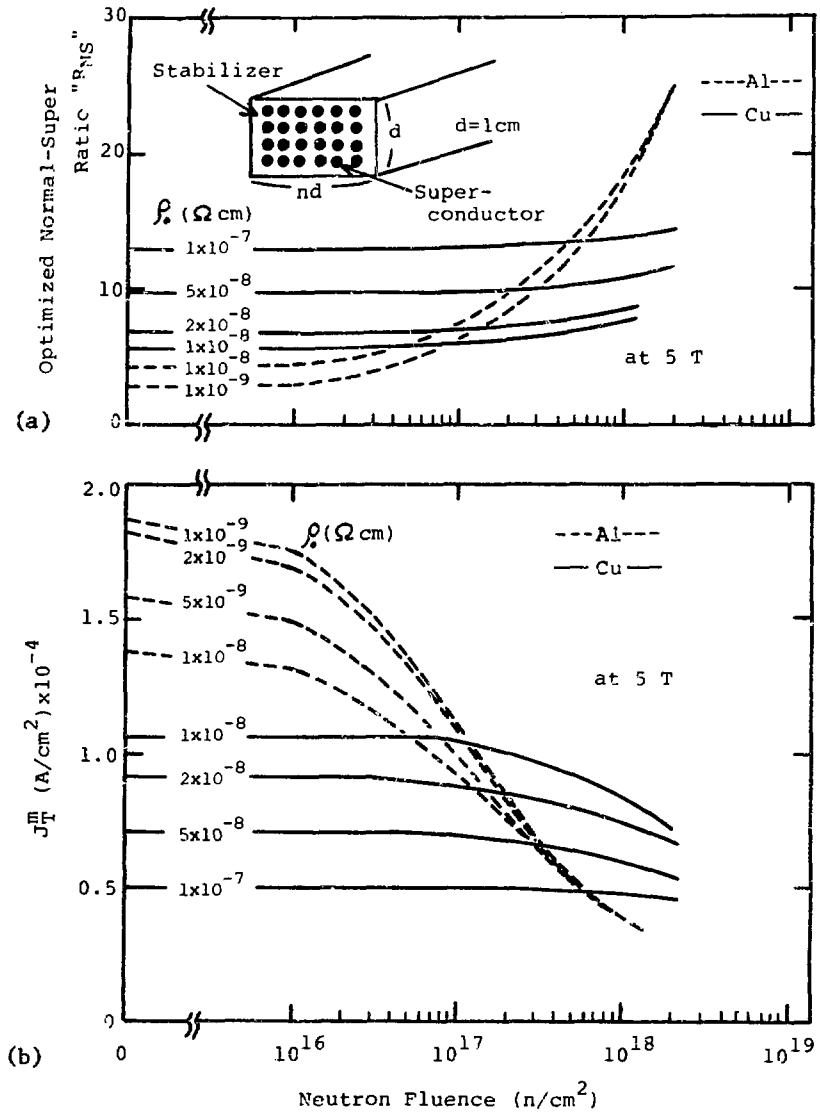

Fig. 6. Influence of the resistivity change of normal conductor on (a) the optimized normal/super ratio vs neutron fluence (b) maximum transport current density J_T^m ; at 5 T.

of superconductivity. Then, the heat generation per unit length of conductor is given by (I^2/A_N). On the other hand the heat released at the surfacesof the conductor is given by $Ph(T_c - T_b)$. If the condition that heat generated is less than the heat removed is satisfied, this composite conductor can recover to superconducting state again with the current flowing. In this case we may call the conductor as stable. Thus the critical value of I can be given by the condition that the heat generated is equal to that being removed. The value of the current satisfying this condition is defined as recovery current (I_r) which gives:

$$I_r^2 = A_N Ph(T_c - T_b)/ \rho \qquad (1)$$

Putting the geometrical figures of the inset of Fig.7(a) into above equation, nemely, replacing the values $A_n = nd^2R_{NS}/(1 + R_{NS})$, P=2nd

$$I_r^2 = 2nd^3hR_{NS}(T_c - T_b)/(1 + R_{NS})\rho \qquad (2)$$

is obtained. It is seen that the recovery current(I_r) can grow larger with increasing T_c or for the smaller value of ρ provided that the cross section of composite conductor is constant. On the other hand critical current (I_c) is given by

$$I_c = nd^2J_c/(1 + R_{NS}) \qquad (3)$$

Thus, for the constant cross section I_c becomes larger for the increasing J_c or smaller N/S ratio. The optimum N/S ratio that makes allowable transport current I_T maximum is given from the condition $I_c = I_r$, ie.,

$$R_{NS} = \frac{1}{2}\left[\sqrt{1 + \frac{20d\rho J_c^2}{3(T_c - T_b)}} - 1\right] \qquad (4)$$

Neutron Irradiation Effect to the Optimized N/S Ratio and Maximum Allowable Transport Current Density

In the following we shall culculate optimized N/S ration and maximum transport current density J_T^m adopting Cu and Al as stabilizer and taking the radiation effects on stabilizer as well as superconductor into consideration. The procedures are as follows:

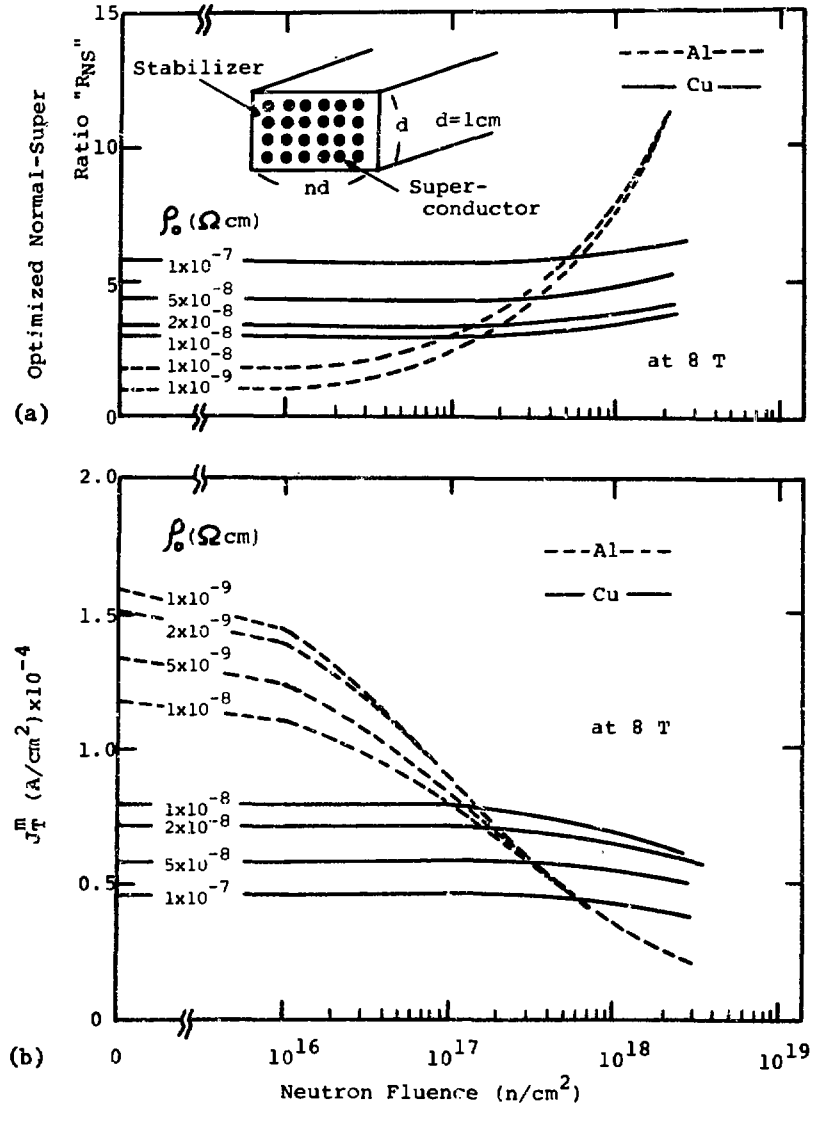

Fig. 7 Influence of the resistivity change of normal conductor on (a) the optimized normal/super ratio vs neutron fluence (b) maximum transport current density J_T^m ; at 8 T.

i) Choice of Nb-Ti--Based on the J_c data presented in the previous section we have chosen Nb-59.8 at% Ti(aged 5 x 10^3 min.) for the use in 5 - 6 T. For the use in magnetic field of 7 - 8 T region Nb-47.6 at % Ti(aged 500 min.) was chosen, and for 9 T region Nb-47.6 at % Ti (10min.).

ii) Normal Conductors--As the stabilizer we have chosen Cu with resistivity from 1 x 10^{-8} to 1 x 10^{-7}ohm.cm at 4.2K: Al with resistivity from 1 x 10^{-8} to 1 x 10^{-9}ohm.cm at 4.2K.

iii) Maximum Transport Current Density, J_T^m--The value of J_T^m was obtained by putting the value of optimized R_{NS} into the equations which gives I_c or I_r and by dividing with total conductor cross section(nd^2). For the sake of convenience d = 1cm was assumed.

Figure 7(a) and (b) illustrate optimized normal/super ratio (R_{NS}) and maximum transport current density(J_T) at 5T in the case of Cu and Al as the stabiliser. It is noted that optimized R_{NS} increases monotonically with neutron fluence. The increasing rate of R_{NS} for Al grows more rapidly than for Cu. This is mainly because of the larger radiation induced increment of resistivity in Al than in Cu. The J_T^m decreases monotonically with increasing neutron fluence. The larger value J_T is obtainable in lower irradiation ($\lesssim 10^{17}$n/cm^2) with Al stabilizer, while in the higher region ($\gtrsim 10^{17}$n/cm^2) Al is not advantageious comared with Cu.

Figures 7(a) and (b) are the results of R_{NS} and J_T^m at 8T. The fact that the value of J_T^m(8T) is lower than J_T^m is mainly because of the decrease in J_c due to magnetic field effect and partly because of the magneto-resistance (ρ_H). The R_{NS} value correspondingly decreases and takes nearly half value at 5T. As we can take the smaller R_{NS} value for 8T, the magnetic field effect on J_T^m was found, therefore, to remain within 10% for Al and 25% for Cu. The behaviors at 8T against neutron fluence are similar to the case at 5T.

EVALUATION OF RADIATION EFFECT CRITERIA IN SUPERCONDUCTING WIRE AND/OR MAGNET

Composite Superconductor

We shall now attempt to evaluate how far a composite suprconducting wire is tolerable to neutron irradiation. To this end it should be convenient to combine Fig.6(b) or Fig.7(b) which give the allowable maximum transport current density J_T^m as a function of neutron fluence. We have shown two examples as Fig.8 and 9 which correspond to the conductors to be used at 5% and 8T, respectively. The log-log diagram on the right hand side of Fig.8 shows neutron fluence against operation time of fusion reactor. Radiation effects on a superconducting magnet for full scale CTR implies two aspects; (1) "flux effect" that involves nuclear heating*) and (2) "fluence effect" that involves integrated radiation damage which have been discussed in this paper. Suppose that a conductor in the SC magnet must be subjected to the neutron flux, say $\Phi = 10^9 n/cm^2/sec$. The fluence then amounts to $\sim 10^{18}$ n/cm^2 after operation of the reactor for 20 years without intermission (without warm-up of the superconducting magnet). We may call a horizontal lines 'F-line' which is drawn passing across point of L_{20} -line(20 years). If we require the superconductor to tolerate up to this fluence under the condition: $J_T^m \geq 5 kA/cm^2$, Al stabilized conductors cannot be used even their residual resistivity is as low as 1×10^{-9} ohm•cm. In case of Cu-stabilised conductor, optimized composite wire stabilised by Cu with residual resistivity lower than 5×10^{-8} ohm.cm can successfully be applicable to this CTR magnet.

If one set a radiation-induced degradation curve of J_c on the left side of the Fig.8 or 9 instead of J_T vs fluence diagram and apply'10 % reduction criteria' for the usability of conductor, we can compare the severeness of radiation damage on superconductor itself and composite case(including stabilizing effect).

---

*) This problem has been discussed by H.Ullmaier in the preceding review paper of this session, this conference.

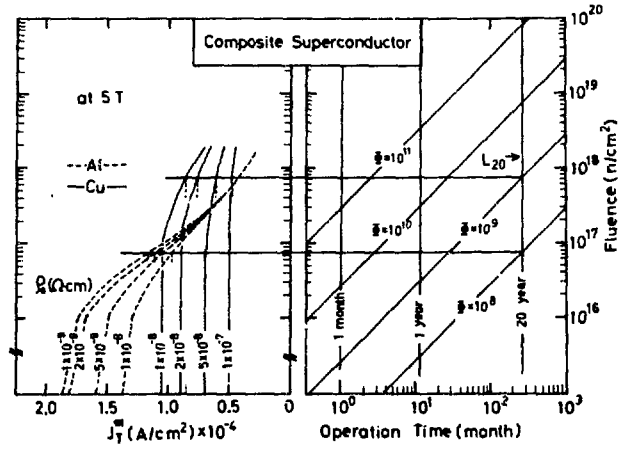

Fig. 8. Knife edge diagram for Nb-Ti/Cu composite superconducting wire; at 5 T.

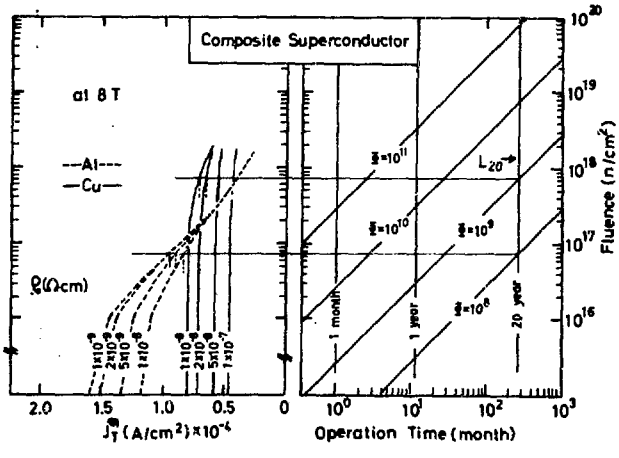

Fig. 9. Knife edge diagram for Nb-Ti/Cu composite superconducting wire; at 8 T.

The utility of this diagram is not limited to the case of short sample but can be conveniently extended to any large magnet system used in CTR taking radiation effects on various components and overall effects into account.

CONCLUSION

In the present study we have made an attempt to evaluate good composite superconducting coil which is tolerable to the use in strong radiation field. To this end we have taken the following factors into consideration: (i) Experimental study(simulation using irradiation by fission reactor) on Cu-stabilized Nb-Ti wire, (ii) Radiation-induced increase in resistivity ($\Delta\rho$) in normal conductor, (iii) Magneto-resistance of stabilizer (ρ_H). The radiation effects were considered in the form of cryogenically stabilized composite conductor. Optimized normal/super ratio and maximum transport current density J_T were obtained and followed as a function of the neutron fluence.

A convenient illustration (a knife-edge-diagram) was proposed to derive the criteria of applicability of superconducting wire under given irradiation conditions. The diagram is considered to be expansible to evaluate the performance in CTR-oriented superconducting magnet.

The authours are grateful to Dr. Ullmaier for informing us about some of his unpublished work. They would like to thank Dr. K. Sako of JAERI for various stimulating suggestions. They also wish to Dr. J. Yamamoto, Y. Tsuji, Y. Wakisaka, and H. Makiyama of Low Temperature Center of Osaka University for their help in the experiment using liquid helium. Acknowledgement is also due to Dr. H. Yoshida for his kind help with neutron irradiation.

REFERENCES

1. R.Hancox, Fusion Reactor Studies in the United Kingdom, ANS Winter Meeting, Washington D.C, Nov.(1972).

2. M.S.Lubell, Superconducting Troidal Magnets for Fusion Feasibility Experiments and Power Reactors (1974).

3. M.S.Lubell, W.F.Gauster, K.R.Efferson, A.P.Fraas, H.M.Long, J.N. Luton, C.E.Parker, D.Steiner and W.C.T.Stoddart, Plasma Physics and Controlled Nuclear Fusion Research (IAEA, Vienna 1971) Vol.III, p.433-446.

4. R.Hancox, General Description of a Possible D-T Toroidal Reactor, International School on Fusion Reactor Technology, September (1972). Cited by K.Sako, J.At.Energy Soc.Japan(Japanese)15, 712(1973).

5. References to Table 1: (a) W.M.Stacey et al., TOKAMAK EXPERIMENTAL POWER REACTOR STUDIES, ANL/CTR-75-2(1975), (b) G.L.Kulcinski and R.W.Conn, The Conceptual Design of a Tokamak Fusion Power Reactor 'UWMAK-1', Sandiego, April(1974), (c) G.L.Kulcinski and R.W.Conn, Design Features of the D-T Tokamak Power Plant 'UWMAK-II', IAEA-CN-33/ G1-2,5th IAEA Conf. Tokyo, November (1975), (d) W.G. Price,Jr., The Princeton Reference Design Rusion Power Plant, IAEA-CN-33/ G1-4, 5th IAEA Conf. Tokyo (1974), (e) K.Sato et al., Design Study of a Tokamak Reactor, IAEA-CN-33/ G1-5 ibid, (f) E. Bertolini et al., Design of a Minimum Size Toroidal D-T Experimental Reactor IAEA-CN-33/G1-1 ibid, (g) A.P.Fraas, Conceptual Design of the Blanket and Shield Region and Related Systems for a Full Scale Toroidal Fusion Reactors, ORNL-TM3096(1973). (h) R.Hancox, ibid Ref.4 and G.M.McCracken and S.Blow, CLM-120, August (1972).

6. References to Table 2: (i) M.Soell, 7th Sympo.on Fusion Technol., p.311 (1972). (j) T.Sugisaki, T.Okada, T.Suita, Technol.Repts. Osaka Univ.,21,385 (1971). (k) J.P.McIvoy, Jr., R.F.Decell, Appl. Phys. Letters,4,43 (1964). (l) J.T.A.Pollock, V.Sadagopan, H.C.Gatos, Trans. Met.Soc.AIME,245,2350 (1969). (m) P.S.Swartz, H.R.Hart,Jr.,

R.L. Fleischer, Appl.Phys. Letters 4 71(1964). (n) H. Tsubakihara, T.Okada, T.Suita, T.Horiuchi, K.Matsumoto, S.Tsurutani, J.Nucl. Sci. Technol. 11 , 452 (1974). (p) M.Couach, J.Doulat, and E.Bonjor, IEEE Trans. Magnetics, MAG-11, 170(1975).

7. I.Kimura, Private communication.

8. T.H. Blewitt, R.R.Coltman, C.E.Claubunde, and T.S.Noggle, J. Appl. Phys. 28,639(1957).

9. G.M.McCracken and S.Blow, The Shielding of Superconducting Magnets in a Fusion Reactor, CLM-R 120, August ,(1972).

THE EFFECT OF STRESS-INDUCED DIFFUSION ON VOID NUCLEATION

W. G. Wolfer and M. H. Yoo
Metals and Ceramics Division
Oak Ridge National Laboratory
Oak Ridge, Tennessee 37830 USA

ABSTRACT

Interstitials and vacancies interact with voids through the image force as well as forces induced by the surface stress and gas pressure in the void. These forces cause a drift motion of the point defects to the void and thereby give rise to a bias. It is found that the bias of voids increases with decreasing void radius. Thus, it mainly influences the nucleation of voids rather than their growth. We have incorporated this bias of voids into the nucleation theory developed by Katz, Wiedersich, and Russell, and studied the effect of surface energy, surface stress, temperature, dislocation bias, and gas pressure on the void nucleation. It is found that the critical void size is to a large extent determined by the condition that the interstitial bias of voids is equal to the bias of dislocations. Although the height of the activation barrier for nucleation depends on the bias factors also, it is affected more by surface energy, temperature, and above all, gas content. Since the bias of dislocations is largest when produced by small dislocation loops, it is concluded that void nucleation depends critically on the evolution of the dislocation structure. To obtain nucleation rates as observed experimentally one or preferably all of the following conditions must be met: A large dislocation bias, a reduction of the surface energy through contamination of the void surface, and a reduction of the void bias through impurity segregation.

INTRODUCTION

In previous theories for void growth[1-3] and void nucleation[4,5] the bias for preferential interstitial absorption at dislocations was considered to be a fixed but not necessarily absolute parameter. In fact, it was generally treated as an adjustable parameter to match the theoretical

*Research sponsored by the Energy Research and Development Administration under contract with the Union Carbide Corporation.

predictions with experimental findings. Recent experiments[6-8] have provided the relaxation volume as well as the elastic polarizabilities of self-interstitials for a few fcc metals. The relaxation volume determines the magnitude of the size-interaction, and the polarizabilities the magnitude of the modulus-interaction of the self-interstitial with stress-fields. Both interactions in turn determine the magnitude of the interstitial bias of a particular sink. Bias factors for voids, small dislocation loops, and edge dislocations have been calculated recently,[9-11] and hence, they can be considered as independent parameters within the context of the swelling and void nucleation theories. Their application to theories for radiation-induced creep has resulted in a successful prediction of the steady-state irradiation creep in neutron-irradiated stainless steel.[12] In this paper we incorporate some of these bias factors into the theory of void nucleation and investigate their effect on void nucleation rates, critical size, and activation barrier.

The Bias Factors

The bias factor of a sink is a convenient measure of the effect of the stress-induced drift on the integrated flux of point defects to the sink. The stress-induced drift is the second term in Fick's law for the flux

$$\underset{\sim}{j} = - D\nabla C - \frac{1}{kT} DC\nabla E \ , \qquad (1)$$

where D is the diffusion coefficient for migration, C the concentration of point defects, k the Boltzmann constant, T the absolute temperature, and E the interaction energy of the point defect with the stress or strain field around the sink. Within the framework of the rate-theories[1-5] the integrated flux, or in short, the current can be written in the form

$$J = AZD\ (C - C^{\circ}) \ , \qquad (2)$$

where C is now the average defect concentration and is determined by solving the rate equations, A is a geometrical factor, C° the concentration of defect in thermal equilibrium with the sink, and Z is the bias factor. For a particular type of sink, the bias factor has the same form for both vacancies and interstitials. However, since it depends on the defect

parameters, v, the relaxation volume, α^G and α^K, the shear and bulk polarizabilities, its value differs for vacancies and interstitials. Using the subscripts v and i, we can state that in general $Z_i > Z_v$. More specifically, the bias factors for small faulted loops, Z^ℓ, are inversely proportional to $(R/b)^2$, where R is the radius of the loop and b the Burgers vector. This is shown in Fig. 1. These bias factors* are, in a strict sense, only valid for infinitesimal loops or very small loops. Hence, it should not be surprising that the bias factors do not approach asymptotically the values for the edge dislocation which are also shown in Fig. 1 by the horizontal lines in the lower right corner. In spite of this shortcoming it is evident that small dislocation loops have an interstitial bias which is substantially larger than the interstitial bias of edge dislocations. Furthermore, there exists a small but non-negligible vacancy bias. The interstitial bias of both edge dislocations and loops are larger than those previously assumed in swelling theories. The two major reasons for their magnitude are the large relaxation volume of 1.4 Ω for interstitials (Ω is the atomic volume) and the large negative shear polarizability α_i^G for interstitials. Both parameters have been measured for Cu (ref. 2) and have also a well-founded theoretical basis.[13]

To arrive at the bias factor of voids we have to consider an additional interaction peculiar to free surfaces: the image interaction. This interaction was derived previously by Moon and Pau[14] from the work of

---

*Detailed expressions are given in Refs. 9 and 10. The parameters used for the calculation are as follows:

Poisson's ratio: $\nu = 0.3$; shear modulus: $G = 10^{12}$ dynes/cm^2; T = 500°C (the small temperature dependence of the bias factors is of no importance to the present results); relaxation volumes: $(v/\Omega)_i = 1.4$ for interstitial, $(v/\Omega)_v = -0.2$ for vacancies; polarizabilities: $\alpha_i^G = -150$, $\alpha_i^K = 10$, $\alpha_v^G = -15$, $\alpha_v^K = -15$, all values in eV.

Bose.[13] Assuming no surface tension or gas pressure in the void, the bias factor due to the image interaction was derived recently.[14] Although a closed-form solution for this bias factor cannot be given (nor has one been used in the subsequent investigations), a good approximation is obtained by the expression

$$Z^{im} = 1 + \left[\frac{G}{kT}\frac{(1+\nu)}{3\pi(1-\nu)}\right]^{1/3}\left(\frac{v}{\Omega}\right)^{2/3}\frac{b}{a}, \qquad (3)$$

where a is the void radius, ν the Poisson's ratio, G the shear modulus, and v the relaxation volume of the point defect. The bias factors of voids due to the image interaction alone are shown by the broken lines in Fig. 2.

The surface tension, σ, which is not necessarily equal to the surface energy, γ, and the gas pressure p give rise to a radial stress component, $(2\sigma/a - p)$, on the void surface. Although the resulting stress field in the matrix does not give rise to a size interaction, it does cause an interaction through the modulus effect. The corresponding bias factor is[2]

$$Z^{s} = 1 - \frac{3}{5\pi}\frac{\alpha^{G}}{kT}\left(\frac{2\sigma/a - p}{G}\right)^{2}. \qquad (4)$$

The compound bias factor, and hence, the void bias factor, Z°, is simply given by the product of Z^{s} and Z^{im}:

$$Z^{\circ} = Z^{im}\,Z^{s}. \qquad (5)$$

The solid lines in Fig. 2 represent Z° for p = 0 and two values of the surface tension, σ = 1000 and σ = 2000 ergs/cm^2, as a function of (a/b). These curves resemble the ones obtained for the bias factors of dislocation loops, Fig. 1, as they also show the rapid decrease of the bias factors with increasing sink radius. This dependence can be understood in qualitative terms if we give the following interpretation to the bias factor:

The geometrical factor A in Eq. (2) is for a spherical sink equal to $4\pi a$ or $4\pi R$. Thus $Z^{\circ}a$ or $Z^{\ell}R$ can be interpreted as the capture radii of voids or loops, respectively. Obviously, capture occurs at a certain distance from the "sink surface," and this distance depends not strongly on the sink dimension. Thus, for increasing sink radius, the capture distance becomes a smaller and smaller fraction of the sink radius. In

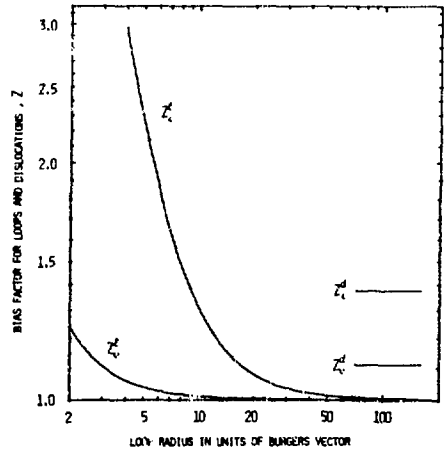

Fig. 1. The Bias Factors for Dislocation Loops, Z^{ℓ}, and Edge Dislocations, Z^{d}.

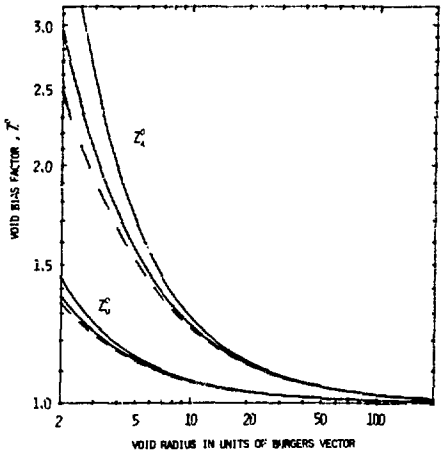

Fig. 2. The Bias Factors for Voids, Z°.

other words, the ratio of capture radius to actual sink radius, that is Z, approaches one with increasing sink radius.

The KWR Theory of Void Nucleation

In the nucleation theory developed by Katz, Wiedersich,[5] and also by Russell[4] the free energy for forming a vacancy cluster with x vacancies is given by

$$\Delta G(x) = -kT \sum_{n=1}^{x-1} \ell n \frac{\beta_v(n)}{\beta_i(n+1) + \gamma_v(n+1)} , \tag{6}$$

where $\beta_v(n)$ is the absorption rate of vacancies by an n-cluster, $\beta_i(n)$ the absorption rate of interstitials, and $\gamma_v(n)$ the thermal emission rate of vacancies. The latter can either be obtained through a constrained equilibrium assumption, or simply and equivalently, by assuming a local thermodynamic equilibrium for the n-cluster and its immediate surrounding. Thus

$$\gamma_v(n) = 4\pi b n^{1/3} Z_v^\circ(n) D_v C_v^\circ(n) , \tag{7}$$

where D_v is the vacancy migration coefficient and

$$\begin{aligned} C_v^\circ(n) &= C_v^{eq} \exp\left\{\{4\pi b^2\gamma [n^{2/3} - (n-1)^{2/3}] - p\Omega\}/kT\right\} \\ &\cong C_v^{eq} \exp\left\{\left(\frac{2\gamma}{a} - p\right)\frac{\Omega}{kT}\right\} , \end{aligned} \tag{8}$$

where a is the radius of the n-cluster.

The absorption rates are given by

$$\beta_v(n) = 4\pi b n^{1/3} Z_v^\circ(n) D_v C_v \tag{9}$$

and

$$\beta_i(n) = 4\pi b n^{1/3} Z_i^\circ(n) D_i C_i \tag{10}$$

where C_v and C_i are determined from the two rate equations

$$P - K D_v C_v D_i C_i = \sum_s N^s A^s Z_v^s D_v (C_v - C_v^s) \tag{11}$$

$$P - K D_v C_v D_i C_i = \sum_s N^s A^s Z_i^s D_i C_i , \tag{12}$$

where

$$K = 504\ b/D_v \tag{13}$$

is the recombination coefficient, P the production rate, N^s is the number of sinks of type s and C_v^s the vacancy concentration in thermal equilibrium with the sink s. It is a simple matter to solve Eqs. (11) and (12) for D_vC_v and D_iC_i and inserting the results into Eq. (6). If we introduce the definitions

$$F = \frac{\bar{Z}_i}{2K\bar{D}_v}\left\{\left[(1 + K\bar{C}_v/\bar{Z}_i)^2 + 4KP/\bar{Z}_i\bar{Z}_v\right]^{1/2} - (1 + K\bar{C}_v/\bar{Z}_i)\right\}, \tag{14}$$

$$\bar{Z}_{i,v} = \sum_s N^s A^s Z^s_{i,v}, \tag{15}$$

and

$$\bar{C}_v = \sum_s N^s A^s Z^s_v C^s_v / \sum_s N^s A^s Z^s_v, \tag{16}$$

then we can write Eq. (6) in the form

$$\Delta G(x)/kT = \sum_n^{x-1} \ell n\left[\frac{(n+1)^{1/3}\ Z_i^\circ(n+1)}{n^{1/3}\ Z_v^\circ(n)}\frac{\bar{Z}_v}{\bar{Z}_i}F + C_v^\circ(n)\right] - (x-1)\,\ell n\,(F + \bar{C}_v). \tag{17}$$

The steady-state nucleation rate is given by

$$I = D_v\,(F + \bar{C}_v)^2\left\{\sum_{x=1}^{\infty} \exp\left[\Delta G(x)/kT\right]/Z_v^\circ(x)\right\}^{-1}. \tag{18}$$

It is apparent that positive contributions to $\Delta G(x)$ are made by all those cluster sizes n for which

$$\frac{(n+1)^{1/3}\ Z_i^\circ(n+1)}{n^{1/3}\ Z_v^\circ(n)}\ \frac{\bar{Z}_v}{\bar{Z}_i}F + C_v^\circ(n) > F + \bar{C}_v. \tag{19}$$

The critical cluster size n* is obtained from the relation (19) if the two sides are equal. $\Delta G(n^*)$ is then the activation barrier for nucleation. Positive contribution to $\Delta G(n^*)$ can be obtained if either $C_v^\circ(n) > \bar{C}_v$ and/or

$$(n+1)^{1/3}\ Z_i^\circ(n+1)/n^{1/3}\ Z_v^\circ(n) > \bar{Z}_i/\bar{Z}_v. \tag{20}$$

The latter condition simply indicates that with a relative void bias, Z_i°/Z_v°, larger than the relative dislocation and loop bias, $\bar{Z}_i/\bar{Z}_v$, void nucleation can be reduced substantially.

To demonstrate this more clearly $\Delta G(x)/kT$ and I were computed according to Eqs. (17) and (18) using the parameters listed in Table 1. Figure 3 shows $\Delta G/kT$ for the more familiar case where $Z_i^+(n+1) = Z_v^-(n)$. Using now the void bias factors discussed in the last section, Fig. 4 is obtained. The inclusion of the void bias causes an increase in the critical size, i.e. a shift in the location of the maximum of $\Delta G/kT$ as well as an increase in $\Delta G(n^*)$ itself. Both effects drastically reduce the steady-state nucleation rates, as shown in the inserted tables. It should also be noted that the nucleation rates, I, in both cases are substantially below the values needed to predict experimentally observed rates even for very large values of the dislocation bias. Meaningful values for reactor irradiation should be of the order of I = 10^{7} to 10^{8} voids/cm^3/sec.

Table 1. List of Parameters

Burgers vector, $b = 2.5 \times 10^{-8}$ cm

Atomic volume, $\Omega = b^3$

Vacancy formation energy, $F_v^f = 1.6$ eV

Vacancy migration energy, $F_v^m = 1.4$ eV

Equilibrium vacancy concentration, $C_v^{eq} = \Omega^{-1} \exp\,(1.5 - F_v^f/kT)$

Vacancy migration coefficient, $D_v = 0.0153 \exp\,(-F_v^m/kT)$

Production rate, $P = 1.125\,\Omega^{-1} \times 10^{-22}\,\phi$, where ϕ is the fast neutron flux

Average equilibrium vacancy concentration, $\bar{C}_v = C_v^{eq}$

In order to obtain meaningful nucleation rates, one may consider various variables as adjustable ones. First, the surface energy, γ, could be lowered substantially by impurities and reactive gases. Indeed, the magnitude of the surface energy determines the initial rise of $\Delta G(n)$ with increasing n^*, and thereby also the maximum value $\Delta G(n^*)$. This is demonstrated by Fig. 5. However, it is seen that for a temperature of T = 500°C a drastic reduction of the surface energy, γ, to as low a value as 600 ergs/cm^2 is needed to bring I close to a reasonable nucleation rate. Thus, if we consider a value of

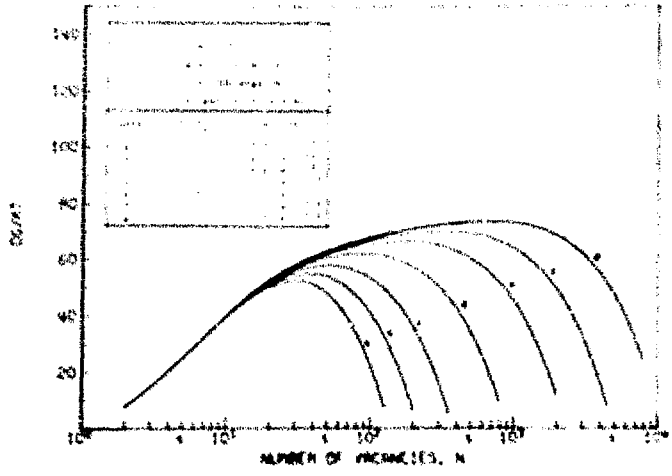

Fig. 3. Free Energy for Void Nucleation with No Void Bias.

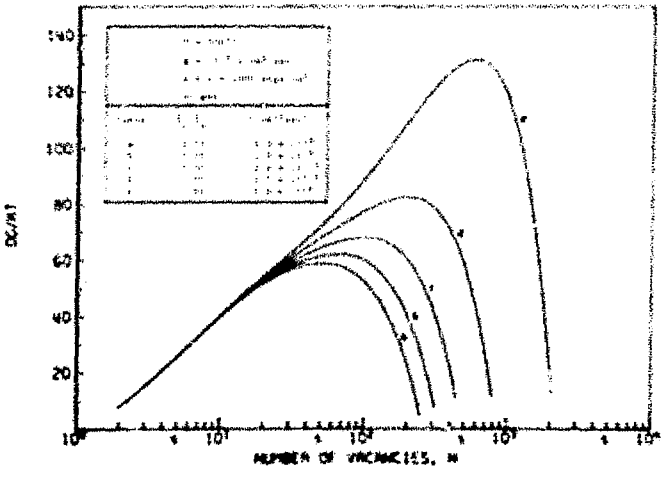

Fig. 4. Free Energy for Void Nucleation with Void Bias.

... erate on as the "effective" surface energy, we can further improve on the nucleation rate by increasing the dislocation bias, Z_i/Z_v, as shown in Fig. . Even further improvement can be achieved when we set the surface stress σ equal to zero, as can be seen from Fig. when compared to Fig. . The last improvement is obvious, since with $\sigma = 0$ the void bias is now due to the image interaction only. The lack of a measurable surface stress has been reported in the literature,[ ] so that the choice of $\sigma = 0$ is not without basis.

An effect similar to the variation in the surface energy, γ, can be studied by varying the temperature, T, as demonstrated by the results shown in Fig. . The increase in temperature raises the nucleation barrier $\Delta G(n^*)$ as well as the critical size, n^*. For the three different temperatures used, different dislocation densities were employed in accordance with the experimental observations. The lower dislocation densities at higher temperatures should compensate for the lowering of the supersaturation of point defects. But in spite of the compensating effects, the nucleation barrier increases rapidly with temperature, and it becomes obvious, that void nucleation at T = (00°C is not feasible without gas.

Gas assisted void nucleation has been discussed recently by several authors.[ ] To compute the nucleation rate the simple formalism used above can no longer be used, as we now have to deal with two-dimensional cluster space. Instead, a vacancy cluster is now characterized by two variables, the number, n, of vacancies and the number, m, of gas atoms contained in it. Although a solution to this nucleation problem has been given recently,[ ] we shall only consider the effect of gas on the activation energy $\Delta G(n,m)$ which is given by

$$\Delta G(n,m) = \Delta G(n) + \Delta F(n,m) \ , \tag{21}$$

where

$$\Delta F(n,m) = - kT \sum_{i=}^{m-1} \ln \left[\beta_g(n,i)/\nu_g(n,i+1) \right] \ , \tag{22}$$

$\beta_g(n,i)$ is the capture rate for gas atoms, and $\nu_g(n,i)$ the emission rate of gas atoms for a cluster containing n vacancies and i gas atoms.

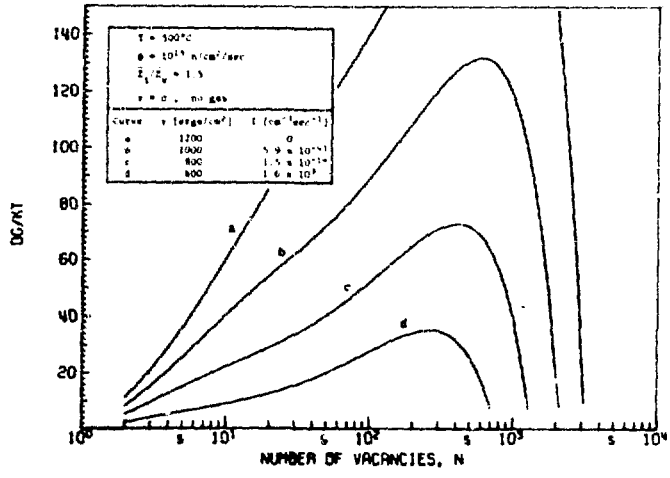

Fig. 5. The Effect of the Surface Energy, γ, on the Free Energy for Void Nucleation.

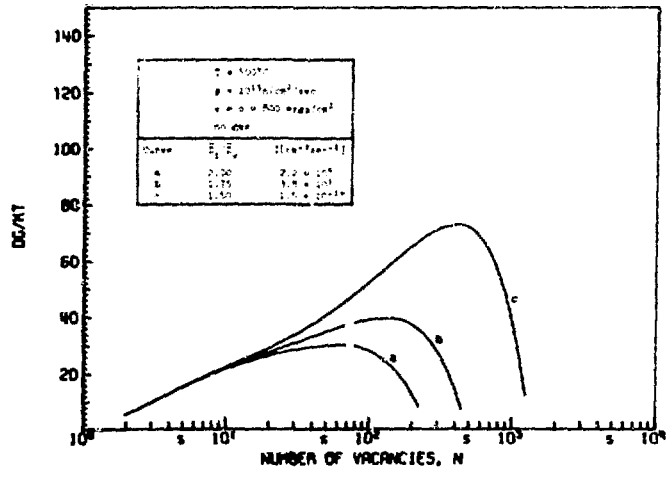

Fig. 6. Free Energy for Void Nucleation for a Surface Energy and Surface Stress of $\gamma = \sigma = 800$ ergs/cm^2.

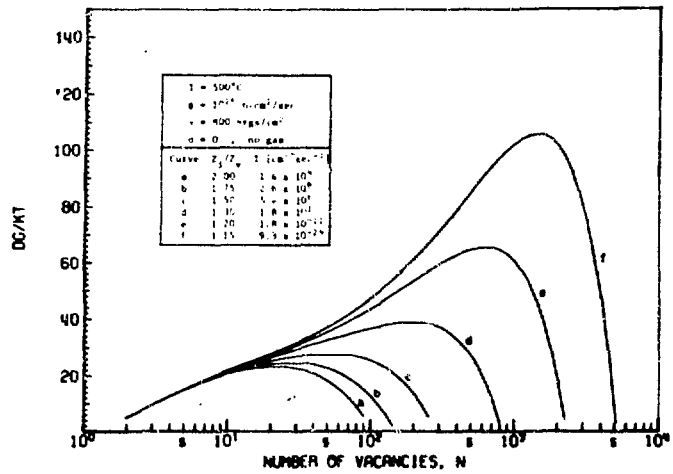

Fig. 7. Free Energy for Void Nucleation for a Surface Energy of γ = 800 ergs/cm^2 but with a Vanishing Surface Stress.

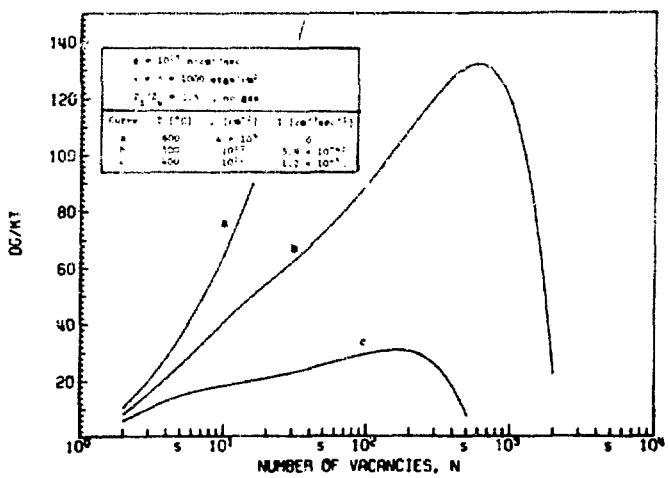

Fig. 8. The Effect of Irradiation Temperature on the Free Energy for Void Nucleation.

The ratio $S_g = \beta_g/\nu_g$ represents an effective supersaturation for gas atoms if we assume that the capture and emission processes involve the same atomic configuration of the gas atom in the matrix. There is, however, recent evidence[13] that the capture process of helium may proceed via interstitial motion and the emission rate through substitutional motion of the helium atom. In such a case, the ratio β_g/ν_g would be much larger than the supersaturation of helium atoms. To demonstrate the effect of gases, it suffices to assign a certain value to this ratio. We have selected the rather low value of $\beta_g/\nu_g = 100$ and assumed that this value does not depend on either n or m. It follows then that $\Delta F(n,m)$ is always negative and leads to a reduction in $\Delta G(n,m)$. In addition to this reduction, the gas atoms inside the void produce a pressure, p, which opposes the surface tension term $2\gamma/a$ in the exponent of Eq. (8). Since the effect of $C_v^e(n)$ and hence the gas pressure on ΔG is only of importance for small voids where $C_v^e(n)$ is large, a good description for the equation of state of gases is needed for large pressures. Thus, the equation of state for a hard-sphere gas was adopted in the form recommended by Carnahan and Starling.[14] This equation has the simple form

$$pV/nkT = (1 + \eta + \eta^2 - \eta^3)/(1 - \eta)^3 , \qquad (23)$$

where $\eta = m\Omega_g/n\Omega$, and Ω_g is the volume of the gas atom. For the present calculations with helium, it is assumed that $\Omega_g = 4 \times 10^{-23}$ cm^3.

Using Eq. (21), $\Delta G(n,m)/kT$ was evaluated for various numbers of gas atoms, m, and the results are plotted in Fig. 9. It is quite apparent that the inclusion of gases in the voids drastically reduces the activation barrier for nucleation. However, it does not change the critical size, n^*. The nucleation rate depends now on the rate with which various vacancy-gas cluster can be formed. If sufficient gas is always available and can readily be incorporated into small void, the nucleation barrier could in fact be completely suppressed. In this case, the voids would start out as gas bubbles, and they would subsequently grow into voids by bias-driven growth. On the other hand, if gas is preinjected before the irradiation, many vacancy-gas clusters could form initially during the irradiation, but since no further gas is supplied, the clusters may not overcome the activation barrier to grow into voids. In this

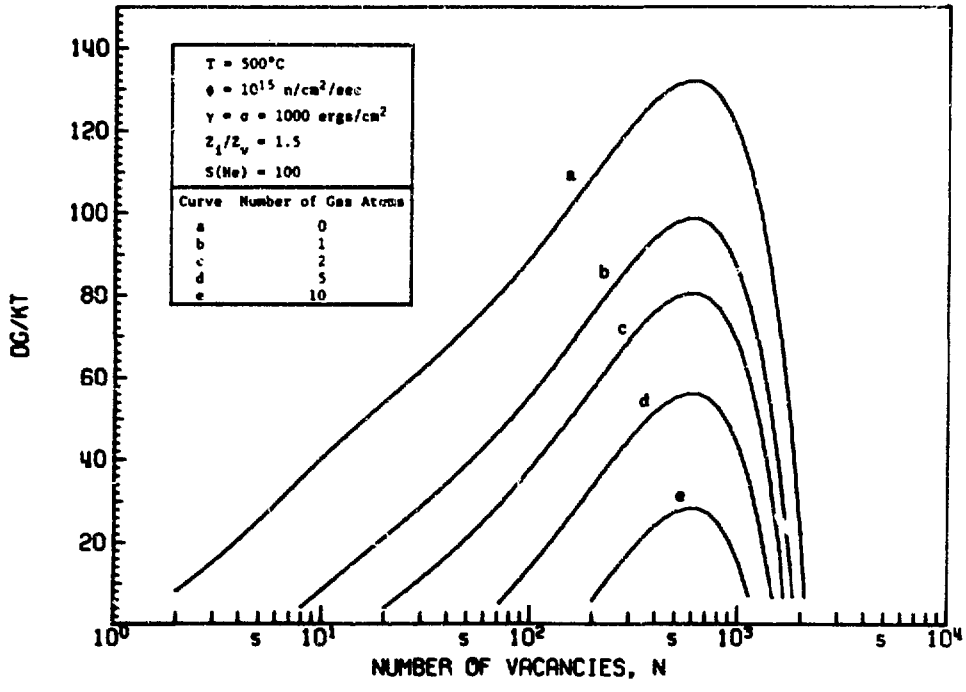

Fig. 9. The Effect of Gas on the Free Energy of Void Nucleation.

situation, the subcritical clusters could act as preferential sinks. They would absorb preferentially interstitials and compensate the accompanying shrinkage through the thermal emission of a vacancy.

CONCLUSIONS

The interaction of the point defects with the void through the image force as well as the surface stress introduces a strong interstitial bias which is comparable to the interstitial bias of dislocations in case of small voids. The inclusion of this void bias reveals that void nucleation without any assisting agents cannot occur significantly. The assisting agents are gases and impurities. The major effect of gases is to oppose the vacancy re-emission rate from small voids or vacancy clusters. This reduces the classical nucleation barrier due to surface tension. However, it may not compensate for the other source of the nucleation barrier, the void bias itself.

Impurity atoms segregated onto the void surface can reduce the surface energy and perhaps the surface stress. A reduction of the former also lowers the nucleation barrier due to vacancy re-emission, whereas a reduction of the latter lowers the void bias. The segregation of impurity or solute atoms at and around the void surface has been reported recently[23] for irradiated stainless steels. Apart from changing the surface energy and stress, this segregation also changes the composition of the surrounding matrix sufficiently to introduce a misfit as well as alter the elastic properties. Thus, voids in stainless steels can be surrounded by a layer of different material. The image interaction with these coated voids is changed so drastically[11] that the interstitial bias of voids not only disappears but that a surface barrier for migration of point defects is introduced. As a result, coated voids are biased against interstitials and their growth kinetics become surface-reaction controlled. Such a growth kinetic was proposed earlier by Mansur et al.[24]

The general conclusion from the present study is that void nucleation is rendered possibly by three major factors, all of which probably act synergetically to assist void nucleation:

(a) Formation of small interstitial loops provides a strong dislocation bias which opposes the void bias.

(b) Contamination of the void surface lowers effectively the surface energy and hence the vacancy re-emission rate.

(c) Segregation of impurities and solute atoms results in an elimination of the void bias and leads to a surface-controlled void growth kinetics.

REFERENCES

1. G. L. Harkness and Che-Yu Li, Met. Trans. 2, 1457 (1971).
2. H. Wiedersich, Radiation Effects 12, 111 (1972).
3. A. D. Brailsford and R. Bullough, J. Nucl. Mater. 44, 121 (1972).
4. K. C. Russell, Acta Met. 19, 753 (1971).
5. J. L. Katz and H. Wiedersich, J. Chem. Phys. 55, 1414 (1971).
6. H. Ehrhart and W. Schilling, Phys. Rev. B8, 2604 (1973).
7. H. Ehrhart and U. Schlagheck, J. Phys. F:Metal Phys. 4, 1575 (1974).
8. L. E. Rehn, J. Holder, A. V. Granato, R. R. Coltman, and F. W. Young, Phys. Rev. B11, 3641 (1975).
9. W. G. Wolfer and M. Ashkin, J. Appl. Phys. 46, 547 (1975); 46, 4108 (1975).
10. W. G. Wolfer and M. Ashkin, to be published in J. Appl. Phys.
11. W. G. Wolfer, paper presented at the Intern. Conf. Fund. Aspects of Radiation Damage in Metals, Gatlinburg, Tenn., Oct. 1975.
12. W. G. Wolfer, Scripta Met. 9, 801 (1975).
13. P. H. Dederichs, C. Lehmann, and A. Scholz, Z. Physik B20, 155 (1975).
14. F. C. Moon and Y. H. Pao, J. Appl. Phys. 38, 595 (1967).
15. S. C. Bose, Indian J. Theoret. Phys. 10, 29 (1962).
16. F. V. Nolfi and C. A. Johnson, Acta Met. 20, 769 (1972).
17. K. C. Russell, Acta Met. 20, 899 (1972).
18. B.T.M. Loh, Acta Met. 20, 1305 (1972).
19. J. L. Katz and H. Wiedersich, J. Nucl. Mater. 46, 41 (1973).

20. H. Wiedersich, J. J. Burton, and J. L. Katz, J. Nucl. Mater. 51, 287 (1974).

21. W. Bauer and W. D. Wilson, Proc. 1971 Intern. Conf. on Radiation Induced Voids in Metals, Albany, NY, p. 230.

22. N. F. Carnahan and K. E. Starling, J. Chem. Phys. 51, 635 (1969).

23. P. R. Okamoto and H. Wiedersich, J. Nucl. Mater. 53, 336 (1974).

24. L. K. Mansur, P. R. Okamoto, A. Taylor, and Che-Yu Li, Defects and Defect Clusters in B.C.C. Metals and Their Alloys, AIME Nuclear Metallurgy, vol. 18, p. 509, National Bureau of Standards, Gaithersburg, Maryland, 1973.

GAS BUBBLES IN STRESS AND THERMAL GRADIENTS*

R. Okray Hall
H. Wiedersich
Materials Science Division
Argonne National Laboratory
Argonne, Illinois 60439

ABSTRACT

Inert gases introduced into the first wall of a CTR by injection from the plasma and by (n,α) reactions occurring in the wall tend to precipitate into bubbles. The forces on gas bubbles that arise from various sources of stress have been explored. The bubble is approximated by a center of dilatation in an elastically isotropic solid. The first-order size interactions of bubbles with elastic fields due to the presence of the surface, dislocations, other gas bubbles, and thermal gradients have been evaluated. The relative magnitudes of the resultant driving forces on the bubbles have been calculated, and their effect on bubble diffusion is discussed. The region of validity of the center of dilatation approximation has been examined. The effects due to a finite bubble size are described.

INTRODUCTION

The predicted high flux of helium at the first wall of a controlled thermonuclear reactor presents a major materials problem for the designer. The low-energy component of the incident particles is in the high

*Work supported by the U.S. Energy Research and Development Administration.

sputtering regime for proposed materials such as niobium, and the helium is deposited in the near-surface region of the wall at concentrations that lead to the formation of gas bubbles and blisters. The detrimental effect of helium on the mechanical properties of metals is also well documented. To minimize these destructive effects, it is important to characterize the behavior of helium in metals. Much experimental work has been done in this area, but many of the results cannot be quantitatively interpreted by available models because of the complexity of helium behavior. As a result of low solubility, helium precipitates out of the matrix at quite low concentrations, and the behavior of aggregates and bubbles differs substantially from that of isolated atoms. The aggregate behavior must be understood if quantitative models of outgassing and wall erosion are to be constructed, and this requires a knowledge of the diffusion of helium atoms and gas bubbles, the nature of trapping by voids and dislocations, and the interactions of point defects with the atoms and bubbles. The purpose of the present work was to examine the elastic interactions between gas atoms or bubbles and the surface, dislocations, thermal stresses and other atoms or bubbles. The possible influence of these elastic interactions on diffusion, trapping, and growth models can then be assessed from the magnitudes.

ELASTIC INTERACTIONS

The first wall is represented for the purpose of the calculations by an elastically isotropic continuum that fills the half-space $z \geq 0$. An inert gas atom or small gas bubble is located a distance c below the surface. As a first approximation, the size of the defect and the fact that its elastic constants differ from those of the matrix are neglected; the defect can then be modeled by a center of dilatation (CD). If ΔV is the change of volume produced by a CD in a body with a free surface, the first-order size interaction between this defect and an arbitrary stress field is

$$E = -\frac{1}{3}\sum_{i} \sigma_{ii}\Delta V = p_H \Delta V \qquad (1)$$

where $p_H \equiv -(\sigma_{11} + \sigma_{22} + \sigma_{33})/3$ is the hydrostatic component of the stress field. The force $\underset{\sim}{F}$ on the defect is given by the negative gradient of the interaction energy

$$\underset{\sim}{F} = - \underset{\sim}{\nabla} E = - \Delta V \, \underset{\sim}{\nabla} p_H \tag{2}$$

Surface Interaction

Following Eshelby,[1] the stress field of the bubble can be written as the sum of the field in an infinite medium and the image field, constructed to satisfy the boundary conditions at the free surface $z = 0$. The stress field of a CD in an infinite medium has no hydrostatic component, but for the image field[2]

$$p_H = \frac{8}{3} \frac{\mu\delta(1 + \nu)}{R_2^3} \left[1 - \frac{3(z + c)^2}{R_2^2}\right] \tag{3}$$

where μ is the shear modulus, ν is Poisson's ratio, δ is the defect strength, and $R_2 = [x^2 + y^2 + (z + c)^2]^{1/2}$. The surface-defect interaction is obtained when the hydrostatic pressure in Eq. (3) is evaluated at the defect site[3]

$$E_s = - \frac{\mu}{36\pi} \frac{(1 + \nu)^2}{(1 - \nu)} (\Delta V)^2 \, c^{-3} \tag{4}$$

Here δ has been expressed in terms of the volume misfit ΔV as

$$\delta = \frac{\Delta V}{12\pi} \frac{(1 + \nu)}{(1 - \nu)}$$

The interaction energy is always negative, indicating the defect is always attracted to the free surface. The force on the defect has the magnitude $-dE_s/dc$, is directed toward the free surface ($-z$ direction), and varies as the inverse fourth power of the distance c. The strength δ of the CD is related to bubble radius a and internal gas pressure p by

$$\delta = \left(p - \frac{2\sigma}{a}\right) a^3/4\mu \tag{5}$$

where σ is the surface stress. If the surface has three-fold or greater rotational symmetry, the surface stress is related to the surface free energy γ by $\sigma = \gamma + d\gamma/d\varepsilon_A$, where ε_A is the elastic areal strain that occurs when the solid is stretched.[4] For equilibrium bubbles, $p = 2\gamma/a$. Thus if $\sigma = \gamma$, the defect strength δ and, consequently, the interaction E_s vanish.

Bubble-Bubble Interaction

Examination of the hydrostatic pressure given by Eq. (3) shows that, for a positive misfit, the hydrostatic component of the stress field immediately surrounding the CD is tensile, with the largest negative values of p_H occurring at the surface (0,0,0) directly above the CD. The tensile region is surrounded by a region of compressive stress that, in any plane parallel to the surface, goes through a maximum and then approaches zero as the distance from the CD approaches ∞. Figure 1 shows a pressure contour map that illustrates these features. Since the force exerted on a second bubble by the first depends on the pressure gradient, one can see from these contours that, depending on the position of defect 2, the interdefect force component $F_{||}$ parallel to the surface can be directed either towards or away from (0,0,z); similarly, the component $F_{\perp}$ can be directed towards or away from the surface. Using Eqs. (2) and (3), these components are

$$F_{||} = \frac{2\mu}{3\pi}\frac{(1+\nu)^2}{(1-\nu)}\Delta V_1 \Delta V_2 \frac{(x^2+y^2)^{1/2}}{R_2^5}\left[1 - \frac{5(c_1+c_2)^2}{R_2^2}\right]$$

$$F_{\perp} = \frac{2\mu}{3\pi}\frac{(1+\nu)^2}{(1-\nu)}\Delta V_1 \Delta V_2 \frac{(c_1+c_2)}{R_2^5}\left[3 - \frac{5(c_1+c_2)^2}{R_2^2}\right] \qquad (6)$$

where c_i is the perpendicular distance of defect i below the surface. Defect 2 is located at (x,y,c_2). The second defect can be a helium atom, a vacancy or an interstitial point defect, or another bubble approximated by a CD.

At large separations between the defects, $F_{||}$ is repulsive (or attractive), if the two defects have the same (or opposite) signs. At a separation

$$r = \left[4(c_1 + c_2)^2 + (c_1 - c_2)^2\right]^{1/2}$$

$F_{||}$ changes sign and becomes attractive (or repulsive). The force component $F_{\perp}$ is repulsive (or attractive) for separation r greater than

$$r = \left[\frac{2}{3}(c_1 + c_2)^2 + (c_1 - c_2)^2\right]^{1/2}$$

and attractive (or repulsive) for smaller separations. The magnitudes of the components depend on the positions of the two defects relative to the surface, but for small separations $F_{||} < F_{\perp}$. If the defect spacing is large, the force exerted on a defect by another is small relative to the force exerted on the defect by the surface. For separations of the order of $(c_1 + c_2)/2$, however, the two forces have the same order of magnitude.

Surface Layer

Bacon[3] has derived an expression for the hydrostatic component of the stress tensor for a center of dilatation beneath a surface layer of arbitrary thickness h with elastic constants that differ from those of the matrix. He finds that

$$P_H = -\frac{4}{3}\mu\delta(1 + \nu)\int_0^\infty k^2 M(k) e^{-k(z + c)} J_0(kr)\,dk \qquad (7)$$

with

$$M(k) = \Big\{-4\Big(1 - \mu_r\Big)\Big[1 + \mu_r(3 - 4\nu')\Big][\cosh(2kh)-1] + 8k^2h^2\Big(1 - \mu_r\Big)^2 + 32\mu_r^2\Big(1 - \nu'\Big)^2\Big\}\Big/\Big\{2[\cosh(2kh)-1]\Big[(3 - 4\nu) + 2\mu_r(1 - 2\nu)(1 - 2\nu') + \mu_r^2(3 - 4\nu')\Big] + 16\sinh(2kh)\mu_r(1 - \nu)(1 - \nu') - 4k^2h^2\Big(1 - \mu_r\Big) \times \Big[(3 - 4\nu) + \mu_r\Big] + 16\mu_r^2(1 - \nu')^2\Big\}$$

where $\mu_r = \mu/\mu'$, μ and ν are the elastic constants of the matrix, and μ' and ν' are those of the layer. The author restricted his attention to the image interaction, which was obtained by evaluating p_H at (0,0,c), and calculated the image force. Equation (7), however, can also be used to determine the force on a second CD in the field of the first. This has been done by a straightforward evaluation of the gradient of p_H. An examination of the results shows that for a surface layer with a shear modulus less than that of the matrix, the CD-layer and CD-CD interactions are qualitatively the same as those with a free surface described in the previous section. If, however, the layer is rigid, i.e., has an infinite shear modulus, the image force changes sign and the CD is repelled by the layer. The interdefect force components also change sign. Thus, for example, at large separations $F_{||}$ is attractive for two defects of like sign, whereas at small separations it is repulsive. For a surface layer with a shear modulus greater than that of the matrix (but not rigid), the image force is directed toward the surface at large distances but away from the surface near the interface.

Dislocation Interaction

An edge dislocation that lies parallel to the y-axis with its slip plane parallel to the free surface of a half-space is stable with respect to slip, since the surface exerts only a force for climb in this geometry. The stress field can be written as the sum of the stress field σ_{ij}^{∞} in an infinite medium, the stress field σ_{ij}^{I} for an image

dislocation oriented as shown in Fig. 2, and the stress field σ^T_{ij} for surface tractions that cancel the shear stress at $z = 0$ arising from the dislocations.[5] Each of these fields has a hydrostatic component:

$$P_H^{\infty} = -\frac{\mu b}{3\pi}\frac{(1+\nu)}{(1-\nu)}\frac{z-\ell}{x^2+(z-\ell)^2}$$

$$P_H^{I} = -\frac{\mu b}{3\pi}\frac{(1+\nu)}{(1-\nu)}\frac{z+\ell}{x^2+(z+\ell)^2}$$

and $$P_H^{T} = \frac{2\mu b}{3\pi}\frac{(1+\nu)}{(1-\nu)}$$

$$\times\left\{\frac{x^4(z+2\ell)+2x^2(z+\ell)^3+(z+2\ell)(z+\ell)^4}{[x^2+(z+\ell)^2]^3}\right\} \qquad (8)$$

The net hydrostatic pressure near the dislocation is plotted in Fig. 3. For comparison, the distribution near the dislocation in an infinite media is plotted in Fig. 4. The force exerted on a CD by the dislocation is normal to the contour lines (which are circles through the dislocation in the infinite medium), and the magnitude is proportional to the gradient. The dashed lines in the figures indicate the positions at which one of the force components vanishes. In the infinite medium, the zeroes for $F_{\perp}$ lie along $x = \pm(z - \ell)$; in the half-space, however, they are shifted down and away from the surface. The extremum line for $F_{||}$ along the z-axis remains unchanged. The line along which p_H vanishes is the x-axis in the infinite space but is shifted down in the half-space. The tensile region beneath the dislocation has thus contracted and the compressive region above the dislocation correspondingly expanded. Arrows indicate the directions of the force components in the various regions. The signs of the components and the hydrostatic pressure change, if the sign of Burgers vector changes.

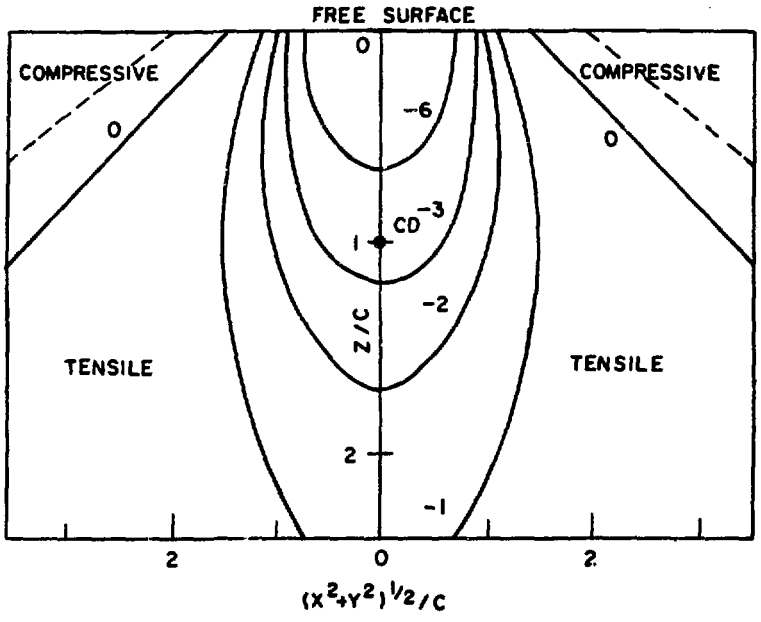

Fig. 1. Contours of Constant Pressure $p_H \cdot 3c^3/\mu\delta$ Near a Center of Dilatation in a Half-space. Poisson's ratio equals 0.38. Dashed lines locate extrema.

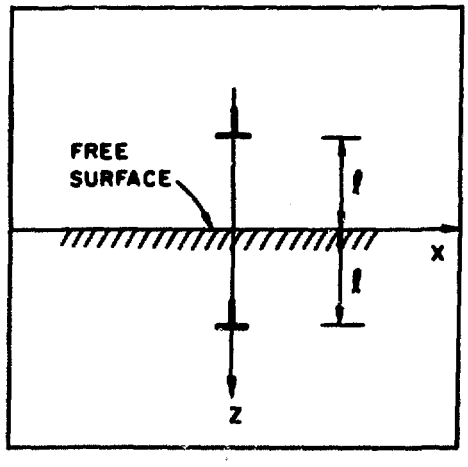

Fig. 2. Image Dislocation Used to Construct Dislocation Stress Function in a Half-space.

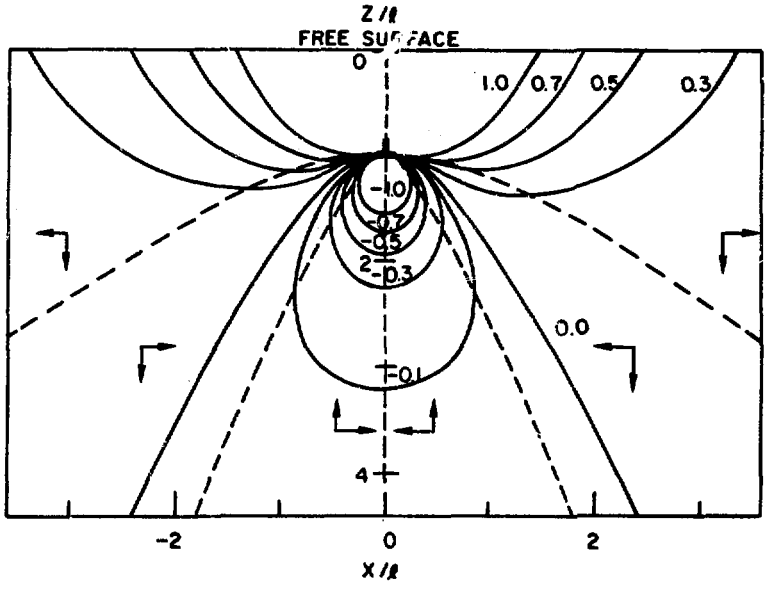

Fig. 3. Pressure Contours $p_H \cdot 3\pi\ell(1 - \nu)/\mu b(1 + \nu)$ Near an Edge Dislocation in a Half-space. Dashed lines locate extrema.

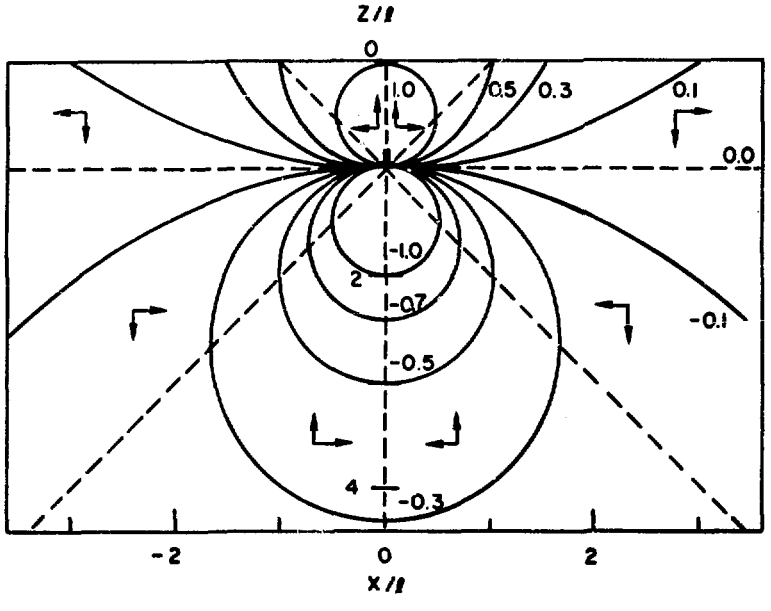

Fig. 4. Pressure Contours $p_H \cdot 3\pi\ell(1 - \nu)/\mu b(1 + \nu)$ Near an Edge Dislocation in an Infinite Medium.

Thermal Stresses

A nonuniform temperature distribution in an elastic material gives rise to a thermal stress field.[6] The stress-strain relations have the form

$$\sigma_{ij} = 2\mu\left\{\frac{\delta_{ij}}{1-2\nu}\left[\nu\sum_{i} e_{ii} - \alpha T(1+\nu)\right] + e_{ij}\right\} \tag{9}$$

where e_{ij} is an element of the strain tensor, α is the coefficient of linear expansion, and T is temperature. If T is a function only of the z-coordinate in the half-space, then the displacements depend only on z, and the normal strains e_{xx} and e_{yy} in the x- and y-directions vanish. The normal stress σ_{zz} in the z-direction also vanishes because of the boundary conditions at the free surface and the equilibrium conditions, but, in the transverse directions,

$$\sigma_{xx} = \sigma_{yy} = -\frac{2\mu(1+\nu)}{(1-\nu)}\alpha T \tag{10}$$

and the hydrostatic component of the stress tensor is

$$p_H = \frac{4\mu}{3}\frac{(1+\nu)}{(1-\nu)}\alpha T \tag{11}$$

Thus, the force exerted on the CD is

$$F_z = -\frac{4\mu}{3}\frac{(1+\nu)}{(1-\nu)}\Delta V\,\alpha\,\frac{\partial T}{\partial z} \tag{12}$$

In general, the temperature in the first wall will decrease as z increase the gradient will be negative, and the elastic force due to thermal stresses will be directed away from the surface.

FINITE BUBBLE SIZE

In the preceding discussion, gas bubbles were represented by centers of dilatation and their finite size was ignored. This approximation is undoubtedly good for small bubbles, but for a large bubble near the surface its validity needs to be examined.

The utility of the CD approximation for the interdefect interaction can be determined by comparing the hydrostatic component of the stress field for a CD with that for a pressurized spherical cavity in a half-space. Chankvetadze[7] has developed an approximate solution for the biharmonic stress function ω for the latter problem, using the form

$$\begin{aligned}\omega(x,y,z) = {} & A \ln \frac{2}{H}\left(R_1 + Z_1\right) + B \ln \frac{2}{H}\left(R + z + \frac{H}{2}\right) \\ & + \frac{C_o}{H}\left[\nu R + \frac{1-2\nu}{2}\left(z + \frac{H}{2}\right) \ln \frac{2}{H}\left(R + z + \frac{H}{2}\right)\right] \\ & + a_o \frac{H}{R} + a_1 \frac{H}{R_1} + b_o \frac{R}{H} + b_1 \frac{R^2}{HR_1} \\ & + b_2 \frac{R^2}{H}\left(\frac{1}{R_1} + \frac{HZ_1}{R_1^3}\right) + d_o \frac{R_1^2}{HR} \\ & + d_1 \frac{R_1^2}{H}\left[\frac{1}{R} - \frac{H}{R^3}\left(z + \frac{H}{2}\right)\right] + d_2 \frac{R_1}{H}\end{aligned} \tag{13}$$

where $R = [x^2 + y^2 + (z + H/2)^2]^{1/2}$, $R_1 = [x^2 + y^2 + (z - H/2)^2]^{1/2}$, and $Z_1 = z - H/2$. The geometrical constant H depends on the bubble radius a and the distance c of the bubble center below the surface, while the prefactors A, B, C_o, a_i, b_i, and d_i are determined by numerically solving a system of linear equations. (The complete set of equations for determining H and the prefactors is given in Ref. 7.) The components of the stress tensor can be obtained from this function by differentiation, and the hydrostatic component p_H^o is

$$p_H^o = \frac{(\nu + 1)}{3}\left\{\frac{\left[(z + H/2)(C_o + 2b_o + 2d_o + 2d_1)H^{-1} - 2(2d_o + 3d_1)\right]}{R^3}\right.$$

$$+ \frac{2(z - H/2)(b_1 + b_2 + d_2)H^{-1} + 2(2b_1 + 3b_2)}{R_1^3}$$

$$+ \frac{6(z - H/2)[(2d_o + 3d_1)(z + H/2) + 6Hd_1]}{R^5}$$

$$- \frac{6(z - H/2)[(2b_1 + 3b_2)(z - H/2) - 6Hb_2]}{R_1^5}$$

$$\left. - \frac{60Hb_2(z - H/2)^3}{R_1^7} - \frac{60Hd_1(z + H/2)^3}{R^7}\right\} \qquad (14)$$

This quantity was evaluated numerically for several values of the ratio a/c in the planes z = 0, z = c, and z = 2c. Figures 5, 6, and 7 show plots of the results as a function of distance $(x^2 + y^2)^{1/2}/c$ in each of the planes.

From Fig. 5, it is apparent that, for ratios a/c > 0.5, the hydrostatic component p_H^o of the stress tensor in the region of the matrix between the bubble and the surface is two to four times larger than that predicted by the CD approximation (dotted line). The most striking result is shown in the plot for z = 2c. An examination of Eq. (3) reveals that along the z-axis for z > c, the hydrostatic component for the CD is always negative, i.e., the stress is tensile. Figure 7, however, shows that, as the ratio a/c increases from 0.5 to 0.8, the stress in the region beneath the bubble becomes compressive. In all three planes, the hydrostatic component of the stress field is well represented by the CD approximation for values of $(x^2 + y^2)^{1/2}$ greater than 2c.

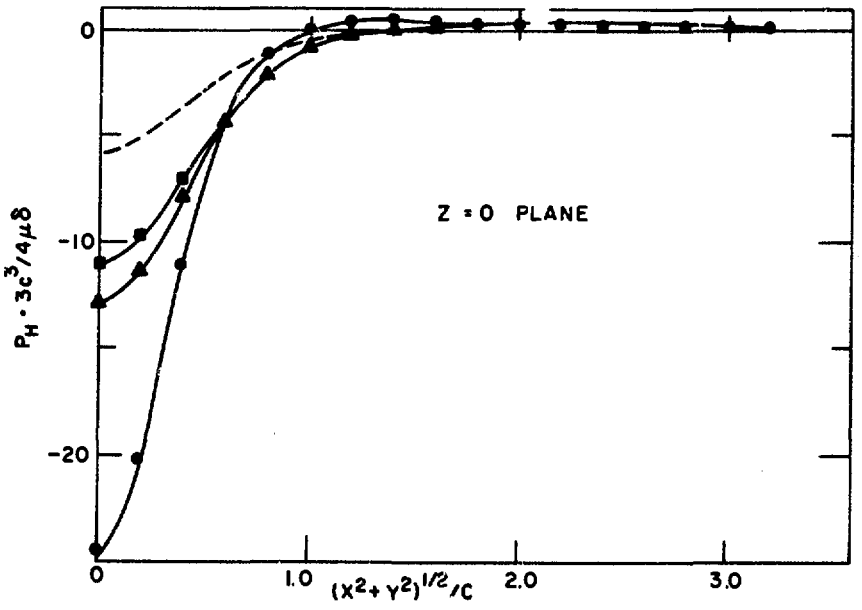

Fig. 5. Hydrostatic Component $p_H \cdot 3c^3/4\mu\delta$ for a Pressurized Cavity in a Half-space in the z = 0 Plane. The Ratios a/c are 0.1 (■), 0.5 (▲), 0.8 (●), and CD (---).

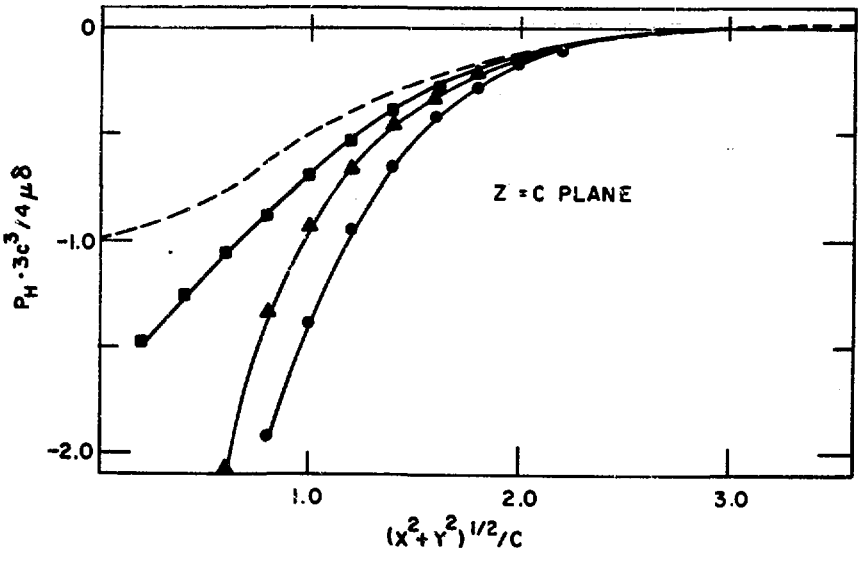

Fig. 6. Hydrostatic Component $p_H \cdot 3c^3/4\mu\delta$ in the z = c Plane. Same notation as in Fig. 5.

These results indicate the hydrostatic stress for a CD is a reasonably good approximation for that of any bubble with $a/c \lesssim 0.3$. This hydrostatic stress is also a good approximation at large distances ($\gtrsim 3c$) for gas bubbles with larger ratios a/c. Any model of the drift diffusion of helium atoms and point defects to a large gas bubble, however, must consider the details of the near field.

NUMERICAL EVALUATION

For niobium (elastic constants $\mu = 3.65 \times 10^{11}$ dyne-cm^{-2} and $\nu = 0.38$), the free surface-bubble interaction given by Eq. (4) is $E_S = -9.91 \times 10^9$ ergs/cm^3 $(\Delta V)^2$ c^{-3}. The volume misfit ΔV must then be 2.03×10^{-21} cm^3 ($\sim$100 atomic volumes) if E_s is to be comparable to kT (300°K) at a depth of 100 Å. At a depth of 10 Å, the required ΔV is 6.41×10^{-23} cm^3. For a gas bubble of radius a = 30 Å with an internal pressure $p = 10^8$ dyne-cm^{-2} and $\sigma = 0$,[4] ΔV is 3.1×10^{-23} cm^3. Thus, the ratio E_s/kT is large only within a distance of a few atomic layers of the surface; the driving force for diffusion is negligible elsewhere. Since the first-order size interaction between the defects is of the same order of magnitude as the image interaction, its driving force on diffusion can also be neglected, except in the near field region.

Because the image interaction due to a free surface is always attractive and small in magnitude except near the surface, it can be argued that gas diffusion to the surface sink is relatively unaffected by the interaction. This is not true, however, if a rigid surface layer is present. The gas diffusion in the bulk will be unaffected by the small repulsive interaction with the layer, but the strong repulsion near the layer-matrix interface acts as a barrier, and gas diffusion through the layer will be negligible. Numerical evaluation of Eq. (7) for a surface layer with a shear modulus greater than that of the matrix (but not rigid) shows that the interaction energy is negative at large distances, goes through a minimum as the distance from the surface decreases, and then rapidly increases, becoming positive near the interface. Figure 8 shows the results for Nb_2O_5 on Nb for several layer thicknesses. The oxide elastic constants used for the calculation were $\nu = 0.38$ and

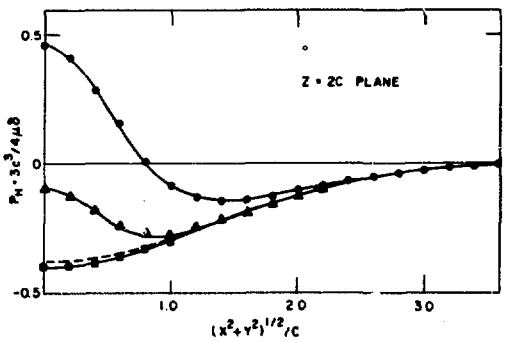

Fig. 7. Hydrostatic Component $p_H \cdot 3c^3/4\mu\delta$ in the $z = 2c$ Plane. Same notation as in Fig. 5.

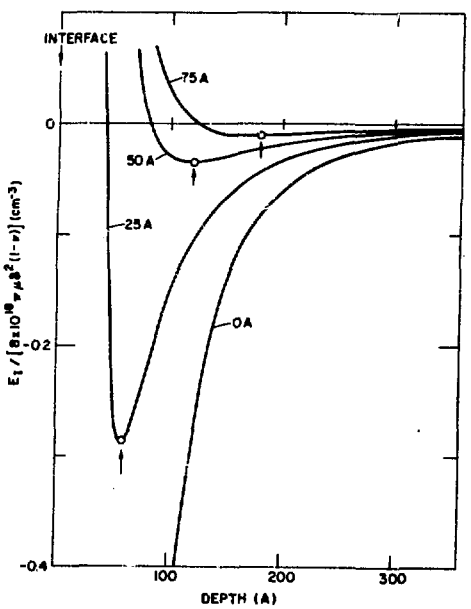

Fig. 8. Interaction Energy of a CD in Niobium with a Layer of Nb_2O_5. Labels on curves give thickness h of oxide layer.

$\mu = 7.30 \times 10^{11}$ dynes-cm^{-2}. It can be seen from the figure that, as the layer thickness increases, the minimum moves deeper into the matrix and becomes both shallower and broader. For a layer of 25 Å, the minimum lies at ∿60 Å from the interface, and each increment of 25 Å in thickness increases the distance by approximately that amount. At the temperatures of interest for the first wall, the effect of the energy minimum will be negligible, but the repulsive force near the interface may significantly inhibit gas diffusion through this region.

For $\ell = c$, the ratio of the dislocation interaction energy E_d to the surface interaction energy E_s at a distance of 4c from the dislocation is of the order

$$\frac{E_d}{E_s} \approx 1.46 \frac{bc^2}{\Delta V}$$

and, for reasonable values of the parameters, E_d is much larger than E_s. The interaction of "point-defect" bubbles with dislocations will therefore provide a significant driving force for diffusion. This result is consistent with experimental observation of helium bubbles located preferentially along dislocation lines in vanadium that has been injected with helium at 750°C.[8]

The coefficient of thermal expansion α for niobium is 7.8×10^{-6} °C^{-1} for the anticipated temperature range in the first wall. For $\Delta V = 3.1 \times 10^{-23}$ cm^3 and $\partial T/\partial z = 2.5 \times 10^3$ °C/cm,[9] the force F_z exerted on a CD by thermal stresses is 6.6×10^{-13} dynes, comparable to the surface image force at 300 Å. For the CD approximation, then, the effects of thermal stresses on drift diffusion of helium bubbles can be neglected.

REFERENCES

1. J. D. Eshelby, Solid State Phys. 3, 79 (1956).
2. R. D. Mindlin and D. H. Cheng, J. Appl. Phys. 21, 926 (1950). The authors give the Galerkin vector from which the stress components σ_{ij} can be derived.
3. An additional factor of 1/2 arises in the interaction energy because the image interaction is induced. See derivation by D. J. Bacon, Phys. Stat. Sol. (b) 50, 607 (1972).
4. F. V. Nolfi, Jr. and C. A. Johnson, Acta Met. 20, 769 (1972).
5. J. P. Hirth and J. Lothe, Theory of Dislocations, McGraw-Hill, New York, 1968. The field associated with core cut-off radius has been neglected.
6. S. P. Timoshenko and J. N. Goodier, Theory of Elasticity, 3rd ed., p. 433, McGraw-Hill, New York, 1970.
7. G. G. Chankvetadze, Inzehener. Sbornik 22, 65 (1955). The equations are complete for use in numerical computations, but they should be used with caution since many typographical errors have been made.
8. R. F. Mattas, private communication.
9. Anticipated maximum temperature gradient discussed in design study. See "An Engineering Design Study of a Reference Theta-Pinch Reactor (RTPR)," Argonne National Laboratory, ANL-8019, March 1974.

PRODUCTION OF POINT DEFECTS IN 14.8 MeV NEUTRON-IRRADIATED MgO*

Y. Chen, M. M. Abraham and M. T. Robinson

Solid State Division, Oak Ridge National Laboratory
Oak Ridge, Tennessee 37830

J. B. Mitchell and R. A. Van Konynenburg

Metallurgy Division, Lawrence Livermore Laboratory
Livermore, California 94550

ABSTRACT

High-purity MgO crystals grown at ORNL have been irradiated in the LLL 14.8 MeV Rotating Target Neutron Source (RTNS) to doses varying from 1.8×10^{15} to 5.7×10^{17} n/cm^2. The optical absorption spectra of these crystals resembled those irradiated in fission reactors and exhibited bands principally at 4.95, 3.5, 2.2 and 1.3 eV. The band with the largest absorption coefficient, that at 4.95 eV, is due to anion vacancies. The bands at 3.5 and 1.3 eV, attended by zero-phonon lines at 3.430 and 1.187 eV respectively, have been attributed to different optical transitions of anion divacancies. Our investigations indicate that the net production rates of the point defects resulting from irradiations with 14.8 MeV neutrons are about twice those resulting from fission neutrons in the Oak Ridge Reactor (ORR). This ratio is in reasonable accord with theoretical estimates based on damage energy calculations.

---

*Research sponsored by the Energy Research and Development Administration under contract with Union Carbide Corporation.

INTRODUCTION

Unlike the situation in metals and semiconductors, the study of defects in insulators has benefited primarily by the powerful techniques of optical and magnetic resonance spectroscopy. This is especially true for magnesium oxide, where many of the basic point defects have been identified using these techniques. It is therefore an ideal host to study the characteristics of the radiation damage resulting from 14.8 MeV neutrons and comparing with those from fission neutrons. Quantitative measurements of the various types of defects are readily accessible. The optical and magneto-sensitive defects in this material are produced by two mechanism: ionization and elastic collisions with energetic particles. For comparisons of defects produced by neutrons of different energies, only the latter are important.[1]

EXPERIMENTAL PROCEDURES

The MgO crystals used in this study were grown from Kanto high purity material at ORNL using a carbon-arc fusion method.[2,3] They were irradiated either in the LLL 14.8 MeV RTNS at T $\sim$ 300 K with doses varying from 1.8×10^{15} to 5.7×10^{17} n/cm^2, or in the fission reactor ORR at T $\sim$ 325 K with neutron doses (>0.1 MeV) ranging from 3.6×10^{15} to 1×10^{19} n/cm^2. Defect concentrations produced by the two neutron sources were determined by measuring intensities of optical absorption bands using a Cary 14R recording spectrophotometer.

RESULTS AND DISCUSSION

The optical absorption spectra of crystals irradiated with neutrons from the RTNS closely resembled those irradiated in fission reactors. The spectra at 5 and 295 K of a crystal irradiated with 14.8 MeV neutrons to a dose of 5.7×10^{17} n/cm^2 are illustrated in Fig. 1. The principal bands occur at 4.95, 3.5, 2.2, and 1.3 eV, corresponding to 250, 355, 574 and 975 nm respectively. The most intense band, that appearing at 4.95 eV, is regarded as arising from isolated anion vacancies, since both the one-electron and two-electron anion vacancies (F^+ and F centers respectively)

absorb at approximately this energy.[4,5,6] The broad bands at 3.5 and 1.3 eV have been attributed in previous studies to optical transitions within the same defect by virtue of their intensities being proportional to one another during irradiation and annealing.[7,8] At low temperatures, they are attended by zero-phonon lines at 3.430 and 1.187 eV respectively. Evidence based on symmetry,[7] dependence of formation on the energy of irradiating electrons,[9] and statistical distributions of isolated anion vacancies[10] supports the argument that the defect in question is an anion divacancy. Hence the intensity of the band at 3.5 eV provides a measure of the concentration of anion divacancies. The defect responsible for the 2.2 eV band has not been identified but is probably some form of divacancy or trivacancy.[9]

The concentration and absorption coefficient of the anion vacancy band at 4.95 eV is plotted in Fig. 2 as a function of neutron dose. The conversion of absorption coefficient to the corresponding concentration is given by Smakula's formula[11] $Nf = 0.87 \times 10^{17}\, n(n^2 + 2)^{-2}\, W\, \alpha$ where N is the concentration of the defect in cm^{-3}, f the oscillator strength, n the index of refraction, and W and α are the half-width and absorption coefficient of the 4.95 eV band respectively. For both the F^+ and F centers in MgO, $N \approx 5 \times 10^{15}\, \alpha$.[4] The dose plotted for samples irradiated in the ORR is for neutrons with energies > 0.1 MeV, a reasonable cut-off point for radiation damage applications. In the past, it has been customary to present neutron exposures in terms of those neutrons with energies greater than 1.0 MeV (e.g. ref. 12). In fact, there are large numbers of neutrons in a reactor like the ORR with lower energies and these can contribute significantly to the damage observed.[13] The fast neutron spectrum in the ORR is similar to that in the HFIR; assuming these spectra to be identical, the choice of 0.1 MeV as a cut-off approximately doubles the stated doses over the older values.[14] Recent calculations[15] show that less than one percent of the damage produced in Al results from lower energy neutrons and the situation in MgO is believed to be similar.

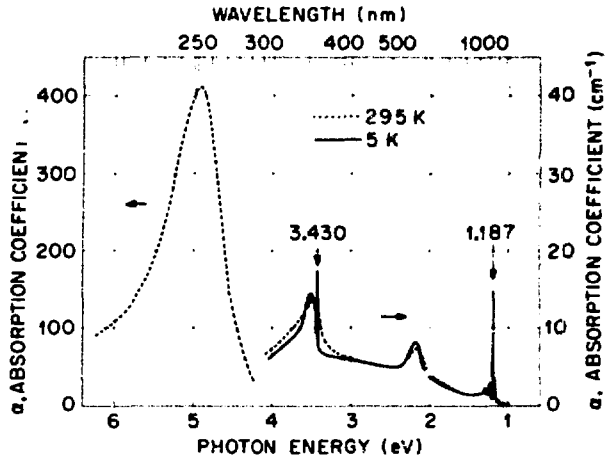

Fig. 1. Optical absorption spectra at 5 and 295 K of an MgO crystal irradiated with 14.8 MeV neutrons to a dose of 5.7×10^{17} n-cm^{-2}.

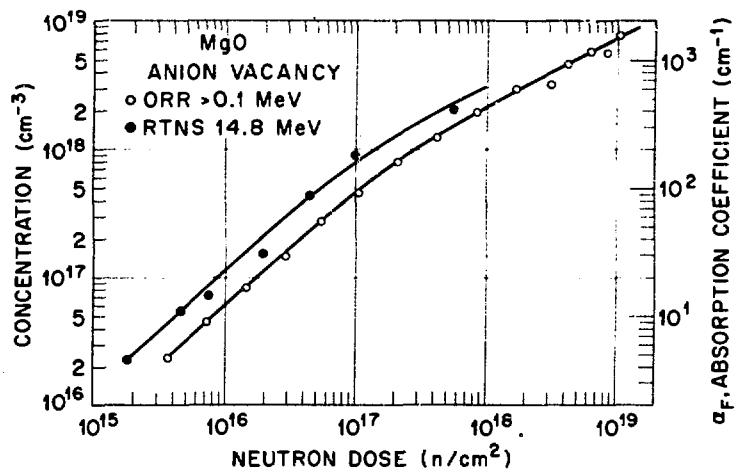

Fig. 2. Concentration of anion vacancies and absorption coefficient of the 4.95 eV band resulting from neutron irradiations in the RTNS and ORR as a function of dose.

The two curves in Fig. 2 are essentially parallel. At a given low dose, the anion-vacancy concentration for the 14.8 MeV irradiations was about twice that for the ORR irradiations. At high doses, saturation becomes significant and the ratio of the concentrations diminishes. For the higher order defects, such as the anion divacancy and the defect responsible for the 2.2 eV band, a similar behavior was noted. At a given dose below 1×10^{17} n/cm^2, irradiations in the RTNS result in larger absorption coefficients for the 3.5 and 2.2 eV band than those obtained in the ORR irradiations, providing support that higher energy neutrons are more efficient in producing higher order defects than lower energy neutrons.

It is interesting to compare the experimentally determined ratio of damage rates between the two neutron sources with the theoretical expectations based on calculations of the damage energy.[13] Although no calculations are available for MgO, those on the nearby element Aℓ should be applicable. Using the spectrum of the similarly constituted HFIR[12] to represent that in the ORR, two different calculations [13,15] both give the ratio 1.94 between the damage rate in a 14.8 MeV D-T neutron spectrum and that in the fission device. The prediction is in good accord with the experiment.

In summary, the experiments show that point defect damage produced in MgO is very similar in character to that produced by fission reactor neutrons and that it agrees quantitatively with the predictions of damage energy calculations.

REFERENCES

1. E. Sonder and W. A. Sibley, in Defects in Crystalline Solids, edited by J. H. Crawford, Jr. and L. M. Slifkin (Plenum Press, New York, 1972) Vol. 1, p. 201.
2. Y. Chen and M. M. Abraham, U. S. Patent 3,829,391 (1975).
3. M. M. Abraham, C. T. Butler and Y. Chen, J. Chem. Phys. 55, 3752 (1971).
4. Y. Chen, J. L. Kolopus and W. A. Sibley, Phys. Rev. 186, 865 (1969).
5. J. C. Kemp, J. C. Cheng, E. H. Izen and F. A. Modine, Phys. Rev. 179, 818 (1969).
6. L. A. Kappers, R. L. Kroes and E. B. Hensley, Phys. Rev. B, 1, 4151 (1970).
7. I. K. Ludlow, Proc. Phys. Soc. 88, 763 (1966).
8. Y. Chen and W. A. Sibley, Phil. Mag. 20, 217 (1969).
9. Y. Chen, D. L. Trueblood, O. E. Schow and H. T. Tohver, J. Phys. C 3, 2501 (1970).
10. Y. Chen, Proceedings of the International Conference on Colour Centres in Ionic Crystals, C 44 (Reading, U. K., 1971).
11. See A. E. Hughes and B. Henderson in Defects in Crystalline Solids, edited by J. H. Crawford, Jr. and L. M. Slifkin (Plenum Press, New York, 1972), Vol. 1, p. 381.
12. Y. Chen, R. T. Williams and W. A. Sibley, Phys. Rev. 182, 960 (1969).
13. M. T. Robinson in Nuclear Fusion Reactors (British Nuclear Energy Society, Culham, U. K., 1970), p. 364.
14. R. D. Cheverton and T. M. Sims, U.S.A.E.C. Report ORNL-4261 (1971).
15. T. A. Gabriel, J. D. Amburgey and N. M. Greenly, to be published, 1975.

NEUTRON IRRADIATION DAMAGE IN Al_2O_3 AND Y_2O_3*

F. W. Clinard, Jr.

J. M. Bunch

W. A. Ranken

University of California
Los Alamos Scientific Laboratory
Los Alamos, NM 87545

ABSTRACT

Two ceramics under consideration for use in fusion reactors, Al_2O_3 and Y_2O_3, were irradiated in the EBR-II fission reactor at 650, 875, and 1025K to fluences between 2 and 6 x 10^{21} n/cm^2 (E>0.1 MeV). Samples evaluated include sapphire, Lucalox, alumina, Y_2O_3, and Y_2O_3-10% ZrO_2 (Yttralox). All Al_2O_3 specimens swelled significantly (1 to 3%), with most of the growth observed in sapphire along the c-axis at the higher temperatures. Al_2O_3 samples irradiated at 875 and 1025K contained a high density of small aligned "pores". Irradiated Y_2O_3-based ceramics exhibited dimensional stability and a defect content consisting primarily of unresolved damage and/or dislocation loops. The behavior of these ceramics under irradiation is discussed, and the relevance of fission neutron damage studies to fusion reactor applications is considered.

INTRODUCTION

Electrical insulators are called for in all fusion reactor concepts. The theta-pinch reactor will require an insulating liner on the first wall, to hold off voltages generated during the implosion heating stage of the D-T burn. The mirror reactor will need electrical insulators in the injector and direct conversion systems. The Tokamak machine will also

*Work performed under the auspices of USERDA.

need injector insulators, may use a low-Z ceramic first wall to reduce problems of plasma contamination, and may require an insulating ring in the torus to break its electrical continuity. Additionally, the above reactors will need magnetic coil insulators and possibly insulating material in the neutron blanket to reduce power losses from eddy current and MHD effects. Conceptual designs for laser fusion reactors are not yet fully developed, so that materials needs in these machines have not been identified in detail. However, such reactors may require transparent ceramic laser windows, and will probably need insulators in the power conversion system.

A major problem for fusion reactor insulators will be neutron radiation damage. Such irradiation will cause atomic displacements, and these can aggregate to cause swelling, reduce mechanical strength and thermal conductivity, and degrade dielectric breakdown strength. In the theta-pinch reactor, the first-wall liner will be irradiated by pulsed fusion neutrons of average flux $\sim 10^{15}$ n/cm^2 sec.[1] In other reactor applications the flux will be of similar or lesser magnitude, and pulsed or steady state, depending on location of the insulator and mode of reactor operation.

At present there are no sources of intense 14 MeV neutrons available for irradiation studies; thus other sources of damaging particles must be used. This paper reports the results of elevated-temperature irradiations of Al_2O_3 and Y_2O_3-based ceramics in the EBR-II fission reactor.*

EXPERIMENTAL PROCEDURE AND RESULTS

Samples Tested

Irradiation samples were in the form of hollow cylinders 1.2 cm

*These irradiations were performed as part of the LASL Thermionic Reactor Project; preliminary results are described in reference 2.

long, 1.5 cm in dia., and 0.05 or 0.09 cm in wall thickness. Four forms of Al_2O_3 were evaluated: single-crystal sapphire furnished by Thermo Electron Corporation (TECO), polycrystalline Lucalox from General Electric Co. (GE), and polycrystalline AD-999b and AD-999x from Coors Porcelain Co. Three polycrystalline Y_2O_3-based ceramics were studied: Y_2O_3 specimens produced at our laboratory from Lindsey Co. and Molybdenum Corp. of America (Moly. Corp.) powder lots, and Yttralox (Y_2O_3 containing ~10% ZrO_2, a densifying agent) made by GE. Characteristics of the samples are given in Table 1.

Irradiation Conditions

Samples were irradiated in capsules which contained heat pipes to maintain isothermal conditions.[3] Test temperatures were 650, 875, and 1025K (±20K). The capsules were irradiated in position 7C1 of the EBR-II fission reactor for a total of 6331 MW-days (~100 days under power). Because sample location varied with respect to the reactor core, neutron fluences ranged from 2 to 6 x 10^{21} n/cm^2 ($E_n > 0.1$ MeV). In the ceramics tested such fluences induce damage levels on the order of 3 DPA.* Fluences were determined by monitoring induced activity from the ^{54}Fe (n, p) ^{54}Mn reaction. Dosimetry techniques and spectral data are described elsewhere.[4]

Evaluation of Samples

Irradiated samples were evaluated for swelling and defect content. Dimensional changes were determined using standard measuring techniques. Volumetric changes as small as 0.2% could be reliably detected. It was found that all Al_2O_3 samples swelled significantly (1 to 3%), with those irradiated at the higher two temperatures generally showing greater growth (Figs. 1 and 2). As irradiation temperature increased, swelling

*Displacements per atom.

Table 1. Characteristics of Test Ceramics

Material	Grain Size, μm	Major Impurities, wt. ppm	% of Theoretical Density
Al_2O_3 (Sapphire)[a]	---	100 Mo[b] 10 Fe 10 Si	100
Al_2O_3 (Lucalox)	20	2000 Mg 30 Si	99.0
Al_2O_3 (AVCO)	3	3000 Mg 3000 Ni 1000 Fe 300 K	99.5
Al_2O_3 (AD-999b)	7	1000 Mg 100 Fe 30 Si	99.5
Al_2O_3 (AD-999x)	4	1000 Mg 100 Fe 30 Si	99.5
Y_2O_3 (Moly. Corp.)	8	30 Mg	97.5
Y_2O_3 (Lindsey)	20	500 Yb 300 Er 300 Dy 200 Al	93
Y_2O_3 - 10% ZrO_2 (Yttralox)	120	1000 Hf 15 Mg	>99

[a] C-axis parallel to axis of cylindrical sample.

[b] Typical analysis.

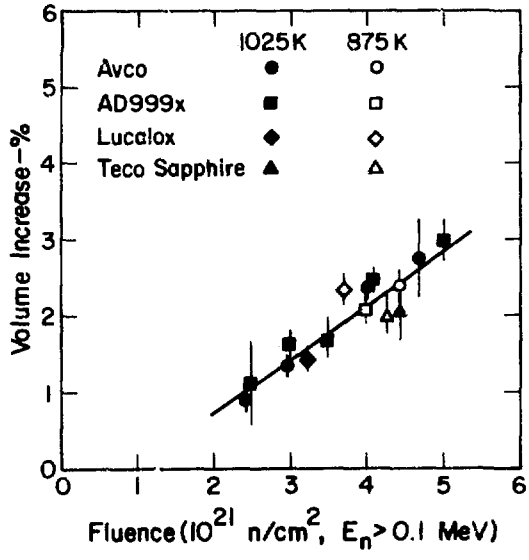

Fig. 1. Volumetric Swelling of Al_2O_3 as a Function of Neutron Fluence at 875 and 1025K.

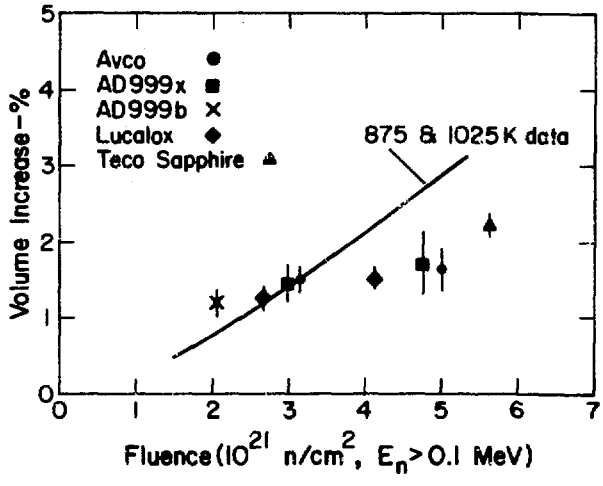

Fig. 2. Volumetric Swelling of Al_2O_3 as a Function of Neutron Fluence at 650K. Data from Fig. 1 are Shown for Comparison.

of sapphire was increasingly concentrated in the c-direction (Fig. 3). Similar results for Al_2O_3 have been reported by Wilks et al.[5] and by Keilholtz et al.[6] Y_2O_3-based samples showed little or no dimensional change (Fig. 4). These results differ from those of Keilholtz et al., who found a volume increase of ~0.2% per 10^{21} n/cm^2 ($E_n > 0.1$ MeV) for Yttralox irradiated at 673K and slightly less than half this amount at 1073K.[6]

Transmission electron microscopy (TEM) was utilized to evaluate the defect content of fourteen irradiated samples. Irradiation conditions and macroscopic swelling observed for TEM samples are given in Table 2. Specimens were prepared by fracturing the samples and making a cellulose acetate extraction replica of the fracture surface, thus removing small flakes of ceramic. A carbon film was then evaporated onto the cellulose acetate and the plastic dissolved, leaving the flakes on the film. Thin edges of these flakes were transparent to 100 keV electrons. This technique eliminates the problem of introduction of radiation damage by ion thinning, but samples tend to have a preferred orientation dictated by cleavage properties of the ceramic being examined. Also, glide dislocations are sometimes introduced during fracture; however, these can usually be distinguished from dislocation loops introduced by irradiation. Electron diffraction patterns were regularly obtained along with photomicrographs of defect structures.

Al_2O_3 samples irradiated at 650K showed only a fine dispersion of unresolved damage. However, those examined after irradiation at 875 and 1025K contained a high density of small "pores"* aligned in the c-direction (Fig. 5). Attempts to tilt into an orientation which exhibited two-dimensional alignment (i.e., a conventional pore lattice) were unsuccessful. Samples irradiated at 1025K showed the larger "pores"

*The significance of the quotation marks is explained in the discussion section.

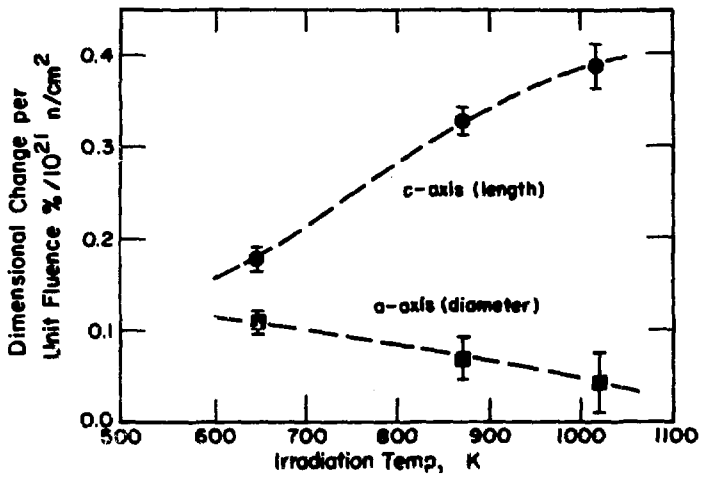

Fig. 3. Dimensional Change per Unit Fluence versus Irradiation Temperature for Sapphire Irradiated to Neutron Fluences from 4.3 to 5.6×10^{21} n/cm^2 ($E_n > 0.1$ MeV).

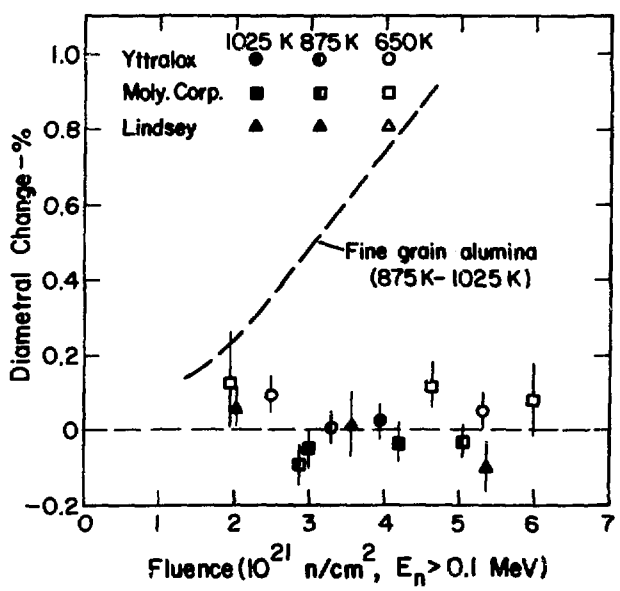

Fig. 4. Diametral Change of Y_2O_3 Made from Moly. Corp. and Lindsey Powders and Y_2O_3 -10% ZrO_2 (Yttralox) versus Neutron Fluence. Data from Fig. 1 are Shown for Comparison.

Table 2. Samples Examined by TEM

Material	Irradiation Temperature, K	Neutron Fluence, n/cm^2 ($E_n > 0.1$ MeV)	Macroscopic Swelling, $\Delta V/V$, %
Al_2O_3 (Sapphire)	650	5.6×10^{21}	2.2
	875	4.3×10^{21}	2.0
	1025	4.4×10^{21}	2.1
Al_2O_3 (Lucalox)	650	4.1×10^{21}	1.5
	875	3.7×10^{21}	2.3
	1025	3.2×10^{21}	1.4
Al_2O_3 (AD-999x)	650	4.8×10^{21}	1.7
	875	4.0×10^{21}	2.1
	1025	4.1×10^{21}	2.4
Y_2O_3	650 (Moly. Corp.)	6.0×10^{21}	0.2
	875 (Moly. Corp.)	5.1×10^{21}	(-0.1)[a]
	1025 (Lindsey)	5.4×10^{21}	-0.3
Y_2O_3 - 10% ZrO_2 (Yttralox)	875	3.3×10^{21}	(0.0)[a]
	1025	3.9×10^{21}	(0.1)[a]

[a]Below level of significance.

and "pore" spacing along a given row (average of ~35 Å and 70 Å, respectively). The defects in samples held at 875K were almost below the limit of resolution, and therefore meaningful dimensions could not be obtained; it is estimated that "pore" diameter and spacing were one-half to three-fourths of the values observed for the 1025K specimens. A rough calculation of swelling for AD-999x irradiated at 1025K was made from Fig. 5, assuming the defects to be cavities. A value of 1.6% was obtained, * in reasonable agreement with the measured macroscopic value of 2.4%.

*Average "pore" diameter was estimated to be ~45 Å and pore density, ~$3 \times 10^{17}/cm^3$. Foil thickness was not measured, but was estimated to be 1000 Å in the area evaluated.

Y_2O_3 contained unresolved damage after irradiation at 650K, a mixture of unresolved damage and small dislocation loops at 875K, and larger loops at 1025K (Fig. 6). The defect structure of Y_2O_3-10% ZrO_2 at both 875 and 1025K was primarily a fine dispersion of unresolved damage (Fig. 7). Small "pores" (~30 Å dia.) can also be seen in Fig. 7; these were occasionally observed in both Y_2O_3 and Y_2O_3-10% ZrO_2, but were not common.

DISCUSSION

Al_2O_3 Samples

The usual interpretation of defect structures such as that shown in Fig. 5 is that irradiation has introduced pores into the material; however, their true nature in Al_2O_3 is difficult to determine. This is why the term "pores" has been put in quotation marks when referring to these defects. In irradiated metals, elevated-temperature swelling is usually the result of condensation into pores* of excess vacancies remaining in the lattice after interstitial atoms are trapped or annihilated. In ceramics, the process of pore formation is not so simple; in order that a cavity be formed in the crystal, a near-stoichiometric ratio of cation and anion vacancies must aggregate.

Hobbs and Hughes[7] have pointed out that two other volumetric defects which resemble pores can occur in irradiated compounds; these are cation metal colloids and high-pressure anion gas bubbles. Colloids could result from migration and agglomeration of cation interstitials and anion vacancies, or simply from the aggregation of anion vacancies into a volume which then contains only cations. In the latter case the colloid might be thought of as an anion pore. High-pressure gas bubbles could result from aggregation of anion interstitials and cation vacancies or migration of cation vacancies into a volume, leaving only lattice anions.

*This term (without quotation marks) here includes voids (empty pores) and bubbles (pores containing impurity gases).

Fig. 5 "Pores" in AD 999x Al_2O_3 after Irradiation at 1025K to 4.1×10^{21} n/cm^2 (E_n>0.1 MeV). 200,000x.

Fig. 6 Dislocation Loops in Y_2O_3 after Irradiation at 1025K to 5.4×10^{21} n/cm^2 (E_n>0.1 MeV). 100,000x.

Fig. 7. Unresolved Damage and Small "Pores" in Y_2O_3-10% ZrO_2 after Irradiation at 1025K to 3.9×10^{21} n/cm^2 ($E_n > 0.1$ MeV). 150,000x.

(The latter defect is in a sense a cation pore.) A complete description of the formation of cation or anion aggregates must account for the behavior of all point defects (for example, in the case of colloid formation, anion interstitials). Models proposed by Hobbs and Hughes address these problems.[7]

It is difficult to distinguish pores, colloids, and high-pressure gas bubbles from one another by TEM, since their imaging characteristics are similar. In the case of oxygen gas bubbles, high lattice strains should cause diffraction effects around each defect.[7] Unfortunately, the "pores" seen in Al_2O_3 were too small to allow examination for these effects. The question of whether the defects are colloidal aluminum particles is presently being studied at our laboratory by evaluation of the Knight shift in nuclear magnetic resonance; results should indicate whether metallic aluminum is present in the irradiated samples.

Measurements of the size and density of agglomerated defects in Al_2O_3 specimens yielded swelling values in reasonable agreement with those obtained from bulk measurements, if the defects are assumed to be pores. However, TEM measurements can be subject to considerable error due to the often nonrepresentative nature of samples examined, and so this is not unambiguous proof that the defects are indeed pores. Estimates of swelling assuming the defects to be colloids or high-pressure gas bubbles cannot be made until the detailed nature and behavior of both aggregated and isolated point defects is specified. *

Pore lattices (i.e., geometric alignment of pores) have been reported in several BCC and FCC metals, and have been seen in one HCP metal.[9] The present studies are apparently the first to report aligned

*Lattice dilation is another possible source of the swelling observed. However, Roof and Ranken[8] measured x-ray dilation of the single-crystal Al_2O_3 studied here, and found that the observed macroscopic swelling could not be explained by this mechanism.

"pores" in a ceramic. Models have been proposed to explain pore lattices based on reduction of elastic energy,[10, 11, 12] presence of a pre-existing impurity lattice,[13] and crowdion motion along preferred crystallographic directions.[14] Since the validity of these theories even when applied to simple metals is not yet known, it does not seem fruitful to speculate at length as to their applicability to a more complex material such as Al_2O_3, where the aligned defects may in fact not even be pores. However, it is interesting to note that hexagonal crystals have a unique lattice direction (the c-axis), that pores in Al_2O_3 are aligned in only one direction (parallel to the c-axis), and that in HCP magnesium porosity is also one-dimensional.[9]

It has been predicted[15] that formation of a pore lattice should restrict further swelling. This is consistent with present results, since swelling increased between 650 and 875K, but not between 875 and 1025K. A high density of random pores can also restrict swelling, by serving as neutral sinks for both vacancies and interstitials.[15]

Another possible explanation for the lack of further swelling at 1025K is that the peak in the swelling-vs.-temperature curve had been exceeded at the highest temperature studied. For Al_2O_3, irradiation temperatures used here are 0.28 T_m, 0.38T_m, and 0.44 T_m. If the temperature range for swelling is the same for ceramics as that for metals (~0.3 to 0.5 T_m), this may explain the fact that "pores" were only seen after irradiation at the two higher temperatures, and that swelling was no greater at 1025K than at 875K.*

The swelling anisotropy observed in single-crystal Al_2O_3 is believed to have occurred in all Al_2O_3 samples, and to have been

*The assumption that swelling ranges for metals and ceramics are similar may not be valid. Preliminary results with Y_2O_3-stabilized ZrO_2 indicate that swelling is at a maximum near 0.30 T_m, and is near zero at 0.22 and 0.36 T_m.[2]

responsible for microcracking observed in polycrystalline Lucalox.[2] Elongation in the c-direction was strongly favored at 875K and 1025K, at which temperatures "pore" alignment in this direction was seen. However, even if the defects are cavities, it does not follow that c-axis pore alignment indicates c-axis swelling. It is the distribution of the atoms from the pores, and not the pores themselves, that dictates swelling direction. The swelling anisotropy observed here may be related to possible preferential movement of interstitial crowdions along certain crystallographic directions as predicted by the Foreman model[14] of pore lattice formation.

Y_2O_3-Based Samples

The defect content of the Y_2O_3-based ceramics is consistent with the observation that macroscopically the materials did not swell. "Porosity" (Fig. 7) was only rarely seen, and the principal defects present (unresolved damage and dislocation loops) were not found in high concentrations. It thus appears that at the temperatures and fluences studied, these ceramics are relatively resistant to permanent radiation damage. (Temperatures of 875K and 1025K correspond to 0.33 T_m and 0.38 T_m for Y_2O_3.)

Two possible explanations for this radiation resistance come to mind. First, Y_2O_3 has a defect structure, with only six of eight cube corners occupied by oxygen ions in each structure cell.[16] This structure may enhance vacancy/interstitial recombination or otherwise affect defect behavior in such a way that excess vacancy concentrations are avoided. Second, the interaction between point defects (vacancies and interstitials) and sinks such as dislocations may be similar, so that preferential removal of interstials from the lattice does not occur. In metals, such interactions are solely controlled by strain fields, and interstitials are usually more strongly attracted to sinks than are vacancies. In ceramics, however, an electrostatic term also contributes, so that it is

possible to postulate equal (or stronger) interaction forces for vacancies.

It is clear that the addition of 10% ZrO_2 to Y_2O_3 dramatically alters the behavior of irradiation-induced defects, since the size of defect aggregates differs greatly from that seen in unalloyed Y_2O_3 (compare Figs. 6 and 7). This behavior may be related to the fact that Yttralox should contain more intrinsic defects than does Y_2O_3, since stoichiometric defects would be expected to result when a ceramic with a cation/anion ratio of 1:2 is added to a ceramic in which the ratio is 2:3. This observation reinforces the suggestion that a defect ceramic may exhibit intrinsically high radiation resistance. Also, solid solutions, of which Yttralox is one, often exhibit better irradiation behavior than do their unalloyed counterparts.

Relevance of Results to Fusion Reactor Technology

Fission neutron irradiation studies of materials for fusion reactor applications are useful in two ways: relative performance of candidate materials in a neutron environment can be evaluated, and baseline information can be established for comparison with results obtained by other irradiation techniques. In considering the accuracy of simulation of a fusion reactor environment by use of fission neutrons, the following must be considered:

total damage energy deposited
rate effects
nature of displacement damage
DPA/gas atom ratio.

The average flux in the core of a fast fission reactor is usually roughly equal to or somewhat greater than that expected at the first wall of a fusion reactor. In the present study, the fluence achieved in the ceramics tested (which were irradiated for ~100 days) was ~5 x 10^{21}

n/cm^2; this is only about 70% of that expected in 100 days' first-wall exposure in a fusion reactor such as the Reference Theta-Pinch Reactor.[1] The reason for the relatively low fluence attained here is that flux is lower in Row 7 than in the core of EBR-II. In addition, the neutron spectrum for the samples tested is somewhat softer than that characteristic of the core location. Considering the fact that a fusion spectrum would cause somewhat more damage than does a core fission spectrum, the present study represents in terms of damage induced perhaps a month's fusion reactor exposure.

A proper damage simulation must take into account not only total damage level, but damage rate. The EBR-II irradiations described here were carried out under quasi-steady-state conditions, at a damage rate roughly a third of that expected at a fusion reactor first wall. The temperature correction for rate differences is in this case small.[17] However, where pulsed damage is to be simulated, differences in rate effects are magnified (e.g., by an additional factor of 100 in the case of the theta-pinch reactor, to account for a duty factor of 1%[1]), and temperature corrections may be significant. An added complication with pulsed damage is that one must take into account the "off" times when no damage is being produced. To properly account for cyclic damage it may be necessary to integrate a dose-rate correction function over that portion of the "off" time during which damage is being removed by annealing processes.

The question of the significance of differences in nature of displacement damage between fission neutrons and fusion neutrons has not been settled. Calculations have shown[18] that there are significant differences in spatial characteristics of defect production for the two cases. In experiments with copper, Mitchell et al.[19] found differences in defect content after irradiation with fission neutrons and 14 MeV neutrons. Kaminsky et al.[20] observed chunk sputtering from the latter particles,

a phenomenon not seen with fission neutrons. However, subsequent work by Thomas and Harling[21] failed to detect chunk sputtering. If details of displacement events differ significantly for fission and fusion neutrons, point defect content of irradiated materials would also be expected to differ. However, Bunch and Clinard[22] compared the nature of optically-active point defects in 14 MeV-neutron-irradiated sapphire with that induced by fission neutrons.[23] The results do not show major differences, other than the expected higher level of damage per neutron from the former particles. Further work is required to define differences in displacement damage in specific materials, and to relate these to changes in physical properties.

A major shortcoming of fission neutron studies is that impurities from neutron-induced transmutations are generated at a much higher rate with 14 MeV neutrons than with fission neutrons. Parkin and Goland have calculated[18] the ratio of spectrum-average normalized damage energy cross section to (n, α) cross-section for several neutron sources and target metals. It was shown that the ratio is 239 times higher for aluminum in Row 7 of EBR-II than for the same material at the first wall of a fusion reactor. Since gaseous transmutation products can enhance pore production, different swelling behavior in the two environments appears likely. Pre-injection of gases into samples before fission reactor irradiation may improve the simulation, but possible differences between impurities injected in this manner and those formed concurrently with lattice damage must be assessed. If ion bombardment techniques which properly simulate displacement damage are developed, concurrent injection of gaseous impurities with a second ion beam may prove to be the best method for simulation of fusion reactor radiation damage.

ACKNOWLEDGMENTS

The authors wish to thank the members of the Thermionic Reactor Project at LASL for their part in conducting this experiment, and D. Rohr for performing the transmission electron microscopy.

REFERENCES

1. An Engineering Design Study of a Reference Theta-Pinch Reactor (RTPR), LA-5336/ANL-8019 (March 1974).

2. Quarterly Report on the Space Electric Power R and D Program, LA-5113-PR (November 1972).

3. C. V. Weaver and W. A. Ranken, Proceedings of the Thermionic Conversion Specialists Conference, Framingham, Mass., p. 96, 1968; W. H. Reichelt, W. A. Ranken, C. V. Weaver, A. W. Blackstock, A. J. Patrick, and M. C. Chaney, Proceedings of the Thermionic Conversion Specialists Conference, Miami, Fla., p. 39, 1970.

4. Quarterly Report on the Space Electric Power R and D Program, LA-5021-PR (August 1972); also see Ref. 2.

5. R. S. Wilks, J. A. Desport, and J. A. G. Smith, J. Nucl. Mat. 24, 80 (1967); R. S. Wilks, Neutron-Induced Damage in α-Al_2O_3, BeO, and MgO, AERE-R-5543 (August 1967).

6. G. W. Keilholtz, R. E. Moore, and H. E. Robinson, Effects of Fast Neutrons on Polycrystalline Alumina and Other Electrical Insulators at Temperatures from 60° to 1230°C, ORNL-4678 (May 1971).

7. L. W. Hobbs and A. E. Hughes, talk presented at the Annual Meeting of the American Ceramic Society, Washington, D. C., May 1975.

8. R. B. Roof, Jr. and W. A. Ranken, J. Nucl. Mat. 55, 357 (1975).

9. A. Risbet and V. Levy, J. Nucl. Mat. 50, 116 (1974).

10. J. H. Evans, R. Bullough, and A. M. Stoneham, Proceedings of the International Conference on Radiation-Induced Voids in Metals, Albany, NY, p. 522, 1971.

11. A. M. Stoneham, J. of Physics (F) 1, 778 (1971).

12. V. K. Tewary and R. Bullough, J. of Physics (F) 2, L69 (1972).

13. J. H. Evans, Nature 229, 403 (1971).

14. A. J. E. Foreman, AERE Report 7135 (1972).

15. J. H. Evans, Rad. Effects 17, 69 (1973).

16. R. C. Anderson, High Temperature Oxides Part II, p. 1, Academic Press, New York, 1970.

17. R. Bullough and R. C. Perrin, as cited in Ref. 15.

18. D. M. Parkin and A. N. Goland, to be published in Radiation Effects.

19. J. B. Mitchell, C. M. Logan, and C. J. Echer, J. Nucl. Mat. 48, 139 (1973).

20. M. Kaminsky, J. H. Peavey, and S. D. Das, Phys. Rev. Letters 32, 599 (1974).

21. M. T. Thomas and O. Harling, talk presented at the American Vacuum Society National Symposium, Anaheim, CA, October 1974.

22. J. M. Bunch and F. W. Clinard, Jr., J. Amer. Ceram. Soc. 57, 279 (1974).

23. P. W. Levy, Phys. Rev. 123, [4], 1226 (1961).

HIGH ENERGY PROTON SIMULATION OF 14-MeV NEUTRON DAMAGE IN Al_2O_3*

D. W. Muir

J. M. Bunch

University of California
Los Alamos Scientific Laboratory
Los Alamos, NM 87545

ABSTRACT

High-energy protons are a potentially useful tool for simulating the radiation damage produced by 14-MeV neutrons in CTR materials. We describe here a comparison of calculations and measurements of the relative damage effectiveness of these two types of radiation in single-crystal Al_2O_3. The experiments make use of the prominent absorption band at 206 nm as an index to lattice damage, on the assumption that peak absorption is proportional to the concentration of lattice vacancies. The induced absorption is measured for incident proton energies ranging from 5 to 15 MeV and for 14-MeV neutrons. Recoil-energy spectra are calculated for elastic and inelastic scattering using published angular distributions. Recoil-energy spectra also are calculated for the secondary alpha particles and ^{12}C nuclei produced by (p, p'α) reactions on ^{16}O. The recoil spectra are converted to damage-energy spectra and then integrated to yield the damage-energy cross section at each proton energy and for 14 Me-V neutrons. A comparison of the calculations with experimental results suggests that damage energy, at least at high energies, is a reasonable criterion for estimating this type of radiation damage.

*Work performed under the auspices of USERDA.

INTRODUCTION

High energy protons are a potentially useful tool for simulating the radiation damage produced by 14-MeV neutrons in CTR materials. Logan[1] has described the application of this approach in niobium. We describe here theoretical and experimental investigations of the validity of such a simulation for a prototype low-Z refractory electrical insulator, Al_2O_3. The theory attempts to estimate pka spectra and damage energy cross sections using existing collision cross section data, and the experiments attempt to assess the quality of the simulation in terms of an easily accessible parameter, the optical absorption induced in damaged material.

EXPERIMENTS

The damage produced in the Al_2O_3 lattice was assumed proportional to the height of the prominent optical absorption band at 6.02 eV (203 nm). Although the specific defect responsible for this absorption has not been identified, it seems plausible by analogy with similar materials[2] that it is a primary damage center produced by lattice collisions. Consequently, the concentration of such defects (and the associated optical absorption density) should be related to the deposited "damage energy" as usually defined. Since the oscillator strength for the optical transition, which would facilitate calculation of absolute defect concentrations, is not known, the experimentally measured absorption coefficients for various proton energies, normalized for proton fluence, are compared directly with the same quantity for 14-MeV neutron irradiated material.

All the samples were of Linde uv grade sapphire* with c axis perpendicular to the surface. One set of 1-cm square by 0.1 cm thick

*Uv-grade sapphire window material, ≈99.999% pure, c axis perpendicular to bombarded surface, obtained from Crystal Products Div., Union Carbide Corp., San Diego, CA.

samples were irradiated at room temperature at the LLL rotating target intense neutron source.*[3] Fluences of the order of 10^{17} n/cm^2 were delivered intermittently during normal 8 hour shifts for a total exposure time of about 40 hours. The flux variation across the samples (~ ±30% across 1 cm) was roughly mapped by cutting the dosimetry foil into quarters and counting the pieces separately; the results agreed within experimental error with variations in optical density obtained by a similar mapping with an aperture in the Beckman DK-1 spectrophotometer, having roughly the same spatial resolution as that of the foil dosimeter technique. The measured optical density thus represents an average across the smallest usable aperture, and the corresponding neutron flux an average over the corresponding section of sample.

Another set of 1-cm square samples was mechanically ground and polished to thicknesses ranging from .01 to .02 cm, thin enough for protons of energies from 5 to 15 MeV to pass through without excessive energy loss. An analyzed beam from the LASL tandem Van de Graaff accelerator was defocussed to give a roughly Gaussian spread ~ 2 cm across. The central portion of the beam was selected by an aperature of area 1 cm^2 and passed into a Faraday cup in which was mounted the sample, attached to a copper heat sink with vacuum grease. A fluorescent quartz plate visible from outside the chamber could be rotated in place of the sample holder, as an aid to aiming and focussing the beam. Although no attempt was made to map precisely the beam current distribution, variations in optical density across the samples were comparable to those seen in the 14-MeV neutron irradiated samples. Thus the proton data also represent averages.

---

*ICT, Lawrence Livermore Laboratory.

The proton beam currents were chosen to give estimated dpa rates equal as nearly as possible to those obtained with the 14-MeV neutrons, in order to avoid confusion from possible rate effects. Because of practical limitations on access to the accelerator, actual proton dpa rates were somewhat larger than (as much as 3 times) the neutron rates. With this criterion proton beam currents were of the order of 0.1 $\mu A/cm^2$; the current tended to fluctuate during a run by ±50% or so. Proton fluences were measured with an integrating Coulombmeter.

The data are summarized in Table I, which gives the peak optical absorption coefficients in the 6.02 eV band for various sources, the corresponding fluences, and the absorption normalized for fluence. Also given are estimated proton energy losses, the implications of which are discussed in the section describing nuclear cross section data. The fluence data for 9 MeV are subject to considerable error; the Coulombmeter reading was inadvertently lost before being recorded, so the recorded datum represents a guess based on estimated average beam current.

Table 1. Optical Absorption vs. Particle Energy

Energy (MeV)		Fluence (cm^2)	Optical Abs. Coeff. (cm^{-1})	Ratio of Abs. to Fluence
In	Out			
5	2	6.75×10^{15}	24	3.6×10^{-15}
9	6	5.6×10^{16}*	55.8	1.0×10^{-15}
12	9.5	2.1×10^{16}	37	1.8×10^{-15}
15	13	2.1×10^{16}	30.5	1.5×10^{-15}
14 MeV	n	1×10^{17}	124**	1.24×10^{-15}

* Estimated

**This may have underestimated by ~30% because of spectrophotometer stray light.

Other data potentially useful for qualitative comparison of neutron and proton damage include (1) the details of the optical absorption spectrum, and (2) the thermal annealing spectrum. Absorption spectra from 14-MeV neutron, 15-MeV proton, and 5-MeV proton irradiated samples are shown in Fig. 1. The spectra are all similar to those reported by Levy[4] for fission neutron irradiated Al_2O_3. He analyzed his spectra in terms of superimposed Gaussian peaks. Although we have not subjected our data to the same kind of detailed analysis, it appears that our spectra have peaks at the same wavelengths as he reported. The differences in spectral shape can apparently be described in terms of differences in relative peak heights.

Isochronal step annealing data for samples heated in air are shown in Fig. 2. Again, the results appear generally similar to Levy's[5] for fission neutrons, with the absorption spectrum returning essentially to that of an unirradiated sample after the sample reaches ~ 600°C. However, there are small differences, which will be discussed later.

THEORY

It seems plausible that a high-energy proton should "look like" a neutron in its nuclear interactions, in terms of having similar reaction cross sections and producing a similar pka spectrum. We attempt here to determine how the accuracy of this statement depends on projectile energy, if indeed it is true for any energy. Given the nuclear cross sections, the pka spectrum can be calculated using simple kinematic considerations.[1] Although a considerable body of data exists for protons of various energies incident on ^{27}Al and ^{16}O targets, extensive smoothing and interpolation were necessary to get the data into useful form, as discussed.

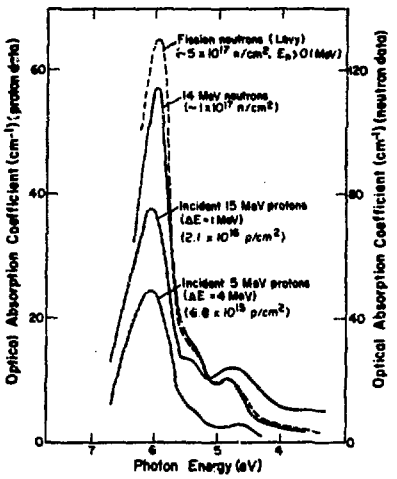

Fig. 1. Optical Absorption of Sapphire Irradiated and Measured at Room Temperature.

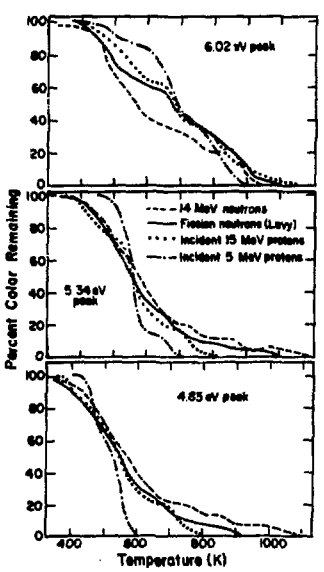

Fig. 2. Isochronal Annealing Curves for the Three Principal Absorption Peaks of Fig. 1.

Since the Al_2O_3 samples were thick enough to produce significant energy loss (2-3 MeV), calculations of the recoil spectra require estimates of nuclear cross sections over the entire proton energy range from 1.5 to 15 MeV. Both the energy dependence of the cross sections and the angle/energy distribution of the reaction products have been reviewed for oxygen (^{16}O) and aluminum (^{27}Al) target nuclei. The choice of nuclear cross section data for these nuclei is somewhat more complicated than it is for heavier nuclei (such as the structural metals). For example, the optical model, which is used extensively in Logan's analysis,[1] is not very useful for ^{16}O, because the cross sections fluctuate strongly with variations in the incident proton energy. In order to reproduce these fluctuations, one must evaluate the optical-model parameters at a large number of proton energies. Further, the optical model does not allow one to directly predict the partitioning of the total reaction cross section into the various possible nonelastic reactions. Thus, in the case of oxygen, we have chosen to obtain the needed cross section data directly from the available measurements. For aluminum, we have made some use of optical-model calculations.

For energies below 5 MeV, we have adopted the oxygen elastic scattering cross section measured by Harris et al.[6] Above 5 MeV, we have used the very extensive measurements of the oxygen elastic scattering cross section by Kobayashi.[7] For inelastic scattering below 10 MeV, we have used the data of Dangle et al,[8] while at higher energies the data of Kobayashi[7] and that of Daehnick[9] are employed. For the reaction $^{16}O(p,\alpha)^{13}N$, we have used the data of Dangle et al[8] up to 10 MeV and the data of Whitehead and Foster[10] at higher energies. Finally, the data for the reaction $^{16}O(p,p'\alpha)^{12}C$ is based on the measurement of Chapman and MacLeod[11] at 13 MeV. The energy dependence of the exitation function is assumed to be the

same as that for the analogous reaction $^{16}O(n,n'\alpha)^{12}C$, as evaluated by Young.[12] For all nonelastic reactions examined the angular distributions are found to be roughly isotropic in the center of mass system (i.e., to within a factor of two or so). For the sake of simplicity then, we have assumed complete isotropy for these reactions in all calculations presented here.

The aluminum elastic scattering data used in this study are taken from a wide variety of sources.[13-19] For the aluminum nonelastic reactions, we have taken a somewhat different approach than that taken for oxygen. This change of method results from the relatively larger number of reactions which are possible for aluminum at any given proton energy. Evaluating each reaction separately might have led to missing a significant fraction of the total nonelastic cross section. Instead, we have used a direct measurement[20] of the total nonelastic cross section at 10 MeV to normalize a theoretical curve based on the optical model.[21] With regard to the kinematics, we observe that the most important reactions have a small nuclear energy release, or Q-value. For example $Q(p,\alpha)$ is + 1.60 MeV, $Q(p,p')$ is -0.84 to -3.00 MeV for the dominant[22] levels, and $Q(p,n)$ is -5.59 MeV. Further, the majority of the reactions result in the emission of either a proton or a neutron. To a good approximation, then, the kinematics of these reactions is the same as elastic scattering. As in the case of oxygen, the angular distributions for the nonelastic reactions are approximated as isotropic.

The damage energy cross section, $\langle \sigma E \rangle_D$, is the quantity of primary interest for quantitative comparison with experiment. It is defined (and calculated) as follows:

$$\langle \sigma E \rangle_D = \int_{Ed}^{E_{max}} \eta(E_2) E_2 \frac{d\sigma}{dE_2} \, dE_2 \qquad (1)$$

where

E_d is the threshold energy for atom displacement from the lattice (or some other lower limit);

E_{max} is the maximum possible value of E_2;

E_2 is the energy of the scattered target atom;

$\frac{d\sigma}{dE_2}$ is the ion recoil spectrum; and

$\eta(E_2)$ is the "Lindhard efficiency factor"[23] which accounts for the partition of energy in the cascade between collisions and ionization.

Table 2 uses calculated values for $\langle \sigma E \rangle_D$ for both atomic species, using the experimental scattering data discussed earlier, down to scattered energies where the scattering can be described as pure Rutherford and then a theoretically derived Rutherford cross section down to the lower limit. The latter was taken to be 300 V, rather than a somewhat lower figure (say 30 V) appropriate for atomic displacements, on the grounds that the scattering is "screened" and consequently decreases rapidly with energy below approximately this limit. The value for $\langle \sigma E \rangle_D$ for 5 MeV incident protons is considerably in error, because the energy of the incident proton, and

Table 2. Proton Damage Effectiveness Relative to 14-MeV Neutrons

Proton Energy	Ratio, Experiment	Ratio, Theory
5	2.9	4.17
9	0.8*	2.38
12	1.4	1.78
15	1.2	1.33

*Subject to large error, as discussed above.

consequently the damage rate, is changing rapidly as the proton slows down. The qualitative conclusions (see "discussion" below) are not altered by the approximations used in deriving the average value given.

It is worth noting here that the contribution to $\langle \sigma E \rangle_D$ of the "non Rutherford" scattering is relatively negligible for 5 MeV incident protons, but comprises about half the total for 15 MeV. The contribution of the various nuclear reactions to the pka spectra for 15 MeV protons are shown in Fig. 3.

A composite $\langle \sigma E \rangle_D$ was calculated for the Al_2O_3 lattice by multiplying the values for the respective species by their atomic fractions. The damage produced in the 14-MeV neutron irradiation was calculated by D. M. Parkin, using the computer program DON.[23] The neutron interaction data used in this calculation were taken from the ENDF/B evaluations for ^{16}O (Ref. 24) and ^{27}Al (Ref. 25). This program computes the pka spectrum and then converts it to a damage-energy cross section using the "Lindhard efficiency factor" discussed above.

The experimental ratio of the values of $\langle \sigma E \rangle_D$ for various proton energies to that for 14-MeV neutrons is also given in Table 2.

DISCUSSION

The comparative damage effectiveness of 15 MeV protons and 14 MeV neutrons is close to 1 both experimentally and theoretically, whereas the agreement is less good at lower energies. The agreement at 15 MeV must be regarded as partially fortuitous, since both numbers were subject to errors estimated to be as large as the observed difference. Also, the thermal annealing spectra and optical absorption spectra as compared with those for 14 MeV neutrons (Figs. 1 and 2) are more similar for protons of 15 MeV than 5 MeV. These effects can be explained qualitatively by observing that the pka

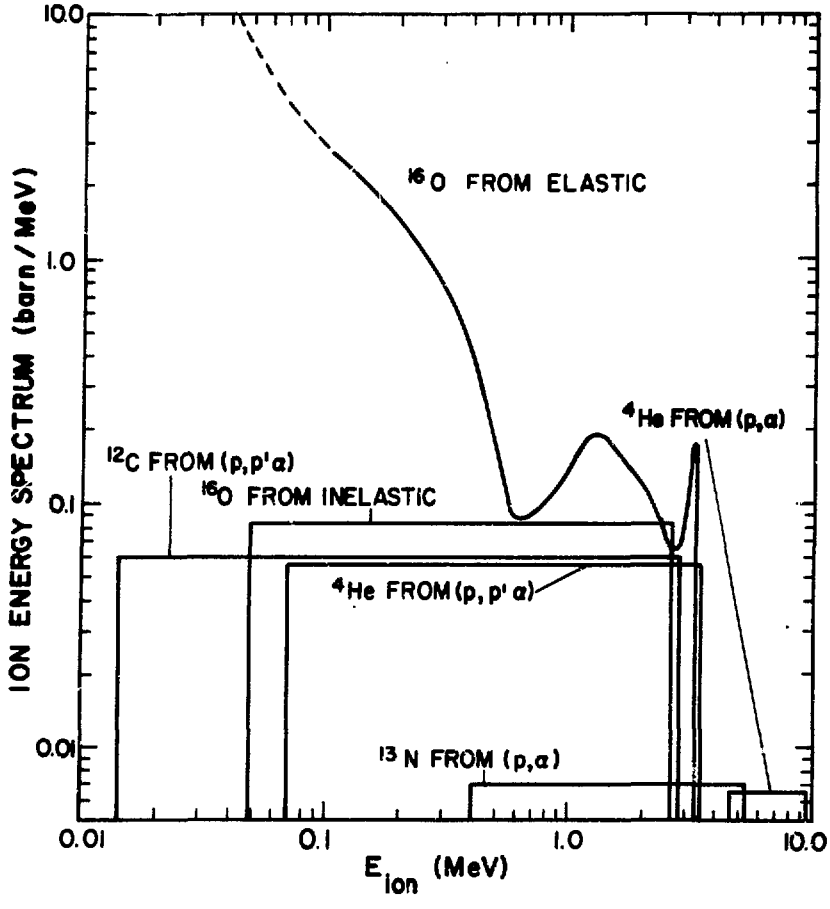

Fig. 3. Recoil Energy Spectra of Various Species due to 15-MeV Proton Reactions on ^{16}O.

spectrum becomes "harder" for the higher incident proton energies. For example, a considerable improvement in the agreement between theory and experiment is obtained if one assumes that primary knock-ons with energy less than 10 keV produce no permanent damage.

The evidence suggests that 15-MeV protons provide a "good" simulation of the damage produced by 14-MeV neutrons, in this material, for the low damage levels investigated.

The main obstacle to the practical use of the technique for materials studies is the low intensity of available proton beams. Although damage rates better than with existing 14-MeV neutron sources are easily available, rates high enough for accelerated material testing at rates 10 times those predicted for reactors (especially for pulsed machines with 1% duty cycle) are not. Even if higher proton fluxes were easily available, heat disposal would present problems, since electronic losses are about 1000 times collisional losses.

REFERENCES

1. C. M. Logan, "Proton Simulation of Displacement Effects Induced in Metals by 14 MeV Neutrons," UCRL-51224, June 14, 1972.

2. A. J. Tench and M. J. Duck, "Radiation Damage in Oxides: I. Defect Formation in MgO," J. Phys. C: Solid State Phys. 6, 1134-48 (1973).

3. P. Booth and H. H. Barshall, "Tritium Target for Intense Neutron Source," Nucl. Instrum. Methods 99, 1-4 (1972).

4. P. W. Levy, "Color Centers and Radiation Induced Defects in Al_2O_3," Phys. Rev. 123, 1226-33 (1961).

5. P. W. Levy, "Annealing of Defects and Color Centers in Unirradiated and Reactor-Irradiated Al_2O_3," Discuss. Faraday Soc. 31, 118-29 (1961).

6. R. W. Harris, G. C. Phillips, and C. Miller Jones, "Phase Shift Analysis of the Elastic Scattering of Protons from Oxygen," Nucl. Phys. 38, 259 (1962).

7. S. Kobayashi, "Elastic and Inelastic Scattering of Protons by Oxygen in the Energy Region of 6.9 to 15.6 MeV," J. Phys. Soc. Japan 15, 1164 (1960).

8. R. L. Dangle, L. D. Oppliger, and G. Hardie, "$^{16}O(p,\alpha)^{13}N$ and $^{16}O(p,p')^{16}O^*$ Differential Cross Sections," Phys. Rev. 133, B647 (1963).

9. W. W. Daehnick, "Elastic and Inelastic Scattering of 13- to 19-MeV Protons by ^{16}O," Phys. Rev. 135, B1168 (1964).

10. A. B. Whitehead and J. S. Foster, "Activation Cross Sections for $^{12}C(p,pn)^{11}C$, $^{16}O(p,\alpha)^{13}N$, and $^{19}F(p,pn)^{18}F$," Can. J. Phys. 36, 1276 (1958).

11. R. Chapman and A. M. MacLeod, "Proton Nuclear Reaction Cross Sections in Oxygen and Neon at 13 MeV," Nucl. Phys. A94, 313 (1967).

12. P. G. Young, private communication.

13. M. K. Mehta, J. John, S. S. Kerekate, and A. S. Divatia, "Reactions Induced by 3.5- to 5.5-MeV Proton Bombardment of Aluminum," Nucl. Phys. 89, 22 (1966).

14. J. Saladin and P. Marmier, "Polarisations-und Streuexperimente mit 4 MeV Protonen," Helv. Phys. Acta, 33, 299 (1959).

15. R. V. Elliot and R. H. Spear, "Proton Scattering from ^{27}Al in the Energy Range from 3.5 to 11.3 MeV," Nucl. Phys. 84, 209 (1966).

16. W. F. Waldorf and N. S. Wall, "Elastic Scattering of 7.5 MeV Protons," Phys. Rev. 107, 1602 (1957).

17. N. M. Hintz, "Proton-Nucleus Elastic Scattering at 9.8 MeV," Phys. Rev. 106, 1201 (1957).

18. G. W. Greenlees, L. G. Kuo, and M. Petravic, "The Elastic Scattering of Protons by Carbon, Aluminum, Nickel, Copper, Zinc, Niobium, Silver and Gold," Proc. Roy. Soc. (London), A243, 206 (1959).

19. B. B. Kinsey and T. Stone, "Elastic Scattering of Protons at 31.5, 20 and 14.5 MeV," Phys. Rev. 103, 975 (1956).

20. B. D. Wilkins and G. Igo, "10-MeV Proton Reaction Cross Sections for Several Elements," Phys. Rev. 129, 2198 (1962).

21. G. S. Mani, M. A. Melkanoff, and I. Iori, "Proton Penetrabilities using an Optical Model Potential," Centre d'Etudes Nucleaires des Saclay report CEA-2379 (1963).

22. J. Kokame, "Inelastic Scattering of Protons from Several Light Odd-Even Nuclei in the Energy Range from 6.0 to 7.5 MeV," J. Phys. Soc. Japan 16, 2101 (1961).

23. D. M. Parkin and A. N. Goland, "A Computational Method for the Evaluation of Radiation Effects Produced by CTR-Related Neutron Spectra," Brookhaven National Laboratory report BNL-50434 (1974).

24. P. G. Young and D. G. Foster, "A Preliminary Evaluation of the Neutron and Photo-Production Cross Sections for Oxygen," Los Alamos Scientific Laboratory report LA-4780 (1974).

25. P. G. Young and D. G. Foster, "A Preliminary Evaluation of the Neutron and Photon-Production Cross Sections for Aluminum," Los Alamos Scientific Laboratory report La-4726 (1972).

THE EFFECTS OF IONIZING RADIATION ON ELECTRICAL PROPERTIES OF REFRACTORY INSULATORS

V. A. J. van Lint, Consultant
J. M. Bunch, Los Alamos Scientific Laboratory
T. M. Flanagan, IRT Corporation

ABSTRACT

The Los Alamos Reference Theta Pinch Reactor (RTPR) requires on the first wall an electrical insulator which will withstand transient high voltage at high temperature 10 sec after severe neutron and ionizing irradiation. Few measurements of electrical parameters for heavily disordered refractory insulators have been reported; we estimate whether breakdown strength or conductivity will be degraded by the irradiation. The approach treats separately short-term ionization effects (free and trapped electrons and holes) and long-term gross damage effects (transmutation products and various lattice defects). The following processes could produce unacceptable conduction across the first wall insulator: (a) delayed electronic conductivity 10 sec after the prompt ionization by bremsstrahlung; (b) prompt electronic conductivity from delayed ionization; (c) electronic breakdown; (d) electronic or ionic conductivity due to thermal motion in the disordered material, possibly leading to thermal breakdown. Worst-case calculations based on lower limits to recombination coefficients limit process (a) to $\sigma << 5 \times 10^{-14}$ mho/cm. Data on ionization-induced conductivity in insulators predict for process (b) $\sigma << 10^{-8}$ mho/cm. Electronic breakdown generally occurs at fields well above the 10^5 V/cm required for RTPR. Thermal breakdown is negligible due to the short voltage pulse. Ionic and electronic conduction must be studied theoretically and experimentally in the type of highly disordered materials that result from neutron irradiation of the first wall.

INTRODUCTION

Insulators for fusion reactors must tolerate considerable abuse. Among the most severe requirements are those imposed on the first-wall insulator of theta pinch reactors. The types of problems resulting from the imposition of severe ionization, thermal, and electrical stresses on such an insulator can be illustrated by using the specific example of

the first-wall insulator in the Reference Theta Pinch Reactor (RTPR). Since it is practically impossible to simulate realistically the insulator environment without first building the RTPR, it is particularly important to illustrate the extent to which knowledge from other research can be used to define and simplify the problem.

In the reference design of the RTPR[1], a 0.03-cm insulator must withstand 10^5 V/cm during a 10^{-7} sec imposion-heating pulse. Soon thereafter, it is exposed to an ionizing dose of $\sim 7 \times 10^7$ rad at a dose rate of 7×10^8 rad/sec during the 0.1-sec thermonuclear burn. It is also subjected to 9×10^{15} fast neutrons/cm^2 at the same time. During the exposure, it also undergoes a temperature excursion from $\sim$1000 to $\sim$1300°K. It does not have to retain any insulating properties during this exposure. However, 10 sec later, it must withstand the electrical stress of the implosion-heating pulse again. At that time, the residual ionization dose rate is probably down to $\sim 2 \times 10^4$ rad/sec.

A very important factor in the insulator's response is the degree to which its original structure may be rearranged by displacements and transmutations produced by the neutron exposure and radiolysis produced by the ionizing dose. The obvious effects on the structural integrity of the insulator will not be discussed in this paper. Instead, we will have to deal with the implications of this disorder for the important electrical properties.

Acceptable limits to the electrical conductivity of the RTPR insulator during impolsion-heating can be derived from various criteria. Since the thermal load on the insulator is already considerable, it would be desirable for the extra heating due to joule heating in the insulator to represent only a small increment. A 0.03-cm-thick layer of conductivity, σ, exposed to 10^5 V/cm for 10^{-7} sec undergoes energy deposition of $W = 10^3 \sigma$ J/cm^3. This corresponds to a 1% increment on the radiation and thermal load for $\sigma = 10^{-2}$ mho/cm. A slightly more severe criterion is that a negligible fraction of the electrical energy delivered to the implosion coil be consumed in the insulator. A value of $\sigma \leq 10^{-3}$ mho/cm appears satisfactory. Actually, it appears possible to assure a much smaller value, say $\sigma \leq 10^{-6}$ mho/cm, as long as certain conditions are met in the disordered insulator.

We consider the following six mechanisms by which insulator conductance could be excessive:

1. Ionization-induced conductivity due to the delayed ionizing dose rate.
2. Delayed conductivity due to thermal release of carriers (electrons and/or holes) 10 sec after the intense ionization pulse.
3. Enhanced electronic conductivity resulting from the high state of lattice disorder.
4. Enhanced ionic conductivity resulting from the high state of the lattice disorder.
5. Electrical breakdown by an electronic mechanism.
6. Electrical breakdown by a thermal mechanism.

It is important to appreciate the degree of lattice disorder that results from the neutron exposure alone. If the insulator were $A\ell_2O_3$, each pulse would produce $\sim 5 \times 10^{17}$ displaced atoms/cm^3, $\sim 3 \times 10^{13}$ He atoms/cm^3, $\sim 2 \times 10^{13}$ H atoms/cm^3, and $\sim 4 \times 10^{13}$ other transmutations/cm^3. Integrated over a year's operation at 0.1 pulse/sec, the impurities amount to a few parts per thousand, and the displacements amount to each atom being displaced on the average $\sim$30 times. Of course, operation at a temperature near 1000°K will ensure sufficient atomic diffusion that a considerable amount of annealing, including recrystallization, can take place. On the other hand, this same diffusion can lead to gas bubble formation which is very deleterious to both mechanical and electrical properties of the insulator.

We will now discuss in order each of the foregoing mechanisms, applying the knowledge that exists in an attempt to scale across the gaps that separate existing data from the RTPR insulator conditions.

IONIZATION-INDUCED CONDUCTIVITY DURING DELAYED IONIZATION

The immediate effect of exposure of an insulator to ionization radiation is the generation of electron-hole pairs at a rate proportional to the dose rate. A portion of the carrier pairs may undergo geminate recombination. The remainder, while they are free, contribute to the conductivity by an amount $\Delta\sigma$, where

$$\Delta\sigma = e_0 (n\mu_n + p\mu_p) ,$$

where n and p are the electron and hole densities and μ_n and μ_p their respective mobilities. Immobilization of these carriers can occur by a number of mechanisms, including:

1. Electron-hole recombination,
2. Trapping at defect sites,
3. Escape from the surface (e.g., into an electrode).

In practical insulators, the second process is the dominant effect. In this case, the electron and hole densities during irradiation at a dose rate $\dot{\gamma}$, which generates K free electron hole pairs per unit dose, are

$$n = K_\gamma \dot{\gamma} \lambda_{tn}/v_n \qquad p = K_\gamma \dot{\gamma} \lambda_{tp}/v_p ,$$

where v_n and v_p are the thermal velocities, and λ_{tn} and λ_{tp} are the mean free paths before trapping for electrons and holes, respectively. It is important to note that λ_{tn} and λ_{tp} may be functions of the accumulated radiation exposure. For example, λ_{tn} will tend to increase as defects serving as electron traps become occupied with electrons, and will tend to decrease as hole traps become occupied with holes, thereby becoming available for electron trapping (the second step in trap-assisted recombination). Therefore, during irradiation,

$$\Delta\sigma = e_0 K_\gamma \dot{\gamma} \left(\frac{\mu_n \lambda_{tn}}{v_n} + \frac{\mu_p \lambda_{tp}}{v_p} \right) .$$

Using the relationship

$$\mu = \frac{e_0}{m^*} \frac{\lambda_s}{v} ,$$

where m* is the effective mass and λ_s is the mean free path before scattering, and also

$$\frac{1}{2} m^* v^2 = k_0 T ,$$

we derive

$$\Delta\sigma = \frac{1}{2} e_0 K_\gamma \dot{\gamma} \left(\frac{e_0}{k_0 T} \right) \lambda_s \lambda_t = K_\sigma \dot{\gamma}$$

We can place a reasonable upper limit on this conductivity. At room temperature, $(e_0/k_0T) = 40\ V^{-1}$. If we assume no geminate recombination and that ∿13 eV is required per electron-hole pair in material of density 2 g/cm^3, then $K_\gamma \simeq 10^{13}$ cm^{-3}-rad^{-1}. At room temperature, phonon-induced scattering alone produces $\lambda_s \simeq 7 \times 10^{-7}$ cm. If we assume a very pure insulator with a trap density of 10^{16} cm^{-3} and a trap cross section of 10^{-15} cm^2, $\lambda_t = 0.1$ cm. In this case, $K_\sigma = 6 \times 10^{-13}$ mho-sec/rad-cm.

As expected by this formulation, insulators exhibit an ionization-induced conductivity proportional to dose rate^2. The magnitude of the proportionality constant, K_σ, decreases with increasing disorder in the insulator, as shown in Table 1, and K_σ can change to either smaller or higher values with accumulated dose[3,4].

We can establish another upper limit on the ionization-induced conductivity by assuming that the rate of carrier removal is at least as fast as the electron-hole recombination rate. In this limit,

$$n = p = \sqrt{K_\gamma \dot{\gamma}/\alpha}\ ,$$

where α is the electron-hole recombination coefficient. A reasonable estimate for α is deduced by the Debye relationship

$$\alpha = \mu \frac{e_0}{\epsilon}\ ,$$

where ϵ is the dielectric constant (assumed to be ∿5 x 10^{-13} F/cm). This effectively establishes the recombination rate by assigning each oppositely charged pair a capture radius at which the attractive potential equals k_0T.

In the RTPR application, high-temperature operation will decrease the term (e_0/k_0T) by a factor of 3, will decrease λ_s by enhancing phonon scattering, and will probably increase λ_t slightly by promptly depopulating shallow traps by thermal excitation. We can then derive estimates of the conductivity at $\dot{\gamma} = 2 \times 10^4$ rad/sec from various arguments:

1. From an upper limit based on electron-hole recombination only:

$$\sigma << 10^{-6}\ \text{mho/cm}\ .$$

2. From an upper limit based on pure insulators estimates of λ_t and λ_s:

$$\sigma << 10^{-8} \text{ mho/cm} .$$

3. From the largest K_σ observed in pure organic insulating crystals:

$$\sigma << 10^{-8} \text{ mho/cm} .$$

4. From K_σ typical of disordered materials,

$$\sigma \lesssim 10^{-12} \text{ mho/cm} .$$

For the RTPR application, even the first limit is satisfactory. For other applications, some of the other arguments may have to be applied. When none of these suffices, it may be necessary to measure K_σ on a highly disordered sample of the insulator material.

This argument does not apply to the contribution to the conductance of any gas bubbles in the insulator. Since the gas in the bubbles is likely to be a non-attaching species such as He, the electron and ion mean free path at low dose rates can be very long, leading to a high ionization-induced conductivity. In the case of He at a pressure of P atmospheres at temperature T°K, we can place an upper limit on the current, I amps, through a bubble of area A cm^2, and thickness a in cm, by assuming that all electrons and ions generated within the volume move to the walls:

$$I \simeq 10^{-8} \frac{P}{T} \dot{\gamma} A a .$$

For the RTPR application, if the entire insulator thickness of 0.03 cm were helium gas at 10 atm pressure and 1000°K, the apparent conductivity at $E = 10^5$ V/cm would be

$$\sigma = \frac{I}{A} / E = 3 \times 10^{-17} \dot{\gamma} .$$

This is also negligible.

DELAYED CONDUCTIVITY DUE TO THERMAL RELEASE OF CARRIERS

After the end of the exposure of an insulator to an ionization pulse, the insulator frequently exhibits a delayed conductivity. Its magnitude is much less than the conductivity during the pulse, but it may persist for a time varying with the insulator from fractions of a microsecond to many hours. Studies of relatively pure crystals, such as MgO, have concluded that the delayed conductivity is due to the thermal release of carriers from traps[4,5]. In this case, each component of the delayed conductivity (associated with a particular trap ionization energy E_i) depends approximately exponentially on time with a lifetime τ that varies with temperature, as

$$\alpha \propto \exp(-E_i/k_0T) \quad .$$

In MgO, such a dependence is observed[5] for a 1.2-eV trap extending over a factor of 10^7 in τ.

In irregular insulators, such as polymers, fitting delayed conductivity to exponential decays usually results in a spectrum of lifetimes. These do not obviously have an exponential dependence on 1/T, but such a dependence can be masked by the multitude of trap levels. Attempts to fit the decays to a hyperbolic dependence on time are also unsuccessful, because the fit works only over a limited range in conductivity[6]. Very recently, the roughly logarithmic dependence on time of the conductance across SiO_2 films grown thermally on silicon has been interpreted by attributing to the holes a very low mobility resulting from hopping with a range of jump distances. (Continuous-time random walk with electric field and planar boundaries[7]; CRTW model.)

Using a trap model with thermal excitation, we can again establish an upper limit on the ionization-induced conductivity at late times (e.g., 10 sec for RTPR). Assume that there exist N_t trap levels with ionization energy E_i and electron capture coefficient α_t. If the electron density is n, the rate of capture of electrons is $\alpha_t\ n\ N_t(1-f_T)$, where f_T is the fraction of the traps occupied by electrons. Detailed balance arguments also predict that the rate of thermal excitation from the trap level is $\alpha_t\ n_1\ N_t\ f_T$, where n_1 is the density of carriers in the conduction band

when the equilibrium Fermi level is at the trap (e.g., $f_{T_e} = 1.2$). With only this trap level, the electrons will continuously be thermally excited and retrapped and the delayed conductivity will be constant at a value determined by the initial dose and the trap ionization energy. This conductivity could be very large and very persistent. However, there exists at least one inescapable means whereby electrons are removed permanently from this cycle: recombination with the holes that were formed with the electrons during the ionization pulse. Whether these holes remain free to move or are trapped, the condition for net charge neutrality is that their density equals the density of free plus trapped electrons. Assuming the rate of recombination is slow compared to the rate of electron trapping, we can write the equations:

$$\alpha_t \, n \, N_t \, (1-f_T) = \alpha_t \, n_1 \, N_t \, f_T \, ,$$

$$\frac{d(f_T N_t + n)}{dt} = -\alpha_r \, n(f_T \, N_t \, n) \, ,$$

where α_r is the electron-hole recombination coefficient. The solution to these equations approaches, for late times when $f_T << 1$,

$$n \to 1/\alpha_r \, t \, .$$

This result is independent of the trap level density or energy. Effectively, if the electrons are all free, they recombine along the hyperbolic curve

$$\frac{1}{n} = \frac{1}{n_0} + \alpha_r \, t \, .$$

If they spend only a fraction, F, of their time out of the trap, the recombination rate is slowed by the factor F but the density of the electrons contributing to the conductivity is also only the fraction F of the total unrecombined electron density.

Therefore, we can assert that an upper limit to the conductivity at late times after an intense ionization pulse independent of dose and independent of trap spectrum is:

$$\Delta\sigma < e_0 \, \mu/\alpha_r \, t = \varepsilon/t \, .$$

For the RTPR first-wall insulator, t = 10 sec and we find $\Delta\sigma < 5 \times 10^{-14}$ mho/cm. This is clearly negligible.

The CTRW model[7] is more difficult to evaluate. Assuming that permanent trapping is not important, we have to compare the diffusion of carriers during a 10-sec waiting period with the possible drift during a 10^{-7}-sec period under a 10^5 V/cm electric field. Actually, the CTRW model predicts an effective mobility that decreases with time. We can again estimate an upper limit to the conductivity by assuming a constant mobility.

During the 10-sec recovery period, the $\sim 7 \times 10^{20}$ carriers/cm^3 formed during the burn can diffuse to the insulator walls. If diffusive loss is to be small, the diffusion constant, D, should be such that

$$\sqrt{Dt} = \sqrt{10D} \ll 0.03 \text{ cm}$$

or

$$D \ll 10^{-4} \text{ cm}^2/\text{sec} .$$

The Einstein relationship then predicts that

$$\mu \ll 4 \times 10^{-3} \text{ cm}^2/\text{V-sec} .$$

The conductivity is then

$$\sigma = e_0 n\mu \ll 1.6 \times 10^{-19} (7 \times 10^{20}) \; 4 \times 10^{-3} \ll 0.4 \text{ mho/cm} .$$

This limit is too large to be acceptable.

If diffusion is significant, the average density in the 0.03-cm layer after 10 sec will be

$$n = n_0 \exp[-DT/(0.03)^2] .$$

The conductivity is then

$$\sigma = \frac{e_0}{kT} D n_0 \exp[-Dt/(0.03)^2] .$$

This has a maximum value at t = 10 sec of

$$\sigma < 0.02 \text{ mho/cm} ,$$

which occurs at $D = 10^{-4}$ cm^2/sec. It is still too large.

The only recourse is to put a lower limit on the density of deep traps (too deep to be thermally ionized during the 10^{-7}-sec pulse), required to ensure that the conductivity is unacceptable. Assuming a conductivity of 10^{-4} mho/cm is acceptable and the worst-case D = 10^{-4} cm^2/sec, the free carrier density must be reduced by a factor of 2000 by trapping during a 10-sec period. Observing that D = 10^{-4} cm^2/sec implies an average jump frequency of 10^{11} sec^{-1}, we find that the untrapped carrier density will decrease by 8 e-foldings at a fractional deep-trap density of

$$\frac{N_{dt}}{N_a} = \frac{8}{10^{11}\ \text{sec}^{-1} \times 10\ \text{sec}} \approx 10^{-11} ,$$

where N_{dt} is the trap density and N_a is the total density of atoms. It is very unlikely that any pure insulator crystal exists with such a low deep-trap concentration, let alone a disordered one.

ELECTRONIC CONDUCTIVITY IN DISORDERED LATTICE

The electronic conductivity in non-crystalline materials has been described in recent literature[8]. The traditional theory of electronic conductivity in crystals is based on the band model of solids. Since the concept of long-range order was involved in the development of the band model, its direct application to highly disordered materials was questionable.

In a crystal possessing long-range order, some electronic wave functions extend over many lattice sites. There are a number of such wave functions with almost a continuum of energy levels. This is the basis for a band of allowed energy states. There is a direct connection between the degree of localization of the wave functions, the spread in energy of the associated energy states, and the effective mobility of the carriers. Localized wave functions imply a narrow band and low mobility. In the limiting case of an electron tightly bound to one atom, it is immobile and the corresponding energy level is discrete.

The model of carrier mobility undergoes a corresponding transition from the ordered to the disordered crystal. When the wave functions have

large extent, the mobility can be evaluated from the concept of a scattering mean free path. When the wave function is more localized, it is better described by a hopping process whereby the electron effectively tunnels from one lattice site to another.

It is observed experimentally that irregular (e.g., amorphous) materials can have good insulating properties (e.g., polymers, dielectric liquids), can have metallic conductivity (e.g., liquid mercury), or can behave as semiconductors (e.g., chalcogenide glasses). It appears on theoretical grounds that whether a material is conductive or insulating depends on the ratio U_0/J, where U_0 is a measure of the electrostatic potential fluctuations from one lattice site to the next, and J is the band width. J is also proportional to the overlap integral of the Hamiltonian multiplied by wave functions centered on adjacent lattice sites. When the wave functions are very localized, J is small and the material tends to be insulating.

It is apparent that the electronic conductivity in a disordered RTPR insulator at operating temperature will depend strongly on the specific material and its equilibrium state of disorder. On the average, the disorder tends to increase the interatomic spacing, which tends to decrease J. Similarly, disorder tends to increase the potential fluctuations, U_0. Both of these changes tend to drive the material toward the insulating state. However, these factors could easily be overcome by pseudo-chemical changes that might produce longer-range wave functions. For example, any changes of effective ion valence that would leave over a considerable density of metallic atoms could increase the overlap integral, J, enough to produce metallic conduction.

The important point of this argument is that the electronic conductivity of the RTPR insulator is strongly affected by its state of disorder. It is necessary but not sufficient for the insulator to have acceptable electrical properties in its undamaged state. It is very likely that an insulator can be selected whose electronic conductivity will not increase (will probably even decrease) as a result of radiation disordering.

IONIC CONDUCTIVITY IN DISORDERED LATTICE

As distinct from electronic conductivity, in which electronic charge (negative or positive) is moved from one lattice site to another, ionic conductivity is produced by the motion of a charged atom between lattice sites[9]. Since the atom is massive, its wave function is always localized and the process can be described in classical terms. Effectively, two conditions must be satisfied for the ion to move and contribute to the conductivity:

1. An adjacent site must be available (i.e., occupied by a vacancy.
2. Random thermal energy fluctuations must enable the ion to surmount the potential barrier (if any) between the site it occupies and the adjacent site.

As a result, in a pure crystal the ionic conductivity depends on temperature approximately as

$$\sigma \propto \exp[-(E_v + E_m)/k_0T] \ ,$$

where E_v is the energy to form a vacancy and E_m is the barrier height to overcome for vacancy motion. In heavily irradiated material, there is likely to be an adequate supply of vacancies due to irradiation and the conductivity will probably depend on

$$\sigma \propto \exp[-E_m/k_0T] \ .$$

This situation is also observed in alkali halides with divalent cationic impurities which probably produce an equal density of cation vacancies to maintain charge neutrality[9]. Furthermore, since the average density of heavily irradiated material is less than for pure material due to disorder, the activation energy for motion, E_m, is likely to be decreased by the damage (at least for those vacancies that find themselves in local strain fields due to displacement disorders).

The point of this discussion for the RTPR insulator is that relevant studies of ionic conductivity must be performed on materials in which at least the proper equilibrium concentration of vacancies is reproduced, and probably also requires a simulation of the effect of the strain fields associated with radiation-induced disorder. Experiments on ionic

conductivity in relatively pure materials (pure from the structural viewpoint) would placed only lower limits on the conductivity, and these limits could be many orders of magnitude less than the magnitude experienced under RTPR conditions.

ELECTRONIC BREAKDOWN

Electronic breakdown in an insulator is assumed to be the result of regenerative changes in the electron (and possibly hole) distribution functions, but does not require for its onset any change in the atom lattice. Of course, the eventual result may be a permanent, thermal-induced defect in the lattice.

Electronic breakdown requires[10]:

1. A supply of electrons (assuming electrons are more mobile than holes), and
2. A means whereby the motion of the electrons under an applied electric field increases the supply of electrons.

The supply of electrons can be within the bulk of the insulator or the cathode contact. In either case, they can be provided by normal thermal excitation (thermal equilibrium carrier concentration in bulk, thermionic emission from the cathode) or field emission (from shallow defect levels in the band gap or from the cathode).

The most obvious means of increasing the supply of electrons is by electron-impact ionization. When the electric field is sufficiently high, a small fraction of the electrons can gain enough energy to be able to produce a secondary electron-hole pair (or perhaps to ionize a defect level). Assuming that the resulting hole or ion is immobile, one direct consequence of the ionization is that the electric field between the hole and the cathode is increased, and between the hole and the anode is decreased. Therefore, the next electron is more likely to produce an ionization event closer to the cathode. If field emission from the cathode is the source of electrons, the emission rate will also be increased.

The available data on the thickness dependence of electronic breakdown appears to favor the combination of field emission from the cathode enhanced by the space charge from electron-impact ionization as the

dominant process for films of thickness between 10^{-5} and 10^{-1} cm. Recent data on 10^{-5}-cm films of SiO_2 on Si strongly support this view[11]. It should be noted that this mechanism implies a delay in achieving breakdown near threshold, since sufficient positive space charge is built up to enhance the cathode field.

The possible modification of this model for porous materials must be considered. If the electric field of 10^5 V/cm is impressed across a bubble, it will certainly create an avalanche in the gas and deliver high-energy electrons to the insulator wall. The bubble need only have dimensions of $\sim 10^{-4}$ cm for the electron to gain sufficient energy in the bubble to produce an ionization event on impact with the wall.

It is also important to note that breakdown rarely occurs uniformly over the area of a sample. Once the conditions for an instability are satisfied at one point on the sample, the current tends to focus on that point.

The relevance of this discussion to the RTPR insulator is that any porous structure of the irradiated insulator may have a significant effect on its breakdown field. The disordered nature of the solid is likely only to have a beneficial effect in shortening the electron mean free path in the solid, thereby decreasing its chances of gaining sufficient energy from the field to cause an ionization.

There is an alternative model of electronic breakdown depending on having a shallow band of immobile states[10]. It is important to avoid materials in which such a mechanism appears.

THERMAL BREAKDOWN

Thermal breakdown is an instability in which the energy deposition by current raises the lattice temperature, which in turn raises the energy deposition. Again, once the onset of the instability is achieved at one point on the surface, there may be a tendency for the current to become filamentary.

High temperatures tend to promote thermal breakdown because the ionic conductivity is exponentially dependent on temperature. Short pulses make thermal breakdown less important since the temperature rise depends on the produce of energy deposition and time.

It is reasonably clear that the limitations discussed in the Introduction (i.e., temperature rise $\lesssim 3°K$ at operating temperatures near 1000°K) should make thermal breakdown a negligible phenomenon for the RTPR insulator. This is a direct consequence on the short voltage pulse and occurs in spite of the high operating temperature. This also implies that dc or long-pulse breakdown data are irrelevant for the RTPR insulator, since at these temperatures such data are dominated by thermal breakdown.

CONCLUSIONS

The potential problems with the electrical characteristic of irradiated insulators in fusion reactors, such as the RTPR, can be evaluated by using data and theories derived from a variety of disciplines including transient ionization effects, photoconductivity, amorphous semiconductors, alkali halides, etc. It appears that ionization-induced conductivity will not be a problem with the RTPR first-wall insulator. As long as the chemical species are chosen to avoid a general valence change upon irradiation and gas bubble fomration is minimized, electronic conductivity and electronic breakdown will probably be acceptable even after irradiation disordering. Thermal breakdown is never expected to be a problem due to the short applied voltage pulse. Ionic conductivity represents a major uncertainty. It is clear that it will be augmented by vacancy introduction during irradiation. Relevant studies of this phenomenon must address the highly disordered material resulting from the equilibrium between radiation disordering and high-temperature annealing.

Table 1

RADIATION-INDUCED CONDUCTIVITY IN SELECTED INSULATORS

Class	Material	T (°C)	$k = \sigma/\dot{Y}$ $\frac{mho/cm}{rad/sec}$	Ref.
Crystalline Inorganic	Al_2O_3 (sapphire)	25	7×10^{-14}	3
	MgO	25	5×10^{-15}	2,4
		800	8×10^{-15}	
	SiO_2	25	2×10^{-16}	12
Polycrystalline Inorganic	SiO_2 (Suprasil)	25	6×10^{-14}	13
	SiO_2 (std. grade)	25	2×10^{-16}	12
	Al_2O_3 (Lucalox)	25	6×10^{-17}	12
	Glass (Corning 0211)	25	1×10^{-17}	12
	$BaTiO_3$ (ceramic)	25	1×10^{-18}	18
Organic Polymer	PTFE (Teflon)	25	2×10^{-18}	14-16
		70	5×10^{-18}	
	H-film	25	4×10^{-19}	14
	Mylar	25	6×10^{-19}	12

REFERENCES

1. "An Engineering Design Study of a Reference Theta-Pinch Reactor, RTPR," LA-5336/ANL-8019, March 1974.

2. V. A. J. van Lint, J. W. Harrity, and T. M. Flanagan, "Scaling Laws for Ionization Effects in Insulators," IEEE Trans. Nucl. Sci. NS-15, No. 6, 194 (1968).

3. J. W. Harrity, "Range of Secondary Electrons in Sapphire," IEEE Trans. Nucl. Sci. NS-17, No. 6, 200 (1970).

4. V. A. J. van Lint and T. M. Flanagan, "Ionization-Induced Conductivity in MgO," Proc. International Conf. on Solid-State Physics Research with Accelerators, Upton, NY, September 25-28, 1967, p. 420 (1968).

5. R. A. Shatar, J. F. Marshall, and M. A. Pomerantz, "Post-Bombardment Conductivity in MgO Crystals," Phys. Rev. 109, 1953 (1958).

6. D. M. J. Compton, G. T. Cheney, and R. A. Poll, J. Appl. Phys. 36, 2434 (1965).

7. H. E. Boesch Jr., F. B. McLean, G. A. Ausman Jr., and J. M. McGarrity, "Charge Relaxation in Irradiated MOS Capacitors," IEEE Trans. Nucl. Sci. NS-22, No. 6 (1975) (to be published).

8. N. F. Mott and E. A. Davis, Electronic Processes in Non-Crystalline Materials, Clarendon Press, Oxford (1971).

9. J. J. O'Dwyer, The Theory of Electrical Conduction and Breakdown in Solid Dielectrics, Clarendon Press, Oxford (1973).

10. H. Fröhlich, Proc. Roy. Soc. A188, 521 (1947).

11. D. Y. Yang, W. C. Johnson, and M. A. Lampert, "A Slow, High-Field Instability in Si-SiO_2-Al Capacitor Structures" (to be published).

12. J. W. Harrity, "Radiation Effects in Dielectric Materials," Final Report on DA 28-043 AMC-2446(E), ECOM report ECOM-02446-F, February 1969.

13. R. C. Hughes, "Transient X-Ray-Induced Conductivity in Single-Crystal and Fused Quartz," Proc. 27th Annual Symp. Frequency Control, June 1973, p. 128.

14. W. H. Sullivan and R. L. Ewing, "A Method for the Routine Measurement of Dielectric Photoconductivity," IEEE Trans. Nucl. Sci. NS-18, December 1971, p. 310.

15. T. M. Flanagan and J. W. Harrity, "Study of Effects of Ionizing Radiation in Capacitors," Final Report on contract DASA-01-C-0014, April 20, 1970.

16. R. H. Bartlett, G. A. Fulk, and R. C. Weingart, "Temperature Dependence of X-Ray-Induced Photoconductivity in Kapton and Teflon," to be published in IEEE Trans. Nucl. Sci., December 1975.

AUTHOR INDEX